

HAVSNÄS – PILOT PROJECT REPORT ON COLD CLIMATE AND HIGH HUB HEIGHT

Project Team/Authors: Alan Derrick, Nicola Atkinson, Iain Campbell, Alex Clerc, Jennifer Cronin, Alice Ely, Simon Feeney, Gail Hutton, Marine Lannic, Malcolm MacDonald, Alastair Oram

Renewable Energy Systems Ltd/NV Nordisk Vindkraft AB

GLOSSARY

PP - Power performance
SA - Site assessment
ABL - Atmospheric boundary layer
RS - Remote sensing
AEP - Annual energy production
ASL - Above sea level
AGL - Above ground level

Sammanfattning

Den Svenska regeringen har som mål att minska kostnaderna för elproduktion av vindkraft. Det finns även ett identifierat behov av särskilda åtgärder för att öka kunskapsbasen, innan denna expansion kan fortsätta. Målet med dessa åtgärder är ett samarbete mellan stat och näringsliv, i syfte att underlätta projektutveckling av vindkraft och samtidigt bidra med kunskap till framtida projekt.

Vindmätningar och vindmodellering av Havsnäs vindkraftspark har pågått sedan en identifiering av området som en potentiell vindkraftspark gjordes 2003, fram till byggstart under 2008. Nu i sin operativa fas, har teknisk forskning genomförts utifrån ett omfattande vindmätningssystem, utplacerat i området såväl före som efter byggnation, samt med driftdata från våra mätstationer i vindkraftsparken.

Detta arbete har utförts som ett pilotprojekt med stöd och bidrag från den Svenska Energimyndigheten, med syfte att bidra till att undanröja hinder för framtida storskalig landbaserad vindkraftsutveckling i norra Sverige. Denna rapport beskriver forskningen i dessa kunskapsområden med inverkan av höga navhöjder och kallt klimat.

Högkvalitativa vindmätningar är nyckeln till korrekt projektering, energibedömning, utformning samt optimering av vindkraftsparksparker. Den stora geografiska omfattningen av Havsnäs och det utbredda nätverket av vindmätningssystem i området har gjort detta till en idealisk plats för att validera metoder, modeller och verktyg kring energibedömningar.

Denna rapport innehåller rekommendationer om hur man bäst genomför mätningar och modeller, som sedan används i förutsägelser av energiutbytet. Rapporten ger värdefull kunskap om faktorer som påverkar avvägningen mellan kostnaden för mätningarna och den osäkerhet, fördelar och minskning som kan förväntas.

En viktig slutsats är att branschstandarder kring vindskjuvningsmodeller kan vara tillräckligt noggranna för att extrapolera vindar i de mer praktiska, måttligt höga mastmätningar som genomförs till de mycket höga navhöjderna som kan tillämpas nu och i framtiden, särskilt när masten används tillsammans med en fjärrstyrd avkänningsanordning för att validera extrapolering till högre höjder. Men extrapolering av vindklimatet från mätmastplats till turbinplats med hjälp av branschstandardens vindflödesmodeller är en av de största källorna till osäkerhet på ett vindkraftsområde med komplex terräng och ytråhet, särskilt där det finns stora säsongsmässiga variationer i klimat, vilket är typiskt för Havsnäs och norra Sverige i allmänhet. Detta stöder uppfattningen att budgetmätningar bättre kan användas för att driftsätta ett större antal kortare master med fjärrstyrda enheter över ett område än att spendera all budget på en eller två mycket höga master. Mer sofistikerade vindflödesmodeller (kopplade till CFD och mesoskalning) kan så småningom ge en mer exakt mätning med extrapolering av vindklimat över ett område, men är fortfarande mycket tidskrävande och dyrt att köra.

Slutligen, att förstå atmosfärens stabilitet och variationer över ett område i form av dygnstid och årstid är nyckeln till att optimera valet och användningen av mätningar och vindflödesmodeller. Dessutom är det bevisat att stabila variationer också påverkar vinden som varje turbin påverkas av genom sin rotor, vilket innebär att en mer komplex bedömning av effekten som produceras av varje turbin kan krävas, än vad som för närvarande representeras av en enkel effektkurva. Ekvivalent "rotorgenomsnittlig" vindhastighetsteknik som föreslås för att utveckla internationella standarder har utvärderats i denna forskning och är nyckeln till en mer omfattande förståelse av verkens elproduktion. Nyttan av denna nya vindhastighetsdefinition stärker valet att använda fjärranalys, eftersom detta är den enda ekonomiska teknik för att mäta vindflödet över hela rotorns höjd (i kombination med kortare mätmast navhöjder).

CONTENTS

1 INTRODUCTION.....	1
2 THE HAVSNÄS WIND FARM.....	2
2.1 <i>Location</i>	2
2.2 <i>Wind Farm Details</i>	2
3 TECHNICAL CHALLENGES OF THE SWEDISH CLIMATE	3
3.1 <i>Implications of High Hub Heights</i>	3
3.2 <i>Cold Climate</i>	4
4 THE PILOT PROJECT	5
5 TEST SITE INSTRUMENTATION	7
5.1 <i>Instrumentation Setup</i>	7
5.2 <i>Cold climate R&D system Power Supply</i>	16
5.3 <i>Data Quality Control</i>	17
5.3.1 <i>Identification of Bad Data Due to Icing</i>	17
5.3.2 <i>Wake Affected Sectors</i>	18
6 IMPLICATIONS OF HIGH HUB HEIGHTS	19
6.1 <i>Shear Extrapolation</i>	19
6.1.1 <i>Introduction</i>	19
6.1.2 <i>Shear Methodologies</i>	19
6.1.3 <i>Model Validity of One Point Theoretical Log Law</i>	20
6.1.4 <i>Model Validity of Alternative Shear Methodologies</i>	26
6.1.5 <i>Shear Methodology Validation Using Remote Sensing</i>	32
6.2 <i>Source and implications of high shear</i>	41
6.3 <i>Atmospheric Stability</i>	41
6.3.1 <i>Atmospheric Stability Background</i>	41
6.3.2 <i>Atmospheric Stability Data Treatment</i>	47
6.3.3 <i>Atmospheric Stability Measurement Results</i>	49
6.3.4 <i>Impact of atmospheric stability on shear Extrapolation</i>	55
6.3.5 <i>Recommendations for Future Campaigns</i>	62
6.4 <i>Effect of Shear on Available Energy</i>	63
6.4.1 <i>Introduction</i>	63
6.4.2 <i>Methodology</i>	63
6.4.3 <i>Justification</i>	66
6.4.4 <i>Results</i>	66
6.4.5 <i>Conclusions</i>	75
7 COLD CLIMATE ISSUES	76
7.1 <i>Mast Instrumentation Availability and Reliability</i>	76
7.1.1 <i>Mast Instrumentation Data Summary</i>	76
7.1.2 <i>Cup anemometer Availability Statistics</i>	76
7.1.3 <i>Wind Vane Availability Statistics</i>	79

7.1.4 Ultrasonic Anemometer Availability Statistics	80
7.1.5 Cup Anemometer Failures	81
7.1.6 Wind Vane Failures	81
7.1.7 Sonic Anemometer Failures	82
7.1.8 Mast Instrumentation Conclusions	83
7.2 LiDAR	84
7.2.1 Wiper replacement	84
7.2.2 LiDAR Reconfiguration	88
7.2.3 Using Remote Sensing for Climatic Conditions Reporting	93
7.3 INSTRUMENTATION RECOMMENDED PRACTICES	98
7.3.1 Mast Instrumentation Recommended Practices	98
7.3.2 Remote Sensing Recommended Practices	103
7.4 Energy Production Losses	108
7.4.1 LiDAR Measured IEC Equivalent Wind Speed	108
7.4.2 Downtime Linked To Icing	121
7.5 Health & Safety - Ice Throw Shutdown	127
7.6 Power Curve Measurement	139
7.6.1 Power Curve Measurement in Cold Climates	139
7.6.2 Practicality Of IEC Equivalent Wind Speed Method	173
7.6.3 Practicality Of IEC Cold Climate Annex	173
7.6.4 Uncertainty Implications Of Power Curve Measurement In Cold Climates	173
7.7 Wind Flow Modelling	177
7.7.1 Uncertainty Of Linearised Models In Cold Climates	177
7.7.2 Usefulness Of CFD And Mesoscales Models	183
7.7.3 Comparison of Linear and CFD Results	205
7.7.4 Annual Average Vs Seasonal Variation	206
8 DISCUSSION	207
9 RECOMMENDATIONS	210
10 FUTURE AREAS OF RESEARCH	212
11 REFERENCES	215
APPENDIX 2A - MAP SHOWING LOCATION OF HAVSNÄS	217
APPENDIX 5A - SITE LAYOUT DRAWINGS	218
APPENDIX 5B - AS BUILT MAST DRAWINGS	222
APPENDIX 7A - M6261 ICING PROGRESS, VECTOR A100L2 ANEMOMETER - PAINTED BLACK	225
APPENDIX 7B - M6282 ICING PROGRESS, VAISALA WAV252 HEATED WIND VANE	227
APPENDIX 7C - M6303 ICING PROGRESS, VECTOR W200P WIND VANE	228
APPENDIX 7D - CUP ANEMOMETER FAILURE PHOTOS	230

APPENDIX 7E - WIND VANE FAILURE PHOTOS	233
APPENDIX 7F - SONIC ANEMOMETER FAILURE PHOTOS	236
APPENDIX 7G - LIDAR DATA FILTERING CRITERIA	238
APPENDIX 7G - LIDAR DATA FILTERING CRITERIA	238
APPENDIX 7H - ACCEPTANCE TEST CRITERIA	239
APPENDIX 7I - AN EXAMINATION OF WINDCUBE TURBULENCE DATA	240
APPENDIX 7J - SENSITIVITY ANALYSIS OF THE ICE THROW MODEL.....	244
APPENDIX 7K - IEC61400-12-1_DRAFT EQUIVALENT WIND SPEED METHODOLOGY	253
APPENDIX 7L - TIME-SERIES COMPARISONS FOR 27 NOVEMBER 2011	255
APPENDIX 7M - TIME-SERIES COMPARISONS FOR 31 DECEMBER 2011	260
APPENDIX 7N - TIME-SERIES COMPARISONS FOR 16 JANUARY 2012	265
APPENDIX 7O - TIME-SERIES COMPARISONS FOR 17 FEBRUARY 2012	270
APPENDIX 7P - TIME-SERIES COMPARISONS FOR 20 FEBRUARY 2012.....	275
APPENDIX 7Q - TIME-SERIES COMPARISONS FOR 6 APRIL 2012	280
APPENDIX 7R - TIME-SERIES COMPARISONS FOR 19 APRIL 2012	285
APPENDIX 7S - TIME-SERIES COMPARISONS FOR 16 MAY 2012	290
APPENDIX 7T - TIME-SERIES COMPARISONS FOR 27 MAY 2012.....	295

1 INTRODUCTION

The Swedish Government is conducting an ambitious plan to reduce the cost of electricity generation from wind power. There is a need for special action to increase the knowledge base before the expansion can continue. The requirements include, amongst other things, a need for risk reduction measures and the creation of strategic actions for further technology and process developments with a resultant reduction of costs. The goal is cooperation between government and business with a view to facilitating other wind developments and to gain knowledge for future projects.

Havsnäs was the first, large onshore wind farm in Sweden. The project had the intention of facilitating future large scale wind farm developments through being a pilot project to stimulate developments in several key areas. The areas of most importance were the development of a project financing model based on creating a framework for legal, financial and technical due diligence and the dissemination of this knowledge to the wider market place; development of cold climate processes particularly in relation to construction and maintenance health and safety and development of the framework for connection to the national electrical grid.

Havsnäs wind farm site has been the subject of wind measurements and modelling since its identification as a potential wind farm site in 2003 until the start of construction in 2008. Now in its operational phase, technical research has been carried out based on comprehensive pre and post construction measurement systems deployed on the site in conjunction with actual operational performance data from the wind farm. This work is carried out with the support of a pilot project grant from the Swedish Energy Agency with an aim to help remove barriers to future large scale on shore wind farm development in northern Sweden.

This report describes research related to the topics; impact of high hub heights and cold climate.

2 THE HAVSNÄS WIND FARM

2.1 LOCATION

Havsnäs wind farm is located in Strömsund commune in the county of Jämtland. This is 110 km North of Östersund, Jämtland (240km West of Umeå) which is an area of national interest for wind power. A map indicating the location of Havsnäs can be seen in Figure 2A.1 in Appendix 2A.

Havsnäs is spread over three hills (Ritjelsberget, Ursåsen and Järvsandberget) occupying 20km x 10km at an elevation of 510m to 650m ASL^{3e}. The wind farm is surrounded by lakes, marshes and forest and the prevailing wind direction at Havsnäs is from the northwest, typical of Northern Sweden. The turbine layout at Havsnäs can be seen in Appendix 5A.

2.2 WIND FARM DETAILS

Havsnäs wind farm was developed, constructed and operated by NV Nordisk Vindkraft AB and comprises 48 Vestas V90 turbines at 95m hub height with an installed capacity of 95.4MW and a predicted annual energy production of 256GWh. The hub height of 95m was necessary to access sufficiently high wind speeds and to minimise the impact of turbulence and high wind shear on the turbine performance and loading. These conditions and hence hub height requirements are typical of all forested sites in the inland areas of northern Sweden and nowadays would represent a minimum viable hub height. Figure 2A.1 in Annex 2A shows the location of the wind farm and the turbine layout.

The pre-construction wind speed measurement campaign included four 50m masts and one 80m mast. Details of these masts are shown in Section 5.1. The prevailing wind directions are from the North West and South East.

Ten hub height (95m) masts were installed in the lead up to construction for the purpose of site calibration and PP testing at 5 turbine locations. The five masts located on the turbine positions were removed at the end of the site calibration to allow the turbines to be constructed. The five remaining masts located 2.5 rotor diameters from the test turbines remained in place for the PP tests. Three of these five remaining masts were subsequently heavily instrumented and supplied with mains power for instrument and boom heating as part of this pilot grant research project. The instrumentation on these masts is described in the instrumentation section. Refer to Annex 5A for maps showing the locations of all the masts.

In addition to the data detailed in the Section 5.1, SCADA data from October 2010 to September 2012 was also available from all 48 turbines.

3 TECHNICAL CHALLENGES OF THE SWEDISH CLIMATE

The Havsnäs wind farm is located in Northern Sweden where a severe, cold climate is experienced for a long period of the year and where consequently significant accumulations of ice form on structures. This makes the process of carrying out wind measurements at the site prospecting stage restrictive in terms of the height of temporary masts that can be deployed at reasonable cost and also limits the data capture rate during the more windy, winter months. Coupled with this, the extensive forestation in Sweden and the location of typical higher altitude sites far in-land results in a relatively low, highly sheared wind resource near the ground. This then requires the use of very high hub heights to capture more of the wind resource and to reduce the loading impact of severe shear and turbulence across the large, low wind speed turbine rotors. The consequence of this is that there is higher uncertainty in the wind resource and energy yield assessment on account of:

- The need to extrapolate from a reduced measurement height (50m-80m) to hub height (80 to 105m +).
- Seasonal variations in wind shear due to atmospheric stability variations and surface roughness changes (snow/no snow) which are not fully captured in the measurements due to instrument icing.
- Lack of knowledge of what shape the wind shear profile takes, especially in the most productive part of the rotor area above hub height.
- The use of simplified, industry standard wind flow models to extrapolate the wind speed distributions from the SA masts to the turbine locations around the site.
- Lack of knowledge of energy loss due to blade icing.
- Poor data capture due to icing.

There are also a number of challenges to overcome in installing and maintaining both wind turbines and measurement devices on site. Remoteness and adverse weather presents challenges for mast and RS measurement campaigns and health and safety on site must be considered i.e. ice throw risk.

More detail of the main research topics focussed on here are given in sections 3.1 and 3.2.

3.1 IMPLICATIONS OF HIGH HUB HEIGHTS

Increasing the turbine hub height based on measurements at 80m (or lower) to an actual hub height of 95m introduces uncertainty associated with the extrapolation of the wind regime. A common assumption is that for every 10m of height extrapolation, the wind speed uncertainty increases by 1% which typically means a 2% increase in energy production uncertainty. In the case of Havsnäs, there was a 3% increase in energy production uncertainty assigned which is worth about 3 million kronor per year.

With the addition of further instrumentation, the existing 95m meteorological masts at Havsnäs were used to investigate the assumptions surrounding extrapolation of wind climates from lower to higher heights.

3.2 COLD CLIMATE

The 95m meteorological masts dispersed across the site provided the opportunity to further investigate and verify the impact of cold climate on the models and methods used to estimate the energy production of the wind farm. Comprehensive instrumentation on these 95m masts allowed detailed investigation of the factors affecting the performance of the turbines adjacent to each mast and to validate new measurement and analysis techniques for deriving measured power curves as are now being proposed for inclusion in future versions of the IEC 61400 12-1 PP standard [1]. The robustness and appropriateness of different instrumentation for use in cold climates has also been assessed.

4 THE PILOT PROJECT

Havsnäs provides a unique opportunity to explore these issues in a cold climate environment. Specifically the network of 5 hub height (95m) reference masts installed for PP testing around the site offered a distributed network of tall masts that has been extensively instrumented at multiple heights to gather measurements over an extended period covering the winter period. More details of the instrumentation can be found in Section 5.1. The fact that the masts are located on an operational wind farm also made it possible to fully heat the instruments using mains power from the wind farm, aiming to achieve 100% availability of instruments through the important winter months.

The following specific tasks have been carried out:

- Design procurement and installation of a cold weather instrumentation set on 3 of the 5 masts (one system on each of the 3 hills) for wind shear measurement and validation.
- Design, procurement and installation of a stability measurement instrumentation set on 3 of the 5 masts (one on each hill) for validation of stability assumptions and model sensitivity investigations.
- Installation of a Leosphere WINDCUBE LiDAR V1 to allow measurement of the wind profile across the entire rotor disk height, to validate shear assumptions and to demonstrate whether such devices have a practical use (in conjunction with standard met masts) as a SA tool in a cold climate environment.
- Investigation of challenges faced in performing PP tests in cold climates
 - Documenting the experience, problems and solutions associated with implementing a PP test in a cold climate environment (making use of the extra, heated instrumentation installed under section 2.1 [1])
 - Implementing high wind shear power curve measurements (in conjunction with LiDAR shear profile measurements) and testing the shear and turbulence normalization procedures being developed by the IEC 61400 12-1 [1] working group (in which RES actively participates).
 - Testing the rotor area averaged power curve measurement procedure (which needs LiDAR data) being developed by the IEC 61400 12-1 [1] working group.
- Investigation of the impact of original met mast based shear assumptions on energy yield prediction by implementing:
 - Wind resource predictions derived from 95m unheated PP anemometers (missing winter data)
 - Wind resource predictions derived from new 95m heated anemometers (all year round data).
 - LiDAR and 95m mast shear measurements to validate original 50m mast based wind shear assumptions.
 - Use of LiDAR to measure the shear profile over the turbine rotor disk and to investigate the validity of the assumption of a power law profile over the entire rotor disk (based on various shear exponent calculations).

-
- Validation of wind flow models in high stability atmospheric conditions
 - Spatial extrapolation validation between 95m masts using the standard, RES linearised flow model (MS3DJH).
 - Investigation of uncertainty associated with MS3DJH linear wind flow models
 - Ventos/M Computational Fluid Dynamics (CFD) wind flow model validation.
 - Developing and validating the icing energy loss prediction techniques based on the observed performance of the 5 Havsnäs test turbines, climate data from the met masts and turbine SCADA data.
 - Modelling and observation of ice-throw from turbines and assessing health and safety implications.

5 TEST SITE INSTRUMENTATION

5.1 INSTRUMENTATION SETUP

Havsnäs Wind Farm has been subject to an extensive measurement campaign over the course of the project development, dating back to November 2003. This research has made use of many different meteorological masts and other measurement systems that have made up this campaign.

The measurement campaign started with the instrumentation of a telecom mast (M192) that is located 11km from the wind farm site. The availability of a constant power source at the telecom mast enabled heated instrumentation and booms to be used and a long term reference wind measurement to be built up. The off-site telecom mast is detailed in Table 5.1.1.

Note that all coordinates and orientations in this section are relative to the following coordinates system: Swedish Grid, RT90, 2.5 gon V. Magnetic to grid offsets have been applied for all direction data - the correction from Magnetic North to Grid North for the Havsnäs Wind Farm in the year 2011-2012 is +3.88°

Mast Name	Mast Coordinates		Anemometer Heights [m] (Boom Orientation) [°]	Wind Vane Heights (Boom Orientations)	Data Range	Instrument types
M192	1481109 E	7102575 N	60.00 (238°), 60.00 (118°)	60.00 (238°), 60.00 (118°)	2/12/2003 - Ongoing	1 x Vaisala WAA252 & 1 x Vector A100 L2-HE1 anemometers 2 x Vector W200P-HE2 Wind Vanes

Table 5.1.1: Off-site Instrumented Telecom Mast near Havsnäs wind Farm.

On site measurements also began in 2003 and the primary wind measurements during this phase took the form of several meteorological masts. These masts are referred to as site-assessment masts as their purpose is to provide a long term assessment of the wind resource on the site. These masts are detailed in Table 5.1.2.

As part of the contractual requirements of the Turbine Supply Agreement for the Havsnäs Wind farm, five test turbines underwent PP testing in accordance with the IEC 61400-12-1 (2005) standard [32]. This testing required the installation of 2 additional masts per test turbine, measuring up to hub height. Five of these masts were temporary masts which were removed prior to this campaign starting - they were located at the test turbine positions as given in Table 5.1.3.

The test turbine and reference mast locations are given in Table 5.1.3, and shown in the drawings Appendix 5A. The masts are 92m guyed lattice towers (with a special, IEC 61400-12-1 [32] compliant top boom for the primary anemometers extending the upper measurement

height to the turbine hub height), manufactured and installed by Wibe in August-September 2008. These masts are referred to as Site Calibration or PP masts.

The instrumentation set up on the Site Calibration reference masts is given in Table 5.1.4. Three of these reference masts were selected for additional instrumentation as part of the cold climate research project, namely M626, M628 and M6303.

The mast nomenclature is explained in Table 5.1.5.

Mast Name	Mast Coordinates		Anemometer Heights [m] (Boom Orientation) [°]	Wind Vane Heights (Boom Orientations)	Data Range	Instrument types
M190	1495920 E	7109137 N	49.8 (263), 49.6 (87), 30.00 (244)	48.5 (258) 47.0 (256)	9/11/2003 - 10/09/2008	3 x Vector A100 L2-HE1 Anemometer 2 x Vector W200P-HE1 Wind Vane
M231	1497395 E	7110421 N	51.02 (286), 50.87 (107), 36.02 (276)	48.72 (265), 47.17 (278)	12/10/2005 - 09/09/2008	3 x Vector A100 L2-HE1 Anemometer 2 x Vector W200P-HE1 Wind Vanes
M278	1492769 E	7103771 N	50.4 (223), 50.2 (40), 36.2 (206)	47.50 (203), 46.70 (223)	10/10/2005 - 18/05/2008	3 x Vector A100 L2-HE1 Anemometer 2 x Vector W200P Wind Vanes
M279	1498439 E	7103936 N	50.4 (262), 50.2 (81), 35.2 (224)	47.50 (249), 46.70 (221)	14/10/2005 - 19/08/2008	2 x Vector A100 L2-HE1 Anemometer 1 x Vector A100 R Anemometer 2 x Vector W200P-HE1 Wind Vanes
M386	1493177 E	7104489 N	80.1 (250), 76.21 (236), 50.0 (239), 35.0 (243)	80.10 (71), 74.71 (236)	24/10/2007 - 19/01/2008	4 x Vector A100L2 Anemometer 2 x Vector W200P Wind Vanes

Table 5.1.2: SA Masts on Havsnäs Wind Farm

Turbine Number	Turbine Mast Name	Reference Mast Name	Turbine/Turbine Mast Location		Reference Mast Location	
D2	M726	M626	1495131 E	7111692 N	1495313 E	7111828 N
E2	M727	M627	1492421 E	7103602 N	1492384 E	7105282 N
E5	M728	M628	1493014 E	7104317 N	1493168 E	7104485 N
F12	M729	M629	1498319 E	7104067 N	1498175 E	7104253 N
F15	M730	M630	1498280 E	7105282 N	1498123 E	7105282 N

Table 5.1.3: Site Calibration or PP Mast locations and numbers at Havsnäs Wind Farm

Mast Name	Anemometer Heights [m] (Boom Orientation) [°]	Wind Vane Heights (Boom Orientations)	Data Range	Instrument types
M626	96.0 (208), 96.0 (28), 89.1 (28), 40.0 (28)	92.6 (24), 92.1 (206), 90.5 (31)	10/09/2008 - 04/03/2010	1 x Risoe P2546A Anemometer 3 x Vector A100L2 Anemometer 2 x Vector W200P Wind Vanes
M627	96.0 (213), 96.0 (33), 89.1 (33), 40.0 (33)	92.6 (33), 92.1 (210), 90.5(31)	30/08/2008 - 04/03/2010	1 x Risoe P2546A Anemometer 3 x Vector A100L2 Anemometer 2 x Vector W200P Wind Vanes
M628	96.0 (211), 96.0 (31), 89.1 (44), 40.0(42)	92.6 (45), 92.1(223), 90.5 (46)	05/09/2008 - 04/03/2010	1 x Risoe P2546A Anemometer 3 x Vector A100L2 Anemometer 2 x Vector W200P Wind Vanes
M629	96.0 (201), 96.00 (21), 88.50 (21), 40.00 (21)	93.20 (21), 92.64 (201), 90.5 (21)	01/10/2008 - 04/03/2010	1 x Risoe P2546A Anemometer 3 x Vector A100L2 Anemometer 2 x Vector W200P Wind Vanes
M630	96.0 (201), 96.0 (21), 88.46 (33), 40.0 (34)	93.2 (31), 92.7 (213), 90.5 (33)	01/10/2008 - 04/03/2010	1 x Risoe P2546A Anemometer 3 x Vector A100L2 Anemometer 2 x Vector W200P Wind Vanes

Table 5.1.4 : Site Calibration Mast instrumentation at Havsnäs Wind Farm

Turbine	Original PP Instrumentation	Cold Climate R&D Instrumentation	Cold Climate R&D Data Range
D2	M626	M6261	16/09/2011 - 02/08/2012
E5	M628	M6282	17/11/2011 - 30/05/2012
F12	M630	M6303	17/11/2011 - 14/07/2012

Table 5.1.5: Mast/Instrumentation Nomenclature

It is important to understand that the additional instrumentation that was added to the reference masts as part of the cold climate research is installed on the same physical mast as the original PP instrumentation. So the reference numbers in columns 2 and 3 of Table 5.1.5 refer to different sets of instruments installed on the same mast. This is necessary as separate data loggers are used to measure and process data from each set of instruments.

Additionally, a Leosphere WindCube V1 LiDAR was deployed adjacent to M626/M6261 system. The LiDAR was deployed on a 2.5m platform to ensure it stayed above the snow level throughout the deployment. The deployment location relative to M626/M6261 is detailed in Figure 5.1.1 and the LiDAR set-up is given in Table 5.1.6.

Mast Name	LiDAR Coordinates		Measurement Heights [m]	Platform Height (m)	Data Range	Instrument types
M814	1495302 E	7111875 N	52.5, 67.5, 77.5, 87.5, 97.5, 107.5, 117.5, 127.5, 137.5, 142.5	2.5	16/09/2011 - 24/07/2012	3D wind speed and direction measured at each measurement height

Table 5.1.6: LiDAR location and measurement heights

M6261						
Instrument type	Identifier	Model	Serial number	Measurement Height	Boom Orientation (° - MAG)	Heated
Anemometer	A1	Vector A100L2	12719 - YUA	87.1m	25	No
Anemometer	A2	Vaisala WAA252	E50301	87.3m	205	Instrument and boom
Anemometer	A3	Vector A100L2	12707 - YTM	72.6m	25	No
Anemometer	A4	Vaisala WAA252	G13310	72.8m	205	Instrument and boom
Anemometer	A5	Vector A100L2	13094 – E458A	50.1m	25	No
Anemometer	A6	Vaisala WAA252	A04106	50.3m	205	Instrument and boom
Anemometer	A7	Vector A100L2	13090 – E454A	30.1m	25	No
Anemometer	A8	Vector A100L2	13088 – E452A	30.1m	205	No
Anemometer	A9	Vector A100L2	11193 – CMER	70.8m	205	No but painted black
Wind Vane	WV1	Vector W200P	55068	85.1m	25	No
Wind Vane	WV2	WAV252	E49504	85.3m	205	Instrument only
Wind Vane	WV3	Vector W200P	54341	70.6m	25	No
Wind Vane	WV5	Vector W200P	12120-01	48.1m	25	No
Wind Vane	WV6	WAV252	E50301	48.3m	205	Instrument only
Ultrasonic Anemometer	S1	Metek USA-1	0102122252	89.3m	267	Instrument and boom
Ultrasonic Anemometer	S2	Metek USA-1	0102122251	10m	267	Instrument only
Temperature Sensor	T1	Campbell Scientific 107 thermistor	23945/6	90.5m	N/A	No
Temperature Sensor	T2	Campbell Scientific 107 thermistor	21506/25	10m	N/A	No
Temperature Sensor	T3	Campbell Scientific 109 thermistor	N/A	-1m (buried in the ground)	N/A	No
Atmospheric Pressure Sensor	Pressure	Vaisala PTB101B	E5040007	8m	N/A	No
Pyranometer	GH Irr	Kipp & Zonen CMP11	091346	25m	185	Yes
Relative Humidity & Temperature Sensor	RH&T	Vaisala HMP11	X3410116	10m	N/A	No

Table 5.1.7: Mast M6261 Instrumentation

M6282						
Instrument type	Identifier	Model	Serial number	Measurement Height	Boom Orientation (° - MAG)	Heated
Anemometer	A1	Vector A100L2	12720 - YUB	87.1m	40	No
Anemometer	A2	Vaisala WAA252	E50302	87.3m	220	Instrument and boom
Anemometer	A3	Vector A100L2	6847 - SAI	72.6m	40	No
Anemometer	A4	Vaisala WAA252	E50204	72.8m	220	Instrument and boom
Anemometer	A5	Vector A100L2	13092 – E456A	50.1m	40	No
Anemometer	A6	Vaisala WAA252	E52021	50.3m	220	Instrument and boom
Wind Vane	WV1	Vector W200P	55204	85.1m	40	No
Wind Vane	WV2	WAV252	E49501	85.3m	220	Instrument only
Wind Vane	WV3	Vector W200P	9749/01	70.6m	40	No
Wind Vane	WV4	WAV252	D46107	70.8m	220	Instrument only
Wind Vane	WV5	Vector W200P	12114/01	48.1m	40	No
Wind Vane	WV6	WAV252	E49503	48.3m	220	Instrument only
Ultrasonic Anemometer	S1	Metek USA-1	0102122248	89.3m	280	Instrument and boom
Ultrasonic Anemometer	S2	Metek USA-1	0102122247	10m	280	Instrument only
Temperature Sensor	T1	Campbell Scientific 107 thermistor	23945/3	90.5m	N/A	No
Temperature Sensor	T2	Campbell Scientific 107 thermistor	22721/4	10m	N/A	No
Temperature Sensor	T3	Campbell Scientific 109 thermistor	N/A	-0.5m (buried in the ground)	N/A	No
Atmospheric Pressure Sensor	Pressure	Vaisala PTB101B	E5040010	9m	N/A	No
Pyranometer	GH Irr	Kipp & Zonen CMP11	091347	25m	180	Yes
Relative Humidity & Temperature Sensor	RH&T	Vaisala HMP11	X3410115	11m	N/A	No

Table 5.1.8: Mast M6282 Instrumentation

M6303						
Instrument type	Identifier	Model	Serial number	Measurement Height	Boom Orientation (° - MAG)	Heated
Anemometer	A1	Vector A100L2	13074 – E438A	87.1m	29	No
Anemometer	A2	Vaisala WAA252	F04510	87.3m	209	Instrument and boom
Anemometer	A3	Vector A100L2	12983 – E109A	72.6m	29	No
Anemometer	A4	Vaisala WAA252	E50205	72.8m	209	Instrument and boom
Anemometer	A5	Vector A100L2	13091 – E455A	50.1m	29	No
Anemometer	A6	Vaisala WAA252	E50203	50.3m	209	Instrument and boom
Wind Vane	WV1	Vector W200P	55079	85.1m	29	No
Wind Vane	WV2	WAV252	D46109	85.3m	209	Instrument only
Wind Vane	WV3	Vector W200P	10181/01	70.6m	29	No
Wind Vane	WV4	WAV252	D46110	70.8m	209	Instrument only
Wind Vane	WV5	Vector W200P	12669/01	48.1m	29	No
Wind Vane	WV6	WAV252	D46108	48.3m	209	Instrument only
Ultrasonic Anemometer	S1	Metek USA-1	0102122249	89.3m	269	Instrument and boom
Ultrasonic Anemometer	S2	Metek USA-1	0102122250	10m	269	Instrument only
Temperature Sensor	T1	Campbell Scientific 107 thermistor	23954/5	90.5m	N/A	No
Temperature Sensor	T2	Campbell Scientific 107 thermistor	23954/9	10m	N/A	No
Temperature Sensor	T3	Campbell Scientific 109 thermistor	N/A	-0.5m (buried in the ground)	N/A	No
Atmospheric Pressure Sensor	Pressure	Vaisala PTB101B	E5040011	8m	N/A	No
Pyranometer	GH Irr	Kipp & Zonen CMP11	091348	25m	173	Yes
Relative Humidity & Temperature Sensor	RH&T	Vaisala HMP11	X07200020	11m	N/A	No

Table 5.1.9: Mast M6303 Instrumentation

All systems are wired into separate CR3000 data loggers with the following serial numbers:

Mast	Data Logger Type	Serial No.	Logger Code
M6261	CR3000	3767	SWEalaM6261_V5.CR3
M6282	CR3000	6317	SWEalaM6282_V5.CR3
M6303	CR3000	4254	SWEalaM6303_V5.CR3

Table 5.1.10: Cold climate R&D Data Loggers

In addition to the instrumentation described in Tables 5.1.7-5.1.9, a Campbell Scientific CC640 Camera was installed on each cold climate R&D mast to provide a time line of ice build-up and melting. These were focussed on particular instruments and programmed to take photos every 30 minutes. In the case of M6261, an unheated anemometer was selected (A9), for M6282 a heated wind vane (WV4) and for M6303 an unheated wind vanes was selected (WV3). A selection of these images are shown in Appendices 7A-7C for M6261, M6282 and M6303 respectively.

5.2 COLD CLIMATE R&D SYSTEM POWER SUPPLY

The power supply for the cold weather instrumentation proved to be a significant challenge due to the remoteness and strict environmental regulations on the site. The high power requirements for the heated booms and instruments ruled out the use of renewable sources and instead the installations were powered directly from the Grid side of the turbine transformer (690V). The power was brought from the turbines to the base of the tower through armoured cable, which was required to be buried as per the site environmental rules. At the base of the tower a 690V/230V transformer was used to step the voltage down to a useable level.

The following voltages were then used (with AC/DC Rectifiers where appropriate) on the installation:

- 230VAC - Boom heaters
- 24VDC - Heated instruments, data loggers
- 12VDC - Unheated instruments

The disadvantage of this setup, as opposed to a stand-alone solution, is that we were dependent on the wind turbine auxiliary supply remaining connected to the grid throughout the installation. Wind turbines are occasionally disconnected from the grid during operation for a variety of reasons, such as maintenance and safety precautions, during which intervals no power was available to the heated instruments or booms. A small backup battery was present at each mast to ensure continued operation of the instrumentation and data loggers during short term disconnections, but these would also drop out during more long term losses of power. Power surges on re-energisation also occasionally caused circuit breakers in the instrumentation power supplies to trip, requiring manual investigation.

5.3 DATA QUALITY CONTROL

All data used in this report has been quality controlled in order that the most accurate and representative data are used for the analysis. In the first phase an instrumentation analyst looked at the data to ensure that all instruments, power supplies and data loggers are operational and no failures have occurred. The data was then looked over by a wind analyst for long term changes in instrument behaviour and sections of data that are thought to be erroneous or bad data values (e.g. -99 or NaN). Data is then removed that is flagged as having an error, either due to site conditions such as icing or through gradual degradations in instrument performance. Further details on identification of bad data due to icing can be found in Section 5.3.1.

Further data filters have been applied dependent upon the analysis taking place and are described in the relevant section for that analysis.

5.3.1 IDENTIFICATION OF BAD DATA DUE TO ICING

As part of the Havsnäs R&D campaign, in conjunction with other ongoing wind measurement campaigns in cold climate, RES have developed an automated algorithm for assisting with the quality checking of data and subsequent removal of any records that are thought to have been affected by ice build up on the instrument. Icing effects can be obvious and stark, such as times when the instrument is prevented from moving, or subtle and difficult to distinguish from measurement noise when motion is only partially restricted.

The icing algorithm relies on calculating the directional relationship between instruments when the temperature is above the freezing zone. This is called the ‘ice-free relationship’. This relationship is then compared to the difference between instrument readings when the temperature is in the icing region and any data that are outside an allowable margin from the ‘ice-free relationship’ are flagged as bad. The icing region is defined by the upper boundary of the expected icing zone. It is recommended that a value a little above freezing is used to account for thaw rates, lapse rate and temperature measurement error, say 5°C. It is preferable to use a heated instrument as a control for icing events, but this is not always possible due to the increased power requirements from heated instruments. It is also preferable to compare instruments at similar heights to minimise variations introduced by changing atmospheric stability and hence wind shear variations clouding the expected relationship.

The choice of the number of directional sectors is based upon the a balance between directional data coverage and resolution of the checks - the algorithm suggests the user starts with 5° bins but this can be increased or decreased as necessary. The standard deviation of the ratio (or difference) between instrument readings in each directional bin is calculated. A sensitivity is then defined as the allowable variation of the ice-region relationship from the ice-free normal directional mean, measured in multiples of the standard deviation in that bin. The sensitivity can again be defined by the user, but after multiple iterations it has been shown that a reliable indication of icing can be obtained when the anemometer ratio difference exceeded three times the ice-free standard deviation.

Mathematically the algorithm can be represented as:

For a given wind direction bin a bad data flag is created when:

$$|ratio_i - ratio_m| > \alpha \sigma$$

Where:

ratio_i = instantaneous ratio below 5°C

ratio_m	=	mean ice-free ratio (above 5°C)
α	=	the sensitivity (or standard deviation multiple) used
σ	=	the standard deviation of the ice-free mean ratio

The algorithm then uses a ‘buffer’ to aggregate individual icing events. For example, with a buffer of six hours, flagged icing events six hours apart will be taken to mark the start and end points of six-hour period of icing; i.e., this whole period will be flagged as icing. The buffer minimises false positives and stops natural random variation within icing events appearing to be a normal, non-iced observation. The length of buffer used at Havsnäs was 4 hours but it is recommended that this buffer be evaluated on a site by site basis, decided upon by evaluating an initial learning period of data.

One of two further sub-algorithms is also used:

- The overall weighted mean ice-free relationship is used to fill any direction bin-specific gaps in the directional ice-free relationship. This was the method used for Havsnäs.
- The overall weighted mean ice-free relationship is used in preference to a direction-specific ice-free relationship - this can offer an advantage when assessing patchy data.

The algorithm may not be suitable for very short data periods, or where the relationship between the two instruments in question is poorly defined.

It is recommended that this icing algorithm is run over all wind measurement data in cold climates and that flagged data be removed from the measurement database.

5.3.2 WAKE AFFECTED SECTORS

As the measurements were carried out on an operational wind farm, the meteorological masts and LiDAR measurements were affected by wind turbine wakes for certain wind directions. Table 5.3.1 shows the wake affected sectors at each measurement location where directional filtering has been used for some analysis in this report. Where directional filtering has been used this will be referred to in that particular analysis section. The wake affected sectors were evaluated according to the method defined in the IEC standard 61400 12-1 (2005) [32].

Mast	Waked Sector Start (°)	Waked Sector End (°)
M626	75	264
M628	122	263
M630	19	214
M814 (LiDAR)	85	297

Table 5.3.1: Wake Affected Sectors

6 IMPLICATIONS OF HIGH HUB HEIGHTS

6.1 SHEAR EXTRAPOLATION

6.1.1 INTRODUCTION

Wind speed is the chief economic driver for wind farm development. As SA masts are often necessarily shorter than turbine hub height, the ability to accurately extrapolate long-term wind speed predictions vertically is extremely important for determining project value and turbine suitability.

There are two main areas which affect how successfully wind speeds above the mast top can be determined: the ability of the model used to characterise the velocity profile and the assumption that this profile holds above the mast top to hub height.

This report aims to investigate these two areas by considering the performance of a variety of vertical wind speed extrapolation models and the relationship observed between the masts and LiDAR on the Havsnäs site.

6.1.2 SHEAR METHODOLOGIES

There are a number of different ways in which a shear exponent can be calculated to permit vertical extrapolations, each with their strengths and weaknesses. For the purposes of this analysis those assessed in the following sections are:

1. One-point theoretical log law

A single wind speed measurement is extrapolated vertically using only theoretical considerations. In practice this is performed using the logarithmic law which is strictly only applicable in flat homogenous terrain. To apply the log law, estimates are required of the surface roughness and displacement height. Both these parameters are normally assumed to be a fixed fraction of the canopy height. Application of such a method requires trust in one wind speed measurement.

2. Two-point power law

A power law exponent is fitted to two wind speed measurements at two different heights. The fitted exponent is then used in conjunction with a power law to extrapolate to the required height. Application of such a method requires trust in two wind speed measurements.

3. Multi-point fitted log law

If three or more measurements are available, then it is possible to fit a logarithmic profile to the data. The fitted profile is then used to predict the wind speed at the required height. In practice judgment must be used to determine whether or not this method is applicable. The correlation co-efficient of the fitted profile will indicate how well it matches the data. If more than three points are available then it may be considered appropriate to exclude one or more erroneous measurements. At the very least three good measurements must be available to apply this method.

Each of these methodologies can be used in conjunction with or without a forest canopy height correction. Using a canopy height, these methodologies would then be classed as *displaced*.

It is also possible, using each of these three methodologies, to calculate an *equivalent* shear exponent. Such a measure of shear is calculated for extrapolation of wind speeds between a specific measurement height and specific hub height. In essence, this is an equivalent non-displaced power law shear exponent which represents a velocity profile that intersects with the ‘true’ displaced wind speed at hub height. This is classed as a *revised* shear methodology and is very useful for comparing the results of the three shear methods on a like-for-like basis.

6.1.3 MODEL VALIDITY OF ONE POINT THEORETICAL LOG LAW

This section presents the results of a comparison between wind speed predictions carried out for the Havsnäs wind farm using SA meteorological masts (installed prior to turbine installation) and subsequent predictions carried out using power PP masts during turbine installation.

The SA masts used were approximately 50.0 m tall¹ tubular masts, somewhat shorter than the 96.0 m PP masts which measure close to hub height, necessitating the vertical extrapolation of long-term predicted site wind speeds.

Therefore, the aim of this analysis is to compare the wind speed predictions from the two types of mast in order to investigate the accuracy of the vertical wind speed extrapolation process.

Vertical extrapolation can be achieved by a variety of methods as described in Section 6.1.2. This analysis concentrates on arguably the least sophisticated, the displaced one point Theoretical Log Law, to establish a baseline uncertainty level for further comparisons of the two- and multi-point shear methods in Section 6.1.4.

DETAILS OF WIND MONITORING

This analysis uses data from nine masts: SA masts M231, M278 and M279; PP masts M626, M627, M628, M629 and M630; and off-site telecoms mast M192. Details of all instrumentation can be found in Section 5.1. The data periods used in this analysis is shown in Table 6.1.1.

Mast	Data Period Used
M192	2 December 2003 - 12 March 2010
M231	12 October 2005 - 17 October 2006
M278	10 October 2005 - 17 October 2006
M279	14 October 2005 - 17 October 2006
M626	10 September 2008 - 4 March 2010
M627	30 August 2008 - 4 March 2010
M628	5 September 2008 - 4 March 2010
M629	1 October 2008 - 4 March 2010
M630	1 October 2008 - 4 March 2010

Table 6.1.1: Wind Monitoring at Havsnäs

¹ These were the tallest, temporary ice-rated masts available in 2003 when measurements started on Havsnäs.

Long term predicted wind speeds have been calculated at each mast. At the SA masts the Vector anemometer mounted on the tower top configuration has been chosen as the primary anemometer. This is to allow fair comparison with the SA prediction (which used Vector instruments).

It should be noted that turbines had been erected at this site during the measurement period of the five PP masts. However, these turbines had not yet been energized so it is not expected that they will have had any significant effect on the PP mast wind speed prediction.

SITE ASSESSMENT MAST WIND SPEED PREDICTION METHODOLOGY

The SA masts' long-term predicted wind speeds have been obtained via a multi-step Measure-Correlate-Predict (MCP) methodology: measured site data at the fully heated, high availability telecoms mast, M192, were correlated with concurrent NCEP/NCAR geostrophic reanalysis reference data to effectively extend the record at M192. M192 was then used as the long-term reference to extend the record at the SA masts.

POWER PERFORMANCE MAST WIND SPEED PREDICTION METHODOLOGY

In order to predict the long-term estimate wind speed at each PP mast, the same multi-step MCP process was followed: the first step uses NCEP/NCAR data as a reference for telecoms mast SWEalaM192; the second step uses the telecoms mast as a reference for the PP masts.

COMPARISON MAST PAIRS

The long term wind speed predictions made at the SA masts and PP masts are compared in this analysis. Since the SA and PP masts are not co-located on site, comparison mast pairs have been selected to minimise their spatial separation, as detailed in Table 6.1.2.

PP Mast	Comparison SA Mast	Approximate distance between masts (km)
M626	M231	2.5
M627	M278	0.6
M628	M278	0.8
M629	M279	0.4
M630	M279	1.4

Table 6.1.2: SA - PP Comparison Mast

SHEAR EXTRAPOLATION TO HUB HEIGHT

The wind speed predictions for SA masts relate to a height above ground level of approximately 50.0 m and 96.0 m for PP masts. Therefore, there is a need to set a common height of comparison.

To achieve this, the long-term wind speed estimates at the SA masts will be extrapolated upwards over approximately 45.0 m using the favoured shear exponent measured at the mast (see Forest Canopy Shear Correction below) and then compared to the long-term estimates obtained at 96.0 m at the PP masts.

FOREST CANOPY SHEAR CORRECTION

In order to vertically extrapolate the long-term wind speed estimates obtained at the SA masts, a reliable shear exponent is needed for each of the masts.

However, as the site is forested, the apparent origin of the velocity profile will be displaced vertically towards the top of the forest canopy by an amount relating to the characteristics of the forest, such as its height and density, for example. It is therefore necessary to correct measured shear exponents by means of a displacement height to gain a more accurate estimate of the velocity profile at the mast position.

Table 6.1.3 shows these corrected “revised” shear exponents used for the vertical extrapolation of long-term wind speeds at each SA mast. The roughness length, which is an input to the one point theoretical Log Law, is assumed to be a fixed portion of the canopy height.

Mast	Anemometer Heights Utilised (m)	Top Anemometer Height (m)	Forest Canopy Height (m)	Minimum Anemometer Height (m)	Extrapolation Height (m)	Revised Shear Exponent	Calculation Method
M231	51.0	51.0	6.0	22.0	96.0	0.251	one-point theoretical log law method
M278	50.4	50.4	5.0	13.8	96.0	0.217	one-point theoretical log law method
M279	50.4	50.4	6.0	22.0	96.0	0.251	one-point theoretical log law method

Table 6.1.3: Revised Shear Exponents Details at Comparison SA Masts

RESULTS

Table 6.1.4 presents the long-term estimate wind speeds at 96.0 m from both the PP masts and their associated SA mast, along with information on measurement altitude and shear.

These results are also featured in Figure 6.1.1 below.

	M626	M627	M628	M629	M630
Base Elevation of PP Mast (m ASL)	521.0	508.0	517.0	518.0	514.0
Measurement Height of PP mast (m AGL)	96.0	96.0	96.0	96.0	96.0
Measurement Height of PP mast (m ASL)	617.0	604.0	613.0	614.0	610.0
Long-Term Estimate of PP Mast (m/s)	7.09	6.95	7.02	7.22	7.26
Long-Term Estimate of PP Mast uncertainty (m/s)	0.36	0.34	0.35	0.37	0.37
Comparison SA] Mast	M231	M278	M278	M279	M279
Base Elevation of Comparison SA Mast (m ASL)	609.0	515.0	515.0	509.0	509.0
Measurement Height of Comparison SA mast (m AGL)	51.0	50.4	50.4	50.4	50.4
Measurement Height of Comparison SA mast (m ASL)	660.0	565.4	565.4	559.4	559.4
Long-Term Estimate of Comparison Mast (m/s)	6.71	5.69	5.69	6.00	6.00
Revised Shear Exponent for Comparison SA Mast	0.251	0.217	0.217	0.251	0.251
Comparison SA Mast LTE Sheared Up to 96 m AGL (m/s)	7.86	6.55	6.55	7.06	7.06

Table 6.1.4: Comparison of Wind Speed Predictions at 96.0 m AGL

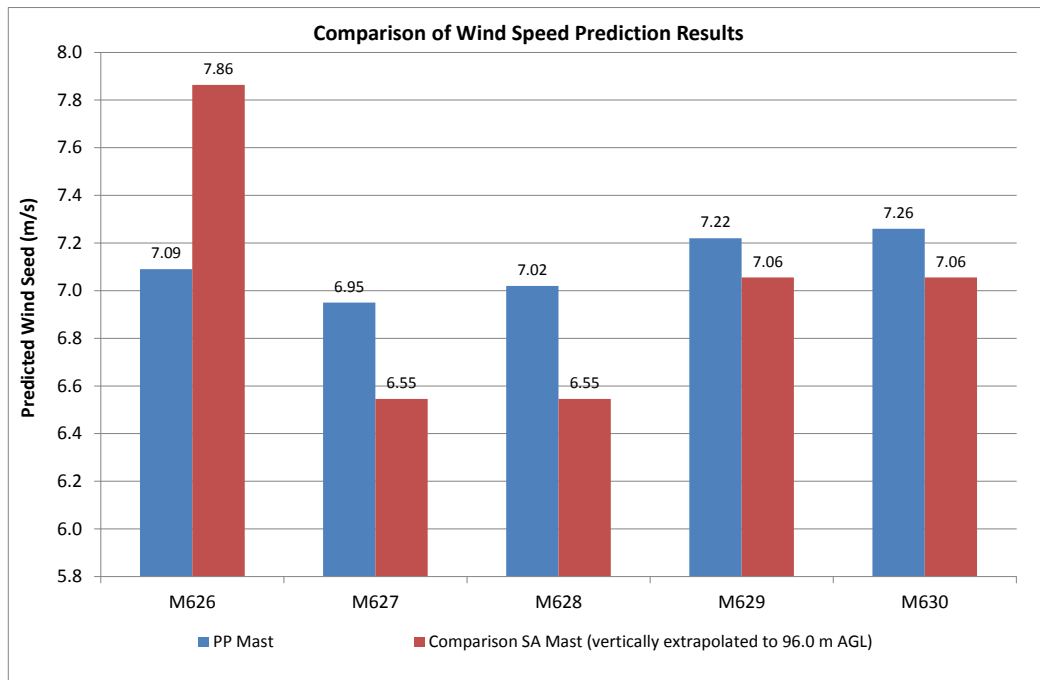


Figure 6.1.1: Comparison of Wind Speed Prediction Results at SA and PP Masts

As can be seen from the results, there is broad agreement between the SA and PP predictions at 96.0 m. However, there is a larger difference observed between M626 and M231, requiring further investigation.

Due to the fact that the comparison masts are not located at the same point as the PP masts, it should be expected that the wind climate will vary at each mast position due to factors such as topography.

Therefore, in order to assess the possible impact of topography on results, a simple linear flow model was run to generate indicative speed-up factors between the mast locations. The speed-up factors and SA wind speeds with speed-up factors applied are presented in Table 6.1.5. Figure 6.1.2 compares the three wind speed predictions obtained from the PP mast at 96.0 m, from the vertical extrapolation of the SA wind speed at 96.0 m and from the application of the speed-up factors to the vertically extrapolated SA wind speed at 96.0 m.

Flow Model Initiation SA Mast	M231	M278	M278	M279	M279
PP Mast	M626	M627	M628	M629	M630
Flow Model Predicted Wind Speed at 96.0 m AGL (m/s)	6.62	6.60	6.52	7.11	7.10
Speed-up Factor (relative to SA mast)	0.84	1.01	1.00	1.01	1.01

Table 6.1.5: Comparison Mast Pair Predicted Speed-Up Factors

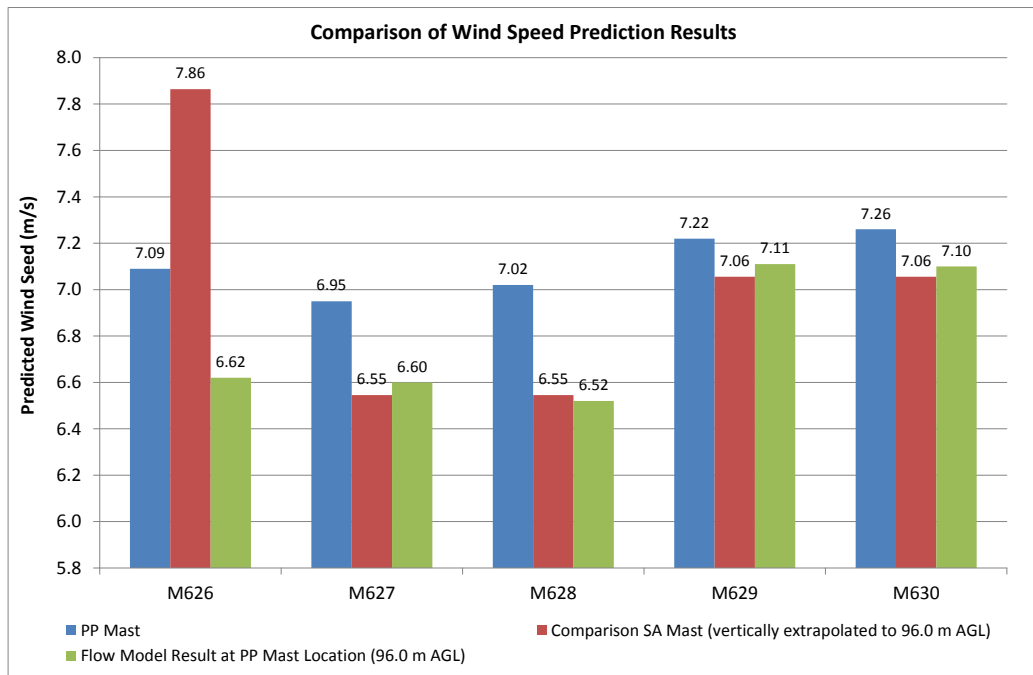


Figure 6.1.2: Comparison of Wind Speed Prediction Results at SA and PP Masts, Including SA wind Speed With Speed-ups Applied to PP Location

The magnitude and direction of the predicted speed-up factors is broadly consistent with the variation in predicted SA and PP long-term 96.0 m wind speeds as shown in Table 6.1.4.

Additionally, since the flow model predicts a large reduction in wind speed at M626 from M231, it can be inferred that topography and roughness account for more of the observed hub height wind speed difference between M231 and M626 than the vertical extrapolation of wind speeds alone.

The overall comparison results are summarised in Table 6.1.6.

	M626	M627	M628	M629	M630
Wind Speed at PP Mast (m/s)	7.09	6.95	7.02	7.22	7.26
PP mast Prediction Uncertainty (m/s)	0.36	0.34	0.35	0.37	0.37
Wind Speed SA Reference Mast vertically extrapolated to 96.0 m (m/s)	7.86	6.55	6.55	7.06	7.06
Wind Speed at PP Mast Location Horizontally Extrapolated From SA Reference Mast at 96.0 m (m/s)	6.62	6.60	6.52	7.11	7.10
[Wind Speed PP mast] - [Wind Speed SA reference mast vertically extrapolated to 96.0 m] (m/s)	-0.77	0.40	0.47	0.16	0.20
Relative difference compared to the PP prediction	-10.9%	5.8%	6.8%	2.3%	2.8%
[Wind Speed PP mast] - [Wind Speed at PP mast location extrapolated from closest SA mast] (m/s)	0.47	0.35	0.50	0.11	0.16
Relative difference compared to the PP prediction	6.6%	5.0%	7.1%	1.5%	2.2%
[Height of measurement ASL at PP mast] - [Height of measurement ASL at SA mast] (m)	-43.0	38.6	47.6	54.6	50.6
Distance from nearest SA mast (km)	2.5	0.6	0.8	0.4	1.4

Table 6.1.6: Difference In Wind Speed Predictions

From Table 6.1.6, it does appear that the one point Theoretical Log Law has a tendency to underestimate hub height wind speed at this site. However, it is difficult to separate out the flow modelling error from the shear extrapolation error using the methodology above. To investigate the effect of vertically extrapolating from lower masts up to hub height more directly, energy yields were modelled for the following scenarios:

- Scenario 1 (EY1) - Original Energy Yield calculations based on SA masts M231, M278 and M239.
- Scenario 2 (EY2) - The original Energy Yield calculated using updated wind climate information derived from the PP reference masts M626-630.

Table 6.1.7 shows that, once the effect of flow model error is fully removed from the comparison, the one point theoretical log law does not consistently underestimate the hub height wind speed and hence underestimate the energy. In fact, these energy yield results indicate that there is very little error introduced by the use of the SA masts with one point theoretical log law with the overall energy only being overestimated by 0.17% as compared to an energy yield using PP mast data.

Wind Farm region	Ritjelsberget	Ursåsen	Järvsand	Havsnäs (all turbines)
Difference [(EY2/EY1) - 1]	-0.94%	1.39%	-0.13%	-0.17%

Table 6.1.7: Difference In Energy Yield Predictions

CONCLUSIONS

It has been shown that, in spite of extrapolating over a relatively large vertical distance, the Theoretical Log Law shear correction methodology results in hub height wind speed estimates that are in good general agreement with those measured at the PP masts. The error introduced by the flow model makes it appear that hub height wind speed is being underestimated using the one point theoretical log law. However, when comparing the predicted energy based on a wind climate derived from the PP reference masts against a wind climate derived from the lower SA masts, we see that the results are in very good agreement. The predicted energy for Havsnäs from using the PP reference mast wind climate is only 0.17% lower than the original energy yield based on SA masts.

This gives some confidence in the use of the one point theoretical log law for vertical extrapolations in cold climates on forested sites where it has proven difficult to measure shear conventionally, or perhaps for scoping purposes.

It should be noted that this method relies on a reliable characterisation of the forest canopy height and roughness length and should be used with caution. It is recommended that no one method is used in isolation, but is considered against alternatives making full use of high quality site measurements of shear wherever available.

6.1.4 MODEL VALIDITY OF ALTERNATIVE SHEAR METHODOLOGIES

The aim of this section is to consider how well the different shear methodologies (see Section 6.1.2) predict hub height wind speed. This analysis considers data from the PP reference masts M626, M628 and M630.

The concurrent period considered in this analysis is 16/09/2011-25/07/2012. However, in order that the most accurate and representative data were used for the analysis, data from each of the three fixed masts were first quality controlled to remove icing (see Section 5.3.1). The data were then further filtered on a directional basis to remove data in wake affected sectors as shown in Table 5.3.1 in section 5.3.2.

Following this, the maximum number of useable 10-minute time periods at each of the three PP reference masts ranges from 8.5 days to 10 days.

A variety of methodologies were used to calculate wind shear at each of the mast locations. In particular, the revised shear approach was used for the vertical extrapolation of wind speed to hub height as it is most amenable to the direct comparison of shear exponents from the one, two and multi-point shear methods.

The vertically extrapolated wind speeds from the different shear methods were then compared against measured wind speeds and the errors compared to highlight the best performing approach.

Additionally, in this analysis:

- Revised shear values were predominantly calculated for a canopy height of 10 m to suit the site, but also for 5 m and 15 m to test the sensitivity of the methodologies to error in canopy height.
- Each mast has an upper anemometer at hub height.
- Each fixed mast has two anemometers at approximately 87 m. These are considered to be the primary anemometers for use in calculating hub height wind speed using the revised shear methodologies.
- Displaced shear values were also tested at each mast using, in turn, all measurement heights below hub height as the primary anemometer.
- For the extrapolation to hub height, measured mean wind speed values were used and global values for the fixed mast shear were used.

It should be noted that the revised shear and displaced shear methodologies are two equivalent ways to extrapolate wind speeds to hub height in the context of this analysis and give the same end result. The reason both are considered here is due to some results being generated initially for different purposes using alternative software.

M626 TWO POINT SHEAR WITH VARYING EXTRAPOLATION DISTANCE

The highest measurement height at M626 is 96 m. Wind speeds at this height have been estimated using measurements from anemometers at the lower heights of 50 m, 72 m and 87 m.

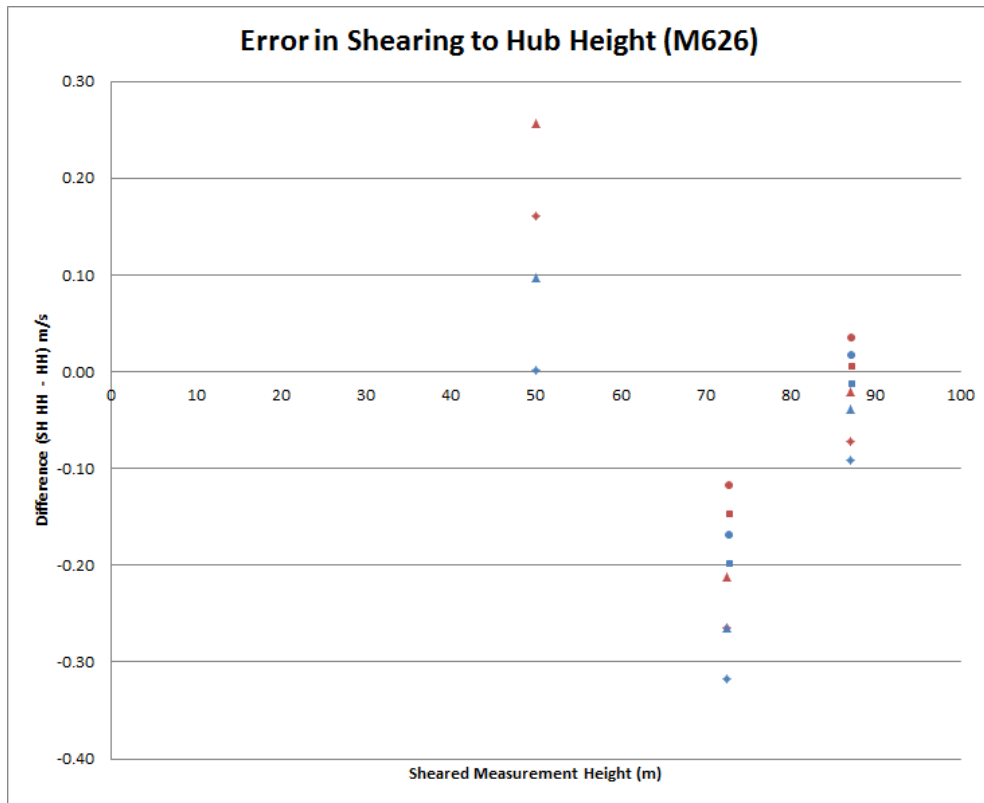


Figure 6.1.3: Vertically extrapolating M626 to Hub Height (Two Point)

Referring to Figure 6.1.3, the 'sheared measurement height' shown on the x axis indicates the primary measurement height from which the wind speed is extrapolated to hub height. The key to the colours and symbols is presented below.

Colour	Shear Value	
Blue	$\alpha = 0.139$	
Red	$\alpha = 0.158$	
Shape	Boom Orientation	
	Measurement Instrument	Hub Height
Diamond	30°	28°
Triangle	30°	208°
Square	210°	28°
Circle	210°	208°

Shear value	Shear Anemometers
$\alpha = 0.139$	50.1 m 30° - 72.6 m 30°
$\alpha = 0.158$	72.6 m 30° - 87.1 m 30°

As may be expected, and as can be seen in Figure 6.1.3, vertically extrapolating over shorter extrapolation distances causes the smallest differences between sheared and measured values of hub height wind speed.

Vertically extrapolating from the 50 m anemometer generally overestimates hub height wind speed, while vertically extrapolating from the 72 m anemometers underestimates the wind speed at hub height. Using the 87 m anemometers, the error approaches zero.

It is also clear in the data that using the shear value obtained from the shear anemometers closest to the primary measurement height also helps to minimise the difference between measured and sheared values of hub height wind speed.

M628 TWO POINT SHEAR WITH VARYING EXTRAPOLATION DISTANCE

As can be seen in Figure 6.1.4, the same general pattern is observed at M628 as at M626; vertically extrapolating over shorter extrapolation distances generally causes the difference between the sheared and measured value of hub height wind speed to converge.

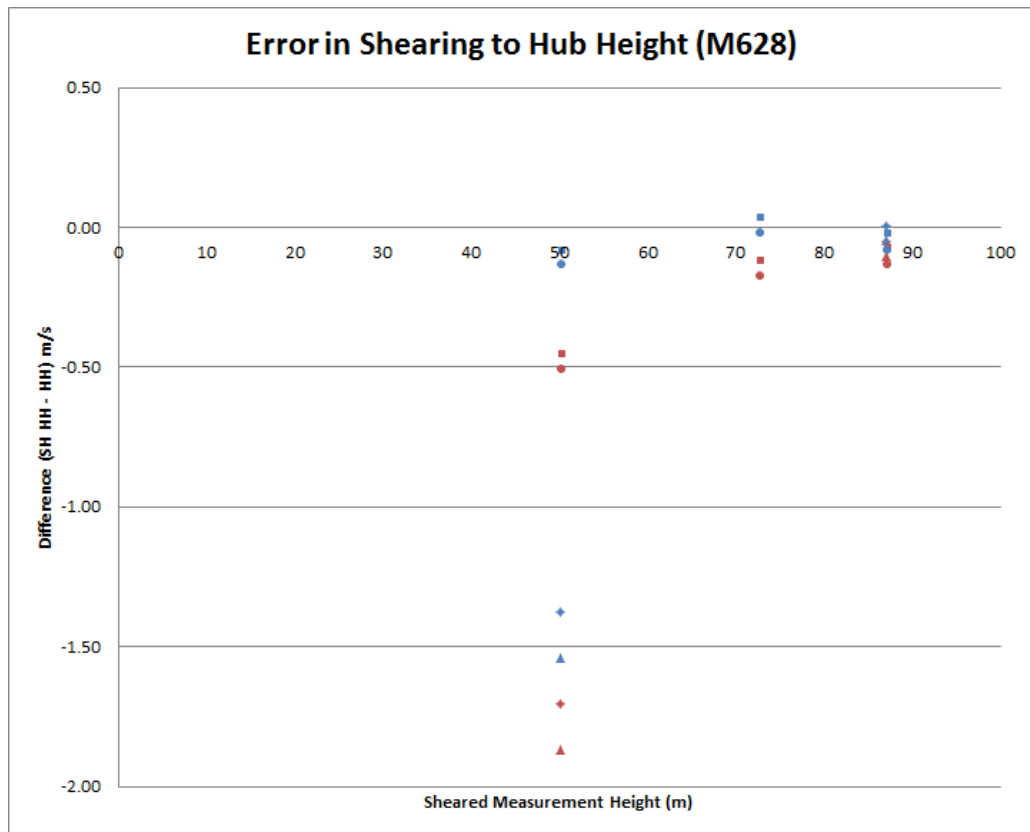


Figure 6.1.4: Vertically extrapolating M628 to Hub Height (Two Point)

Referring to Figure 6.1.4, the 'sheared measurement height' shown on the x axis indicates the primary measurement height from which the wind speed is extrapolated to hub height. The key to the colours and symbols is presented below.

Colour	Shear Value	
Blue	$\alpha = 0.219$	
Red	$\alpha = 0.166$	
Shape	Boom Orientation	
	Measurement Instrument	Hub Height
Diamond	45°	31°
Triangle	45°	210°
Square	225°	31°
Circle	225°	210°

Shear value	Shear Anemometers
$\alpha = 0.219$	50.3 m 225° - 72.8 m 225°
$\alpha = 0.166$	72.8 m 225° - 87.3 m 225°

The Anemometer at 50.1 m and orientation of 45 degrees has a very poor data capture compared with all other instruments which results in the large differences observed in the data. This anemometer would not normally have been used in a prediction or for vertically extrapolating wind speed to hub height.

The largest underestimations, or worst errors, are associated with the largest extrapolation distances.

At M628, using the shear value obtained from the lower shear anemometers helps, in all cases, to minimise the difference between measured and sheared values of hub height wind speed.

This is in contrast to M626 where the shear pairing closest to the primary measurement height helped minimise the differences between measured and sheared values of hub height wind speed.

M630 TWO POINT SHEAR WITH VARYING EXTRAPOLATION DISTANCE

As can be seen in Figure 6.1.5, the data from M630 indicate that vertically extrapolating over shorter extrapolation distances causes the difference between the sheared and measured value of hub height wind speed to converge.

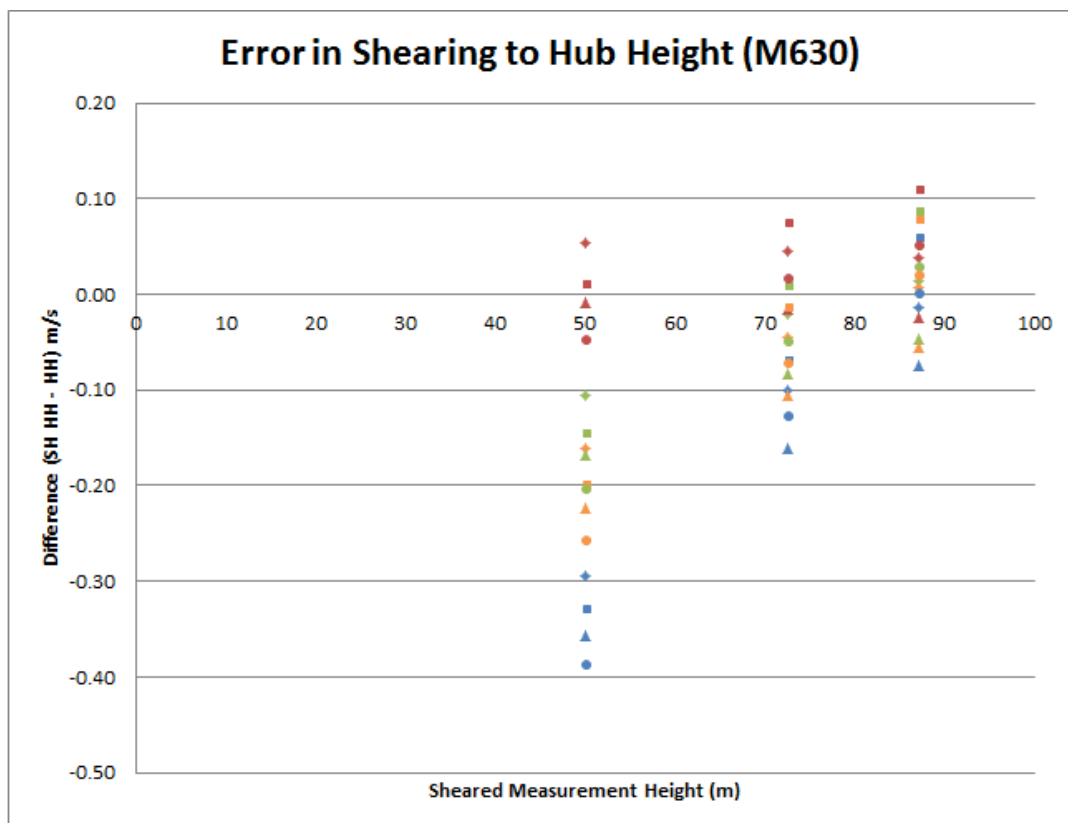


Figure 6.1.5: Vertically extrapolating M630 to Hub Height (Two Point)

Referring to Figure 6.1.5, the 'sheared measurement height' shown on the x axis indicates the primary measurement height from which the wind speed is extrapolated to hub height. The key to the colours and symbols is presented below.

Colour	Shear Value	
Blue	$\alpha = 0.201$	
Red	$\alpha = 0.245$	
Green	$\alpha = 0.225$ (heated)	
Orange	$\alpha = 0.218$ (heated)	
Shape	Boom Orientation	
	Measurement Instrument	Hub Height
Diamond	37°	21°
Triangle	37°	201°
Square	217°	21°
Circle	217°	201°

Shear value	Shear Anemometers
$\alpha = 0.201$	50.1 m 37° - 72.6 m 37°
$\alpha = 0.245$	72.6 m 37° - 87.1 m 37°
$\alpha = 0.225$ (heated)	50.3 m 217° - 72.8 m 217°
$\alpha = 0.218$ (heated)	72.8 m 217° - 87.3 m 217°

Generally, when vertically extrapolating from the 50 m and 72 m anemometers, there is an underestimation of wind speed when vertically extrapolating up to hub height.

M626 COMPARISON OF SHEAR METHODS WITH VARYING CANOPY HEIGHT

When comparing shear methods at M626, it can be said that, generally, the two point and multi-point methods help to minimise the difference between measured and sheared values of hub height wind speed. The multi-point method does return the smallest error, however this is dependent on which anemometer orientation is used for extrapolating to hub height.

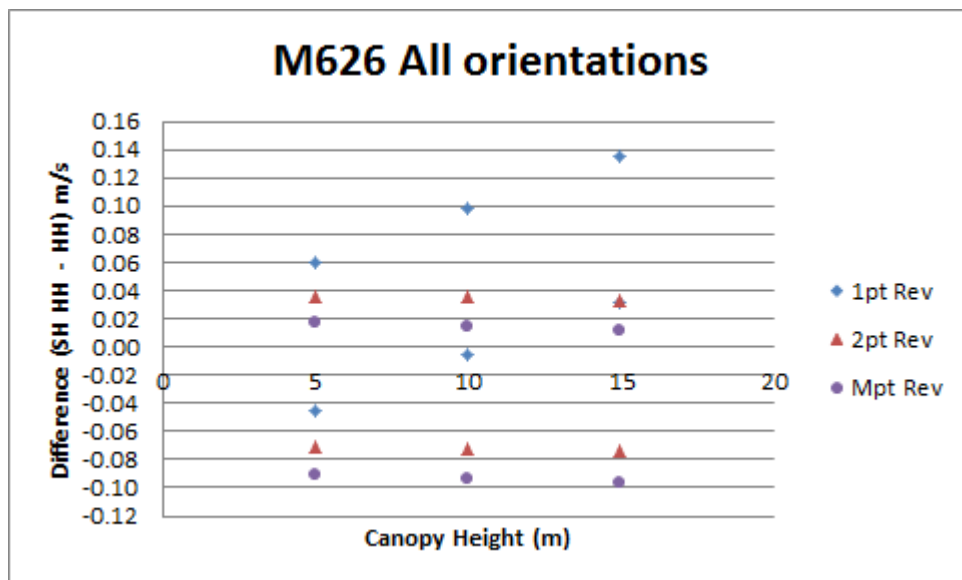


Figure 6.1.6: Vertically extrapolating M626 to Hub Height (Revised)

Of particular note is the very small variation in error when varying the canopy height for the two point and multi-point methods. This suggests that these methods may not be very sensitive to uncertain or approximate canopy heights.

The same is not true for the one point method, however. Due to the manner in which it is calculated, the one point method requires an accurate value for the canopy height. It is

therefore possible that where there is variation in the tree canopy across a site, the one point method may not provide a sufficiently accurate measure of shear.

M628 COMPARISON OF SHEAR METHODS WITH VARYING CANOPY HEIGHT

When comparing shear methods at M628, it can be said that, generally, all methods help to minimise the difference between measured and sheared values of hub height wind speed. Again, the multi-point method does return the smallest error, but again this is dependent on which anemometer orientation is used for extrapolating to hub height.

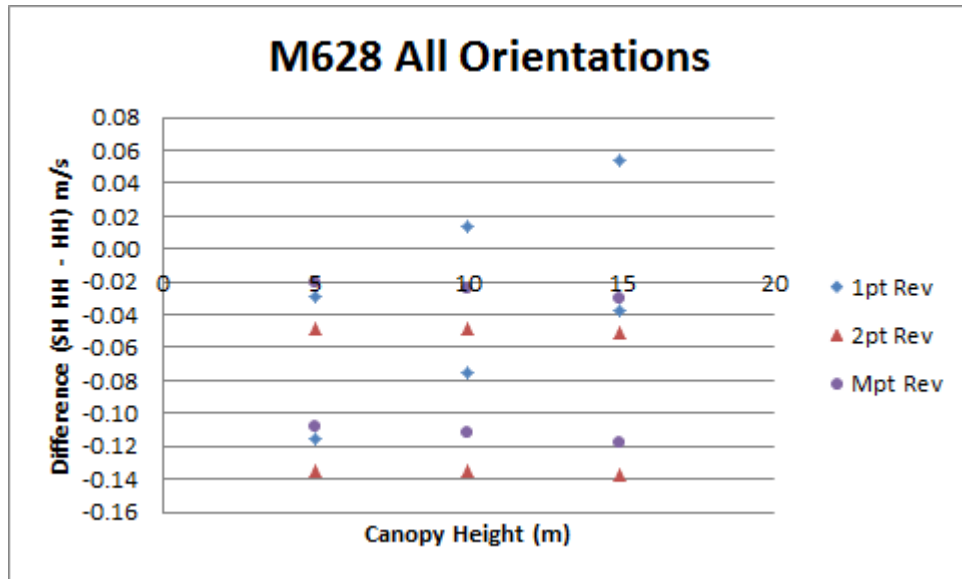


Figure 6.1.7: Vertically extrapolating M628 to Hub Height (Revised)

Again, the data suggest that both the two point and multi-point revised shear methods may not be very sensitive to uncertain or approximate canopy heights.

M630 COMPARISON OF SHEAR METHODS WITH VARYING CANOPY HEIGHT

When comparing shear methods at M630, it can be said that, generally, all methods help to minimise the difference between measured and sheared values of hub height wind speed.

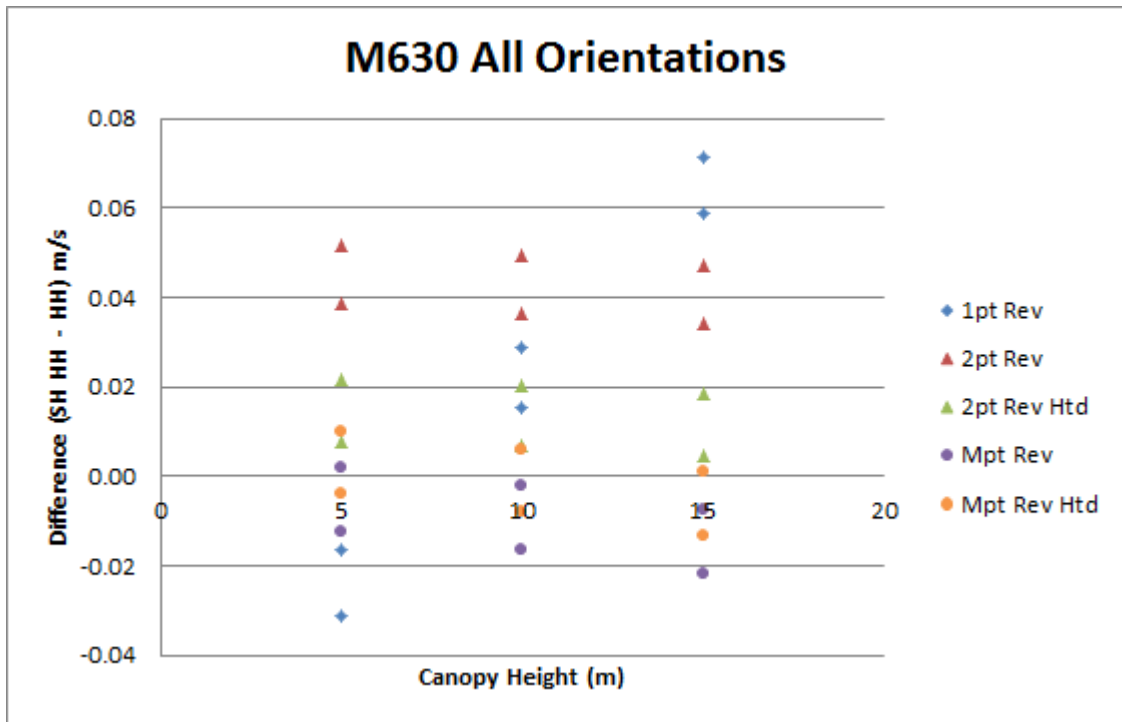


Figure 6.1.8: Vertically extrapolating M630 to Hub Height (Revised)

The multi-point method does return the smallest error, but this is dependent on which anemometer orientation is used for vertically extrapolating to hub height.

The data suggest that both the two point and multi-point revised shear methods may not be very sensitive to uncertain or approximate canopy heights.

6.1.5 SHEAR METHODOLOGY VALIDATION USING REMOTE SENSING

The aim of this section is to consider how shear varies across the site, how well correlated the mast data are and how well the different shear methodologies (see Section 6.1.2) predict hub height wind speed. This analysis considers the WINDCUBE V1 LiDAR deployment M814 which is co-located with the PP reference mast M626 and also considers data from masts M628 and M630.

The concurrent period considered in this analysis is 16/09/2011-25/07/2012. However, due to icing and wake filters, the data used in this analysis represent only a small subset of the concurrent period.

Once suspected icing periods had been removed (see Section 5.3.1) the maximum number of useable 10-minute time periods is 1440 at the LiDAR, which is the equivalent of 10 days of data. The amount of data available at each of the three PP reference masts ranges from 8.5 days to 10 days.

The data were then further filtered on a directional basis to remove data in wake affected sectors as shown in Table 5.3.1 in Section 5.3.2.

VELOCITY PROFILE AND SHEAR COMPARISONS

Shear exponents were calculated and compared for each mast-mast or mast-LiDAR pair over the concurrent period, using a data period of maximum possible length. (This means that when making shear comparisons between the LiDAR and the fixed masts each comparison uses a slightly different concurrent period as a result of different icing conditions at each fixed mast.)

By assessing the spatial variability of shear, it should be possible to determine the likely reduction in shear uncertainty achievable across a site of this type via the installation of RS devices.

The shear comparisons are detailed below.

M814-M626

Figure 6.1.9 illustrates the relationship between measurement height and mean wind speed at that height for both the LiDAR and fixed mast M626. The distance between the fixed mast and LiDAR is 51 m in this case.

It is clear that there is excellent agreement between the WINDCUBE V1 LiDAR and its co-located fixed mast, M626, both in measured profile and in wind shear, as indicated by the closeness of the two data series and gradient of the fitted lines. Using the multi-point fitted log law the value of LiDAR shear is 0.223 compared to the fixed mast shear value of 0.218.

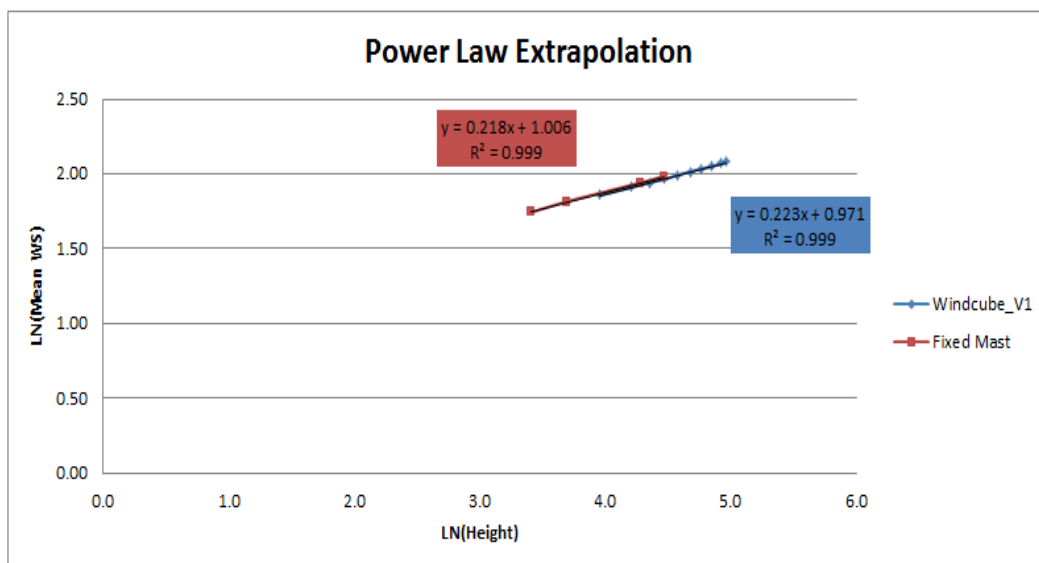


Figure 6.1.9: M814-M626 Multi-point Shear

M814-M628

Figure 6.1.10 illustrates the relationship between measurement height and mean wind speed at that height for both the LiDAR and fixed mast M628. Mast M628 is located a distance of 7699 m from the LiDAR and so some variation in wind climate would be expected.

When comparing the LiDAR profile with the profile at M628, it is clear that the LiDAR location is less windy than that at M628. Nevertheless, there is still good agreement between the mast and the LiDAR shear values by comparison of the gradients of the fitted lines.

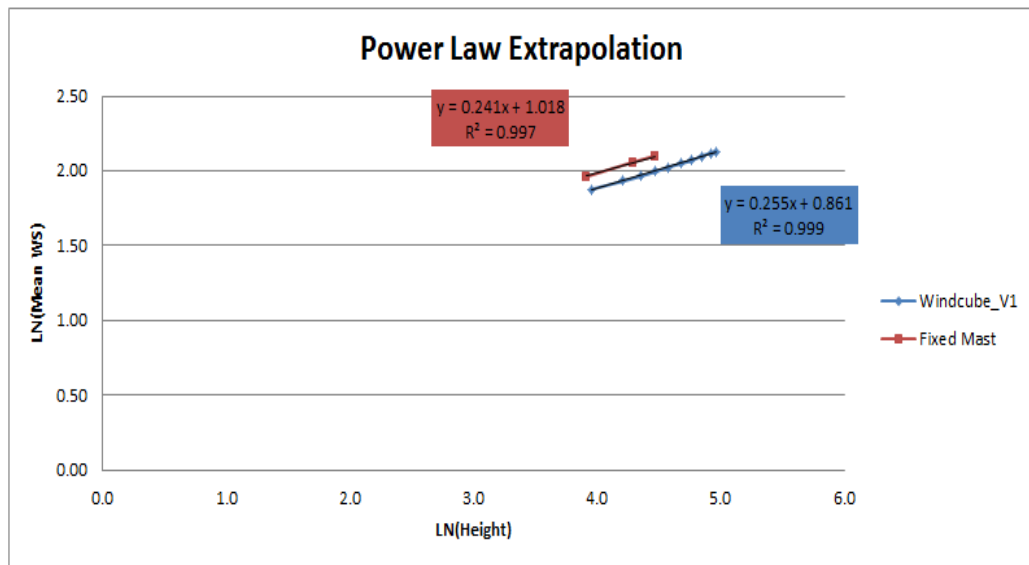


Figure 6.1.10: M814-M628 Multi-point Shear

M814-M630

Figure 6.1.11 illustrates the relationship between measurement height and mean wind speed at that height for both the LiDAR and fixed mast M630. Mast M630 is located a distance of 7181 m from the LiDAR and so some variation in wind climate would be expected.

When comparing the LiDAR profile with the profile at M630 it can be seen that the LiDAR location is less windy than that at M630. Nevertheless, although the shear at M630 is higher than at M626 or M628, there is still good agreement between the mast and the LiDAR shear values.

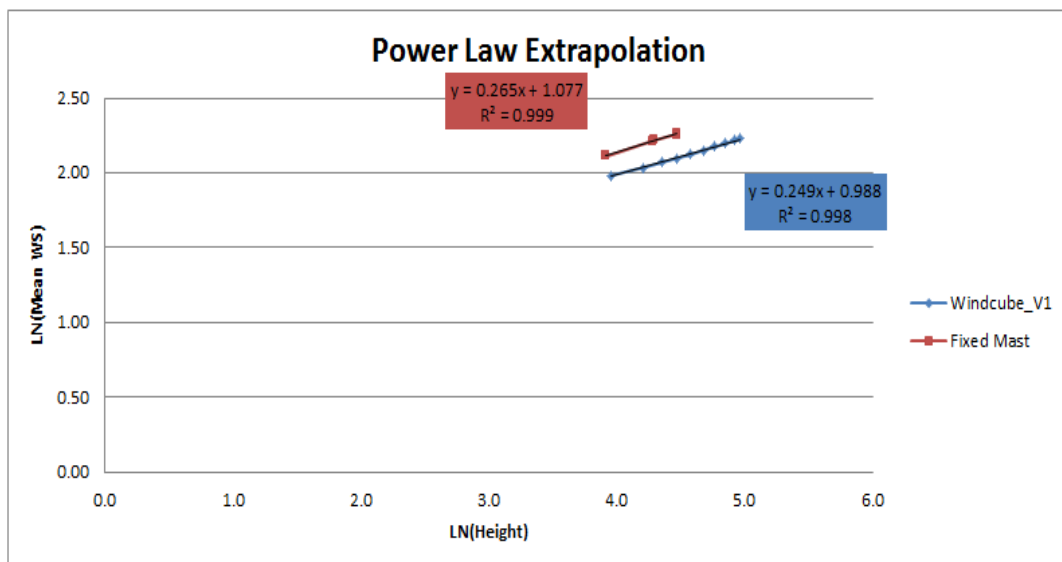


Figure 6.1.11: M814-M630 Multi-point Shear

In summary, based on the above comparisons, even at distances of up to 7 km, a very good agreement in shear is observed across the site and heights assessed.

This gives confidence that, at least qualitatively, RS devices should be able to represent velocity profiles above mast top heights over the course of fairly large separations on sites with similar topography, forestry and climate as Havsnäs.

INTER-MAST CORRELATIONS

In an attempt to parameterise the mast-LiDAR agreement, the relationship between wind speed and separation distance between measurements was further investigated as follows.

Correlation by Separation Distance

The correlation (r-value) between the concurrent time series (10-minute means) of measured wind speed data between each mast pair was calculated and plotted as a function of separation distance in Figure 6.1.12. These correlations were calculated using similar heights on each mast.

Mast and LiDAR separations are detailed in Table 6.1.8.

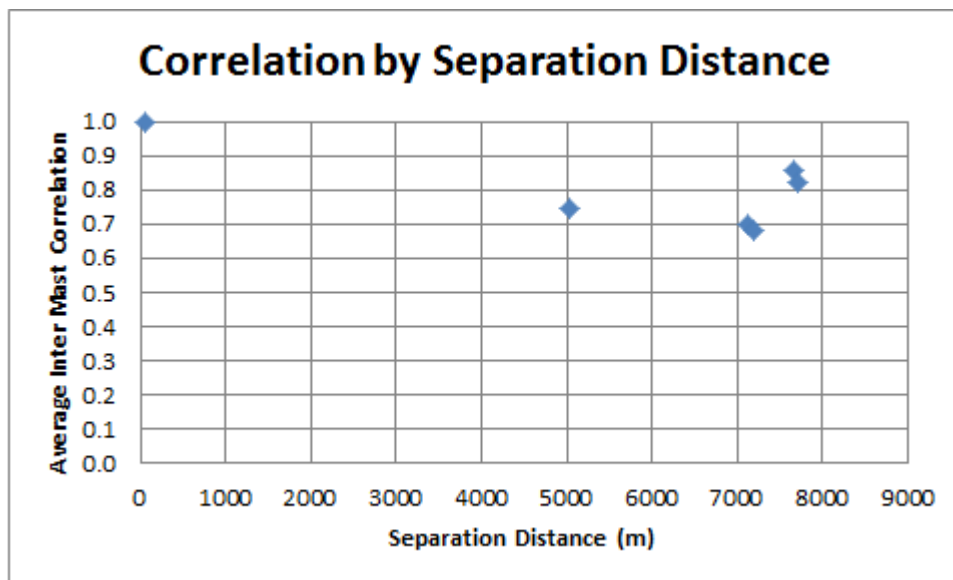


Figure 6.1.12: Correlation by Separation Distance

As would be expected, increasing the separation distance between masts reduces their correlation of wind speeds. For this site, it can be seen that, for every km increase in distance separation, correlation between wind speeds decreases by approximately 0.03.

Taking into account Figure 6.1.11 and Figure 6.1.12, for example, it can be concluded that the lowest observed r-value of around 0.7 (for the M814-M630 pairing) still corresponds to a good agreement in wind speed over coincident heights.

From experience, a high level of coincident agreement between LiDAR and mast velocity profile gives a good indication that the logarithmic profile at a given mast position will persist upwards to hub height.

This relationship between separation distance and correlation is likely to vary from site to site and will be dependent upon the site terrain, but, from the Havsnäs, study, it is suggested that even with 10-minute average r-values of 0.7, the LiDAR-measured velocity profile can be considered to give confidence in the mast-measured shear even at relatively large separations.

	M626	M628	M630
M626	7653		
M626	7131	5025	
M814 (LiDAR)	51	7699	7181

Table 6.1.8: Separation Distances

Correlation by measurement height

The correlations between mast-mast wind speeds and mast-LiDAR wind speeds at a variety of measurement heights were also calculated; however, in general, whilst there was a small indication that correlation improves with height, the extent was hard to distinguish from noise in the dataset.

As a result, it can be concluded that spatial separation is the dominant factor in determining the r-value between devices and masts and is therefore a reasonable descriptor for terrain and roughness conditions and, therefore, shear similarity.

With a larger dataset, (and concurrent measurements from two or more LiDAR devices) it should be possible to determine thresholds to help define shear validation and uncertainty criteria based on an extension of the above study and uncertainty analysis.

LIDAR SHEAR EXTRAPOLATION

A variety of methodologies were used to calculate wind shear at the LiDAR locations in a similar way to that described in Section 6.1.3 for the PP masts.

The LiDAR has a 97.5 m AGL measurement height which is taken to be hub height for this analysis. Note, that actual turbine hub height is 95m. Measurement heights below hub height range from 52.5 m to 87.5 m giving a minimum extrapolation distance of 10 m and a maximum extrapolation distance of 45 m.

Shear anemometers on the fixed masts are typically at measurement heights of 87, 72 and 50 m, and so the two-point power law shear values for the LiDAR were calculated using the wind speeds measured at heights of 87.5, 67.5 and 52.5 m. Multi-point values of LiDAR shear were also used. Results are illustrated in Figure 6.1.13 to Figure 6.1.15.

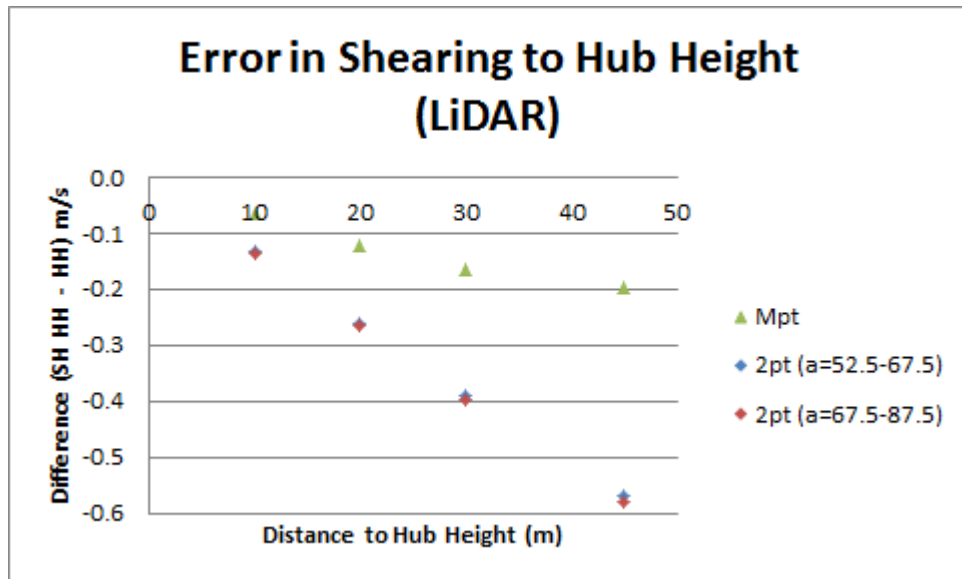


Figure 6.1.13: Vertically extrapolating LiDAR to Hub Height (non-Displaced)

Figure 6.1.13 shows that vertically extrapolating wind speed at the LiDAR using a two point power law or multi-point shear value routinely underestimates the hub height wind speed. As the vertical extrapolation distance increases the error in predicting hub height wind speed also increases.

However, the increase in error with extrapolation distance is different depending on the shear method used. The underestimation from the two point method increases more rapidly than that of the multi-point method as the shear extrapolation distance increases.

Further, given that there is a 10 m tree canopy at Havsnäs, which has not been considered in Figure 6.1.13, the Figure indicates that the two point method is more greatly affected by the use of an incorrect tree height than the multi-point method. Indeed, Figure 6.1.13 illustrates that the multi-point method performs comparatively well without the consideration of a canopy height.

This might be expected as the LiDAR multi-point shear value is derived using all ten of the LiDAR measurement heights and will likely be less affected by one or two affected measurement heights. However, for the two point shear method, just one affected measurement height can result in a shear value that is not representative of the shear profile at higher elevations.

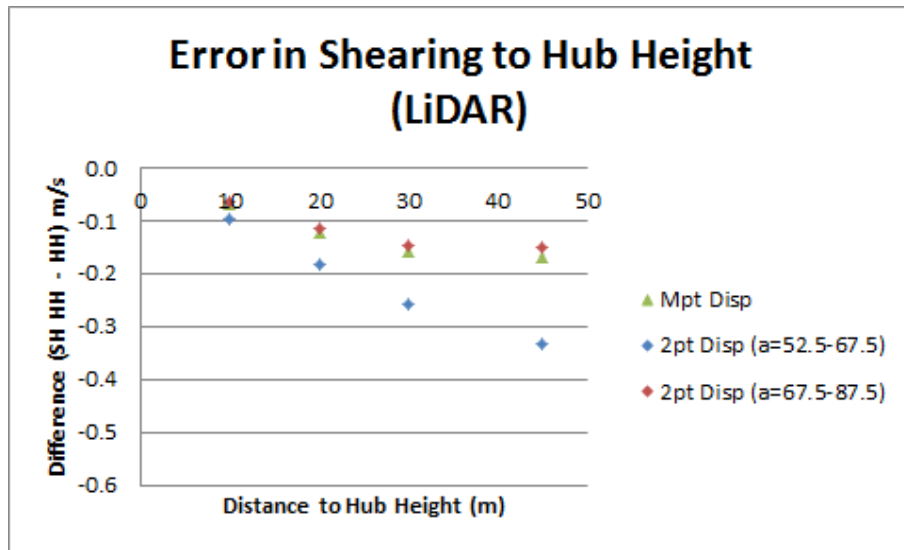


Figure 6.1.14: Vertically extrapolating LiDAR to Hub Height (Displaced)

When using the canopy height in the analysis, as in Figure 6.1.14, the data show that the two point shear value obtained from the lower measurement heights (52.5-67.5 m) gives the largest underestimation of shear. Figure 6.1.14 suggests that, for the LiDAR, measuring shear further above the tree canopy and or closer to hub height (67.5-87.5 m) will help reduce the error in extrapolating to hub height.

It can be seen from Figure 6.1.14 that the two point shear method (using the shear value obtained closest to hub height) performs slightly better than the multi-point method. This may be a result of some variation in the shear profile across the measurement range, meaning that because the two point value is obtained close to hub height it is more representative of the shear in this part of the measurement range than the multi-point method.

Nevertheless, the multi-point method is in excellent agreement with the two point method and is an effective method for minimising the difference between the sheared and measured values of hub height wind speed.

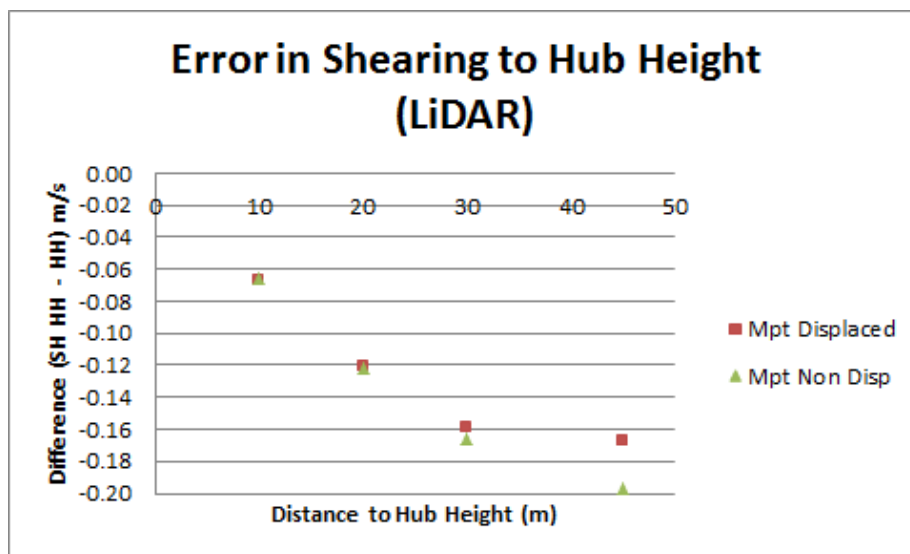


Figure 6.1.15: Vertically extrapolating LiDAR to Hub Height (Multi-point)

Figure 6.1.15 shows that, for the canopy of 10 m at Havsnäs, the multi-point method is not particularly sensitive to canopy height. This suggests that, at least for canopy heights up to 10 m, the multi-point shear method performs equally well with or without the use of a canopy height. However, in order to minimise the error in extrapolation, the extrapolation distance should be minimised and where the canopy height is known it should still be used.

CONCLUSIONS

In this analysis, two main areas of potential error in the vertical extrapolation of wind speeds were investigated:

1. The characterisation of the wind velocity profile (incorporating the influence of forestry on measurements)
2. The assumption of a smooth continuation of velocity profile above the mast top

There are a variety of methods available which attempt to achieve (1.); this analysis assessed the performance of single, two and multi-point displaced shear models by comparing their extrapolated wind speeds against equivalent hub height values using PP mast measurements.

From this study, it can be concluded that:

- a. Where forestry is well parameterised, and when relying on IEC-compliant measurements and class 1 anemometry, all three methods perform acceptably well
- b. On more complex sites or where the above conditions cannot be met, use of the single point method (except as a comparative value) is not recommended
- c. The two point method was the second best performer, slightly behind the multi-point method
- d. The multi-point shear model performed best overall, leading to the lowest extrapolated wind speed error
- e. The multi-point method also demonstrated the least sensitivity to the canopy height errors tested

By virtue of the fact that the overall error on the best performing multi-point extrapolations was small, it can be concluded that the profile assumptions of (2.) are also reasonable for this site.

However, while the velocity profiles appear to be well defined through the extent of measurement heights at Havsnäs, there is no guarantee that this will be the case across a given site, or even in the upper region of the turbine rotor swept area. Therefore, the potential for RS devices to aid in the reduction of extrapolation error was also explored, detailed as follows:

- f. When considering the full range of measurement heights at the LiDAR, the velocity profile was very well described by the multi-point log law and well approximated by the two point power law (though which specific two points are chosen needs to be given careful consideration).

As a result, the LiDAR has been observed to offer great potential in mitigating errors in (1.) and (2.) when co-located with a fixed mast of longer measurement duration. It follows that this would also be the case in standalone use when seasonal variation in climate can be accounted for.

-
- g. Further to point (f.) above, the potential for the LiDAR to give increased confidence in velocity profile across a site was also investigated. Good correlations in coincident wind speeds corresponded with good agreement in velocity profiles at separations of up to 7 km. That this agreement can give confidence from LiDAR measurements in the behaviour of the velocity profile above the mast tops is borne out by the small errors in the best performing vertical extrapolation models.

FURTHER WORK

With longer datasets, more measurements, including multiple RS deployments, and additional time, it should be possible to derive an empirical relationship that quantifies the reduction in mast shear uncertainty from the availability of RS device measurements based on proximity.

It may be interesting to investigate how increasing the extrapolation distance between measurement height and hub height affects the ability of the shear methodologies to accurately predict hub height wind speed.

It would also be informative to investigate the effect higher canopy heights have on these findings.

6.2 SOURCE AND IMPLICATIONS OF HIGH SHEAR

A further important aspect of accurately representing and understanding wind shear profiles is the energy content of the profile across the wind turbine rotor swept area and how this varies with time of day and season. The shape and hence energy content of the shear profile can be influenced by a range of atmospheric and site characteristics, particularly the variation in surface roughness as a function of wind direction and season (e.g. snow or no snow cover on ground, leaves on trees or no leaves on trees) and atmospheric stability which typically varies substantially between night and day in the summer months and between summer and winter in Sweden. Section 6.3 discusses the background to atmospheric stability in detail, how it was measured at Havsnäs and its general impact on turbulence and shear. It then goes on to investigate the relationship between atmospheric stability and shear based on measurements at Havsnäs. Section 6.4 investigates the theoretical energy content of modelled and measured shear profiles and how this relates to stability via time of day and season.

6.3 ATMOSPHERIC STABILITY

6.3.1 ATMOSPHERIC STABILITY BACKGROUND

Atmospheric stability is an important parameter in the context of wind energy. It is a measure of how the vertical temperature gradient affects the vertical motion of air flows in the ABL. The ABL is described as the lowest layer of the troposphere which is directly affected by contact with the earth surface. Thus it describes how much impact thermal or buoyant effects, caused by the diurnal cycle of solar heating and ground cooling, have on the measured wind parameters.

The effects of atmospheric stability can be observed through diurnal and seasonal changes to the turbulence intensity and wind shear that a potential wind farm site will experience. Measurements of atmospheric stability are thus important for the location and planning of wind farms, especially in climates where thermal effects are significant

Atmospheric stability stratification can be split into three classes, stable, unstable and neutral.

In order to understand the distinction between the three classes it is useful to consider a parcel of air displaced vertically upwards adiabatically (no energy transfer in or out of the parcel). The parcel will decrease in temperature as its altitude increases due to the lowering of atmospheric pressure. The rate at which this temperature change occurs is known as the Adiabatic Lapse Rate [8];

$$\frac{dT}{dz} \cong - 1^{\circ}C/100m \quad \text{Equation 6.3.1}$$

UNSTABLE STRATIFICATION

The atmosphere is described as unstable when the parcel of air displaced vertically upwards continues to rise. The lapse rate of the parcel in this case is lower than the adiabatic lapse rate.

During a typical day the sun heats the earth's surface causing a layer of the ABL closest to the ground to become hotter and less dense than the air directly above it. This heated air will

rise, resulting in increased vertical flow due to thermal effects and the atmosphere becomes unstably stratified.

Unstable stratification results in an increase in turbulence intensity and a decrease in vertical wind shear relative to neutral conditions due to increased mixing and transfer of turbulent energy from lower to upper atmospheric levels.

STABLE STRATIFICATION

The atmosphere is described as stable when a parcel of air displaced vertically upwards returns to its original position. The lapse rate of the parcel is now greater than the adiabatic lapse rate.

At night the ground cools quicker than the air above it. This results in any air displaced vertically being hotter and less dense than the air that it moves into, causing it to sink back down. The atmosphere is in effect suppressing vertical flow and results in a stable stratification.

Turbulent effects are diminished through a reduction in the vertical mixing of the air, which in turn allows greater wind shear exponents to develop.

Stable stratification can also occur on cold winter days, particularly when snow covers the ground. On these days, the snow acts to cool the air near the ground and maintain a temperature inversion. This prevents the occurrence of buoyancy-driven turbulent mixing, which on warmer days would normally encourage the atmosphere into neutral or unstable conditions. Due to the cold climatic conditions during the winter months, the atmosphere at Havnäs is expected to be stable for a larger proportion of the time than would be the case in a more temperate climate.

NEUTRAL STRATIFICATION

The atmosphere is described as neutral if the parcel of air remains in the same place when displaced vertically. The lapse rate of the parcel equals (or closely approximates) the adiabatic lapse rate in the case of neutral stratification.

When the thermal effects on the vertical wind flow are very slight the atmosphere is said to be neutrally stratified. This is either due to a lack of surface heating and cooling, or due to the thermal effects being dwarfed by mechanically induced turbulence (due to very high winds for example)

In this case the atmospheric stability effects can effectively be ignored.

QUANTIFYING ATMOSPHERIC STABILITY

Atmospheric stability can be quantified through two main techniques, flux based methods and gradient based methods. These are discussed below

Flux Method

The Monin-Obukhov Length, also known simply as the Obukhov Length, is generally accepted by meteorologists as the most robust and reliable quantification of Atmospheric stability [2, 3]. It can be thought of as the ratio of production/destruction of buoyancy-driven turbulence to the production of mechanically-driven turbulence.

In its most frequent form it is represented as the dimensionless Obukhov stability parameter, ξ :

$$\xi = \frac{z}{L} = -\frac{(g/\theta_v)\overline{(w'\theta_v')}}{u_*^2/kz} \quad \text{Equation 6.3.2}$$

Where:

L = Obukhov Length

z = Measurement height

g = Acceleration due to gravity

θ_v = Virtual potential temperature (this is simply temperature corrected for moisture and atmospheric pressure effects)

w = Vertical wind velocity

k = Von Karman constant. Taken as 0.4 [8,3]

u^* = Friction velocity.

The term $\overline{(w'\theta_v')}$ is the vertical virtual potential temperature flux, a measure of the thermal energy passing through a slice of space at a given time. The over-bar indicates a time average.

The Obukhov Length is a difficult parameter to measure accurately due to the very high measurement frequency required to capture very small perturbations from the mean conditions. This requires special instrumentation capable of measuring at frequencies in excess of 20Hz and a dedicated logging system to process and store the calculated values.

Gradient Method

For this report the simpler gradient method was used (the heavy icing environment of Havsnaäs made it almost impossible to maintain reliable winter operation of the instruments required to make flux measurements and so prevented meaningful data capture, as is discussed in Section 7.1.4), and an alternative metric to the Monin-Obukhov Length was calculated to quantify stability - the Gradient Richardson Number. The physical meaning of this number is very similar however, in that it is simply a ratio of thermal to mechanical turbulence effects.

Gradient methods are empirical in nature, and require the temperature and momentum fluxes in the wind to be expressed as simple gradients of temperature and wind speed. The instrumentation and logging equipment required to measure these gradients are much simpler than the flux method. This is down to the lower sampling frequencies required as the measured values are averaged over typically a ten minute period.

The Gradient Richardson Number in its most common form is expressed as follows:

$$Ri = \frac{g\Delta\theta_v}{\theta_v(\Delta\bar{v})^2} z_g \Delta \ln Z \quad \text{Equation 6.3.3}$$

Where:

Z = measurement height

z_g = geometric mean height of the layer (between Z_{upper} and Z_{lower})

θ_v = Potential temperature

v = horizontal wind speed

Δ refers to the difference between the value at the upper and lower level

The value of Gradient Richardson Number that applies to each stability class varies depending on site conditions so a calibration must be completed to find the neutral range. In general the following applies however:

Stability class as a function of the Gradient Richardson Number, Ri		
$Ri < 0$	$Ri \sim 0$	$Ri > 0$
Unstable	Neutral	Stable

Table 6.3.1: Stability class as a function of the Gradient Richardson Number, Ri

It is desirable for the upper and lower levels to be separated by as great a distance as possible so as to maximise the value of the gradients and minimise the relative impact of instrumentation error.

It should also be noted that gradient methods work best in uniform flat terrain and may suffer from additional uncertainties for complex sites.

WIND SHEAR AND TURBULENCE INTENSITY

The main effect that varying stability conditions will have on a wind measurement campaign are different values of wind shear and turbulence intensity than would be predicted by classical (log law based) theories. This is caused by a variation in the shape and depth of the ABL. The changing shape of the ABL, along with the effects on wind shear and turbulence are illustrated in Figure 6.3.1.

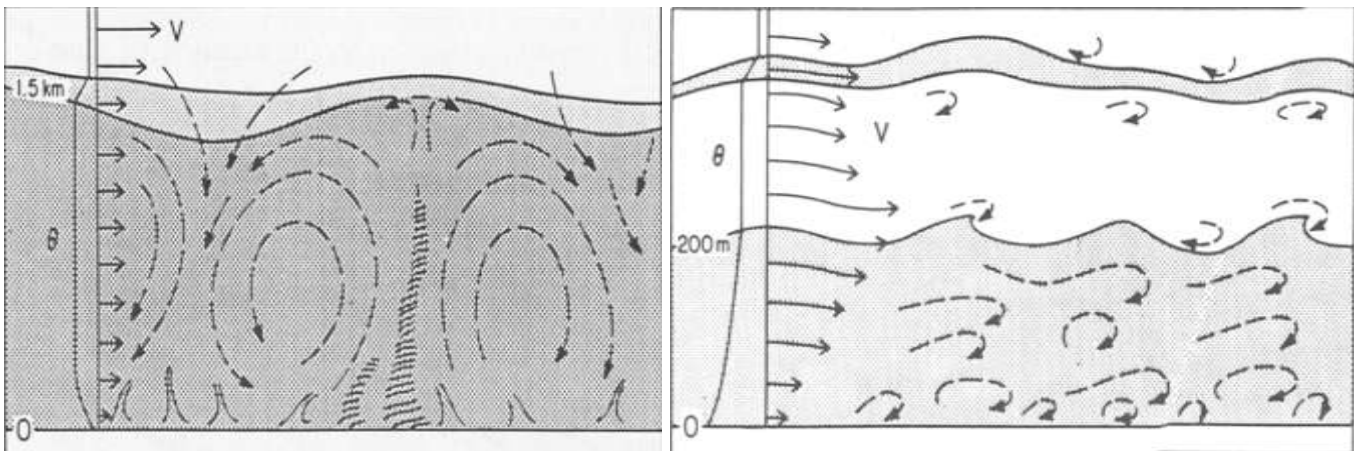


Figure 6.3.1: ABL depth and idealised shear profile for unstable (left) and stable (right) conditions [4].

A simplified shear profile for the three stability classes is shown in Figure 6.3.2.

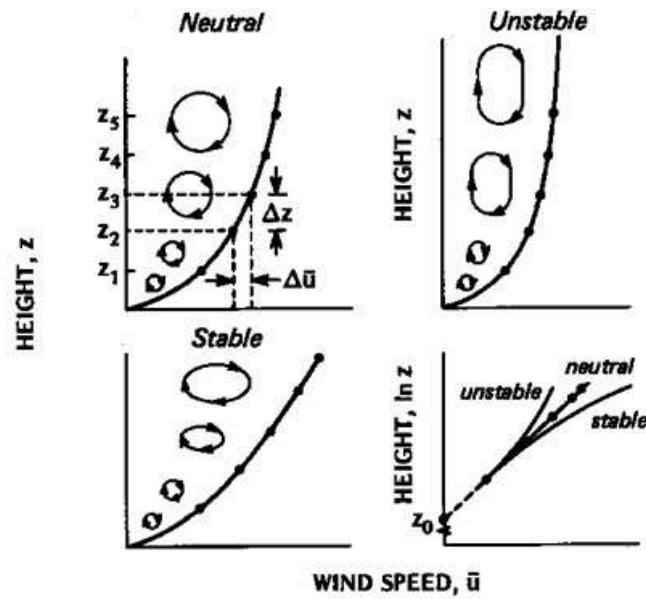


Figure 6.3.2: Shear profile and eddy schematic for each stability class. [5]

As a general rule:

Condition	Neutral	Unstable	Stable
Turbulence intensity	Varies with wind speed	Increases relative to neutral conditions for a given wind speed	Decreases relative to neutral conditions for a given wind speed
Shear Exponent	Follows log law	Decreases relative to log law	Increases relative to log law

Table 6.3.2: Generalised rules for turbulence intensity and shear for each stability class.

Figure 6.3.3 shows the seasonal and diurnal turbulence intensity patterns at Havsnäs as recorded by the long term SA mast M231. Figure 6.3.4 shows the monthly and diurnal variation in shear exponent. From October to January the shear exponent remains at close to night time levels throughout the day, suggesting that the atmosphere typically remains stable. The persistence of high shear during these months is characteristic of cold climates and is accompanied by low turbulence intensity, remaining close to night time levels throughout the day.

For the remaining months, both the turbulence intensity and shear show diurnal patterns. During daylight hours the turbulence intensity increases and the shear exponent decreases, suggesting neutral or unstable conditions are prevalent.

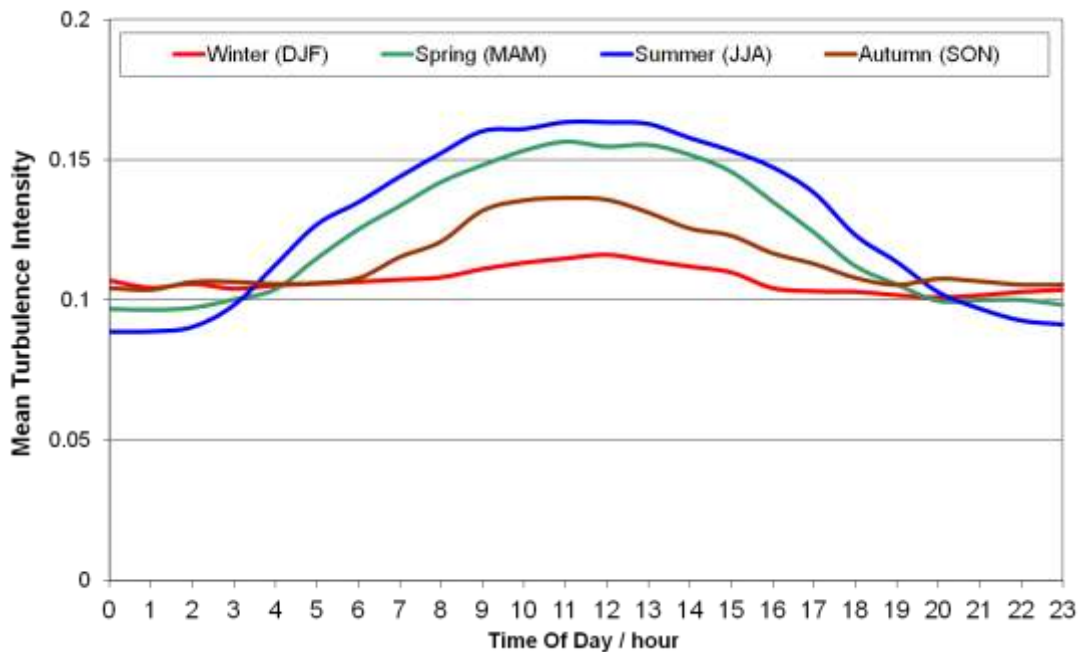


Figure 6.3.3: Variation in seasonal and diurnal turbulence intensity at M231.

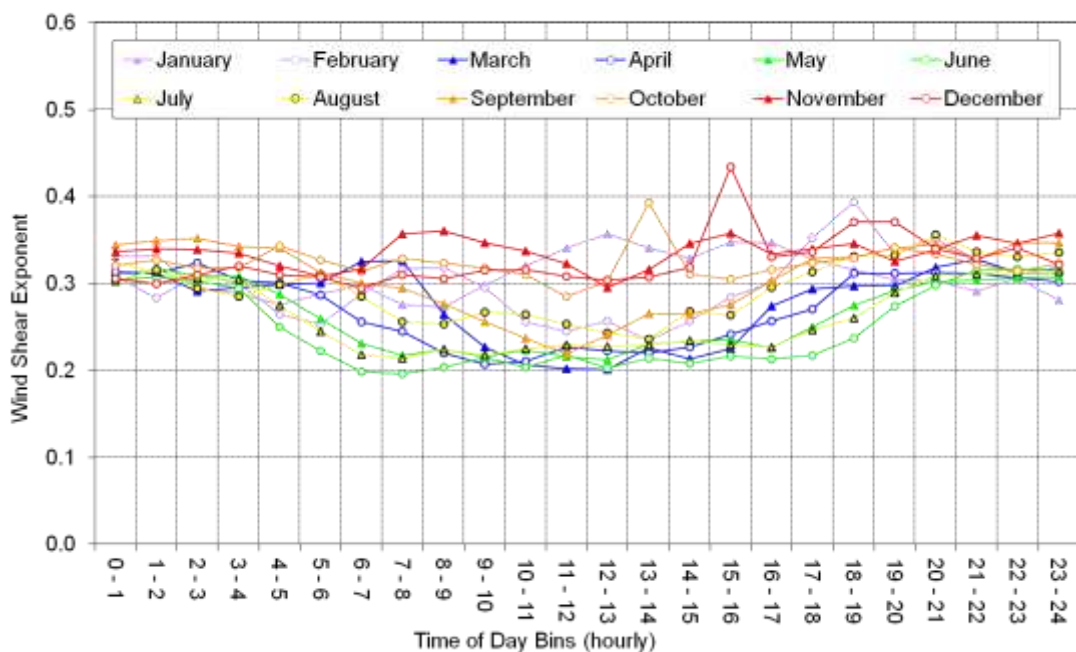


Figure 6.3.4: Variation in monthly and diurnal shear exponent at M231.

TEMPERATURE GRADIENT

The vertical temperature gradient is also affected by the stability of the atmosphere and can be used as a very approximate indication of stability by comparing to the adiabatic lapse rate. However, this approach does not take into consideration mechanical turbulence or the humidity of the air and therefore cannot precisely determine stability. Temperature gradients are investigated in Section 6.3.3 and in the CFD modelling section of this report (Section 7.7.2).

6.3.2 ATMOSPHERIC STABILITY DATA TREATMENT

Stability measurements were taken at two masts at Havsnäs during the cold climate R&D project, M6261 and M6282.

Ideally the wind speed measurements and the temperature measurements would be at the same measurement height for gradient measurements. For this study however the instruments selected for the lower wind speed measurement were not at the same height as the lower temperature sensor. A virtual lower level, mid way between the lower temperature sensor and the lower anemometer was used. This was necessitated by the multiple failures of the ultrasonic anemometers as detailed in the instrumentation section.

The following instruments were selected based on data availability and quality and used for the stability study:

Mast/Turbine	Upper Wind speed	Lower Wind speed	Upper Temperature	Lower Temperature	Upper Pressure	Lower Pressure
M6261/D2	Vector A100L2 @ 87.1m (S/N 12719-YUA)	Vector A100L2 @ 30.1m (S/N 13090-E454A)	CS 107 thermistor @ 90.5m (S/N 23946/6)	CS 107 thermistor @ 10m (S/N 21506/25)	Vegabar 17 @93m (S/N 12318143)	Vaisala PTB101B @ 8m (S/N E5040007)
M6282/E5	Vaisala WAA252 @ 87.3m (S/N E50302)	Vaisala WAA252 @ 50.3m (S/N E52021)	CS 107 thermistor @ 90.5m (S/N 23945/3)	CS 107 thermistor @ 10m (S/N 22721/4)	Vegabar 17 @93m (s/N 12318138) - NOT USED	Vaisala PTB101B @ 9m (S/N E5040010)

Table 6.3.3: Summary of instruments used.

Each instrument was checked against nearby instruments for accuracy where possible and any erroneous data was removed from the record.

VIRTUAL AND POTENTIAL TEMPERATURE

The Gradient Richardson Number uses the virtual potential temperature to calculate the temperature difference between the two levels. This allows the values to be corrected for different atmospheric pressure and moisture levels, allowing like for like comparisons of two different “packets” of air.

Unfortunately no relative humidity data was available during the majority of the winter months which prevents the virtual temperature correction being calculated. For this reason only the potential temperature, θ , was considered. It is not thought that the humidity levels would change much over the first hundred metres of the ABL, and as such this shouldn't have a major effect on the results.

The potential temperature is calculated relative to a reference pressure of 1000 mBar, P_{ref} , through the following formula (T is in Kelvin):

$$\theta = T \left(\frac{P_{ref}}{P_{air}} \right)^{2/7}$$

Equation 6.3.4

Where P_{air} is the measured atmospheric air pressure.

This relies on the pressure measurements being performed at the same measurement height as the wind speed and temperature measurements. The pressure measurements were taken at 93m (part of the original instrumentation of the PP masts) and 8m for D2 or 9m for E5. Potential temperature corrections were not used for the E5 stability calculations as the distance between the lower wind speed measurement (at 50m) and the lower pressure measurement (at 9m) was too great.

NEUTRAL CALIBRATION

In order to establish what constitutes neutral conditions at each mast a neutral calibration was performed. First filters are applied on the wind direction sensor to remove speed wind data affected by tower shadow, and then a filter is applied on the wind speed to leave only data above a certain threshold where it is assumed the conditions will be neutral due to the high levels of mechanically produced turbulence. The remaining values after the filters should be relatively homogeneous and free from any large spikes or deviations)

The following parameters were used for the neutral calibration for each mast:

Mast	Wind Directions Sensor	Wind Direction Filter ²	Wind speed filter (using upper wind speed sensor)	No of data points remaining	Minimum value of Ri	Maximum value of Ri
M6261 (N.B. using Potential temperature)	Vector W200P @ 70.6m (S/N 54341)	165-225°	>14 m/s	1183	-0.37	1.24
M6282 (N.B. Using measured air temperature)	Vector W200P @ 85.1m (S/N 55204)	20-80°	>16 m/s	436	-3.45	0.12

Table 6.3.4: Data used for neutral calibration

Note that the apparent large differences in the minimum and maximum values for the Ri neutral conditions at either mast are caused by the difference in calculation method. The corresponding values for M6261 if simple air temperature is used instead of potential temperature are max $R_i = 0.19$ and min $R_i = -2.5$.

² Wind direction has not been corrected from Magnetic North to Grid North

Based on the neutral calibration results the following criteria were used to indicate stability classes.

Mast	Unstable	Neutral	Stable
M6261	$Ri < -0.5$	$-0.5 \leq Ri \leq 1.5$	$Ri > 1.5$
M6281	$Ri < -3.5$	$-3.5 \leq Ri \leq 1.5$	$Ri > 0.2$

Table 6.3.5: Criteria to identify stability classes

6.3.3 ATMOSPHERIC STABILITY MEASUREMENT RESULTS

The results of the atmospheric stability measurements are presented in this section.

M6261 RESULTS USING POTENTIAL TEMPERATURE

The statistics for the Gradient Richardson Number for the M6261 mast are presented below using the potential temperature calculation.

The overall statistics for the mast are presented in Table 6.3.6.

Time Period	Valid Observations	Unstable Stratification	Neutral Stratification	Stable Stratification
Full Year	24586	18.97%	58.07%	22.97%

Table 6.3.6: M6261 Percentage of time in each stability class

The results are bunched into three month periods in Table 6.3.7 to demonstrate how the stratification varies from season to season with the degree of solar heating.

Time Period	Valid Observations	Unstable Stratification	Neutral Stratification	Stable Stratification
Sep - Nov	7466	1.85%	62.05%	36.10%
Dec - Feb	3203	0.81%	72.84%	26.35%
Mar-May	7125	19.27%	63.86%	16.87%
Jun-Jul	6792	46.02%	40.64%	13.34%

Table 6.3.7: M6261 Seasonal Variation of Atmospheric Stability

It is evident that unstable stratification is more common in summer months as the daylight hours increase. Conversely in the winter months, when there are very few hours of sunlight, stable conditions are far more frequent than unstable conditions.

Grouping stability class by wind speed bin, in Figure 6.3.5, shows how neutral conditions, that assumed by the majority of wind flow models used in the wind industry, are less common at lower wind speeds. As expected when the wind speed picks up the mechanical turbulent effects outweigh any thermal effects resulting in neutral conditions. The wind speed bin is simply the integer value of the measured wind speed at the upper anemometer. So the wind speed bin 1 covers wind speeds between 1 and 2 m/s. Wind speed bin 2 covers wind speeds between 2 and 3 m/s and so on. Wind speed values less than 1 m/s have been omitted.

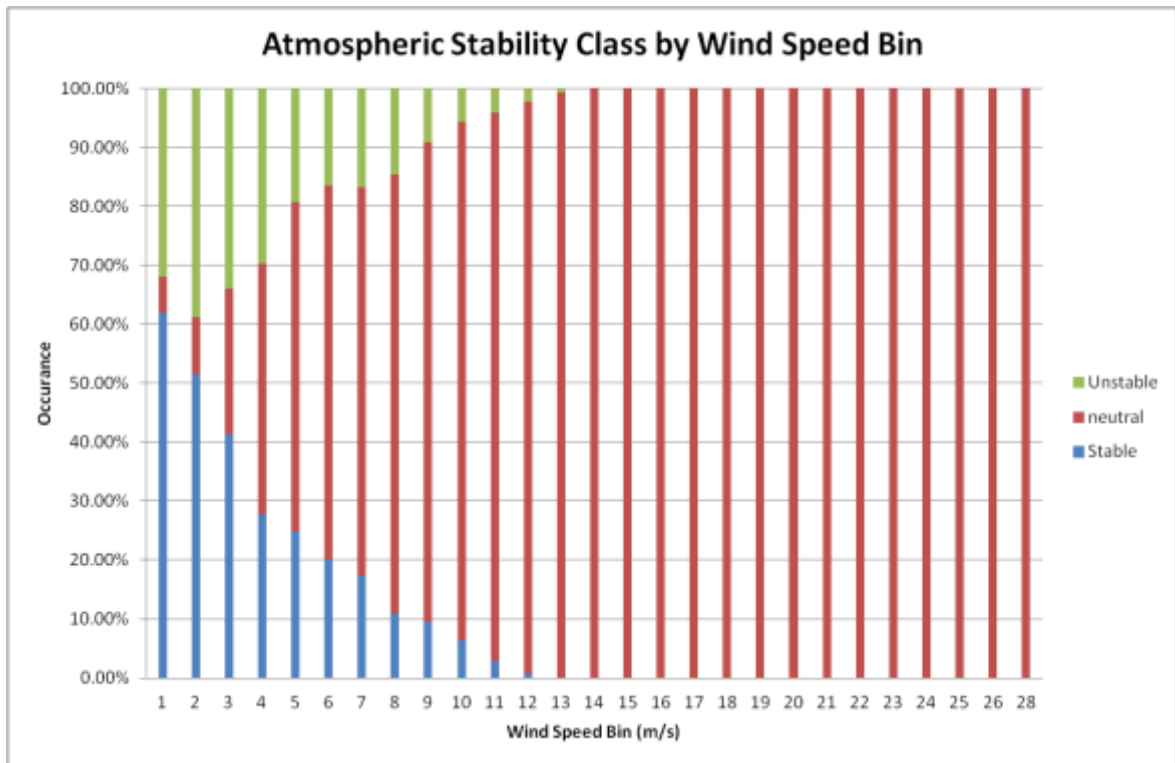


Figure 6.3.5: M6261 Atmospheric Stability Class by Wind Speed Bin

Figure 6.3.6 shows how the results of the stability measurements follow a diurnal cycle with unstable conditions being far more prevalent during the daytime and stable conditions more common at night. The hour of day displayed in this graph is Greenwich Mean Time, thus one hour should be added to give local time. The hour of day is again the integer value, so 12 covers the period from 12.00 to 13.00 GMT.

As the hours of daylight vary greatly in this part of Sweden from Summer to Winter, it is also instructive to look at the stability results binned by incident solar radiation. This is shown in Figure 6.3.7.

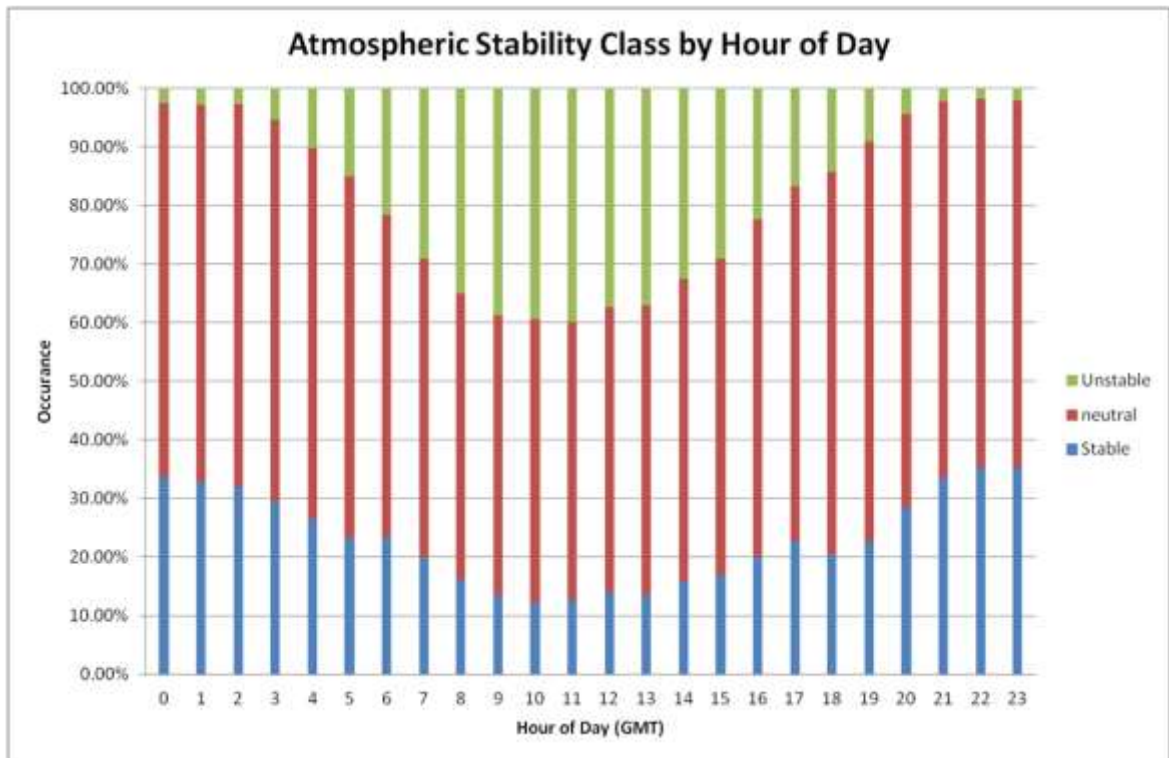


Figure 6.3.6: M6261 Atmospheric Stability Class by Hour of Day

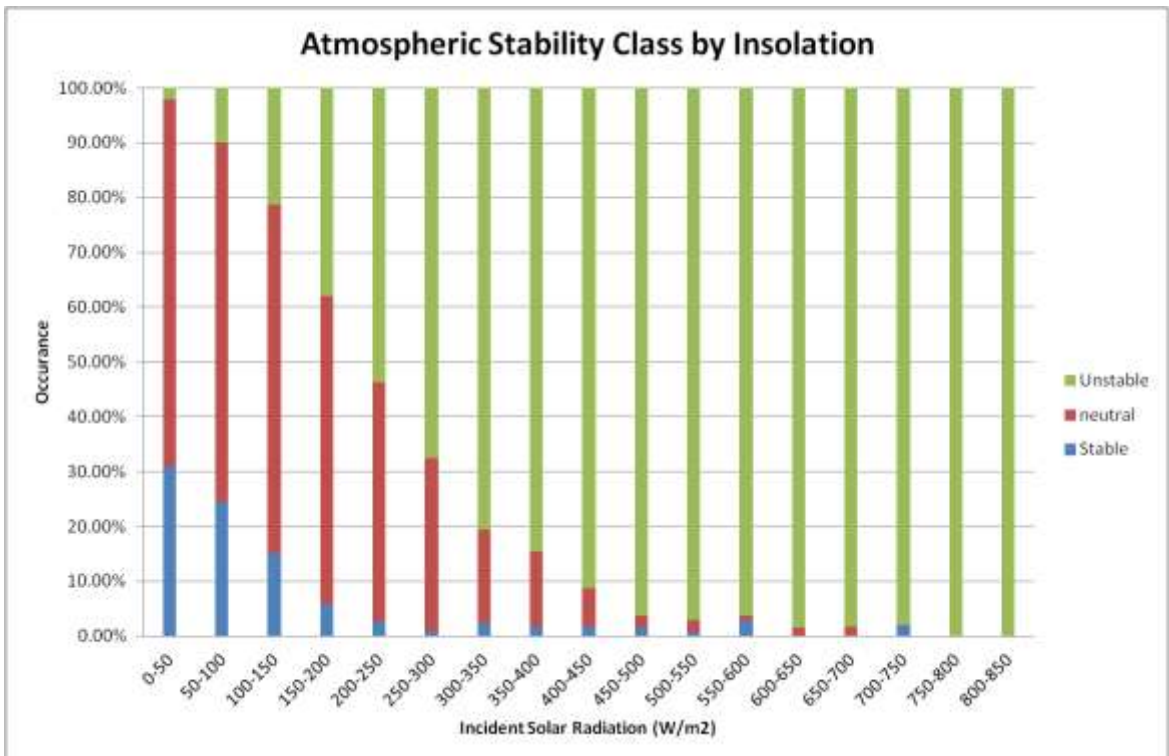


Figure 6.3.7: M6261 Atmospheric Stability Class by Insolation

For low radiation levels when the pyranometer reading is less than 50W/m^2 , the breakdown is 30.88% stable stratification and only 2.03% unstable stratification.

The effects of the stability effects can be seen in other parameters observed on site. Figures 6.3.8 and 6.3.9 show how the power law shear exponent and the upper anemometer turbulence intensity vary with hour of day. These follow a diurnal pattern as expected.

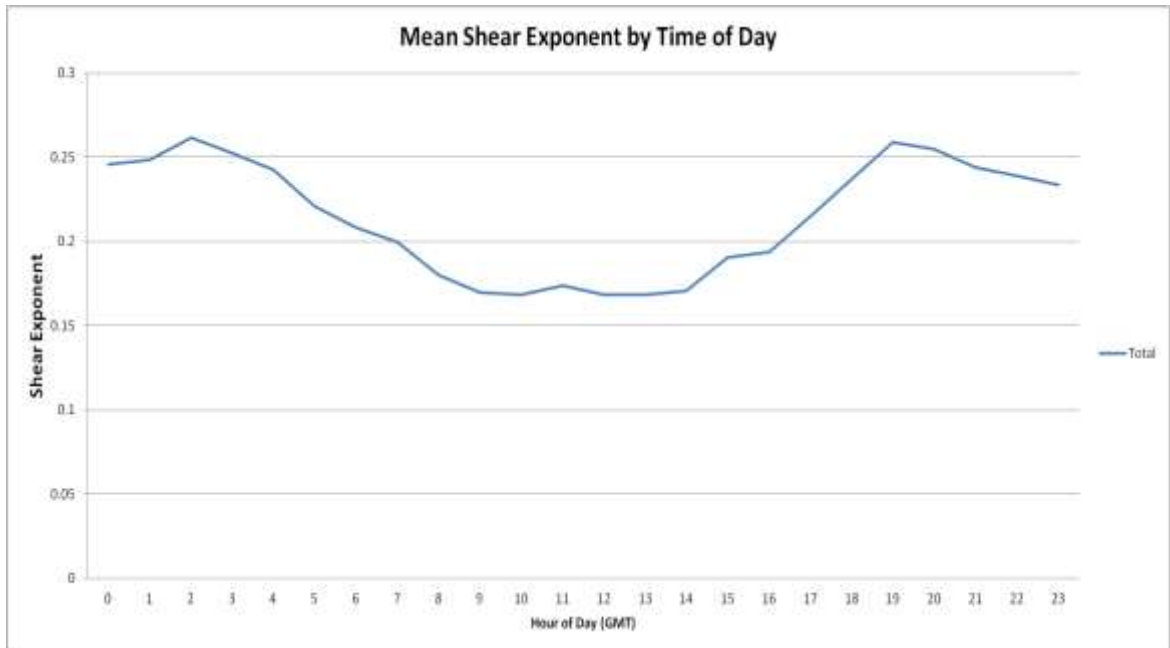


Figure 6.3.8: Mean Shear Exponent by Time of Day

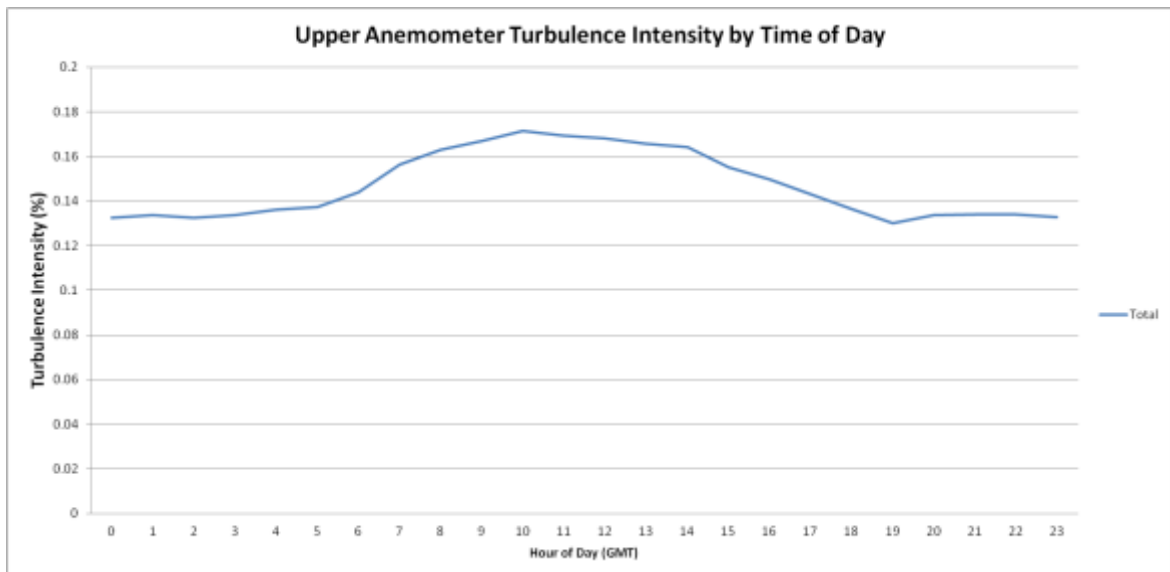


Figure 6.3.9: Turbulence Intensity by Time of Day

Finally the potential temperature difference between the upper and lower measurement level, $\Delta\theta$, is shown in Figure 6.3.10 for various summer and winter months. There is a strong diurnal pattern visible in summer months resulting in temperature inversions during the middle of the day which is not present in winter. This is most likely as a result of the solar heating effects during the summer months.

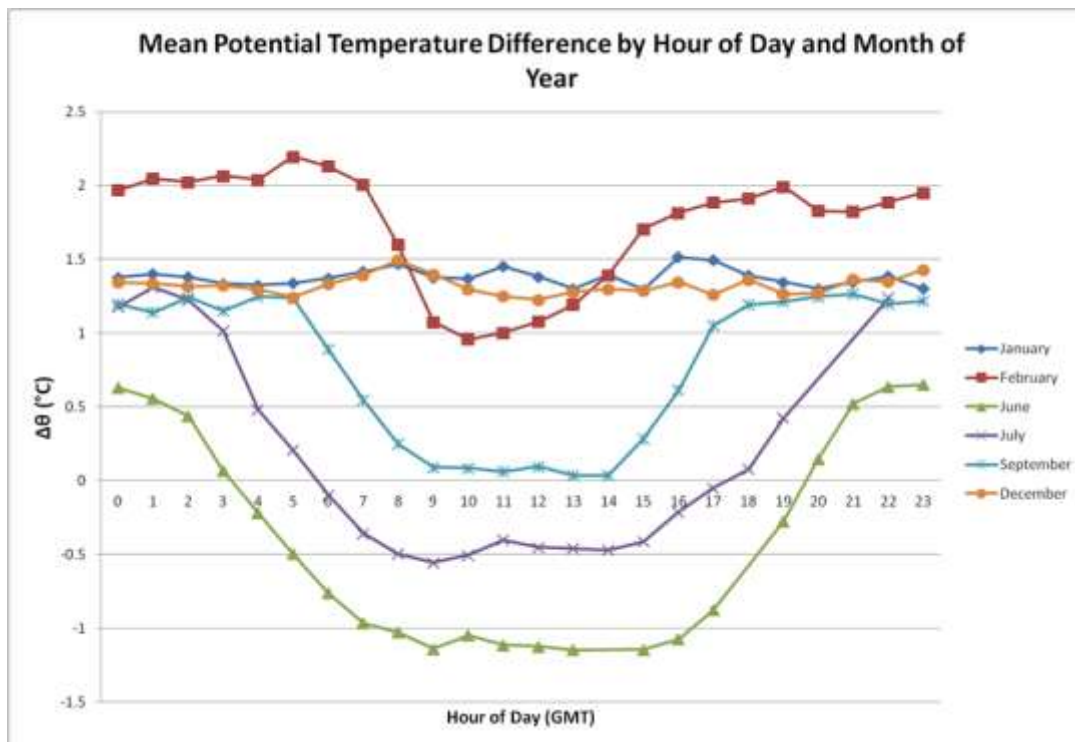


Figure 6.3.10: Mean Potential Temperature difference by Hour of day and Month of Year

M6282 RESULTS USING MEASURED AIR TEMPERATURE

The statistics for the Gradient Richardson Number for the M6282 mast are presented below using the measured air temperature in place of the potential temperature.

Time Period	Valid Observations	Unstable Stratification	Neutral Stratification	Stable Stratification
Full Year	15721	27.54%	48.86%	23.6%

Table 6.3.8: M6282 Percentage of time in each stability class

Time Period	Valid Observations	Unstable Stratification	Neutral Stratification	Stable Stratification
Nov	1518	2.44%	58.43%	39.13%
Dec - Feb	3481	11.58%	47.89%	40.53%
Mar-May	10722	36.28%	47.82%	15.90%
Jun-Jul	0	N/A	N/A	N/A

Table 6.3.9: M6282 Seasonal Variation of Atmospheric Stability

Note that no measurements were taken during June-October at the M6282 mast.

The comparable periods are shown in Table 6.3.10. It is evident that the gradient method shows a decrease in neutral observations at M6282 relative to M6261. It is unknown whether this effect is due to local conditions at the masts or due to the slightly different methods and instrumentation used for the M6282 calculation. It is hypothesized that there is more

mechanical mixing caused by the higher winds and better exposure at M626, increasing the prevalence of neutral conditions in Winter.

Time Period	Mast	Unstable Stratification	Neutral Stratification	Stable Stratification
Dec - Feb	M6261	0.81%	72.84%	26.35%
	M6282	11.58%	47.89%	40.53%
Mar-May	M6261	19.27%	63.86%	16.87%
	M6282	36.28%	47.82%	15.90%

Table 6.3.10: Comparison of results from nM6261 and M6282

As before, atmospheric stability classes are shown binned by wind speed, time of day and incoming solar radiation for the M6282 mast in Figures 6.3.11, 6.3.12 and 6.3.13. Similar patterns are evident to the M6261 results although the reduction in neutral observations is apparent.

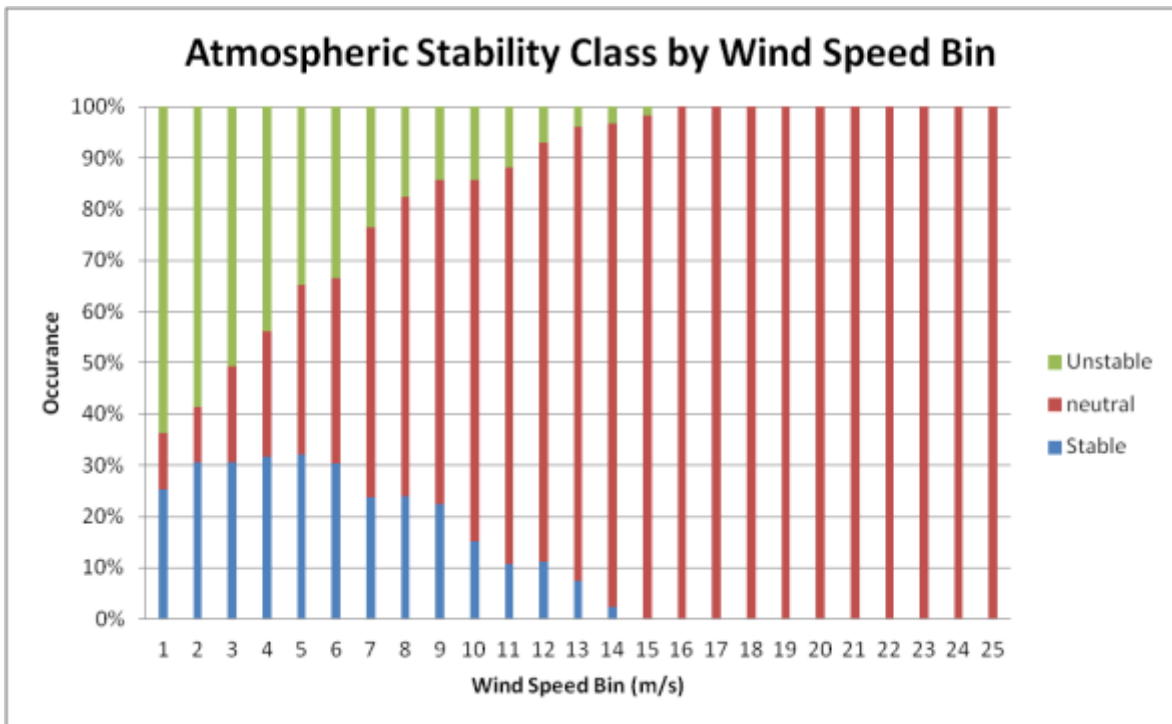


Figure 6.3.11: M6282 Stability Class by Wind Speed Bin

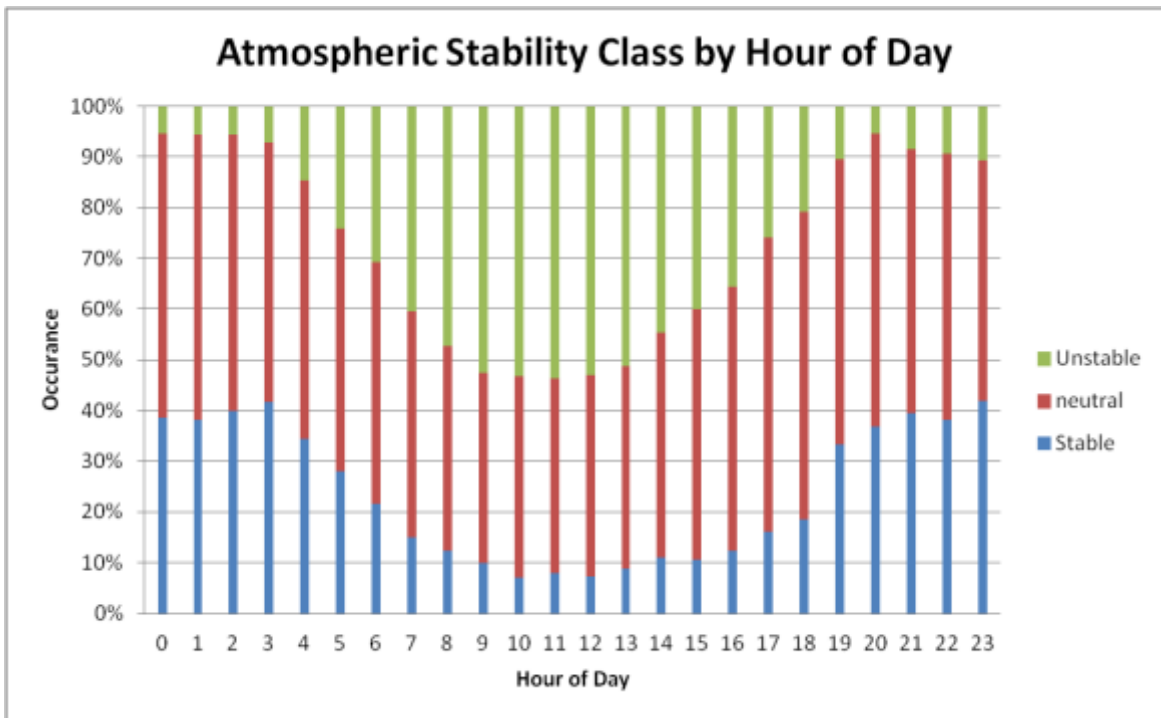


Figure 6.3.12: M6282 Atmospheric Stability Class by Hour of Day

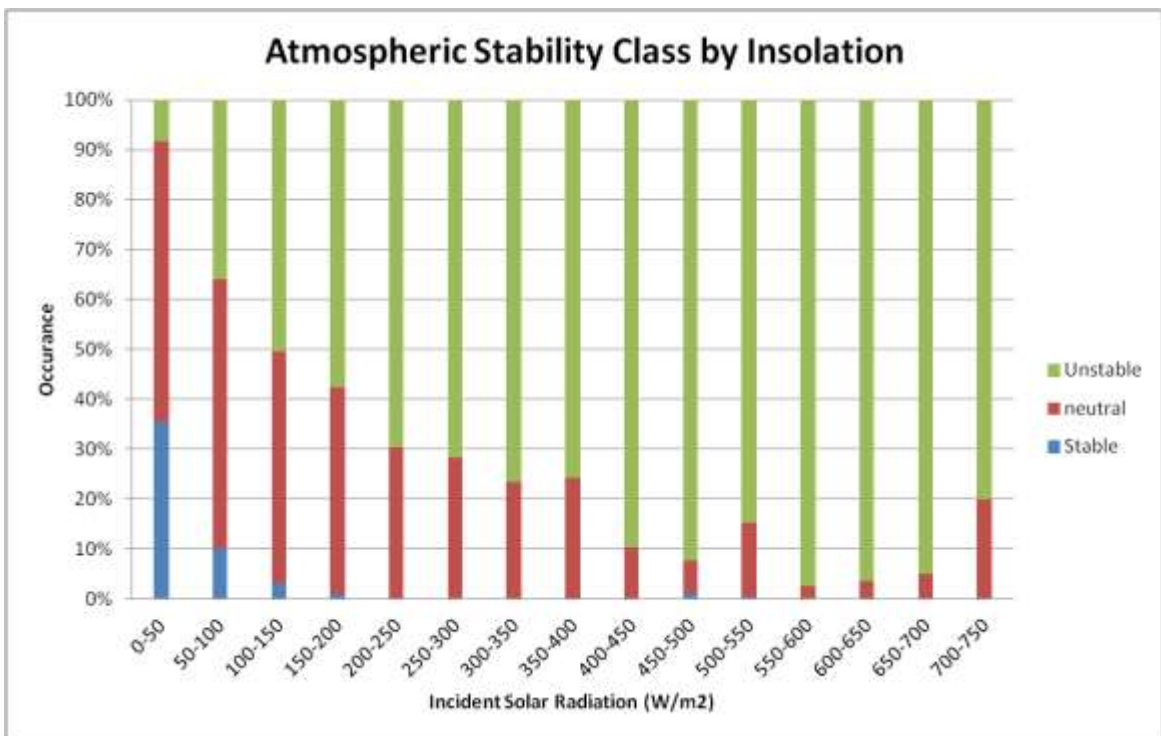


Figure 6.3.13: M6282 Atmospheric Stability Class by Insolation

6.3.4 IMPACT OF ATMOSPHERIC STABILITY ON SHEAR EXTRAPOLATION

This section presents the results of a comparison of shear and vertical extrapolation error as a function of atmospheric stability at the two atmospheric stability measurement mast locations discussed in the previous sections (M6261 & M6282).

METHODOLOGY

The analysis is based on wind speed, wind direction and temperature data measured at masts M6261 and M6282. The analysis followed the process described below:

- The 10-minute Richardson numbers were calculated for both masts from the 10-minute data measured following the methodology outlined in the atmospheric stability analysis (Section 6.3.2)³.
- 10-minute shear exponents were calculated on each mast. Table 6.3.11 below presents the calculation heights.

	M6261	M6282
Shear 1	72.6 m – 87.1 m	72.8 m – 87.3 m
Shear 2	50.1 m – 72.6 m	50.3 m – 72.8 m
Shear 3	30.1 m – 50.1 m	-
Global shear 1	50.1 m -87.1 m	50.3 m – 87.3 m
Global shear 2	30.1 m -87.1 m	-

Table 6.3.11: Shear combinations⁴

- The shear time series were then filtered to remove any measurements affected by the presence of wake effects from turbines under operation (See Table 5.3.1 in section 5.3.2). the data was also filtered to remove sectors affected by tower shadow:

	M6261	M6282
Tower shadow sector	165° - 225°	20° - 80°

Table 6.3.12: Direction sectors filtered at M6261 and M6282.

- The 10-minute shear exponents calculated were plotted against the 10-minute Richardson number.
- The atmospheric stability criteria presented in Table 6.3.5 of Section 6.3.2 were then highlighted on the charts.
- The wind speeds at 87.1 m on M6261 were vertically extrapolated to 96.0 m using the shear exponent presented in Table 6.3.13. The vertically extrapolated wind speeds were then compared to the measured wind speed at PP mast top measurement height, 96.0 m. Note that the shear exponent used was deemed the most suitable for this mast among several possible values calculated.

	Shear exponent	Methodology	Canopy height (m)	Anemometers used
M6261	0.149	Multi-Point Fitted Log-Law	10	87.1 m, 72.6m, 50.1 m

Table 6.3.13: Characteristics of the shear exponent used in the vertical extrapolation.

³ Note that due to the bad quality of the measurements of the sonic anemometers present on the masts, only one of the two methods to quantify the atmospheric stability could be used: the gradient method.

⁴ Note the anemometers used in this analysis were heated on M6282 and unheated on M6261.

RESULTS

Shear versus Richardson Number

All the charts in this section feature 10-minute shear exponents versus the 10-minute Richardson number. Note that the 10-minute Richardson numbers are mast-dependant. On each chart, the area in red relates to the neutral atmospheric state. The black area on the left is the unstable state, while the black area on the right relates to the stable state of the atmosphere.

M6261

Figure 6.3.14 below presents the 10-minute shear exponent plotted against the Richardson number at M6261.

When the atmosphere is stable, highest shear exponents are expected. It can be seen on Figure 6.3.14 that the atmospheric stability criterion is mostly in agreement with the shear exponents observed: the highest shear exponents are experienced in a stable atmosphere.

However, a significant part of the high-shear peak is happening in neutral atmosphere according to the criterion based on the Richardson number. Therefore, this may indicate that the criterion adopted using only the Richardson number may not always be the most accurate method of determining when high shear will occur. It could also be the case that the neutral conditions are coincident with wind directions where higher shear is present due to higher surface roughness.

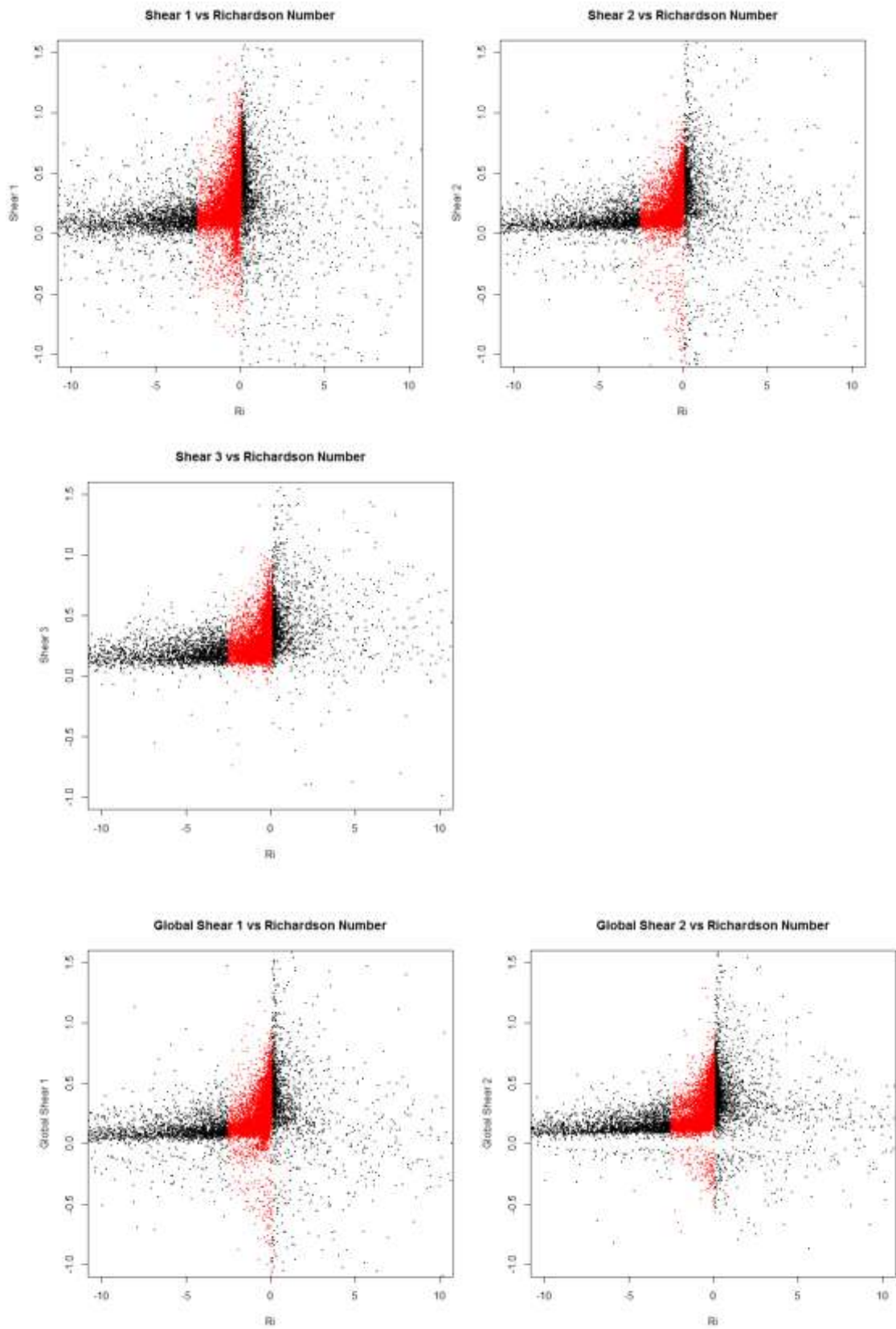


Figure 6.3.14: Shear exponents at different heights versus Richardson number at M6261.

M6282

Figure 6.3.15 below presents the 10-minute shear exponent plotted against the Richardson number at M6282.

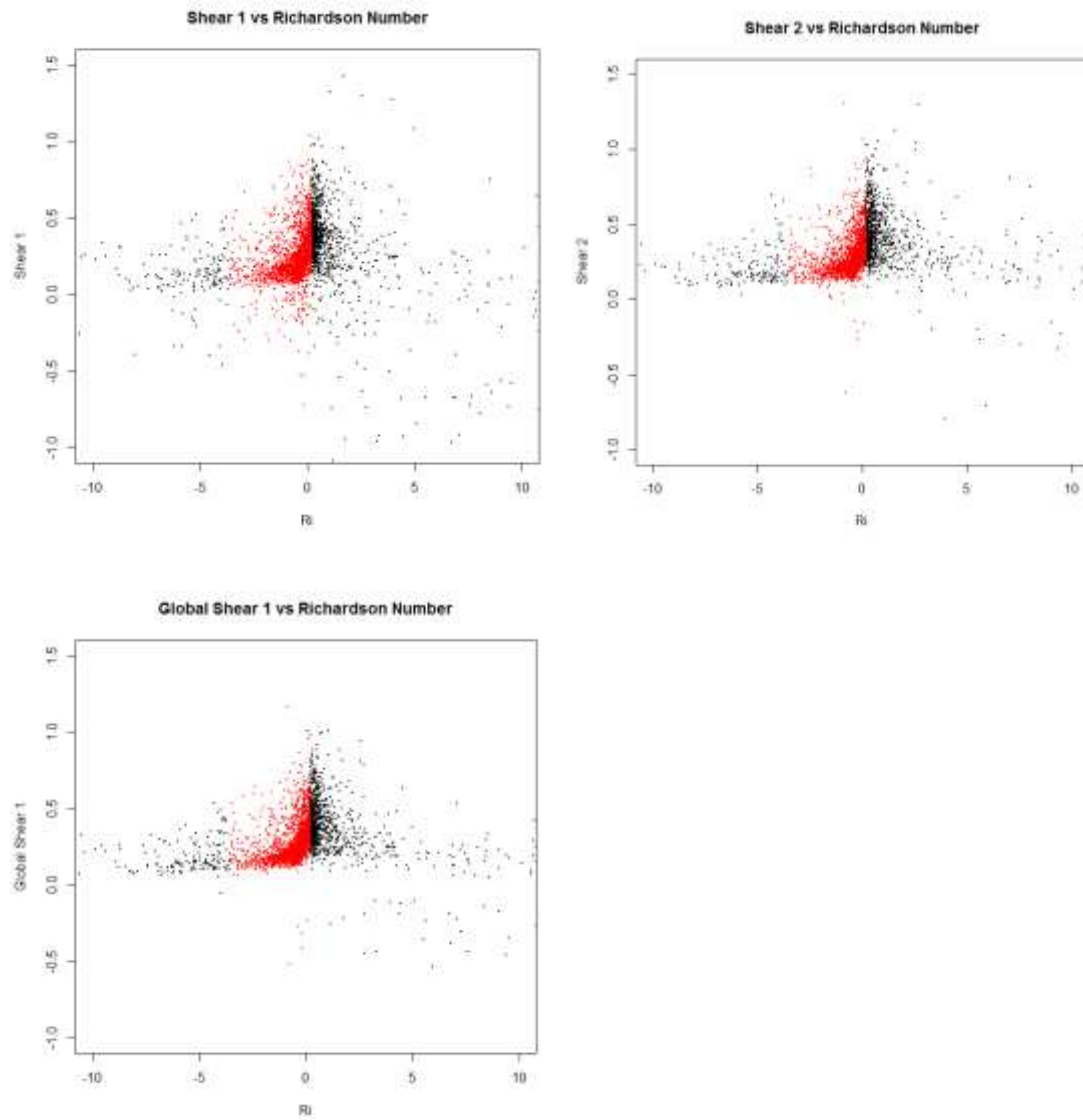


Figure 6.3.15: Shear exponents at different heights versus Richardson number at M6282.

The same observations as for mast M6261 can be made for mast M6282.

UNCERTAINTY IN VERTICALLY EXTRAPOLATED WIND SPEEDS AT M6261 VS. ATMOSPHERIC STABILITY

In order to assess the uncertainty related to the vertical extrapolation, and thus, the suitability of the use of a global shear exponent, the wind speed measured at 96.0 m was compared against the wind speed extrapolated using the global shear exponent (Table 6.3.11) from 87.1 m to 96.0 m.

Table 6.3.14 presents the difference between the two wind speeds for each of the three stability conditions.

	Unstable Atmosphere	Neutral Atmosphere	Stable Atmosphere	Global
Number of observations	7688	9045	808	17804
Mean difference [Vertically extrapolated at 96.0 m - Measured at 96.0 at Vector on M626] (m/s)	0.02	-0.09	-0.02	-0.04
Min (m/s)	-4.14	-3.89	-1.97	-4.14
Max (m/s)	8.22	5.97	2.36	8.22
stdDev (m/s)	0.563	0.364	0.352	0.462

Table 6.3.14: Difference between vertically extrapolated and measured wind speeds at 96.0m.

It can be observed that the extreme differences between 10-minute measured and extrapolated mean wind speeds are bigger for unstable and neutral atmospheres.

This result seems to go against the expectation of unusually high shears in stable atmosphere that would enlarge the gap between vertically extrapolated and measured wind speeds. However, these extremes could be based on only a few points and not be representative of the whole sample.

The absolute difference relative to the measured wind speed at 96.0 m was then calculated. Table 6.3.15 presents a few statistics related to this new index number.

	Unstable Atmosphere	Neutral Atmosphere	Stable Atmosphere	Global
Mean Absolute Relative Difference	2.23 %	2.47 %	7.04 %	2.58 %
Min	0.00 %	0.00 %	0.02 %	0.00 %
Max	42.97 %	32.36 %	59.05 %	59.05 %
Std Dev	0.031 %	0.026 %	0.076 %	0.034 %

Table 6.3.15: Relative difference between vertically extrapolated and measured wind speeds at 96.0m.

It can be seen in Table 6.3.14 that the mean absolute relative difference is much higher for stable atmosphere (7.04 %) than for neutral (2.47 %) and unstable (2.23 %) atmospheres.

In a stable atmosphere, the extrapolated wind speed thus seems to be further from the measured wind speed.

CONCLUSIONS

This analysis shows that determining the stability of the atmosphere based on the Richardson number gives satisfying results.

However, note that this atmospheric stability criterion needs to be handled very carefully as there are questions over the reliability of the gradient method for predicting the neutral class and the data used in this analysis come from measurements which were not specifically designed for implementing the gradient method in relation to atmospheric stability analysis.

The atmospheric stability criterion based on the Richardson number is not in perfect agreement with the shear exponents observed. This could be due to the design of the masts as stated above. Further work is required to verify or improve this method using measurements optimised for this kind of atmospheric stability analysis. Shear and turbulence intensity may be good complementary index rates to improve the methodology and better define the atmospheric stability criterion.

Comparing the extrapolated wind speed at 96.0 m with the measured wind speed at 96.0 m for each of the three stability conditions shows that vertically extrapolating the wind speed in a stable atmosphere using a global shear exponent could include some bias in the predicted wind speeds.

Therefore, it would be worth isolating the stable atmosphere events and adopting a specific methodology to vertically extrapolate the wind speeds during these occurrences. If the stable events' measurements were to be isolated and a shear exponent calculated from this data and applied to wind speed in order to vertically extrapolate wind speeds during stable atmosphere events, the bias may be reduced. Further work is required to verify this hypothesis.

Despite the measurement campaign lasting almost a year, the equivalent of only four months of data was used in this analysis. This is because part of the data was affected by icing, instrument failure, mast effects or wake effects. Given that stable atmospheric conditions occur mostly in winter, data filtered due to icing events may result in also filtering most of the events that show atmospheric stability. Therefore, the 4.5% of stable atmosphere observations is suspected to be unrepresentative of the reality: there may be much more stable events than what these figures suggest⁵. Some further analysis using measurements with a better availability over a full year of data or more could give useful complementary information to assess the bias introduced by the use of a global shear exponent to vertically extrapolate wind speeds.

⁵ Note that Section 6.3.1 records 23.6% of stable conditions over the period analysed but the two periods used are not comparable and different filtering criteria have been used.

6.3.5 RECOMMENDATIONS FOR FUTURE CAMPAIGNS

The cold climate R&D campaign highlighted various difficulties associated with measuring atmospheric stability, particularly in a cold climate. There are lessons that can be learnt for future campaigns in order to improve the scope and quality of atmospheric stability measurements.

If gradient based measurements are to be performed, all sensors should be located at the same level with as little a vertical separation as possible. At each level the following measurements should be taken:

- Wind speed
- Air temperature
- Atmospheric Pressure
- Relative humidity

And the wind direction should be measured at an intermediate measurement height.

Redundancy should be a large consideration for all instrumentation campaigns, thus redundant instrumentation with stand alone logging systems should be deployed. This will ensure as wide a data coverage as possible and give confidence in the results by allowing comparisons between the measured values of each redundant system.

Gradient measurements should be performed over multiple levels, as opposed to just two, which will also provide redundancy and additional confidence in the results.

For future atmospheric stability campaigns it would be beneficial to deploy a flux based atmospheric stability system in conjunction with the gradient measurements. This approach should eliminate some of the assumptions inherent in the Gradient Richardson Number and provide a more direct measurement of vertical thermally driven flow. The Monin-Obukhov Length could be measured directly by a flux system.

The downside of flux measurements is that more powerful and complex logging systems are required and three dimensional wind measurements are necessary. Given the very poor performance of the Metek USA-1 ultrasonic anemometers during this measurement campaign (see instrumentation statistics section), flux measurements in cold climates may prove difficult, but would offer improved stability measurements should a more robust ultrasonic anemometer be available.

6.4 EFFECT OF SHEAR ON AVAILABLE ENERGY

6.4.1 INTRODUCTION

Pre-construction energy yield predictions currently assume the hub height wind speed is representative of the wind speed across the whole rotor. For turbines with large rotor diameters, where the shear across the rotor is likely to be significant, this assumption is invalid.

The difference between the predicted and actual energy due to shear, $\delta\alpha$, is likely to have components due to the effect of shear on available energy and the turbine conversion efficiency:

$$\delta\alpha = \delta\alpha_A + \delta\alpha_p \quad \text{Equation 6.4.1}$$

where: $\delta\alpha_A$ = Energy difference due to the effect of shear on the available energy

$\delta\alpha_p$ = Energy difference due to the effect of shear on the turbine's conversion efficiency.

This work evaluates $\delta\alpha_A$ by comparing the energy predicted using the hub height wind speed and assuming no shear across the rotor with the energy predicted using a number of other wind speed calculation methods.

6.4.2 METHODOLOGY

The latest draft IEC PP standard 61400-12-1 [1 and section 7K.1 in Appendix 7K] recommends the use of the 'rotor-equivalent wind speed', v_{eq} , to better represent the energy available to the turbine. This is the wind speed corresponding to the kinetic energy flux through the rotor:

$$v_{eq} = \left(\sum_{i=1}^n v_i^3 \frac{A_i}{A} \right)^{\frac{1}{3}} \quad \text{Equation 6.4.2}$$

where: n = number of measurement heights ($n \geq 3$)

v_i = wind speed measured at height i

A = total area swept by the rotor

A_i = area of the i^{th} segment.

The IEC standard intends Equation 6.4.2 to be used with wind speeds measured at several heights across the rotor. However, it can also be used to derive the rotor equivalent wind speed theoretically. In this case, the wind speed at several heights is first calculated by applying the two point power law with an assumed shear exponent to the hub height wind speed, v_{hh} .

In either case, the segments are defined such that the horizontal division lines are equidistant between each pair of measurement heights. The top and bottom segments extend to the edge of the rotor disk. See Figure 6.4.1.

It is assumed that the available energy would be perfectly represented by a v_{eq} derived from wind speeds at an infinite number of rotor segments. Therefore, $\delta\alpha_A$ is defined as the difference between the energy yields calculated with the rotor equivalent wind speed and the hub height wind speed:

$$\delta\alpha_A = \frac{(E_{Shear} - E_{hub})}{E_{hub}} \quad \text{Equation 6.4.3}$$

where: E_{shear} = energy calculated using v_{eq}

E_{hub} = energy calculated using v_{hh} which assumes there is no shear across the rotor.

Two pieces of analysis are described in this report. In the first (Theoretical V_{EQ}), $\delta\alpha_A$ was evaluated with the theoretical v_{eq} derived with a large number of segments for a range of combinations of shear exponent and mean v_{hh} . In the second (Time Series Analysis), a time series based energy yield model was used with data from Havsnäs Wind Farm. The energy difference $\delta\alpha_A$ was calculated for a number of types of v_{eq} , derived from combinations of measured LiDAR data and derived shear exponents. The time series energy results are also examined by time of day.

As three of the 48 x V90 turbines at Havsnäs are de-rated from 2MW to 1.8MW, two power curve cases are presented. The hub height of all turbines on site is 95m, however this analysis takes the hub height to be 97.5m as this is the central LiDAR measurement. No comparisons with measured production data are used in this study so this assumption is valid.

THEORETICAL V_{EQ}

The theoretical v_{eq} was calculated for a range of combinations of v_{hh} and shear exponent. A large number of rotor segments (91) was used so that the theoretical profile was described at high-resolution across the rotor height. For each value of v_{eq} , the theoretical power was looked up from the warranted power curve (both 1.8MW and 2MW cases). The ratios of these powers with the corresponding no shear cases gave the power ratio for each combination of wind speed and shear.

For each combination of v_{hh} and shear exponent, a theoretical energy yield ratio was then derived by convolving the appropriate power ratio results with a Weibull wind speed distribution with the given mean. A Weibull shape factor of 2 was assumed in every case.

Note that it is unlikely that the real wind speed frequency distribution is well described by a Weibull distribution at all heights during the whole year. The simulation also assumes the wind speed profile is perfectly described by a theoretical power law and that the shear exponent is constant.

The results show how the effect of using v_{eq} depends on the mean wind speed (measured at hub height) and shear exponent. The results are quite sensitive to the site air density due to the density adjustment applied to the power curve. The power curves used here were adjusted to the long term average density of the Havsnäs Ritjelsberget hill. Warranted power curves have been used in this analysis to convert wind speed to power in order to be consistent with common energy yield prediction methodologies.

TIME SERIES ANALYSIS WITH LIDAR DATA

Wind speed time series

Ten-minute wind speed data were collected by a LiDAR on Havsnäs Ritjelsberget hill, situated close to the PP turbine D2. Measurements were made at 9 heights, spaced symmetrically about the hub height, for one year, excluding the months August, September and October.

The LiDAR data set was filtered to exclude the following:

- Timestamps with any wind speed measurements or hub height wind direction measurement missing
- Timestamps with less than 90% data capture at any measurement height
- Timestamps with hub height direction in a sector affected by turbine wakes.

To examine the seasonal variation in the wind speed profile, the filtered LiDAR data were aggregated into monthly average profiles. This identified a difference between the average profiles for summer and winter months so the data were then aggregated into hourly average profiles for each of the seasons separately. These are shown in the time series analysis results in Section 6.4.4.

Time series of three shear exponents were derived from the filtered LiDAR data using different measurement height pairs to define the shear exponent:

Shear Case		Measurement heights (metres AGL)	
Lower rotor half	α_{Lower}	52.5	97.5
Upper rotor half	α_{Upper}	97.5	142.5
Full rotor	$\alpha_{\text{RotorFull}}$	52.5	142.5

Table 6.4.1: Shear cases

The shear exponents were calculated using the two point power law presented in Equation 6.4.4 where v_1 and v_2 are the LiDAR measured wind speeds at heights h_1 and h_2 respectively.

$$\alpha = \frac{\ln(v_1 / v_2)}{\ln(h_1 / h_2)} \quad \text{Equation 6.4.4}$$

The filtered LiDAR data and shear time series were used to generate the following wind speed time series. In cases B-E the segments were defined as shown in Figure 6.4.1.

- A. v_{hh} : hub height wind speed, assuming no shear across the rotor
- B. $v_{eq_AllLiDAR}$: v_{eq} calculated directly using all the LiDAR measurement heights
- C. v_{eq_Lower} : v_{eq} calculated using the LiDAR hub height wind speed and speeds generated at the other 8 heights using α_{Lower}
- D. v_{eq_Upper} : v_{eq} calculated using the LiDAR hub height wind speed and speeds generated at the other 8 heights using α_{Upper}
- E. $v_{eq_RotorFull}$: v_{eq} calculated using the LiDAR hub height wind speed and speeds generated at the other 8 heights using $\alpha_{\text{RotorFull}}$

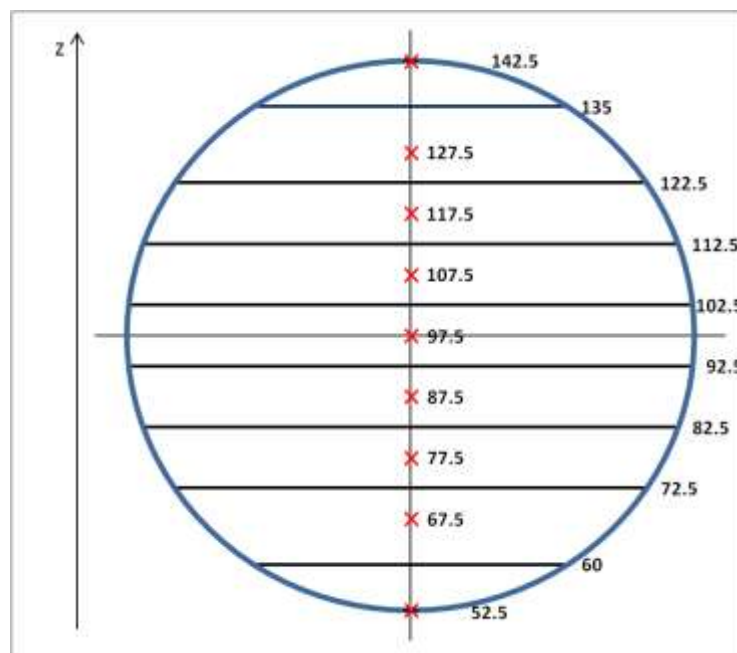


Figure 6.4.1: Segments used for v_{eq} with LiDAR wind speeds measurements (Heights in metres AGL)

Time series EY model

A time series based energy yield model was then used to create time series of predicted energy yield from each input wind speed time series. This performs the full energy yield calculation, including topography, roughness and wake modelling for each ten-minute timestamp.

To avoid the introduction of error due to the wake and topography model, the time series model was run for a single turbine (1.8MW and 2.0MW cases) at the location of the LiDAR. The model was also run for the same cases for the whole wind farm layout, from which the results for the D2 turbine could be extracted for comparison with PP test results. D2 is less than 220m from the LiDAR location with little change in altitude so the speed up due to topography is very small.

The results show $\delta\alpha_A$ for each v_{eq} case normalised to the no shear case. It is assumed the available energy is best described by the v_{eq} calculated directly using all the LiDAR measurement heights. Therefore, how well it is described by each other v_{eq} case is judged by the similarity between that $\delta\alpha_A$ and the $\delta\alpha_A$ for the ALLiDAR case.

6.4.3 JUSTIFICATION

The current methodology for pre-construction energy yields, widely used in the wind energy industry, assumes there is no shear across the rotor. Alternatives to this assumption include using RS devices or more anemometers to obtain measurements over the whole rotor height which can then be combined into a rotor equivalent wind speed. This study aims to evaluate the magnitude of the difference this could make to the energy yield predicted. In this context, in the interest of practicality, the possible merits of using multiple anemometers and shear exponents versus RS devices are considered.

6.4.4 RESULTS

As defined by Equation 6.4.3, the energy difference $\delta\alpha_A$ is positive when the use of v_{hh} underestimates the energy yield and negative when the energy yield is overestimated. In these cases, $\delta\alpha_A$ is referred to as an energy gain and an energy loss respectively (i.e. using v_{eq} appears as an apparent energy loss or gain as compared to the current energy yield methodologies which use v_{hh} .)

THEORETICAL V_{EQ}

Figures 6.4.2 - 6.4.5 show $\delta\alpha_A$ for a 1.8MW and 2.0MW turbine for a range of combinations of mean v_{hh} and constant shear exponent α .

For all mean v_{hh} , the model predicts an energy loss for $0 < \alpha \leq 0.33$ and an energy gain for higher or lower values of α . The magnitude of the loss or gain depends on the v_{hh} .

For a given constant v_{hh} , i.e. not a Weibull distribution, $\delta\alpha_A$ is zero below turbine cut-in and above rated wind speed. It is greatest when the v_{hh} is just above cut-in, decreasing in magnitude with increasing v_{hh} . For the cases of a v_{hh} Weibull distribution, Figures 6.4.2 - 6.4.5, this trend with wind speed is smoothed.

Note these theoretical results take account of the Weibull v_{hh} distribution but assume the shear exponent is constant in each case. In reality, the shear exponent is likely to vary considerably with the season and time of day. The effect of this is shown in the following section on the time series analysis with LiDAR data.

These results are marginally dependent on the turbine model, even though the turbine dimensions remain unchanged. This is due to differences between the warranted power curves: it is expected they account for aerodynamic behaviour of the turbine within a range shear and turbulence conditions. However, as the results are ratios of energy (with both energies calculated with the same warranted

power curve), it is expected that this effect is small compared to the effect of shear on the available energy, as is shown by the small differences between the 1.8MW and 2MW cases.

$\alpha \backslash$ mean v_{hh}	1.0	2.0	3.0	4.0	5.0	6.0	7.0	8.0	9.0	10.0	11.0	12.0	13.0	14.0	15.0
-0.10	0.00	0.14	0.53	0.79	0.88	0.88	0.82	0.75	0.66	0.59	0.52	0.46	0.41	0.37	0.33
-0.05	0.00	0.06	0.22	0.32	0.36	0.37	0.34	0.31	0.28	0.25	0.22	0.20	0.18	0.16	0.14
0.00	0.00	0.00	0.00	0.00	0.00	0.00	0.00	0.00	0.00	0.00	0.00	0.00	0.00	0.00	0.00
0.05	0.00	-0.04	-0.14	-0.20	-0.24	-0.24	-0.23	-0.21	-0.19	-0.17	-0.16	-0.14	-0.12	-0.11	-0.10
0.10	0.00	-0.06	-0.23	-0.34	-0.39	-0.39	-0.38	-0.35	-0.32	-0.28	-0.25	-0.23	-0.20	-0.18	-0.16
0.15	0.00	-0.08	-0.27	-0.39	-0.45	-0.46	-0.44	-0.41	-0.37	-0.33	-0.30	-0.27	-0.24	-0.21	-0.19
0.20	0.00	-0.07	-0.26	-0.38	-0.44	-0.45	-0.43	-0.40	-0.36	-0.32	-0.29	-0.26	-0.23	-0.21	-0.18
0.25	0.00	-0.06	-0.20	-0.29	-0.34	-0.35	-0.33	-0.31	-0.28	-0.25	-0.22	-0.20	-0.18	-0.16	-0.14
0.30	0.00	-0.03	-0.10	-0.14	-0.16	-0.17	-0.16	-0.15	-0.13	-0.12	-0.11	-0.10	-0.09	-0.08	-0.07
0.35	0.00	0.02	0.06	0.08	0.09	0.10	0.09	0.09	0.08	0.07	0.06	0.06	0.05	0.04	0.04
0.40	0.00	0.08	0.30	0.44	0.49	0.50	0.47	0.42	0.38	0.34	0.30	0.26	0.23	0.21	0.19
0.45	0.00	0.17	0.61	0.90	1.01	1.01	0.94	0.85	0.76	0.67	0.59	0.53	0.47	0.42	0.37
0.50	0.00	0.27	0.98	1.44	1.62	1.61	1.50	1.36	1.21	1.07	0.94	0.83	0.74	0.66	0.59

Figure 6.4.2: δa_A for 1.8MW turbine.

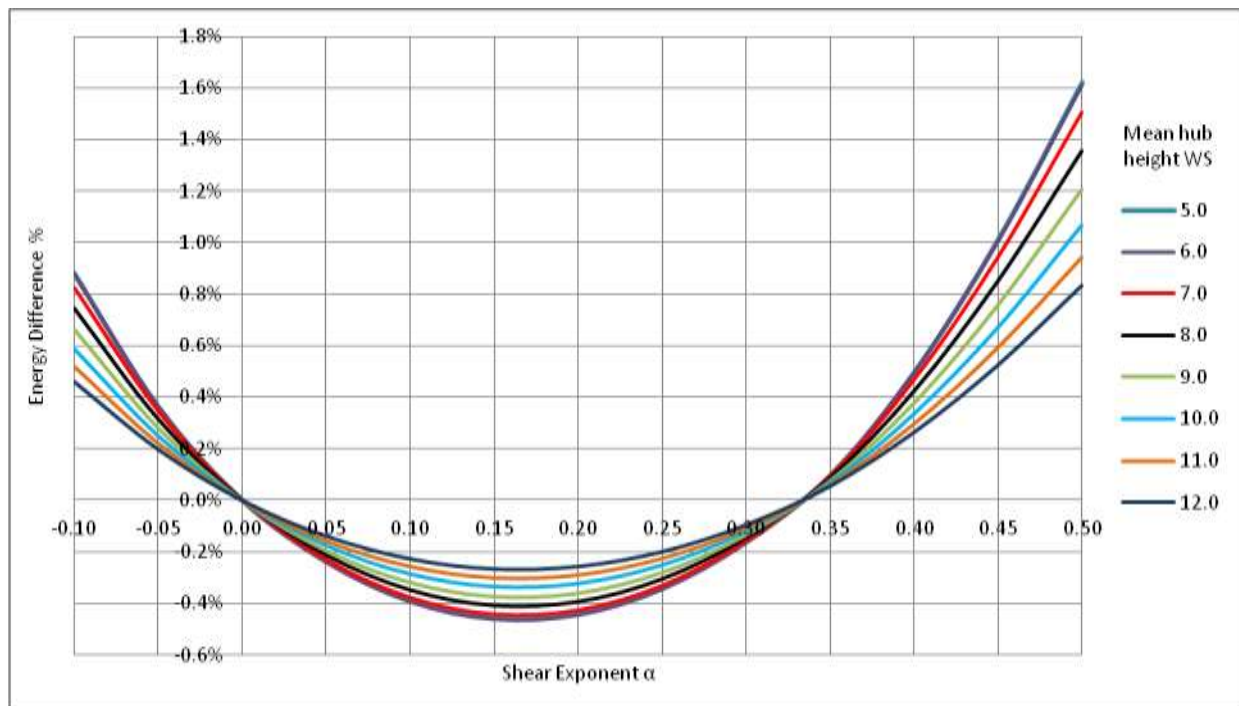


Figure 6.4.3: δa_A for 1.8MW turbine.

$\alpha \backslash$ mean v/h	1.0	2.0	3.0	4.0	5.0	6.0	7.0	8.0	9.0	10.0	11.0	12.0	13.0	14.0	15.0
-0.10	0.00	0.12	0.44	0.65	0.75	0.77	0.74	0.69	0.63	0.57	0.51	0.46	0.41	0.37	0.33
-0.05	0.00	0.05	0.19	0.28	0.33	0.34	0.33	0.30	0.28	0.25	0.22	0.20	0.18	0.16	0.15
0.00	0.00	0.00	0.00	0.00	0.00	0.00	0.00	0.00	0.00	0.00	0.00	0.00	0.00	0.00	0.00
0.05	0.00	-0.04	-0.14	-0.21	-0.24	-0.25	-0.24	-0.22	-0.20	-0.18	-0.16	-0.15	-0.13	-0.12	-0.11
0.10	0.00	-0.07	-0.23	-0.34	-0.39	-0.40	-0.39	-0.36	-0.33	-0.30	-0.27	-0.24	-0.22	-0.19	-0.17
0.15	0.00	-0.08	-0.27	-0.40	-0.46	-0.47	-0.46	-0.43	-0.39	-0.35	-0.31	-0.28	-0.25	-0.23	-0.20
0.20	0.00	-0.07	-0.26	-0.38	-0.44	-0.46	-0.44	-0.41	-0.37	-0.34	-0.30	-0.27	-0.24	-0.22	-0.20
0.25	0.00	-0.06	-0.20	-0.30	-0.34	-0.35	-0.34	-0.32	-0.29	-0.26	-0.24	-0.21	-0.19	-0.17	-0.15
0.30	0.00	-0.03	-0.10	-0.14	-0.16	-0.17	-0.16	-0.15	-0.14	-0.13	-0.11	-0.10	-0.09	-0.08	-0.07
0.35	0.00	0.02	0.06	0.08	0.10	0.10	0.09	0.09	0.08	0.07	0.07	0.06	0.05	0.05	0.04
0.40	0.00	0.07	0.25	0.38	0.43	0.45	0.43	0.40	0.37	0.33	0.30	0.26	0.24	0.21	0.19
0.45	0.00	0.14	0.50	0.74	0.85	0.87	0.84	0.79	0.72	0.65	0.58	0.52	0.46	0.42	0.38
0.50	0.00	0.22	0.79	1.17	1.35	1.39	1.34	1.25	1.13	1.02	0.92	0.82	0.74	0.66	0.60

Figure 6.4.4: δa_A for 2MW turbine.

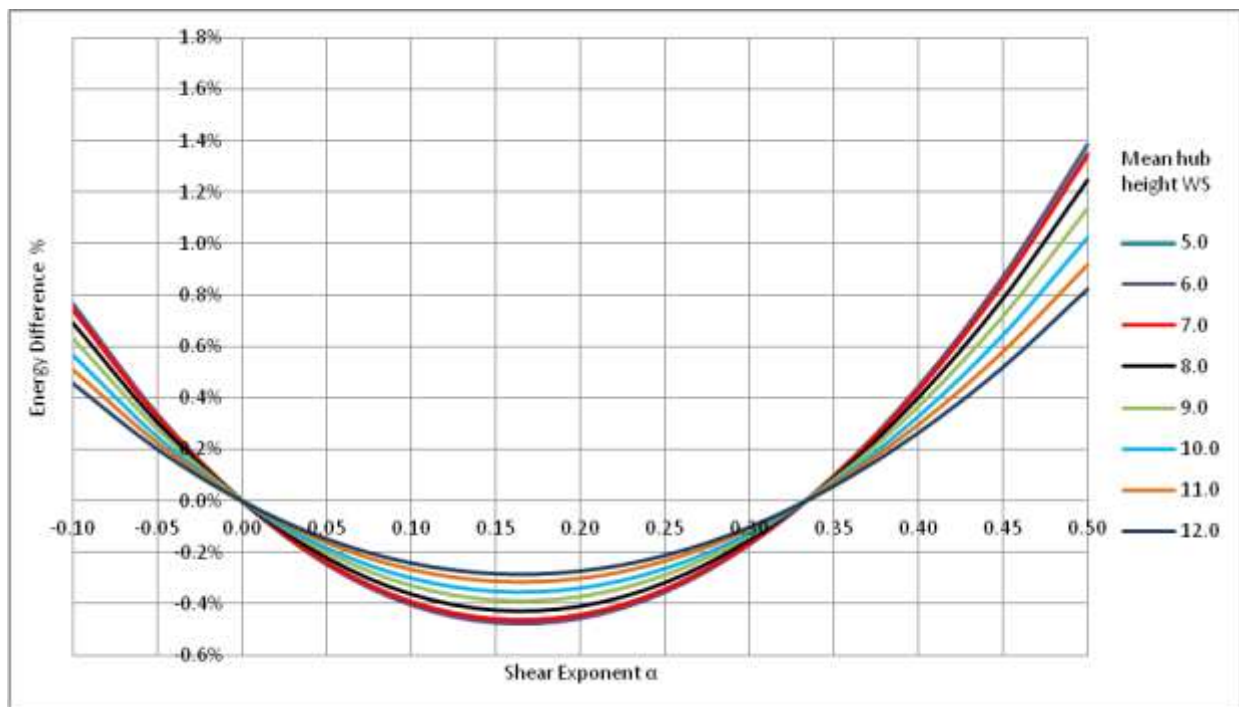


Figure 6.4.5: δa_A for 2MW turbine.

TIME SERIES ANALYSIS WITH LIDAR DATA

Average wind speed profiles

The average monthly LiDAR wind speed profiles are shown in Figure 6.4.6. The average profiles for the warmer months (Apr-Jul, “summer”) generally show lower shear than the colder months (Nov-Mar, “winter”)⁶. This is as we expect from the atmospheric stability discussion (Section 6.3) and the CFD study (Section 7.8.2), as the thermal effects, which are more common in the summer, increase

⁶ Note that no LiDAR data were collected during the months August, September or October.

the vertical mixing, leading to reduced shear. The shape of some of the winter profiles - increased shear high up - is also indicative of stable conditions.

The average hourly LiDAR profiles using data from the whole measurement period show no clear diurnal trend. However, the average hourly profiles for the separate seasons (Figures 6.4.8 and 6.4.9) show strong diurnal variation in the summer, with higher shear in the day time. Again, this is consistent with expectation from the stability theory and the CFD results. The hourly data coverage is shown in Figure 6.4.7.

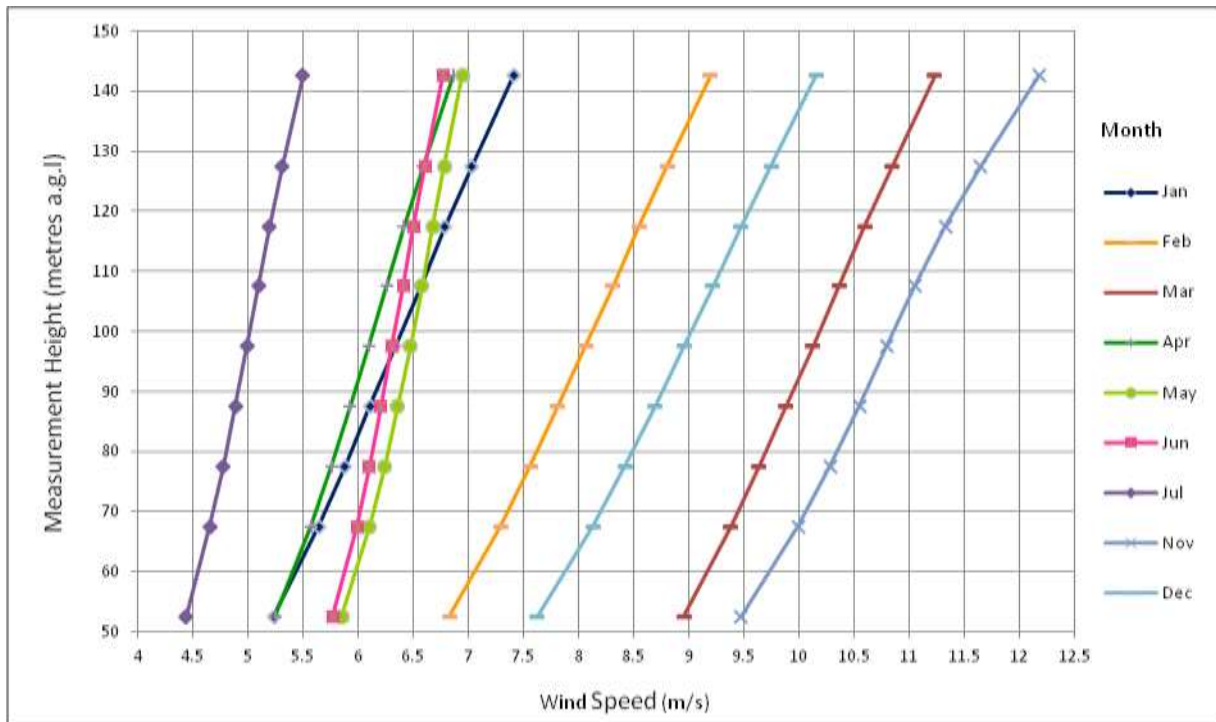


Figure 6.4.6: Average monthly LiDAR profiles

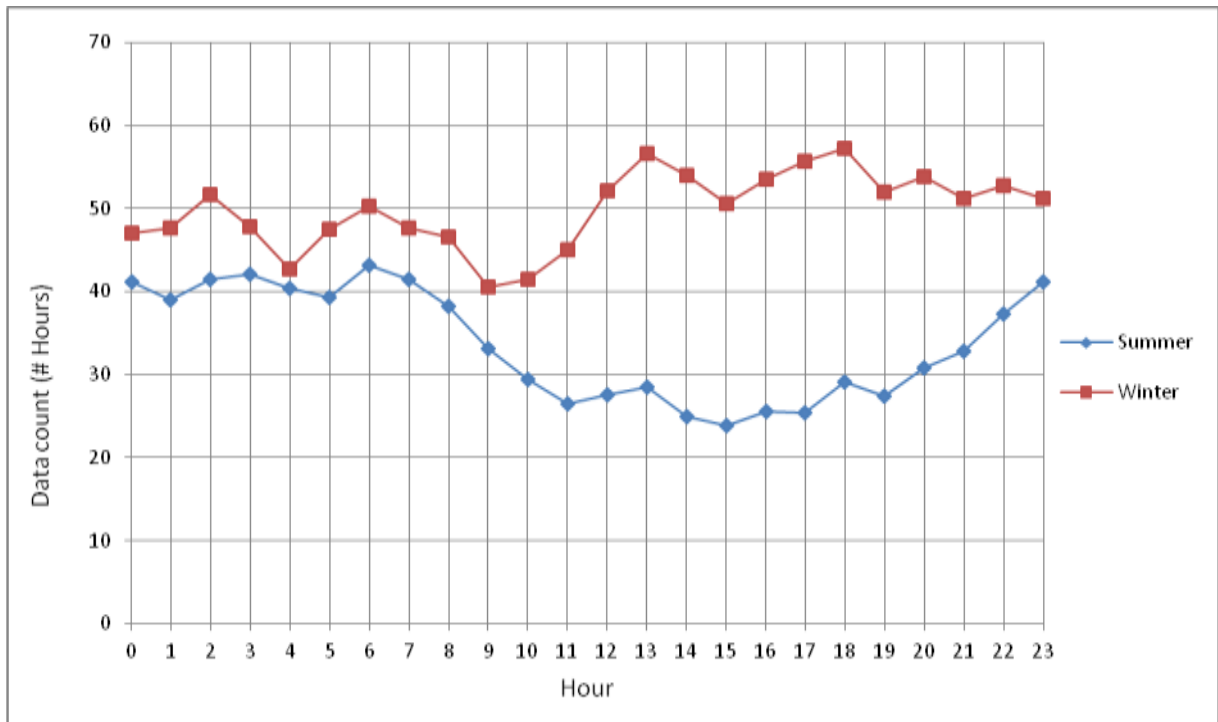


Figure 6.4.7: Hourly data coverage

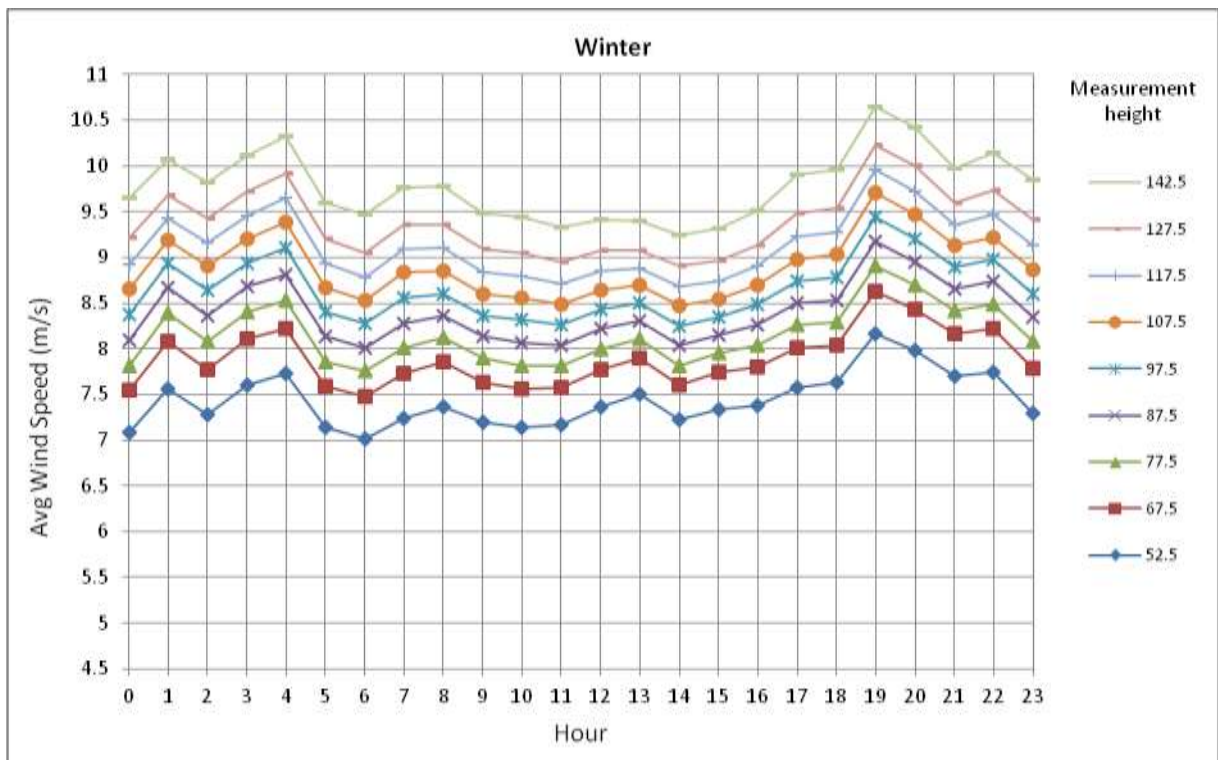


Figure 6.4.8: Hourly average LiDAR wind speeds - Winter

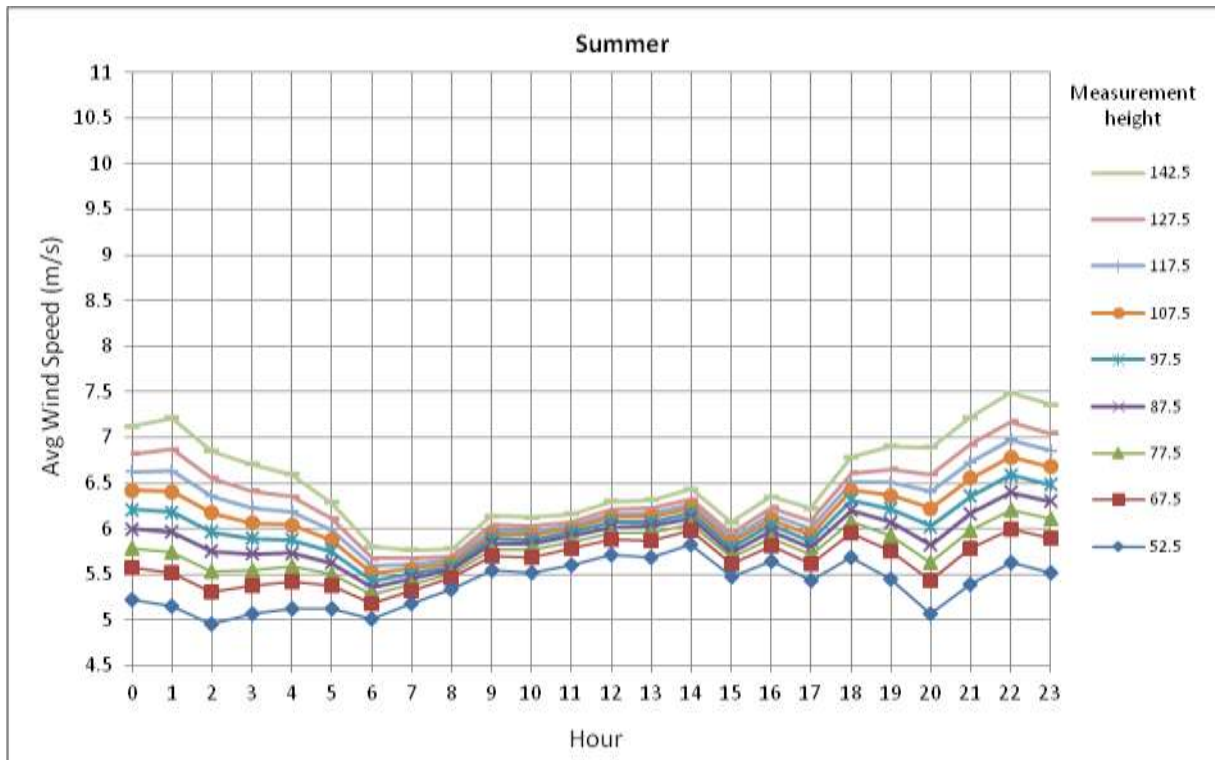


Figure 6.4.9: Hourly average LiDAR wind speeds - Summer

Shear time series

Details of the shear time series derived from the LiDAR data and used to generate the time series of v_{eq} are shown in Table 2. Note the large spread of values in all three cases.

Shear Case	Mean	Standard Deviation	Min	Max
α_{Lower}	0.236	0.225	-1.866	2.443
α_{Upper}	0.304	0.309	-3.889	3.419
$\alpha_{RotorFull}$	0.262	0.216	-1.410	2.393

Table 6.4.2: Shear time series details

Average shear exponents have also been derived for mast M6261. Although this mast was only 51m from the LiDAR used in this study, no comparison can be drawn with the shear values quoted for each as different data periods and measurement heights were used.

Time series energy comparisons

The results of the time series energy yield model runs were summed over the whole data period and $\delta\alpha_A$ calculated for five combinations of shear cases (Table 6.4.3 and Figure 6.4.10).

The rotor equivalent wind speed $v_{eq_AllLiDAR}$ is the draft IEC recommendation for best practice. The energy difference $\delta\alpha_A$ for the comparison $v_{eq_AllLiDAR}$ vs v_{hh} indicates the full error in our current energy yield due to the effect of shear on the available energy. Each other v_{eq} case was compared to v_{hh} to ascertain the extent to which it represents the available energy.

The case $v_{eq_AllLiDAR}$ vs v_{eq_Lower} was calculated to show the error that remains if v_{eq_Lower} is used. Measurement across the lower rotor half is the most likely alternative to RS as mounting anemometers at the height of top of the rotor is unlikely to be cost effective.

Shear Comparison		Energy difference due to available energy, $\delta\alpha_A$		
		2MW turbine	1.8MW turbine	2MW PP turbine
1	$v_{eq_AllLiDAR}$ vs v_{hh}	0.79%	0.80%	0.81%
2	v_{eq_Lower} vs v_{hh}	0.12%	0.14%	0.12%
3	v_{eq_Upper} vs v_{hh}	0.49%	0.50%	0.49%
4	$v_{eq_FullRotor}$ vs v_{hh}	0.11%	0.13%	0.11%
5	$v_{eq_AllLiDAR}$ vs v_{eq_Lower}	0.67%	0.66%	0.69%

Table 6.4.3: Energy differences between shear cases - whole data period

The theoretical comparison (Figures 6.4.2 to 6.4.5) predicts that using v_{eq} rather than v_{hh} results in an energy loss for all values of v_{hh} for shear exponents in the range ~ 0.0 - 0.33 . The averages of all three shear exponent time series (Table 6.4.2) are in this range. However, the time series model predicts an energy gain for all cases (Table 6.4.3 and Figure 6.4.10). This is due to each shear time series including a number of timestamps with high positive and negative exponents. The sensitivity of $\delta\alpha_A$ to the shear exponent, shown in Figures 6.4.3 and 6.4.5, means the total $\delta\alpha_A$ calculated for an extended time period will be skewed towards more positive values by any small number of data points with very high or very low shear.

Note that v_{hh} is taken from LiDAR data. In reality, for energy yields that do not use rotor equivalent wind speed, the v_{hh} is sometimes obtained by extrapolating up from below hub height measurements. This introduces additional uncertainty to the $\delta\alpha_A$ calculation.

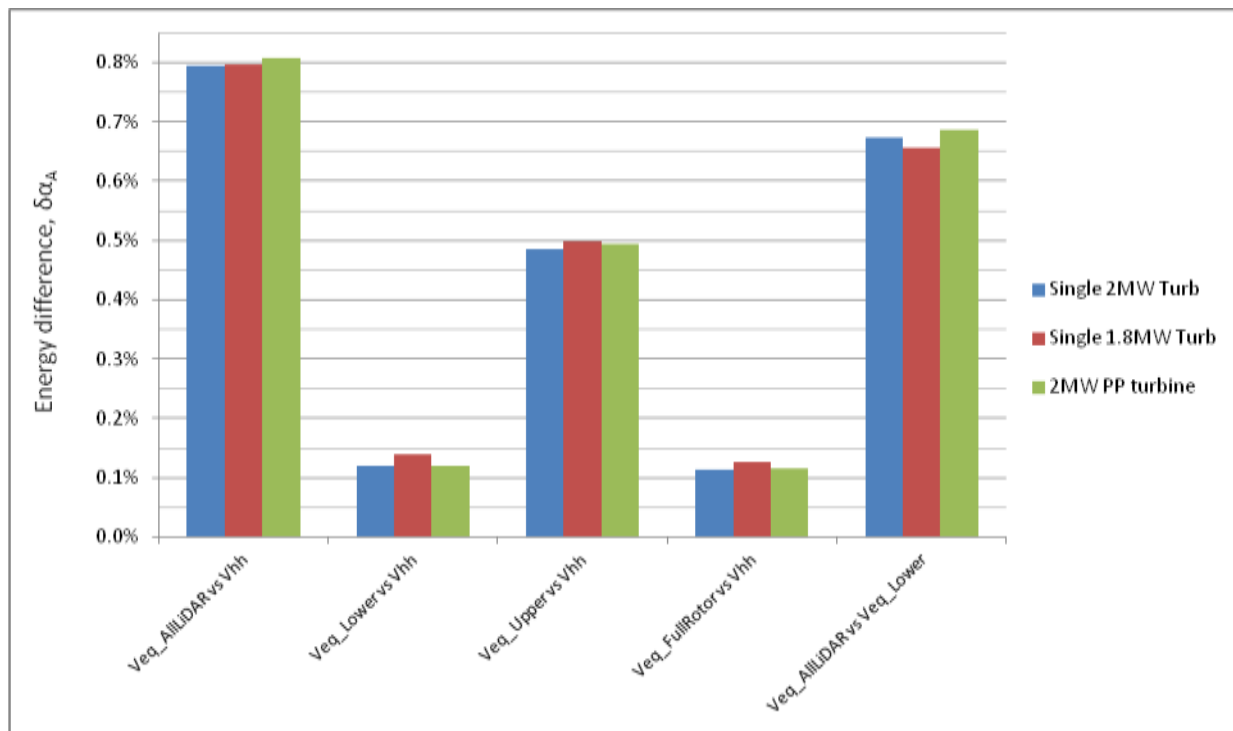


Figure 6.4.10: Energy differences between shear cases - whole data period

The results are very similar for the single 2MW and 1.8MW turbines at the LiDAR location so the seasonal hourly results are shown for the 2MW case only in Figures 6.4.11- 6.4.14. The same trends are observed in the seasonal hourly results for the PP test turbine.

It is assumed that the available energy is best described by $v_{eq_AllLiDAR}$. The plots of average hourly $\delta\alpha_A$ (Figures 6.4.11 and 6.4.13) for this case show the energy yield is currently underestimated quite consistently by approximately 1% in winter months. In summer, it is underestimated at night but overestimated during the day.

The ability of the other v_{eq} cases to describe the available energy can be judged by the similarity of each $\delta\alpha_A$ to the $\delta\alpha_A$ of the $v_{eq_AllLiDAR}$ case. In winter, $\delta\alpha_A$ of the v_{eq_Upper} case is consistently closest to the $v_{eq_AllLiDAR}$ case. In summer, $\delta\alpha_A$ of the v_{eq_Upper} case is closest to the $v_{eq_AllLiDAR}$ case at night but most different during the day when the average shear is low and $\delta\alpha_A$ is negative.

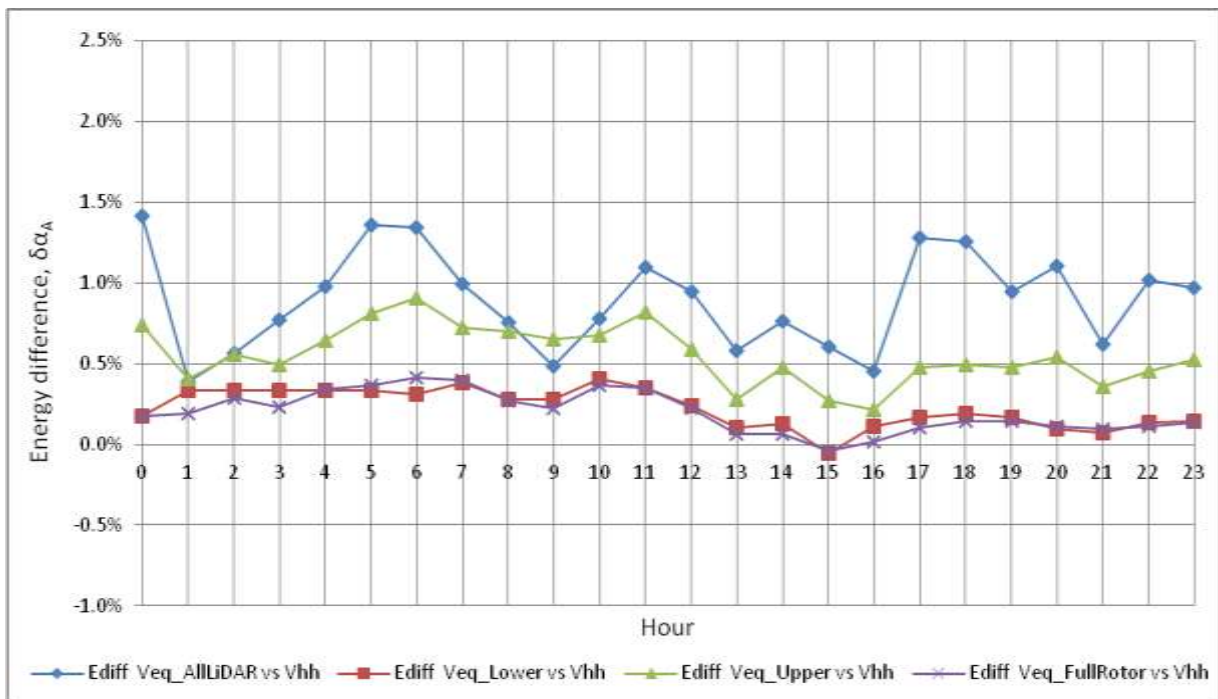


Figure 6.4.11: 2MW turbine at LiDAR location - Hourly mean energy differences - Winter

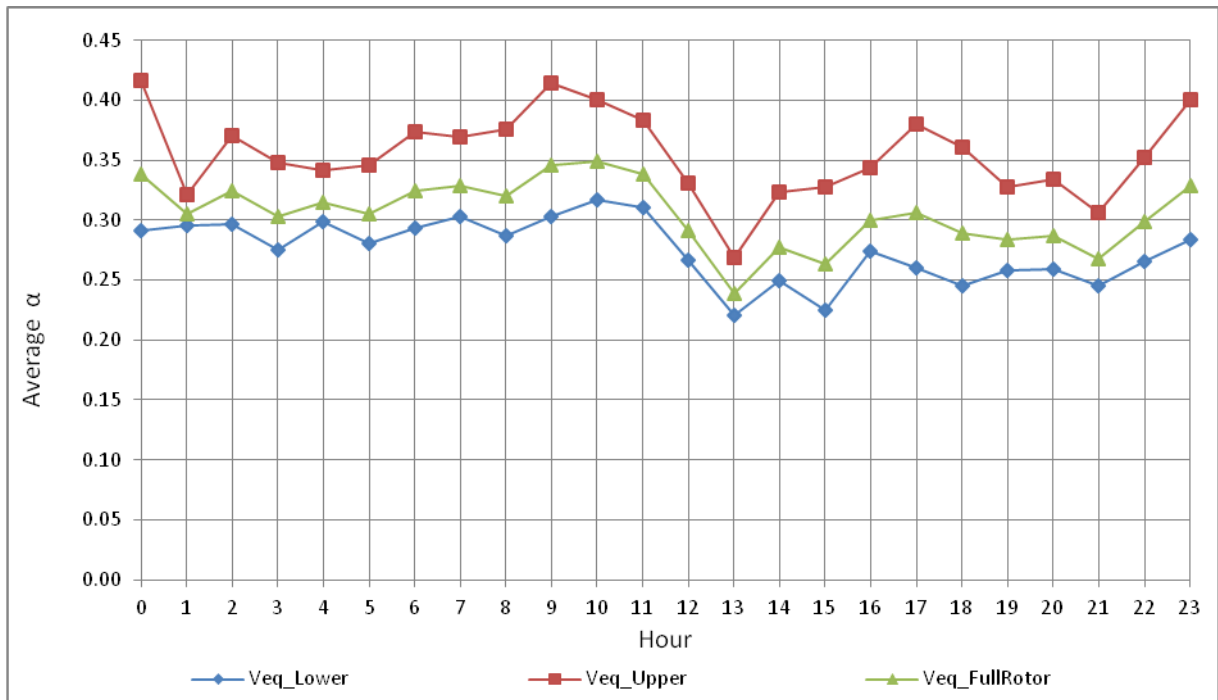


Figure 6.4.12: 2MW turbine at LiDAR location - Hourly mean shear exponents - Winter

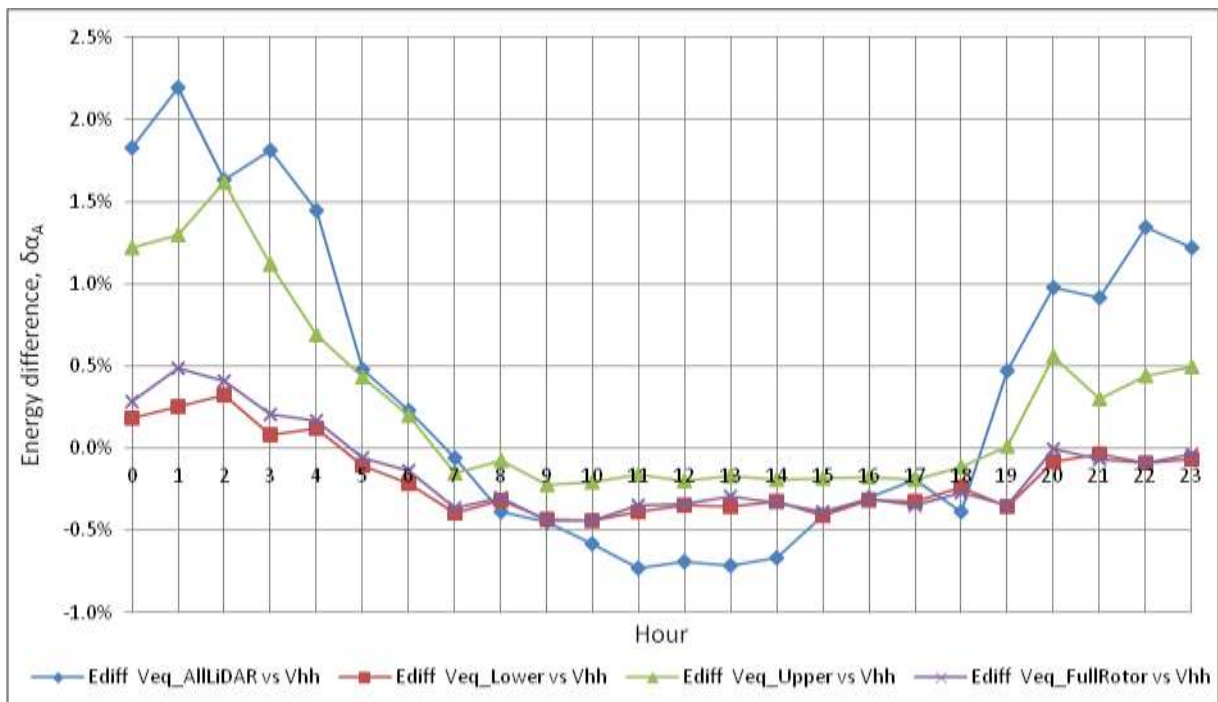


Figure 6.4.13: 2MW turbine at LiDAR location - Hourly mean energy differences - Summer

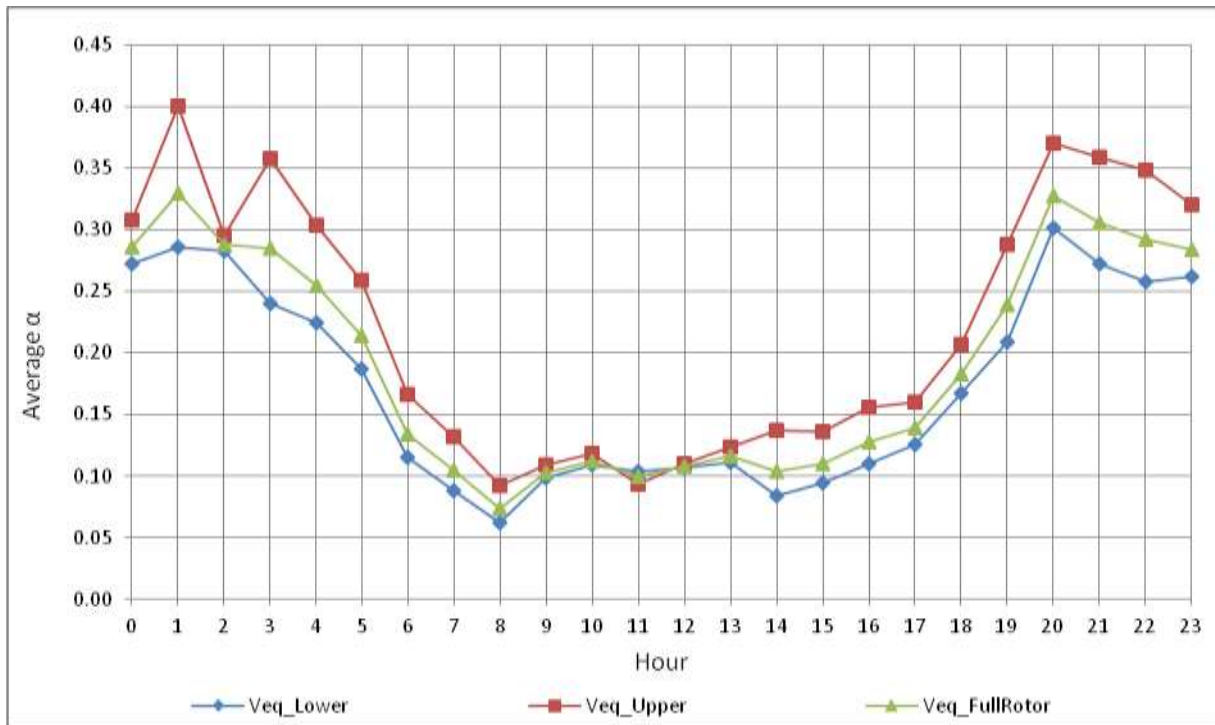


Figure 6.4.14: 2MW turbine at LiDAR location - Hourly mean shear exponents - Summer

6.4.5 CONCLUSIONS

A significant difference is observed between energy yields predicted by the rotor equivalent wind speed and hub height wind speed. The magnitude and sign of this difference, $\delta\alpha_A$, is sensitive to the shear exponent across the turbine rotor, the hub height wind speed and the shape of the vertical wind speed profile.

The energy difference $\delta\alpha_A$ is negative for shear exponents in the range $-0.0-0.33$, which are typical average values for Havsnäs. However, due to the way in which $\delta\alpha_A$ is dependent on α , the variation in the shear exponent means using v_{hh} underestimates the energy yield for the whole data period. The energy difference $\delta\alpha_A$ for the comparison $v_{eq_AllLiDAR}$ vs v_{hh} indicates that, on average, using v_{hh} underestimates the energy yield at Havsnäs by approximately 0.8%.

The ability of each theoretical v_{eq} case to describe the available energy was judged by the similarity of its $\delta\alpha_A$ to the $\delta\alpha_A$ of the $v_{eq_AllLiDAR}$ case. In the absence of RS data, v_{eq_Upper} is the most appropriate method in winter and in summer night time (stable conditions). In the summer days (unstable conditions) the v_{eq_Lower} and $v_{eq_RotorFull}$ are more appropriate.

It should be noted that mounting anemometers at the height of the top of the rotor is unlikely to be cost effective compared to RS. The rotor equivalent wind speed v_{eq_Lower} would be relatively easy to implement with the data gathered from a met mast measuring up to and at hub height. Section 6.4.4 shows this would represent the wind profile more effectively than using the hub height wind speed. However, the energy difference due to using $v_{eq_AllLiDAR}$ rather than v_{eq_Lower} shows the total energy over the whole data period would still be underestimated by approximately 0.66-0.67%.

7 COLD CLIMATE ISSUES

7.1 MAST INSTRUMENTATION AVAILABILITY AND RELIABILITY

7.1.1 MAST INSTRUMENTATION DATA SUMMARY

This section looks at the performance of the additional instrumentation that was added to the D2, E5 and F15 PP reference masts as part of the Havsnäs cold climate R&D system. The instrumentation systems are referred to by the mast names M6261, M6282 and M6303 respectively. The details of the instrumentation can be found in Section 5.1.

Data has been analysed, where possible, for the following periods:

	M6261	M6282	M6303
Data start point	16/09/2011 13:50	17/11/2011 13:00	17/11/2011 14:00
Data end point	25/07/2012 07:00	30/05/2012 07:30	14/07/2012 05:00
Number of 10 minute averaged data rows	45032	28047	34507

Table 7.1.1: Data analysed

In the case of an instrument failure, either prior to the start of measurements or during the measurement campaign, the subsequent bad data from this instrument was not included in the analysed statistics. All instrument failures are detailed in Sections 7.1.5 to 7.1.7.

Images of instruments on each mast were recorded throughout the installation so the build up of ice could be monitored. These images offer an insight into the difficulty of wind measurement campaigns in cold weather climates and can be seen in Appendices 7A-7C for masts M6361, M6282 and M 6303 respectively. Note these images are for illustration only and not evenly spaced in time so do not necessarily constitute a typical ice build up pattern

7.1.2 CUP ANEMOMETER AVAILABILITY STATISTICS

The primary reason for removing cup anemometer data in cold weather climates is the presence of ice which prevents the rotor from rotating freely and accurately measuring wind speed. Two possible solutions are evaluated; heated anemometry and an anemometer painted black as discussed in the following sections.

Heated versus Unheated Anemometry Statistics

Using heated instrumentation which has enough power to melt the ice that builds up on the anemometer rotor is one solution to icing affecting wind speed measurements.

Statistics are presented for the valid data obtained from the Vector A100L2 unheated anemometers and the Vaisala WAA 252 heated anemometers. Data is only considered for the periods that the data logger was operational, (i.e. not considered when the system was powered down for maintenance or as a result of a power failure).

M6261					
Instrument	No of instruments analysed	No of data points analysed	Bad Data Removed %	Bad Data attributed to icing %	Bad Data Removed Due other causes %
Unheated Anemometers (A100L2)	5	190865	20.8	20.75	0.05
Heated Anemometers (WAA252)	2	90064	12.81	1.43	11.38

Table 7.1.2: M6261 Anemometer Statistics

M6282					
Instrument	No of instruments analysed	No of data points analysed	Bad Data Removed %	Bad Data attributed to icing %	Bad Data Removed Due other causes %
Unheated Anemometers (A100L2)	2	56094	42.56	Breakdown unavailable	Breakdown unavailable
Heated Anemometers (WAA252)	3	84141	34.47	Breakdown unavailable	Breakdown unavailable

Table 7.1.3: M6282 Anemometer Statistics

M6303					
Instrument	No of instruments analysed	No of data points analysed	Bad Data Removed %	Bad Data attributed to icing %	Bad Data Removed Due other causes %
Unheated Anemometers (A100L2)	3	103521	29.83	27.81	2.02
Heated Anemometers (WAA252)	3	103521	14.05	1.86	12.19

Table 7.1.4: M6303 Anemometer Statistics

We can see from the Tables 7.1.2 - 7.1.4 that the by far the major source of bad data for unheated cup anemometers is icing. Heated anemometers suffer from icing during those periods where the ice build up was so severe as to outweigh the heating capacity of the heated anemometers.

Based on the results of the data analysed, we can say that deploying heated anemometers has resulted in, on average, an additional 21.75% of data being available after filtering to remove data affected by icing.

However, although icing only definitively occurred on heated anemometers 1.43% and 1.86% of the time for the M6261 and M6303 masts respectively, the bad data figures are much higher at 12.81% and 14.85%. This data includes times when the power supply to the heated anemometers failed and other system faults. It also includes a relatively large amount of data that has been removed by the quality checking process because it can't be said with certainty that the anemometer has been operating ice free for every sample in the record. For example should there be a large drop in the minimum wind speed value recorded this could be caused by ice or snow settling on the anemometer cups and would be removed. In total 11.38% for M6261, and 12.19% for M6303, of the heated anemometer data has been removed as it could have been affected by snow or ice (this is included in the Bad Data Removed % columns above). It is much easier to attribute icing to unheated anemometers as they can be checked against their heated counterparts at the same measurement level.

This highlights that the relative increase in data coverage by using heated anemometry ends up less than expected after a robust quality assurance process where the conservative approach is to remove any data there is any uncertainty about. It also highlights how icing can have a very subtle effect and removing data due to icing can be a subjective process.

Painting Unheated Anemometers Black

Another idea for limiting the build up of ice on the anemometer rotor is to paint the rotor black. This should result in a greater absorption of solar energy during times when the anemometer is in direct sunlight. Indeed, Figure 7.4.16 (in Section 7.4.2) from the production loss assessment suggests that solar radiation alone is sufficient to reduce some of the production lost due to icing.

To test this theory an additional Vector A100L2 anemometer was spray-painted black and added to the M6261 mast in place of one of the heated wind vanes. This anemometer was then wired into a logger through an analogue channel which results in a generic voltage to wind speed calibration being applied to the instrument. It should be noted that the wind tunnel calibration that had been applied to this instrument is therefore invalid, both because of this wiring setup and also the change to the rotor surface as a result of the paint. However the absolute wind speed measurement is not being analysed here.

The black anemometer is compared against the other three anemometers of the same make that were operational on the same mast for the same period (the black anemometer was installed at a later date than the other instruments on the mast). 33069 data points have been used for this analysis, for the period covering 16/11/2011 08:40 to 27/07/2012 07:00

Instrument Serial No.	Installation Height	Bad Data %
12719/YUA	87.1m	30.39
12707/YTM	72.6m	29.77
13090/E454A	30.1m	28.33
Combination of Above	N/A	29.50
11193/CMER-Black	70.8m	29.65

Table 7.1.5: Bad data summary

Based on the results presented above there is no benefit in terms of data availability observed as a result of painting the anemometer black.

7.1.3 WIND VANE AVAILABILITY STATISTICS

Wind vanes rely on the ability of the vane to move freely with the wind in order to accurately measure wind direction. Ice build up on the vane results in the vane sticking in a particular position and not measuring the correct direction. Heating the vane should allow higher measurement availability.

Statistics are presented for the valid data obtained from the Vector W200P unheated wind vanes and the Vaisala WAV 252 heated wind vanes. Again data is only considered for the periods that the data logger was operational.

M6261			
Instrument	No of instruments analysed	No of data points analysed	Bad Data Removed %
Unheated Wind Vane (W200P)	3	107786	8.94
Heated Wind Vane (WAV252)	2	90064	7.15

Table 7.1.6: M6261 Wind Vane Statistics

M6282			
Instrument	No of instruments analysed	No of data points analysed	Bad Data Removed %
Unheated Wind Vane (W200P)	3	84141	26.51
Heated Wind Vane (WAV252)	3	84141	24.48

Table 7.1.7: M6282 Wind Vane Statistics

M6303			
Instrument	No of instruments analysed	No of data points analysed	Bad Data Removed %
Unheated Wind Vane (W200P)	2	69014	27.22
Heated Wind Vane (WAV252)	3	103521	20.53

Table 7.1.8: M6303 Wind Vane Statistics

There is an average of 19.44% of data removed for unheated wind vanes as compared to 17.39% of data being removed for heated wind vanes. In the case of wind vanes it is very difficult to distinguish between data that has been removed due to icing and data that has

been removed for other reasons, as the symptoms are often identical (wind direction flat lines). For this reason a breakdown of icing statistics is not available

7.1.4 ULTRASONIC ANEMOMETER AVAILABILITY STATISTICS

Ultrasonic anemometers measure both wind speed and direction simultaneously by sending sound pulses between pairs of transducers and measuring the time of flight between them.

There are other advantages of using Ultrasonic anemometers for wind measurement campaigns.

- The air temperature can be calculated concurrently with the wind speed measurements.
- There are no moving parts so in theory there should be less degradation of the instrument performance over time.
- Higher sample frequencies are possible allowing higher resolution measurements of the wind profile, which can be used for atmospheric stability and turbulent eddies studies.

Two heated Metek USA-1 3-axis ultrasonic anemometers were deployed on each reference mast. Ultrasonic anemometers record data quality for each sound pulse that is sent, and the average data quality is recorded every 10 minutes (600 samples) and displayed as a percentage of time that the measurement isn't valid.

There were multiple failures experienced on the ultrasonic anemometer during this campaign as detailed in the following section. Four of these failures occurred during the period between the time when the instruments were installed on the mast and when power was applied to the system so they appear as having no valid data. This is discussed in the following section. The data from the sonic anemometers was only used when the error rate was less than 10% (i.e. >540 valid measurements over ten minutes) and this is taken as the cut-off for bad data.

Mast	Mast Position	% of time that Error = 100	% of time that Error = 0	% of time that Error < 10
M6261	Upper (89m)	18.78	70.82	79.83
M6261	Lower (10m)	52.18	37.11	47.40
M6282	Upper (89m)	100	0	0
M6282	Lower (10m)	100	0	0
M6303	Upper (89m)	99.05	0.68	0.73
M6303	Lower (10m)	100	0	0

Table 7.1.9: Ultrasonic Anemometer Availability Statistics

It is apparent that the performance of the ultrasonic anemometers is very poor. The decision was taken to prioritise the measurements on the M6261 mast for comparison with the LiDAR measurements and PP research, and the ultrasonic anemometers were moved around so as to achieve this. Virtually no Ultrasonic anemometer data was thus recorded at either the M6282 or M6303 masts.

7.1.5 CUP ANEMOMETER FAILURES

The instrumentation and associated support systems suffered numerous failures as is expected for a campaign in extreme winter environments. Photos of the failures shown in Table 7.1.10 can be seen in Appendix 7D.

Instrument Serial Number	Instrument Type	Mast	Failure Date	Failure reason	Photo number
13094/E458A	Vector A100L2	M6261	27/11/2011	Broken boom	7D.1
13088/E452A	Vector A100L2	M6261	17/01/2012	Smashed cups, likely due to falling ice	7D.2
A04106	Vaisala WAA252	M6261	16/09/2011	Electrical issue - Over reads throughout	N/A
X34202	Vaisala WAA252	M6261	Between commissioning and powering on	Missing cup. Possible lightning strike	7D.3
6847/5AI	Vector A100L2	M6282	18/11/2011	Detached rotor	7D.4
13092/E456A	Vector A100L2	M6282	01/01/2012	Detached from boom - cracked cups found on ground near mast. Body never located	7D.5

Table 7.1.10: Cup anemometer failures

7.1.6 WIND VANE FAILURES

Instrument Serial Number	Instrument Type	Mast	Failure Date	Failure reason	Photo number
55068	Vector W200P	M6261	01/03/2012	Broken boom	7E.1
E49501	Vaisala WAV252	M6282	23/03/2012	Vane detached	7E.2
9749/01	Vector W200P	M6282	17/01/2012	Broken boom	7E.3
55079	Vector W200P	M6303	18/11/2011	Vane detached	7E.4
12669/01	Vector W200P	M6303	17/01/2012	Broken boom	7E.5

Table 7.1.11: Wind vane failures

Photos of the wind vane failures shown in Table 7.1.11 can be seen in Appendix 7E.

7.1.7 SONIC ANEMOMETER FAILURES

Instrument Serial Number	Instrument Type	Mast	Failure Date	Failure reason	Photo number
0102122252	Metek USA-1 Heated	M6261	09/03/2012	Ice build up changing path length	7F.1
0102122251	Metek USA-1 Heated	M6261	26/05/2012	Flat line following power loss from turbine - fails to recover	N/A
0102122248	Metek USA-1 Heated	M6282	Prior to commissioning	Ice build up changing path length	7F.2
0102122247	Metek USA-1 Heated	M6282	Prior to commissioning	Ice build up changing path length	No photo as recovered prior to decommission
0102122249	Metek USA-1 Heated	M6303	Prior to commissioning	Ice build up changing path length	7F.3
0102122250	Metek USA-1 Heated	M6303	Prior to commissioning	Ice build up changing path length	No photo as recovered prior to decommission

Table 7.1.12: Sonic Anemometer Failures

Photos of the wind vane failures shown in Table 7.1.12 can be seen in Appendix 7F.

The main reason for failures of the ultrasonic anemometers was ice build-up on the transducer heads during periods when the heating was not operational. The ice build-up causes the transducer orientation, and hence distances for the time of flight measurements, to change. Even relatively small changes in the transducer geometry can cause all data to be discarded and render the instrument useless.

In the majority of cases the change in sensor head orientation occurred prior to the systems being turned on as there was a delay between the installation of the instruments on the mast and power being available from the turbine. However there was ice build-up on the transducer heads throughout the campaign, which caused the orientation to change.

The ultrasonic anemometers were recovered from the mast mid way through the campaign and the sensor head orientation was recalibrated where possible. In the case of four out of the six deployed instruments this proved impossible due to the bending of the transducer arms to the point where the instrument was permanently damaged.

These results point out a very serious design flaw in these instruments, and as such they should not be used except in cases where a guaranteed power source adequate for the full heating load is available, such as a permanent grid connection.

7.1.8 MAST INSTRUMENTATION CONCLUSIONS

There was more than 20% unheated anemometer data lost due to icing on all masts and painting the anemometer black showed no benefit. There was only 1-2% heated anemometer data lost due to icing but the heated sonic anemometers suffered numerous failures. These failures were caused by ice build up during periods power supply was non-functional or intermittent and highlighted a design flaw in instruments.

A reliable power supply must be used for all equipment if good data coverage is to be obtained over the winter period in cold climates. This is especially important if relying upon delicate sonic anemometers for wind speed or stability measurements.

Half of all other failures were caused by broken booms. These booms were box section aluminium booms not optimised for the unheated instrumentation. This is thought to have caused a resonance issue. It is recommended that boom suitability should be assessed when mounting non-standard instrumentation.

7.2 LIDAR

As detailed in Section 5.1 of this report, the WINDCUBE V1 (WLS7-69) was installed in September 2011.

The WINDCUBE V1 (identified as M814) is located 51 m to the north of the co-located fixed mast M626 (Shown in Figure 5.1.1 in Section 5.1). The altitude at the V1 location is 520 m.

7.2.1 WIPER REPLACEMENT

Following its installation the LiDAR suffered from a wiper unit failure, where the wiper repeatedly stopped in the middle of the lens, obstructing the line of sight. The wiper unit was replaced in November 2011. In this report, the period prior to the wiper unit replacement is compared with the period following the installation of the new wiper unit.

The improvement in data capture is clearly observed, however, the qualified data capture rates remain low, partly due to the assumed low aerosol density at the site coupled with the north westerly prevailing wind direction.

Nevertheless, comparing the data capture at Havsnäs with that from a Scottish site with a reasonable approximation of the Havsnäs climate, suggests that data capture could be considered low.

Data exist at Havsnäs from 16/09/2011 until 17/11/2011 with the original wiper unit and from 21/11/2011 until 06/01/2012 with the replacement unit.

AVAILABILITY STATISTICS

This section aims to investigate the data capture rates realised by the device during the deployment period and understand why the qualified data capture rates are lower than might be expected.

The operational availability of the WINDCUBE V1 prior to and following wiper replacement is 91% and 99.9% respectively. However, the availability of useable data is reduced due to bad data values and reduced quality data.

Impact of Bad Data Values on Data Capture

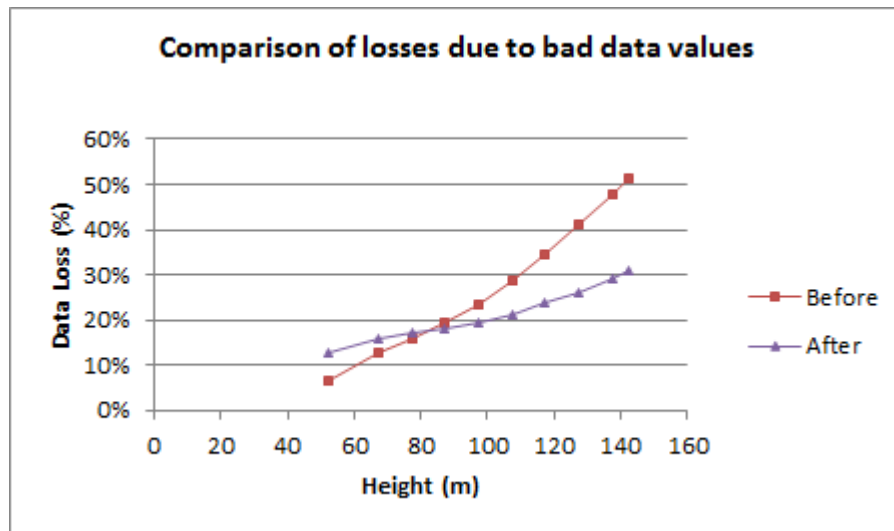


Figure 7.2.1: Comparison of losses due to bad data values before and after wiper replacement

Figure 7.2.1 shows that following the wiper replacement, fewer data periods are lost as a result of bad data⁷ values. Following the wiper replacement a larger percentage of data is lost for each of the three lowest measurement heights. This may be as a result of the appearance of a northerly component in the wind rose during the latter period, resulting in lower aerosol densities and contributing to more periods with bad data values.

Impact of Data Quality on Data Capture



Figure 7.2.2: Comparison of losses due to data quality before and after wiper replacement

⁷ Bad data values are returned by the WINDCUBE when it is unable to calculate useable data values. Bad data values include NaN (Not a Number) and 5000.

Figure 7.2.2 shows that following the wiper replacement, fewer data periods are lost as a result of low quality data⁸.

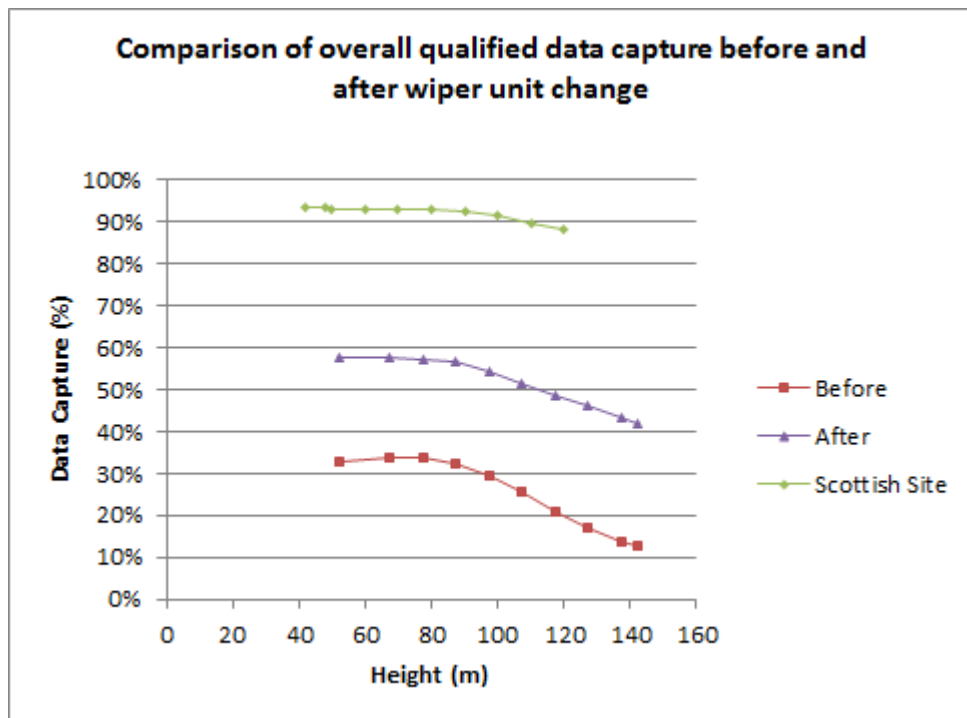


Figure 7.2.3: Comparison of overall data capture before and after wiper replacement and at a Scottish site

Figure 7.2.3 shows that following the wiper replacement, there is a large increase in qualified data capture⁹. However, the qualified data capture at the Scottish site is still considerably higher than the Havsnäs values. The Scottish site data period is similar to the period at Havsnäs following the wiper replacement.

The following things should be noted about the comparison between data capture at Havsnäs and the Scottish site:

- The Scottish site uses WINCUBE V2 whereas Havsnäs uses WINDCUBE V1.
- The data period at the Scottish site is from 14/11/2011 to 03/01/2012 (The data period at Havsnäs after the wiper replacement is from 21/11/2011 until 06/01/2012).
- The altitude at the Scottish site V2 location is 745 m (225 m higher than the V1 at Havsnäs).
- The prevailing wind direction is from the southwest at the Scottish site (northwest at Havsnäs).
- The data filters applied to the V1 at Havsnäs (the same as those applied at the Scottish site) can be found in Appendix 7G.

⁸ Low quality data are data that do not meet the filtering criteria and are therefore deemed unsuitable for analysis purposes. Further detail can be found in Appendix 7G.

⁹ Data Capture will always reduce with measurement height above 80 m. This is because with increasing measurement height it is increasingly difficult for the WINDCUBE to distinguish the return signal from the noise.

ACCEPTANCE TESTS

This section shows the results of LiDAR acceptance tests before and after the wiper replacement. Information on NORSEWInD and Sgurr acceptance test criteria can be found in Appendix 7H. Data from tower shadow sectors and wake affected sectors have been removed from the analysis.

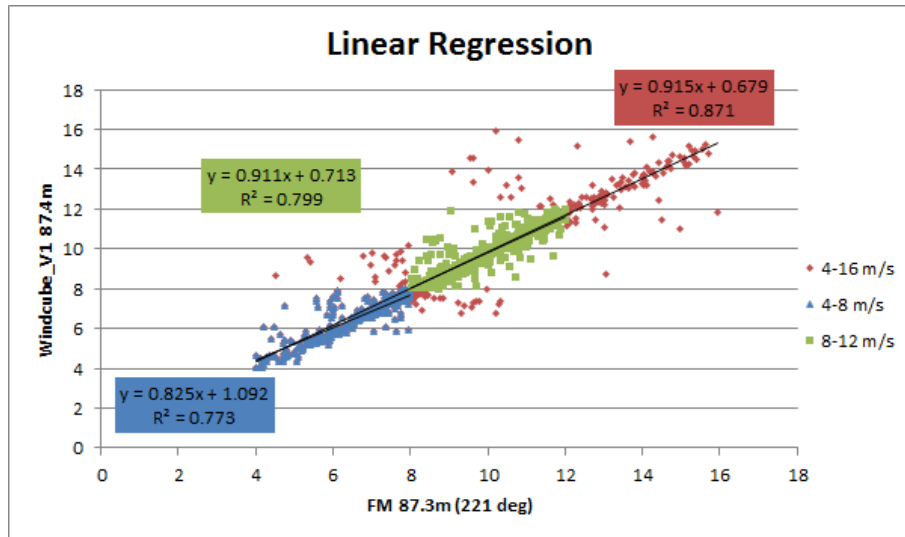


Figure 7.2.4: NORSEWInD acceptance test results for period prior to wiper replacement (FM refers M626)

It is clear from the Figure 7.2.4 that the correlations between the V1 and the fixed mast are not ideal. For both the slope and R^2 values, the WINDCUBE V1 fails the NORSEWInD criteria (note that it also fails the Sgurr criteria).

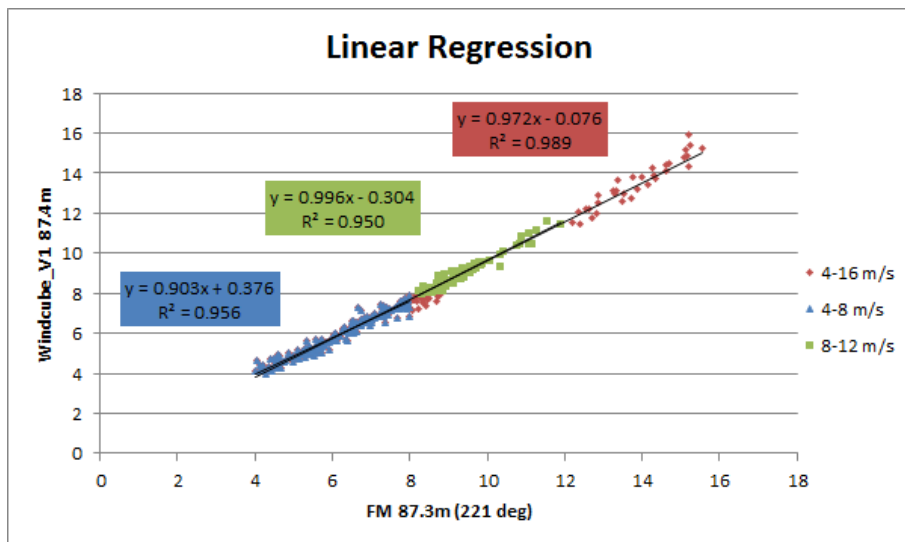


Figure 7.2.5: NORSEWInD acceptance test results for period following wiper (FM refers M626)

From Figure 7.2.5 in comparison to Figure 7.2.4, it can be seen that there is a marked improvement in the correlations between the V1 and the M626 following the wiper replacement. Nevertheless, following the wiper replacement, the V1 still does not pass the NORSEWInD criteria, it does pass the Sgurr criteria however.

CONCLUSIONS

Following the wiper unit replacement, the quality of the correlations improves markedly, such that correlations may now be considered acceptable.

While the qualified data capture improves considerably following the wiper unit replacement, the qualified data capture is still lower than expected.

The qualified data capture remains below 60 % at 50 m and drops as low as 42 % at 140 m. This is in contrast to the Scottish site where at 120 m the qualified data capture rate is 88 %.

If it is assumed that the Scottish site is similar to that of Havsnäs, then it might be expected that similar data capture rates would be observed at both sites. This suggests that signal quality at Havsnäs is not sufficient.

The low data capture at Havsnäs was assumed to be as a result of low aerosol density. This may be due to cleaner air from the prevailing north-west sector. Note, though, that the effect of altitude on aerosol density should not be as great as at the Scottish site where the site elevation is 225 m higher than Havsnäs. It is more likely that this aerosol density is associated with the much more northerly latitude of Havsnäs in comparison to the Scottish site.

The main difference between the WINDCUBE V1 and WINDCUBE V2 is that they fire 10,000 and 20,000 pulses respectively. After discussions with the manufacturer it was thought possible that the difference in data capture was due to this difference in configuration. Section 7.2.2 of this report shows the results of reconfiguring the LiDAR number of pulses per line of sight.

7.2.2 LIDAR RECONFIGURATION

Following the investigation into the data capture of the WINDCUBE V1 at Havsnäs shown in Section 7.2.1, which revealed poor data capture, it was recommended by the device manufacturer that the number of pulses for each line of site be increased and the signal to noise threshold be decreased appropriately.

This section reviews the performance of the WINDCUBE V1 at Havsnäs following the reconfiguration of its firing sequence. This section also reviews the effectiveness of the reconfiguration in improving data quality and considers whether any aspect of the device's performance has been degraded as a result.

BACKGROUND

LiDAR devices depend upon the presence of aerosols in the atmosphere to back scatter the laser pulses. The devices can then use the information from the back scattered laser pulses to calculate the various wind parameters necessary to characterize the wind flow through the measurement volume.

The origins of the aerosols are various but generally at remote, cold climate sites the air is much cleaner with lower aerosol densities. This results in less back scattered light and therefore lower signal quality and lower data capture.

Following discussions with the device manufacturer, it was recommended that the number of pulses per line of sight be increased to 40,000 and the carrier to noise ratio (CNR) threshold be reduced by 2 dB. These changes can be effected remotely by dialling into the device and altering the configuration.

Each line of site firing sequence produces one data point to be used in calculating the 10-minute average. As increasing the number of pulses increases the time taken in each line of sight position, increasing the number of pulses decreases the number of data points in each 10-minute average. For example, increasing the number of pulses to 20,000 pulses would reduce the number of measurements from 600 to 300 and increasing to 40,000 pulses would reduce the number of measurements to 150 for each ten minute average. The greatest impact of this could be on the standard deviation values returned.

RECONFIGURING THE WINDCUBE V1 AT HAVSNÄS

For the comparison, the test period prior to reconfiguring the WINDCUBE was from 21/11/2011 until 06/01/2012.

During this period the WINDCUBE was configured as follows (the standard WINDCUBE V1 configuration):

- Number of averaged shots per line of sight: 10,000
- CNR threshold: -22 dB
- 600 data points going into 10-minute average

Following the reconfiguration, the test period used for comparison purposes was from 01/02/2012 until 16/02/2012.

The WINDCUBE was reconfigured as follows (according to the manufacturer's recommendations):

- Number of averaged shots per line of sight: 40,000
- CNR threshold: -24 dB
- 150 data points going into 10-minute average

IMPACT OF RECONFIGURING THE WINDCUBE V1 AT HAVSNÄS

Following the reconfiguration it was important to ensure that not only did the data capture increase but that no other aspect of the data had been adversely affected. In particular it was important to understand what impact the reduced number of points in the 10-minute average would have on the values returned for the standard deviation of mean wind speed.

This section considers a number of aspects of the WINDCUBE operation to confirm that no aspect of its operation has been degraded as a result of the reconfiguration.

Operational Availability

The data availability describes those periods when the WINDCUBE V1 LiDAR is operational, i.e. returning data. Operational availability should be independent of the device configuration. Nevertheless, it is still useful to check that for both periods the device has similar levels of operational availability.

For the test period prior to the reconfiguration of the device, the operational availability of the device was approximately 100%. Following the reconfiguration, the operational availability is also excellent at approximately 99%. The 1% reduction in operational availability is due to a small period of missing data.

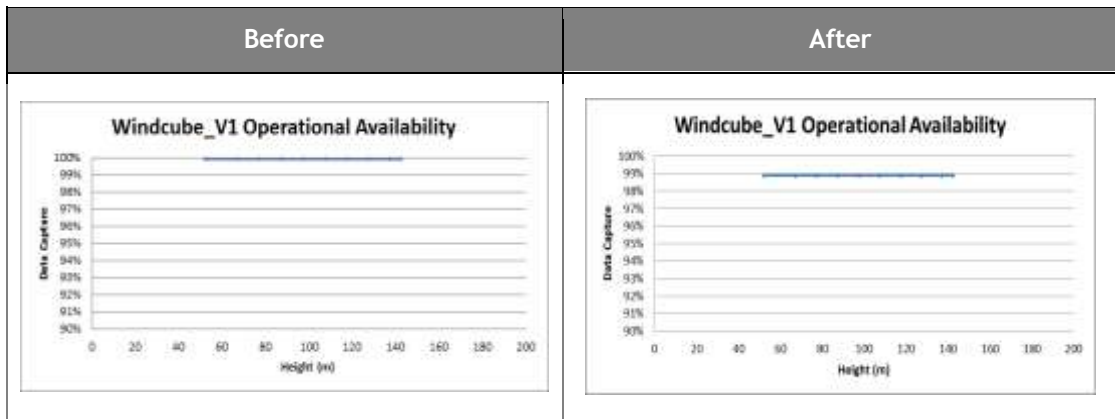


Figure 7.2.6: Operational Availability of WINDCUBE V1 before and after reconfiguration

Device Geometry

Dividing the components of wind speed by the mean wind speed and then plotting the resulting values (See Figure 7.2.7) by direction provides a visual indication of the orientation of the laser beams (or device ‘geometry’). The ‘peaks’ and troughs’ indicate the orientation of the LiDAR beams. Using the highest LiDAR measurement height illustrates how the device is performing at the height with lowest qualified data capture.

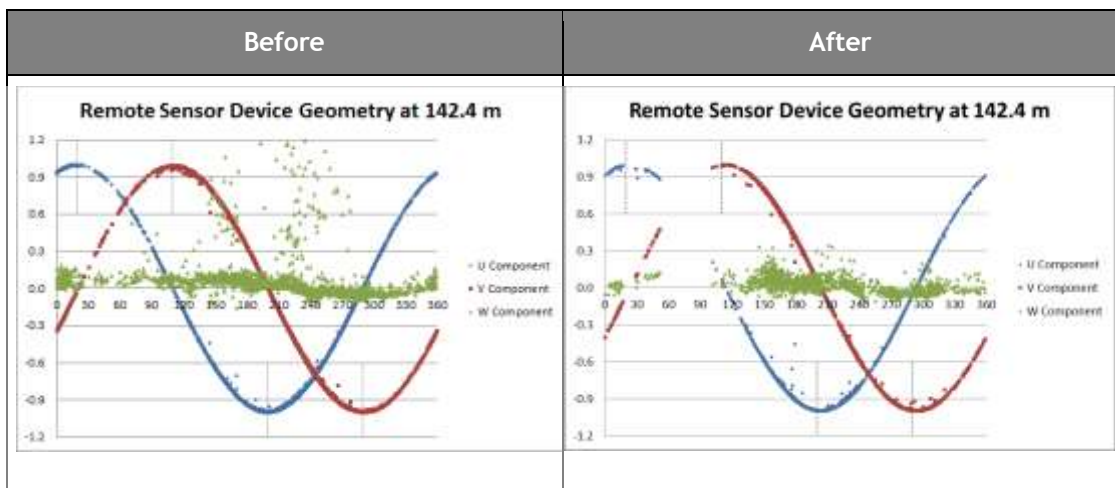


Figure 7.2.7: Device Geometry of WINDCUBE V1 before and after reconfiguration.

It is clear that both before and after the device reconfiguration, there is very little scatter in the u and v components (the two horizontal components of wind speed). Following the reconfiguration, the scatter in the w component (the vertical component of wind speed) is reduced. This could be as a result of different wind conditions in the period following the reconfiguration or it could be as a result of the increased number of pulses allowing the vertical component of wind speed to be more accurately calculated.

Qualified Data Capture

The qualified data capture describes the percentage of data remaining after the necessary quality filters have been applied. The ultimate aim of reconfiguring the WINDCUBE firing sequence was to increase the qualified data capture to obtain sufficient data for analysis purposes.

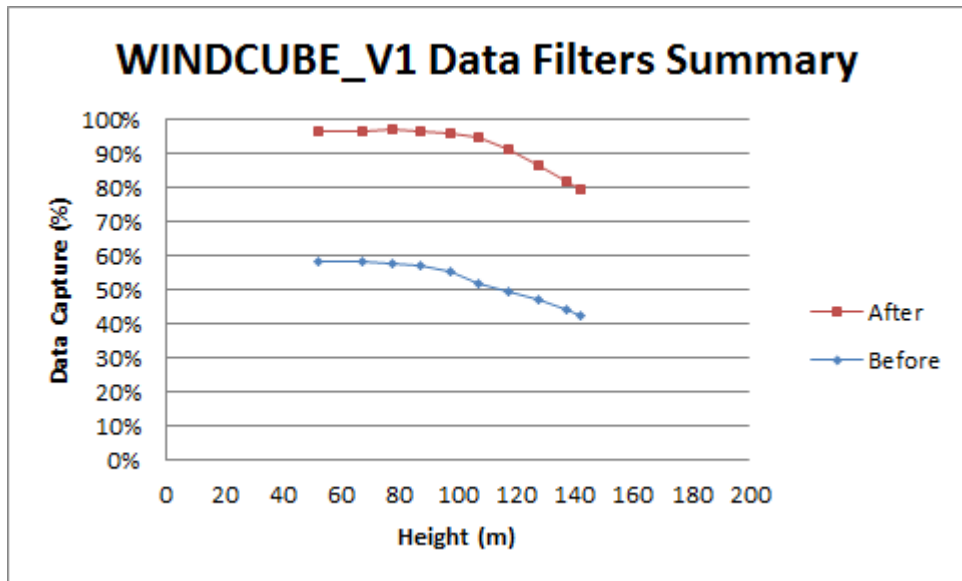


Figure 7.2.8: Data Capture of WINDCUBE V1 before and after reconfiguration

Figure 7.2.8 and Table 7.2.1 show that following the reconfiguration of the WINDCUBE, the qualified data capture increases dramatically. On average, the absolute increase in qualified data capture as a result of the reconfiguration is approximately 37 %. This increase is a result of the factor of four increase in the number of pulses per line of site.

Windcube_V1 Data Filters Summary (Before)				Windcube_V1 Data Filters Summary (After)				Improvement (Absolute)
Height (m)	Data Capture	Expected	%	Height (m)	Data Capture	Expected	%	%
52.4	3716	6378	58.26%	52.4	2081	2166	96.08%	37.82%
67.4	3704	6378	58.07%	67.4	2088	2166	96.40%	38.33%
77.4	3684	6378	57.76%	77.4	2094	2166	96.68%	38.92%
87.4	3627	6378	56.87%	87.4	2090	2166	96.49%	39.62%
97.4	3504	6378	54.94%	97.4	2077	2166	95.89%	40.95%
107.4	3308	6378	51.87%	107.4	2041	2166	94.23%	42.36%
117.4	3138	6378	49.20%	117.4	1970	2166	90.95%	41.75%
127.4	2975	6378	46.64%	127.4	1863	2166	86.01%	39.37%
137.4	2806	6378	43.99%	137.4	1765	2166	81.49%	37.50%
142.4	2703	6378	42.38%	142.4	1721	2166	79.46%	37.08%

Table 7.2.1: Data Capture of WINDCUBE V1 before and after reconfiguration.

Correlations of Standard Deviation

As a result of increasing the number of pulses per line of sight by a factor of four to 40,000 pulses per line of sight, there is a factor of four decrease in the number of wind speed measurements in each 10-minute average.

It is possible, therefore that the standard deviation value returned by the WINDCUBE could be affected as a result of the reduction in data points in the 10-minute average.

In all further graphs in section 7.2, the RS device is the WINDCUBE V1 LiDAR and ‘FM’ refers to fixed mast which is mast M626 in this case.

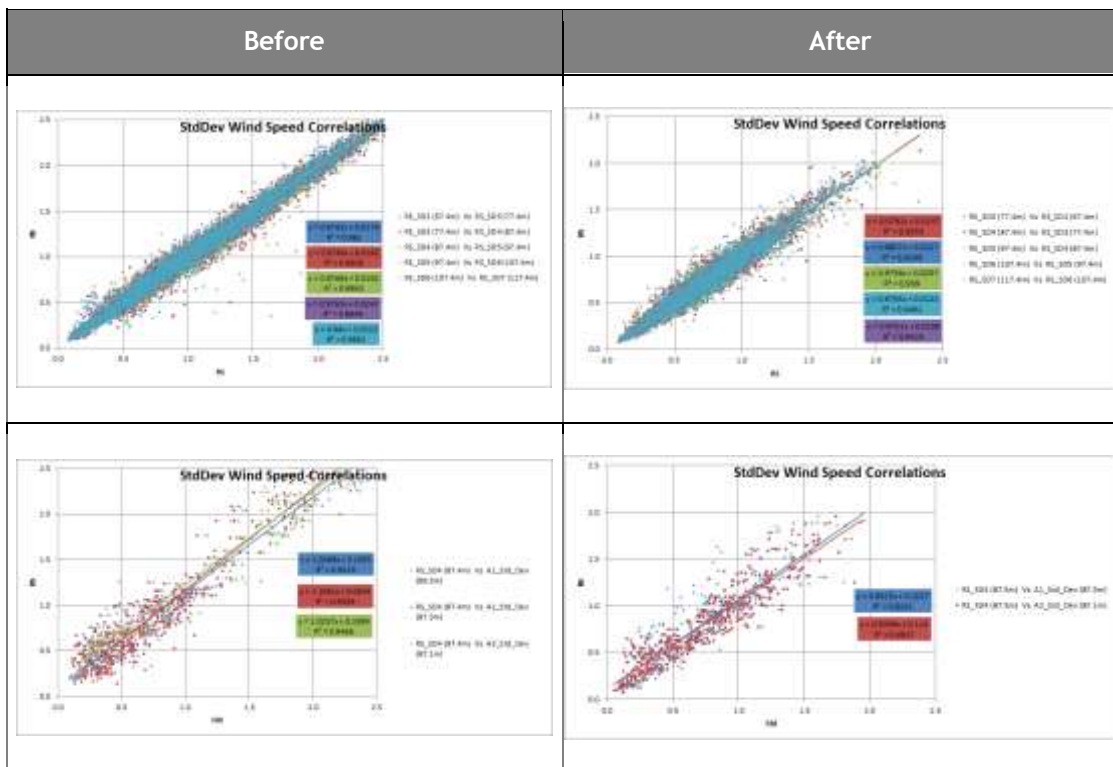


Figure 7.2.9: Correlations of standard deviation of mean wind speed

The charts in Figure 7.2.9 show correlations of standard deviation of mean wind speed. Initially correlations were made between adjacent WINDCUBE measurement heights. WINDCUBE measurements were also correlated with fixed mast data. The bottom charts show WINDCUBE data on the y-axis and fixed mast data on the x-axis¹⁰.

The WINDCUBE-WINDCUBE correlations following the reconfiguration are consistent with those prior to the reconfiguration. While there is very little data for the WINDCUBE-fixed mast correlations (due to icing and wake filters), the correlations following the reconfiguration are also consistent with those prior to the reconfiguration, with the slopes from both periods being similarly close to unity.

Correlations of Mean Wind speed

When considering the correlations of mean wind speed, between the WINDCUBE and the fixed mast, for both periods, it is clear that there is very little variation between the periods. Prior to the reconfiguration the slope is within 1 % of unity and following the reconfiguration the slope is within 2 % of unity.

¹⁰ In the WINDCUBE versus fixed mast ‘After’ chart, one correlation is missing due to low data capture at the fixed mast.

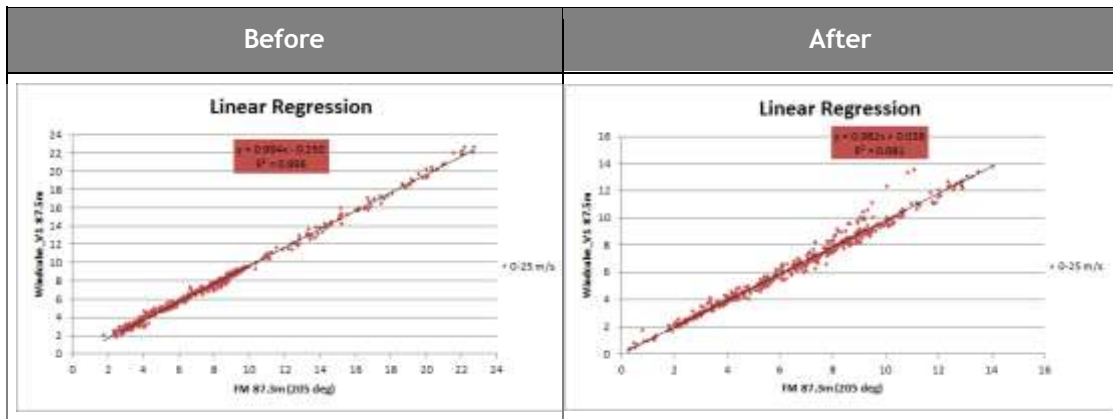


Figure 7.2.10: Correlations of mean wind speed from Windcube versus fixed mast (M626)

The scatter above the main trend for the period following the reconfiguration is due to periods of subtle icing at the fixed mast and may contribute to the small change in slope.

Such periods are difficult to identify when assessing the fixed mast data on their own but in combination with RS data it is possible to identify these periods. At such times, the fixed mast anemometers appear to be operating correctly but are in actual fact, to some extent, inhibited by icing.

CONCLUSIONS

Using the standard WINDCUBE V1 device configuration resulted in low data capture. It was expected that the low data capture was as a direct consequence of low aerosol densities at the Havsnäs site.

Following discussions with the device manufacturer, the WINDCUBE was reconfigured to increase the number of pulses per line of site. The number of pulses was increased to 40,000. It was also appropriate to reduce the carrier to noise threshold by 2 dB.

Various checks were made to confirm that no aspect of the WINDCUBE operation was degraded as a result of the reconfiguration.

The reconfiguration of the WINDCUBE has resulted in a marked increase in qualified data capture. The absolute increase in data capture is approximately constant across all heights at around 37 %. The quality of the qualified data remains consistent.

It is therefore recommended that, at sites where there is likely to be low aerosol densities, the WINDCUBE should be reconfigured. The recommended device configuration for such sites is 40,000 pulses per line of sight and a reduction in the carrier to noise threshold of 2dB.

7.2.3 USING REMOTE SENSING FOR CLIMATIC CONDITIONS REPORTING

This report investigates the validity of using RS data for the purposes of climatic conditions reporting (CCR) at Havsnäs wind farm, Sweden. Specifically, this report considers the WINDCUBE V1 LiDAR deployment M814 which is co-located with the PP reference mast M626 as described in Section 5.1.

BACKGROUND

Climatic conditions data are important in ensuring that appropriate turbines are selected for a given wind farm site.

In cold climates, the expense of installing hub height ice-rated meteorological masts can be prohibitive, particularly with the availability of taller hub heights up to around 120 m.

As an alternative or in addition to existing site masts, it may be possible to use RS devices to provide the necessary data for climatic conditions reporting (wind shear, maximum wind speed and turbulence intensity data). Not only would it be possible to provide data at hub height but it would be possible to provide data for a range of measurement heights across the rotor diameter.

RES has previously investigated turbulence intensity data from RES sites where a WINDCUBE has been deployed. This investigation found that there is a good relationship between the fixed mast values of turbulence and the WINDCUBE values of turbulence and that the WINDCUBE turbulence data are suitable for climatic conditions reporting (See Appendix 7I).

It was noted however, that there is likely to be variability between sites and world regions and therefore data should be examined on a site-by-site basis.

CCR VERIFICATION

In this analysis standard deviation of mean wind speed data and maximum wind speed data have been considered. The ability of RS devices to provide reliable data for wind shear is widely accepted and is not considered in this analysis.

The data set used in this analysis has been filtered to remove wake affected data (Section 5.3.2) and the fixed mast data have been filtered to remove data when the temperature is below two degrees Celsius. The LiDAR quality filter has been set to 100 %. A $4 \text{ m}\cdot\text{s}^{-1}$ wind speed censor has been applied.

STANDARD DEVIATION OF MEAN WIND SPEED

It can be seen in Figure 7.2.11 that there is a well-defined relationship between the standard deviation of mean wind speed recorded by the mast and that recorded by the WINDCUBE V1. However, the WINDCUBE data do slightly overestimate standard deviation on average as compared to the fixed mast. The slope of the correlations varies from 5 % to 1 % from unity and the R^2 value is between 0.86 and 0.88.

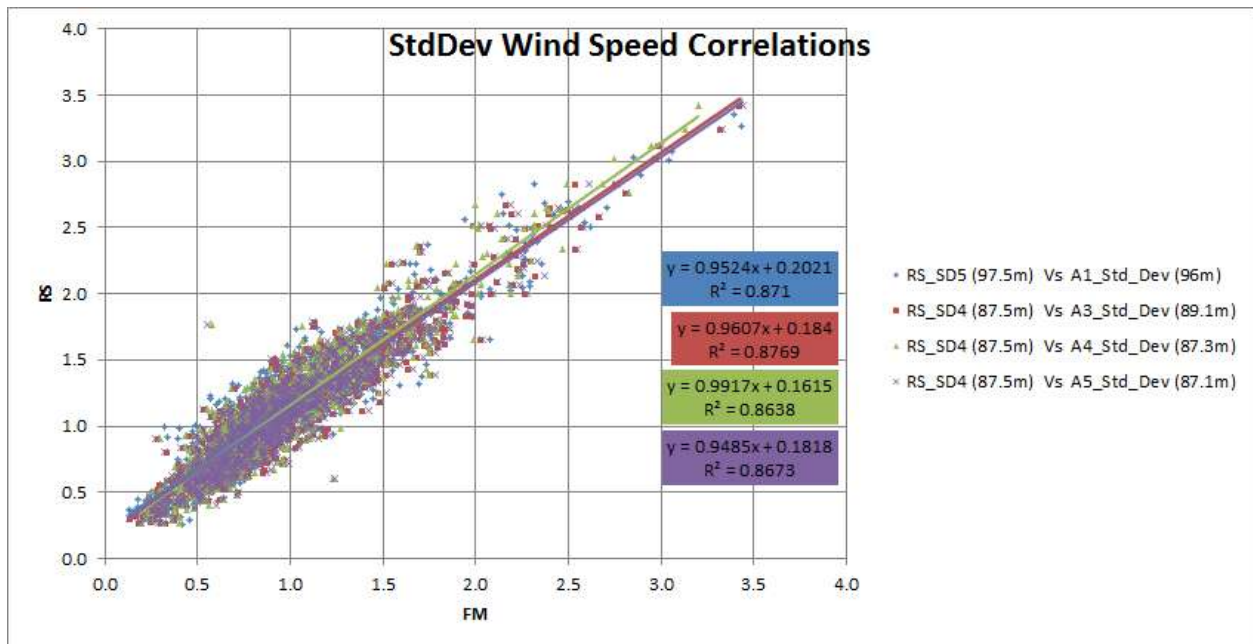


Figure 7.2.11: Correlation of the Standard Deviation in Wind Speed from the RS device and the fixed mast, M626.

While there is greater variation in the correlation slope than would be expected for mean wind speed correlations, the standard deviation relationship is strong.

It should be noted that for the same WINDCUBE measurement height and three slightly different anemometer measurement heights, the correlation slopes vary between 5 % and 1 %. This suggests that flow distortion experienced by the anemometers based on their boom orientation and position is responsible for some of the observed variation between the fixed mast and WINDCUBE. Overall, the level of agreement observed between the WINDCUBE and fixed mast data is acceptable.

MAXIMUM MEAN WIND SPEED

In Figure 7.2.12 it can be seen that there is a well-defined relationship between the maximum wind speed recorded by the mast and that recorded by the WINDCUBE V1. However, the fitted trend lines suggest that, compared to the fixed mast, the WINDCUBE data do slightly overestimate maximum wind speed at speeds up to $10 \text{ m}\cdot\text{s}^{-1}$, and slightly underestimate maximum wind speed at speeds beyond $10 \text{ m}\cdot\text{s}^{-1}$. For gust calculations, the WINDCUBE may underestimate maximum gust.

The slope of the correlations varies from 6 % and 5 % from unity and the R^2 value is 0.97. This level of agreement, observed between the WINDCUBE and fixed mast data, is acceptable.

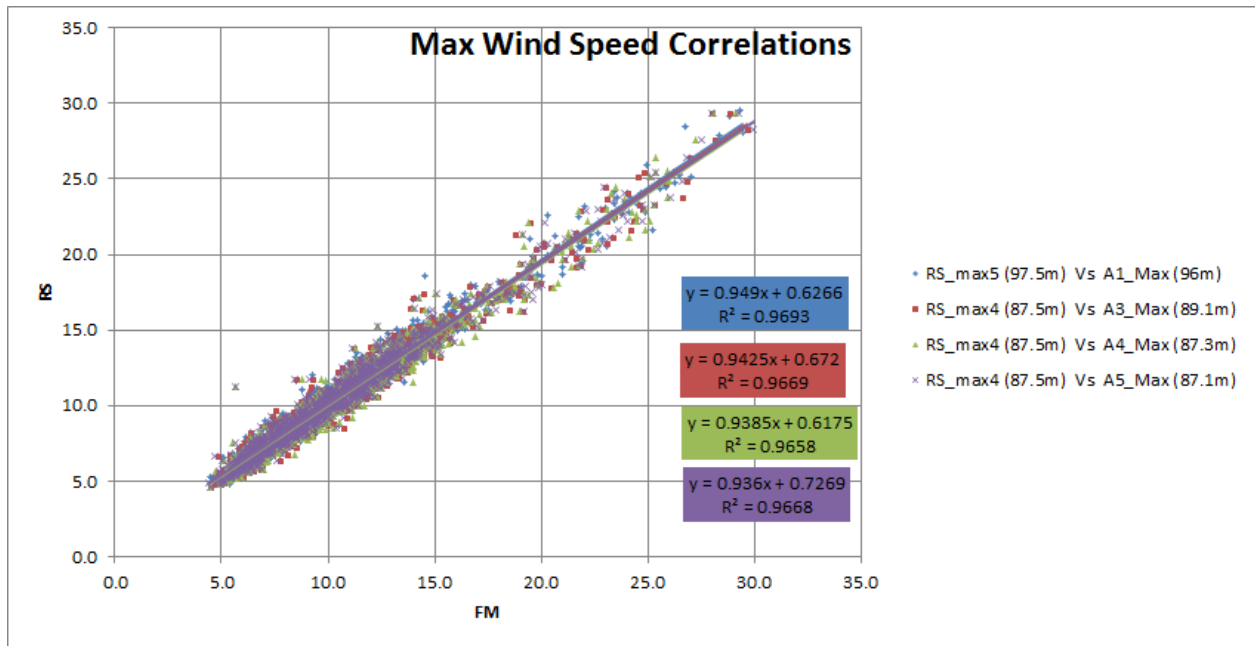


Figure 7.2.12: Correlation of the Maximum Wind Speed from the RS device and the fixed mast, M626.

CHARACTERISTIC TURBULENCE

The characteristic turbulence intensity from the WINDCUBE is in good agreement with the fixed mast data as can be seen in Figure 7.2.13. However, the WINDCUBE does return higher values of characteristic turbulence intensity than the fixed mast.

Due to the different measurement principles for the LiDAR compared to the cup anemometers on the mast (volume averaged versus point measurement), we do not expect the turbulence intensities to agree exactly but it is encouraging to note that the turbulence trend is well captured by the LiDAR.

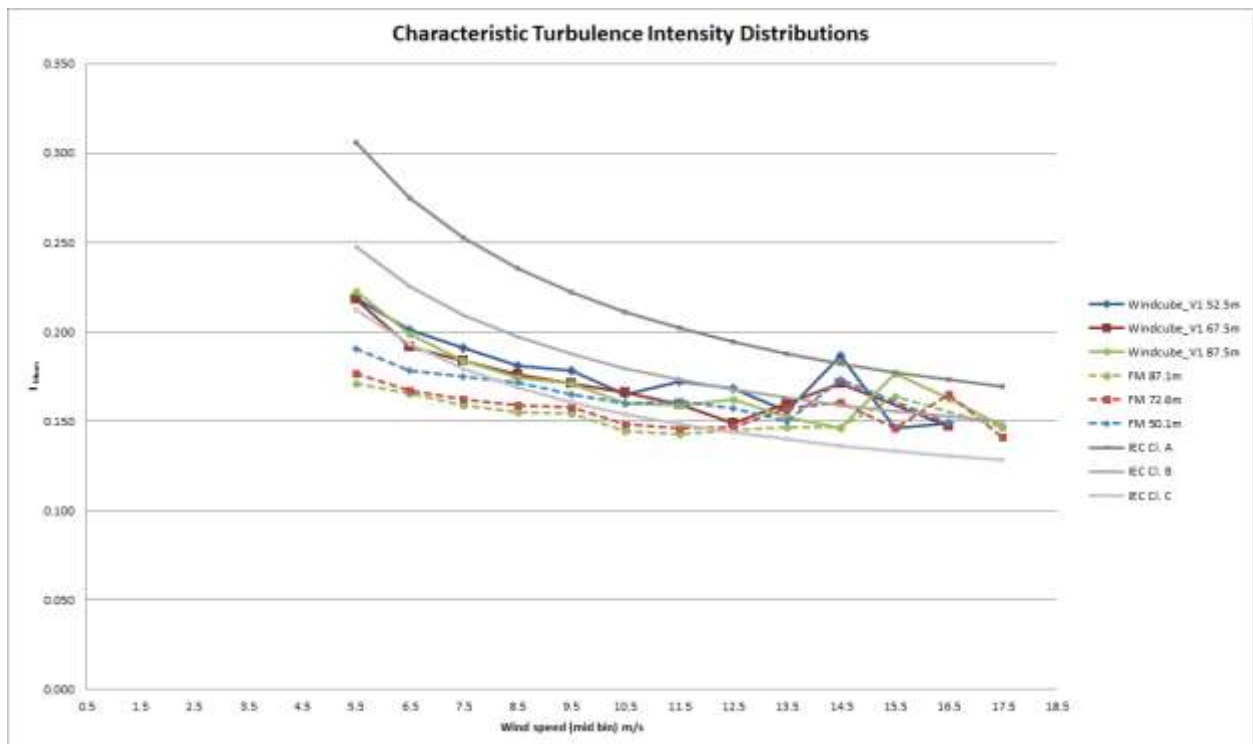


Figure 7.2.13: Characteristic turbulence intensity distributions of RS device and the fixed mast, M626.

CONCLUSIONS

Considering the data from Havsnäs, it has been found that there is a well-defined linear relationship between the WINDCUBE and fixed mast data both for the standard deviation of mean wind speed data and the maximum wind speed data.

In both cases the correlation slope is around 5 % from unity which is an acceptable difference¹¹ and similar in magnitude to the implied flow distortion effects on anemometer measurements from the (IEC compliant) mast.

As further demonstrated in Appendix 7I, RES has seen that WINDCUBE turbulence intensity data are suitable for climatic conditions reporting at a variety of sites with differing levels of complexity. However, as there is likely to be variability between sites (and even across sites) and world regions, WINDCUBE LiDAR data should be examined on a deployment-by-deployment basis to ensure they can be used for climatic conditions reporting.

In summary, on sites similar in nature to Havsnäs wind farm, where using a RS device may result in a small overestimation of turbulence intensity and an underestimation of maximum wind speed, a suitable RS device (that can return climatic conditions data) would potentially have most value when co-located with a fixed mast. In conjunction with a fixed mast it should be possible to characterise any difference between the fixed mast and the RS device measurements but also provide increased coverage of measurement heights across the rotor diameter.

¹¹ As the dataset used in this analysis is equivalent to a period of 10 days in length, the observed relationships between the fixed mast and WINDCUBE may change slightly with the availability of more data.

7.3 INSTRUMENTATION RECOMMENDED PRACTICES

This section aims to define the recommended instrumentation practices for cold weather climates that have been developed over the course of the cold climate R&D campaign at Havsån Wind Farm and other experience RES have gained in Northern Sweden.

7.3.1 MAST INSTRUMENTATION RECOMMENDED PRACTICES

REQUIREMENTS SPECIFICATION

It is essential when considering the deployment of any data acquisition system that a clearly defined set of objectives and required outcomes are agreed as a starting point for the campaign.

SYSTEM DESIGN

The design stage of a cold weather measurement campaign is one of the most critical parts of the entire process. Sufficient time and resource must be budgeted to ensure that the installed system is suitable for a remote location that is frequently exposed to extended periods of extreme weather. Particular attention must be paid to:

- System Feasibility
- System Complexity
- Selection of Data Acquisition Equipment
- Selection of Mast Structure and Associated Hardware
- Available Sources of Power
- Measurement System Configuration
- System Installation, Decommissioning and Maintenance Activities

SYSTEM FEASIBILITY

The question must be asked: is it actually possible and practical to install a measurement system at the intended location? Various factors must be taken into account when considering the feasibility of a measurement campaign. These include, but are not limited to:

- Where is the site with respect to local dwellings?
- What is the risk of damage to people or property due to total mast failure?
- What is the risk of damage to people or property due to instrument or instrument boom failure?
- What is the risk of damage to people or property due to ice fall from the mast or supporting guy wires if present?
- What if any access routes are available to site?
- Can equipment be easily transported to site?
- Are access routes available during periods of extreme weather?
- Is there a reliable local mains fed power source?
- What alternative power sources are available? (wind resource / solar resource)
- Is there a local supplier of suitable vehicles that will allow access to site during adverse weather conditions?
- Is there local skilled manpower available to carry out unplanned maintenance at short notice?

SYSTEM COMPLEXITY

It is especially important for cold weather measurement systems to ensure that a design is as simple as possible while still meeting all required objectives. The need for unplanned maintenance due to complex component failures invariably leads to data loss and the need to visit site during periods of adverse weather conditions.

SELECTION OF DATA ACQUISITION EQUIPMENT

All equipment must be selected with consideration given to manufacturer limits on operational environment.

A 'tried and tested' approach must be adhered to as a remote environment prone to extreme weather is not the best place to experiment with new equipment.

Heated instruments should be used where reliable power sources capable of covering the full heating load are available. If intermittent instrument heating power availability is likely,

advice should be sought from manufacturers of heated equipment in order to confirm that the equipment is designed to survive in an unheated state as quoted environmental specifications frequently assume heating to be present 100% of the time.

Where economically and practically viable, redundancy should be built into a cold weather measurement system. A strategy should be formulated, where each instrument that is considered essential to the success of the project having a backup device that can be used in the event of primary instrument failure in order to maintain continuity of data. This strategy allows extra time for adequate preparation of an intervention to recover the system to full working order as data is not being lost during primary instrument down time.

SELECTION OF MAST STRUCTURE AND ASSOCIATED HARDWARE

Mast Structure

Consideration must be given to suitability of the mast for the intended environment, the following information at a minimum must be presented to a prospective mast supplier for inclusion in the design calculations for the structure and foundation:

- Coordinates of proposed location.
- Details of proposed equipment to be mounted onto the structure.
- Predicted ice build up on structure.
- Wind climate.

Instrument Booms/Lightning Finial

Instrument booms and lightning finials must be designed with due consideration being given to:

- Weight of instrument to be installed.
- Required separation distances.
- Increased weight due to ice build up on equipment.
- Wind climate.
- Change in dynamic response due to changes in mast oscillation as ice build up increases.

POWER SUPPLY

Available Sources of Power

A reliable, robust and simple power supply is essential to the success of a cold weather measurement system. The following sections gives an indication of possible sources of power to a measurement system located in an area prone to extended periods of extreme cold weather in order of preference:

1) Reliable grid connection

Where a suitably rated constant reliable grid connection is available, this is by far the simplest option as it involves the minimum equipment i.e. a cable. This solution however depends on 100% availability of mains power.

There are however some inhibitive factors to be considered, for example:

- Distance of location from grid source
- Protection of source from possible mast lightning strikes
- Local electrical regulations are very likely to require cable burial
- Cable losses due to voltage drops across long cable runs

2) A battery based power supply maintained by an intermittent grid connection

It is possible to utilise a less reliable grid connection to provide charge to a battery bank but only if there is sufficient autonomy built into the battery system to run at full load for the duration of a mains power outage.

3) A battery based power supply maintained by a diesel generator

For many wind monitoring projects, which tend to be remote and off-grid, a mains fed power supply is not practical and alternative solutions are required. The use of diesel generator systems to charge battery banks is a possible solution. There are however issues that must be considered in order to determine the practicality of such systems, for example:

- Generators will require refuelling and servicing, therefore increased maintenance will be required.
- Generators add complexity and this drastically increases the likelihood of component failure, usually at times of high demand or adverse weather conditions.
- Specialist vehicles may be required for refuelling / maintenance interventions in order to get fuel and equipment to site.
- Special fuel treatment or heated fuel lines are required to prevent an increase in fuel viscosity due to low temperature.
- There is the risk of diesel spillage or leakage.

4) A battery based power supply maintained by a renewable energy sources

While theoretically possible, the use of renewable sources of energy as a primary means of recharging battery banks, present some major technical issues, for example:

- Battery bank sizes would have to be significantly increased to maintain a charge level beyond the manufacturer recommended minimum state of charge during periods where no energy is being generated.
- Photovoltaic systems - Sunlight is in short supply during winter months, therefore the number of panels required to recover a battery depleted by loads due to instrument heaters would normally prove to be impractical.

-
- Micro Wind turbines - While significant energy can be recovered by wind chargers, these devices are prone to freezing, mechanical failure and damage due to icefall from the mast.

Instrument Power Supply Cabling Issues

When supplying heated instruments with DC power, losses in cables become significant, steps must be taken to ensure that the voltage drop is accounted for. This can be achieved by:

- Adjusting the voltage of a power supply in order to ensure the required supply voltage is present at the instrument heater
- Increasing the cable diameter in order to minimise voltage drop.
- Stepping up the supply voltage significantly at the source then stepping down again at the load, thus minimising the voltage drop by reducing load current in the cable.

Effect of Low Temperature on Battery Bank Storage Capacity

When sizing battery banks for cold weather measurement systems, it is critical that the de-rated storage capability of a battery at low temperature be accounted for in any system autonomy calculations.

Battery banks must have a safety cut off switch that will isolate a battery from a system when the battery is depleted to the manufacturer quoted minimum state of charge. Should a battery bank fall below the minimum recommended state of charge while at low temperature, damage to the battery bank is likely to occur.

For clarification, system autonomy is defined as the length of time it takes a battery bank, under normal load conditions to reach the manufacturers minimum recommended state of charge when no sources of charge recovery are available.

Instrument Heater Inrush Current

When specifying the rating of circuit protection devices such as circuit breakers and earth leakage residual current devices, it is important to factor in the short duration rush current that will be present when an instrument heater is activated. Failure to do so will result in phantom trips each time a heater is powered.

SYSTEM INSTALLATION, DECOMMISSIONING AND MAINTENANCE ACTIVITIES

The installation, decommissioning and planned maintenance of cold climate instrumentation campaigns should be performed outside of winter conditions where possible. This is primarily to increase the safety of the installation engineers and contractors. Where unplanned interventions are required during winter, cold weather equipment and ensuring the familiarity of all persons with the risks involved with working in cold climates are essential.

Careful consideration should be given to boom orientation to remove as much as possible the chance of ice falling on lower instruments. A staggered approach, where the lower instruments don't sit directly beneath the upper one, seems to work well, with the downside being that all instruments won't see identical tower shadow effects.

7.3.2 REMOTE SENSING RECOMMENDED PRACTICES

RS devices such as SoDARs and LiDARs are an attractive proposition for cold climate measurement campaigns as they can operate down to very low ambient temperatures without data quality being affected.

This section highlights key aspects of best practice that should be considered when deploying a RS device. These practices are particularly relevant for the deployment of RS devices at cold climates sites. This section reflects the experiences of deploying a WINDCUBE V1 LiDAR device at Havsnäs wind farm but also draws on experiences from other RS device deployments.

When deploying any RS device it is important that the device is appropriately deployed. This will help ensure that the data recorded by the RS device are suitable for the intended purpose. When planning a RS deployment at a cold climate site there can be additional aspects of the deployment that should be considered as discussed in the following sections.

DEVICE SITING

Ensure that device is sited according to manufacturer guidelines, taking account of aspects such as beam direction and any obstacles or trees. Where possible site the device as close to the reference mast as possible. Difficulties can arise in deploying RS devices in very remote locations with poor vehicular access. Particularly in cold weather sites with the potential for deep snow, it will not always be possible to site the RS device in the most appropriate location. Therefore, when planning the RS measurement campaign, it is sensible to decide upon an alternative appropriate siting location.

While many sites will be quite remote it is still sensible to take precautions against theft. Therefore, ensure that the device and any other equipment is, where possible, suitably secured.

POWER SUPPLY

Adequate consideration must be given to the power supply. The power demands of RS devices increase in very low temperatures as internal components must be maintained at operating temperatures.

Many of the comments in the Power Supply section of Section 7.3.1 are also relevant for RS devices.

SNOW PLATFORM

When deploying a RS device in a cold climate, serious consideration should be given to the use of a snow platform (Figure 7.3.1). For some devices, for example the AQ500 Wind Finder with its trailer, this is not necessary, but even larger devices like the Secondwind Triton SoDAR can be deployed on a snow platform. In particular, the smaller LiDAR devices are more susceptible to the impacts of drifting snow (Figure 7.3.2) and it is strongly recommended that a snow platform is utilised. Using a snow platform will allow devices to continue to operate even when there is deep snow or a large build-up of drifting snow.



Figure 7.3.1: Leosphere WINDCUBE V1 on snow/hunting platform at Havsnäs



Figure 7.3.2: Leosphere WINDCUBE V2 on a scaffold snow platform in Scotland.

If an external generator is being used to power a RS device, consideration should be given to protecting the generator from the effects of snow build-up. If the generator ventilation becomes blocked then it is likely that the generator will shut down and there is a risk of data loss. Building a 'tent' with suitable ventilation as shown in Figure 7.3.3 will allow the generator to continue operating in deep and drifting snow.



Figure 7.3.3: 'Tent' with ventilation covering generator

The snow platform can be constructed from a variety of materials (for example, an elk shooting platform or scaffolding). Whatever type of platform is used it is essential that it is stable, causes no obstructions to the device and in particular, for SoDAR devices, causes no fixed echoes.

IEC MEASUREMENT HEIGHT RECOMMENDATIONS

If obtaining a measure of rotor equivalent wind speed is part of the deployment campaign objectives, then it is important to follow the IEC recommendations. The IEC recommends that measurement heights are distributed as symmetrically as possible around hub height and as evenly as possible over the vertical range of the rotor diameter.

It is also important to ensure that the RS measurement heights match as closely as possible the anemometer measurement heights of the co-located fixed mast.

Therefore, it may be necessary to compromise slightly the lower measurement heights to ensure that agreement between RS devices and fixed masts is retained at key heights. Nevertheless, for most user-configurable RS devices it should still be possible to achieve both coincident measurement heights and measurement heights suitable for calculating rotor equivalent wind speed.

CORRECTLY CONFIGURED MEASUREMENT HEIGHTS

When configuring the RS measurement heights, it is important to take account of any measurement offset that there is in the system set up. This will ensure, as closely as possible, that the actual measurement heights above ground level match the anemometer measurement heights and the correct measurement heights for rotor equivalent wind speed calculations.

For example, the WINDCUBE LiDAR is approximately 0.5 m high, from the bottom of the device to the zero height of the WINDCUBE window (this height can change depending on the extension of the levelling legs). Then if a 2 m snow platform is used the height above ground to the platform level needs to also be considered. For this example, to configure a WINDCUBE device for a 90 m AGL measurement, the actual LiDAR measurement height (above LiDAR window) is:

$$90 - 0.5 - 2 = 87.5 \text{ m.}$$

For the WINDCUBE, measurement heights or range gates can only be set to 1 m resolution. Therefore the measurement height should be rounded to the nearest metre, in this case 88 m.

LOW AEROSOL CONFIGURATION

LiDAR devices depend upon the presence of aerosols in the atmosphere to back scatter the laser pulses. The devices can then use the information from the back scattered laser pulses to

calculate the various wind parameters necessary to characterise the wind flow through the measurement volume.

The origins of the aerosols are various but generally at remote, cold climate, sites the air is much cleaner with lower aerosol densities. This results in less back scattered light and therefore lower signal quality and lower data capture.

For LiDAR deployments in cold climates and where the specific device allows, it is recommended that the number of measurements made by each line of sight is increased.

Following discussions with the manufacturer, for the case of WINDCUBE LiDAR devices, it is recommended that the number of pulses per line of sight is increased to 40,000 and the CNR threshold is reduced by 2 dB. This was as a result of the analysis presented in Section 7.2.2 of this report. Depending on the WINDCUBE version deployed, this will result in a factor of two or four increase in the number of laser pulses per line of sight. This means that there will be more back scattered signals and therefore as a result of the increased signal quality it will be easier to identify the back scattered signal from the 'noise'. The carrier to noise ratio (CNR) threshold can therefore be reduced by 2 dB. This will increase qualified data capture but should not adversely affect the reliability of values of standard deviation of mean horizontal wind speed.

COLD WEATHER INSULATION

In order to combat the effects of cold weather on RS devices (small LiDAR devices in particular), it is important to ensure that any device is suitably insulated against cold weather. However, it is also important to ensure that all air vents remain clear to allow system cooling. Taking suitable measures to protect the device from cold weather will help ensure that the device continues to operate during cold weather.



Figure 7.3.4: Insulation in the LiDAR device.

It may be necessary to remove the insulation once the air temperature starts to rise. Otherwise data may be lost due to overheating and system shutdown.

At Havsås a cold weather insulation cover was used, as provided by the manufacturer. However, to ensure that snow could not build up on top of the WINDCUBE, modifications were made. RES Instrumentation developed a heating grid to help keep the WINDCUBE window clear of snow. The heating grid was positioned on top of the device, between the WINDCUBE unit and the outer insulation cover.

The heating grid consisted of a layer of insulation, a layer of heat reflecting foil and a grid of heating wire (the same heating wire used for boom heating). The insulation ensured the device remained warm while the protective foil prevented any damage to the device from the heating wire. The grid of heating wire provided heating to the top of the outer cover to ensure it remained free from snow. This modification was very effective and allowed the WINDCUBE to continue operating, unaffected by the snow.

DEVICE MONITORING

Once the RS device is deployed and operational, and to maximise device operational availability and maximise qualified data capture, it is essential to closely monitor the RS device, paying attention to any status indicators or alarm emails. Responding to these, where necessary in close liaison with the device manufacturer, will help ensure that device down time is minimised and qualified data capture maximised.

DEPLOY WEBCAM

Deploying a webcam as part of the RS deployment can prove useful. This will enable remote viewing of the system which could help to identify any issues or isolate the cause of a specific fault. For example, snow build up can be monitored and for devices with a wiper it will be possible to confirm if the wiper has failed over the window of the RS device.



Figure 7.3.5: Clear window on Leosphere WINDCUBE V2.

The ability to remotely identify and isolate faults could help to reduce the cost of a RS campaign. Multiple and frequent site visits, particularly to a remote site with difficult access requirements can result in large costs in terms of staff time and expenses.

With a webcam it may be possible to locate the cause of a fault and therefore ensure that any visit to site will be suitably equipped to deal with the fault. If for example there is some snow build up that needs to be removed, it may be possible in the short term to employ someone local to the site to remove the snow build up.

7.4 ENERGY PRODUCTION LOSSES

7.4.1 LIDAR MEASURED IEC EQUIVALENT WIND SPEED

INTRODUCTION

This section uses RS data to investigate the evolving industry assumption that energy yield predictions are over-estimated in the stable atmospheric conditions characteristic of Scandinavian wind farm sites.

Using data from RS devices and co-located fixed masts, this report investigates the validity of this assumption for Havsnäs wind farm and another site in Sweden. This report initially considers the WINDCUBE V1 LiDAR deployment at Havsnäs, M814, which is co-located with M6261. Data from another RES site in Sweden is also considered.

BACKGROUND

At sites in the USA where stable atmospheric conditions are prevalent it has been found that the average performance of turbines in particular wind conditions, characterised by low turbulence (turbulence intensity < 8 %) was materially lower than those not characterised by low turbulence [30]. As a result an energy loss adjustment factor is now applied at such sites in the USA.

It is important to understand if what has been observed at sites in the USA is globally applicable at sites characterised by stable atmospheric conditions. It may be that the different atmospheric drivers in different parts of the world mean that the results from the USA cannot be globally applied. Indeed, for sites characterised by stable atmospheric conditions, it may be necessary to investigate this phenomenon on a site by site basis.

In [31]¹², it is suggested that in stable atmospheric conditions, lower shear is experienced across the upper part of the rotor diameter than in the lower part of the rotor. For low turbulence conditions it is reported that, the high shear observed across the fixed mast measurement range is not observed across the upper half of the rotor.

¹² WINDPOWER Presentation by Tony Roger, DNV KEMA, June 2012. Used with permission.

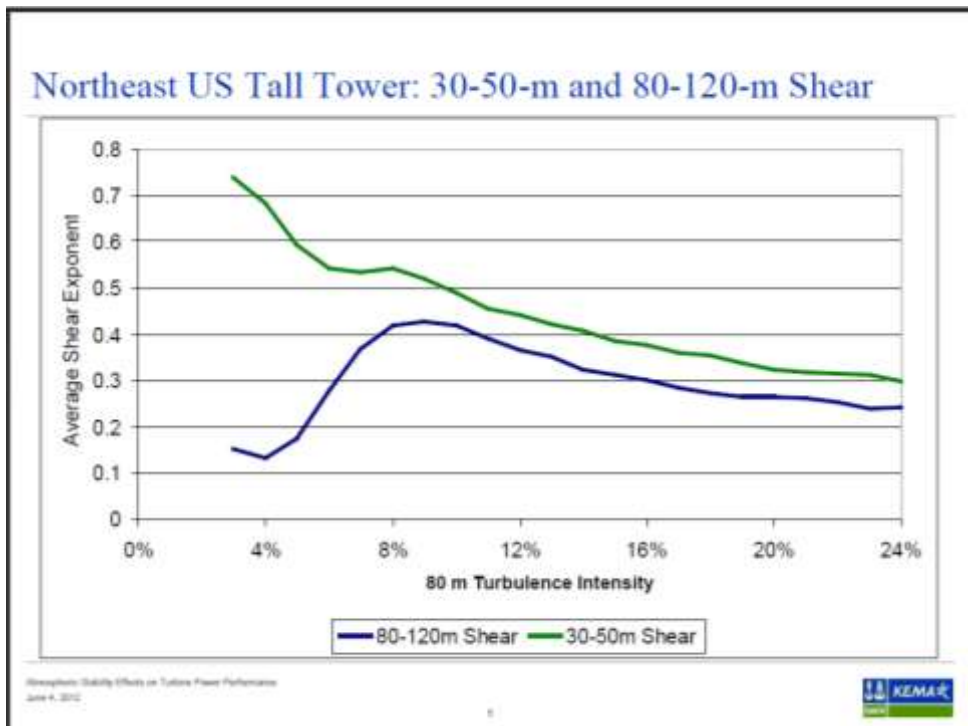


Figure 7.4.1: Shear by Turbulence Intensity (DNV KEMA Data from USA).

Further, the presentation shows how for low turbulence conditions, the measured or shear extrapolated hub height wind speed overestimates the actual hub height wind speed as given by the rotor average wind speed.

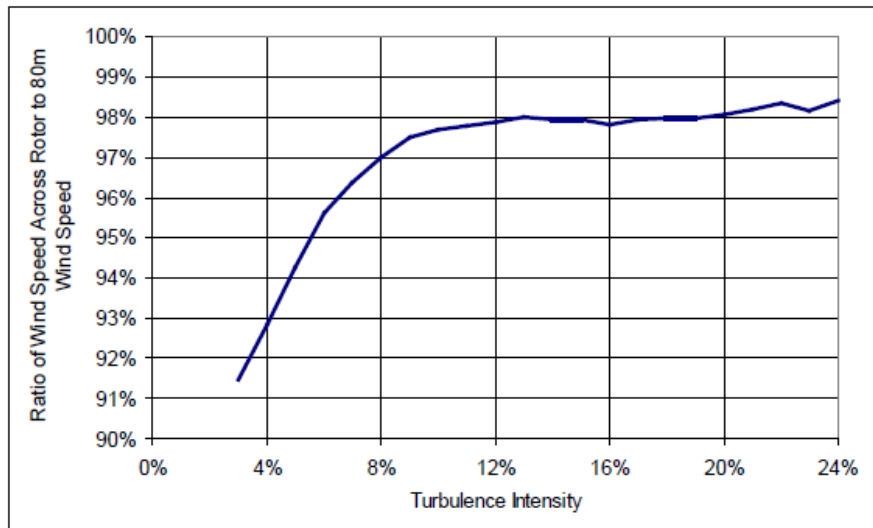


Figure 7.4.2: Shear Correction Factor by Turbulence Intensity (DNV KEMA Data from USA)

For turbulence intensity below 10 % it is clear that the ratio of hub height wind speed to rotor average wind speed falls dramatically away from the general trend of the ratio.

EQUIVALENT WIND SPEED ANALYSIS

One approach to investigating this problem is to compare measured or shear extrapolated hub height wind speed to the equivalent wind speed across the rotor.

Wind shear and turbulence are closely linked according to atmospheric stability. Low turbulence is associated with high wind shear (stable conditions) and high turbulence with low wind shear (unstable conditions).

It can be hypothesised that if turbines are underperforming in low turbulence conditions (and therefore high wind shear conditions) then hub height wind speeds are overestimated for such conditions.

Therefore, in low turbulence conditions, the standard approach of using a shear value obtained from fixed mast measurements, to extrapolate to hub height should result in an overestimation of hub height wind speed and therefore an overestimation in the turbine energy yield.

Using RS data and the guidance in the IEC draft standard (IEC61400-12-1) for calculating rotor average wind speed, it is possible to calculate an equivalent hub height wind speed that takes account of the variation in wind speed (and hence shear) across the rotor diameter.

It is then possible to compare equivalent hub height wind speed to that derived by extrapolating from the measurement height to hub height.

IEC DEFINITIONS

Equivalent wind speed and the shear correction factor are defined in the IEC draft standard [1] as follows:

Equivalent Wind Speed

The rotor-averaged or equivalent wind speed is defined as in Equation 6.4.2 of Section 6.4.

Shear Correction Factor

A shear correction factor is defined as a ratio of the equivalent wind speed relative to the wind speed measured at hub height according to

$$f_{r,X} = v_{eq,X} / v_{h,X} \quad \text{Equation 7.4.1}$$

where

$v_{eq,X}$ is the equivalent wind speed as defined in Equation 6.4.2 of Section 6.4;

$v_{h,X}$ is the wind speed measured at hub height;

and the index X specifies the instrument or instrument setup both, $v_{eq,X}$ and $v_{h,X}$, are measured with.

It is also possible to calculate a shear correction factor for wind speed extrapolated to hub height, something that is done in this analysis.

SHEAR INVESTIGATIONS AT HAVSNÄS

At Havsnäs, the rotor centre, lower tip and upper tip heights were taken to be 96m, 51m and 141m respectively, based on a rotor diameter of 90m.

Figure 7.2.13 in Section 7.2.3 shows that, generally there is good agreement between the fixed mast and WINDCUBE characteristic turbulence intensity. However, the WINDCUBE does measure higher turbulence than the fixed mast.

Due to the different measurement principles for the LiDAR compared to the cup anemometers on the mast (volume averaged versus point measurement), we do not expect the turbulence intensities to agree but it is encouraging to note that the turbulence trend is reasonably well captured by the LiDAR.

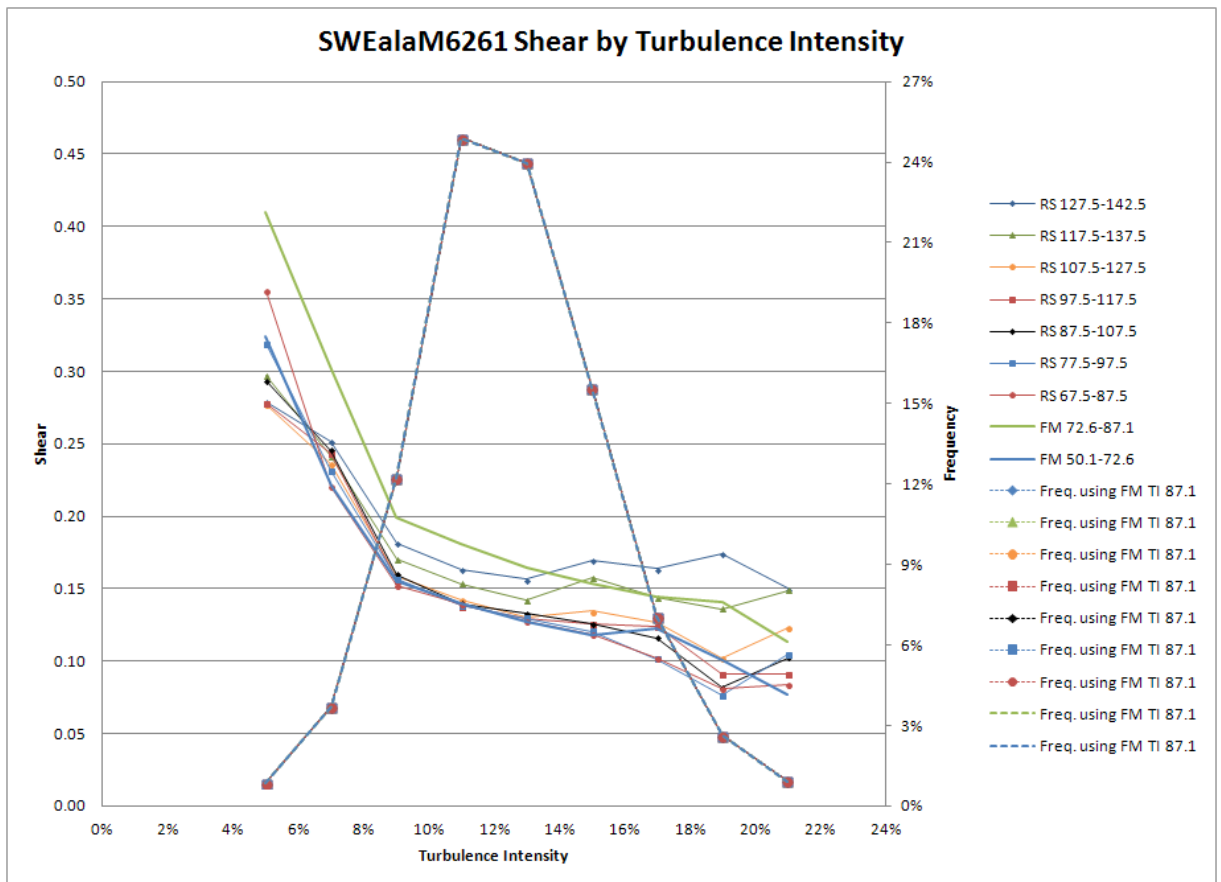


Figure 7.4.3: Shear by Turbulence Intensity at Havsnäs (FM denotes fixed mast M626).

Plotting shear by turbulence intensity for the full range of shear measurements, it can be seen that at low turbulence intensity high shear is present. However, it is clear from Figure 7.4.3 that, at these low turbulence intensities, high shear persists across the full range of shear measurements from lower rotor tip to upper rotor tip.

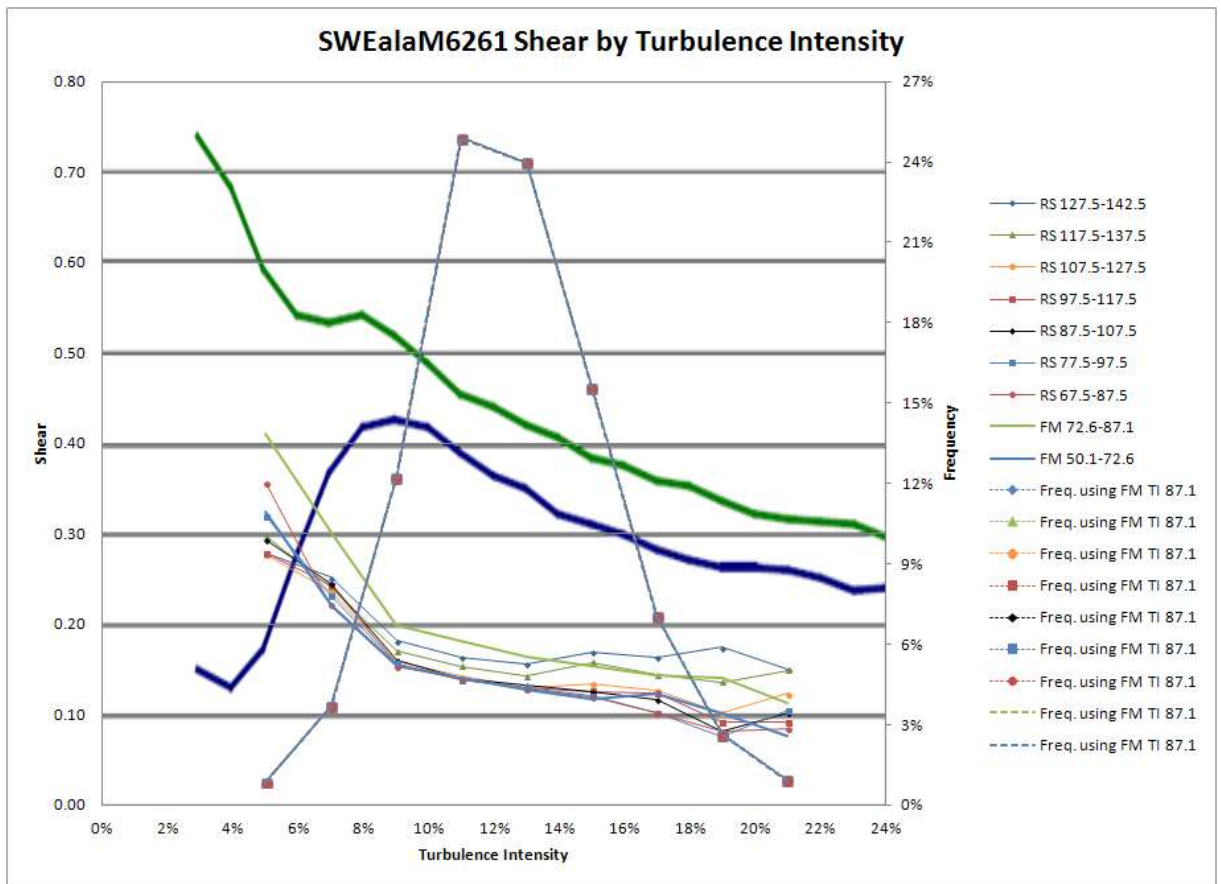


Figure 7.4.4: Shear by Turbulence Intensity at Havsnäs (As Figure 7.5.3 but including DNV KEMA Data).

From Figure 7.4.4, it does appear that the shear versus turbulence relationship changes slope at around 9 % in both DNV KEMA (see Figure 7.4.1 also) and RES analyses. Critically, however, we do not see a decrease in shear at higher measurement heights; the shear versus turbulence relationship remains similar irrespective of the measurement heights.

One of the assumptions forming the basis for applying an energy loss adjustment factor would be that the shear behaviour in the upper half of the rotor would be different from what is measured in the lower half of the rotor.

In the DNV KEMA case, the implication is that by measuring shear only between 30 and 50m, the average shear profile across the entire rotor disk (averaged over all turbulence conditions) would be overestimated due to missing the low turbulence turning point and hence the argument for applying an energy loss adjustment factor.

However, the Havsnäs data suggest that the average shear profile does contain this low turbulence turning point, irrespective of whether the shear is measured on the mast or LiDAR and irrespective of the measurement height and hence the shear profile is not significantly over estimated by basing it on below hub height measurements only.

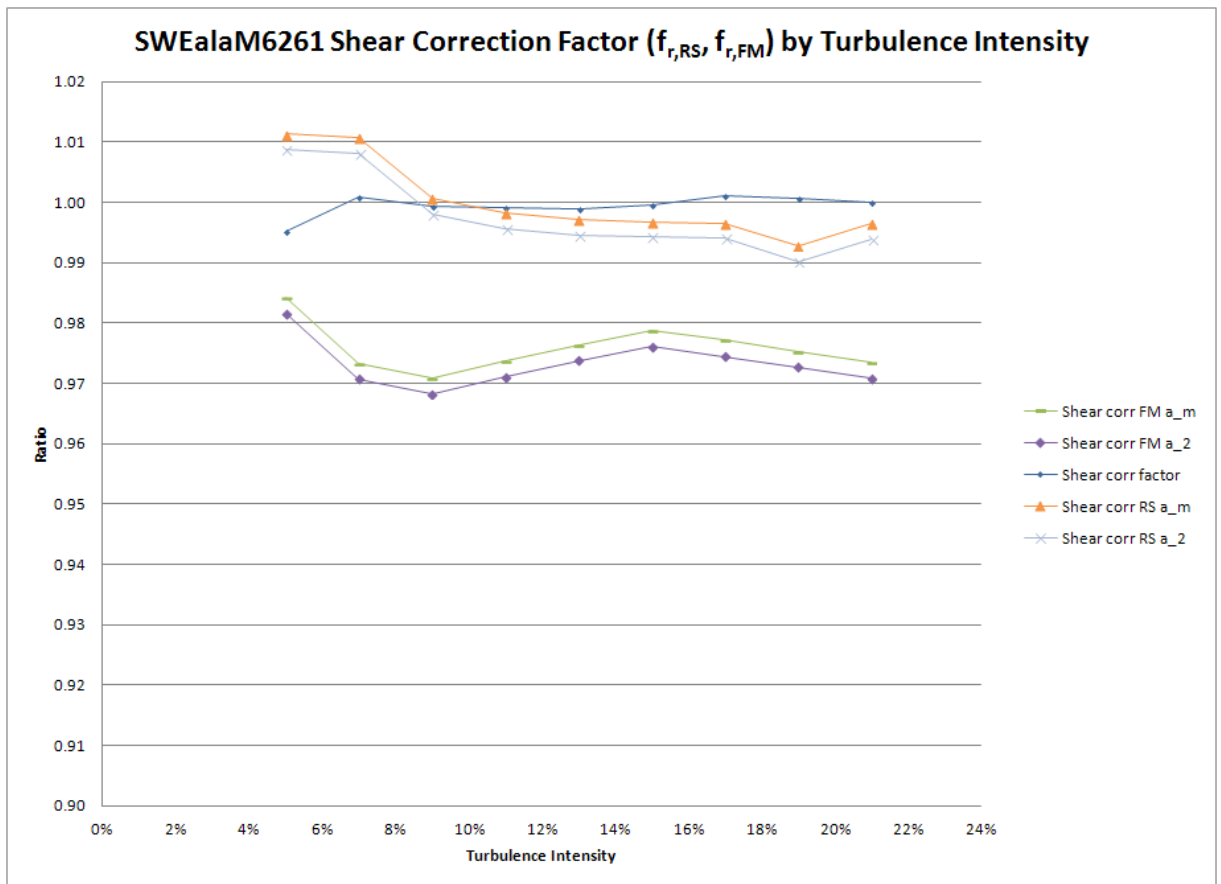


Figure 7.4.5: Shear Correction Factor by Turbulence Intensity at Havsnäs (FM denotes fixed mast M626).

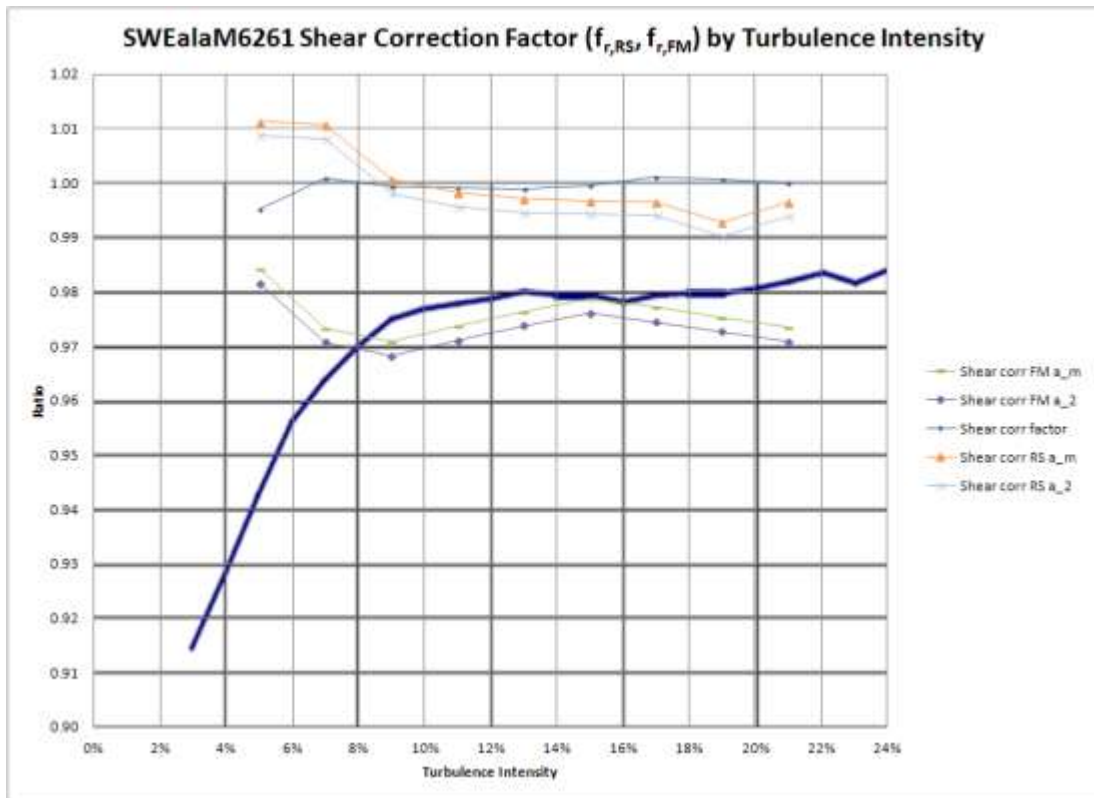


Figure 7.4.6: Shear Correction Factor by Turbulence Intensity at Havsnäs (As figure 7.4.5 but including DNV KEMA Data)

Series		
Number	Name	Description
1	Shear corr FM a_m	Equivalent wind speed / hub height measure of shear calculated by extrapolating 87.1 m fixed mast data using a multi-point value of shear
2	Shear corr FM a_2	Equivalent wind speed / hub height measure of shear calculated by extrapolating 87.1 m fixed mast data using a two point value of shear
3	Shear corr factor	Equivalent wind speed / hub height measured RS data
4	Shear corr RS a_m	Equivalent wind speed / hub height measure of shear calculated by extrapolating 87.5 m RS data using a multi-point value of shear
5	Shear corr RS a_2	Equivalent wind speed / hub height measure of shear calculated by extrapolating 87.5 m RS data using a two point value of shear
Notes		<ul style="list-style-type: none"> Equivalent wind speed is calculated with RS data using equation (1) above, with $n = 9$. Shear correction factor is calculated using equation (2) above. The methodologies used to obtain multi-point and two point shear values are described in Section 6.1.2.

Table 7.4.1: Shear Correction Factor at Havsnäs (Legend Descriptions).

In Figure 7.4.2 (and as can also be seen in Figure 7.4.6) The DNV KEMA data suggest a situation where the rotor average wind speed is significantly less than the hub height wind speed in low turbulence situations and therefore the energy content across the rotor disk will also be less.

From Figure 7.4.5 (and Figure 7.4.6) however, the Havsnäs LiDAR data show very little variation in the shear correction factor as the turbulence intensity decreases. In particular, series 3 in Table 7.4.1 (as derived using LiDAR measured data only) is very stable. There is no dramatic plunge in rotor averaged wind speed for turbulence intensities less than 9 %. Note that the hub height wind speed used in the shear correction factor is the LiDAR measured (approximate) hub height wind speed at 97.5 m.

When using fixed mast data extrapolated to hub height (series 1 & 2 in Table 7.4.1), the resultant shear correction factors do not vary strongly with turbulence intensity but are quite steady. Generally across the full range of turbulence intensity, the fixed mast overestimates the LiDAR based equivalent wind speed by approximately 2-3 %.

However, as turbulence intensity drops below 9 %, this overestimation decreases, suggesting that the presence of low turbulence intensity at a site does not lead to an overestimation of hub height wind speed.

These results do not suggest that an energy loss factor is appropriate at Havsnäs.

The LiDAR measures lower wind speeds at Havsnäs when compared to the fixed mast. As the mast and LiDAR are not at the same location, this wind speed difference could be a real, spatial wind speed variation. However the important point is that the difference remains consistent as a function of turbulence intensity.

Using seasonal campaign LiDAR or other RS device measurements in conjunction with a long-term, shorter than hub height meteorological mast can therefore provide a clearer understanding of the impact of using a shear value from lower measurement heights on the met mast to extrapolate the wind climate to hub height.

Using the warranted power curve for the 2 MW turbines installed at Havsnäs, it is possible to calculate an energy yield for each measure of hub height wind speed. Table 7.4.2 presents a matrix of the ratios of energy yield derived from each wind speed definition in combination with the power curve.

	Energy (GWh)	Energy Ratios		
		/FM 96	/RS HH 97.5	/v equiv
RS HH 97.5	6.64	0.97	1.00	0.99
v equiv	6.69	0.98	1.01	1.00
FM 96	6.86	1.00	1.03	1.03
FM 87.1 sheared to HH (a_m)	6.74	0.98	1.02	1.01
FM 87.1 sheared to HH (a_2)	6.78	0.99	1.02	1.01
RS 87.5 Sheared to HH (a_m)	6.55	0.96	0.99	0.98
RS 87.5 Sheared to HH (a_2)	6.61	0.96	0.99	0.99

Table 7.4.2: Ratios of Energy Yield at Havsnäs (Standard sea level density, 1.225 kg/m³, has been used in the energy yield calculations).

The equivalent wind speed using LiDAR measurements (v equiv) is around 1% more energetic than that of the measured LiDAR time series at 97.5 m (RS HH 97.5).

The fixed mast measured data at 96 m (FM 96) are 3% more energetic than the LiDAR measured data at 97.5 m and about 2.5% more energetic than the equivalent wind speed data.

Therefore, when extrapolating fixed mast measured data from 87.1 m to 97.5 m and calculating the energy content, similar energy content as compared to the 96 m fixed mast data would be expected. Similar differences in energy when compared to the 97.5 m LiDAR data would also be expected. As Table 7.4.2 shows, similar differences are indeed observed.

When considering the LiDAR extrapolated data against the equivalent wind speed data this suggests that using a measure of shear derived from measurements over the fixed mast measurement heights will result in an underestimation of the energy content.

Similarly, when considering the fixed mast extrapolated data against the fixed mast measured data at 96 m, this also suggests that using a measure of shear derived from measurements over the fixed mast measurement heights will result in an underestimation of the energy content.

These results do not suggest that an energy loss factor is appropriate at Havsnäs.

SHEAR INVESTIGATION AT ANOTHER SWEDISH SITE

At another Swedish site, a turbine hub height of 118 m and a rotor diameter of 113 m have been used. This means the lower tip height is at 61.5 m and the upper tip height at 174.5 m.

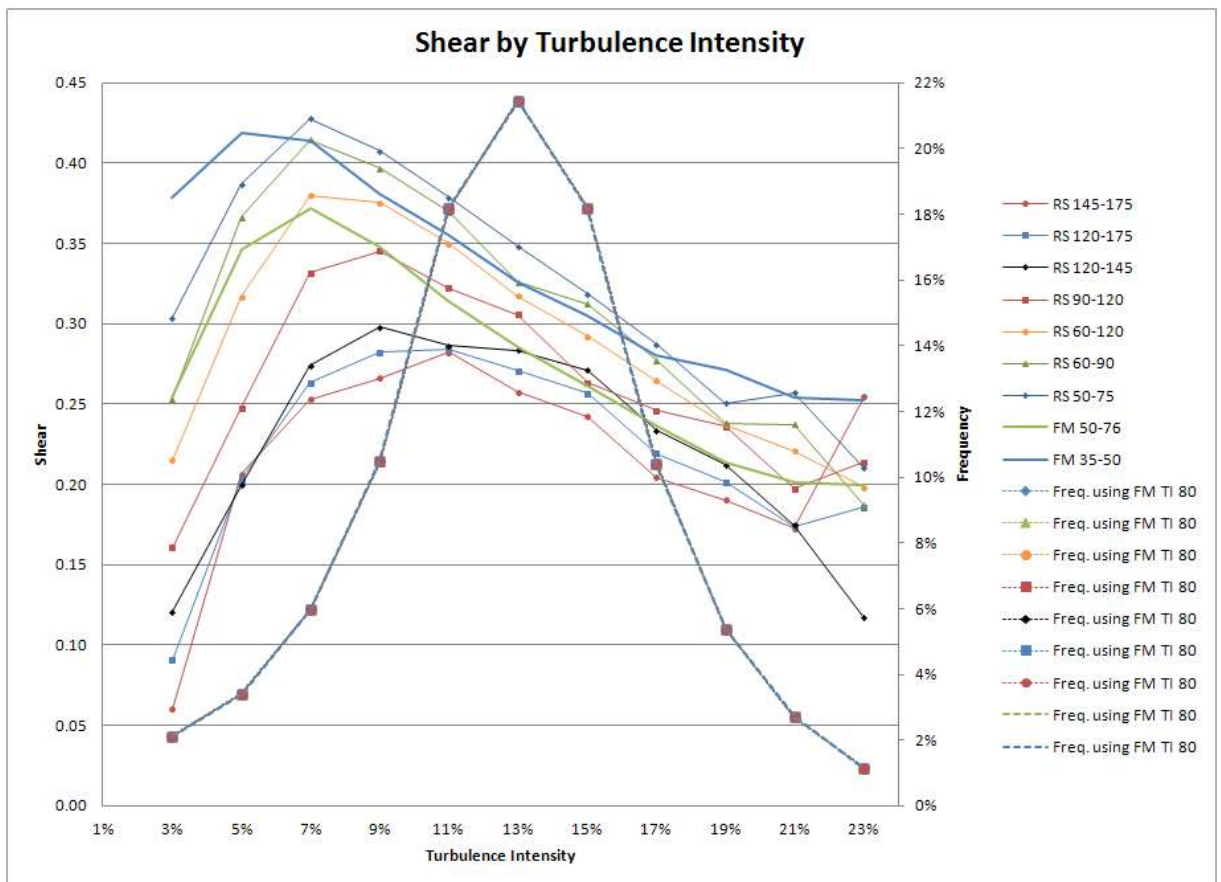


Figure 7.4.7: Shear by Turbulence Intensity at Other Swedish Site

When considering this other Swedish site, the RS data in Figure 7.4.7 show a shear versus turbulence relationship similar to that obtained by DNV KEMA in so much that there is a turning point at low turbulence (8% in this case). However, this relationship is followed irrespective of the measurement height. The data do not support the view that met mast shear measurements at low elevations overestimate the shear exponent at low turbulence intensity when compared to shear measurements based on measurements at higher elevations.

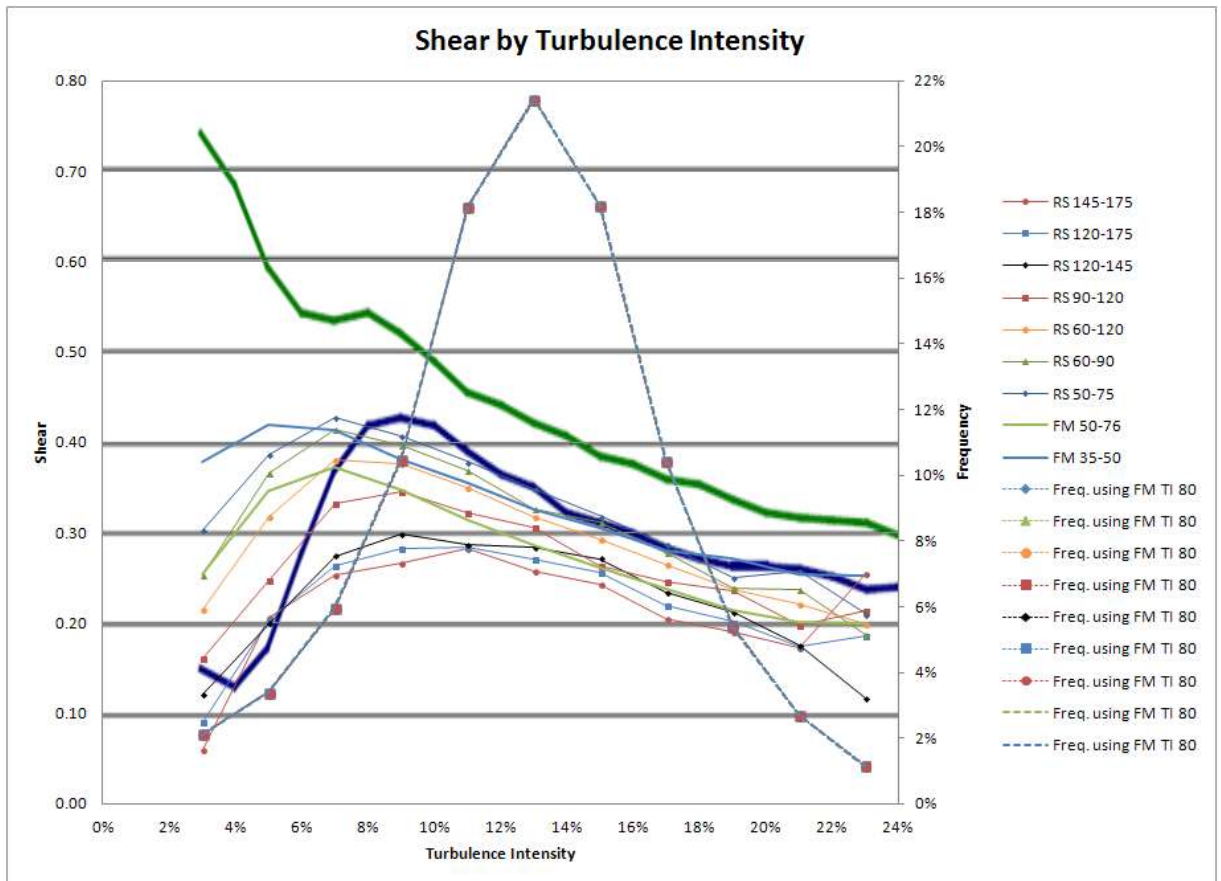


Figure 7.4.8: Shear by Turbulence Intensity at Other Swedish Site (As Figure 7.4.7 but including DNV KEMA Data).

In this case and as shown in Figure 7.4.8, all the measurements, whether low elevation or high elevation, mast or RS device, exhibit a similar characteristic of decreasing shear exponent in turbulence less than 8%. Consequently the average shear exponent from the met mast measurements is not as significant an overestimate of the rotor disk shear as the DNV KEMA data (see Figure 7.4.1 also) would suggest.

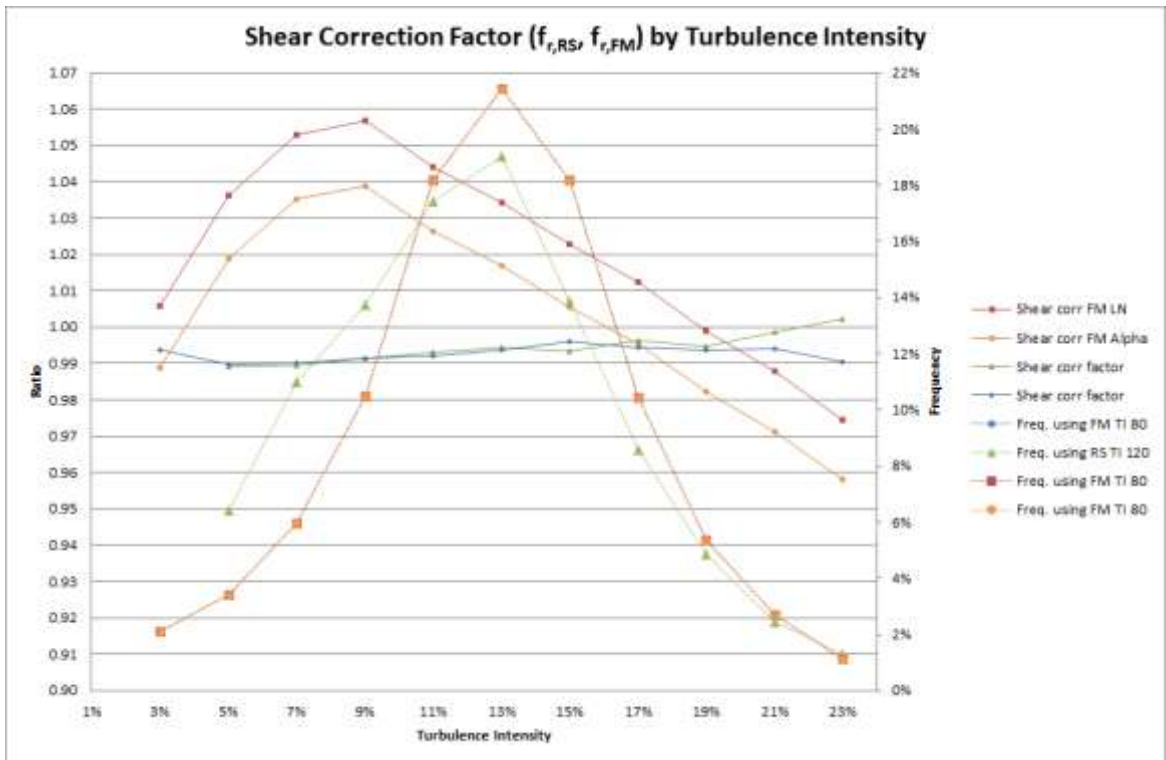


Figure 7.4.9: Shear Correction Factor by Turbulence Intensity at Other Swedish Site.

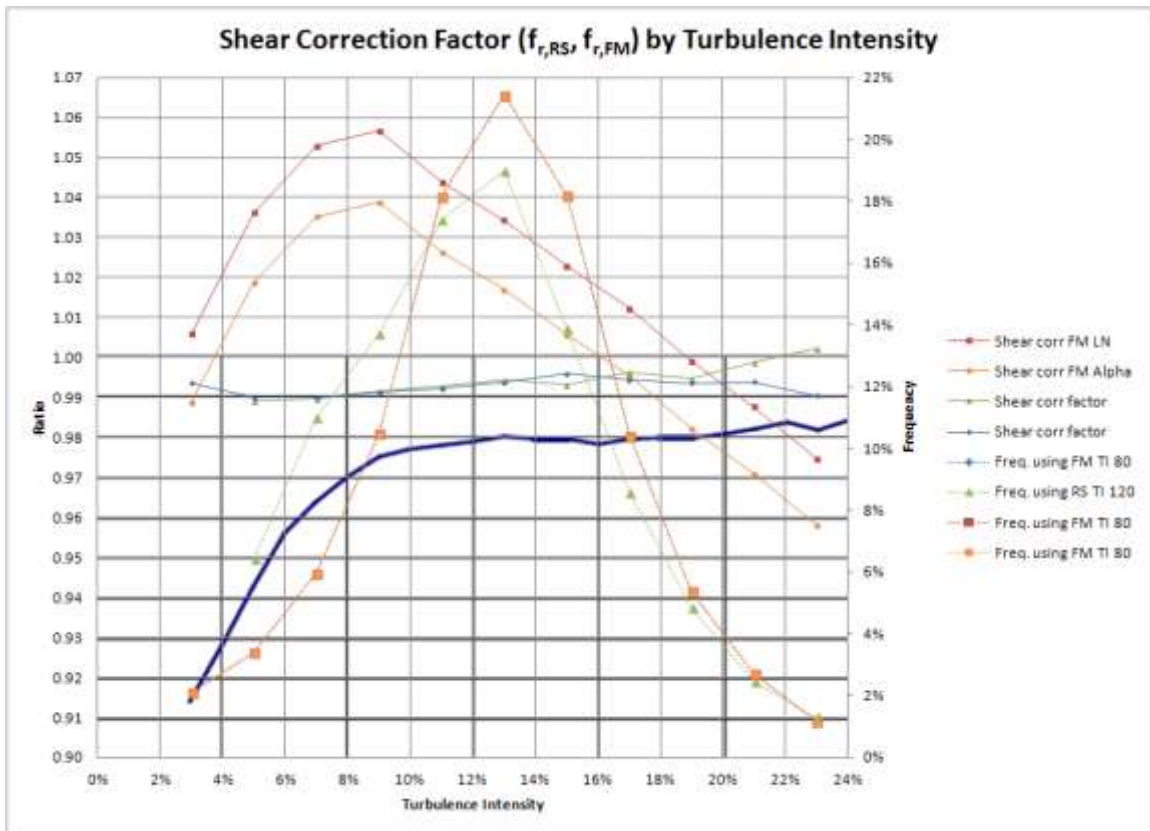


Figure 7.4.10: Shear Correction Factor by Turbulence Intensity at Other Swedish Site (As Figure 7.4.9 but including DNV KEMA Data).

Series		
Number	Name	Description
1	Shear corr FM LN	Equivalent wind speed / hub height measure of shear calculated by extrapolating 79.8 m fixed mast data using a one point value of shear
2	Shear corr FM Alpha	Equivalent wind speed / hub height measure of shear calculated by extrapolating 79.8 m fixed mast data using a two point value of shear
3	Shear corr factor	Equivalent wind speed / hub height measured RS data (using RS turbulence distribution measured at hub height)
4	Shear corr factor	Equivalent wind speed / hub height measured RS data (using fixed mast turbulence distribution measured at 79.8 m)
Notes		<ul style="list-style-type: none"> • Equivalent wind speed is calculated with RS data using equation (1) above, with $n = 5$. • Shear correction factor is calculated using equation (2) above. • The methodologies used to obtain one point and two point shear values are described in Section 6.1.2.

Table 7.4.3: Shear Correction Factor at Other Swedish Site (Legend Descriptions).

The RS data (series 3 & 4 in Table 7.4.3) show very little variation in the shear correction factor as the turbulence intensity decreases. There is no dramatic plunge in rotor averaged wind speed for turbulence intensities less than 9 %. Note that in this case the hub height wind speed used in the shear correction factor is the RS device measured (approximate) hub height wind speed at 120m.

For the fixed mast data extrapolated to hub height (Series 1 & 2 in Table 7.4.3), as turbulence decreases towards 9 %, the hub height wind speed tends to underestimate the wind speed through the rotor diameter. As the turbulence continues to decrease this underestimation decreases. This is due to the fixed shear exponent not capturing the turbulence dependency of shear. However, the result does not suggest that an energy loss factor is appropriate.

Using the warranted power curve for a 3 MW turbine, it is possible to calculate an energy yield for each measure of hub height wind speed. Table 7.4.4 presents the energy ratios derived from each wind speed definition in combination with the power curve.

	Energy (GWh)	Energy Ratios	
		/RS HH 120	/v equiv
RS HH 120	11.90	1.00	1.01
v equiv	11.78	0.99	1.00
FM 80	9.52	0.80	0.81
FM 80 sheared to HH (Alpha)	11.55	0.97	0.98
FM 80 sheared to HH (Log law)	11.21	0.94	0.95
RS 80 Sheared to HH (Alpha)	11.59	0.97	0.98
RS 80 Sheared to HH (Log Law)	11.26	0.95	0.96

Table 7.4.4: Ratios of Energy Yield at Other Swedish Site (Standard sea level density, 1.225 kg/m³, has been used in the energy yield calculations).

The equivalent wind speed using RS measurements (v_{equiv}) is around 1% less energetic than that of the measured RS time series at 120 m. This suggests that the hub height measured wind speed data will marginally overestimate the energy through the rotor diameter.

When considering the wind speed data extrapolated to hub height, from both the fixed mast and the RS device, against the equivalent wind speed data, all extrapolated data are less energetic than the equivalent wind speed data. This suggests that using a measure of shear derived from measurements across the fixed mast will result in an underestimation of the energy content.

These results do not suggest that an energy loss factor is appropriate at this site.

CONCLUSIONS

In considering the available data from these two Swedish sites, it is evident that the manner in which shear varies with turbulence intensity is site dependent and will vary from site to site, even when both sites are characterised by stable atmospheric conditions. Neither of the sites considered exhibit the same trend observed by DNV KEMA on sites in the USA, suggesting that the precise characteristics of the climate, topography and surface roughness are altering the shear characteristics in some critical way.

At one Swedish site, shear decreases with decreasing turbulence intensity below 9 % whereas at Havnäs shear increases with decreasing turbulence intensity below 9 %.

The RS and fixed mast measured data at both sites do not support the view that meteorological mast shear measurements at low elevations overestimate the shear exponent at low turbulence intensity when compared to shear measurements based on measurements at higher elevations.

Indeed, at both sites the manner in which shear varies with turbulence intensity is consistent across the full rotor diameter and between fixed mast and RS device. There is therefore no dramatic over estimation of hub height wind speed at turbulence intensities below 9 %.

From these two sites, it could be argued that using a measure of shear obtained from fixed mast measurements made below hub height is likely to underestimate energy through the rotor diameter.

Considering the data from these two Swedish sites, the justification for a universal energy loss adjustment factor to account for periods of high atmospheric stability is not evident.

It can be said therefore that what has been observed in the USA cannot simply be applied in other regions where stable atmospheric conditions prevail. The climatic mechanisms that create stable atmospheric conditions may vary from region to region and it is clear that not all stable atmospheric conditions result in an overestimation of energy through the rotor diameter.

Such an energy loss adjustment factor should not be applied generally. In particular, each region should be treated separately on the basis of data gathered from that region and each individual site, where the necessary data exist, should be considered on its own merits.

It is only with the deployment of a RS device in conjunction with a long-term reference mast at each wind farm site that the necessary data to make an informed judgement on the appropriateness of an energy loss adjustment factor can be obtained.

7.4.2 DOWNTIME LINKED TO ICING

This document describes an evaluation of lost production due to icing at Havsnäs wind farm. It is assumed that the primary mechanism of energy loss due to icing (hereafter icing loss) is decreased aerodynamic efficiency of the turbine, which causes reduced power output while the turbine is operating. Other mechanisms of icing loss such as the inability to start after a shutdown, incorrect wind speed reading or increased probability of component failure may be possible but have not been evaluated in this work.

METHODOLOGY

Dataset

Active power, wind speed, ambient temperature and blade pitch data from the Havsnäs SCADA system were analysed for the time period October 1, 2010 to September 30, 2012. Data coverage for this time period was 97.4%.

Data Processing

In this work, icing loss in a 10-minute period is defined as:

$$\text{Icing Loss} = (\text{Warranted Power} - \text{Actual Power})/1000/6$$

where *Icing Loss* is in MWh, *Warranted Power* and *Actual Power* are 10-minute means and in kW, and *Warranted Power* is a function of nacelle-measured wind speed. This calculation is performed only when the following conditions are met:

- There are no stopping alarms active (note that these turbines do not have a specific icing alarm)
- Measured wind speed is above cut-in (4m/s)
- Measured wind speed is below cut-out restart (20m/s); this is to prevent the effects of high wind speed shutdown from being interpreted as icing loss
- Curtailment is not occurring (this is determined by analysing the pitch behaviour)
- *Actual Power* is less than 100kW of *Warranted Power*
- *Actual Power* is shifted right of the warranted curve by more than 1 m/s (see Figure 7.4.12)

Uncertainty Assumptions

The uncertainty associated with icing loss was assumed to be dominated by the uncertainty in the nacelle-measured wind speed. The uncertainty in nacelle-measured wind speed is believed to be 10%. Therefore, the uncertainty of the Icing Loss calculation is assumed to be 20% (10% wind speed and a sensitivity factor of 2). Note there may also be a bias associated with the nacelle anemometer during Iced conditions as suggested by Figure 7.4.11.

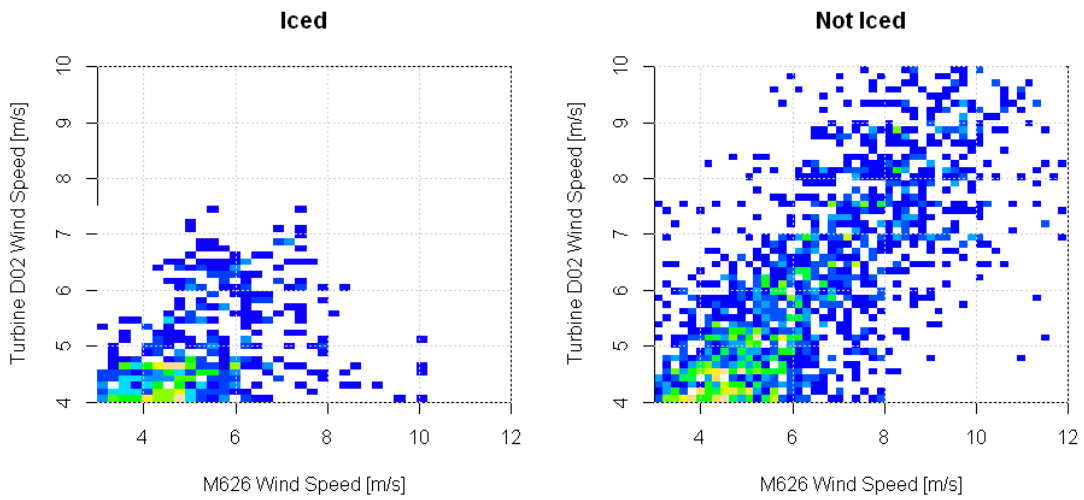


Figure 7.4.11: Nacelle-measured wind speed (sonic anemometer) vs mast-measured wind speed (cup anemometer) in Iced and Non-Iced conditions for the predominant wind sector (300).

RESULTS

The data used for the icing loss calculation is shown in Figure 7.4.12. The majority of the data is at wind speeds below 7m/s and with active power above 0.

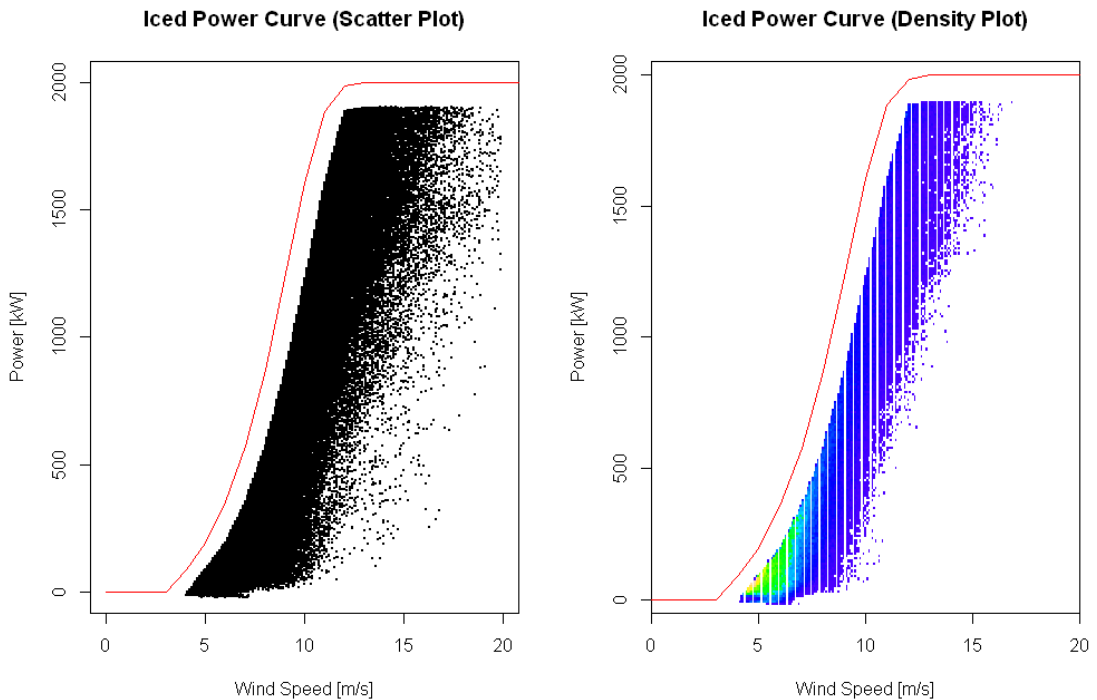


Figure 7.4.12: Data used for the icing loss calculation. In the density plot on the right, yellow indicates the highest data density.

Data for the same period which was not used for the icing calculation is shown in Figure 7.4.13. This data includes normal operations and also some curtailment events. Figure 7.4.13 suggests that some iced data may have been filtered out at low wind speeds.

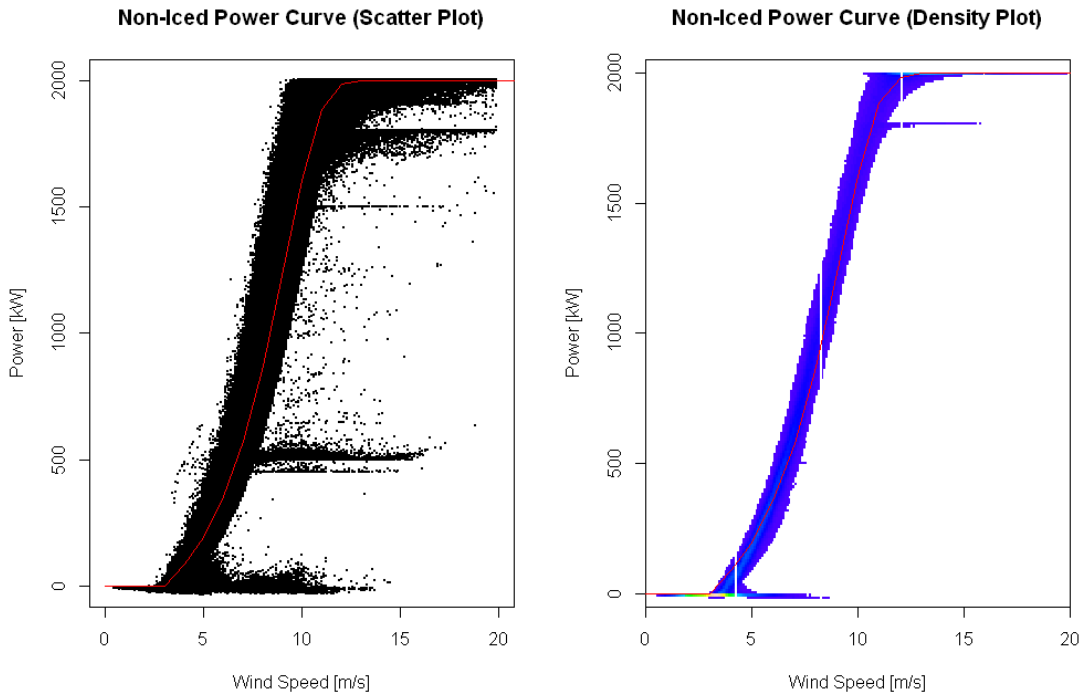


Figure 7.4.13: Data not used in the icing loss calculation

The overall icing loss was 2.9% of the expected annual yield. The results are broken down by month in Table 7.4.5. These Figures indicate the icing loss due to the decreased aerodynamic efficiency of the turbine and do not consider times when the turbine is unable to restart after shutdown because of iced conditions.

Month	Icing loss as % of expected monthly yield
Jan	11.0%
Feb	13.3%
Mar	0.1%
Apr	0.4%
May	0.2%
Jun	0.0%
Jul	0.0%
Aug	0.0%
Sep	0.0%
Oct	0.5%
Nov	2.1%
Dec	4.7%

Table 7.4.5: Measured icing loss by month

The probability of icing loss occurring is shown in Figure 7.4.14. This was determined by dividing the iced data count by the total data count of each temperature bin. Note that this reflects the temperature when icing loss occurred, not the temperature when the ice may have formed. Furthermore, although lower temperatures have very high icing probability, the majority of icing loss occurs near 0 degrees because this temperature is more common.

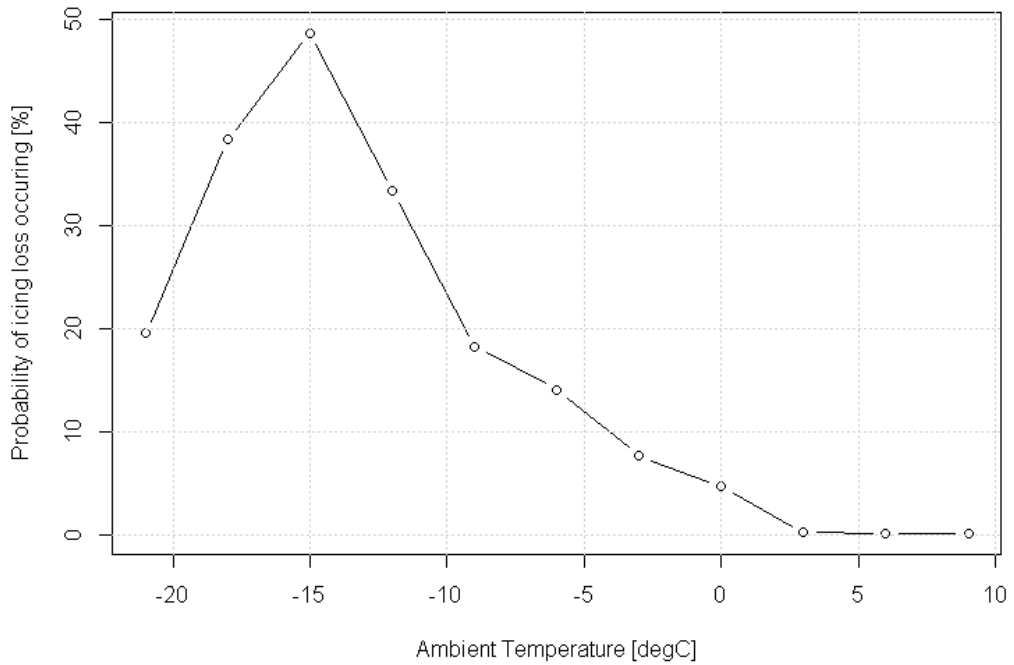


Figure 7.4.14: Probability of icing loss occurring by temperature

Finally, there is a strong correlation (0.8) between icing loss and elevation as shown in Figure 7.4.15.

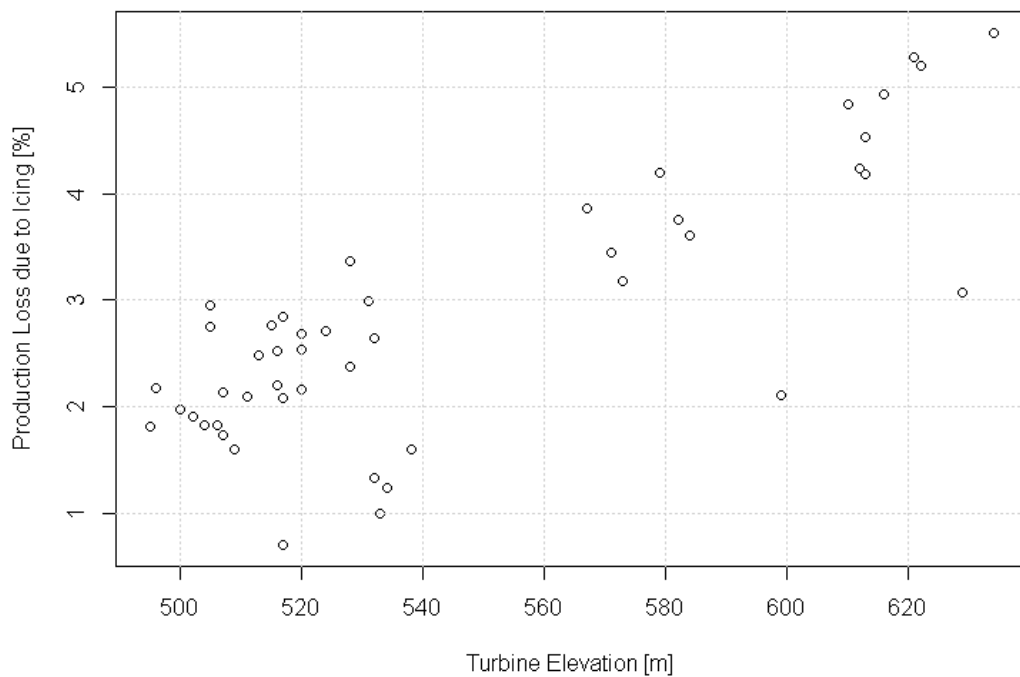


Figure 7.4.15: Icing Loss as a percentage of expected turbine production vs turbine elevation above sea level.

The analysis was repeated without the curtailment filter so that the icing loss calculation disregarded pitch behaviour. This was done so that cases where the turbine had not cut-in correctly after shutdown because of iced conditions could be included. The result was 4.1%, with the increased loss predominantly occurring with no power being produced as expected. A very small part of this increase is also due to curtailment loss being counted as icing loss.

Finally, an interesting relationship between time of day and overall wind farm icing loss was discovered as illustrated in Figure 7.4.16, suggesting that there is a strong correlation between solar insolation and reduction in the icing loss. On average, the solar radiation reduces the icing loss by approximately 0.6% through the course of the day.

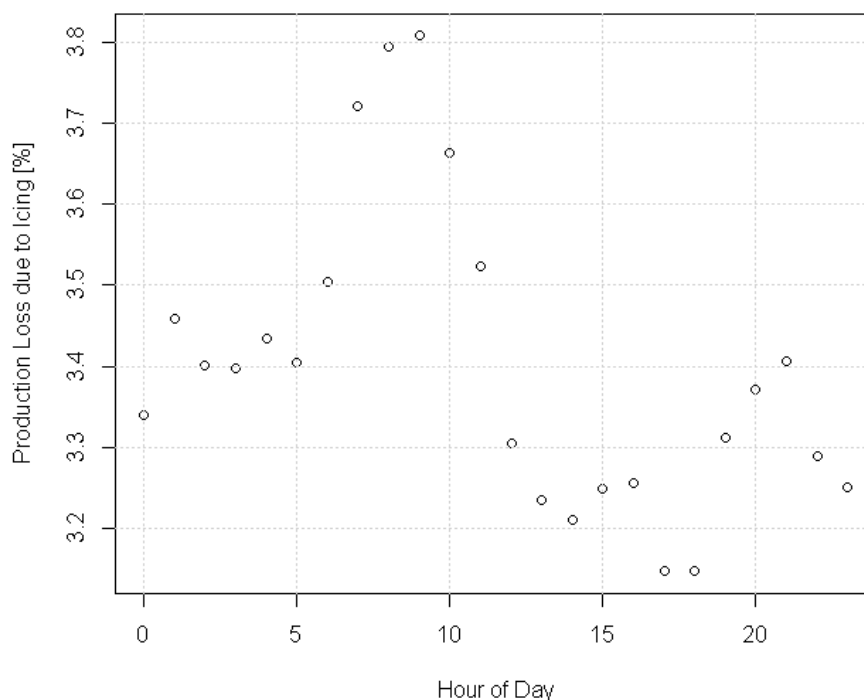


Figure 7.4.16: Wind farm average icing loss as a function of time of day.

COMPARISON TO PRECONSTRUCTION PREDICTION

Before Havsnäs was constructed, the energy loss due to icing was predicted to be 4.0% based on comparisons with another Swedish operational project. This is in good agreement with the 4.1% loss calculated in this study.

Since the construction of Havsnäs there is now a commonly applied heuristic in the wind industry for predicting icing loss [reference to GH CanWEA paper]. The total percentage energy loss due to icing is predicted as 3/8 of the total data loss at the SA mast anemometers due to icing. This rule refers to unheated anemometers. If this heuristic is applied to the unheated anemometers at the Havsnäs PP reference masts an energy loss between 8.4% and 10.5% is predicted. This is more than double the calculated value for Havsnäs in this study, and the difference is over 5 times larger than the standard uncertainty of 0.8%. The breakdown at the different masts is shown in Table 7.4.6.

Reference Mast	Anemometer	Data loss due to	Predicted energy loss (3/8 of
----------------	------------	------------------	-------------------------------

	height (m)	icing (%)	anemometer data loss) (%)
M6261	87.1	23.9	9.0
M6261	72.6	23.5	8.8
M6261	30	22.4	8.4
M6303	87.1	27.5	10.3
M6303	72.6	27.8	10.4
M6303	30	28.1	10.5

Table 7.4.6: Predicted energy loss due to icing for Havsnäs using unheated anemometer data and the 3/8 heuristic.

This comparison shows that the measured icing loss at Havsnäs is significantly lower than the predicted icing loss using the industry heuristic. However, only two years of data have been analysed for Havsnäs so the long-term average icing loss is still unknown. The industry heuristic does not seem sensitive to anemometer height but will be sensitive to the method used to identify bad data due to icing.

CONCLUSIONS

Icing loss at Havsnäs has been estimated as $2.9 \pm 0.6\%$ during the time period October 1, 2010 to September 30, 2012. As stated in the Introduction, this loss is due to decreased aerodynamic efficiency of the turbine which causes reduced power output while the turbine is operating.

Furthermore, the calculation was repeated without a pitch filter to include cases where the turbine had not cut-in correctly due to icing (i.e. was not operating due to decreased aerodynamic efficiency). This calculation shows that the total icing loss due to aerodynamic efficiency does not exceed $4.1 \pm 0.8\%$.

It appears that solar radiation alone can result in a significant reduction in icing loss through the course of daylight hours.

7.5 HEALTH & SAFETY - ICE THROW SHUTDOWN

INTRODUCTION

If turbine blades ice over whilst in motion then there is a risk of ice throw. This results in a risk of ice strike to the area surrounding the turbine.

Current guidelines are for a 'safe zone' around an operating turbine to be represented by a circle of radius

$$d = 1.5(D + H), \quad \text{Equation 7.5.1}$$

[9] and [10] where D is the rotor diameter of the turbine and H is the hub height (both in m).

This guideline does not account, however, for wind climate or other physical conditions on-site which will affect the distance over which ice is likely to be thrown.

To assess more accurately the zone of ice strike risk surrounding a turbine RES has developed an ice throw simulation model. The physics of this are based on the work of reference [11]. The benefit of the ice throw model is the ability to quantify with some accuracy the risk of ice strike in the vicinity of a turbine. The results of the model are then widely applicable, for example to planning, regulation and engineering, and to inform shutdown strategy if appropriate. In addition, the results of the model are then compared to the radius of risk given by Equation 7.5.1 to determine whether current guidelines are appropriate.

METHODOLOGY

The RES ice throw simulation model pairs a three-dimensional physical model of the way in which a piece of ice travels after being released from the blade of a turbine with stochastic models of wind speed, wind direction, angle of detachment, position of detachment and rotational speed to create a three-dimensional risk map around each turbine. This map represents not only the likely impact positions of the ice fragments but also the probability density of ice strike at each location given that ice is thrown.

Each simulation requires inputs related to:

1. Turbine type (including blade radius, hub height, cut-in wind speed, cut-out wind speed and the range of rotational speeds)
2. Wind climate (including wind speed distribution, wind speed uncertainty, wind rose and wind shear)
3. The physical characteristics of each ice fragment thrown and the conditions on-site (including the mass and surface area of an ice fragment, air density and drag).

Appendix 7J describes the outcome of RES' sensitivity analysis to these input conditions.

The turbine type being used for the Havsnäs ice throw simulation is a Vestas V90 machine with a hub height of 95 m and a maximum rotational speed of approximately 15 rpm [12]. Although there are three turbines at Havsnäs that have been de-rated (D15, D17 and D21), the effect of this on the wind speed at which the turbine reaches maximum power output is minimal, and so the effect on modelling of rotational speeds is also minimal. A general profile of rotational speed is assumed to apply to all turbines.

The wind speed frequency distributions and wind roses used in simulation have been derived from the wind speed predictions for this site. Note that there were two predictions for this site; one of these predictions uses SA mast data and the other prediction uses PP mast data. The ice throw simulation uses data from both sources, calculating four different risk maps based on data from M190 and M231 (SA masts) and M628 and M629 (PP masts). The risk map associated with the mast closest to each turbine is then assumed to apply to that turbine. This is summarised in Table 7.5.1.

Mast	Turbines
M190	D1, D5, D9, D11, D12, D13, D14, D16 (8 turbines)
M231	D2, D3, D4, D6, D7, D8, D10, D15, D17, D18, D19, D20, D21 (13 turbines)
M628	F1 to F16 (16 turbines)
M629	E1 to E11 (11 turbines)

Table 7.5.1: Reference masts for turbines at Havsnäs for ice throw modelling. Turbine locations can be seen in Appendix 5A.

For all reference masts a Weibull distribution estimated from the long term frequency distribution (in 12 sectors) has been used as the distribution from which wind speeds are sampled for the ice throw model. Wind direction roses have been estimated on a seasonal basis, where missing information at the SA or PP mast has been interpolated with reference to the relationship between each of these masts and a heated telecoms mast located a short distance off-site. This accounts for seasonal variations in wind rose that would not otherwise be captured. Estimates of wind speed and uncertainty, wind shear and air density have been taken from RES' calculations specific to this site. Icing is considered most likely to occur in Winter, Spring and Autumn and so, for any given measurement mast, the ice throw simulation is run over 100,000 iterations for each of three seasons and a final risk map created from the weighted average of the seasonal maps. By overlaying the appropriate risk map (see Table 7.5.1) on each turbine the risk to safety in the area surrounding each turbine is assessed. This is a map of conditional risk for one thrown particle of ice - i.e. it represents the probability of the ice landing at any position on a 1 m x 1 m grid, given that it is thrown from the turbine blades.

JUSTIFICATION

Ice throw simulation has already been used within RES for advising on public safety at sites in Sweden and for informing engineering and infrastructure decisions. For wind farms not yet built then running the risk model prior to construction could be used to inform layout decisions.

The benefit of running the ice throw model specifically at Havsnäs is in its ability to quantify the area of risk around each turbine and therefore assess whether there are any public safety implications from this. If so, then it can be used to quantify public safety risk and to inform shutdown strategy where necessary. It also offers an assessment of whether the radius of risk given by Equation 7.5.1 is appropriate. For Havsnäs - where the turbines have radius 45 m and a hub height of 95 m - this implies leaving a circle of radius 277.5 m clear around each turbine.

RESULTS

The risk contours from the ice throw model when applied across the full Havsnäs site are depicted in Figure 7.5.1.

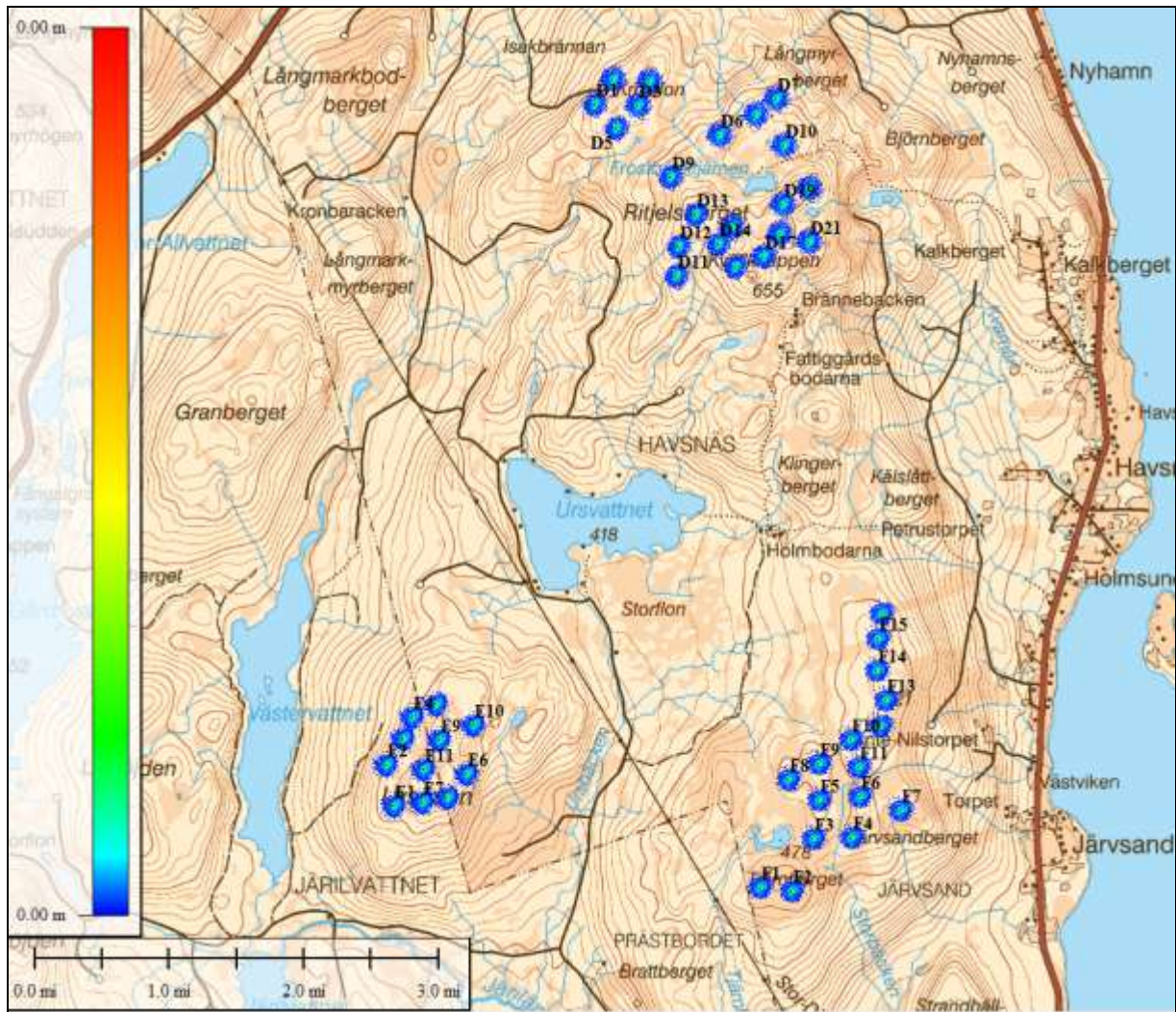


Figure 7.5.1: Ice throw risk contours at Havsnäs (all turbines).

COMPARISON TO GUIDELINES

The maximum simulated throw distance given the variation in input conditions at each mast is shown in Table 7.5.2. Note that the maximum throw distance in each case is less than the safe distance of 277.5 m derived from Equation 7.5.1.

Mast	M190	M231	M628	M629
Maximum Throw Distance (m)	196	229	207	211

Table 7.5.2: Maximum ice throw distances based on wind climate at four masts at the Havsnäs site

Figure 7.5.2 shows the cumulative probability of ice being thrown within a given radius based on each of the four measurement masts used for the modelling. These are similar for all masts; however note that the lowest gradient is on cumulative density for M231 as this is the mast associated with the highest maximum throw distance. Hence Figure 7.5.2 gives an indication of not just the throw distance but also the probability of being within that throw distance for any one piece of ice thrown from the turbine blades. For example, based on M231 there is (approximately) an 80% chance of a piece of ice thrown from a turbine on this site landing within 100 m of the turbine base, and therefore a 20% chance of it landing further away. The 95% limit is at a distance of 133 m from the turbine base at most whilst the 99% limit is at a distance of 159 m from the turbine base. In other words the RES ice throw model indicates that for this site there is little risk of ice strike outside of a distance of 160 m from the turbine.

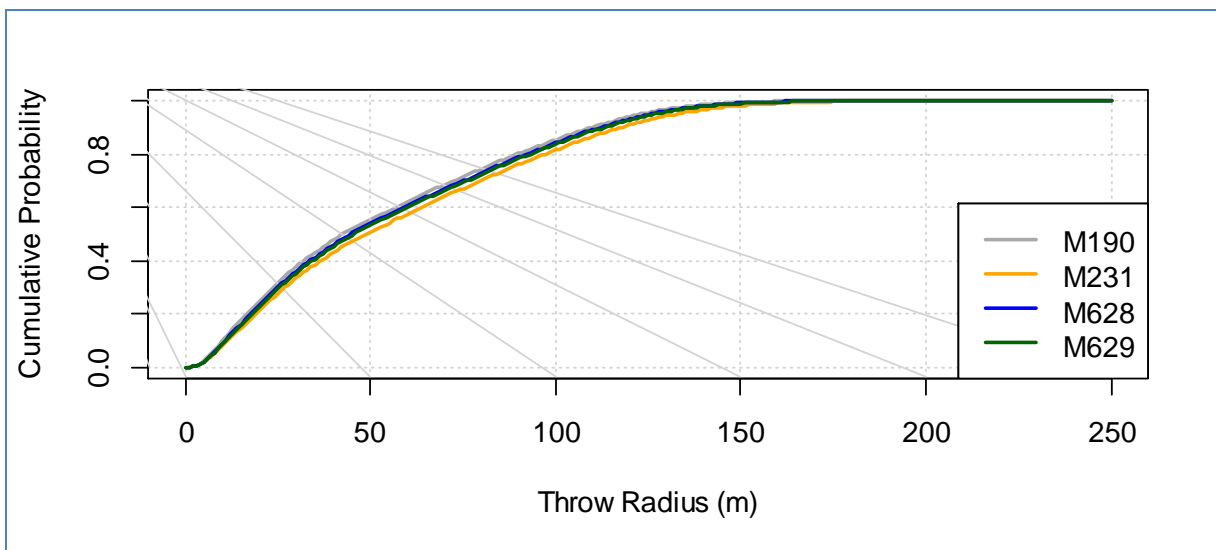


Figure 7.5.2: Cumulative probability of an ice particle landing within a given distance of a turbine, given that ice is thrown.

Figure 7.5.3 then shows the risk map derived from M231 overlaid with smoothed risk contours to represent the risk of ice strike per square metre per release. For example, the 1E-04 contour represents the locations at which the probability of ice strike in any particular square metre of land is 1 in 10,000. Note that the risk contours are not circular, although the contour at 1E-7 could be reasonably approximated by a circle of radius 190 m (red dotted line), which contains 99.96% of total probability.

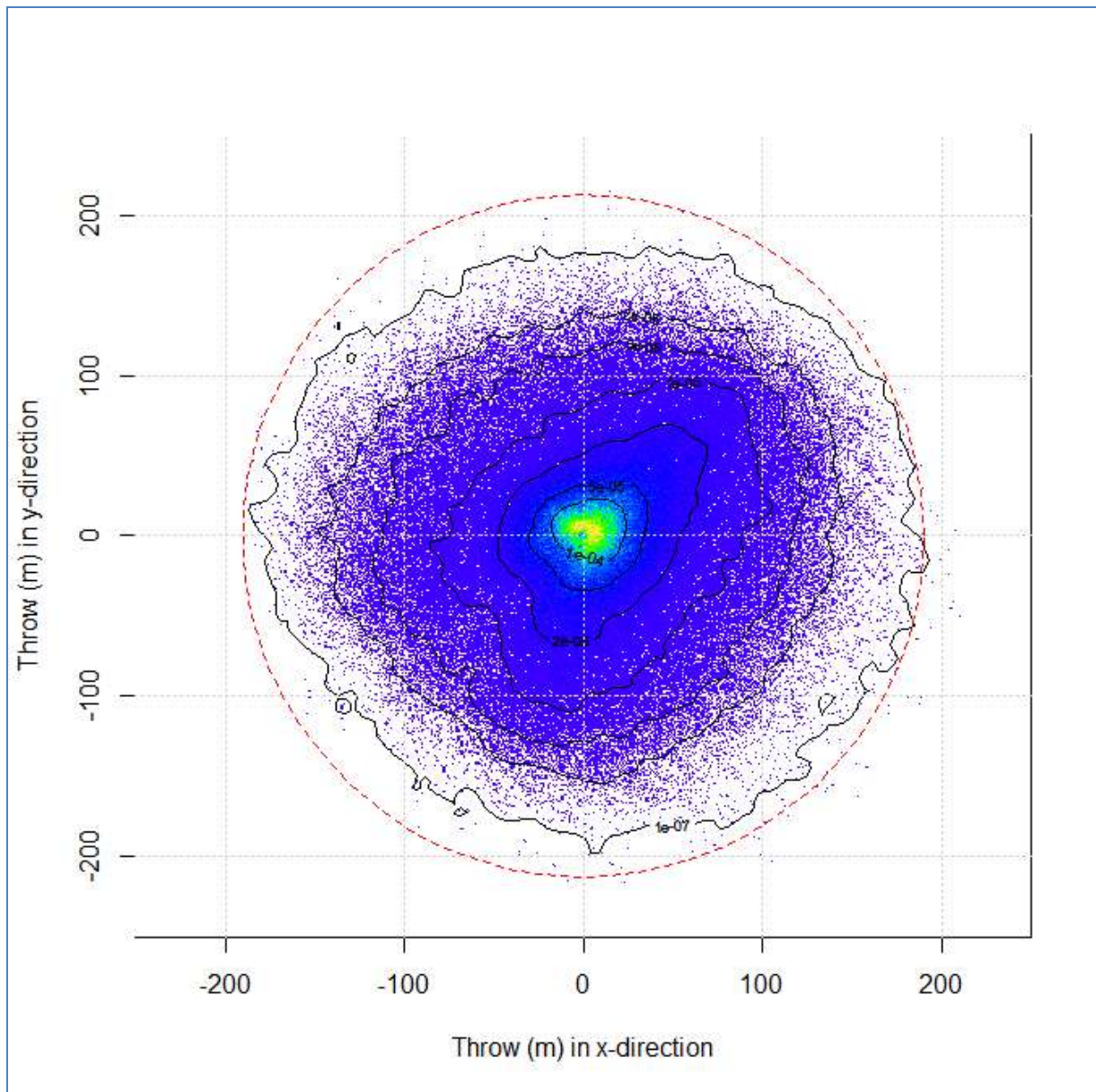


Figure 7.5.3: Risk contours for M231.

ASSESSMENT OF RISK TO PUBLIC SAFETY

Each turbine group (D, E and F) is shown individually in Figure 7.5.4 to Figure 7.5.6 with roads and snowmobile tracks marked. It can be seen from these that for the group of turbines labelled F there is no significant overlap between the ice throw risk contours and nearby roads or tracks. Further, there are no cabins or houses (denoted by black squares on the map) within the zones of risk around the turbines.

Figure 7.5.4 shows that turbines D1 and D2 are located close to an access road and that the ice throw contours from these turbines overlap with this. Road usage during icing months is, however, likely to be low and so risk of ice strike to transport will be mitigated naturally.

The main risk of ice strike during icing months will derive from the overlap of the ice throw risk contours with the snowmobile tracks denoted in red on Figure 7.5.4 to Figure 7.5.6. Areas of overlap for the most risky turbines have been calculated as given in Table 7.5.3. The highest risk associated with any individual turbine is 1.9%.

Turbine	D3	D4	D14	D17	E4	D16	E5	F6	F11
Probability of ice strike intersecting with snowmobile track (%)	0.5%	1.9%	1.1%	0.6%	1.9%	0.1%	0.03%	0.02%	0.01%

Table 7.5.3: Areas of overlap between risk contours and snowmobile tracks.

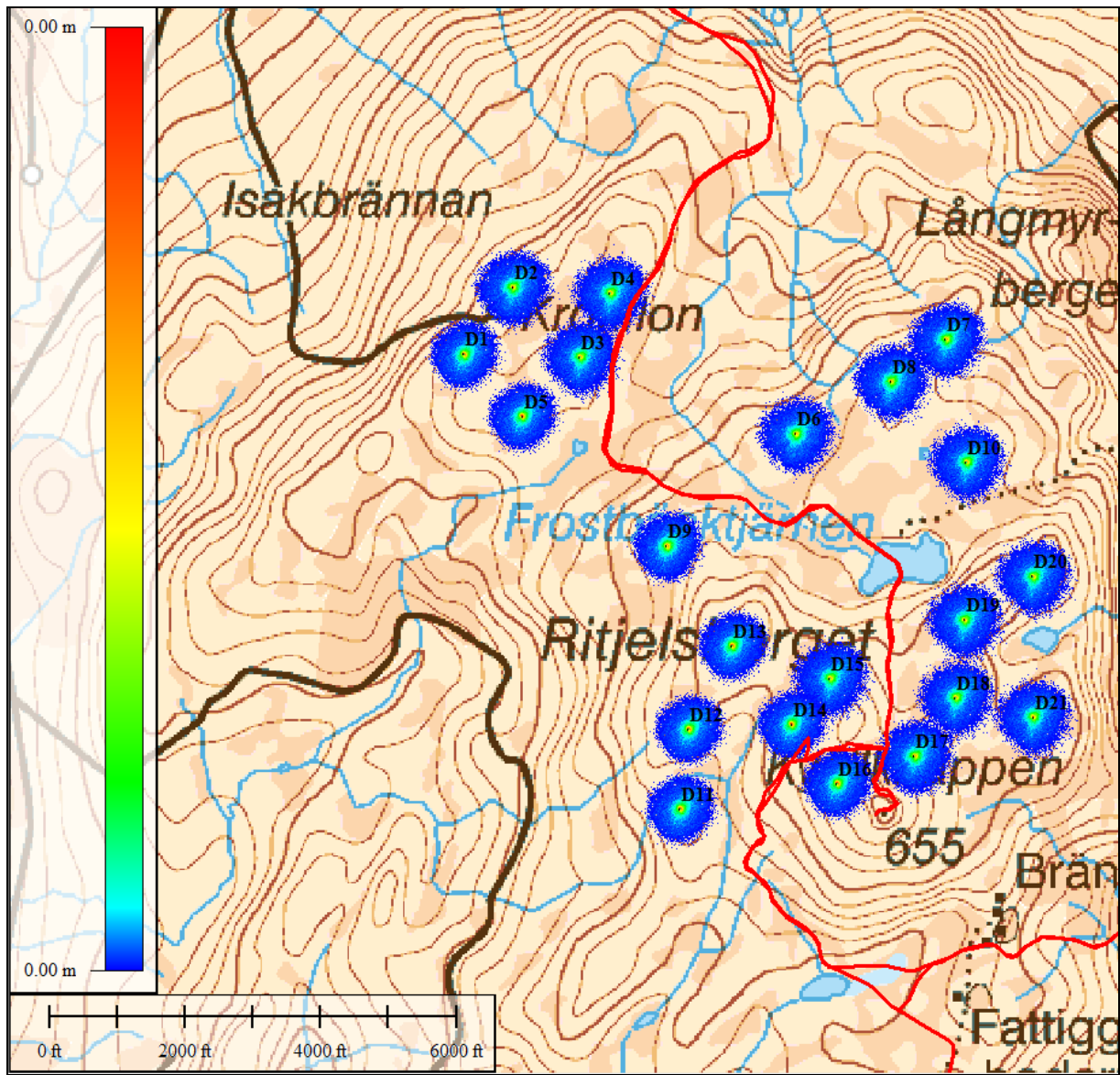


Figure 7.5.4: Ice throw risk contours at Havsnäs (D Turbines) - Red line is snowmobile track.

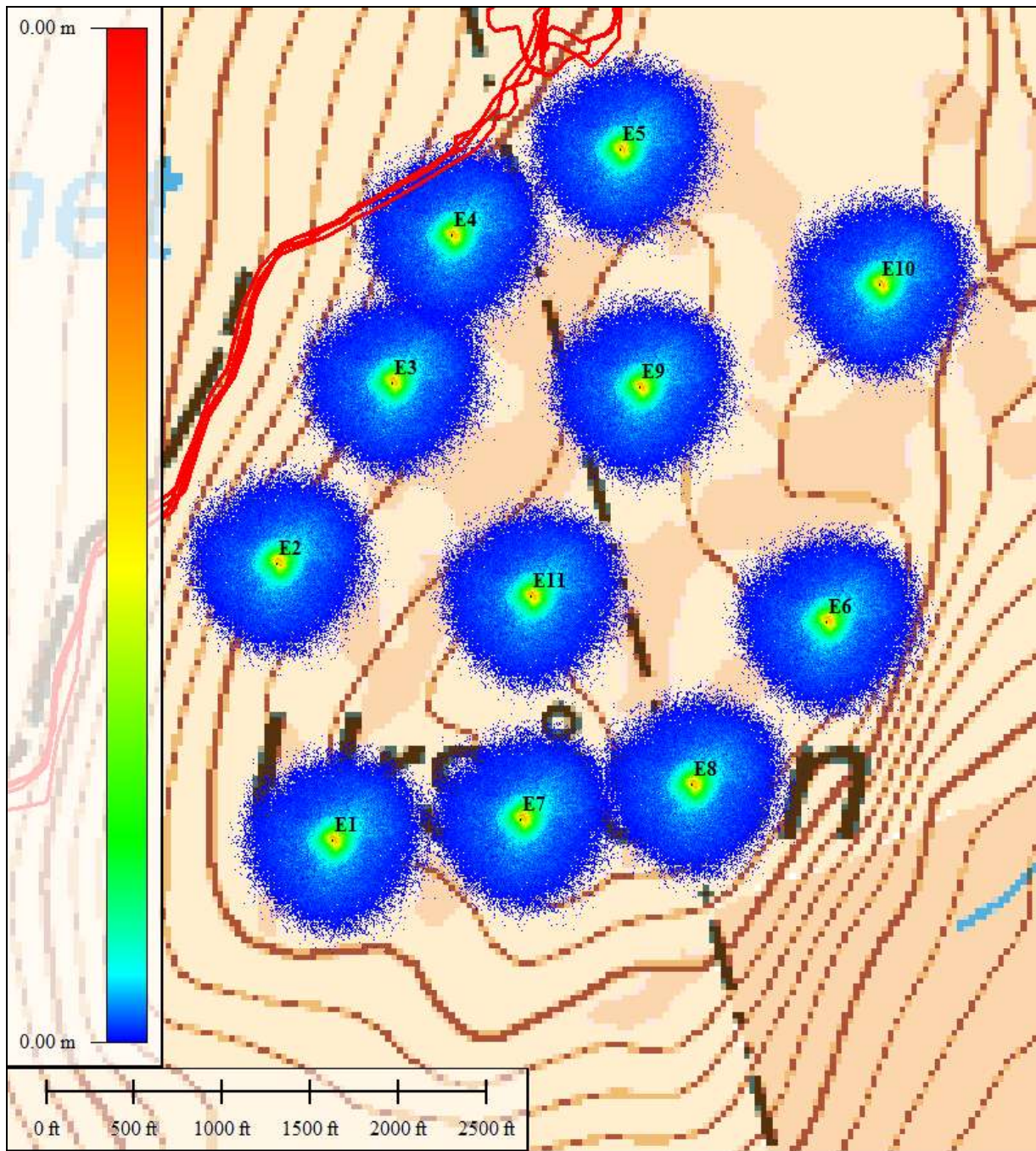


Figure 7.5.5: Ice throw risk contours at Havsnäs (E Turbines) - Red line is snowmobile track.

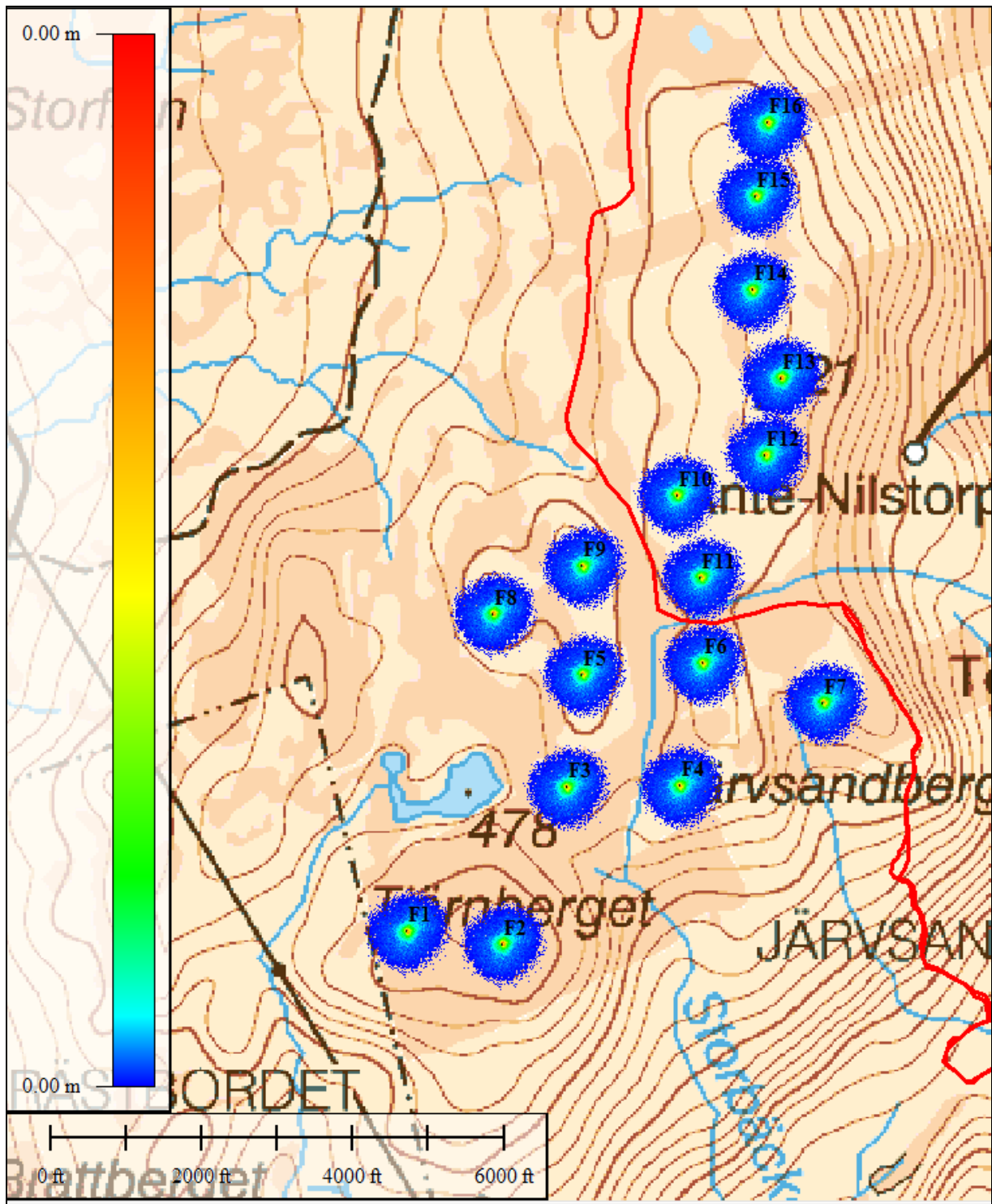


Figure 7.5.6: Ice throw risk contours at Havnsäs (F turbines) - Red line is snowmobile track.

EXPECTED ICE STRIKES TO SNOWMOBILES

The overall risk of an ice strike to a single snowmobile is a function of the probability maps shown in Figure 7.5.1, the number of pieces of ice expected to be thrown and the time spent by a snowmobile in the risky zones, as per Table 7.5.3.

Based on icing identified during data quality control, the number of days of icing at Havsnäs ranges from 37 per year (at measurement mast SWEala190) to 127 per year (at measurement masts SWEala628 & SWEala629). The mean number of icing days per year across each of the four measurement masts used in this study is 87.

The total number of ice particles released per icing day is more difficult to estimate. Reference [13] assumes approximately 100 thrown pieces of ice per day to be in line with reference [14], although notes that this is likely to be a conservative assumption. Reference [15] documented 228 ice fragments from 32 icing events over 4 Winters in the Swiss Alps, giving an estimate of approximately 7 ice particles per icing event. Given that this is based on observational data it is unlikely to have captured all ice thrown and so is very likely to be low.

For purposes of this analysis we will assume that the number of thrown particles per icing day lies somewhere between 10 and 100 and that turbines are operational at all times during icing. Under these assumptions, and applying the mean number of icing days at Havsnäs to all turbines, then the number of pieces of ice released from the blades of one turbine in any year could range from 870 to 8,700.

Based on the areas of overlap between the risk contours and the snowmobile tracks the total number of ice fragments that would be expected to land on the tracks during any one day of icing is around 6 at most (based on 100 fragments being thrown per turbine per day). This has been calculated by assuming that the landing positions of ice are independent, i.e. the probability of ice thrown from turbine D3 landing on the snowmobile tracks is unrelated to the probability of ice thrown from turbine D4 landing on the tracks. In practice, due to a degree of correlation between wind direction at turbines this is unlikely to hold true, and the accuracy of the risk assessment could be improved upon by developing a model of correlated wind directions for the ice throw model. This may imply moving towards a time series analysis.

The number of these ice fragments expected to intersect with the path of a given snowmobile will be small: intersection depends on both the ice landing in the risky zone and the snowmobile concurrently passing through that zone. Say, for example, that a snowmobile uses all areas of the track, travels at 35 km/h and has a plan area of approximately 4 m² [16]. Then, the length of time spent on the risky areas of the snowmobile tracks will be approximately 8.5 minutes (assuming that the snowmobile travels once over all risky areas of the tracks).

During this time there is a very small probability that a piece of ice will coincide with the snowmobile, given that the likelihood of the ice landing on the track is already very small. The expected number of ice fragments to strike one snowmobile on any given day at Havsnäs is 6.5E-06. The total number of strikes per year depends on this expected value, the number of snowmobiles travelling on the tracks at Havsnäs per day and the number of icing days per year. For example, if there are two snowmobiles per day, on average, and 87 icing days per year then there would be one strike on a snowmobile expected every 882 years.

This risk assessment is based on an assumption that each snowmobile only uses each part of the track once per journey, and that they do not idle in the most risky areas. Hence, again the accuracy of this risk assessment could be improved by temporal modelling. To enable a better understanding of the routes typically taken by snowmobiles, the frequency of use of

each route and the number of snowmobiles travelling at the Havsnäs site daily would be required.

VALIDATION

Further research is required to validate fully the RES ice throw model. Validation of both the landing positions of ice particles given wind direction, and the number of particles thrown per icing day, would add greatly to existing research.

This would require on-site observation similar to the program of research described in reference [15]. Sector-by-sector maps of the likely landing locations of ice particles when thrown from the turbine blades given wind direction could be created and then compared to on-site observations of ice strike given the prevailing wind direction for the icing day.

For example, if it is known that the prevailing wind direction is Northerly, then the predicted locations for ice strike based on reference mast M231 is shown in Figure 7.5.7**Figure**. This shows a high density of points to the South of the turbine base and a maximum throw distance of 189 m.

Implementation of such an on-site observation scheme over the Winter of 2011-12 at the most heavily iced locations proved somewhat inconclusive as virtually no thrown ice was discovered. This reflects the difficulty of actually finding evidence of ice throw in a remote, snow covered location as it is most likely that ice particles bury themselves in the snow and are covered over or shatter on contact with hard packed snow and hence are impossible to find. A more focussed on-site observation is being carried out through Winter 2012-13 looking at the specific areas where the model predicts that most ice should be thrown for a particular wind direction.

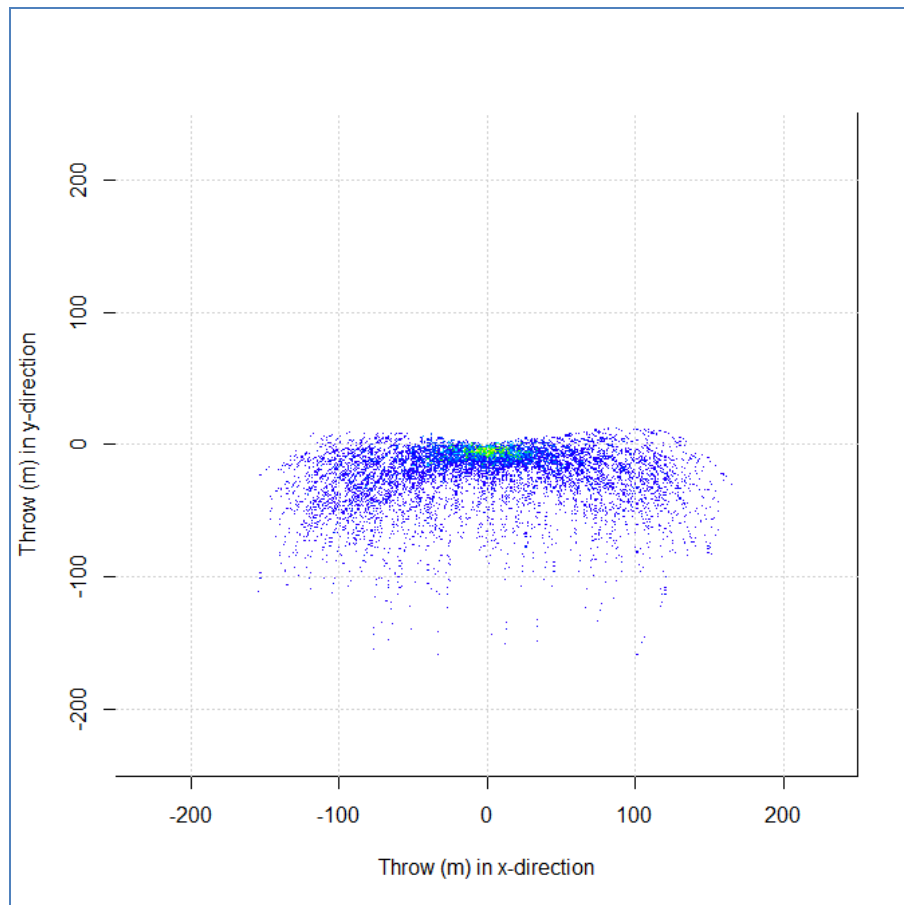


Figure 7.5.7: Ice strike locations for Northerly wind speeds, Havsnäs.

This validation would require additional research time and participation from on-site staff.

CONCLUSIONS

Overall, the RES simulation model of ice throw model indicates that there is no substantial risk to public safety due to ice throw from the turbines at Havsnäs. Although there are two turbines located close to an access track use of this should be occasional during icing months and so risk is naturally mitigated. The main risk to public safety derives from ice thrown on to snowmobile tracks and it has been demonstrated that the likelihood of ice throw which lands on the tracks coinciding with a snowmobile passing is small.

Further, the ice throw model indicates a maximum throw distance of just over 200 m for this site, based on Vestas V90 machines with a hub height of 95 m. This is less than the rule of thumb safe distance given in references [9] and [10].

Ice throw modelling could be improved by validation in terms of the predicted locations of ice strike and the number of ice particles released from the turbine blades when iced and operational. It is proposed that such validation should be on a sector-by-sector basis, whereby maps of simulated ice throw could be compared to observed locations of ice strike given prevailing wind direction. This would require a campaign of on-site measurements and is an area for future research. Finally, the estimation of risk to public safety could be enhanced by a better model of the frequency of movement of snowmobiles around the site.

7.6 POWER CURVE MEASUREMENT

7.6.1 POWER CURVE MEASUREMENT IN COLD CLIMATES

The remit of this component of the project is to test out and research the methods for measuring power curves proposed in the most recent draft of the IEC standard IEC 61400-12-1 (Draft Edition September 2012) [1].

The principal aspects of this are;

- 1) Apply IEC (draft) equivalent wind speed definition to LIDAR data and investigate the power curve obtained over a range of conditions.
- 2) Bring in winter data with potential icing events by using heated instrumentation.
- 3) From 1+2 investigate high shear/ low temperature/ potential icing impact on the power curve and whether the new equivalent wind speed power curve definition helps to reduce or explain scatter in the measured power curves.

PROJECT BACKGROUND

This research is driven by the need to understand better the effects of wind flow on the PP of modern multi megawatt wind turbines, the consequences of which have direct effects on the uncertainty in wind resource and energy yield assessment.

As turbines' physical size and the complexity of the environments in which they are built have evolved, the challenges associated with accurately measuring their performance have been compounded. Specifically, in practical and cost efficiency terms, the met mast based cup anemometry is not capable of measuring wind flow over the full extent of the rotor (typically rotor diameters are now in the region of 90 to 120 m). Further, the wind speed at hub height is not necessarily representative of the wind over the whole rotor. Consequently, the economic wisdom of deploying a generally very expensive hub height met mast (say 100m or more high), or more usually a pair of met masts for site calibration, is called into doubt as the measured hub height wind speed alone may poorly represent what the turbine rotor actually sees.

The IEC standard presents an alternative definition of wind speed to the hub height wind speed typically measured by cup anemometry. This new definition, the rotor-averaged or equivalent wind speed, is particularly suited (but not restricted to) the use of RS technologies like LiDAR (Light Detection And Ranging). The new definition essentially uses the wind speed and direction measurements from the multiple measurement heights available from an RS device to calculate the wind speed equivalent to the average wind power available across the full wind turbine rotor area and enables a more accurate representation of the wind speed experienced by the turbine.

Havsnäs provides a unique opportunity in which to conduct research into cold climate effects on wind energy. Its location in Northern Sweden where a severe, cold climate is experienced for a long period of the year give rise to atmospheric conditions (in particular low wind speed and high shear) which necessitate the use of very large hub height wind turbines. This coupled with the existing measurement infrastructure (from the 5 existing PP reference masts) and the accessibility of power supplies for supplying heated instrumentation enable an extensive measurement system to be installed and cold-climate and icing conditions to be investigated.

According to the draft standard [1], the site conditions at Havsnäs in terms of terrain and wind flow complexity somewhat exceed the conditions defined for application of RS technology for power curve measurement. However, a pragmatic approach has been taken here to show that despite this, useful and meaningful improvements to our understanding of turbine performance in these more complex environments can be made using these more sophisticated measurement and analysis techniques. It is the purpose of projects such as this to contribute to the body of scientific evidence and experience that will eventually allow wider adoption of these improved techniques.

There still remain many aspects of wind measurement and flow modelling which are not fully understood and so further research is still required in these areas. The work of this project seeks to contribute to the future reduction in wind resource uncertainty and improvement of future wind and PP measurement campaigns.

MEASUREMENT SYSTEMS

There are four measurement systems involved in this work, namely;

- M626 - Reference mast for test turbine D2
- M6261 - Reference mast heated instrumentation
- M726 - Power measurement at test turbine (previously the site calibration mast)
- M814 - Leosphere Windcube LiDAR

The relative locations of the above systems can be found in the schematic, Figure 5.1.1, in Section 5.1. The locations and altitude of each measurement system can be found in Table 7.6.1.

The met mast “M626” is at the reference position for the PP test (completed November 2011) on Havsnäs turbine D2. This is a 93m Wibe W1200 mast with the standard RES, IEC compliant 3m extension anemometer mounting boom. The mast supports both the original PP test measurement system M626 and the pilot project heated instrument system denoted M6261.

The primary anemometer from system M626 used in this study is the Vector A100L2 (unheated) instrument. Direction measurement is taken from the side boom mounted Vector W200P (unheated) wind vane. Temperature and pressure sensors are installed at 93m elevation. The instrumentation used for this analysis is summarised in Table 7.6.2 (All instrumentation at M626 can be found in Section 5.1, Table 5.1.7). Appendix 5B contains the general arrangement of the fully instrumented met mast.



Figure 7.6.1: Windcube LiDAR and Reference Mast M626.

Mast ID	X	Y	Mast Base Altitude [m]
M626	1495312	7111825	521
M6261	1495312	7111825	521
M726	1495120	7111763	517
M814	1495302	7111885	517

Table 7.6.1: Measurement System Location/ Height

Mast ID	Instrument (Channel/Type)	Serial Number	Instrument Height (m)	Boom Orientation (° Mag.)
M626	A2 / Vector A100L2	11179/MEB	96	24
	WV2 / Vector W200P	11654/654	92.1	202
	Temperature / CS 107 Thermistor	18491/1	93	-
	Pressure / Vega Bar 17	12318143	93	-
M6261	A2_HE / Vaisalla WAA252 Heated	E50301	87.3	205
	A2 / Vector A100L2	12719/ YUIA	87.1	25
	DIR2_HE / Vaisalla Heated vane		85.3	205
	Temp_Upper / CS 107 Thermistor	23954/6	90.5	-
	Pressure / Vaisalla PTB101B	E5040007	8	-

Table 7.6.2: Measurement System Instrumentation

Acronym	Definition
V_{m626}	Free stream wind speed at turbine position D2 - represented by the hub height met mast anemometer (from m626) corrected with original PP test site calibration
V_{m6261}	Free stream wind speed at turbine position D2 - represented by met mast heated anemometer (from m6261), close to hub height, corrected with the 'second step' site calibration process for heated anemometer data applied as shown in the Methodology section.
V_{eq}	Free stream wind speed at turbine position D2 - represented by the IEC defined equivalent wind speed from LiDAR data over the complete rotor disc. This has the 'second step' site calibration process for LiDAR data applied as shown in the Methodology section.
V_{eq_Veer}	As per V_{eq} but with the IEC prescribed veer correction ($\cos\varphi$ term) applied to the equivalent wind speed.
V_{m814_97}	Free stream wind speed at turbine position D2 - represented by LiDAR data wind speed measurement at hub height. This has the 'second step' site calibration process for LiDAR data applied as shown in the Methodology section.
V_{D2}	Free stream wind speed at turbine position D2
V_{LiDAR}	Wind speeds measured by LiDAR system m814

Table 7.6.3: Definition of Wind Speeds.

METHODOLOGY

Analysis - Power Curve Comparisons

Four tests are defined for purposes of power curve comparisons;

- Test 1 - Standard met mast anemometer (V_{m626}) vs met mast heated anemometer (V_{m6261})
- Test 2 - LiDAR equivalent wind speed (V_{eq}) vs met mast anemometer wind speed (V_{m626})
- Test 3 - LiDAR hub height wind speed (V_{m814_97}) vs met mast anemometer wind speed (V_{m626})
- Test 4 - LiDAR equivalent wind speed (V_{eq}) vs met mast heated anemometer wind speed (V_{m6261})

In each case the datasets are defined by the availability of the measurement systems. The datasets for M6261 and M814 were quality controlled prior to analysis to remove periods of instrument failure. It is noted (section 7.1) that this results in substantial loss of available data throughout the winter months.

Further investigation was made on the Test 4 set up with LiDAR based shear and veer data.

Wind Speed Corrections

The wind speed obtained from the fixed mast hub height anemometer (V_{m626}) is corrected using the site calibration determined from the original PP test at the turbine. This is therefore providing the free stream wind speed at the turbine hub height position.

Further to this both the LiDAR wind speed measurements (at all heights), and the heated anemometer from M6261 were corrected using a newly defined site calibration to the corrected anemometer V_{m626} mentioned above. These wind speeds in turn therefore provide the free stream wind speed at turbine position.

Wind Speed Correction: 'Site Calibration' Process for LiDAR Data

- 1) Derive LIDAR site calibration with respect to V_{m626} (D2 site calibration has been applied first: corrects M626 hub height anemometer wind speed to turbine position free stream wind speed), then $VD2 = f(V_{m626}, V_{LiDAR})$.
- 2) Derive normalised wind speeds with respect to hub height, for each LiDAR height measured wind speed for each ten minute period.
- 3) Convert normalised wind speeds to absolute wind speed by applying site calibration from above.
- 4) Apply IEC equivalent wind speed technique, see Appendix 7K section 7K.1.
- 5) Apply density correction to wind speeds to enable comparison with warranted power.

Note: For calculation of the V_{eq_veer} term step 4 is modified with application of the veer correction method, see Appendix 7K, section 7K.2.

Wind Speed Correction: 'Site Calibration' Process for Heated Anemometer Data

- 1) Derive heated anemometer from M6261 site calibration with respect to V_{m626} (D2 site calibration has been applied first: corrects M626 hub height anemometer wind speed to turbine position free stream wind speed), so $V_{D2} = f(V_{m626}, V_{m6261})$.
- 2) Apply this correction to the V_{m6261} heated anemometer data.
- 3) Apply density correction to wind speeds to enable comparison with warranted power.

DATASET

Data were analysed over the period 22 November 2011 to 24 July 2012. Over this time period the data availability was 51% (where data were concurrently available from the LiDAR, heated and un-heated met mast systems and the turbine power measurement system).

Data Filtering

Only direction sectors free from wakes from other turbines and significant obstacles were considered. The sectors were also limited by the original site calibration result which was valid for sectors 265° to 325° . The direction sectors analysed throughout were thus narrowed to 276° to 324° degrees. The wake interference on the LiDAR measurement volume is the main limiting defining the lower limit of the useable direction sector. The test results presented below are based on these same directional filters, irrespective of whether the LiDAR data are used in the test or not and hence all the resulting power curves are consistent in that respect.

The filters listed in Table 7.6.4 were applied throughout the tests defined below. For ice free power curves a temperature filter of $\geq 2^\circ\text{C}$ was applied. Turbine faults and shut downs were removed via application of the three filters 3, 4 or 5.

Filter	Description
1	$276 < [\text{Wind Direction (mean)}] < 324$
2	$[\text{Wind speed (mean)}] < 3 \text{ OR } [\text{Wind speed (mean)}] > 30$
3	$[\text{Power (minimum)}] < -50$
4	$[\text{Turbine Generating}] < 600 \text{ OR } [\text{Turbine Generating}] \geq 601$
5	$[\text{Turbine Grid Connect}] < 600 \text{ OR } [\text{Turbine Grid Connect}] \geq 601$

Table 7.6.4 Data Filters

ICE DETECTION

Ice detection is carried out by utilising the heated instrumentation from system M6261; the ratio of the output of the heated anemometer with that from an unheated anemometer on the same mast and comparing the ratio (binned by direction) to that derived during known ice-free conditions ($T > 5^{\circ}\text{C}$). When the ratio deviates from the ice-free condition then it is known that icing is occurring on the unheated anemometer. See Section 5.3.1 for more detail.

RESULTS

Within each power curve comparison, for the synchronised datasets an initial correlation on the two wind speeds representing the free stream at turbine are compared. Thereafter the scatter plot, binned power curves and power coefficients are compared. The set of figures and tables corresponding to each test are arranged according to the format described by this table:

Wind Speed Correlation (where x axis is wind speed from source 1 and y axis is wind speed source 2, e.g. $x = V_{m626}$ and $y = V_{m6261}$ for Test 1).	Summary of Energy Yield Comparison
Power Curve Scatter Plot (Ten minute averaged data, corrected to nominal air density 1.225 kg/m^3)	
Binned Power Curve	Power Coefficient

Test 1- (V_{m626}) vs (V_{m6261})

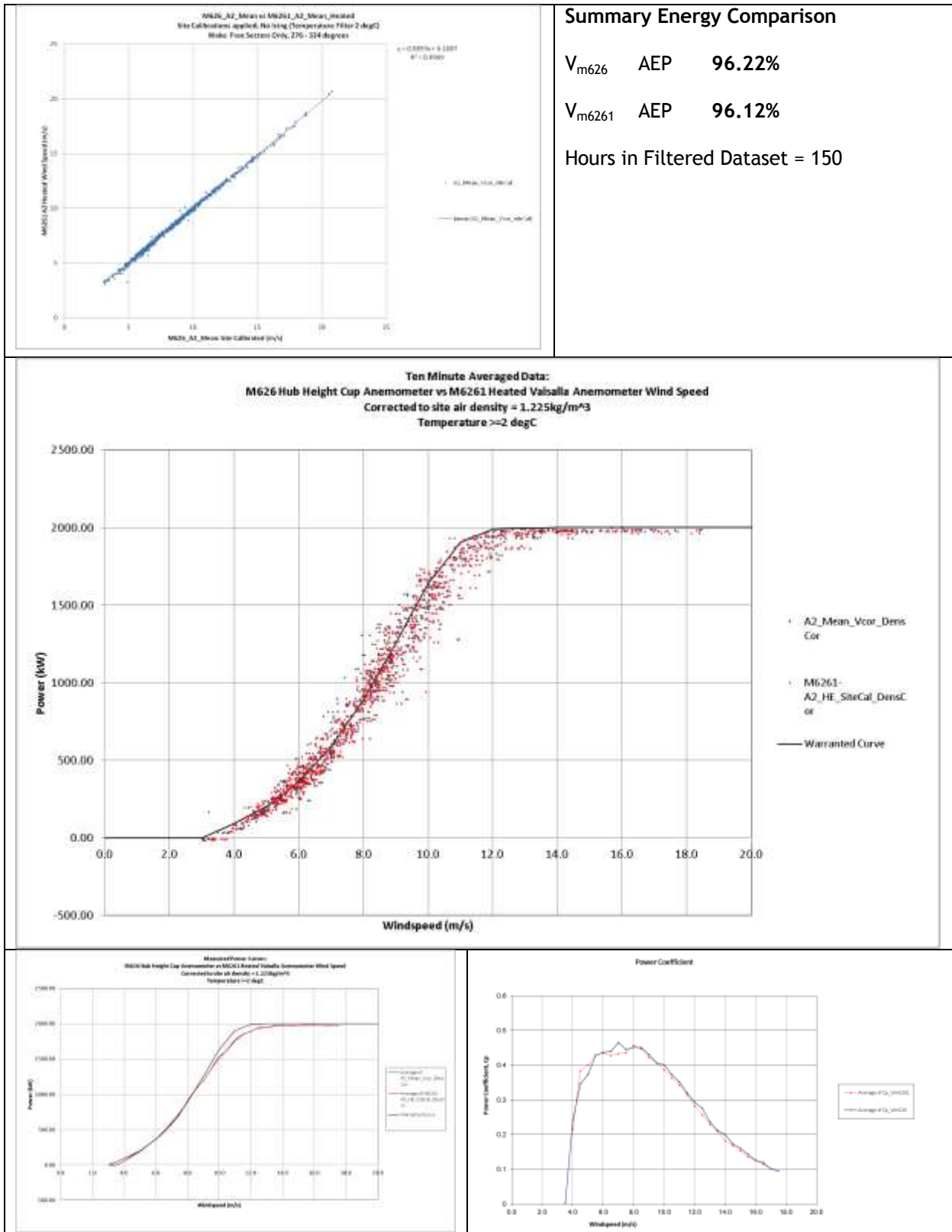


Figure 7.6.2: Test 1 Results Summary.

Test 2 - (V_{eq}) vs (V_{m626})

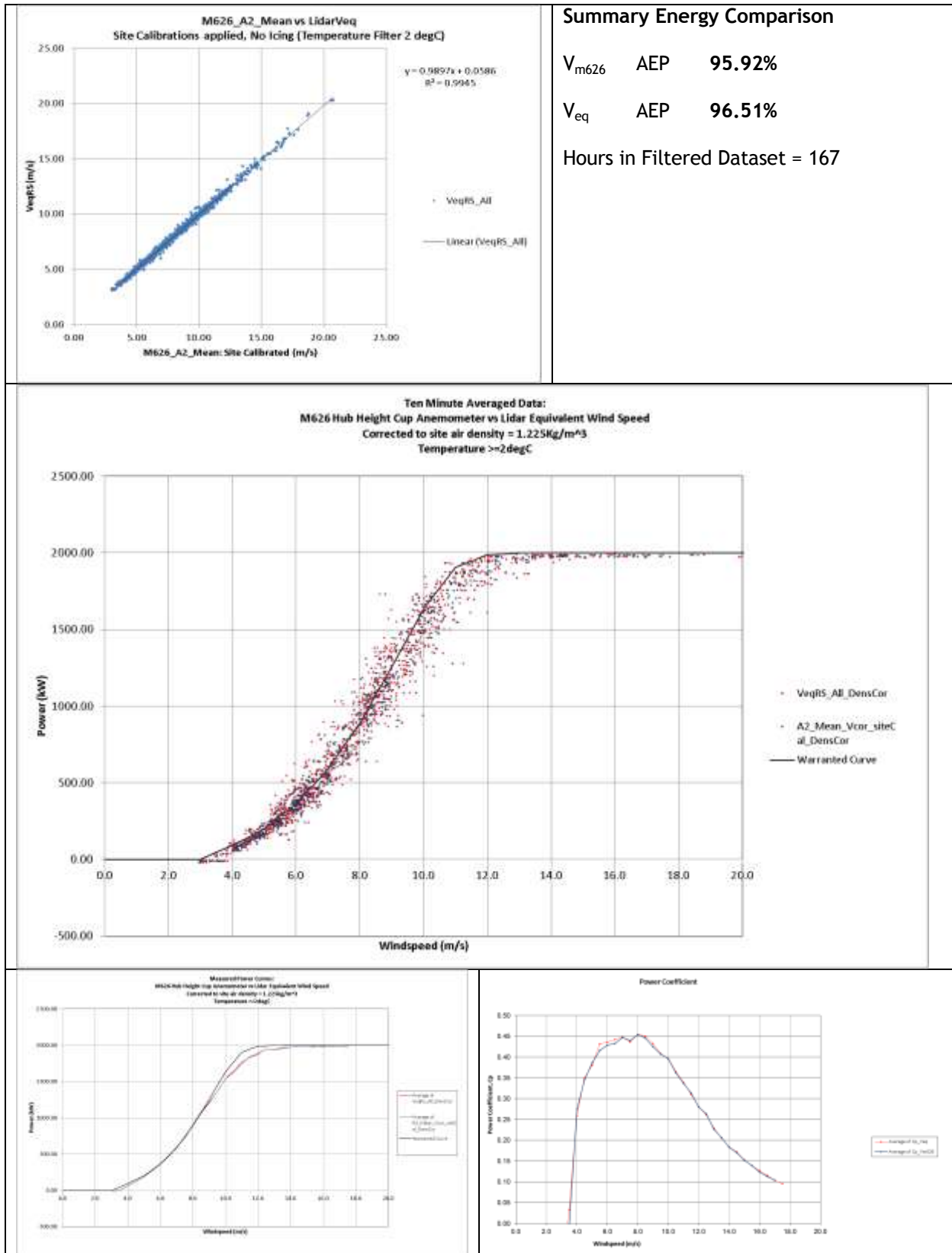


Figure 7.6.3: Test 2 Results Summary.

Test 3 - (V_{m814_97}) vs (V_{m626})

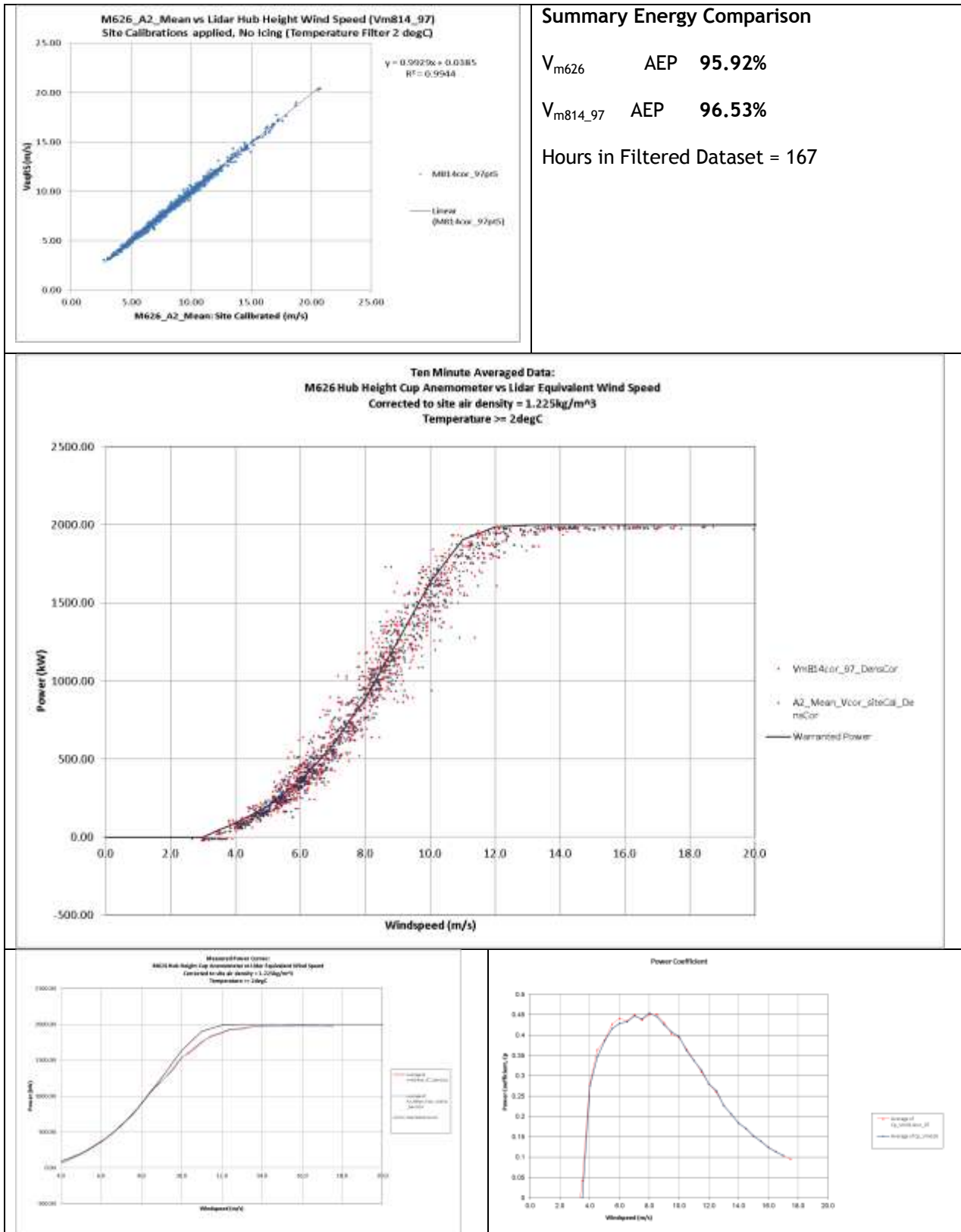


Figure 7.6.4: Test 3 Results Summary.

Test 4 - (V_{eq}) vs (V_{m6261})

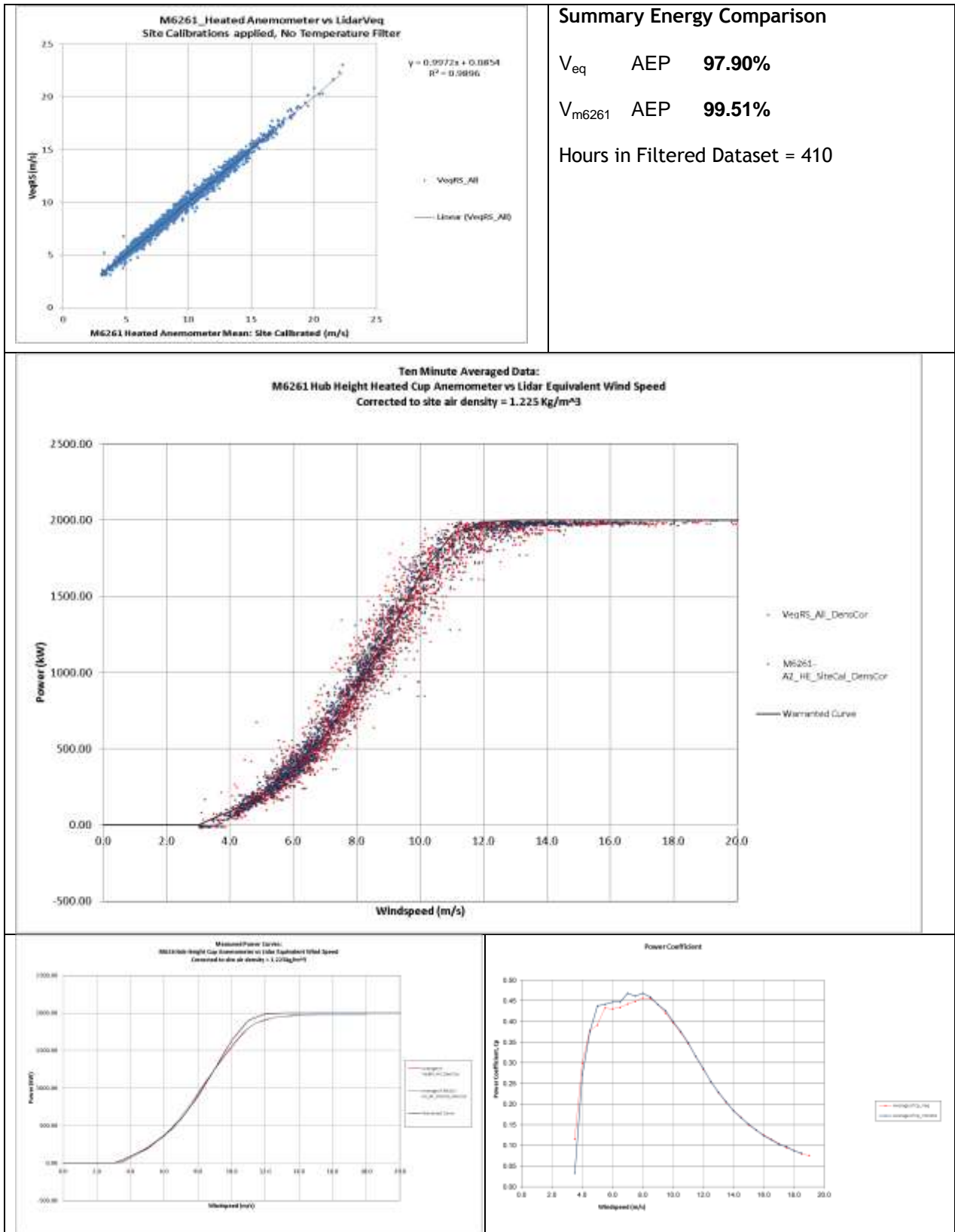


Figure 7.6.5: Test 4 Results Summary.

ANALYSIS OF RESULTS; FOCUS ON LIDAR BASED POWER CURVES

LiDAR measurements enable the shear exponent to be defined across different heights and therefore specific areas of the rotor disc. For the purpose of these tests the effect of shear was investigated, focusing on three principal shear exponents . 'lower', 'upper' and 'rotor full'. These different shear exponents were derived as described in Section 6.4.2 in Table 6.4.1 and Equation 6.4.4 (power law) and are summarised below;

- i) Lower: Shear across lower half of the rotor (hub height - lower tip height)
- ii) Upper: Shear across upper half of the rotor (upper tip height - hub height)
- iii) Rotor Full: Shear across full rotor height (upper tip height - lower tip height)

Comparing the distribution of shear exponents reveals the shear 'lower' and shear 'rotor full' definitions in reasonably similar quantities but the shear 'upper' following a slightly different pattern, in particular exhibiting more negative shear.

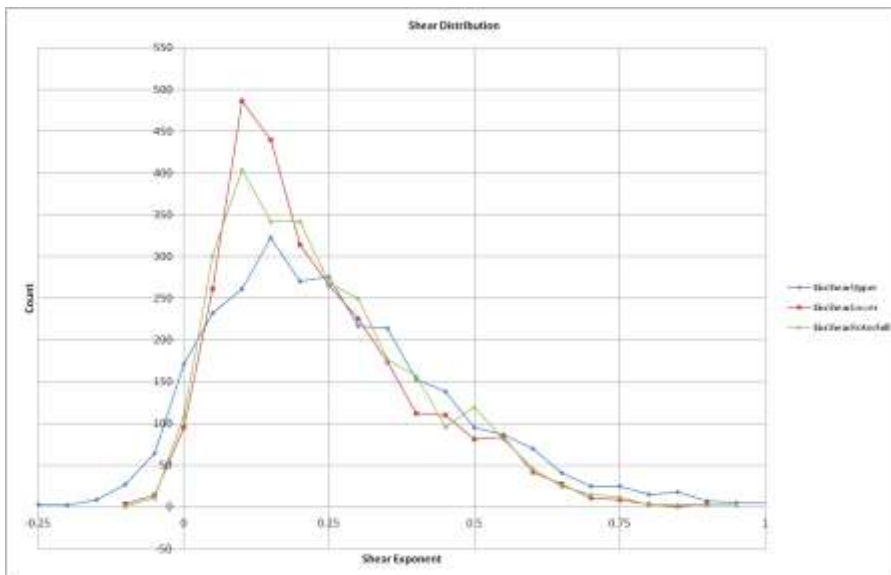


Figure 7.6.6: LiDAR Measured Shear Exponent Distributions.

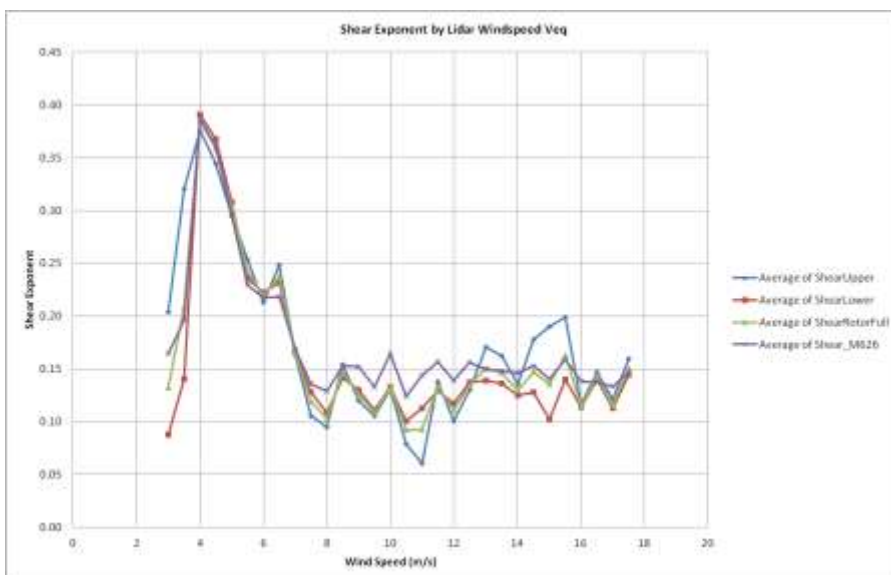
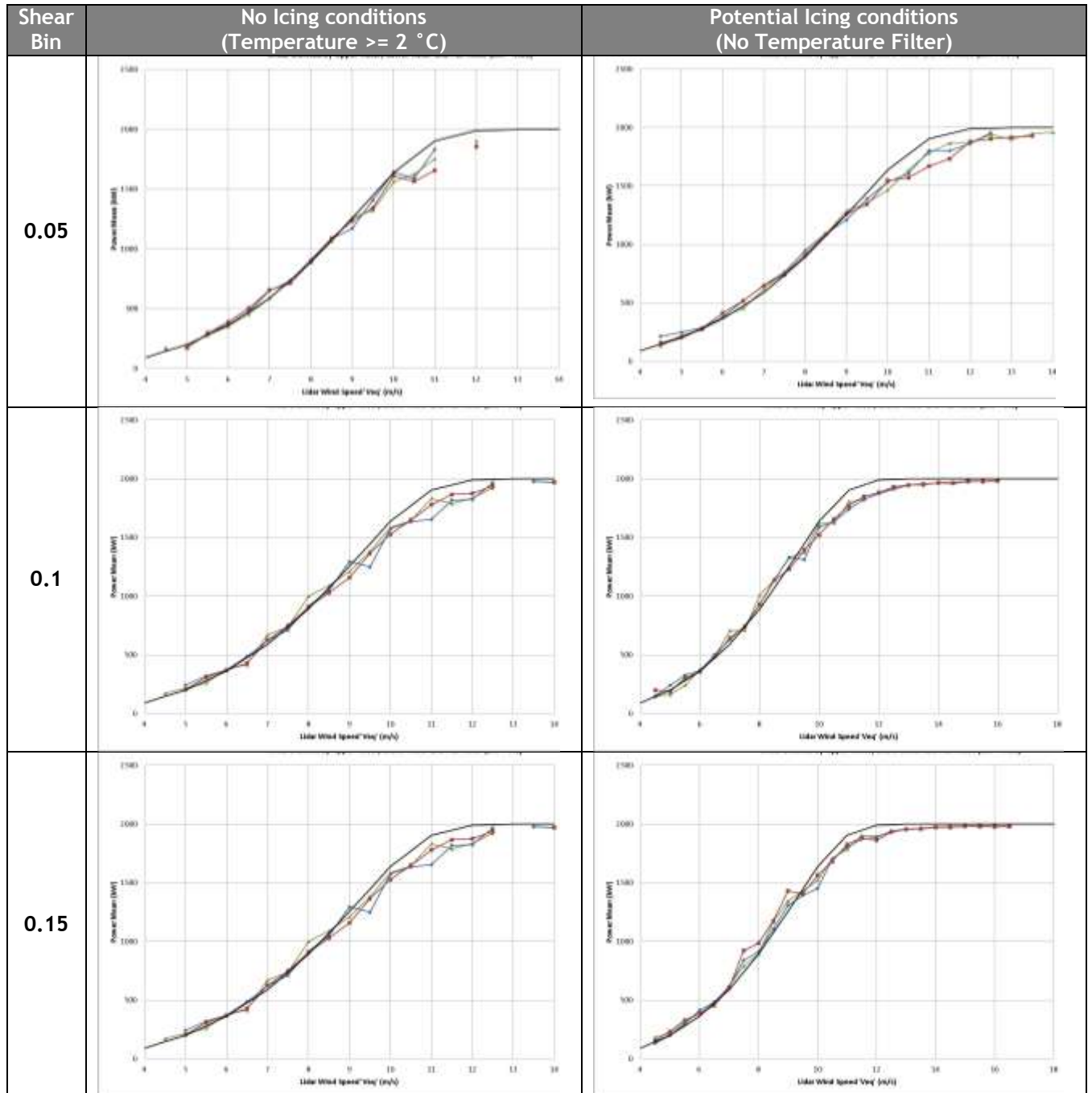


Figure 7.6.7: Shear Exponent LiDAR and M626 Measured by Wind Speed.

Power curve comparisons

Binned power curves obtained in Test 2 and Test 4 compared over a range of shear exponents are shown in Table 7.6.5. The key to the line colours used in each graph is as follows:

- Green represents Shear 'Upper'
- Blue represents Shear 'Lower'
- Red represents Shear 'Rotor Full'
- Black represents warranted power curve



Shear Bin	No Icing conditions (Temperature $\geq 2\text{ }^{\circ}\text{C}$)	Potential Icing conditions (No Temperature Filter)
0.2		
0.25		
0.3	Insufficient Data	
0.35	Insufficient Data	

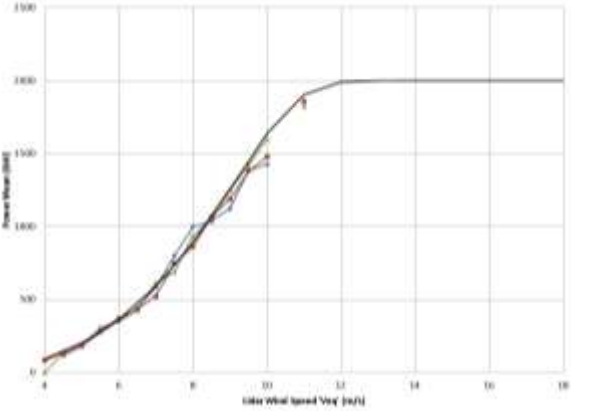
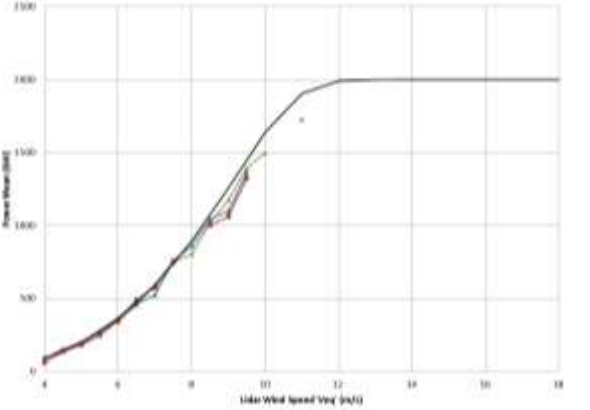
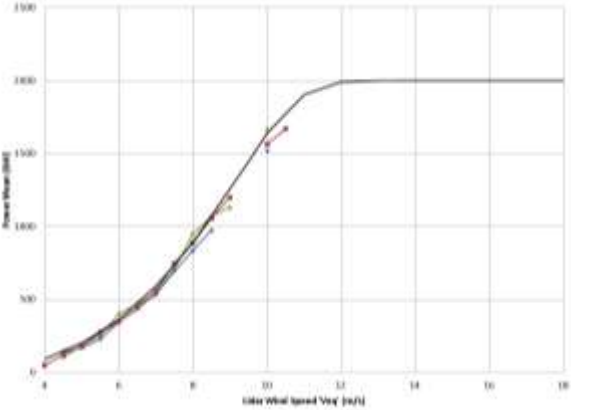
Shear Bin	No Icing conditions (Temperature ≥ 2 °C)	Potential Icing conditions (No Temperature Filter)
0.4	Insufficient Data	
0.45	Insufficient Data	
0.5	Insufficient Data	

Table 7.6.5: Binned Power curve Comparison Over Range of Shear Exponents.

The power curves obtained with shear defined over different parts of the rotor reveal generally good agreement between the power curves but with deviations becoming more apparent at higher shear values. This trend is shown more clearly in Table 7.6.6 which focuses on the heated anemometer data from Test 4. The key to the line colours used in Table 7.6.6 is as follows:

- Red represents Shear Lower V_{eq}
- Blue represents Shear Lower V_{m6261}
- Black represents warranted power curve

Shear Bin	Potential Icing conditions (No Temperature Filter)
0.1	<p>This graph shows the potential icing rate for a shear bin of 0.1. The x-axis represents Mean Wind Speed in m/s, ranging from 4 to 18. The y-axis represents Potential Icing Rate in %, ranging from 0 to 2500. The data points, connected by a line, show a sigmoidal increase in icing rate as wind speed increases, reaching a plateau of approximately 2000% between 17 and 18 m/s.</p>
0.15	<p>This graph shows the potential icing rate for a shear bin of 0.15. The x-axis represents Mean Wind Speed in m/s, ranging from 4 to 18. The y-axis represents Potential Icing Rate in %, ranging from 0 to 2500. The data points, connected by a line, show a sigmoidal increase in icing rate as wind speed increases, reaching a plateau of approximately 2000% between 17 and 18 m/s.</p>
0.2	<p>This graph shows the potential icing rate for a shear bin of 0.2. The x-axis represents Mean Wind Speed in m/s, ranging from 4 to 18. The y-axis represents Potential Icing Rate in %, ranging from 0 to 2500. The data points, connected by a line, show a sigmoidal increase in icing rate as wind speed increases, reaching a plateau of approximately 2000% between 17 and 18 m/s.</p>
0.25	<p>This graph shows the potential icing rate for a shear bin of 0.25. The x-axis represents Mean Wind Speed in m/s, ranging from 4 to 18. The y-axis represents Potential Icing Rate in %, ranging from 0 to 2500. The data points, connected by a line, show a sigmoidal increase in icing rate as wind speed increases, reaching a plateau of approximately 2000% between 17 and 18 m/s.</p>

0.3	<p>Graph showing Power (Watt) vs. Inlet Water Speed (m/s) for 0.3. The x-axis ranges from 4 to 18 m/s, and the y-axis ranges from 0 to 2500 W. The curve shows a sharp increase in power between 6 and 12 m/s, reaching a plateau of approximately 2000 W at 12 m/s.</p>
0.35	<p>Graph showing Power (Watt) vs. Inlet Water Speed (m/s) for 0.35. The x-axis ranges from 4 to 18 m/s, and the y-axis ranges from 0 to 2500 W. The curve shows a sharp increase in power between 6 and 12 m/s, reaching a plateau of approximately 2000 W at 12 m/s.</p>
0.4	<p>Graph showing Power (Watt) vs. Inlet Water Speed (m/s) for 0.4. The x-axis ranges from 4 to 18 m/s, and the y-axis ranges from 0 to 2500 W. The curve shows a sharp increase in power between 6 and 12 m/s, reaching a plateau of approximately 2000 W at 12 m/s.</p>
0.45	<p>Graph showing Power (Watt) vs. Inlet Water Speed (m/s) for 0.45. The x-axis ranges from 4 to 18 m/s, and the y-axis ranges from 0 to 2500 W. The curve shows a sharp increase in power between 6 and 12 m/s, reaching a plateau of approximately 2000 W at 12 m/s.</p>

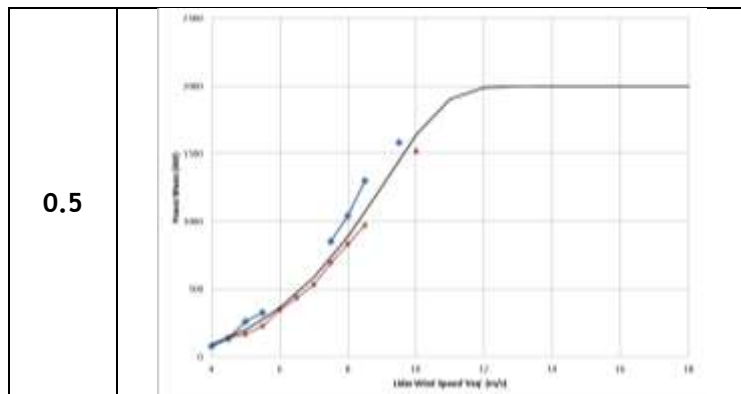


Table 7.6.6: Divergence of measured power curves (LiDAR ‘V equivalent’ wind speed vs met mast heated anemometer wind speed) with progressively higher shear.

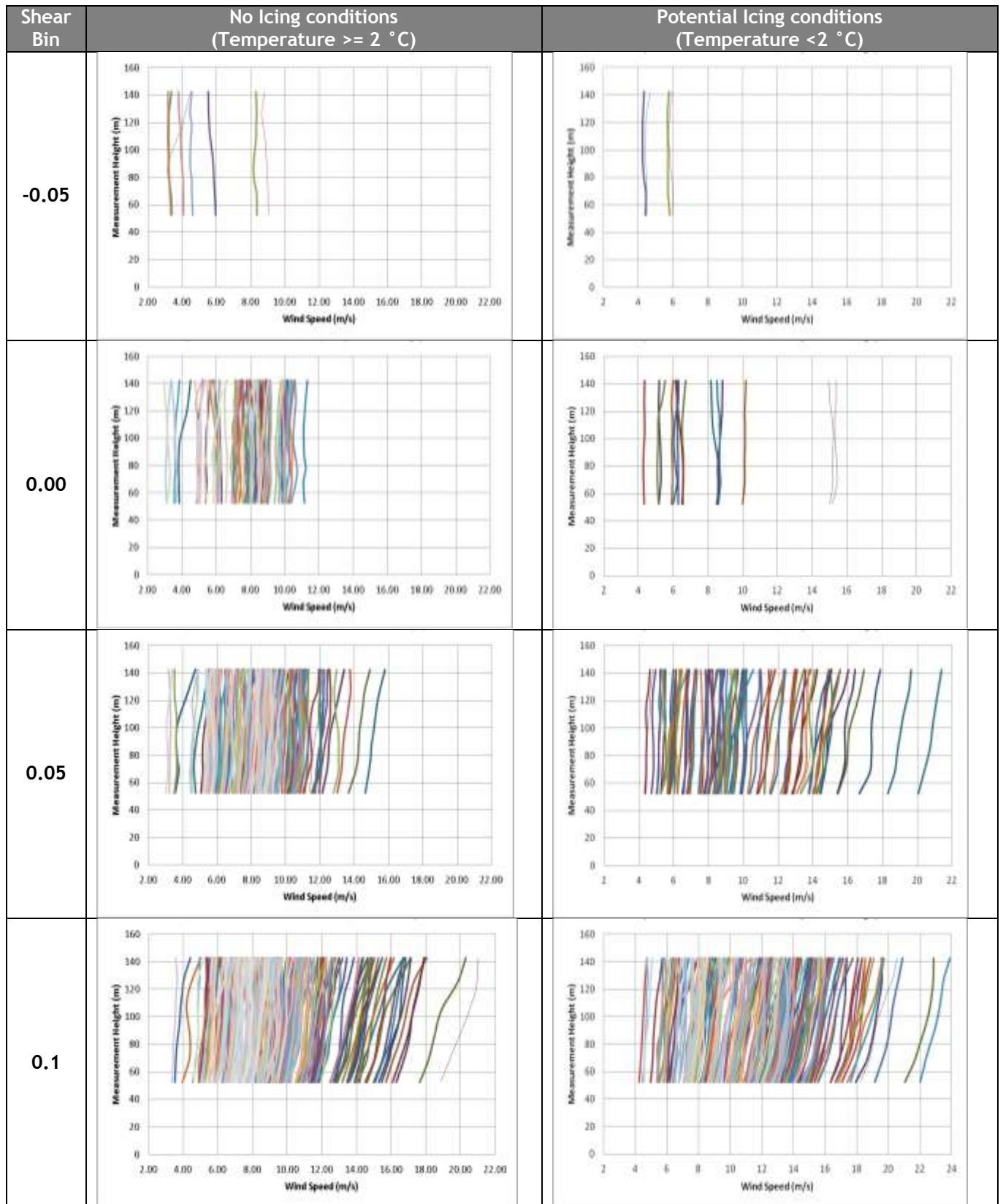
However, irrespective of the shear measurement method or definition, the performance of the turbine does appear to improve with respect to the warranted power curve as the shear increases. This is attributable more to the reduced turbulence conditions which accompany the high shear than any mechanism directly attributable to shear (see following section on ‘Effect of Turbulence on Performance’).

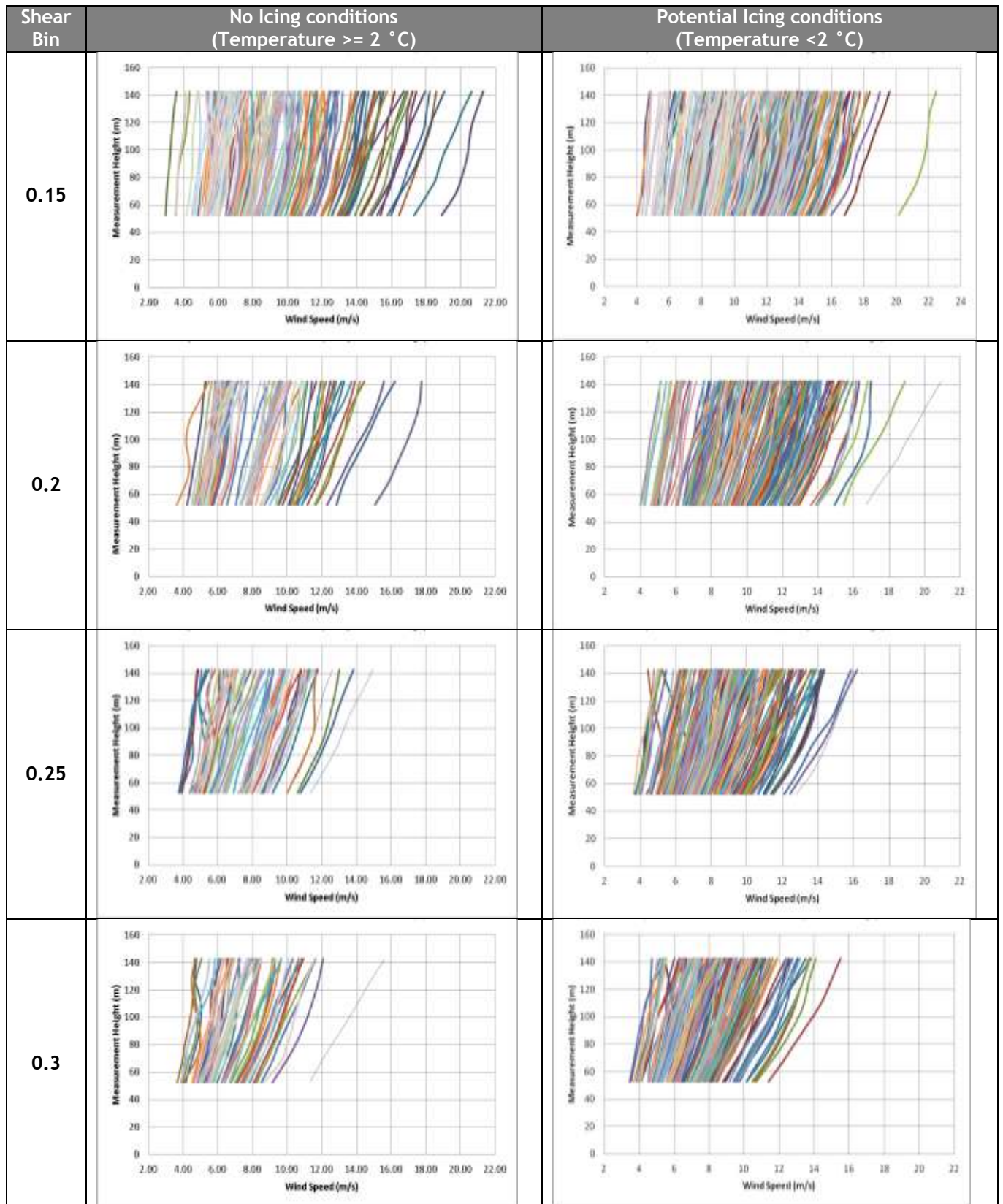
The impact of shear is captured in the comparison between the equivalent wind speed power curves and the hub height wind speed power curves. In that respect it appears that the hub height wind speed derived power curve is over-estimating the actual performance of the turbine in high shear as the equivalent wind speed power curve generally shows lower performance than the hub height power curve in higher shear conditions. In other words, there is more wind energy available through the area of the rotor disk than is suggested by the hub height wind speed alone.

This may sound counterintuitive but another way of thinking about it is that the cup anemometer wind speed is underestimating the actual wind speed seen by the full rotor area. When the wind speed is underestimated this has the effect of pulling the measured power curve to the left and thus making it appear that there is more energy being produced. If we accept that the wind speed is being underestimated then there is in reality more energy available because greater wind speed of course equals greater energy.

LiDAR Wind Speed Profiles

Plots of wind speed profiles obtained from LiDAR under different atmospheric conditions defined by shear measured across the lower half of the rotor are displayed below. Note that many of the measured profiles deviate considerably from exponential profiles, with evidence of negative shear, low level jets and other complex profile shapes. A comparison of data from warm temperatures and cold temperatures is made in Table 7.6.7.





Shear Bin	No Icing conditions (Temperature $\geq 2\text{ }^{\circ}\text{C}$)	Potential Icing conditions (Temperature $< 2\text{ }^{\circ}\text{C}$)
0.35		
0.4		
0.45		
0.5		

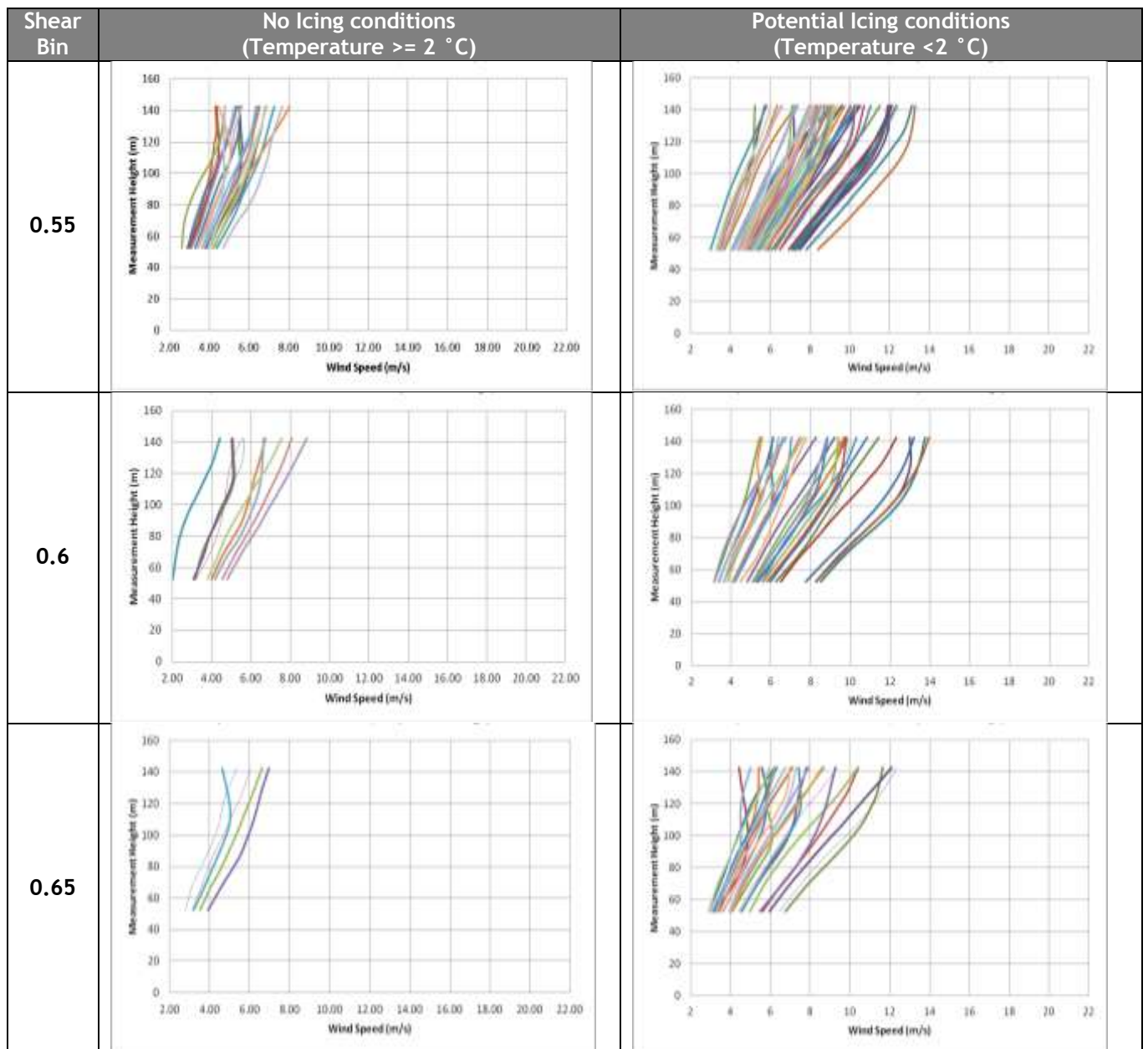


Table 7.6.7: LiDAR Wind Speed Profile by Shear: Compare Warm/Cold Climate Conditions.

Atmospheric Conditions

It is noted that the difference between the shear exponent measured on the upper half and the lower half of the rotor is at its greatest in conditions of high air density resulting from low temperatures ($< -2\text{ }^{\circ}\text{C}$) and high atmospheric pressure ($> 960\text{mBar}$) as shown in Figure 7.6.8. These low temperature, high pressure situations are most often associated with highly stable atmospheric conditions.

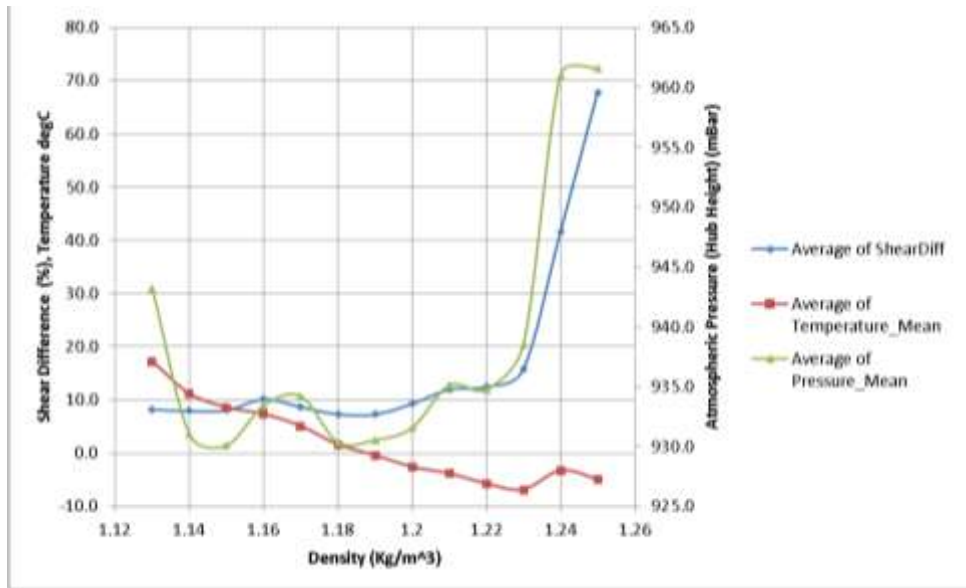


Figure 7.6.8: Density Effect on Shear 'Difference' Across Rotor.

Impact of Profile Consistency across Rotor

Profiles which do not follow the power law (those with a large difference between the shear exponent measured on the upper half and the lower half of the rotor) were isolated such that their effect on the power curve can be seen. By comparing the variation in measured shear with that expected by application of the power law, several profiles with either a negative shift in the wind speed profile or a large positive deviation¹³ can be identified. The power curves obtained from these datasets are shown in figure 4.4.1 in the scatter plot on the left (the scatter plot on the right hand side shows the power curve with these points removed). The distribution of these points which constitute approximately 12% of the power curve dataset is shown in figure 7.6.9.

The scatter plot shows there are several points which are indicative of either poor or exaggerated turbine performance. In most cases however these more extreme wind profiles do not have an obviously adverse effect on the power curve (hub height definition of wind speed).

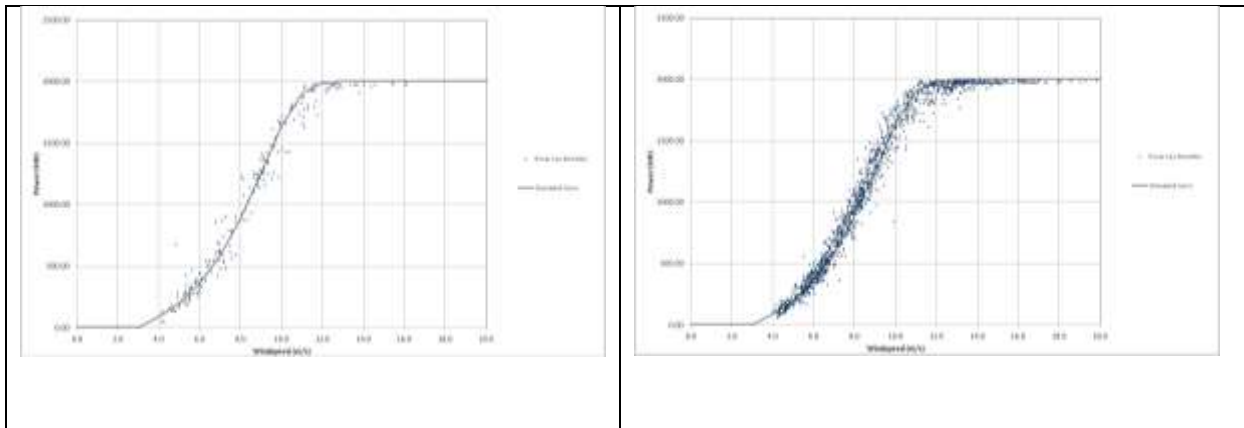


Figure 7.6.9: Power Curve Scatter Plot; Data with Large Deviation from Power Law in Left Panel, Remaining Data on Right.

¹³ $\text{SUM}(dV/dh \text{ measured} / dV/dh \text{ theoretical}) > 1.9$

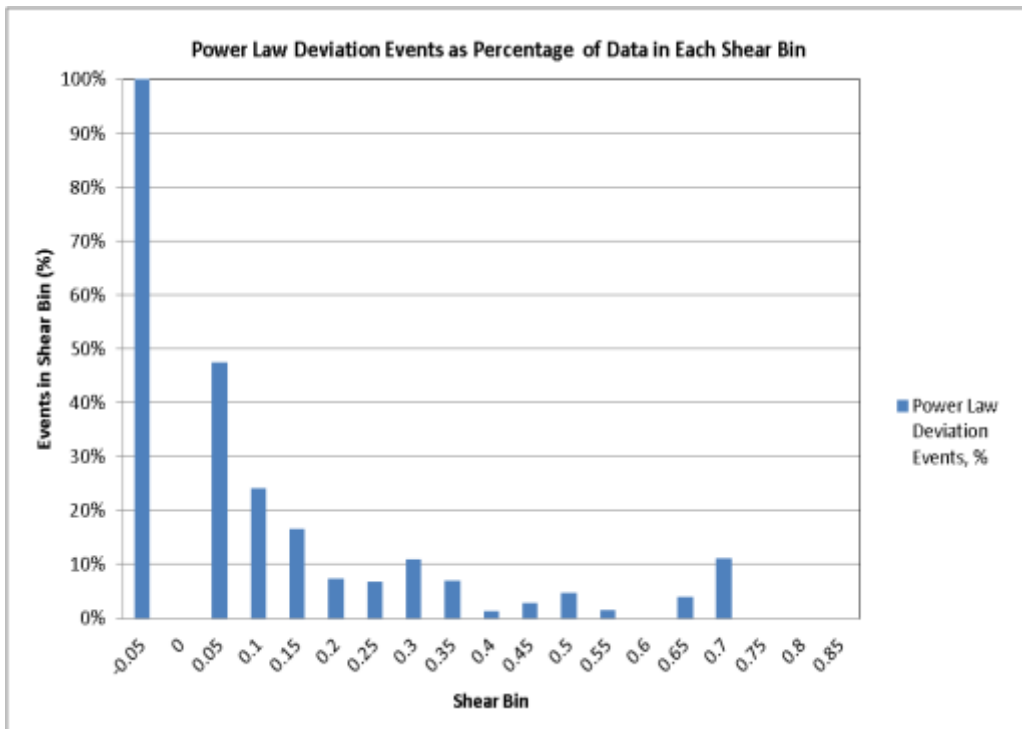


Figure 7.6.10: Distribution of Points with Large Deviation from Power Law as Percentage of Data in each Bin.

Veer Effect on Power Curve

Direction measured at each LiDAR measurement height shows that there can be a substantial change of direction in the wind profile across the rotor (see Table 7.6.8). In figure 7.6.11 the maximum veer¹⁴ measured in each ten minute period is presented relative to direction, temperature and turbulence. Figure 7.6.12 shows the distribution of veer by shear measured across the rotor. This appears to show that incidence of higher veer increase with increasing shear.

Direction Sector	No Icing conditions (Temperature ≥ 2 °C)	Potential Icing conditions (Temperature < 2 °C)
280		

¹⁴ Maximum Veer = Direction at rotor upper tip height - direction at rotor lower tip height

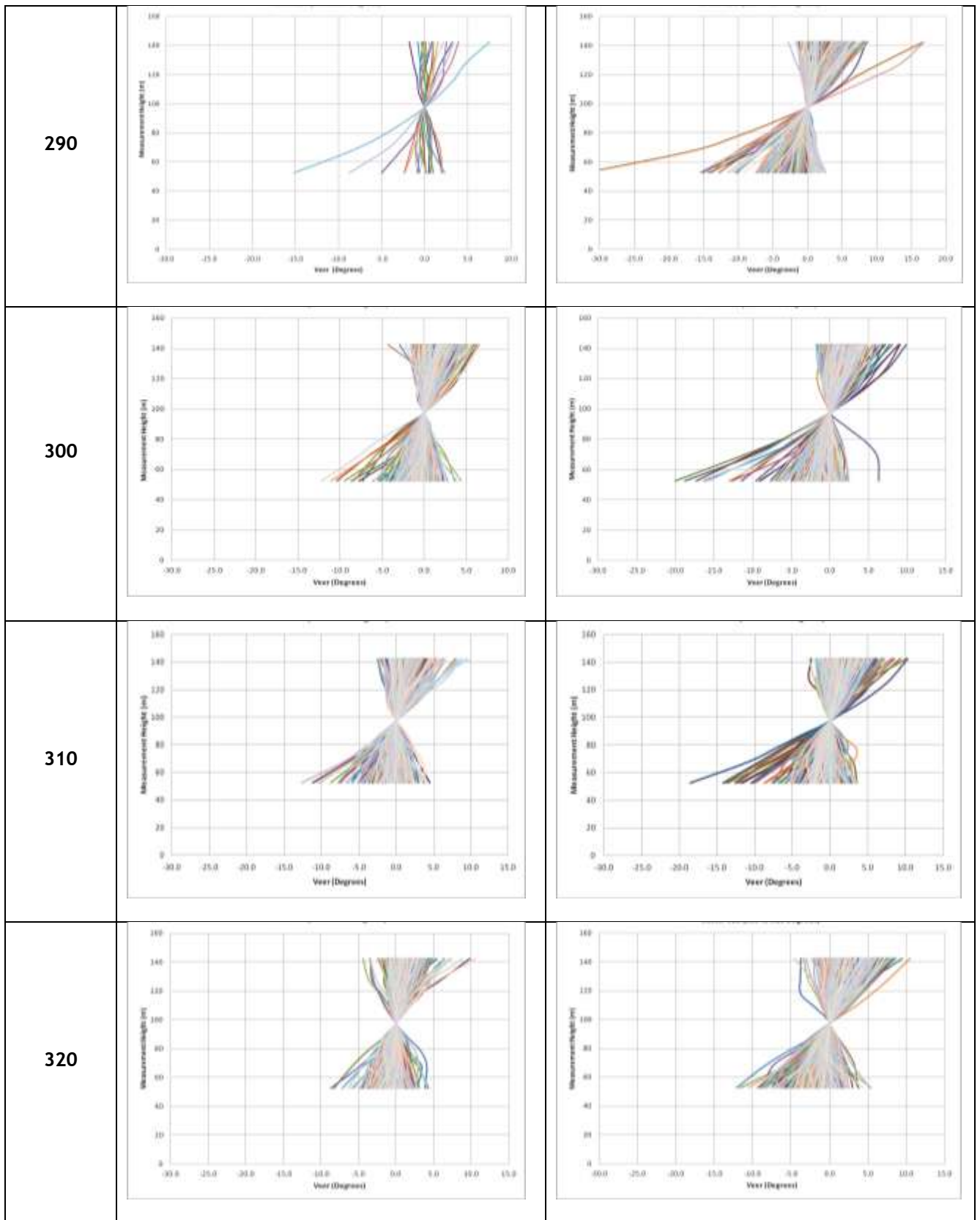


Table 7.6.8: Veer Profiles Across Rotor: Compare Warm/Cold Climate Conditions.

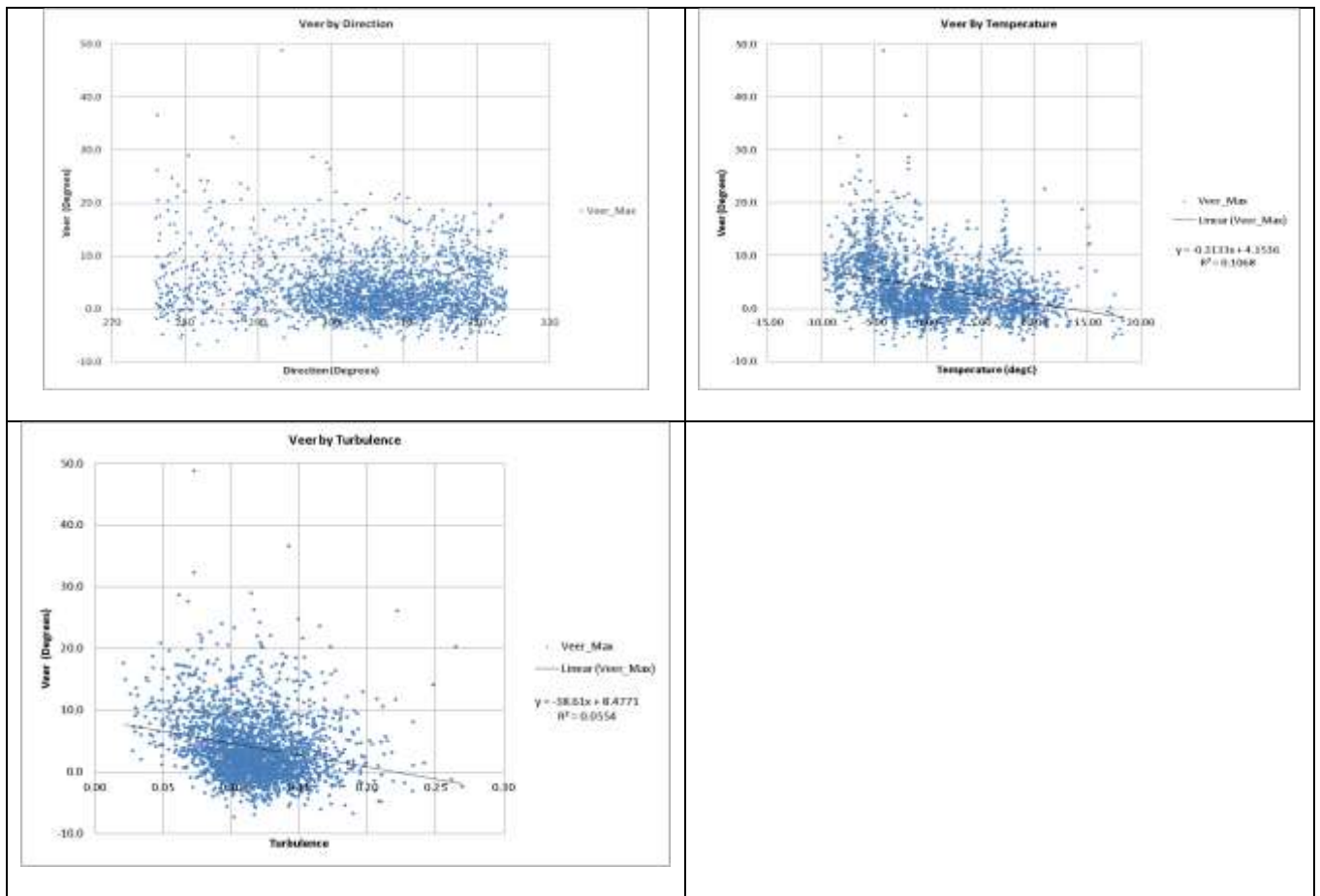


Figure 7.6.11: Plots of Veer against Direction and Temperature and Turbulence.

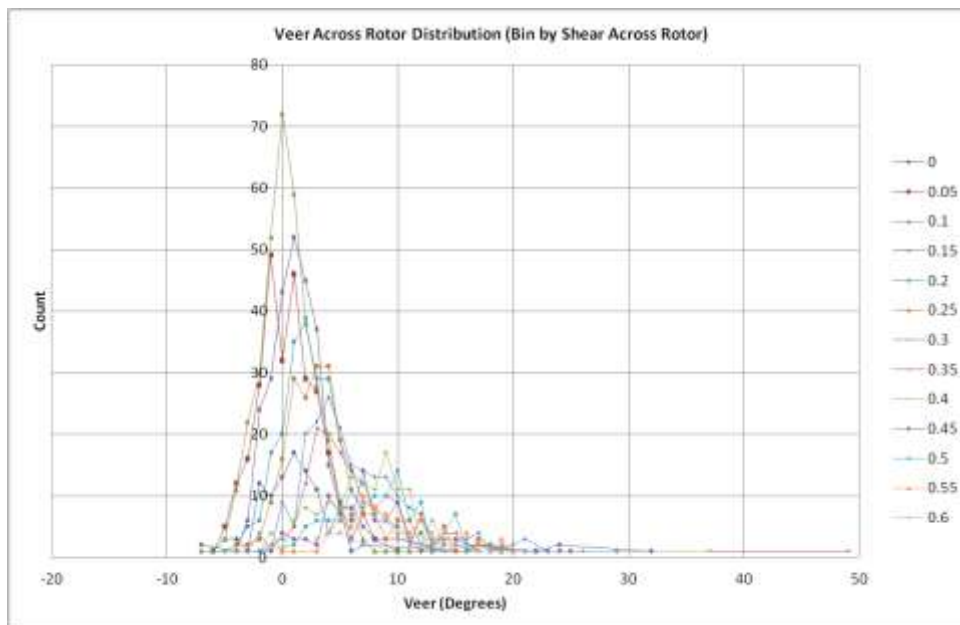


Figure 7.6.12: Veer Across Rotor Distribution - Binned by Shear across Rotor.

The effect of veer on the power curve is investigated in Figure 7.6.13. Low veer is considered to be a value between -5 and +5 degrees. High veer is considered to be any value outside this range.

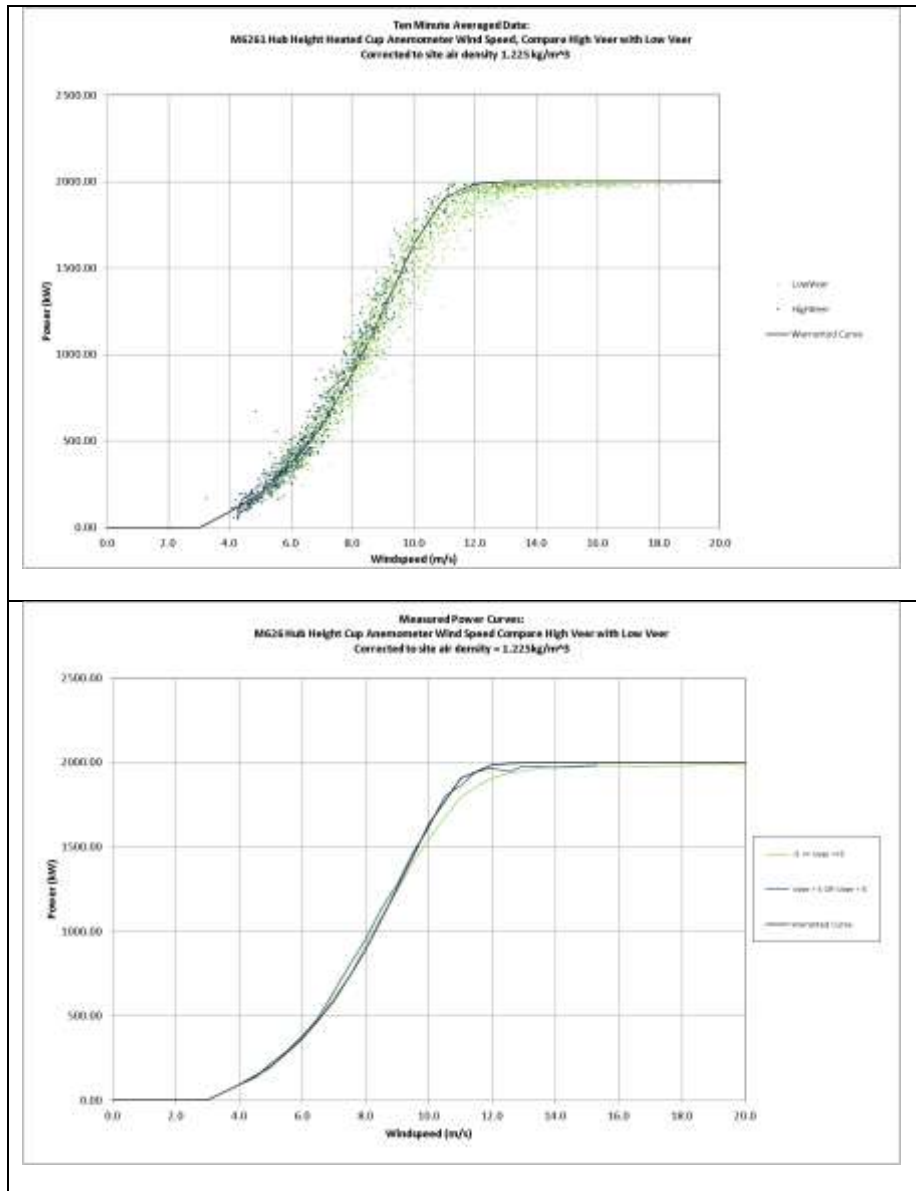


Figure 7.6.13: Veer Effects on Power Curve; Compare High Veer with Low Veer.

There is evidently a marked difference between the two power curves although it is likely these differences are dominated by the turbulence effect (high veer is associated mainly with high shear which is associated with low turbulence). In figure 7.6.14 a narrower range of turbulence is considered (7.5 to 12.5%). The same pattern exists suggesting that veer (albeit in conjunction with high shear) does have a substantial impact on the power curve and hence measured performance.

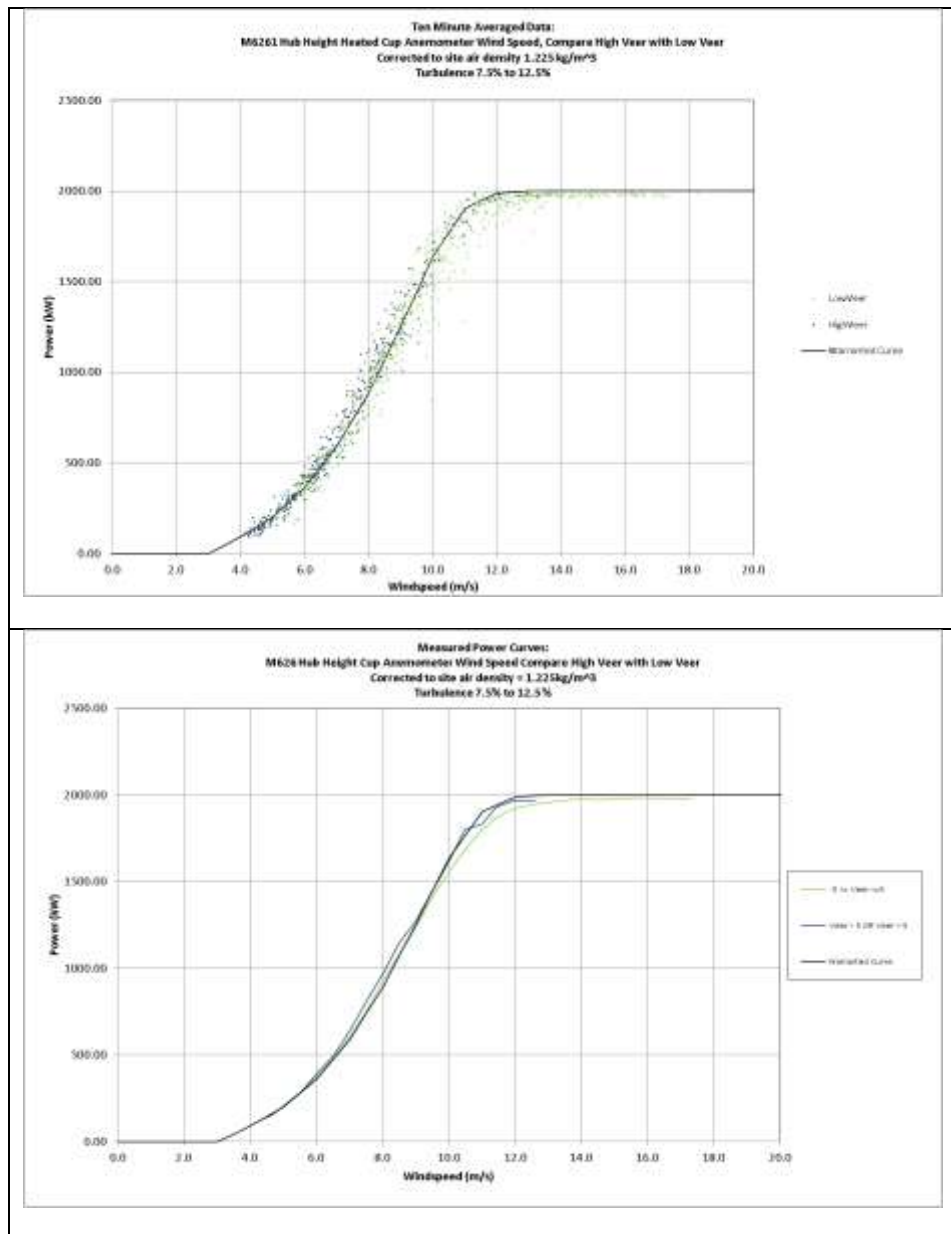


Figure 7.6.14: Veer Effects on Power Curve; Compare High Veer with Low Veer (Turbulence 7.5% to 12.5%).

The effect of the veer correction method (defined in 3.2.1) on the power curve has been tested. With the veer correction applied to the LiDAR equivalent wind speed, ‘test 4’ is repeated for comparison as shown in Figure 7.6.15. This results in an improvement to the AEP of 0.15% compared to the use of non veer corrected data. The set of graphs and tables in Figure 7.6.15 are arranged according to the format described by this table:

Wind Speed Correlation (where x axis is wind speed from source 1 and y axis is wind speed source 2, e.g. x = Vm626 and y = Vm6261 for Test 1).	Summary of Energy Yield Comparison
Power Curve Scatter Plot (Ten minute averaged data, corrected to nominal air density 1.225 kg/m ³)	
Binned Power Curve	Power Coefficient

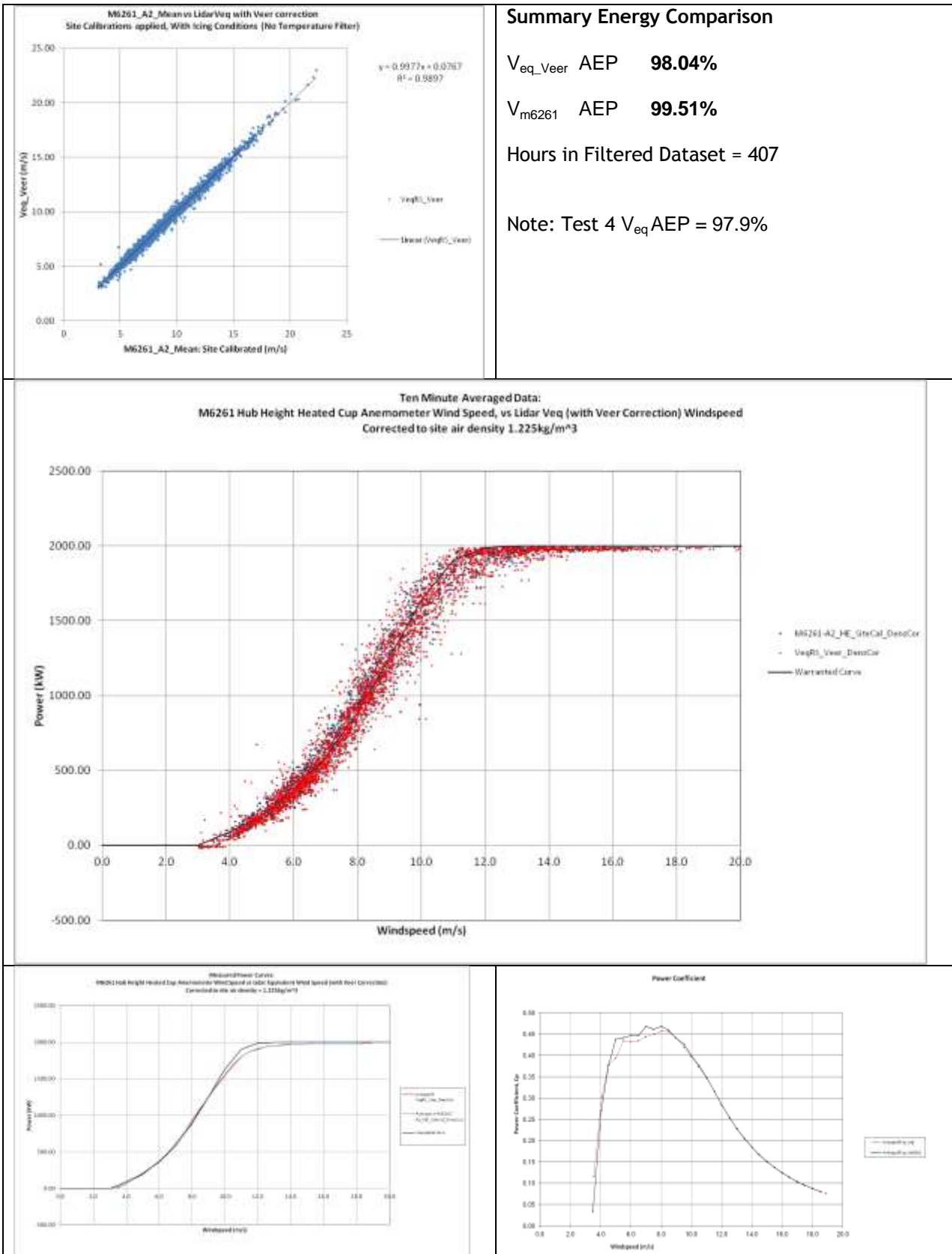


Figure 7.6.15: Veer Corrected Equivalent Wind Speed Power Curve; Test 4c - (V_{eq_Veer}) vs (V_{m6261}).

EFFECT OF TURBULENCE ON PERFORMANCE

The effect of turbulence on power curves is generally well documented. In particular the pattern is that for high turbulence, the performance at the knee of the curve reduces and a corresponding increase occurs on the lower portion or ankle of the curve.

Because the effects of shear and turbulence do not happen in isolation, it is important to acknowledge the effect of turbulence in these previous shear investigations. Essentially the relationship is that as shear increases turbulence decreases as shown in Figure 7.6.16.

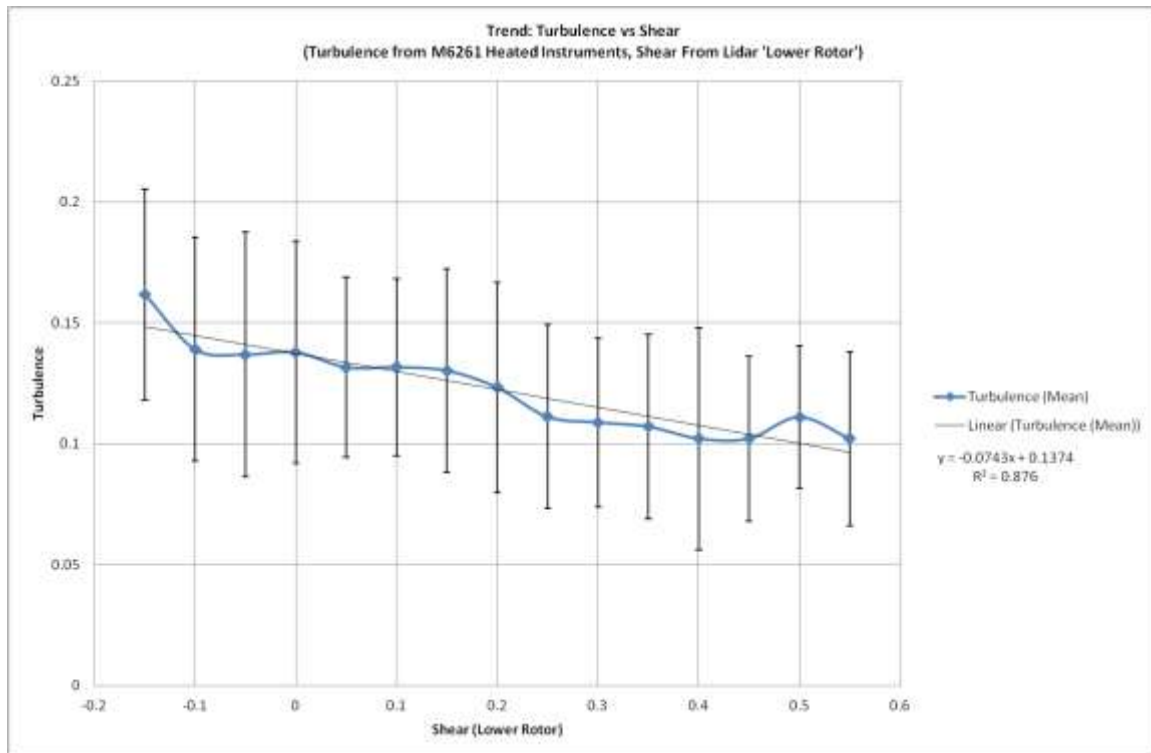


Figure 7.6.16: Turbulence vs Shear Trend from m6261 and LiDAR Measurements.

A study was carried out into the effects of turbulence on the PP test turbines at Havsnäs. The results of this study are summarised here.

The 5 test turbines at Havsnäs D2, E2, E5, F12 and F15 showed similar under performance or energy loss at the knee of the power curve in comparison to the warranted power curve (and over performance below rated). It is suspected that these effects are attributable to the effects of turbulence and therefore shear across the rotor disc.

Turbulence Normalisation

This method [33] accounts only for the effect of 10-minute averaging on the power curve and allows the 10-minute average measured power curve to be normalised to any turbulence level. An example of the method as applied to turbine D2 is shown in Figure 7.6.17.

The warranted power curve is stated to be valid for a turbulence range of 11 to 16%. The measured power curve data for this test were filtered to this turbulence range.

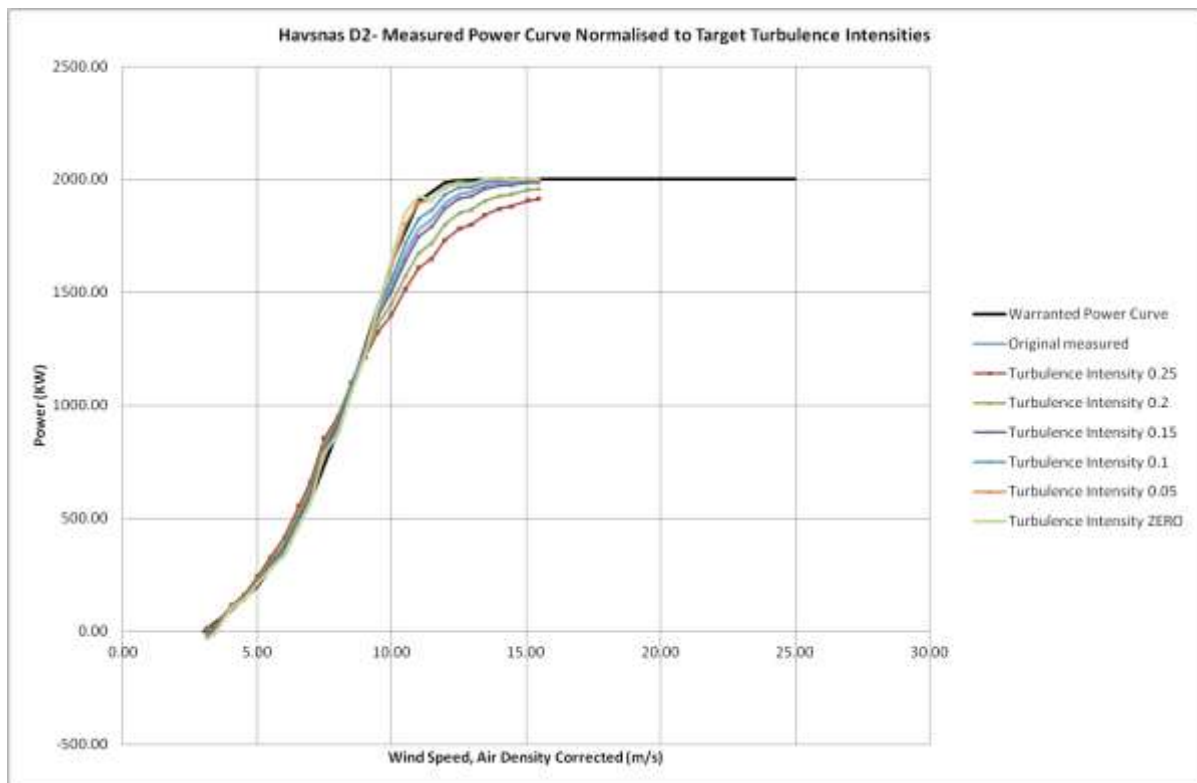


Figure 7.6.17: D2 Power Curve Normalised to Target Turbulence intensities.

The actual measured power curve sits between the power curves normalised to target turbulence intensities of 10% and 15%. This would be as expected as a high proportion of the measured data lie within this range. Additionally, the data was filtered for turbulence within the contractually specified 11 to 16% range.

The warranted power curve however sits closest to a power curve normalised to a target turbulence intensity of 5%.

It is concluded that either the turbulence has some other impact on the turbine performance over and above the impact of the 10-minute averaging process or that the warranted power relates to a lower turbulence intensity level than the warranted turbulence intensity range of 11 to 16%.

ICE DETECTION

Test 4 is effectively repeated with the addition of the ice detect signal as described in Section 5.3.1. The ice signal identifier is shown in Figure 7.6.18; note that only directions 276 to 324 are usable. Figure 7.6.19 then shows application of this signal to identify points in the dataset exhibiting ice effects. Figure 7.6.20 is a verification test on the difference of iced to ice free wind speed ratios.

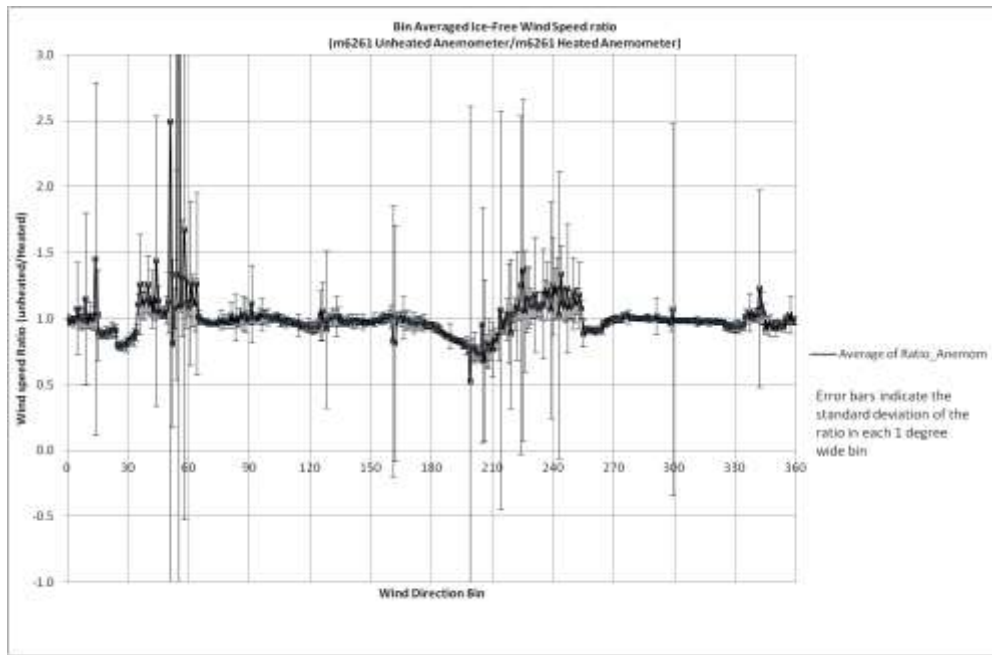


Figure 7.6.18: Ice Detect 'Signal'; Bin Averaged Wind Speed ratio Relationship Defined for Temperature > 5°C.

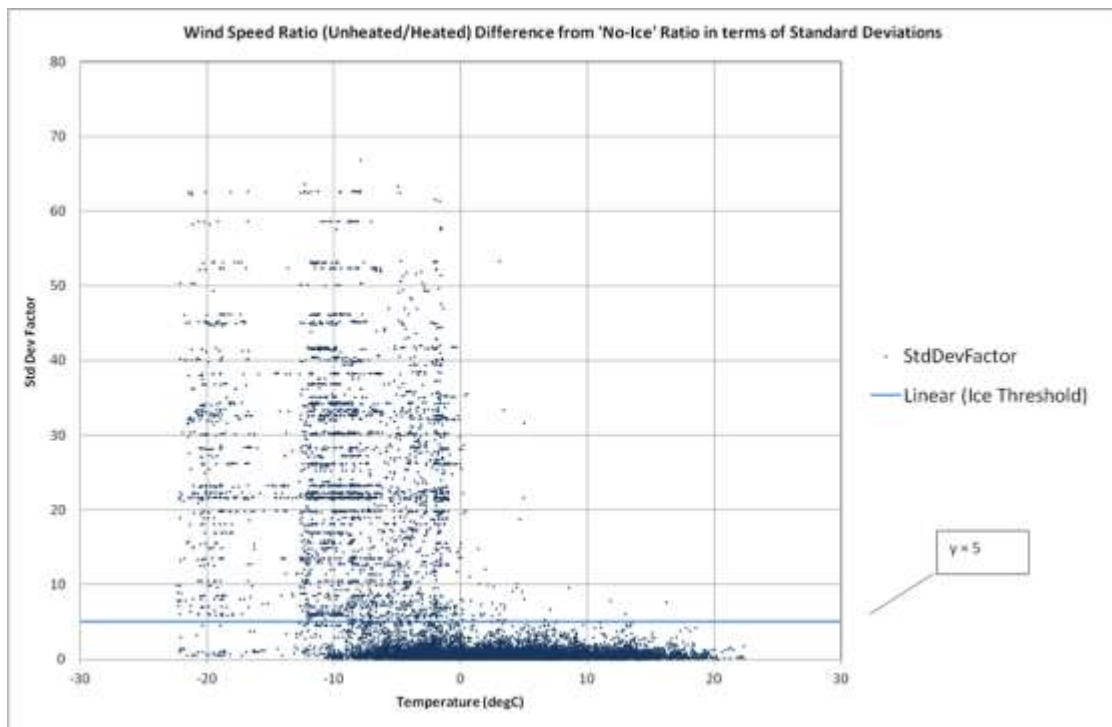


Figure 7.6.19: Ice Detect Events.

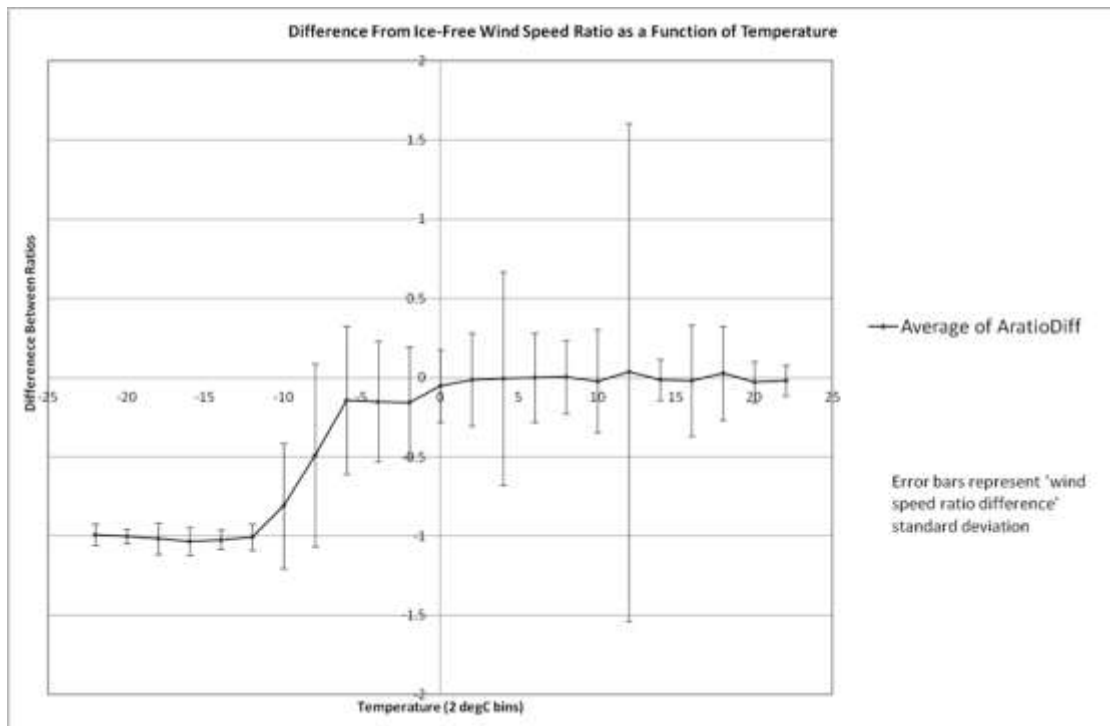


Figure 7.6.20: Difference from ice-free wind speed as a function of temperature.

Application of the ice detect signal to the dataset obtained from joining the LiDAR and M6261 heated systems results in very low data counts. This is due in part to the data lost to instrument faults and power loss but also to the unfortunate dominance of southerly wind directions (which are wake affected and hence excluded) as shown in figure 7.6.21.

In summary, of the 13306 data points in the combined LiDAR and M6261 dataset, there were 2743 ice events. However within the wake free sector there were only 150 icing events remaining. This is insufficient to develop any power curve and thus draw conclusions on ice impact on the turbine operation.

In order to try and increase the data count, only data obtained from the heated system M6261 is selected. As the data contains many incidents of instrument icing there is still a substantial amount of non-usable data. In this case of the 35272 data points in the M6261 dataset, there were 7429 ice events. However within the wake free sector there were only 419 icing events.

Figure 7.6.22 shows that the measured power curve is obviously affected by icing of the heated anemometer (power curve data points shifted to the left) to a more significant extent than any deterioration in the turbine performance (reduction in power). Consequently the power curve measurement is invalidated due to anemometer icing, despite using a heated anemometer. This suggests that measurement of power curves in icing conditions remains impractical even when fully heated instrumentation is used.

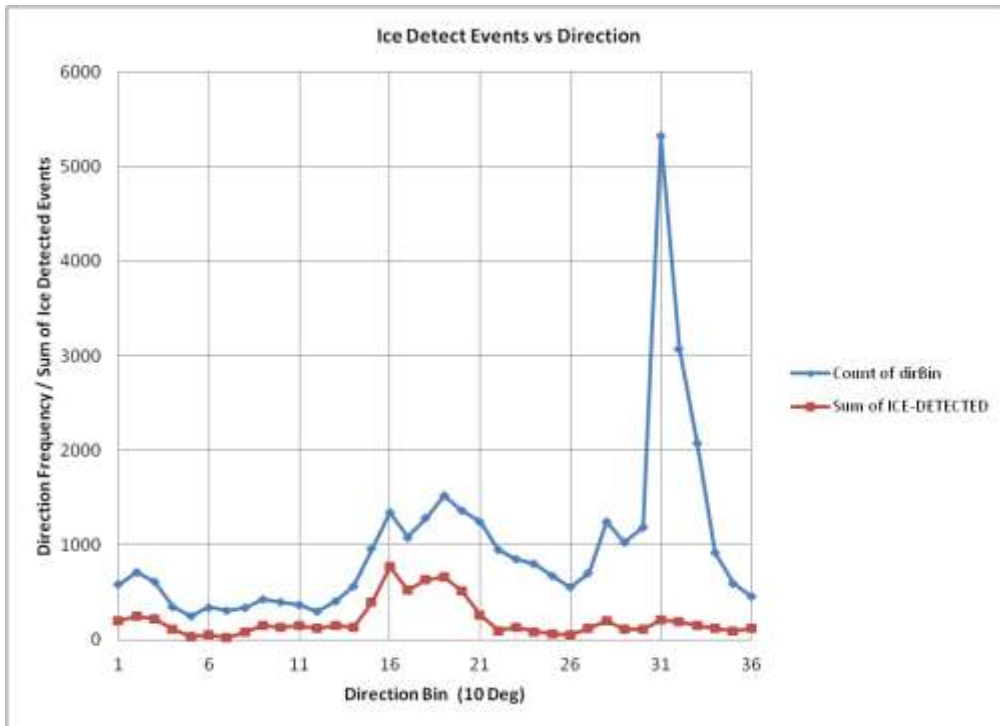


Figure 7.6.21: Distribution of Ice Events By Direction.

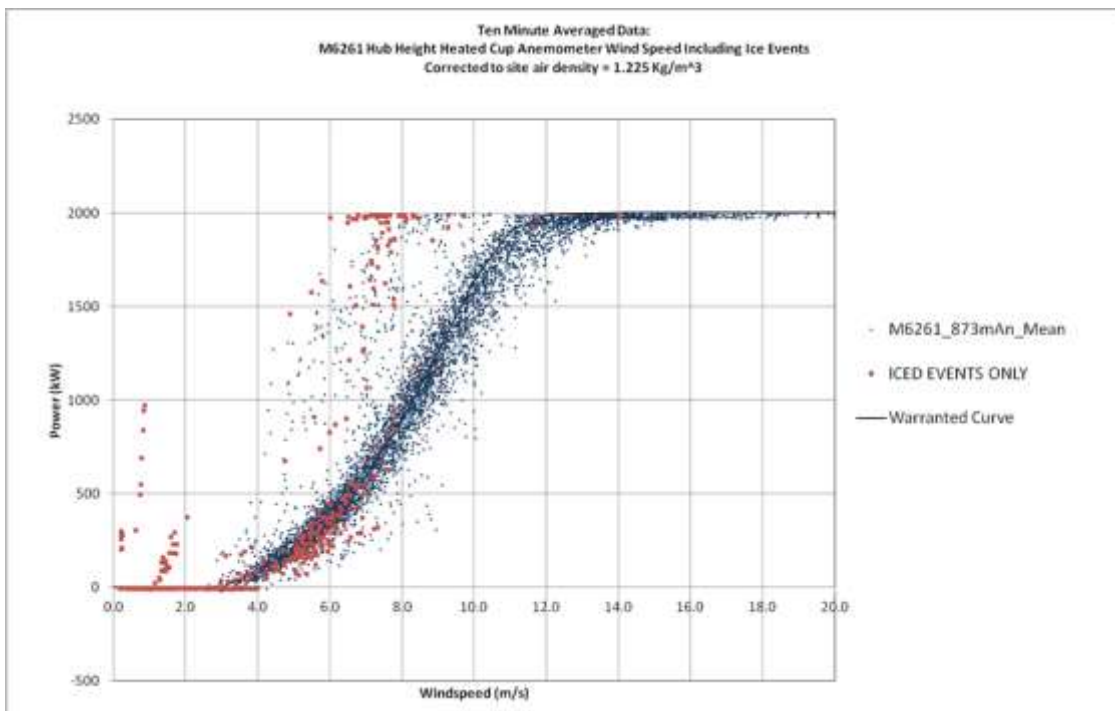


Figure 7.6.22: Power Curve with Ice Events.

CONCLUSIONS

The power curve and measured AEP obtained with hub height LiDAR data were in very good agreement with the hub height cup anemometer results (Test 3 - differing by approximately 0.7%) suggesting that LiDAR present a reliable alternative to use of fixed masts in PP assessment.

The IEC equivalent wind speed definition has been successfully applied to the data thus enabling detailed investigation of the turbine performance under different atmospheric conditions. Compared to the hub height power curve derived from LiDAR data (Test 3), the rotor equivalent wind speed power curve (Test 2) demonstrated an approximately 0.02% difference in AEP (or a 0.7% difference with respect to the hub height anemometer power curve). Due to using the same measurement technique (LiDAR volumetric measurement), the comparison between the LiDAR hub height power curve AEP and the LiDAR equivalent wind speed power curve AEP is a more meaningful comparison than comparing to the hub height anemometer power curve. This therefore allows a comparison to be made with the theoretical investigations of “Available Energy” presented in Section 6.4, where for the actual site conditions it was predicted that there should be 0.8% more available energy through the rotor than suggested by the hub height wind speed alone (Table 6.4.3 of Section 6.4). Then this measured power curve result suggests that the turbine is actually only able to extract 0.02% more energy than that suggested by the hub height wind speed. Consequently, referring to Equation 6.4.1 of Section 6.4.1:

$$\delta\alpha = \delta\alpha_A + \delta\alpha_P$$

And substituting

$$\delta\alpha = 0.02\%$$

$$\delta\alpha_A = 0.8\%$$

Then (rounding to the nearest 0.1%),

$$\delta\alpha_P = -0.8\%$$

In other words, the turbine is 0.8% inefficient with respect to its ability to extract the available energy through the rotor disk. Note that the available energy is with respect to the warranted power curve and not to the total kinetic energy through the rotor disk area. Therefore this 0.8% inefficiency is a performance reduction with respect to the warranted power curve derived energy production rather than to the total theoretical energy content. Of course these numbers are very small with respect to typical power curve measurement uncertainties (5 to 10% - see the next section for further discussion) but the impact of these uncertainties on the final energy difference calculation has been minimised by using only the measurements from the LiDAR. Consequently there is a degree of cancellation of uncertainties present. However, this result is not generic and is specific to the particular turbine type tested and the specific inflow conditions experienced during the measurement campaign. For example, Tables 7.6.5 and 7.6.6 suggest that for this specific turbine, the inefficiency may increase with increasing shear.

LiDAR data have enabled investigations into effects of shear and veer on the power curve which has previously been impossible with the practical and cost limitations of met mast based instrumentation.

This work reveals that performance appears to improve with respect to the warranted power curve as the shear increases however this is attributable more to the corresponding reduced

turbulence conditions which accompany the high shear than any mechanism directly attributable to shear.

Comparison of the equivalent wind speed power curves and the hub height wind speed power curves reveals the impact of shear and the limitations of the hub height wind speed to fully describe the inflow on the turbine. In the situation investigated here, it appears that the hub height wind speed derived power curve is over-estimating the actual performance of the turbine in high shear as the equivalent wind speed power curve generally shows lower performance than the hub height power curve in higher shear conditions. In other words, there is more wind energy available through the area of the rotor disk than is suggested by the hub height wind speed alone. A RS device used in conjunction with a conventional hub height met mast can indeed provide further understanding of the performance of a wind turbine in a complex flow environment.

7.6.2 PRACTICALITY OF IEC EQUIVALENT WIND SPEED METHOD

This project has provided an ideal test case for application of the equivalent wind speed definition of a power curve. Although the complex terrain and high surface roughness of the Havnäs site invalidate the procedure as defined in the draft IEC standard (which allows a RS device of proven quality to be used in conjunction with a possibly shorter than hub height mast on flat sites only), when deployed in conjunction with a conventional, hub height mast, it has been demonstrated that a RS device provides reliable data from which the equivalent wind speed can be easily derived. The implication of applying this new procedure on a complex site is connected mainly to the uncertainty of the final result rather than any practical implication. The uncertainty implications are discussed further in Section 7.6.4.

There are still major issues with applying this technique in Winter although these are mainly connected with icing of the conventional instruments on the meteorological mast used as references rather than the RS device.

With present RS technology, the technique is better suited to LiDARs than SoDARs due to the need to retain a reference mast and for the RS device to be as close to the mast as possible to maximise the correlation. The possibility of fixed echoes from the mast means that a SoDAR would generally need to be placed further away from the mast than a LiDAR.

The increased knowledge on the wind speed and direction profiles across the rotor disk and the measurement of an equivalent wind speed through the rotor enables a more detailed assessment of true wind turbine inefficiencies than can be determined from hub height wind speed alone.

7.6.3 PRACTICALITY OF IEC COLD CLIMATE ANNEX

The work carried out has underlined the difficulties associated with making meteorological measurements in cold climates. Difficulties associated with maintaining full functionality of the instrumentation resulted in very limited datasets. Ultimately the winter power curve measurement is invalidated due to anemometer icing, despite using a heated anemometer. In summary the use of heated instrumentation does not guarantee our ability to carry out PP tests in severe icing conditions. The cold climate annex of the PP standard is therefore of limited practical use.

7.6.4 UNCERTAINTY IMPLICATIONS OF POWER CURVE MEASUREMENT IN COLD CLIMATES

As previously noted, the implementation of the new rotor equivalent wind speed power curve measurement procedure at Havnäs was carried out under conditions which are technically not valid according to restrictions defined within the proposed draft standard. This is on account of the terrain

and hence wind flow complexity. The problem is not that the definition of equivalent wind speed is invalid in complex flow, rather that the measurement assumption of the RS wind speed measurement devices presently commercially available is invalid in non-homogeneous flow and hence the wind speed measurements from which the equivalent wind speed is derived become more uncertain or possibly totally erroneous in complex flow conditions. However, considering the shortcomings in the original, hub height wind speed power curve which the rotor equivalent wind speed power curve is intended to address, the implication is that power curves measured using the rotor equivalent wind speed definition should have lower uncertainty than those measured on the basis of hub height wind speed alone. This section assesses whether that is a reasonable statement or not. Furthermore, the hub height wind speed power curve should become significantly more uncertain the greater the flow complexity (i.e. more complex wind flow profiles across the rotor) and the larger turbine rotor diameters become.

The treatment of uncertainty in the existing standard ignores the fact that the hub height wind speed may not be representative of the true average wind speed which the wind turbine rotor sees. Indeed, the basic assumption behind the existing standard is that the hub height wind speed as measured at a point in space by a cup anemometer is representative of the average wind speed through the wind turbine rotor. If the terrain and hence flow is complex, then according to the existing standard, this is accounted for by carrying out a site calibration. The site calibration is simply a measurement to relate the wind speed at one point in space (the reference mast located between 2 and 2.5 rotor diameters from the turbine) to the wind speed at another point in space at the precise location of the turbine rotor hub (measured using a temporary hub height met mast located at the turbine location before turbine construction). However, even with a site calibration, the existing standard still relies on the assumption that the site calibration corrected point-in-space hub height wind speed represents the average wind speed through the wind turbine rotor. This assumption becomes less likely to be true the more complex the flow and the larger the turbine rotor. The new draft standard recognises this deficiency by defining extra components of uncertainty to be added to the hub height wind speed power curve uncertainty to account for the lack of knowledge of the wind flow through the entire rotor. Where a rotor equivalent wind speed is used this component of uncertainty can be reduced. It is therefore necessary to understand that hub height power curve uncertainties derived according to the existing standard should most likely have the uncertainty increased if the flow is complex and/or the turbine rotor diameter is large.

SUBJECTIVE COMPARISON OF UNCERTAINTY FOR HUB HEIGHT AND ROTOR EQUIVALENT WIND SPEED POWER CURVES

The uncertainty annexes of the draft standard dealing with the equivalent wind speed method have only come into existence in recent months. To fully implement the uncertainty analysis, additional verification and classification tests would have been required to be carried out on the LiDAR on a test site before commencing the actual Havsnäs measurements. This was clearly not possible. Therefore a somewhat subjective assessment of where the new test increases and decreases uncertainty with respect to a “standard” hub height power curve measurement is presented in this chapter. Where numerical estimates of uncertainty are possible then they are presented. However, in most cases it is only possible to say whether there is likely to be an increased or decreased overall uncertainty with respect to the hub height power curve uncertainty.

The following table assesses the likely relative impact on uncertainty of each aspect of the Havsnäs rotor equivalent wind speed power curve implementation.

Component	Discussion	Relative Uncertainty Impact
First stage site calibration from turbine hub height mast to reference hub height mast.	This step is common to the hub height power curve and the equivalent wind speed power curve.	No relative impact.
Second stage site	This component affects only the rotor equivalent wind	The site calibration

Component	Discussion	Relative Uncertainty Impact
calibration from reference hub height mast to LiDAR hub height wind speed (this is effectively the LiDAR performance verification test as defined in the draft standard).	speed power curve. The correlation is over a short distance (ca 50m) although compares wind speeds derived from different measurement principles (cup anemometer point measurement and volumetric LiDAR measurement). The correlation is good however. The uncertainty is assumed to be the mean deviation between the corrected LiDAR hub height wind speed and the met mast site calibration corrected hub height wind speed.	linear regression relationship suggests that this is of the order of 1%.
LiDAR wind speed at hub height.	As the absolute LiDAR wind speed at hub height is corrected with respect to the reference mast hub height wind speed via the second stage site calibration, the uncertainty of this wind speed cannot be less than the uncertainty of the reference mast wind speed measurement combined with the site calibrations.	Defined in the step above and hence already accounted for.
LiDAR wind speeds across rotor disk height range.	The uncertainty at each measurement height will vary with height. The change of wind speed with height and turbulence is larger at lower elevations and reduces with height. Consequently the flow through each measurement volume is more complex at lower elevations than higher elevations. Therefore the measurement uncertainty reduces with increasing height. Such uncertainties would be derived from the RS device classification test (as proposed and defined in the draft standard) where such a test has been carried out (not implemented in this case). This uncertainty component cannot be less than the uncertainty of the reference mast measurement to which each of these individual measurements is referenced. However the reference mast uncertainty is common to the hub height and equivalent wind speed power curves, so here we are considering only the uncertainty over and above the reference mast anemometer uncertainty.	This is assumed to be the relative difference between the wind speed range in the highest measurement volume compared to that across the lowest measurement volume. Assuming a worst case shear exponent of 0.5, this evaluates to 0.4% uncertainty.
Uncertainty Due to Limited number of measurement heights across the rotor disk.	In this case we have 10 measurement heights across the rotor disk. At least in the case of a power law shear profile, a theoretical analysis has shown that the equivalent wind speed does not change to the second decimal place irrespective of whether there are 3 or 100 measurement heights across the rotor. This may not be the case for a non-power law shear profile.	Assumed to be zero in this case.
Uncertainty due to lack of wind shear/equivalent wind speed measurement.	Starting from the assumption that only hub height wind speed is measured, then the extra uncertainty to account for the lack of knowledge of the wind profile across the rotor is estimated to be 2.5% of wind speed according to the worst case assumptions defined in the draft standard. This is 2.5% over and above the uncertainty associated with the reference anemometer.	Applies to the hub height wind speed power curve only.
Uncertainty due to lack of wind veer measurement and correction across the rotor.	In the case of a hub height wind speed power curve there is no knowledge of the variation of wind veer across the rotor. The draft standard provides a method to evaluate the uncertainty assuming a worst case veer of 40 degrees/100m. This evaluates to a wind speed	Applies to the hub height wind speed power curve only.

Component	Discussion	Relative Uncertainty Impact
	uncertainty of 0.7%.	
Derivation of equivalent wind speed from LiDAR measurements.	As the reference wind speed is a common factor to this summation, this defines the lower limit of the equivalent wind speed uncertainty. Additional, incremental components associated with the components described above (but not double counting the reference mast uncertainty) combine in quadrature to define the total, equivalent wind speed uncertainty.	Combining only those components which are over and above the reference anemometer wind speed uncertainty on the assumption that the components are uncorrelated: $\sqrt{(1\%^2+0.4\%^2)}= 1.1\%$
Additional Uncertainty Applicable to Hub Height Wind Speed Power Curve	Combined uncertainty due to lack of shear and veer measurements.	$\sqrt{(2.5\%^2+0.7\%^2)}= 2.6\%$

The absence of a LiDAR classification for these site conditions is in itself a potential uncertainty in the above analysis for which further uncertainty components may be required. However, it is noted that the uncertainty associated with not implementing this more sophisticated power curve measurement technique is at least 2.6%. Even if the equivalent wind speed uncertainty estimate of 1.1% is an underestimate, there would have to be significant further uncertainty so far unaccounted for (at least 2.4%) for the overall uncertainty to be worse than not carrying out the equivalent wind speed measurements at all. The challenge is therefore to ensure that the RS instruments, measurement and analysis methods applied result in significantly less than the 2.6% extra uncertainty associated with not carrying out these measurements. From the above relative assessment, this does seem achievable. It is most likely that for complex sites a hub height mast should still be used in conjunction with the RS device to provide further in-situ verification of the RS measurements and to assist in reducing some components of uncertainty.

The above discussion is concerned with the relative uncertainty impact compared to a hub height wind speed power curve. Furthermore, the above discussion is in terms of wind speed uncertainty rather than energy yield uncertainty. The absolute uncertainty of the hub height wind speed power curve derived energy yield according to the current standard, which ignores the above effects, was 9.5% of warranted AEP¹⁵. Assuming a sensitivity factor of 2 for the wind speed to energy yield uncertainty conversion, including the extra 2.6% wind speed uncertainty would increase the combined uncertainty in AEP to 10.8%, assuming the uncertainty components are uncorrelated.

¹⁵ This relatively high overall uncertainty was dominated by the relatively poor uncertainty characteristics of the contractually specified anemometer type when exposed to the turbulent in-flow of the Havsnäs site. A different anemometer type could have reduced this overall uncertainty significantly.

7.7 WIND FLOW MODELLING

7.7.1 UNCERTAINTY OF LINEARISED MODELS IN COLD CLIMATES

This section describes an evaluation of wind flow model performance at Havsnäs wind farm. The wind flow model used in this work (hereafter referred to as “the linear flow model”) is a combination of the well-established orography model MS3DJH/3R [18] and empirical roughness and obstacle models which are consistent with the European Wind Atlas [19], Kaimal and Finnigan [20] and Perera [21]. It is broadly similar to other industry standard flow models such as WASP [19].

The output of the wind flow model is the speed-up, S , defined as:

$$S = \frac{v_T}{v_M}$$

Equation 7.7.1

where v_T is the modelled wind speed at the turbine location at hub height above ground level and v_M is the modelled wind speed at the meteorological mast location, also at hub height.

METHODOLOGY

A mast pairs database was created using four 50m SA masts and ten 96m PP masts. Mast locations are shown in Figure 7.7.1. Masts were processed in pairs in order to compare the flow model’s predicted speed-up between two masts with the real wind speed ratio.

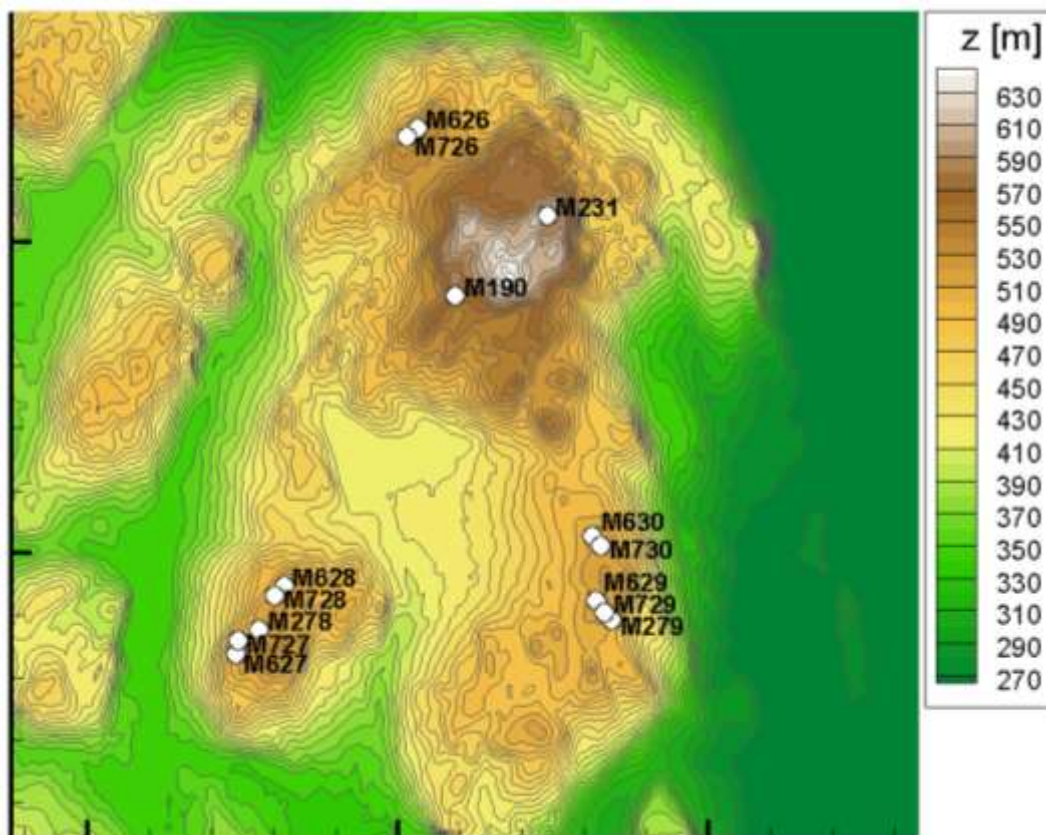


Figure 7.7.1: SA (M190, M231, M278 and M279) and PP mast locations. The elevation (z) is in metres above sea level. Major tick marks are 5km.

For each mast pair, anemometer and wind vane data were processed by 30° direction sectors for concurrent data only. The wind speed and direction data analysed in this work are 10-minute averages. Data affected by icing, instrument failures and tower shadow were removed where necessary. The wind speed ratio for a mast pair, R , was defined as the ratio of the measured mean wind speeds of the two masts. The speed-up error, ε_s , was calculated as:

$$\varepsilon_s = 2 \left(\frac{S - R}{S + R} \right) \quad \text{Equation 7.7.2}$$

which means swapping the masts changes the sign of ε_s but not the magnitude.

More details of this methodology can be found in Reference [22].

RESULTS

After data count filters were applied (minimum 5000 data points for SA masts, 500 for PP masts), 90 directional observations were included in the Havsnäs dataset. A directional observation constitutes a long-term wind speed ratio measurement for a mast pair in a 30 degree sector (thus up to 12 directional observations are possible per mast pair). The three most common direction sectors which passed the data count filters are 300°, 270° and 330°. The mean absolute speed-up effect is 3.2% (where speed-up effect is the speed-up minus 1) which indicates that this site has moderate wind speed variation. Figure 7.7.2 shows a histogram of distances between mast pairs in the Havsnäs dataset; low distances are well-covered by PP masts and larger distances are well-covered by SA masts. The mean distance between masts is 1.75km.

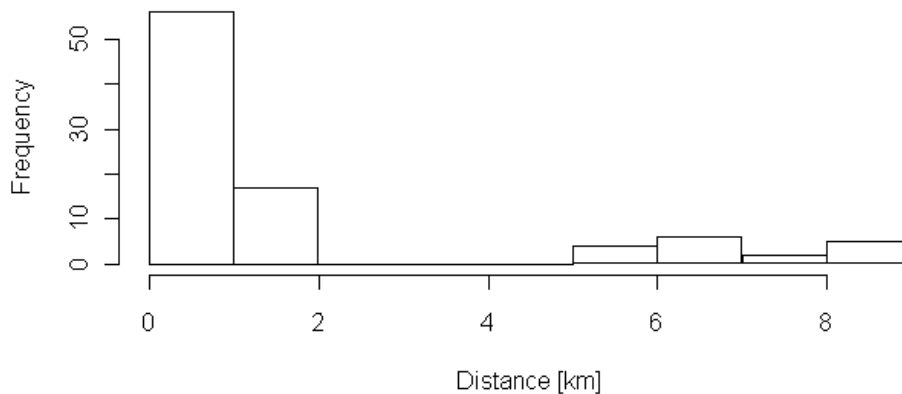


Figure 7.7.2: Histogram of distances between mast pairs (30 degree sectors)

The overall standard deviation of speed-up error is 5.0%. This is better than the 7.8% observed in Reference [22] but distances in the Havsnäs dataset are relatively small (mean distance was 1754m compared with 4939m in Reference [22]). Figure 7.7.3 shows a histogram of speed-up error in the Havsnäs dataset.

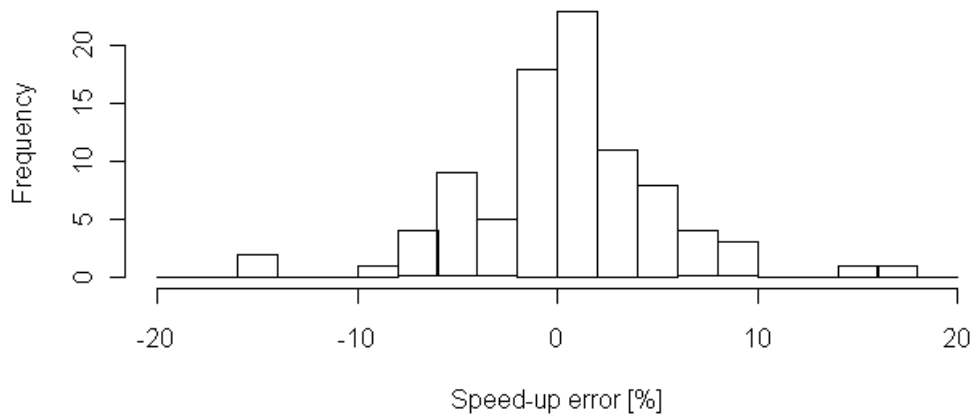


Figure 7.7.3: Histogram of speed-up errors (30 degree sectors)

As explained in Reference [22], distance between a mast pair is the strongest predictor of speed-up error. Figure 7.7.4 shows a plot of speed-up error against distance for the Havsnäs dataset along with the expected uncertainty based on Reference [22]; this plot confirms there is good agreement with the expected relationship.

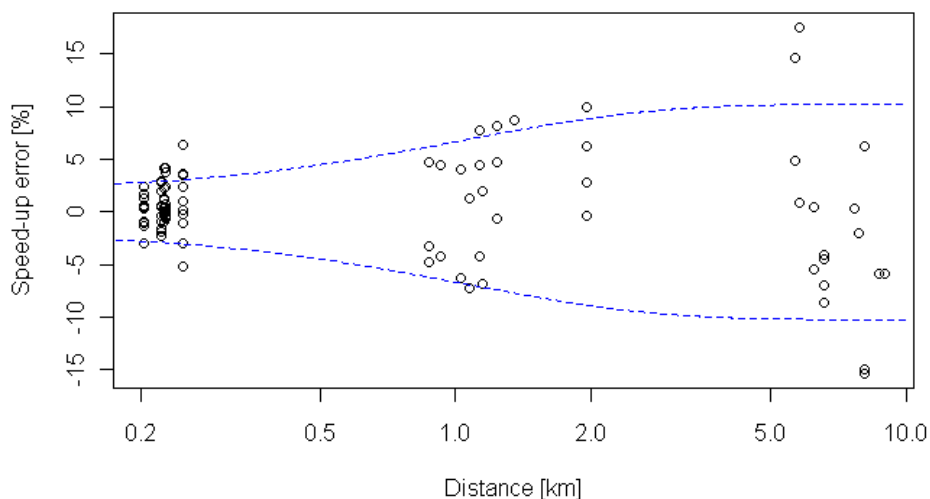


Figure 7.7.4: Speed-up error vs. distance between mast pairs (30 degree sectors). The dashed lines show the expected standard deviation from the results in Reference [22].

Finally, speed-up was analysed by time of day. The most striking pattern noticed was a tendency for the measured wind speed variation across the site to be much higher at night than during the day. As shown in Figures 7.7.5-7.7.10, the linear flow model predictions also tend to be more accurate during the day. Note that the mean wind speeds in these Figures are overstated due to a 5 m/s wind speed filter.

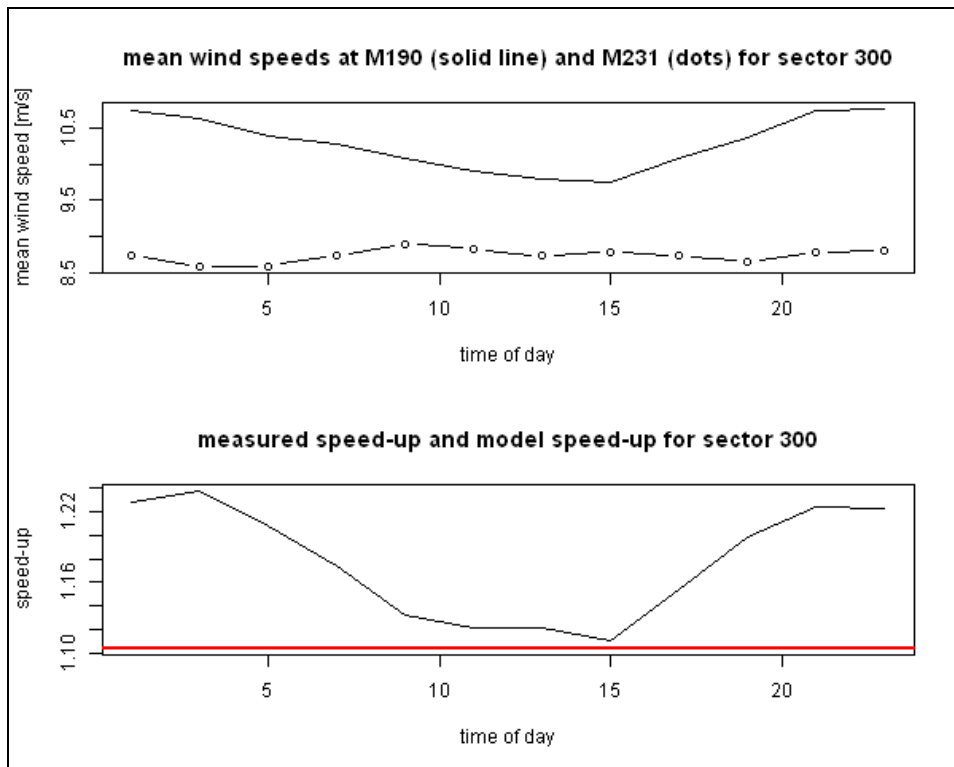


Figure 7.7.5: Measured wind speeds and speed-ups for M190 and M231 for direction sector 300°. In the second plot, the red line shows the speed-up predicted by the linear model.

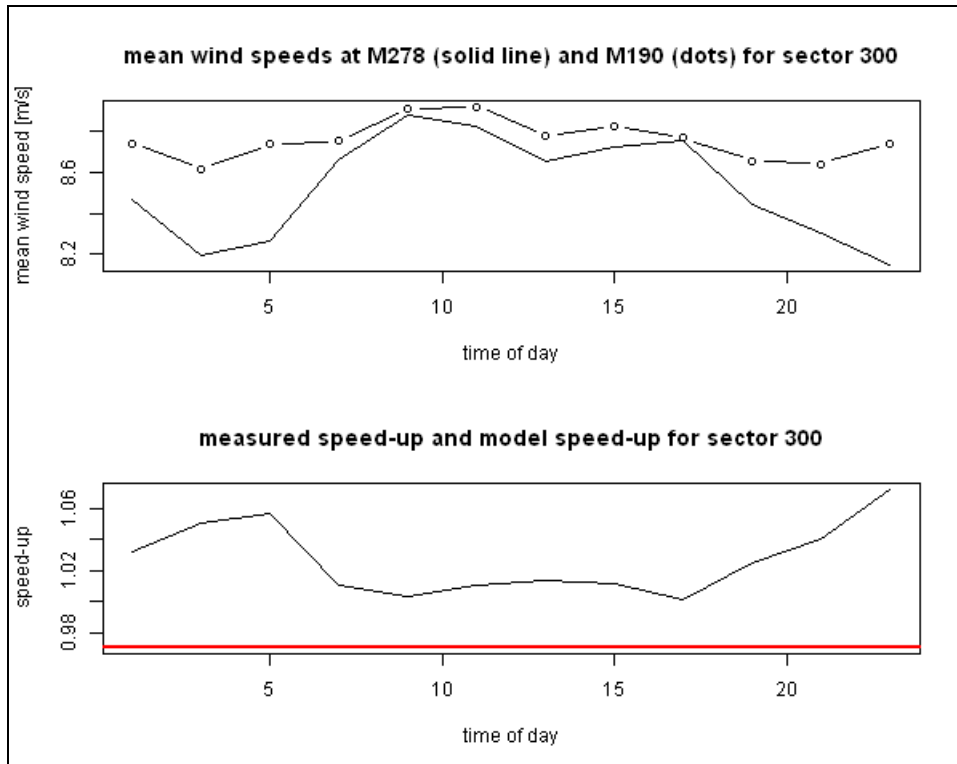


Figure 7.7.6: Measured wind speeds and speed-ups for M190 and M278 for direction sector 300°. In the second plot, the red line shows the speed-up predicted by the linear model.

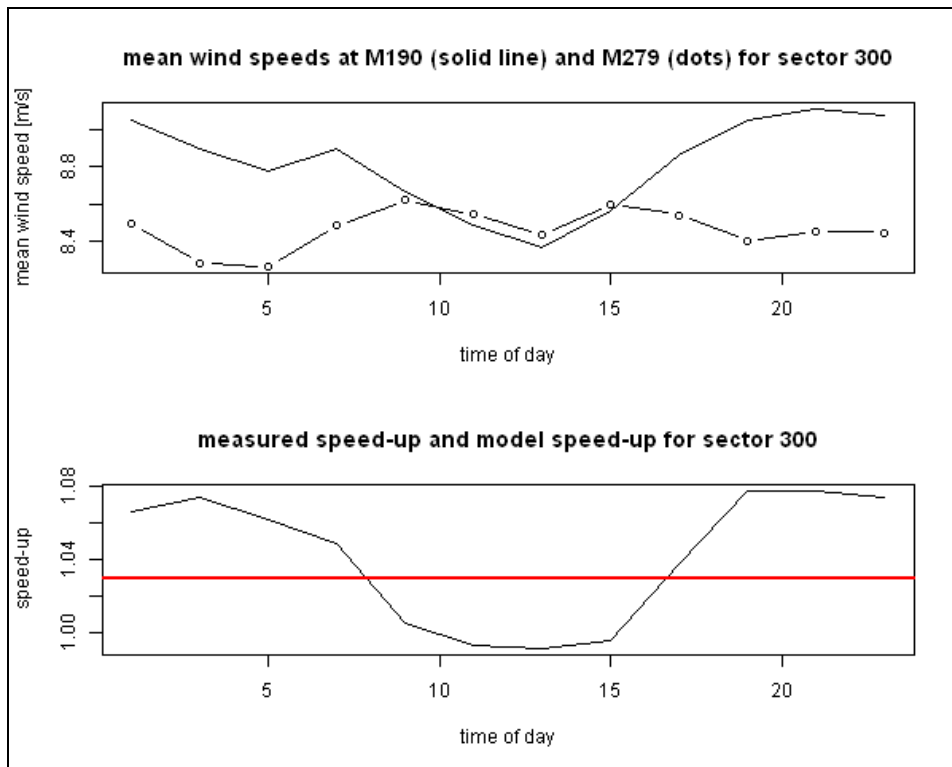


Figure 7.7.7: Measured wind speeds and speed-ups for M190 and M279 for direction sector 300°. In the second plot, the red line shows the speed-up predicted by the linear model.

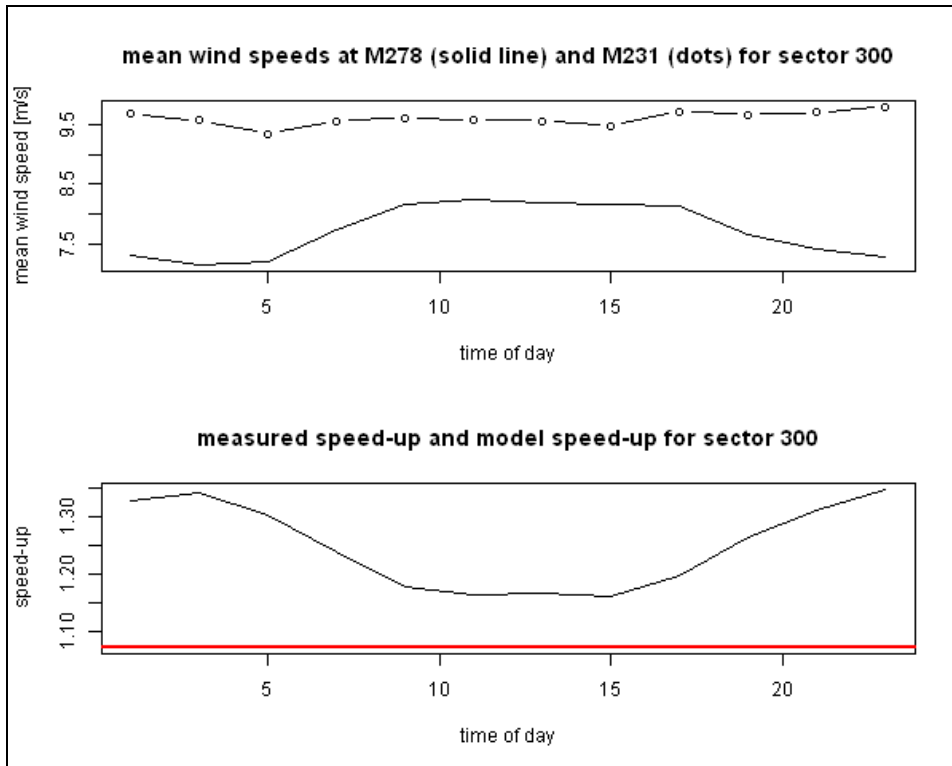


Figure 7.7.8: Measured wind speeds and speed-ups for M231 and M278 for direction sector 300°. In the second plot, the red line shows the speed-up predicted by the linear model.

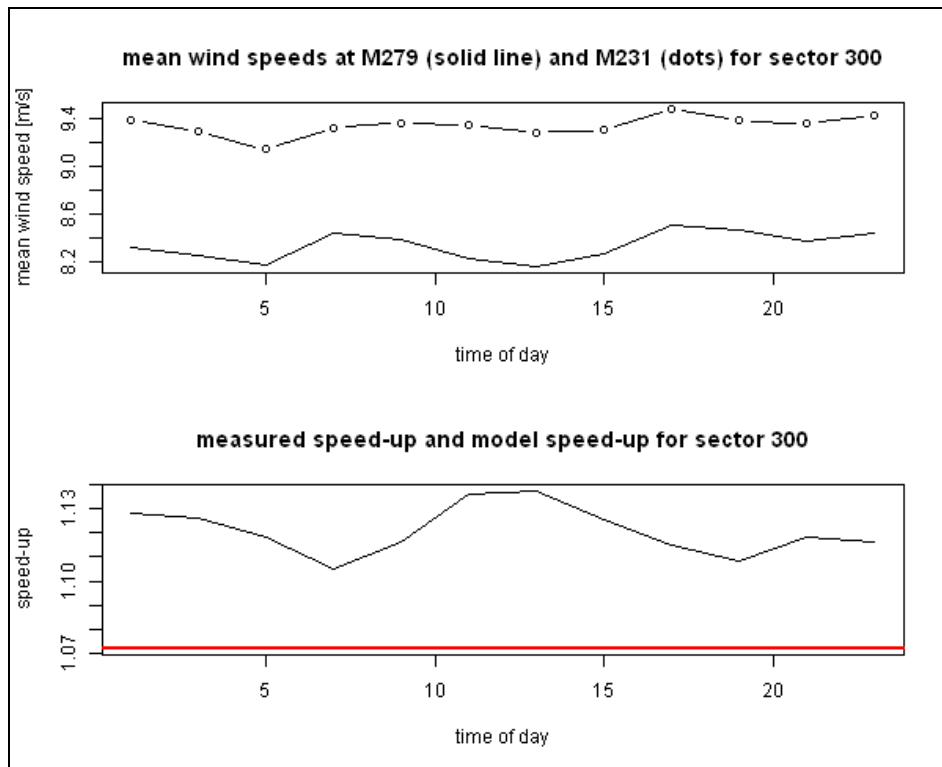


Figure 7.7.9: Measured wind speeds and speed-ups for M231 and M279 for direction sector 300°. In the second plot, the red line shows the speed-up predicted by the linear model.

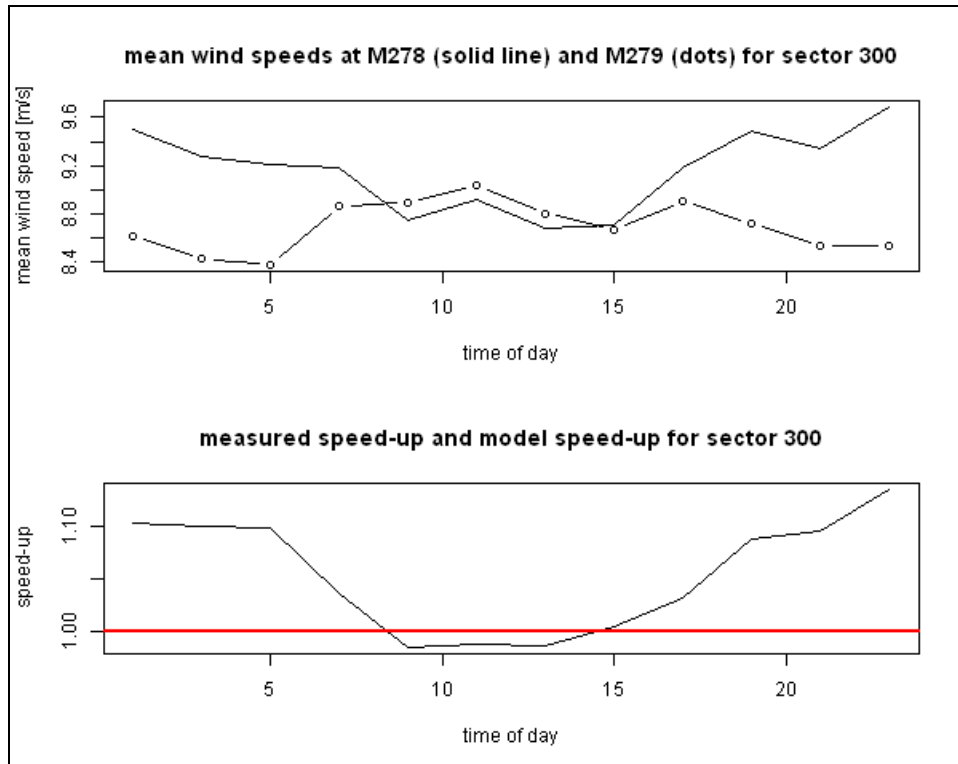


Figure 7.7.10: Measured wind speeds and speed-ups for M278 and M279 for direction sector 300°. In the second plot, the red line shows the speed-up predicted by the linear model.

CONCLUSIONS

The linear flow model performs with similar accuracy at Havsnäs as for sites in warmer climates. The relationship of speed-up error against distance agrees well with the results reported in Reference [22]. Figures 7.7.5-7.7.10 indicate a strong diurnal trend in the performance of the linear model.

7.7.2 USEFULNESS OF CFD AND MESOSCALES MODELS

INTRODUCTION TO CFD MODELLING AT HAVSNÄS

Standard linear and CFD flow models assume neutral atmospheric stability. Whereas this may be a reasonable assumption in many temperate climates, in both hot and cold climates the stability of the atmosphere has been observed to deviate from this, particularly at wind speeds below 10m/s. This has important effects on the wind climate in terms of the wind speed and direction, turbulence intensity and shear. Since the average wind speed at Havsnäs is just under 8m/s at hub height, a considerable proportion of the energy generated at the site occurs at times when the wind climate is likely to be affected by non-neutral atmospheric conditions. Due to the cold climatic conditions during the winter months, the atmosphere at Havsnäs is expected to be stable for a larger proportion of the time than would be the case in a more temperate climate.

CFD analysis at Havsnäs has been carried out to investigate flow model behaviour under cold climatic conditions and also to gain a qualitative understanding of flow conditions across the site. Simulations have been performed using the coupled mesoscale-CFD model, VENTOS®/M, which takes atmospheric stability into account. Verification of the model results is sought by comparison with measured data and the strengths and weaknesses of the CFD model in cold climates are explored. A literature review of other relevant CFD studies is also included.

Havsnäs wind farm is located in northern Sweden on relatively high altitude terrain and is therefore exposed to a cold climate for much of the year. The terrain is reasonably complex, with some steep slopes located on the hills to the west of the site. The site is surrounded by forestry and extensive snow cover is typically present through the winter months.

Stable atmospheres in cold climates result in the suppression of vertical flow and the wind having a stronger tendency to be driven through the valleys between hills, rather than being pushed upwards and over the top. Therefore, speed-ups between masts and turbine locations calculated by traditional flow models, where neutral conditions are assumed, may be inaccurate if the atmosphere is stable for a large proportion of the time.

The orography and location of the atmospheric stability masts, M6261 and M6282, are shown in Figure 7.7.1 in Section 7.7.1. The wind at Havsnäs is predominantly from the North-West, with secondary predominant sectors from the South-East.

LITERATURE REVIEW

Recently, several studies have been carried out showing the effects stability has on wind climates, turbulence intensity, shear, energy yield predictions and PP. Since these studies have often demonstrated that varying stability can have a significant effect on results, including atmospheric stability in mesoscale and CFD models has also become important.

Work carried out in [23], which involved analysing data from multiple wind farm sites, showed that atmospheric stability can significantly affect turbine PP. This can pose particular problems in stable atmospheres, where the turbulence is low but the shear profile is high at lower altitudes and very low at high altitudes. This results in a reduction in the energy

produced across the rotor diameter relative to the wind speed at hub height. They also found that in stable atmospheres with high turbulence, the turbine performance increases at low wind speeds, but decreases at higher wind speeds, which affects parts of the power curve. They suggest that using an empirical model to correct linear flow model results for varying atmospheric stability would be beneficial in non-complex terrain. Research into the effects of atmospheric stability on power curves and wakes for offshore sites by [24] also concluded that thermal stratification is of crucial importance.

Various methods have been used to include atmospheric stability in CFD models. The VENTOS®/M model used for the study, and described later in this report, forms the tail end of a model chain, receiving WRF mesoscale results as input in the form of transient boundary conditions. The nature of the model chain implies that atmospheric stability is inherently taken into account. The model used in [25] also makes use of the model chain, but uses the WRF results at a single point located within the CFD model domain to scale the CFD results after first correcting for bias in the WRF model. This approach means that CFD look-up tables can be created from simulations carried out with a standard CFD model, rather than re-running CFD simulations for various atmospheric conditions. The methodology is designed for short-term forecasting, and for this purpose, they found the results to be promising. Another approach, used by [26], takes atmospheric stability into account within the CFD model by altering a parameter in the turbulence model according to the stability class indicated by mast measurements. The CFD model is then used to extrapolate conditions at the meteorological mast to the rest of the site.

In common with VENTOS®/M, the approach used by [27] solves a transport equation for potential temperature in their CFD model, whilst including extra buoyancy terms in the turbulence equations, to take into consideration atmospheric stability. However, the stability is defined by the temperature profile used as the inlet condition, rather than using the model chain to pass down results, and only the free-stream stability is included. Their work shows that by including atmospheric stability in the CFD model a significant reduction in the error of speed-ups calculated between different mast locations can be achieved when compared to results calculated whilst always assuming neutral conditions. Improvements were also observed in the prediction of turbulence intensity ratios. In a study carried out by [28], atmospheric stability predictions from a WRF mesoscale model were used to assess the long-term effect of stability on shear profiles offshore, with the aim of finding long-term correction. Since terrain effects do not exist offshore, the resolution of the mesoscale model should be sufficient for this purpose and CFD is not required.

ANALYSIS

Coupled Mesoscale-CFD Model

Model Description

The coupled mesoscale-CFD VENTOS®/M model was selected for this study. VENTOS®/M uses the output of the WRF mesoscale model as its input. This allows realistic atmospheric conditions, including thermally driven flows and changes in atmospheric stability, to be modelled at microscale resolution. The model simulates real periods in time and takes surrounding regional atmospheric conditions into consideration.

The benefits of using VENTOS®/M are particularly apparent when modelling sites where the atmosphere is non-neutral for a significant proportion of the time. Standard CFD models assume neutral conditions, so are unable to capture the profound effect changes in the atmosphere's stability can have on wind flow patterns, turbulence intensity and shear, as outlined in Section 6.3.1. Since VENTOS®/M models real periods in time, it is possible to verify the model results by comparing to time-series of measured data at mast locations, whilst also gaining an understanding of transient flow conditions across the site. For these reasons, VENTOS®/M was selected over a standard CFD model for this study at Havsnäs.

Model Setup

VENTOS®/M forms the tail-end of a flow modelling chain. At the top of the model chain, six hourly output data was taken from the NCEP/NCAR T62 global model with 2.5° x 2.5° horizontal resolution. This data was used to drive the WRF mesoscale model, which forms the middle link in the model chain. The WRF modelling was carried out using a triple-nested domain. The inner-most domain was approximately 420km x 420km in the horizontal, with a 2000m resolution, and extending to 20km above ground level. The WRF model was run for individual days: 30 hours were simulated, with the first six hours being discounted as they were considered to be model spin-up time.

Finally, output from the WRF model was passed hourly to the VENTOS®/M model in the form of transient boundary conditions. The VENTOS®/M model was also run for individual days, using the 24 hours worth of useful WRF output data. Spin-up time for the VENTOS®/M model was considered to be negligible. The VENTOS®/M model domain covers a horizontal area of 17km x 20km, with a 100m resolution at the centre, expanding up to around 300m at the domain edges. The vertical domain extends to 7km above ground level. The VENTOS®/M model results used in this study were output as ten minute average records, making it possible to compare directly to the measured data which is stored in the same format.

Model Limitations

At both the WRF and VENTOS®/M stages of the model chain, some limitations were found which may affect the accuracy of the results. First, it was not possible to include the snow cover in the WRF model. The main effect of this is in the modelling of solar insolation, which may result in differences in the stability of the atmosphere on certain days. However, this may also affect the wind speed, since snow cover would reduce the roughness length. This is also the case in the CFD model. If the days with snow cover were known, then it would be possible to include time-varying roughness in VENTOS®/M. Additionally, VENTOS®/M does not include a canopy model at present. Therefore, it was only possible to take the trees surrounding the Havsås site into consideration through a standard roughness model.

The days selected for modelling are all since the wind farm began operating. This implies that the measured wind speed at the mast locations may be influenced by wakes from the turbines. However, the turbines and wake effects were not included in the flow models. The locations of each of the three masts used in this study mean that they will have been unwaked for the predominant wind directions from the north-west, but are waked for some less predominant directions from the South and South-East.

Day Selection

Nine days between 17th November 2011 and 30th May 2012 were selected for simulation. The days were chosen from the period when both masts M6261 and M6282 were recording data with minimal loss of data due to icing. Within this period, days were selected to cover a range of typical conditions throughout the seasons, with around average wind speed. Over the winter period, the availability of days with sufficient measured data was very limited due to prolonged spells of icing. The selected days, along with a brief summary of conditions on the day, are given in Table 7.7.11.

Date	Approximate wind speed at 90m AGL	Approximate temperature at 90m AGL
27/11/2011	8m/s decreasing to 1m/s, then increasing to 14m/s	-2°C decreasing to -4°C, then increasing to -2°C
31/12/2011	12m/s decreasing to 4m/s, then increasing to 10m/s	-6°C decreasing to -10°C
16/01/2012	9m/s decreasing to 5m/s	1°C all day
17/02/2012	Average of 8m/s all day, but oscillating	-3°C decreasing to -5°C

20/02/2012	5m/s increasing to 10m/s	-8 °C increasing to -4 °C
06/04/2012	9m/s decreasing to 4m/s, then increasing to 8m/s	-10 °C increasing to -4 °C, then decreasing to -8 °C
19/04/2012	Average of 6m/s all day, but spread between 4m/s and 8m/s across site	-3 °C increasing to 2 °C, then decreasing to -2 °C
16/05/2012	Average of 4m/s all day	5 °C increasing to 10 °C, then decreasing to 6 °C
27/05/2012	3m/s increasing to 14m/s	8 °C increasing to 18 °C, then decreasing to 4 °C

Table 7.7.11: Days selected for simulation with descriptions of the wind speed and temperature.

Limitations of the Study

This CFD study at Havsnäs has been carried out to gain qualitative insight into the effect cold climates may have on flow model results. Where possible, time-series results extracted from the CFD are verified by comparison with measured data. However, since only nine selected days have been modelled, it is not possible to draw quantitative or statistical conclusions from the results. In order to do this, a statistically significant number of days would need to be simulated and the results analysed to obtain a wind map and calculate average speed-ups, with thorough validation against measured data.

Post-processing Procedure

The CFD results were used to produce two-dimensional movies of the changing flow conditions throughout the day. Horizontal slices through the domain at 90m were extracted to show the vertical flow as well as horizontal wind speed and direction. Vertical planes were also extracted through each of the mast locations, showing flow patterns, turbulence intensity and potential temperature. A few selected images from the movies are presented in this report to illustrate the flow conditions predicted by the model and highlight non-neutral flow characteristics.

Time-series of various parameters have also been extracted from the CFD at the two mast locations, M6261 and M6282, at close to the installation heights of the relevant instruments. The CFD time-series are compared to measured mast data in order to assess the accuracy of the results. The parameters extracted for comparison are wind speed, wind direction, potential temperature gradient, turbulence intensity and shear. Since the output from the CFD is saved as ten minute averages, the results can be directly compared with the measured data where and when measured data exists. Although the CFD outputs potential temperature, the mast measures actual temperature. For simplicity, the measured temperature was converted to potential temperature using the measured pressure, rather than converting the CFD potential temperature to actual temperature. In reality, the difference between actual and potential temperature is very small and could probably be ignored.

The time of day specified in all the Figures presented in the following section is local time, which is UTC+1 over winter and UTC+2 from 25th March 2012.

RESULTS

CFD Model Results across the Site

The results presented in this section demonstrate how a better understanding of flow conditions across the site can be gained through looking at the CFD model results as a whole. In the following Figures horizontal and vertical wind speed, along with wind direction, are presented on horizontal isosurfaces at 90m AGL, whilst flow patterns, turbulence intensity and potential temperature are presented on vertical planes through the mast locations. These

have been used to construct movies showing how the flow conditions vary throughout the day. For obvious reasons, it was only possible to include still images in this report.

Figure 7.7.12 shows vertical and horizontal wind flow patterns across the site. The vertical motion is indicated by the coloured contours, where red areas show rising flow and blue areas show downward flow. The horizontal wind speed and direction is indicated by the vector arrows. Figure 7.7.12 shows flow patterns on 16th January 2012, not long after sunrise when the wind speed was relatively high and the air temperature was cool, at around 4 °C in the CFD (1 °C in the measured data). The only vertical motions shown in this Figure are mechanically driven and due to the air moving over the hills. Looking along the direction of the horizontal wind, the flow is pushed up over hills and rolls down on the leeward side. On this day, there is no evidence of any thermals rising and the temperature remains at about 4 °C all day at the measured heights in the CFD, suggesting a stable atmosphere. Figure 7.7.13 shows a vertical cross-section of turbulence intensity and wind vectors through M6282, as indicated by the thick grey line in Figure 7.7.12, and taken at the same time. The slice is taken at 310°, which is approximately parallel to the wind direction at this time. The wind vectors confirm that the flow follows the slopes of the hills, with the high band of turbulence intensity remaining close to the ground. Figure 7.7.14 shows the same cross-section as Figure 7.7.13, but with the potential temperature shown in the coloured contours. This shows a strong temperature inversion, with higher temperatures higher up in the atmosphere and the contour lines following the changes in elevation. Again, this suggests the atmosphere is stable at this time.

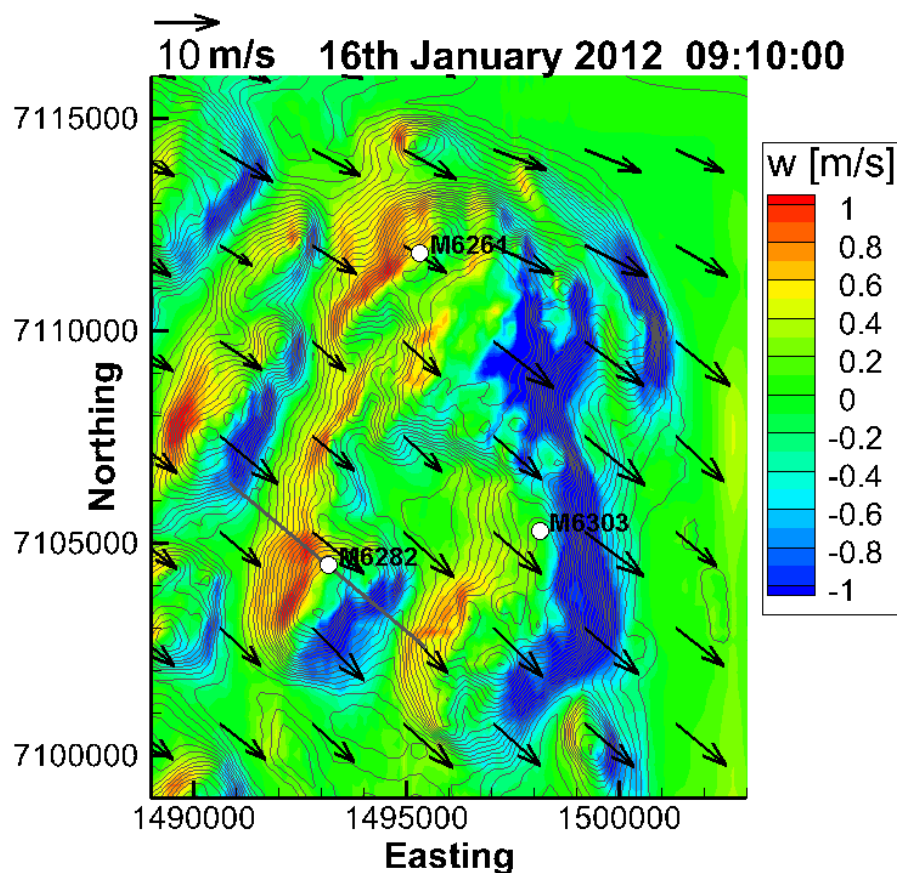


Figure 7.7.12: Contour and vector plot showing both vertical and horizontal flow 90m AGL at a selected time on 16th January 2012. Vertical wind velocity is shown as coloured contours and horizontal wind speed and direction are shown as vector arrows. The thick grey line through M6282 indicates the location of the vertical plane used for the following two Figures.

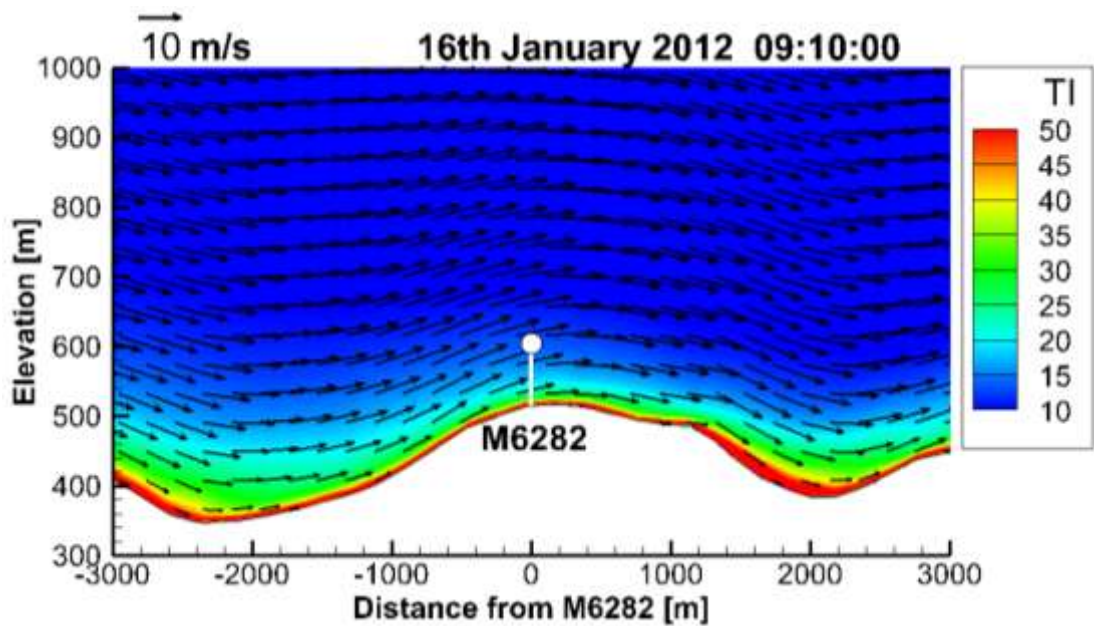


Figure 7.7.13: Contour and vector plot showing turbulence intensity and wind flow patterns, taken through M6282 at 310° (parallel to the wind direction) at a selected time on 16th January 2012. Turbulence intensity is shown as coloured contours and wind speed and direction are shown as vector arrows. The vertical scale, including the velocity vectors, has been multiplied by a factor of 5.

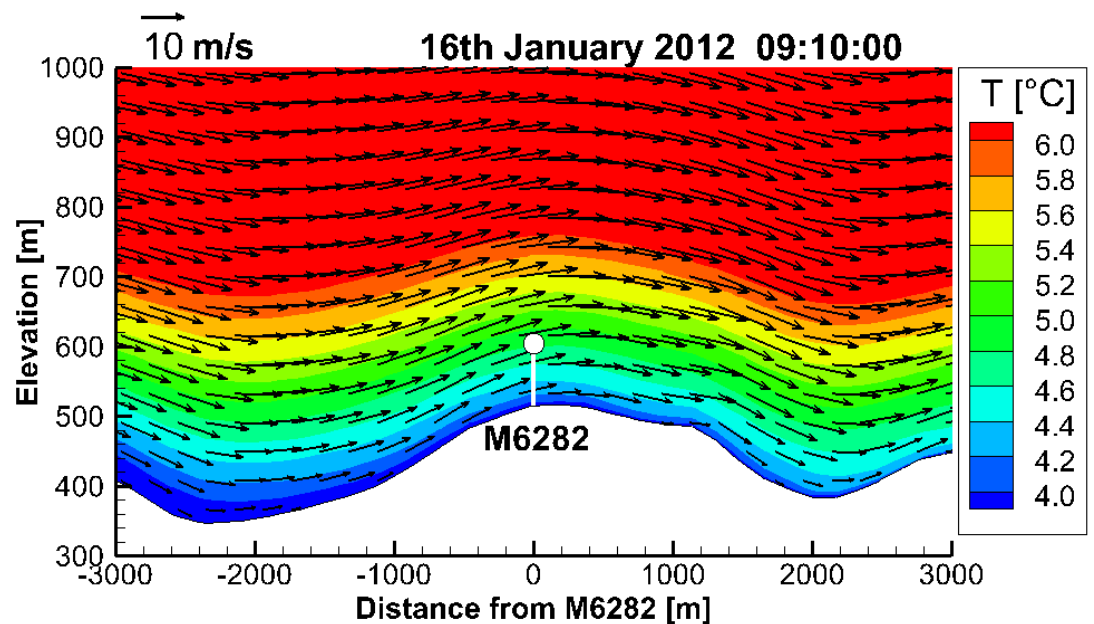


Figure 7.7.14: Contour and vector plot showing potential temperature and wind flow patterns, taken through M6282 at 310° (parallel to the wind direction) at a selected time on 16th January 2012. Potential temperature is shown as coloured contours and wind speed and direction are shown as vector arrows. The vertical scale, including the velocity vectors, has been multiplied by a factor of 5.

Figure 7.7.15 shows flow patterns on 6th April 2012 during the middle of the day. In the north-west of the site, the wind direction varied considerably between each of the points plotted. Flow characteristics of this nature would not be fully captured by traditional CFD models. Although this was a cold day, the relatively high solar insolation during daylight hours appears to have generated thermals rising from the ground. These appear as red and blue stripes of upward and downward motion parallel to the wind direction, bearing little relationship to the

underlying topography. Figure 7.7.16 shows a vertical cross-section of turbulence intensity and wind vectors taken through M6282, as indicated by the thick grey line in Figure 7.7.15, and at the same time. The slice is taken at 230° , which is approximately perpendicular to the flow direction at this time. Here, the upward and downward motion of the flow is clear. Where the thermals rise, mixing is induced, and so buoyancy-driven turbulence intensity increases. Figure 7.7.17 shows the same cross-section as Figure 7.7.16, but with the potential temperature shown in the coloured contours. This shows some weak thermals rising with the increased turbulence intensity, confirming that the vertical motions observed in Figure 7.7.15 are buoyancy driven.

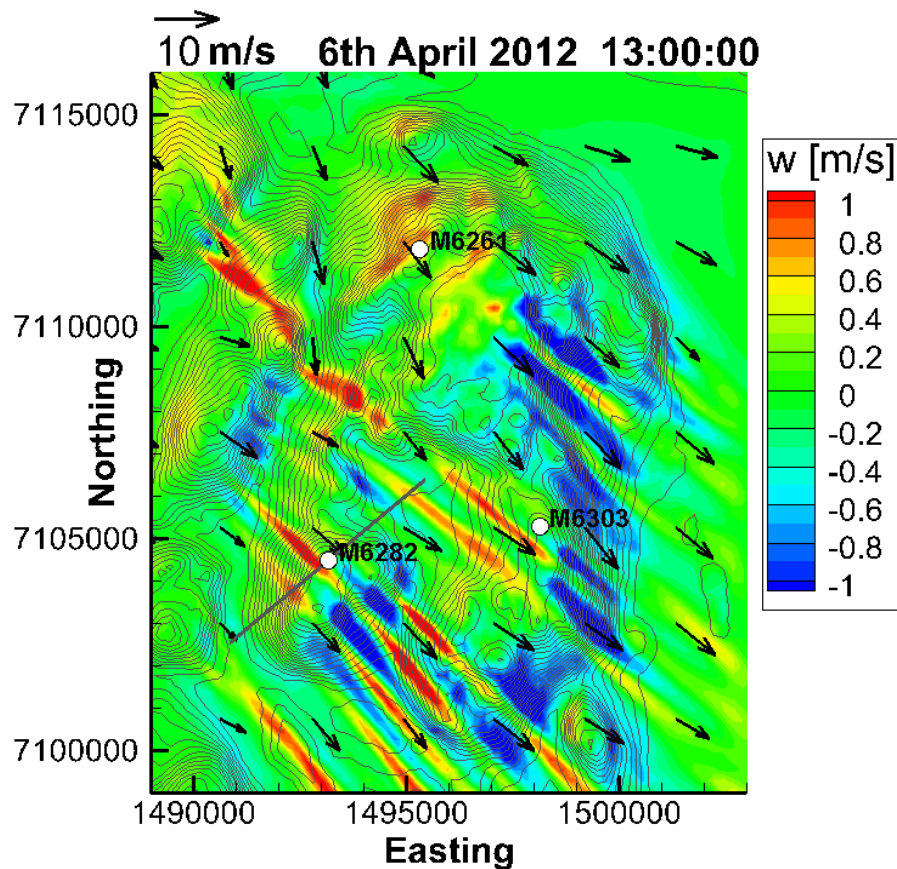


Figure 7.7.15: Contour and vector plot showing both vertical and horizontal flow 90m AGL at a selected time on 6th April 2012. Vertical wind velocity is shown as coloured contours and horizontal wind speed and direction are shown as vector arrows. The thick grey line through M6282 indicates the location of the vertical plane used for the following two Figures.

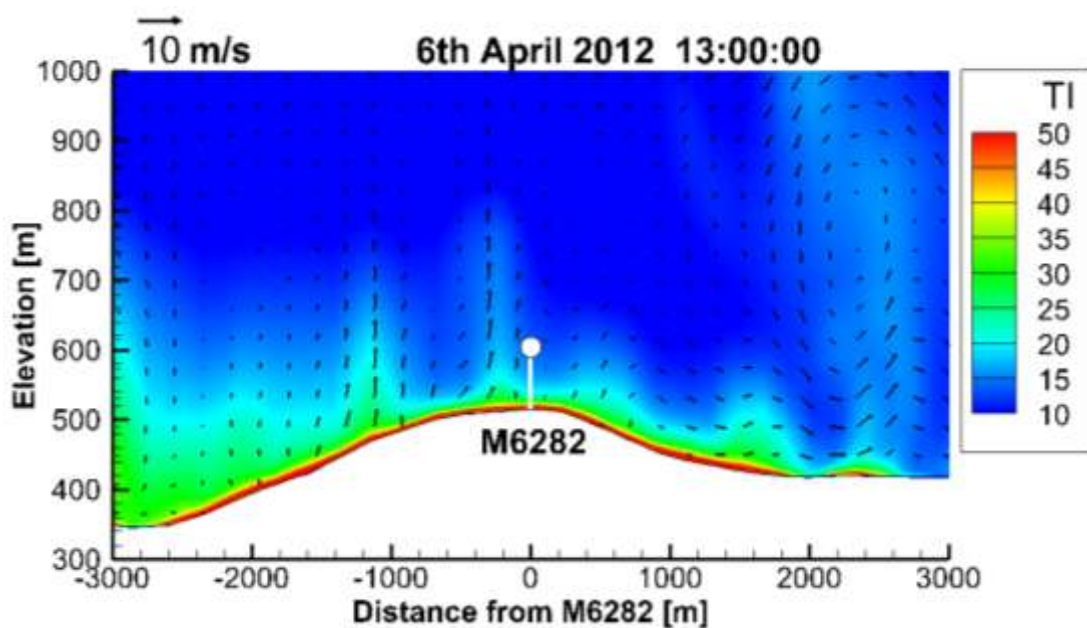


Figure 7.7.16: Contour and vector plot showing turbulence intensity and wind flow patterns, taken through M6282 at 230° (perpendicular to the wind direction) at a selected time on 6th April 2012. Turbulence intensity is shown as coloured contours and wind speed and direction are shown as vector arrows. The vertical scale, including the velocity vectors, has been multiplied by a factor of 5.

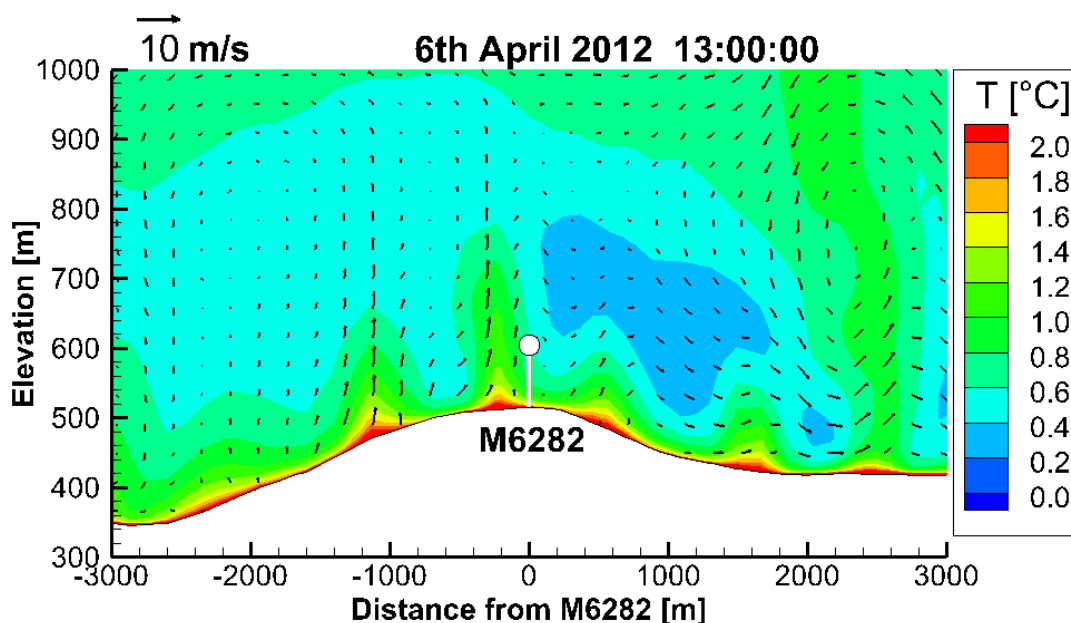


Figure 7.7.17: Contour and vector plot showing potential temperature and wind flow patterns, taken through M6282 at 230° (perpendicular to the wind direction) at a selected time on 6th April 2012. Potential temperature is shown as coloured contours and wind speed and direction are shown as vector arrows. The vertical scale, including the velocity vectors, has been multiplied by a factor of 5.

Figure 7.7.18 shows flow patterns on 16th May 2012 during the afternoon. In this image, thermals appear to be rising across most of the site. Figure 7.7.19 shows a vertical cross-section of turbulence intensity and wind vectors taken through M6261, as indicated by the thick grey line in Figure 7.7.18, and at the same time. The slice is taken at 250°, which is approximately perpendicular to the flow direction at this time. Since this day was considerably warmer than 6th April 2012, the rising and falling motion of the thermals is much

stronger and the bands of increased turbulence intensity are drawn further upwards. Figure 7.7.20 shows the same cross-section as Figure 7.7.19, but with the potential temperature shown in the coloured contours. This shows some stronger thermals rising than those on 6th April 2012, with cooler air descending in between. This confirms that the vertical motions observed in Figure 7.7.18 are buoyancy driven.

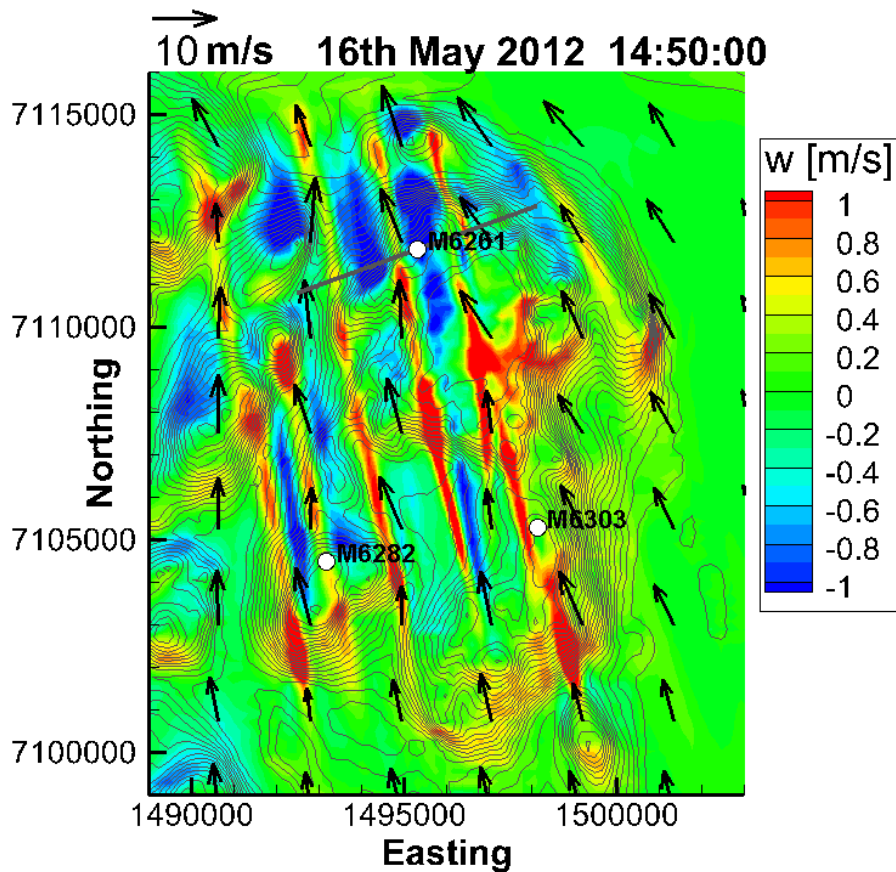


Figure 7.7.18: Contour and vector plot showing both vertical and horizontal flow 90m AGL at a selected time on 16th May 2012. Vertical wind velocity is shown as coloured contours and horizontal wind speed and direction are shown as vector arrows. The thick grey line through M6261 indicates the location of the vertical plane used for the following two Figures.

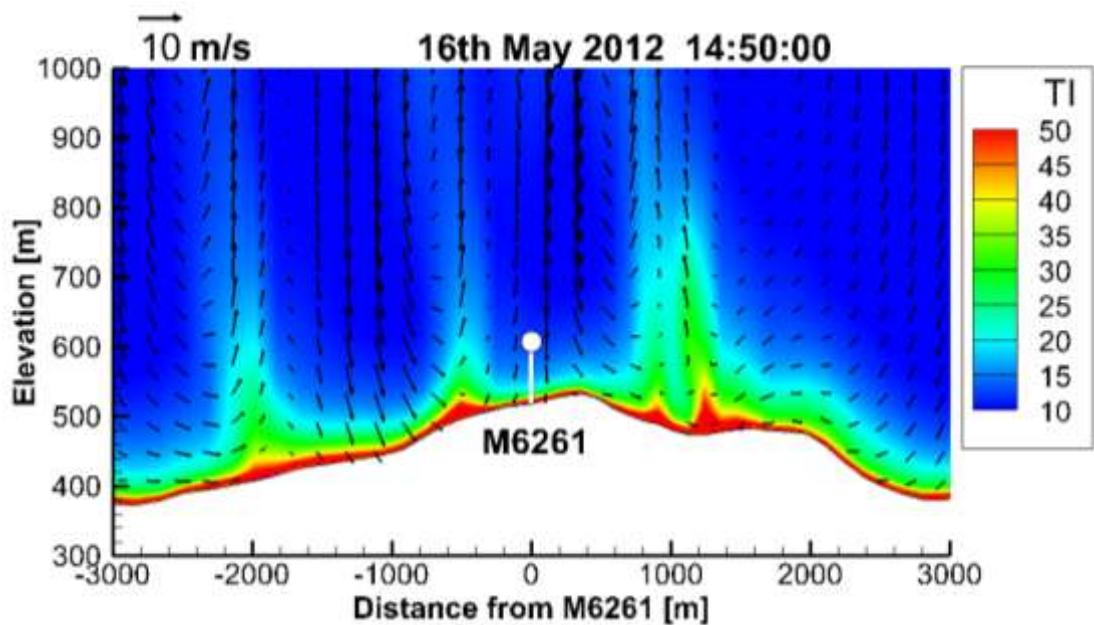


Figure 7.7.19: Contour and vector plot showing turbulence intensity and wind flow patterns, taken through M6261 at 250° (perpendicular to the wind direction) at a selected time on 16th May 2012. Turbulence intensity is shown as coloured contours and wind speed and direction are shown as vector arrows. The vertical scale, including the velocity vectors, has been multiplied by a factor of 5.

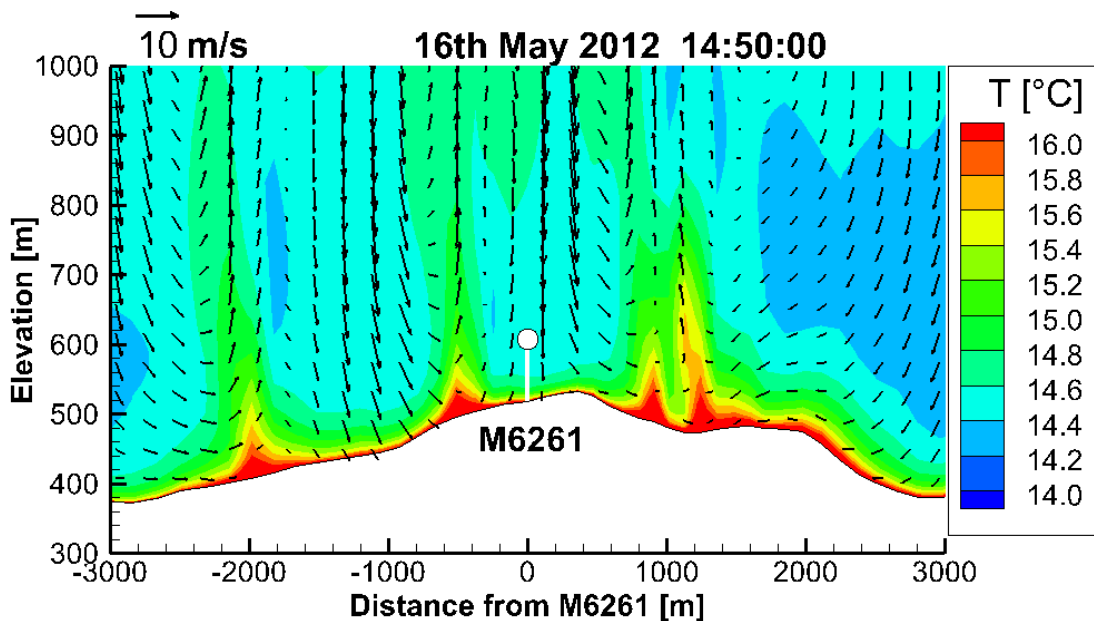


Figure 7.7.20: Contour and vector plot showing potential temperature and wind flow patterns, taken through M6261 at 250° (perpendicular to the wind direction) at a selected time on 16th May 2012. Potential temperature is shown as coloured contours and wind speed and direction are shown as vector arrows. The vertical scale, including the velocity vectors, has been multiplied by a factor of 5.

Further CFD Model Results across the Site

This section of the results shows some other interesting flow characteristics associated with varying atmospheric stability and cold climates.

Figure 7.7.21 shows a vertical cross-section taken through M6282 on 20th February 2012 during the night. Since this is night time following a very cold winter's day, it is highly likely that the atmosphere was stable at this time. Large eddies are visible in the cross-section, which appear to be drawn out in the horizontal direction. This is what is expected in a stable atmosphere. Figure 7.7.22 shows the same cross-section as Figure 7.7.21, but with the potential temperature shown in the coloured contours. A temperature inversion is observed, with higher temperatures higher up in the atmosphere. This is also consistent with a highly stable atmosphere.

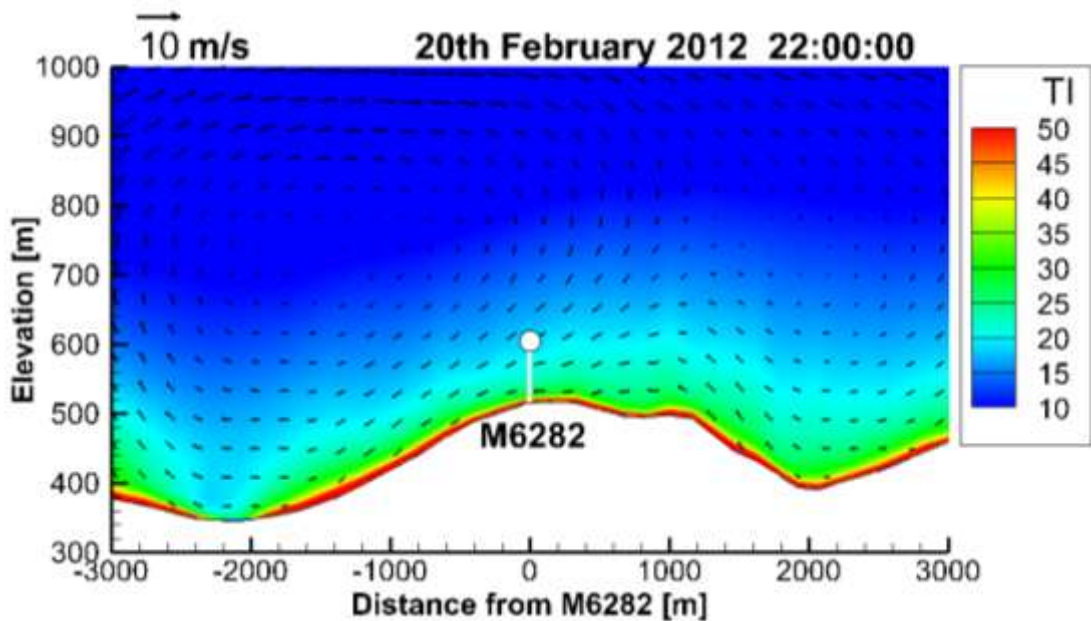


Figure 7.7.21: Contour and vector plot showing turbulence intensity and wind flow patterns, taken through M6282 at 300° at a selected time on 20th February 2012. Turbulence intensity is shown as coloured contours and wind speed and direction are shown as vector arrows.

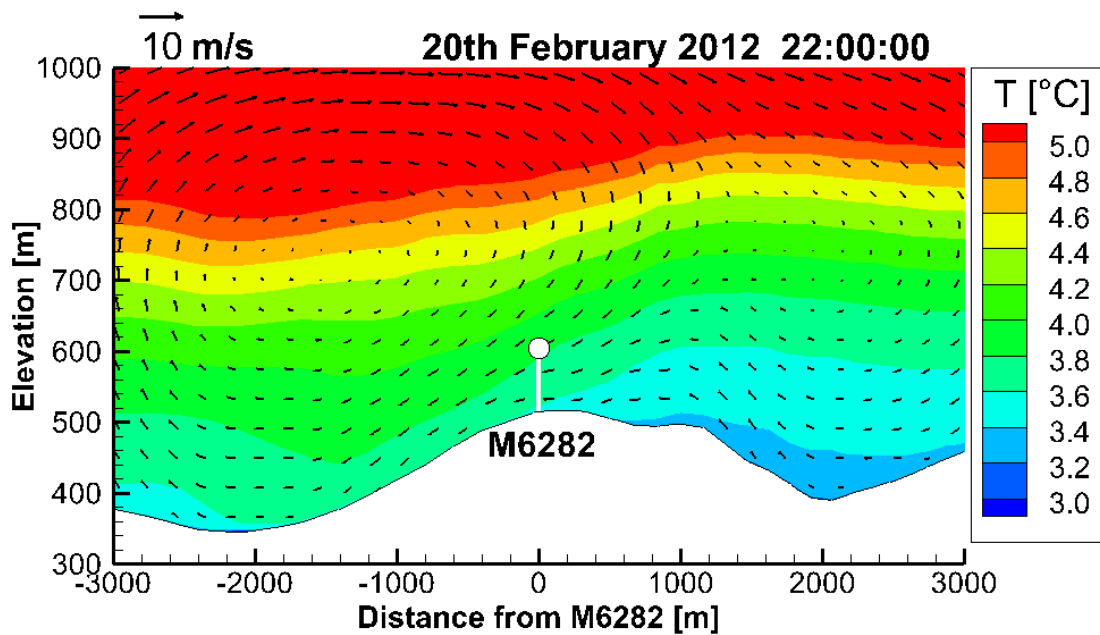


Figure 7.7.22: Contour and vector plot showing potential temperature and wind flow patterns, taken through M6282 at 300° at a selected time on 20th February 2012. Potential temperature is shown as coloured contours and wind speed and direction are shown as vector arrows.

Figure 7.7.23 shows a vertical cross-section taken through M6282 on 27th May 2012 in the middle of the day. Large eddies are visible in this cross-section. However, in contrast to those shown in Figure 7.7.21, the eddies visible in Figure 7.7.23 are drawn out vertically, which is typical of an unstable atmosphere. Figure 7.7.24 shows the same cross-section as Figure 7.7.23, but with the potential temperature shown in the coloured contours. This appears to show a warm front that has moved in over the top of cooler air immediately underneath. Strong mixing is induced as warm air is drawn up from the ground, resulting in the tall eddies observed in Figure 7.7.23.

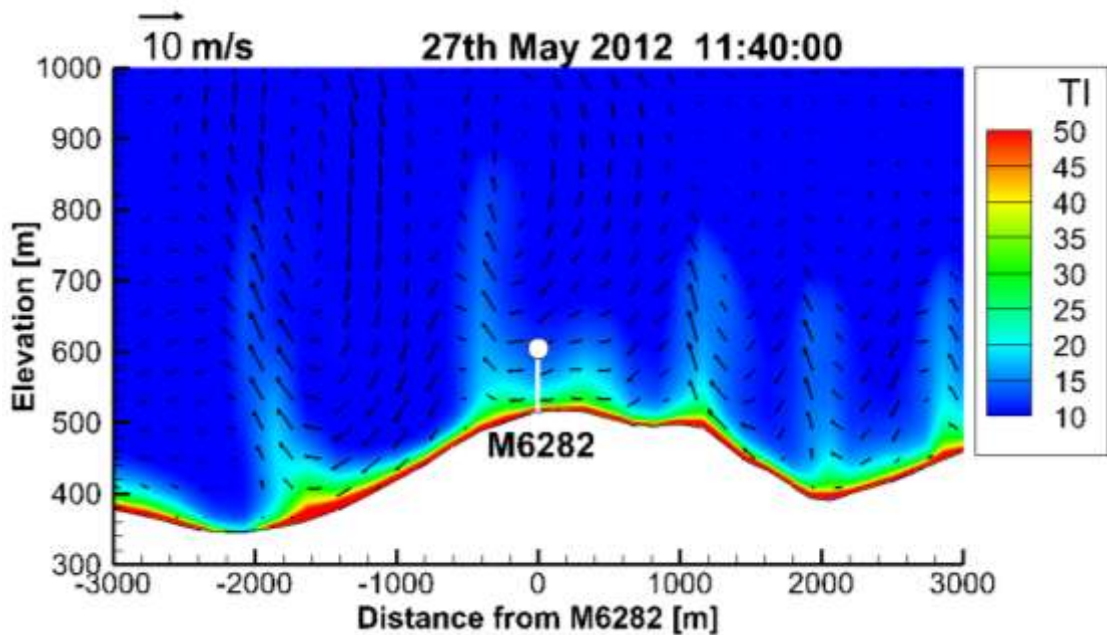


Figure 7.7.23: Contour and vector plot showing turbulence intensity and wind flow patterns, taken through M6282 at 300° at a selected time on 27th May 2012. Turbulence intensity is shown as coloured contours and wind speed and direction are shown as vector arrows.

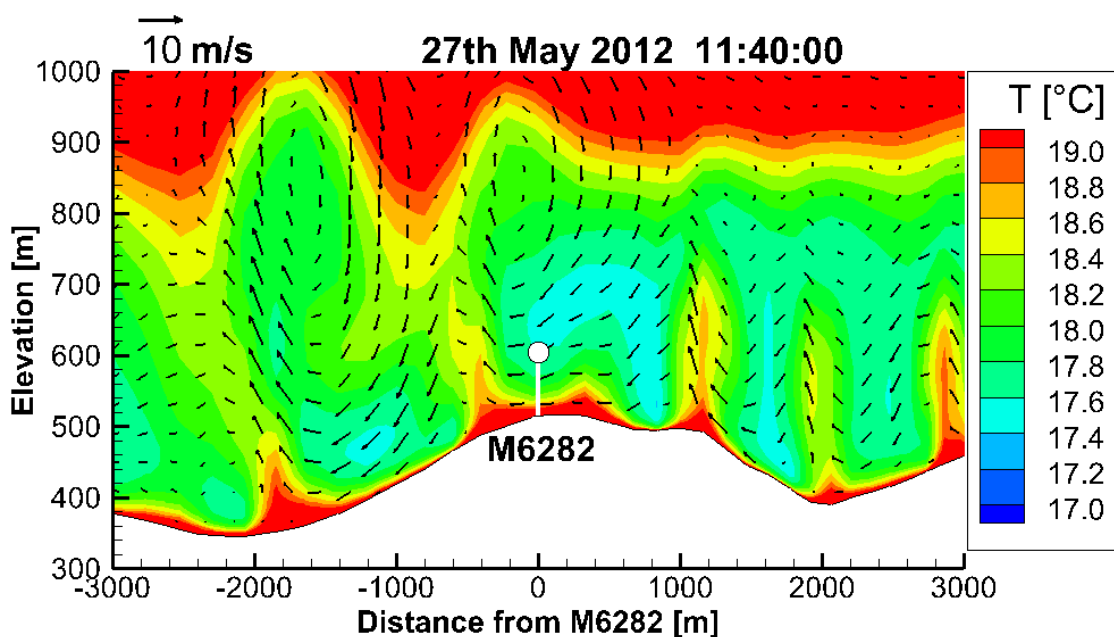


Figure 7.7.24: Contour and vector plot showing potential temperature and wind flow patterns, taken through M6282 at 300° at a selected time on 27th May 2012. Potential temperature is shown as coloured contours and wind speed and direction are shown as vector arrows.

Figure 7.7.25 shows a vertical cross-section taken approximately parallel to the wind direction through M6282 on 16th January 2012. The image appears to show standing gravity waves. The regions of high turbulence intensity in the valleys are trapped below the waves, where the wind speed is very low. Figure 7.7.26 shows the same cross-section as Figure 7.7.25, but with the potential temperature shown in the coloured contours. There is a strong temperature inversion, with the isotherms following the wave pattern. Gravity waves are common in stable boundary layers when the underlying surface is colder than the air. This often occurs when warm-air is advected over a colder surface [29]. The air temperature was above freezing on this day, but snow is likely to still have been on the ground since the air temperature on the preceding days was well below 0°C. Therefore, it seems plausible that this modelled observation may have occurred.

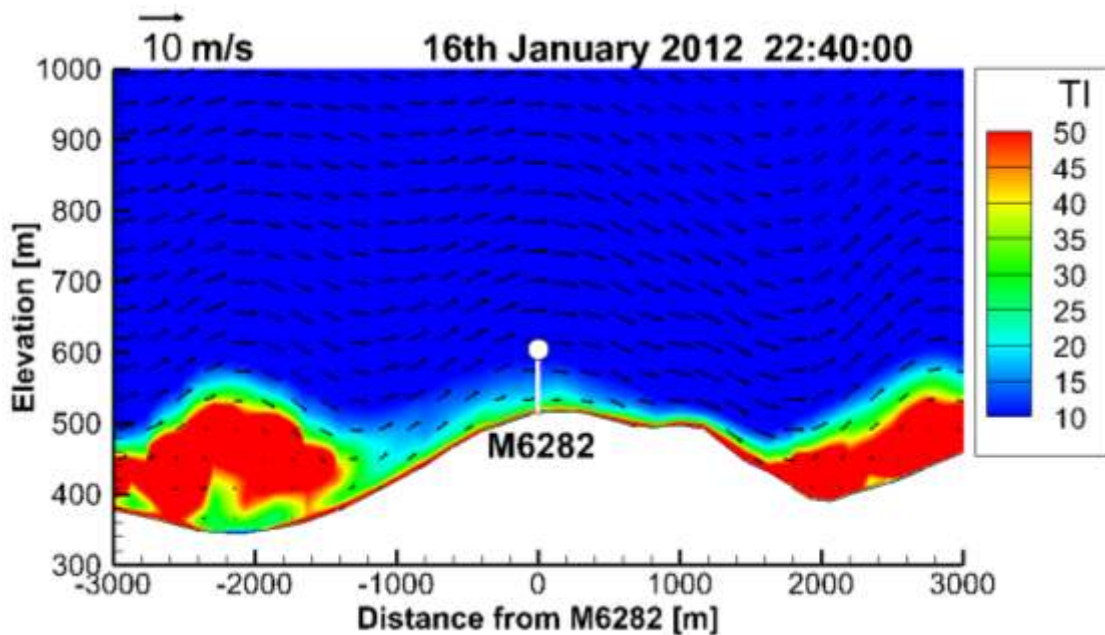


Figure 7.7.25: Contour and vector plot showing turbulence intensity and wind flow patterns, taken through M6282 at 300° (parallel to the wind direction) at a selected time on 16th January 2012. Turbulence intensity is shown as coloured contours and wind speed and direction are shown as vector arrows.

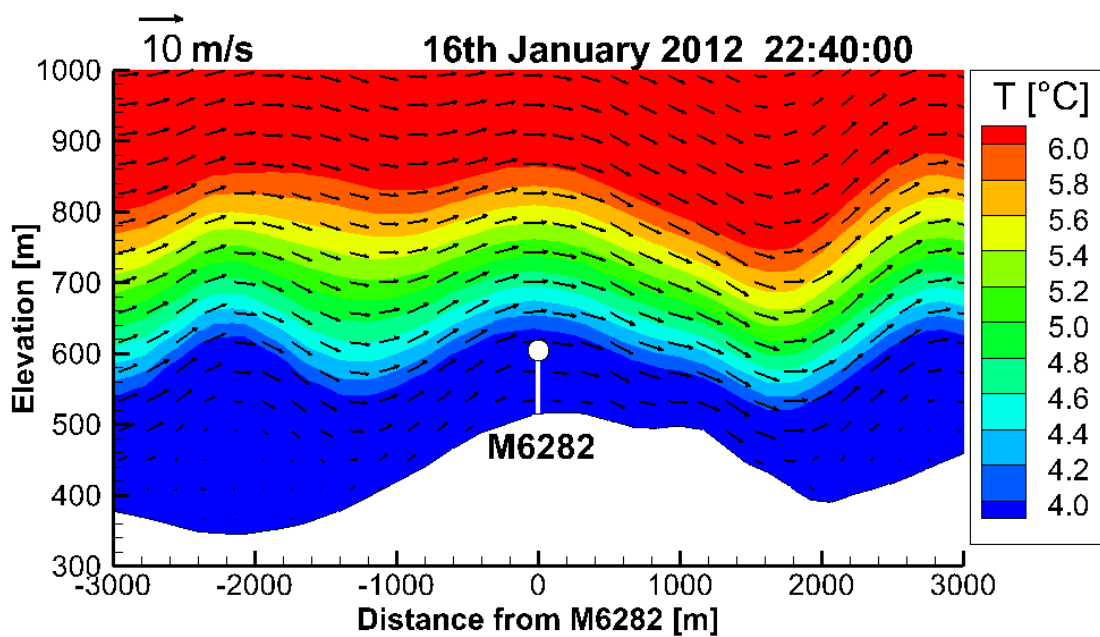


Figure 7.7.26: Contour and vector plot showing potential temperature and wind flow patterns, taken through M6282 at 300° (parallel to the wind direction) at a selected time on 16th January 2012. Potential temperature is shown as coloured contours and wind speed and direction are shown as vector arrows.

Model Verification of Wind Speed and Direction

In this section, time-series of the CFD model results are compared to time-series of measured data at the mast locations in order to assess the accuracy of the CFD results. Highlights of the results from the nine days are given in this section, with the full set of time-series comparisons for each day given in Appendices 7L-7T. The full set of comparisons compare wind speed, wind direction, potential temperature gradient, turbulence intensity and shear at all three mast locations.

An example of a typical wind speed comparison is given in Figure 7.7.27. This is taken at M6282, 87m above ground level on 19th April 2012. The general trend of the variation of wind speed is captured by the WRF model, with the small scale features being added at the CFD modelling stage. In this example, the trend follows the measured data reasonably well. The small scale fluctuations are a result of using higher resolution topographical data as well as recording results at a higher time frequency. Although not all the fluctuations happen at exactly the same time as they do in the measured data, they often follow a similar pattern. Due to the turbulent nature of the flow and wide range of parameters affecting the model, it is unlikely that the CFD model would ever predict the fluctuations at exactly the same time and of the same size as the measurements. Nevertheless, it is encouraging to observe similar patterns in the CFD results as in the measured data.

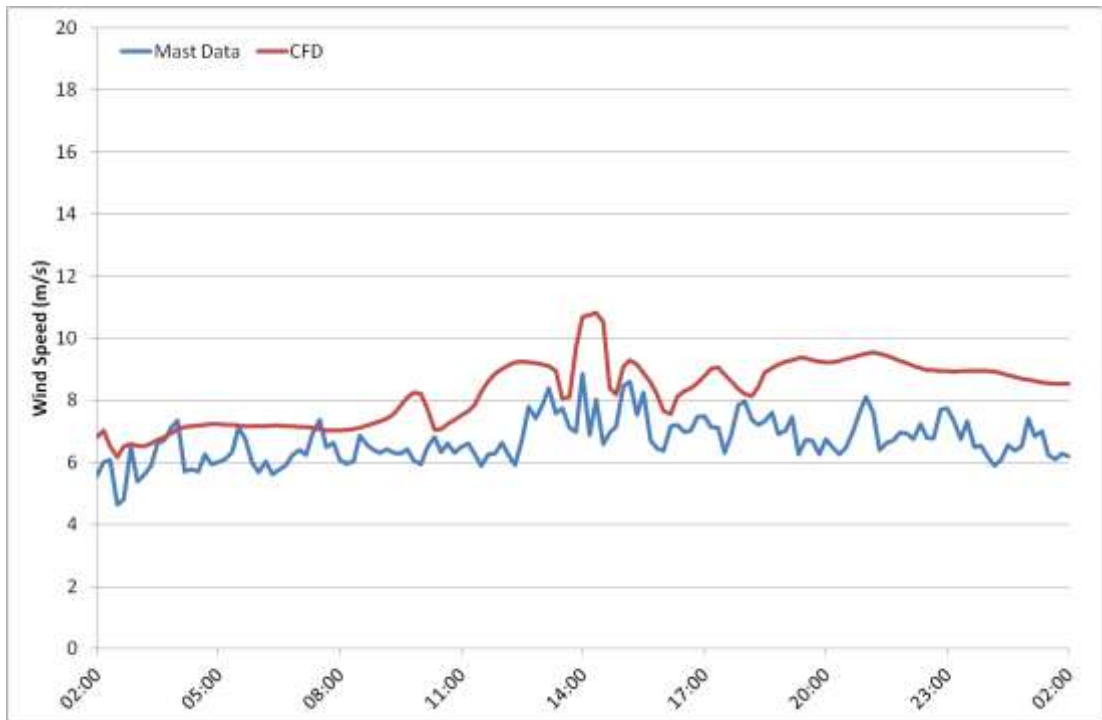


Figure 7.7.27: Wind speed time-series for 19th April 2012 at M6282, 87m AGL. Comparison between measured data and CFD.

A similar comparison between the CFD results and measured data was made for wind direction. An example time-series is shown in Figure 7.7.28, taken at M6282, 85m above ground level on 19th April 2012. In general, the wind direction is captured reasonably well by the CFD model.

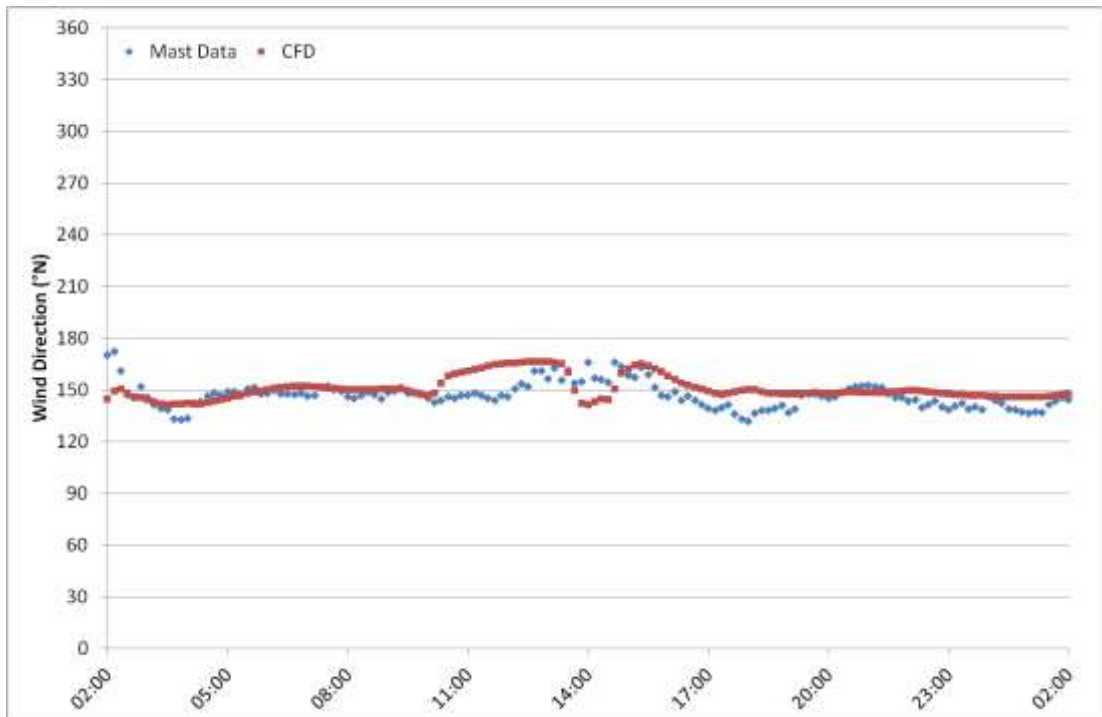


Figure 7.7.28: Wind direction time-series for 19th April 2012 at M6282, at 85m AGL. Comparison between measured data and CFD.

Model Verification of Potential Temperature Gradient, Turbulence Intensity and Shear

The results presented in this section demonstrate the CFD model's ability to reproduce flow characteristics associated with varying atmospheric stability and, in particular, cold climates.

Although the potential temperature was, in general, over-predicted by the CFD model, the potential temperature gradient is both more relevant to the flow conditions of interest and better predicted. The potential temperature gradient between two heights can be used as an approximate indicator of atmospheric stability, as is outlined in Section 6.3.1.

Before comparing the modelled results to the measured data, time-series of temperature gradient taken from the measured data are presented to demonstrate both the relationship between temperature gradient and solar irradiance, and how temperature gradient can be used as an indicator of stability. Figure 7.7.29 shows the variation of measured temperature gradient and solar irradiance throughout an example winter day and an example summer day at Havsnäs. The winter day measurements are taken from mast M6261 on 27th November 2011 and the summer day measurements are taken from mast M6282 on 16th May 2012. The time-series show that on the winter day, when there is very little solar irradiance even during daylight hours, the temperature gradient remains higher than the adiabatic lapse rate throughout the day, suggesting that the atmosphere remains stable. On the summer day, the temperature gradient dips below the adiabatic lapse rate during the warmest parts of the day, when the solar irradiance is at its highest. This suggests that during daylight hours the atmosphere becomes neutral or slightly unstable. At night time on 16th May 2012 and at some times during the day on 27th November 2012 the temperature gradient is positive, implying that the temperature profile is inverted. This is consistent with highly stable atmospheres [23].

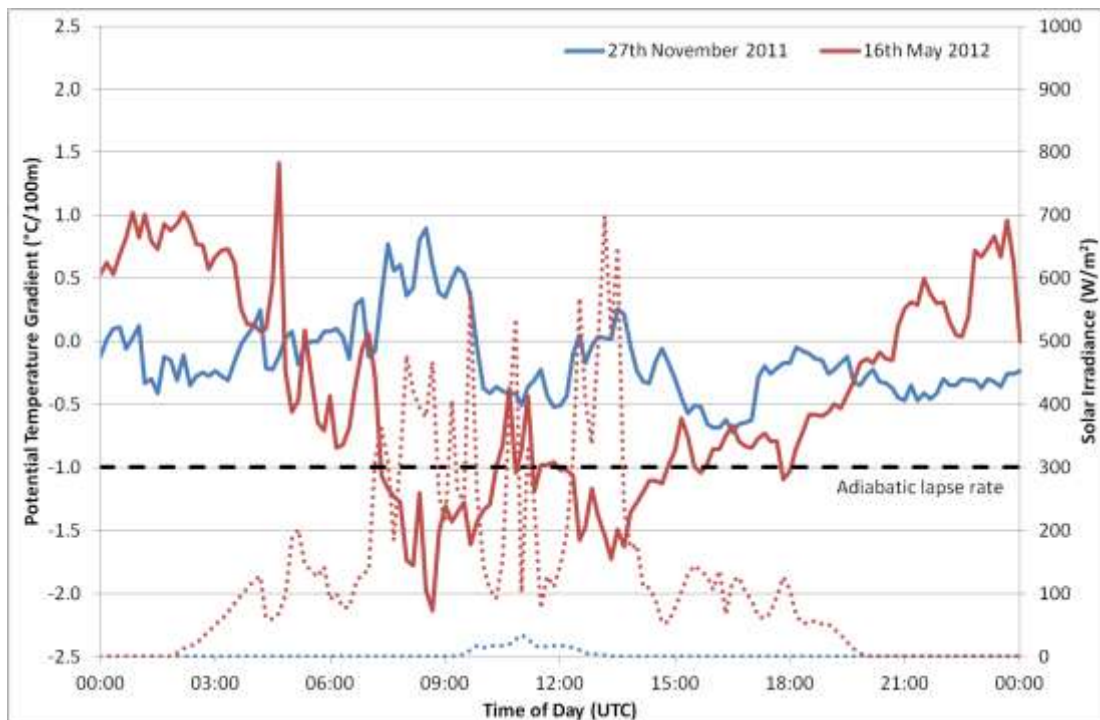


Figure 7.7.29: Measured temperature gradient (solid lines) and solar irradiance (dotted lines) on example winter and summer days at Havsnäs.

Both flux based methods and gradient based methods are considered better for quantifying atmospheric stability than considering temperature gradient on its own. These are outlined in Section 6.3.1 since the Gradient Richardson Number was used to assess atmospheric stability measurements (Section 6.3.3). Although this could also be calculated from the modelled VENTOS®/M results, this has not been done under the current scope of work.

Figure 7.7.30 shows an example time-series comparison of temperature gradient taken at M6261 on 27th November 2011. The CFD time-series stays reasonably close to the measured time-series all day, with the temperature gradient remaining comfortably above $-1^{\circ}\text{C}/100\text{m}$. This suggests that the atmosphere remained stable all day, as is typical of a cold winter's day with little variation in temperature. A second example is given in Figure 7.7.31, taken at M6261 on 6th April 2012. Again, the CFD stays reasonably close to the measured time-series, although slightly under-predicts the considerable drop in temperature gradient during the day. Despite 6th April being a very cold day, a large increase in temperature was observed during daylight hours, from around -10°C to around -2°C (or from -3°C to 3°C in the CFD results due to the over-prediction of temperature). Although the measured temperature remains below freezing, the large temperature increase is enough to push the temperature gradient below $-1^{\circ}\text{C}/100\text{m}$, suggesting the atmosphere becomes unstable during daylight hours. Even though the CFD slightly under-predicts the shift in temperature gradient, it still goes below $-1^{\circ}\text{C}/100\text{m}$, therefore representing similar atmospheric conditions.



Figure 7.7.30: Temperature gradient time-series for 27th November 2011 at M6261, taken between 90m and 10m AGL. Comparison between measured data and CFD.



Figure 7.7.31: Temperature gradient time-series for 6th April 2012 at M6261, taken between 90m and 10m AGL. Comparison between measured data and CFD.

A third example of the variation in temperature gradient is given in Figure 7.7.32. This is taken at M6282 on 16th May 2012. The air temperature on this day reached around 12°C, so is considerably warmer than the days used in the examples above. Again, the CFD remains close to the measured temperature gradient all day. The temperature gradient goes from being positive at night, to around -1°C/100m during daylight hours. This suggests that the stable night atmosphere becomes neutral during the day.

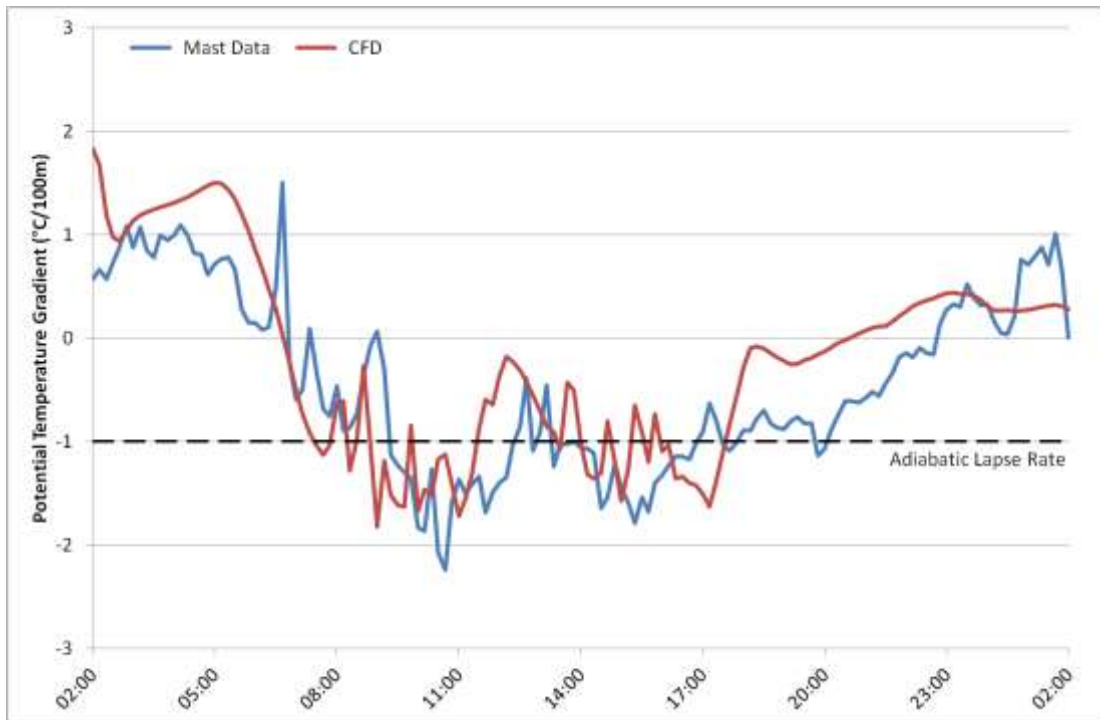


Figure 7.7.32: Temperature gradient time-series for 16th May 2012 at M6282, taken between 90m and 10m AGL. Comparison between measured data and CFD.

Differences in turbulence intensity and shear would also be expected in cold climates, where the atmosphere remains stable for more of the time. Often turbulence intensity is found to be the best indicator of stability. However, for most of the days simulated for this study, no clear patterns in turbulence intensity or shear relating to the temperature gradient on particular days were observed. Two example days were selected, which appeared to be representative of stable and unstable conditions respectively, but it should be noted that the patterns seen on these days were not clearly repeated at all masts on all days as might have been expected.

Figures 7.7.33 and 7.7.34 show time-series comparisons of the turbulence intensity and shear, respectively, at M6282 on 16th January 2012. In both Figures the CFD follows the measured time-series reasonably well throughout the day. The turbulence intensity remains relatively low all day, whilst the shear exponent stays high. These conditions are typical of a stable atmosphere.

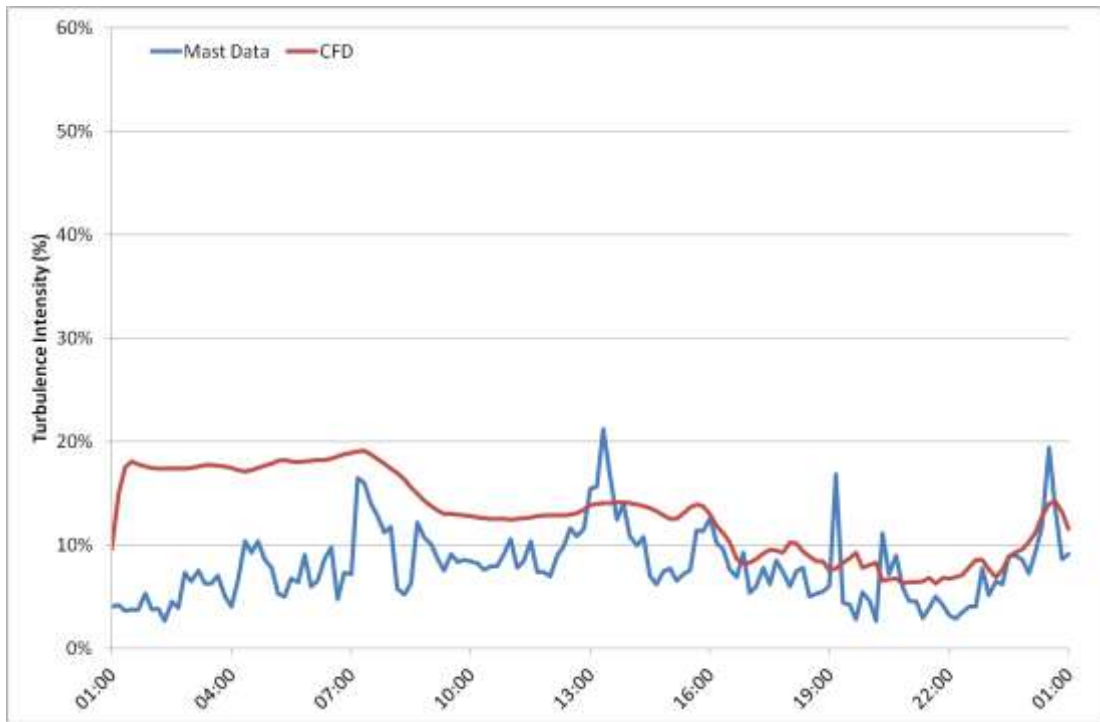


Figure 7.7.33: Turbulence intensity time-series for 16th January 2012 at M6282, 87m AGL. Comparison between measured data and CFD.

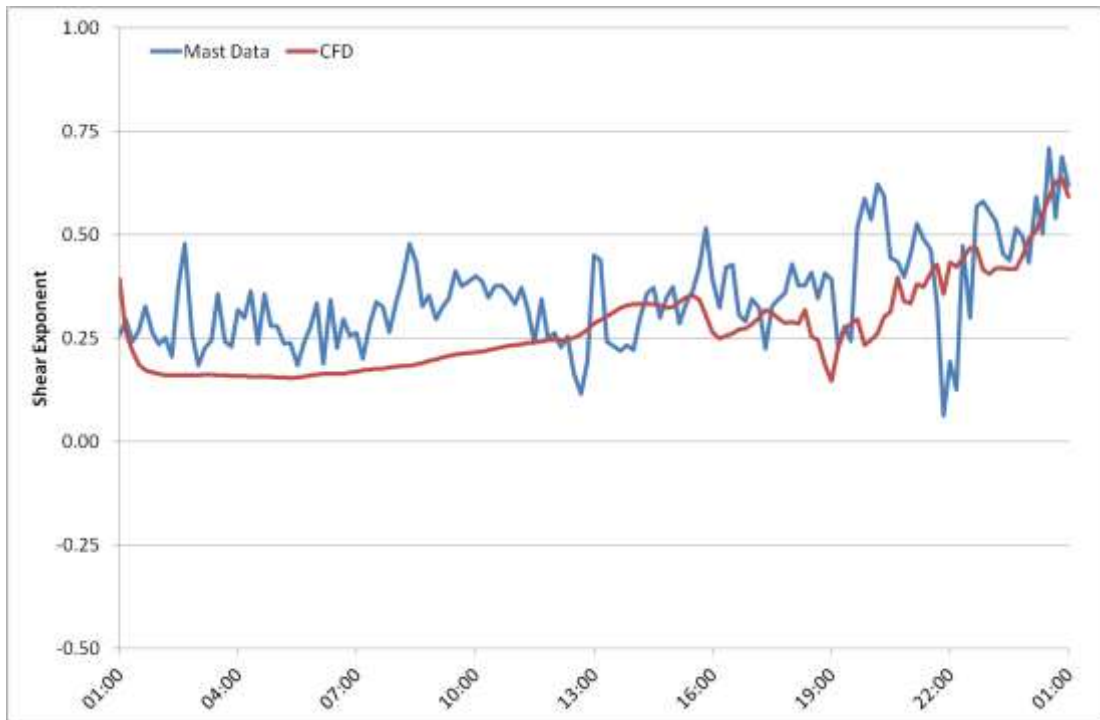


Figure 7.7.34: Shear exponent time-series for 16th January 2012 at M6282, taken between 73m and 50m AGL. Comparison between measured data and CFD.

Figures 7.7.35 and 7.7.36 show time-series comparisons of the turbulence intensity and shear, respectively, at M6282 on 16th May 2012. Again, the CFD models both the turbulence intensity and shear reasonably well throughout the day. Here, the turbulence intensity rises during daylight hours, which would be typical of a neutral or unstable atmosphere. Compared to the turbulence intensity plotted for 16th January in Figure 7.7.33, the turbulence intensity on 16th

May oscillates considerably more during daylight hours in both the measured results and the CFD. This reflects the observed spatial turbulence intensity patterns shown in the vertical cross-section in Figure 7.7.19, where peaks and troughs in the turbulence intensity can be seen along the cross-sectional plane. The shear remains reasonably constant all day and is of the same order as that measured on 16th January 2012. During daylight hours, the shear is slightly lower than the following night, which would be typical if conditions were neutral to unstable during the day, but this is inconclusive since the shear does not reduce from levels during the previous night.

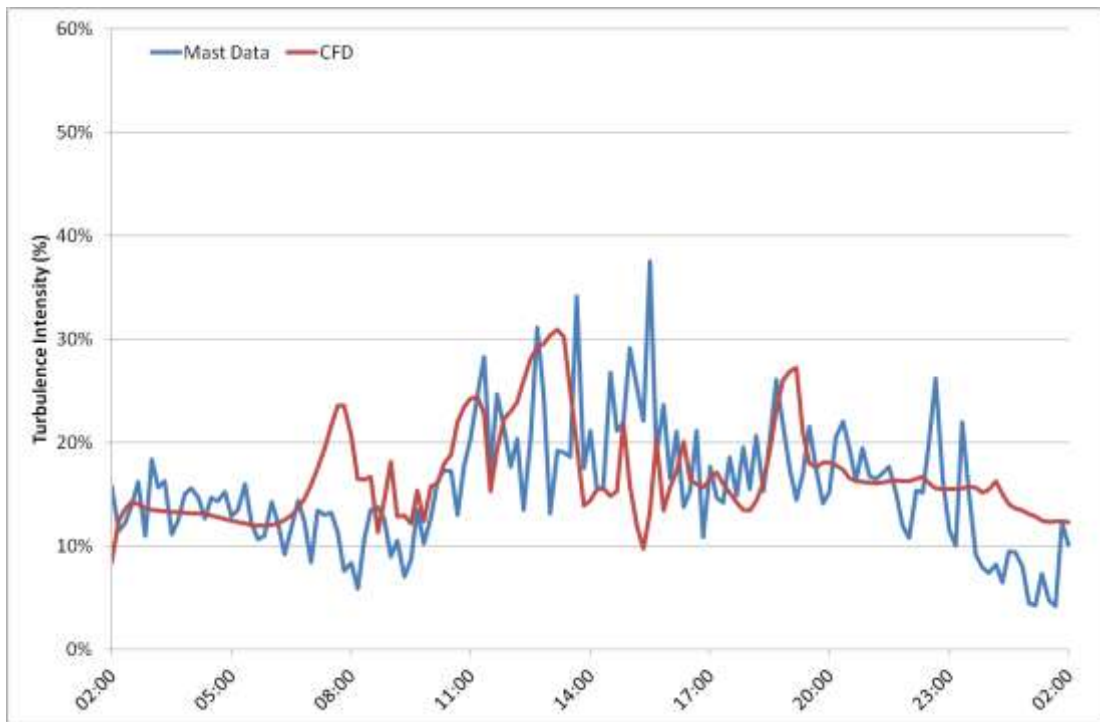


Figure 7.7.35: Turbulence intensity time-series for 16th May 2012 at M6282, 87m AGL. Comparison between measured data and CFD.

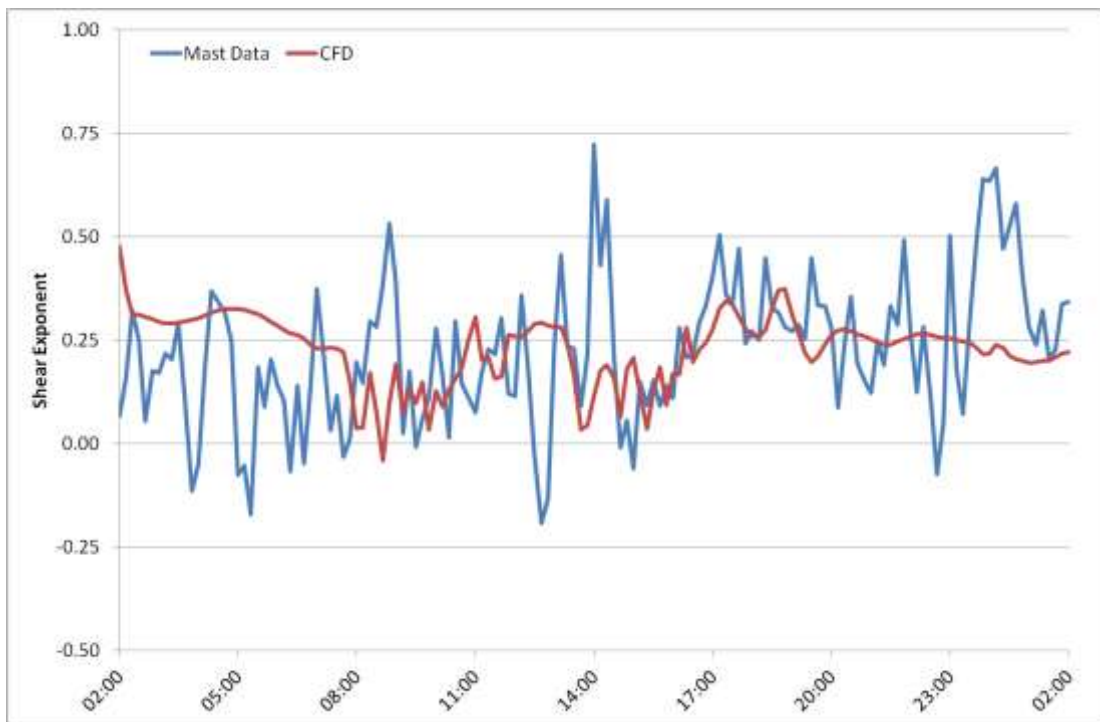


Figure 7.7.36: Shear exponent time-series for 16th May 2012 at M6282, taken between 73m and 50m AGL. Comparison between measured data and CFD.

CONCLUSIONS

Contour and vector plots showing horizontal isosurfaces and vertical planes through the CFD domain were used to demonstrate how the CFD model can provide insight into flow conditions across the site as a whole. These results also highlighted some interesting flow patterns associated with varying atmospheric stability. Movies constructed from the isosurfaces and planes can be used to show how the flow conditions vary with time. Visualisations of this nature are valuable for understanding the underlying flow characteristics that contribute towards observations in the measured mast data.

Time-series comparisons of wind speed, wind direction, potential temperature gradient, turbulence intensity and shear have shown that in general the CFD model captures the varying atmospheric conditions at Havsnäs reasonably well on the days selected for simulation. Although fairly substantial errors were observed in the modelling of potential temperature, this did not appear to have a serious effect on the results, probably because the more relevant potential temperature gradient was well represented.

Qualitatively, many effects of cold climates were observed in the CFD model results on the days simulated. Several of the selected days appeared to have flow conditions representative of stable atmospheres during daylight hours. This was observed through looking at variations in temperature gradient, turbulence intensity and shear throughout the day, alongside results presented on the horizontal isosurfaces and vertical slices. If further CFD modelling were to be carried out at Havsnäs, it would be beneficial to calculate either the Monin-Obukhov Length or the Gradient Richardson Number to quantify atmospheric stability with more confidence.

Standard CFD models and linear flow models are not able to capture this large variation in flow conditions, since they assume neutral atmospheric conditions. At Havsnäs, the cold climate suggests that assuming neutral conditions throughout the year may not be appropriate and this could affect flow parameters used to estimate energy yield and calculate damage to the turbine blades. Therefore, carrying out flow modelling with a more appropriate model, such as that used for this study, may increase the accuracy of overall results.

Although the results of this study show evidence of varying atmospheric stability and that the CFD model is able to capture this, the effect on the overall wind climate and relevance to parameters involved in wind energy, such as speed-ups, turbulence intensity, shear, inflow angles and wind veer, remains to be seen. In order to investigate this properly, it would be necessary to model a statistically significant number of days and form a wind map from the results.

The flow patterns observed in the CFD model through looking at the horizontal isosurfaces and vertical planes show some interesting features of the flow which seem to coincide with what would be expected at those times given the measured data available for comparison in the form of time-series. However, further validation should be carried out to confirm that these flow characteristics also occur in reality.

If further CFD modelling were to be carried out, as well as simulating a statistically significant number of days, some improvements should be made to both the WRF model and VENTOS®/M to try to reduce the model limitations discussed in the 'Model Limitations' text. It would also be worth investigating the cause of the discrepancy in the modelled and measured potential temperature, as this could be contributing to errors in the CFD predictions. Once a statistically significant number of days have been simulated, the results should also be compared to linear flow model results, standard CFD model results and results from the WRF model to confirm that VENTOS®/M is adding value to the flow predictions. Undertaking uncertainty analysis on the results, similar to that carried out for the linear flow model results in Section 7.7.1 would also be beneficial.

7.7.3 COMPARISON OF LINEAR AND CFD RESULTS

The analyses presented in Section 7.7.1 and Section 7.7.2 cannot be compared in a like-for-like manner due to differences in both the models themselves and the methods used to carry out the two studies. However, some qualitative comparisons can be made to highlight these differences. In order to compare the two models, a time-series of speed-ups between two masts was created for one day (27 May 2012), as presented in Figure 7.7.37. This shows the measured speed-up (measured wind speed at M626 divided by measured wind speed at M628), the VENTOS®/M predicted speed-up and the linear model predicted speed-up, which only varies by wind direction. The VENTOS®/M predicted speed-up better represents short-term variation in time. This is because the VENTOS®/M model takes into consideration more atmospheric physics than the linear model, allowing diurnal and seasonal variations to be observed in the model results. The linear model cannot do this since it provides a steady-state solution and assumes a neutrally stable atmosphere.

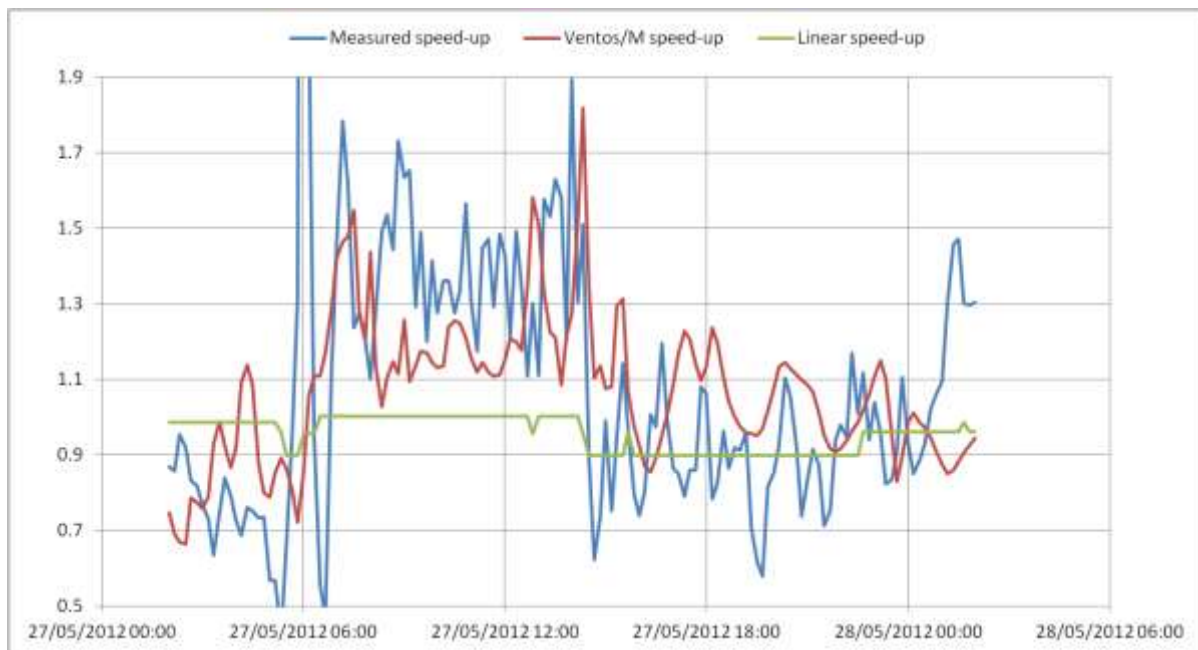


Figure 7.7.37: Time-series of the speed-up from M628 to M626 for 27 May 2012.

However, the time-series shown in Figure 7.7.37 does not necessarily imply that VENTOS®/M is more accurate than the linear model in predicting a long-term average speed-up. In order to make this comparison a statistically significant number of days would need to be simulated by VENTOS®/M. The results of the study carried out in Section 7.7.2 show that VENTOS®/M can capture characteristics of a changing atmosphere that the linear flow model cannot, but more days must be simulated in order to analyse the data in a similar way to the linear model.

7.7.4 ANNUAL AVERAGE VS SEASONAL VARIATION

The CFD results presented above indicate that different flow conditions can be observed at different times of year. Although only a few days were simulated, the combination of the results presented above and the findings of the atmospheric stability analysis from the measured data (Section 6.3.3) suggest that seasonal variation has an important effect on wind flow parameters such as turbulence intensity and shear.

This suggests that energy yield prediction methodologies would benefit from inclusion of seasonal variation in shear and turbulence intensity rather than global averages.

8 DISCUSSION

SHEAR EXTRAPOLATION

Section 6.1.3 shows that there is some wind speed variation across the Havsnäs site, despite the relatively flat terrain, simply due to spatial variation. Nevertheless, there is good agreement in shear across the site.

The nature of the relationship between separation distance and correlation is likely to be site dependent but at Havsnäs it has been found that, for every 1 km increase in separation distance, correlation between wind speeds decreases by approximately 0.03. Generally, this spatial variation in wind speeds does not vary with measurement height.

From the Havsnäs analysis, it is suggested that even with 10-minute average r-values as little as 0.7, and distance separations as great as 7.7 km, the LiDAR-measured velocity profile can be considered to validate mast-measured shear assumptions.

The sensitivity of the hub-height wind speed prediction to the canopy height is proportional to the relative size of the canopy height compared to the measurement heights. If the canopy height is small compared to the measurement heights, the influence of the canopy height will be negligible. This is found in the analysis in Section 6.1.4, where the two point and multi-point shear methodologies appear insensitive to changing canopy height.

The one point theoretical log law shear methodology is shown in this analysis to return the largest error on average. In particular, the one point theoretical log law method is only applicable in simple, homogenous, terrain. Despite resulting in conservative wind speed predictions, the one point method was still in broad agreement with measurements and this gives some confidence in its use for vertical extrapolations in cold climates on forested sites where it is difficult to measure shear conventionally, or perhaps for scoping purposes. It should be noted that this method relies on a reliable characterisation of the forest canopy height and roughness length and should be used with caution.

The two point and multi-point shear methods investigated in Section 6.1.4 have been shown to be best at minimising the error between measured and sheared values of hub height wind speed. Preference would be given to using the multi-point shear method where possible since it has been shown to be the least sensitive to the choice of canopy height. However, it is recommended that no single method is used in isolation, but is considered against alternatives making full use of high quality site measurements of shear wherever available.

Calculating shear using any method leads to an under-prediction of wind speed at hub height at the LiDAR location. However, vertically extrapolating over shorter distances causes the difference between the sheared and measured value of hub height wind speed to converge.

ATMOSPHERIC STABILITY AND WIND FLOW MODELLING

Instrument failures caused difficulties in atmospheric stability measurement, especially with the lower ultrasonic anemometers removing the lower wind speed measurement. This meant that several assumptions were necessary in order to assess stability.

Overall statistics show neutral stratification roughly 50% of the time, unstable and stable roughly 25% each. Stability effects follow strong diurnal and seasonal patterns which correspond with the degree of incoming solar radiation. The diurnal and seasonal stability effects can be seen in the measured turbulence intensity and shear exponent values on site (Section 6.3.3) and have also been noted in the energy content section (Section 6.4.4) and wind flow modelling section of this report (Sections 7.7.1 and 7.7.2).

Continuing to omit the inclusion of seasonal and diurnal variation in energy yield predictions will lead to errors and bias in energy yield results. It is seen in Section 6.3.4 that use of a global shear exponent for vertically extrapolating the wind speed in a stable atmosphere could include a bias in the predicted wind speeds. Likewise, the linear flow modelling in Section 7.7.1 shows that the model performs best during the day. Standard CFD models, as discussed in Section 7.7.2, assume neutral atmospheric stability so will not predict conditions associated with stable or unstable atmospheres.

MAST INSTRUMENTATION AVAILABILITY AND RELIABILITY

The analysis in Section 7.1 found that there was more than 20% unheated anemometer data lost due to icing on all masts and painting the anemometer black showed no benefit. There was only 1-2% heated cup anemometer data lost due to icing but the heated sonic anemometers suffered numerous failures. These failures were caused by ice build up during periods the heating power supply was non-functional or intermittent and highlighted a design flaw in the instruments in the case where ice can form and heating power is intermittent.

Half of all other failures were caused by broken booms. These booms were box section aluminium booms not optimised for the unheated instrumentation. This is thought to have caused a resonance issue.

LIDAR

Low aerosol density resulted in poor data capture at the WINDCUBE V1. The reconfiguration of the LiDAR to more pulses per line of sight resulted in a marked increase in qualified data capture and a reduction in the carrier to noise threshold of 2dB. The absolute increase in data capture was approximately 37% across all heights as shown in section 7.2.2. The quality of the qualified data remained consistent and other aspects of device performance were unaffected by reconfiguration, with acceptance tests being passed.

Considering the data from Havsnäs, it has been found that there is a well-defined linear relationship between the WINDCUBE and fixed mast data both for the standard deviation of mean wind speed data and the maximum wind speed data. RES has seen that WINDCUBE turbulence intensity data are suitable for climatic conditions reporting at a variety of sites with differing levels of complexity. The LiDAR at Havsnäs has also provided reliable data from which the equivalent wind speed could be easily derived in accordance with the draft IEC power performance standard [1] in the analysis in Section 7.6.1.

EQUIVALENT WIND SPEED AND ENERGY CONTENT

The PP analysis (Section 7.6), energy content analysis (Section 6.4.4) and shear section (Section 6.1) all show that using a measure of shear obtained from fixed mast measurements made below hub height is likely to underestimate energy through the rotor diameter. The extent of this is dependent on the shear methodology used and the vertical extrapolation distance.

There is no evidence seen in this report for the justification of a universal energy loss adjustment factor to account for periods of high atmospheric stability (and hence high shear) as shown in Section 7.4.1. In fact PP test results binned by shear exponent in Section 7.6.1 show that performance improves with increasing shear. The analysis also indicates that whilst the hub height wind speed power curve appears better than the equivalent wind speed power curve, if it is accepted that the hub height wind speed is an underestimate of the rotor-averaged equivalent wind speed then in fact there is more energy available than suggested by the hub height wind speed. The time series study of energy content (Section 6.4.4) also shows

that using the hub height wind speed and assuming no shear across the rotor height is likely to underestimate the available energy by up to ~2% in high shear conditions.

It can be said therefore that a global energy loss based on that observed in the USA (as discussed in Section 7.4.1) cannot simply be applied in other regions where stable atmospheric conditions prevail. The climatic mechanisms that create stable atmospheric conditions may vary from region to region and it is clear that not all stable atmospheric conditions result in an overestimation of energy through the rotor diameter.

ICING PRODUCTION LOSSES

Production losses due to icing were shown to be broadly in line with that predicted at preconstruction from experience from other Swedish wind farms.

Application of a standard heuristic based upon a fraction of the amount of data loss due to icing at the site assessment mast anemometers may be sensitive to the icing detection algorithm used.

ICE THROW MODELLING

Overall, the RES simulation model of ice throw model in section 7.5 indicates that there is no substantial risk to public safety due to ice throw from the turbines at Havsnäs. The ice throw model indicates a maximum throw distance of just over 200 m for this site which is less than the rule of thumb safe distance given in references [9] and [10].

9 RECOMMENDATIONS

SHEAR EXTRAPOLATION

The analysis in this report finds that a LiDAR-measured velocity profile can be used to validate mast-measured shear assumptions.

Vertically extrapolating over shorter vertical extrapolation distances generally causes the difference between the sheared and measured value of hub height wind speed to converge. It is recommended that masts are as close to hub height as economically viable or that a RS device is used to measure hub height wind speed.

The two point and multi-point shear methods have been shown to be best at minimising the error between measured and sheared values of hub height wind speed and are the most insensitive to canopy height. Preference would be given to using the multi-point shear method extrapolating wind speed to hub height where possible but it is recommended that multiple methods are considered in conjunction with one another making full use of high quality site measurements of shear wherever available.

It is recommended that the one point theoretical log law method is only applied in simple, homogenous, terrain. This methods sensitivity to canopy height suggests that it may not be appropriate for use at sites where the canopy height varies significantly across the site.

ATMOSPHERIC STABILITY

If gradient based measurements of stability are to be performed, they should be performed over multiple levels, as opposed to just two, which will also provide redundancy and additional confidence in the results. At each level the following measurements should be taken; wind speed, air temperature, atmospheric pressure and relative humidity. All of these sensors should be located at the same level with as little a vertical separation as possible. The wind direction should be measured at an intermediate measurement height (i.e. between the upper and lower measurements used for the gradient analyses).

Flux based measurements would allow stability to be assessed more directly with less assumptions needing to be made.

MAST INSTRUMENTATION AVAILABILITY AND RELIABILITY

Recommendations to instrumentation best practices can be found in section 7.3. The main recommendations are included here too.

It is recommended that boom suitability should be assessed when mounting non-standard instrumentation.

A reliable power supply must be used for all equipment if good data coverage is to be obtained over the winter period in cold climates. This is especially important if relying upon sonic anemometers for wind speed or stability measurements since ice build up was seen to be very detrimental not only to their performance but also to their survivability.

Redundancy should be a large consideration for all instrumentation campaigns, thus redundant instrumentation with stand alone logging systems should be deployed. This will ensure as wide a data coverage as possible and give confidence in the results by allowing comparisons between the measured values of each redundant system.

LIDAR

Standard device configuration is not appropriate for cold climate sites with low aerosol density. It is recommended that the pulses per line of sight are increased to 40,000 and the signal to noise threshold is decreased appropriately.

As there is likely to be variability between sites (and even across sites) and world regions, WINDCUBE LiDAR data should be examined on a deployment-by-deployment basis to ensure they can be used for climatic conditions reporting. A suitable RS device (that can return climatic conditions data) is thought to have most value when co-located with a fixed mast.

In cold climates thought must be given to the mounting of a LiDAR on a snow platform and measurement heights altered accordingly. Further recommendations can be found in the LiDAR best practice section (Section 7.3.2).

EQUIVALENT WIND SPEED AND ENERGY CONTENT

The draft IEC standard is useable and it is advised that where appropriate data is available the equivalent wind speed will offer an improved estimate of energy through the rotor over hub height wind speed. This is particularly important for large rotor diameters and high hub heights where the increased wind speed and size of the rotor makes the available energy more sensitive to changes in the wind speed used to estimate the available energy.

It has been shown that the stable atmospheric conditions at Havsnäs do not result in an overestimation of energy through the rotor diameter. Such an energy loss adjustment factor should therefore not be applied generally. Each region should be treated separately on the basis of data gathered from that region and each individual site, where the necessary data exist, should be considered on its own merits.

It is only with the deployment of a RS device in conjunction with a long-term reference mast at each wind farm site that the necessary data to make an informed judgement on the appropriateness of an energy loss adjustment factor can be obtained.

ICE THROW MODELLING

It is recommended that the rule of thumb safe distance given in references [9] and [10] should continue to be followed for health and safety purposes.

10 FUTURE AREAS OF RESEARCH

SHEAR EXTRAPOLATION

It has been shown that spatial separation is the dominant factor in the r-value of correlation between LiDAR and mast data. With a larger dataset, it may be possible to determine separation thresholds to help define shear validation and uncertainty criteria based on device-mast agreement.

It has been shown that the larger the vertical extrapolation distance (up to 45m), the larger the error in predicting hub height wind speed. It may be interesting to investigate how increasingly large extrapolation distances between measurement height and hub height affect the ability of the shear methodologies to accurately predict hub height wind speed.

It would also be informative to investigate the effect higher canopy heights have on these findings since this report only looks at the sensitivity or varying the canopy height when the actual canopy height is 10m.

Vertically extrapolating the wind speed in stable atmosphere using a global shear exponent could include some bias in the predicted wind speeds. Therefore, it would be worth isolating the stable atmosphere events and adopt a specific methodology to vertically extrapolate the wind speeds during these occurrences. If the stable events' measurements were to be isolated and a shear exponent calculated from this data and applied to wind speed in order to vertically extrapolate wind speeds during stable atmosphere events, the bias may be reduced. Further work is required to verify this hypothesis.

Time series based energy yield modelling, without the use of average shear exponents may also improve results. Tests could be done using 10-minute shear exponents to extrapolate wind speeds from a mast below hub height to hub height. This could then be compared to the same timeseries modelling where the wind speeds are sheared up to hub height using the same shear exponent for each 10-minute average. This constant shear exponent would be the average shear exponent for the period used which would be representative of the current energy yield methodology which is widely used in industry. These results could then be compared the measured hub height wind speed to assess the amount of improvement through applying varying shear exponents.

ATMOSPHERIC STABILITY

Further work is required to verify or improve the method to determine the atmospheric stability criterion. Suitable instrumentation for atmospheric stability measurements would be considered in all future cold weather system R&D designs to include the ability to conduct flux based measurements. Shear and turbulence intensity may be good complementary index rates to improve the methodology and better define the criterion.

For future atmospheric stability campaigns it would be beneficial to deploy a flux based atmospheric stability system in conjunction with the gradient measurements. This approach should eliminate some of the assumptions inherent in the Gradient Richardson Number and provide a more direct measurement of vertical thermally driven flow. The Monin-Obukhov Length could be measured directly by a flux system.

The downside of flux measurements is that more powerful and complex logging systems are required and three dimensional wind measurements are necessary. Given the very poor performance of the Metek USA-1 ultrasonic anemometers during this measurement campaign (see sections 7.1.4 and 7.1.7), flux measurements in cold climates may prove difficult, but

would offer improved stability measurements should a more suitable ultrasonic anemometer be available.

LENGTH OF MEASUREMENT PERIOD

Despite the measurement campaign lasting almost a year, the equivalent of only four months of data was used in this analysis. This is because part of the data was affected by icing, instrument failure, mast effects or wake effects.

Given that stable atmospheric conditions occur mostly in winter, data filtered due to icing events may result in also filtering out most events that show atmospheric stability and introduce some bias into the results of stability class percentages.

Some further analysis using measurements with a better availability over a full year of data or more could give useful complementary information to assess the bias introduced by the use of a global shear exponent to vertically extrapolate wind speeds. Further Winter measurements would also enable a more thorough assessment of the use of equivalent wind speed and of the impact of icing on power curves.

ICING DETECTION IN DATA

Further work would be appropriate to develop the icing algorithm used to identify iced data. Use of a webcam with improved availability would enable validation of data removed as iced periods. This would then allow an appropriate buffer, mentioned in Section 5.3.1, to be found.

VENTOS®/M CFD & WIND FLOW MODELLING

The most beneficial addition to the CFD analysis using VENTOS®/M would be to model a statistically significant number of days. At least 100 days should be simulated, from which a wind map can be created showing the modelled distribution of wind speed and direction. This would also allow analysis of CFD-predicted speed-ups, turbulence intensity, shear, inflow angles and veer as averages per direction, season, time of day and stability class. The results can then be compared to the linear flow model results and also to standard CFD and WRF mesoscale results to assess the value added to the flow predictions through using VENTOS®/M CFD analysis. The model could also be validated further by making more comparisons with measured data. Finally, uncertainty analysis, similar to that carried out for the linear flow model and presented in Section 7.7.1, could be undertaken.

The model itself could also be improved in a number of ways. Snow cover could be included in the WRF model, which could then be taken into consideration in the CFD roughness model. Ideally a canopy model should also be included in VENTOS®/M, however, this is non-trivial due to the canopy's contribution to the prediction of turbulence. An investigation into the origin of the errors arising in the modelled potential temperature would also be beneficial.

It would also be interesting to extract shear exponents from the CFD results in order to calculate the rotor equivalent wind speed. A comparison could then be made with the results of Section 6.4.

ICE THROW MODELLING

Ice throw modelling could be improved by model validation in terms of the predicted locations of ice strike and the number of ice particles released from the turbine blades when iced and operational. Maps of simulated ice strike locations could be compared to observed locations of ice strike given prevailing wind direction. This would require a campaign of on-site measurements and is an area for future research. The estimation of risk to public safety could

be enhanced by a better model of the frequency of movement of snowmobiles around the site.

11 REFERENCES

- [1] IEC draft standard International Electrotechnical Commission (2011), “*Wind Turbines - Part 12-1: Power performance measurements of electricity producing wind turbines*”, dated September 2011.
- [2] Foken, T., “*50 Years of the Monin-Obukhov Similarity Theory*”, University of Bayreuth, Department of Micrometeorology, Germany
- [3] Hogstrom, U. (1996), “*Review of Some Basic Characteristics of the Atmospheric Surface Layer*”, *Boundary Layer Meteorology*, Vol. 78 p 215-246
- [4] Wyngaard, J.C. (1990), “*Scalar fluxes in the planetary boundary layer - theory, modelling and measurement*”, *Boundary Layer Meteorology*, Vol.50, 49-75.
- [5] Gardiner, B., “*Airflow over forests and forest gaps*”, British Wind Energy tree workshop, http://www.bwea.com/pdf/trees/Barry_Gardiner.pdf
- [6] Clive, P. (2007), “*LiDAR wind profiling*”, Sgurr Energy presentation, dated 03 July 2007.
- [7] Oldroyd, A., Courtney, M., Kindler, D. (2009), “*Testing and Calibration of Various LiDAR Remote Sensing Devices for a 2 Year Offshore Wind Measurement Campaign*”, EWEC 2009 Presentation, 19 March 2009.
- [8] Stull, R.B. (1988), “*An Introduction to Boundary Layer Meteorology*”, Springer Science, ISBN: 978-90-277-2769-5
- [9] Seifert, H., Westerhellweg, A. & Kröning, J. (2003), “*Risk Analysis of Ice Throw from Wind Turbines*”, Paper presented at BOREAS VI, 9-11 April 2003
- [10] IEA Wind Expert Group Study on Recommended Practices (2011), 13. “*Wind Energy Projects in Cold Climates*”, dated May 22 2012,
- [11] Biswas, S., Taylor, P. and Salmon, J. (2011), “*A Model of Ice Throw Trajectories from Wind Turbines*”, *Wind Energy*
- [12] Martin, D. (2008), Annex 5.1.1(i) “*WTG General Specification 950019 V06*”, dated 29 Feb 2008
- [13] Taylor, P., Brothers, C.F. & Salmon, J.R. (2012), “*Zephyr North South Branch Wind Farm Ice Throw Report*”, Prowind Canada, Revision 2
- [14] LeBlanc, M.P. (2007), “*Recommendations for Risk Assessments of Ice Throw and Blade Failure in Ontario*”, Report from Garrad Hassan to the Canadian Wind Energy Association
- [15] Cattin, R. (2012), “*Ice Throw Studies in the Swiss Alps*”, Meteotest
- [16] Snowmobile speed limits, accessed at <http://www.snokoterradet.se/english/> on 15 November 2012
- [17] Snowmobile specifications, accessed at <http://yamaha-motor.ca/products/products.php?model=4075§ion=td&group=S#contentTop> on 15 November 2012

-
- [18] Walmsley, J.L., Taylor, P.A. and Keith, T. (1986), "A simple model of neutrally stratified boundary-layer flow over complex terrain with surface roughness modulations (MS3DJH/3R)", *Boundary-Layer Meteorology* 36 (1986) 157-186.
- [19] Troen, I. and Petersen, E.L. (1989), "European Wind Atlas", Published by Riso.
- [20] Kaimal, J.C. and Finnigan, J.J (1994), "Atmospheric Boundary Layer Flows: Their Structure and Measurement", Oxford University Press.
- [21] Perera, M.D.A.E.S. (1981) "Shelter behind two-dimensional solid and porous fences", *Journal of Wind Engineering and Industrial Aerodynamics* Vol. 8, pp. 93-104.
- [22] Clerc, A., Anderson, M., Stuart, P. and Habenicht, G. (2012), "A systematic method for quantifying wind flow modelling uncertainty in wind resource assessment", *Journal of Wind Engineering & Industrial Aerodynamics*, pp. 85-94
- [23] Rogers, T., Randall, G., Hughes, H., & Mault, J. (2012), "New Methods for Predicting the Impact of Stability on Energy Production", EWEA 2012 Conference Proceedings
- [24] Tambke, J., Doerenkaemper, M., Steinfeld, G. & Wolff, J-O., (2012), "Influence of Offshore Wind Conditions on Power Curves and Wakes of Multi-Mega-Watt Turbines", EWEA 2012 Conference Proceedings
- [25] Meissner, C., Reidar Gravdahl, A., (2012), "Short-term Forecasting using Mesoscale Simulations, Neural Networks and CFD Simulations", EWEA 2012 Conference Proceedings
- [26] Texier, O., Bezault, C., Girard, N., Houbart, J.C. & Pham, S., (2012), "Results of integration of atmospheric stability in wind power assessment through CFD modelling", EWEA 2012 Conference Proceedings
- [27] Montavon, C., Jones, I., Malins, D., Strachan, C., Spence, R. & Boddington, R., (2012), "Modelling of Wind Speed and Turbulence Intensity for a Forested Site in Complex Terrain", EWEA 2012 Conference Proceedings
- [28] Peña, A., Gryning, S.E., Mikkelsen, T., Hasager, C. & Kelly, M, (2012), "The Modeling and Observation of the Long-term Offshore Vertical Wind Profile and Wind Shear", EWEA 2012 Conference Proceedings
- [29] Stull, R. B., (1988), "An Introduction to Boundary Layer Meteorology", Atmospheric Sciences Library, Kluwer Academic Publishers
- [30] Tindal, A., Johnson, C., LeBlanc, M., Harman, K., Rareshide E & Graves A (2008), "Site-Specific Adjustments to Wind Turbine Power Curves", 2008 AWEA WINDPOWER Conference, dated June 2008.
- [31] Rogers, T. (2012), "Atmospheric Stability Effects on Turbine Power Performance", DNV KEMA, WINDPOWER 2012 Presentation, dated 4 June 2012.
- [32] International Electrotechnical Commission (2005), "Wind turbines Part 12-1:Power performance measurements of electricity producing wind turbines", International Standard IEC 61400-12-1 First Edition, 2005-12
- [33] Albers A. (2009), "Turbulence Normalisation of Wind Turbine Power Curve Measurements", Deutsche WindGuard consultation GmbH, dated 29 August 2009.

APPENDIX 2A - MAP SHOWING LOCATION OF HAVSNÄS

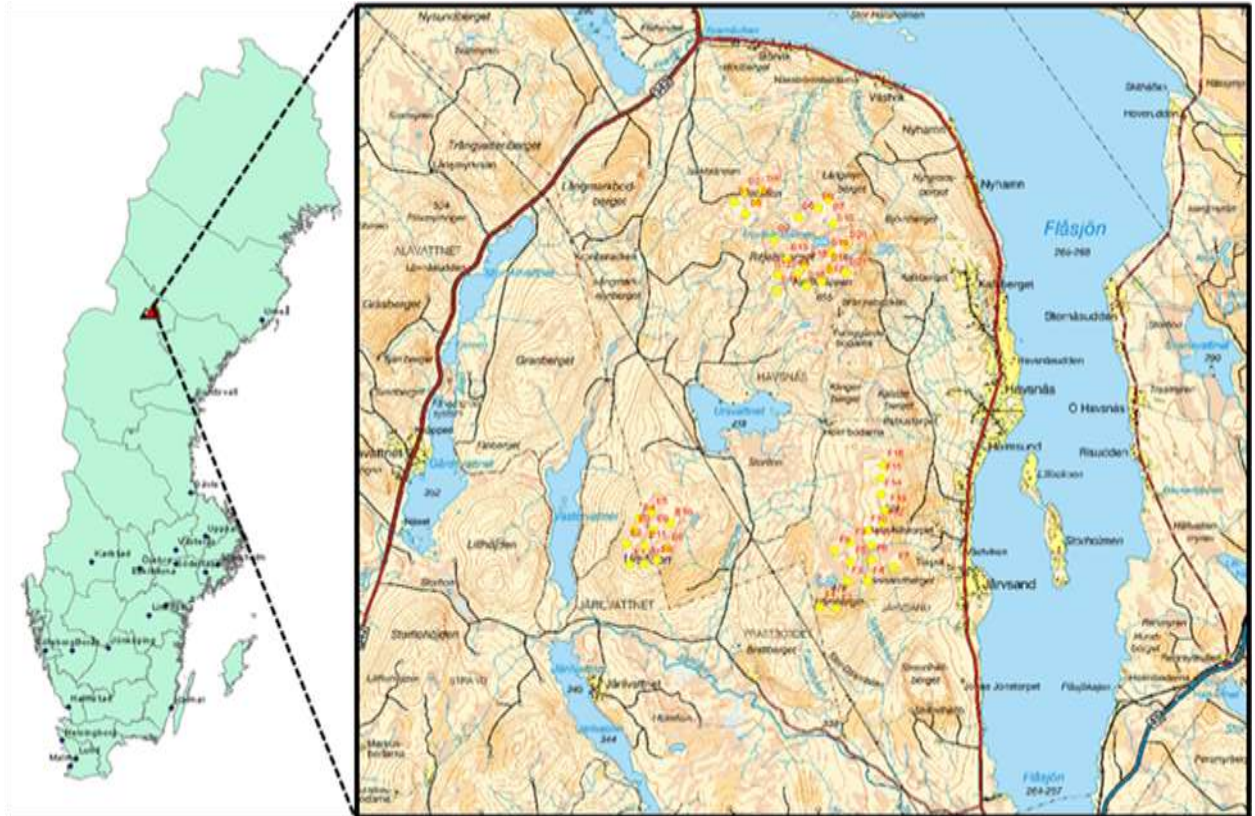


Figure 2A.1: Location of Havsnäs.

APPENDIX 5A - SITE LAYOUT DRAWINGS

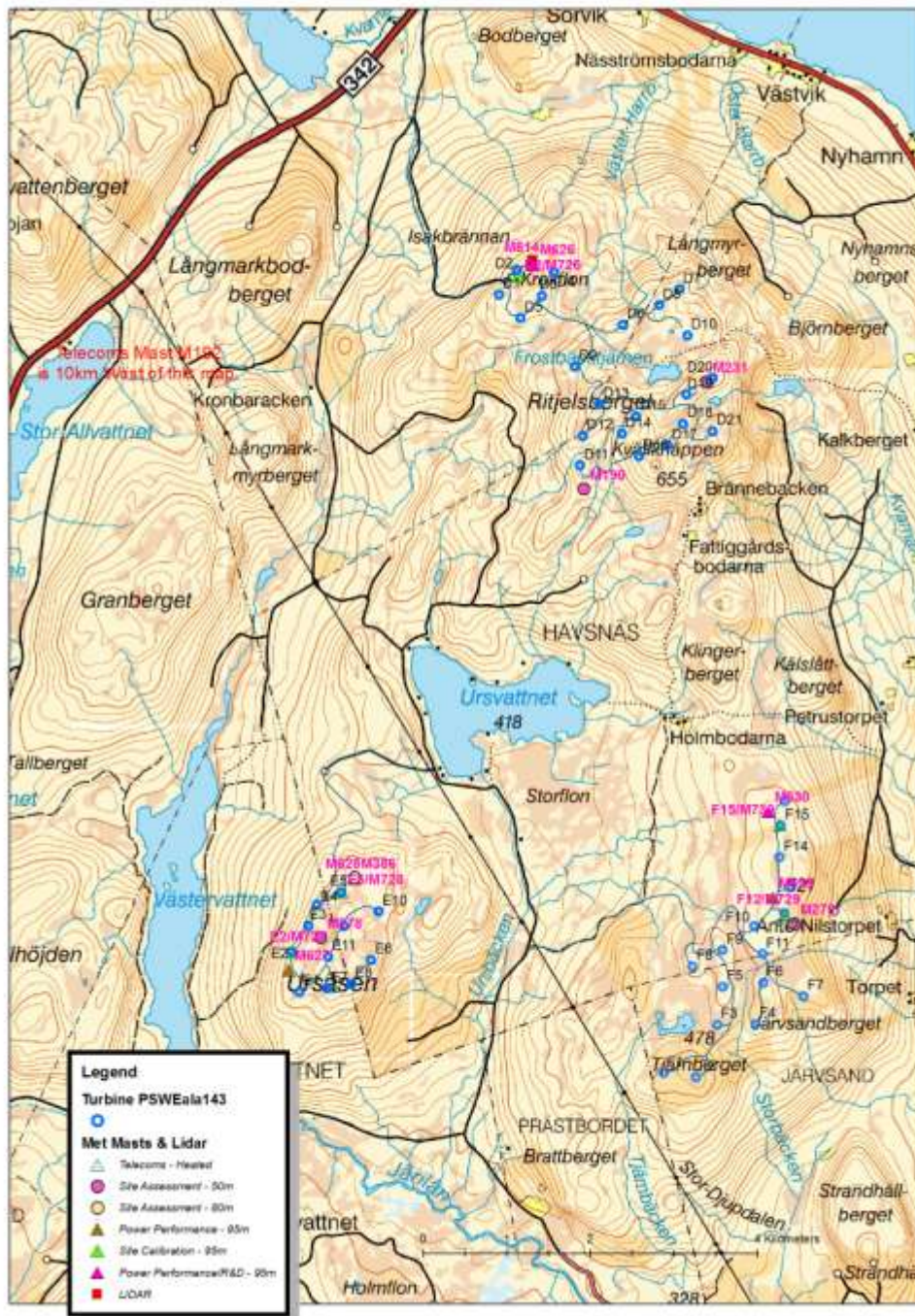


Figure 5A.1: Map of entire Havsnäs site. Note that the heated telecoms mast is not shown on these drawings since it is to the West of the area shown.¹⁶

¹⁶ Mast naming convention - each mast location is uniquely identified by the first three digits of its reference number (e.g. M628). Where a fourth digit is present then this indicates which of the multiple instrumentation systems on that mast is being referred to (e.g. M6282 refers to instrumentation system 2 on mast M628).

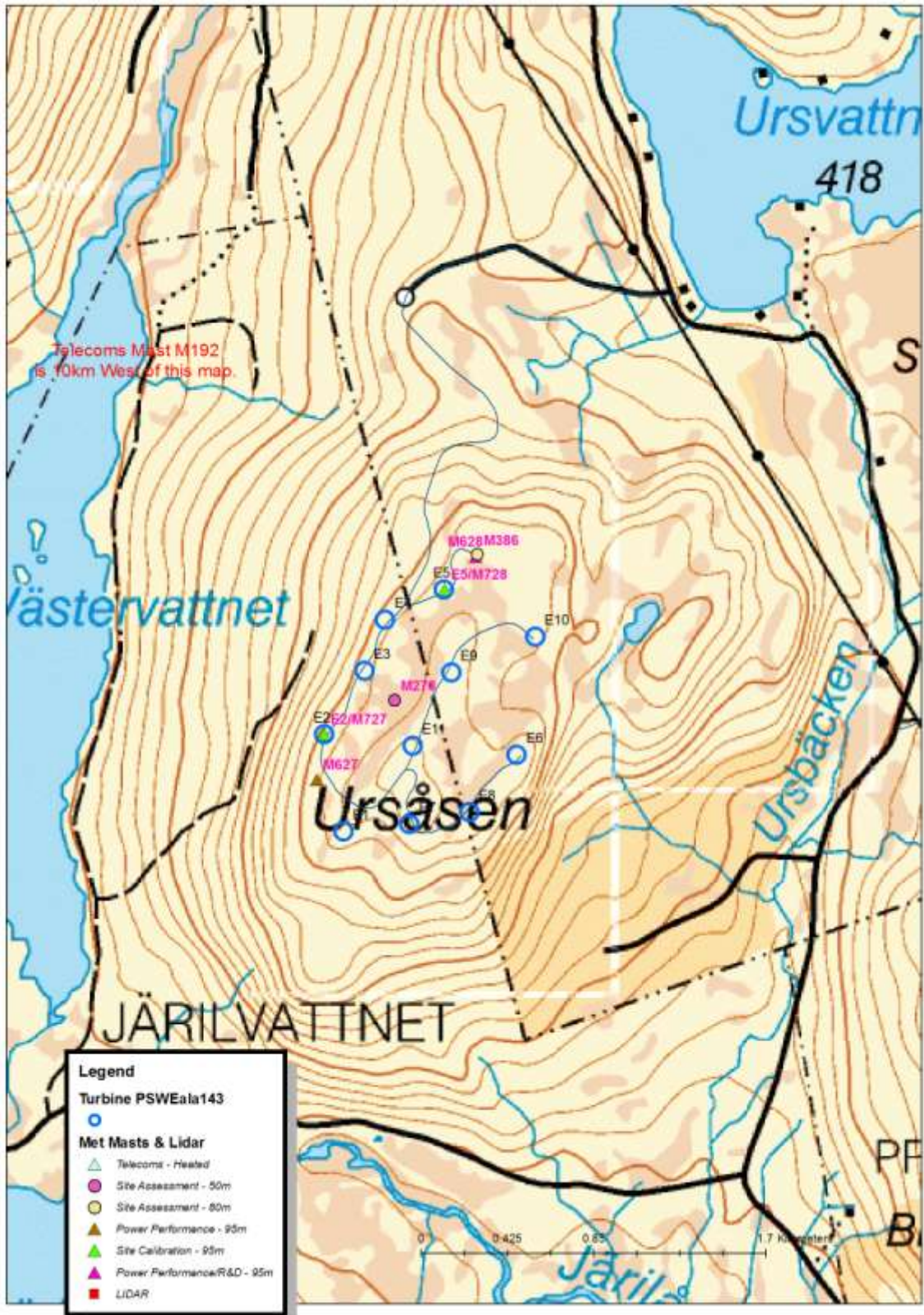


Figure 5A.2: Map of the Uråsen hill of Havsnäs project.

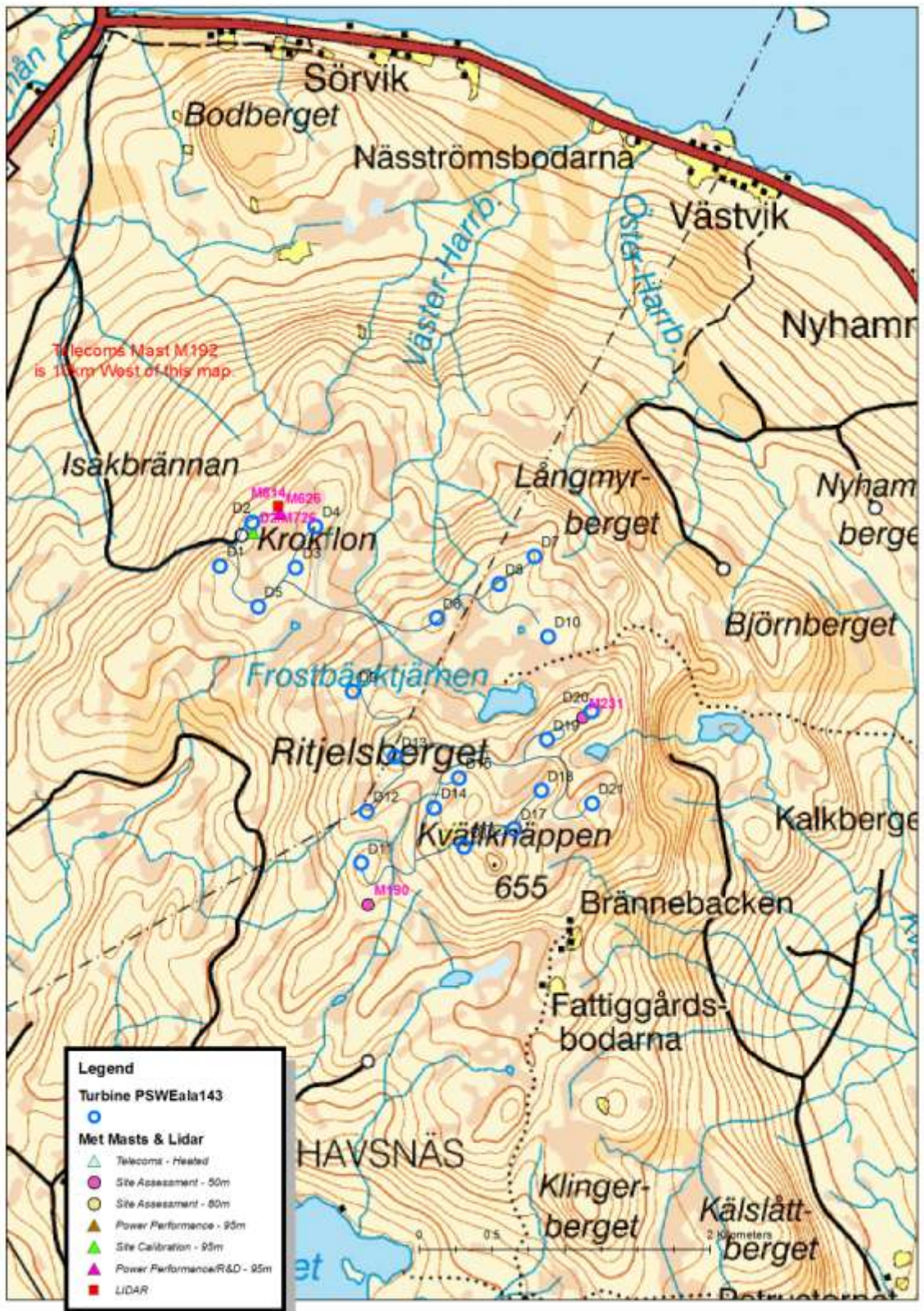


Figure 5A.3: Map of the Ritjelsberget hill of Havsnäs project.

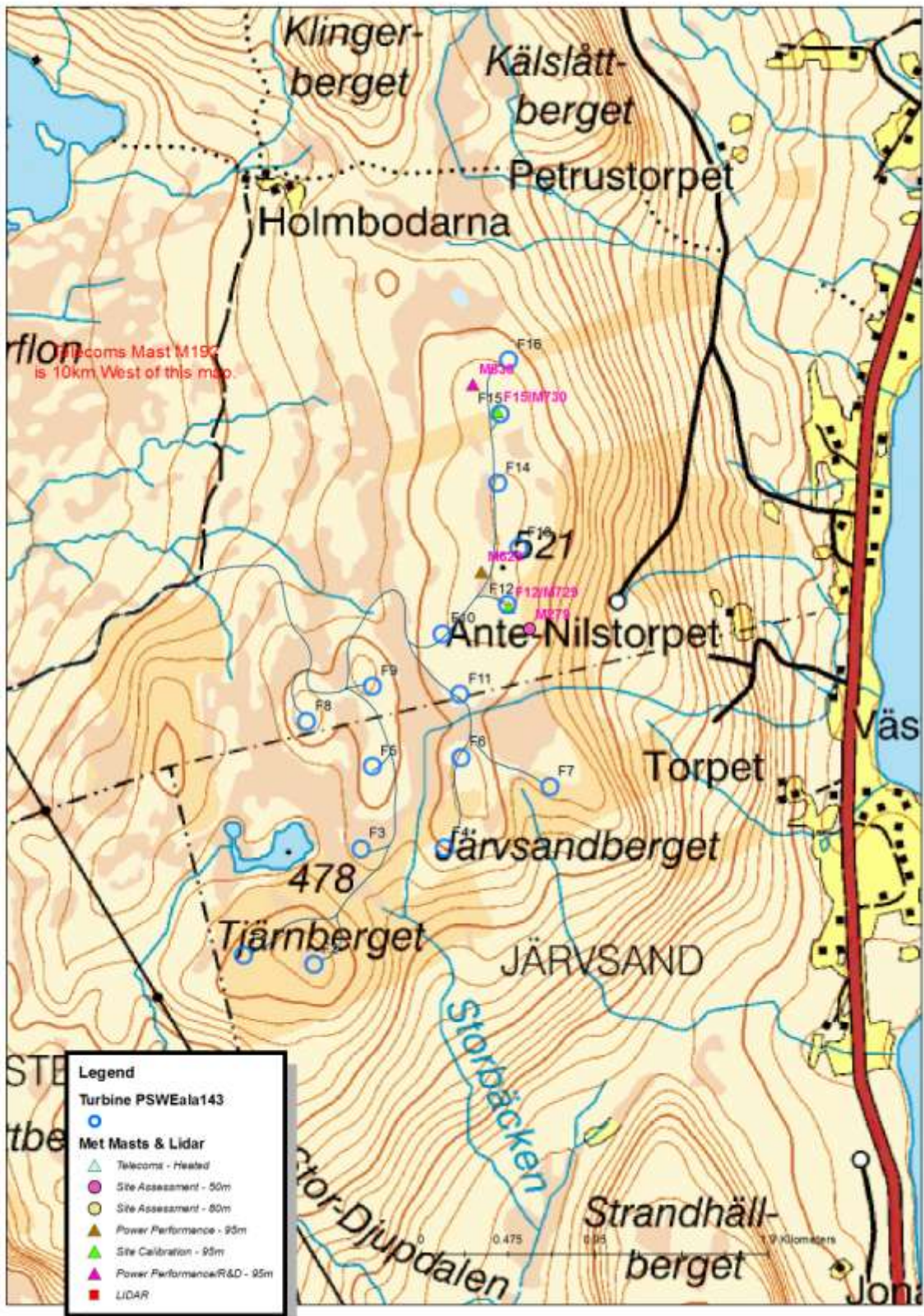


Figure 5A.4: Map of the Jarvsandverget hill of Havsnäs project.

APPENDIX 5B - AS BUILT MAST DRAWINGS

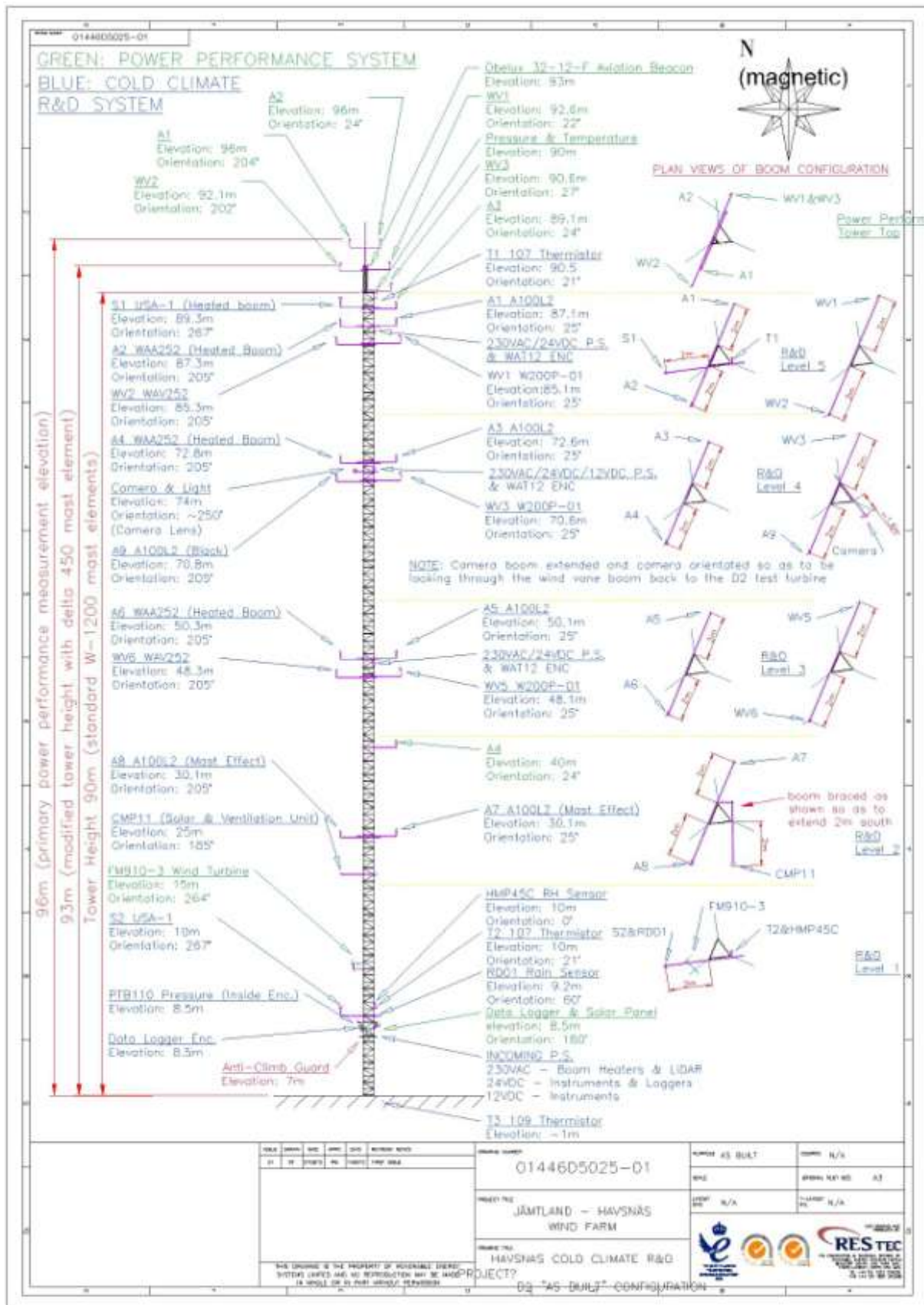


Figure 5B.1: M6261

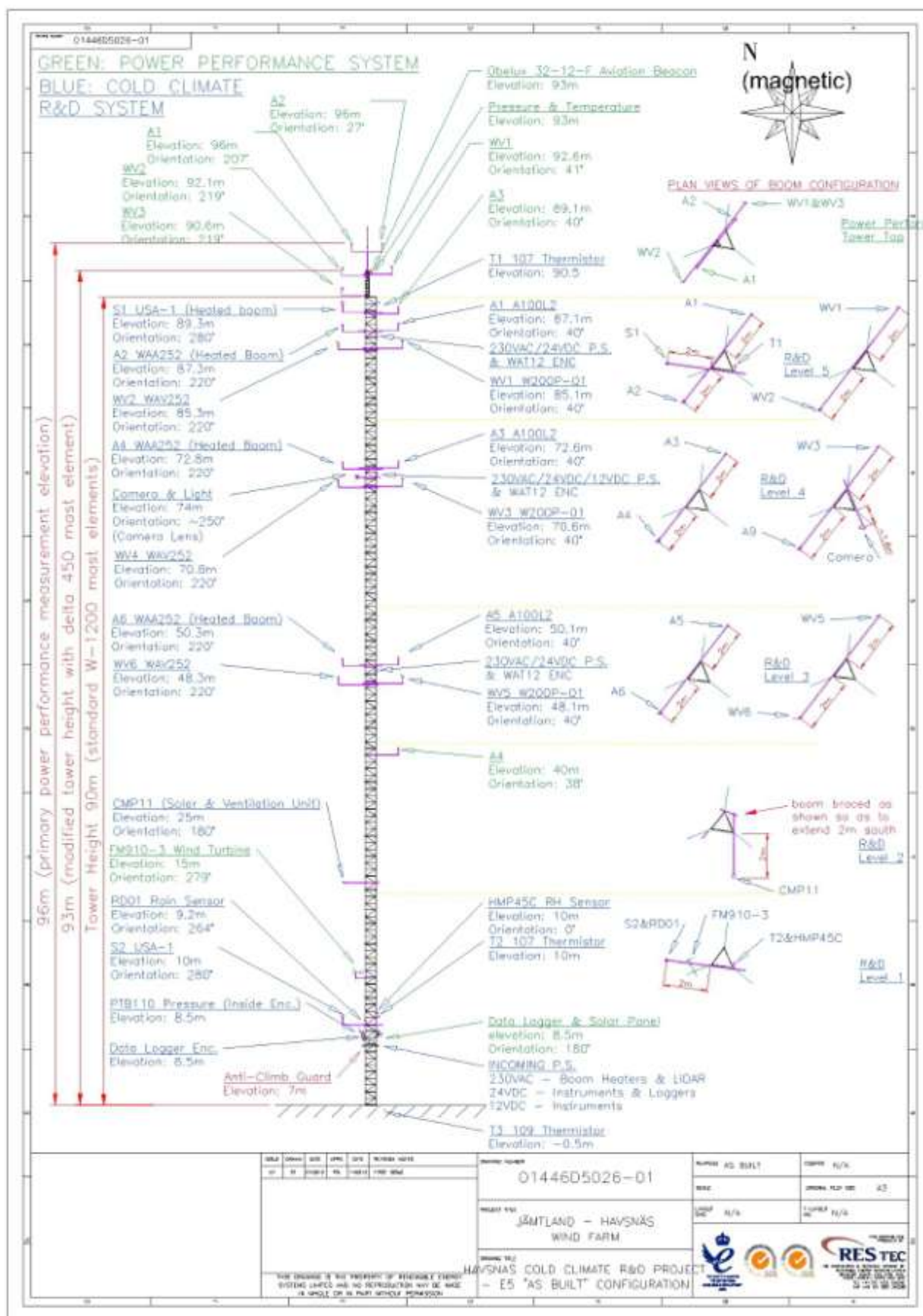


Figure 5B.2: M6282

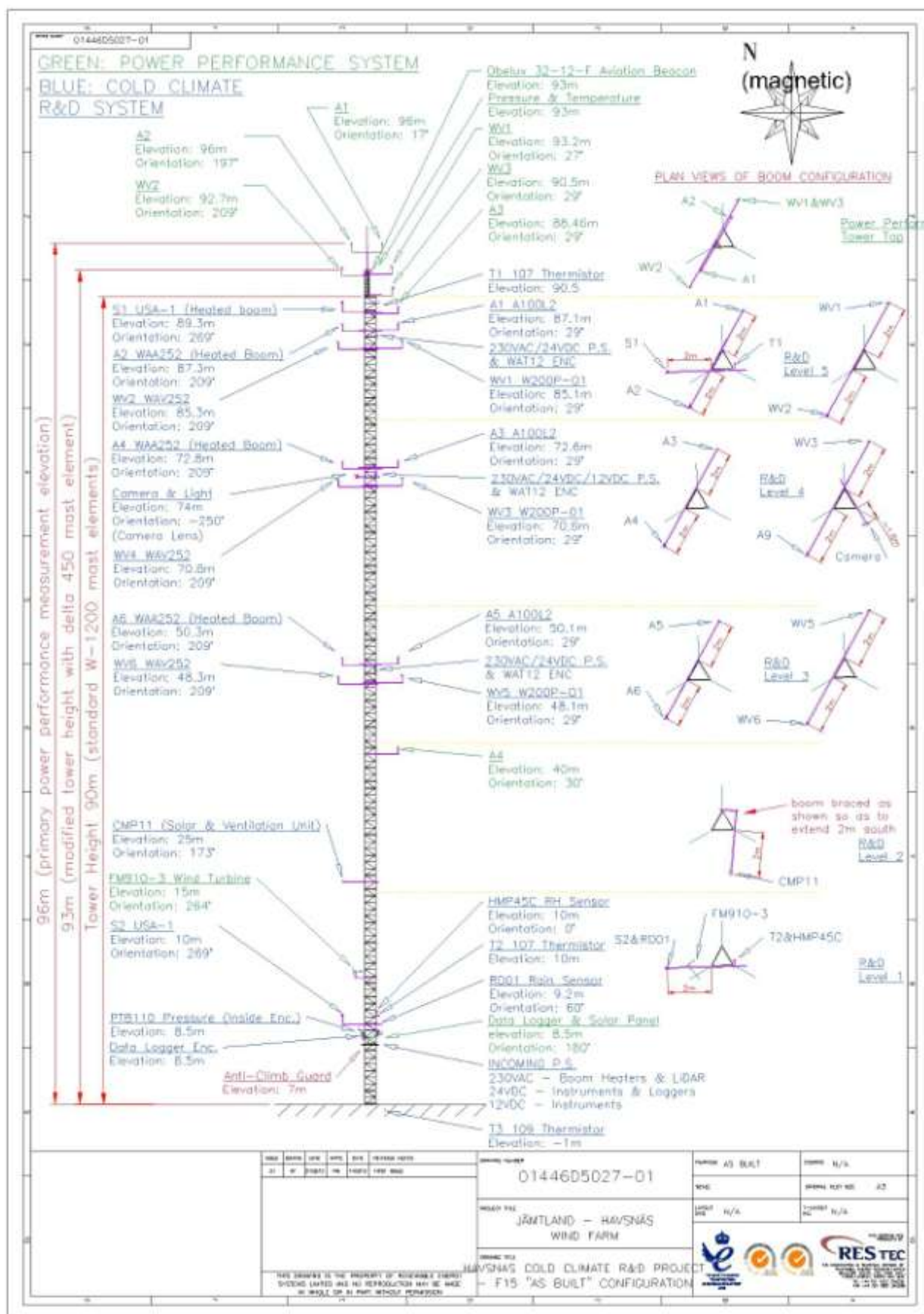


Figure 5B.2: M6303

APPENDIX 7A - M6261 ICING PROGRESS, VECTOR A100L2 ANEMOMETER - PAINTED BLACK.





APPENDIX 7B - M6282 ICING PROGRESS, VAISALA WAV252 HEATED WIND VANE



APPENDIX 7C - M6303 ICING PROGRESS, VECTOR W200P WIND VANE





APPENDIX 7D - CUP ANEMOMETER FAILURE PHOTOS



Photo 7D.1



Photo 7D.2



Photo 7D.3



Photo 7D.4



Photo 7D.5

APPENDIX 7E - WIND VANE FAILURE PHOTOS



Photo 7E.1



Photo 7E.2



Photo 7E.3



Photo 7E.4



Photo 7E.5

APPENDIX 7F - SONIC ANEMOMETER FAILURE PHOTOS



Photo 7F.1



Photo 7F.2



Photo 7F.3

APPENDIX 7G - LIDAR DATA FILTERING CRITERIA

Prior to the analysis of data from RS devices, it is important to apply data filters to remove any data that cannot be said to be representative of any given time period. For the WINDCUBE V1 the two key filters are the vertical wind speed censor and the availability filter. These filters remove data which are not deemed to be of suitable quality or have been affected by precipitation. Table 7G.1 shows the filters that have been applied to the WINDCUBE V1 data.

WINDCUBE V1 Filters	
Vertical wind speed censor (m.s^{-1})	1.5
Availability	90
Rain filter	N/A
Low wind speed censor (m.s^{-1})	N/A
Check max ws greater than min ws?	No
Check that the Stdev value is present?	No

Table 7G .1: WINDCUBE V1 Filters.

APPENDIX 7H - ACCEPTANCE TEST CRITERIA

The following acceptance test criteria are suggested by Peter Clive in his July 2007 presentation, ‘LiDAR wind profiling’ [6]. These acceptance tests are designed for onshore LiDAR devices.

Acceptance criteria

The following criteria for acceptance tests have been adopted and easily satisfied in the past by lidar operators under contract

- 1) 2 week data period
- 2) R^2 value on wind speed correlations >0.96
- 3) Slope of wind speed correlation: $0.97 < x < 1.03$
- 4) RMS on wind direction difference $< 5^\circ$
- 5) Units located adjacent to a tall mast ($>40m$):
 - Calibrated instruments
 - Mounting in accordance with IEC Pt .11
 - Sited to minimise differences in wind between locations

In addition data availability $>95\%$ is typical. The IEA expert committee, on which SgurrEnergy is represented, will publish guidelines by the end of the summer.

© SgurrEnergy Ltd
www.sgurrenergy.com

Figure 7H.1: Sgurr Energy acceptance test criteria.

The following acceptance tests developed by the NORSEWInD project [7] are intended for LIDAR device deployments in an offshore environment. However it is still possible to use the NORSEWInD criteria in an onshore environment but it will be more difficult for the LiDAR device to meet those criteria due to likely increased complexity of flow in an onshore environment.

Parameter	Criteria	Ranges (height & speed)
Absolute error	$<0.5m/s$ for WS range 2-16m/s Within 5% above 16 m/s Not more than 10% of data to exceed those values	All valid data
Data Availability	Assessed case by case – Environmental conditions dependent	All valid data
Linear Regression - Slope	Between 0.98 and 1.01 <0.015 variation in slope etween WG-ranges (b) and (c)	Heights all 60 to 116m WS-ranges: (a) 4-16m/s, (b) 4-8m/s & (c) 8-12 m/s
Linear Regression – R^2	>0.98	Heights: all 60 to 116m WS-ranges: 4-16m/s, 4-8m/s & 8-12 m/s

Figure 7H.2: NORSEWInD acceptance test criteria.

APPENDIX 7I - AN EXAMINATION OF WINDCUBE TURBULENCE DATA

7I.1 SIMPLE SITE (V1)

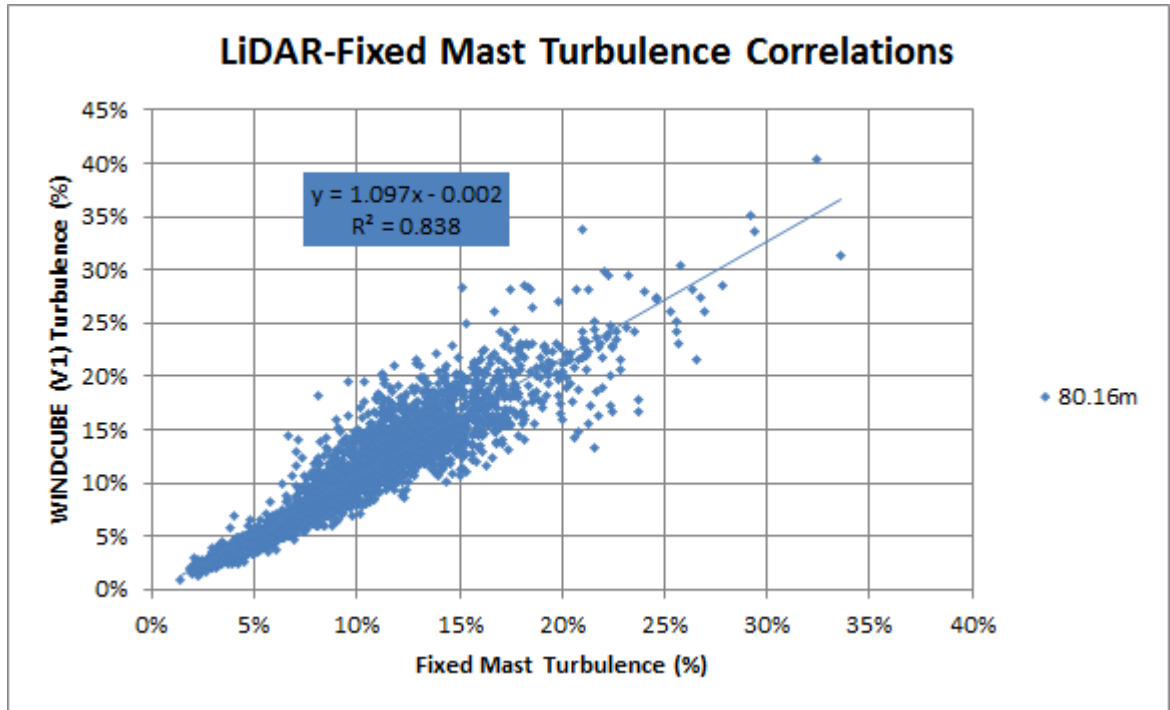


Figure 7I.1: Correlation of turbulence between RS device and fixed mast on a simple site.

Notes:

- The data from the 80.16 m anemometer have been compared with the data from the 80 m WINDCUBE V1 measurement height.
- A tower shadow sector of 60° centred on the boom inverse has been used.
- A $5 \text{ m}\cdot\text{s}^{-1}$ wind speed censor has been applied.
- There is a large amount of scatter and the slope is 10 % from unity. Nevertheless, there is a clear relationship between the turbulence values from the fixed mast data and those from the WINDCUBE V1 data.

71.2 OFFSHORE SITE (V2)

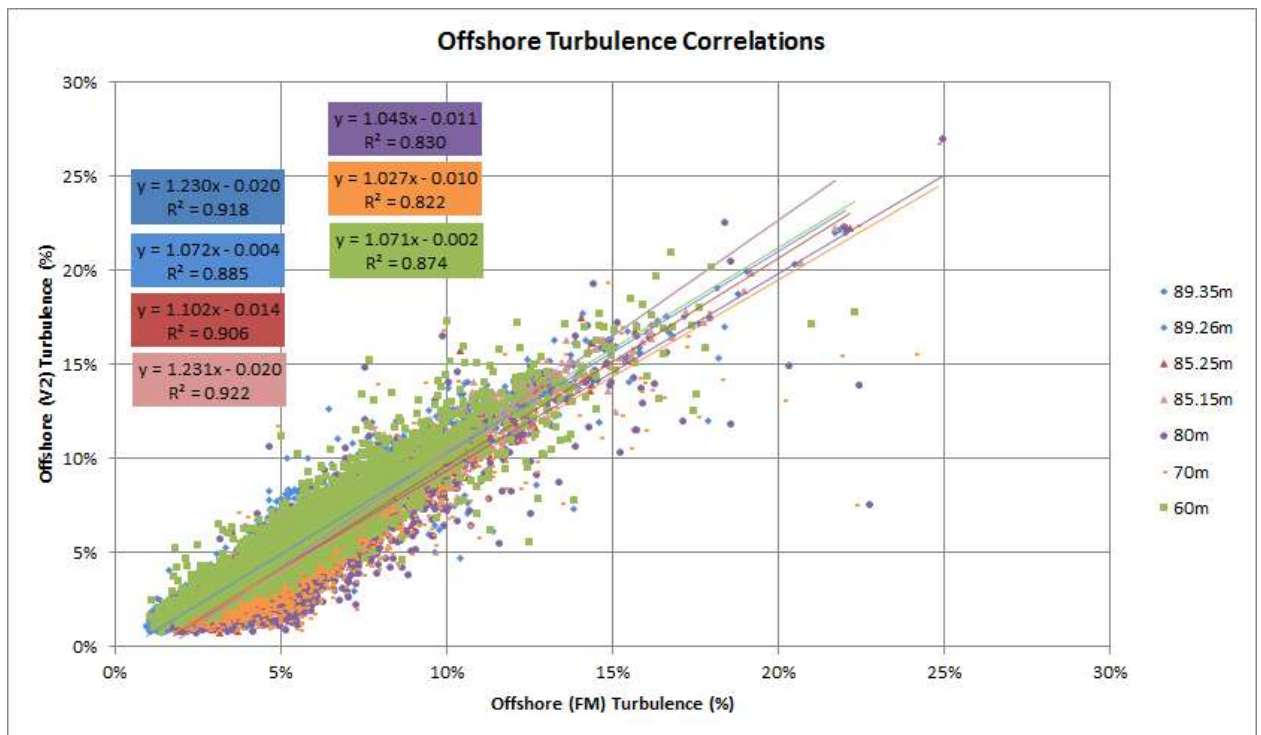


Figure 71.2: Correlation of turbulence between RS device and fixed mast on an offshore site.

Notes:

- The data from the 89.35, 89.26, 85.25, 85.15, 80, 70 and 60 m anemometers have been compared with the data from the 89.5, 84.5, 79.5, 69.5 and 59.5 m WINDCUBE V2 measurement heights.
- A tower shadow sector of 120° centred on the boom inverse has been used.
- A 5 m.s⁻¹ wind speed censor has been applied.
- While there is a large amount of scatter and the slopes of the correlations vary from 3-23 % from unity, there remains a clear relationship between the turbulence values from the fixed mast data and those from the WINDCUBE V2 data, particularly at 90 and 85 m.

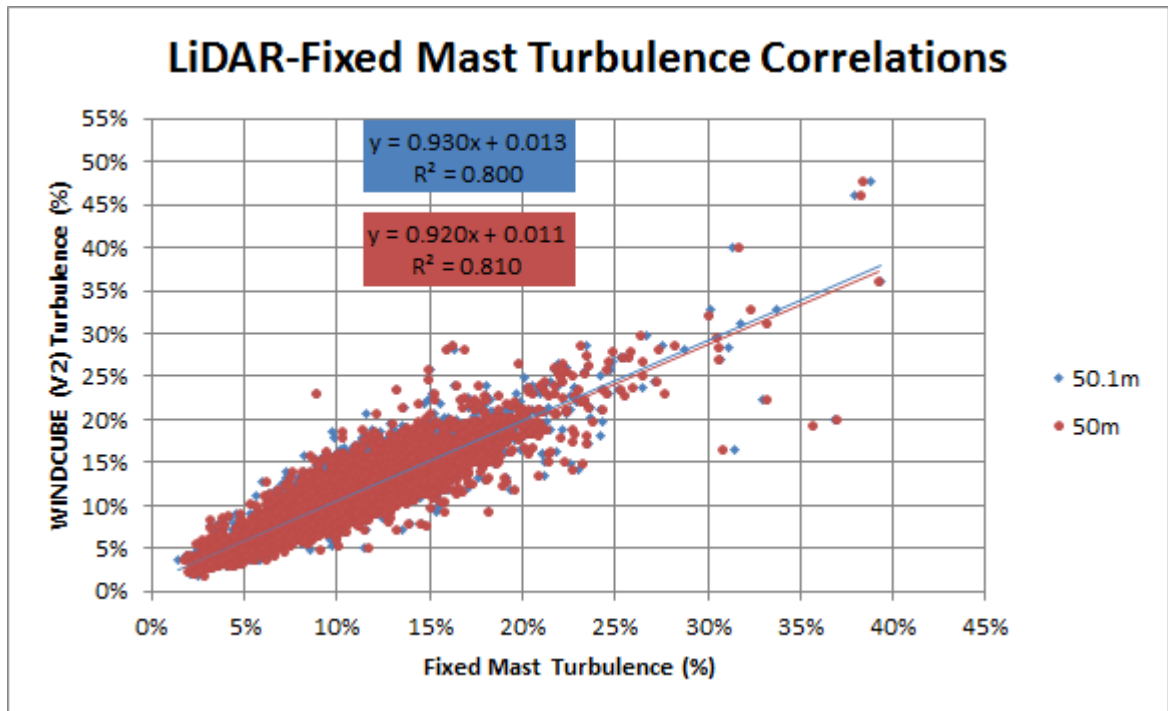


Figure 71.3: Correlation of turbulence between RS device and fixed mast on a moderately complex site.

Notes:

- The data from the 50.1 and 50 m anemometers have been compared with the data from the 50 m WINDCUBE V2 measurement height.
- A tower shadow sector of 60° centred on the boom inverse has been used.
- A $5 \text{ m}\cdot\text{s}^{-1}$ wind speed censor has been applied.
- There is a large amount of scatter and the slopes of the correlations are 7 and 8 % from unity. Nevertheless, there is a clear relationship between the turbulence values from the fixed mast data and those from the WINDCUBE V2 data.

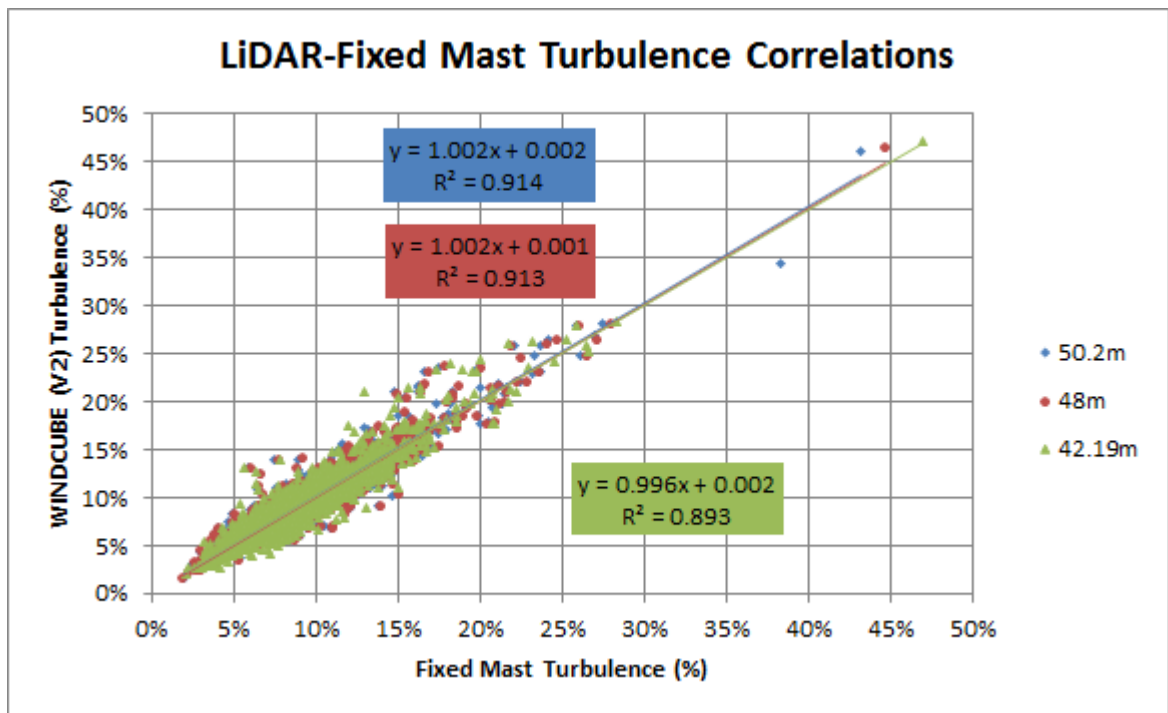


Figure 71.4: Correlation of turbulence between RS device and fixed mast on a moderately complex site.

Notes:

- The data from the 50.2, 48 and 42.19 m anemometers have been compared with the data from the 50, 48 and 42 m WINDCUBE V2 measurement heights.
- A tower shadow sector of 60° centred on the boom inverse has been used.
- A 5 m.s⁻¹ wind speed censor has been applied.
- There is some scatter but the slopes of the correlations are within 1 % of unity and the R² values are very good. There is a very well defined relationship between the turbulence values from the fixed mast data and those from the WINDCUBE V2 data.

APPENDIX 7J - SENSITIVITY ANALYSIS OF THE ICE THROW MODEL

Sensitivity of the ice throw model to

1. Wind Direction
2. Wind Speed
3. Angle of Detachment
4. Rotational Speed
5. Position of Detachment from the Blade

has been assessed via simulation based on 1,000 iterations of the Monte Carlo model for each variable. This validates the model by checking that it responds correctly to each input.

7J.1 WIND DIRECTION

Consider a site with the wind direction rose shown in Figure 7J.1 and with a mean wind speed of approximately 7 ms^{-1} at a hub height of 95 m. Assume that the angle of detachment from the turbine blade is 45° , that the rotational speed is fixed at 14.9 rpm and that the ice detaches from the tip of the blade at 45 m.

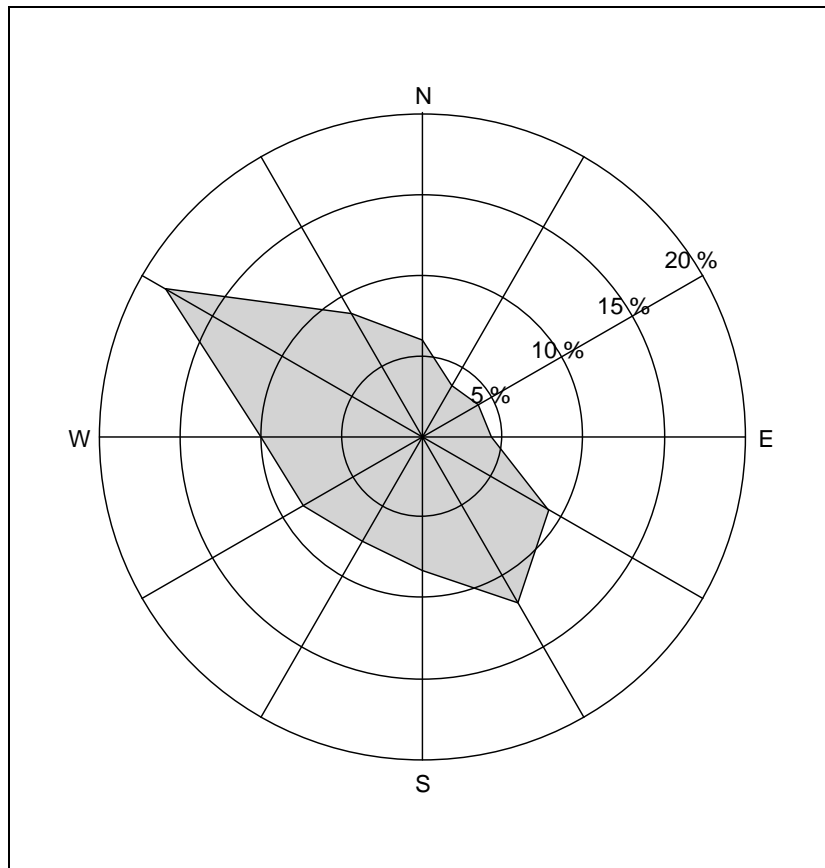


Figure 7J.1: Model validation wind rose.

Then, the distribution of impact locations based on Figure 7J.1 is as per Figure 7J.2. This has been generated by assuming that wind arrives from the centre of a directional sector (giving one landing position per sector). Note that the density plot shown in Figure 7J.2 has smoothed contours for illustration of probability density.

In this illustration the base of the turbine is at position (0,0). For wind from 270° the ice fragment lands in position(61,-99), making an angle of approximately -60° with the horizontal. In other words, the landing position of the ice particles from each directional sector is offset by just under -60° relative to that wind direction. Hence the density of points is also offset by around -60° relative to the wind rose, i.e. the highest density of points relates to the ice being affected by winds from the 300° sector, as expected, but these do not land directly downwind.

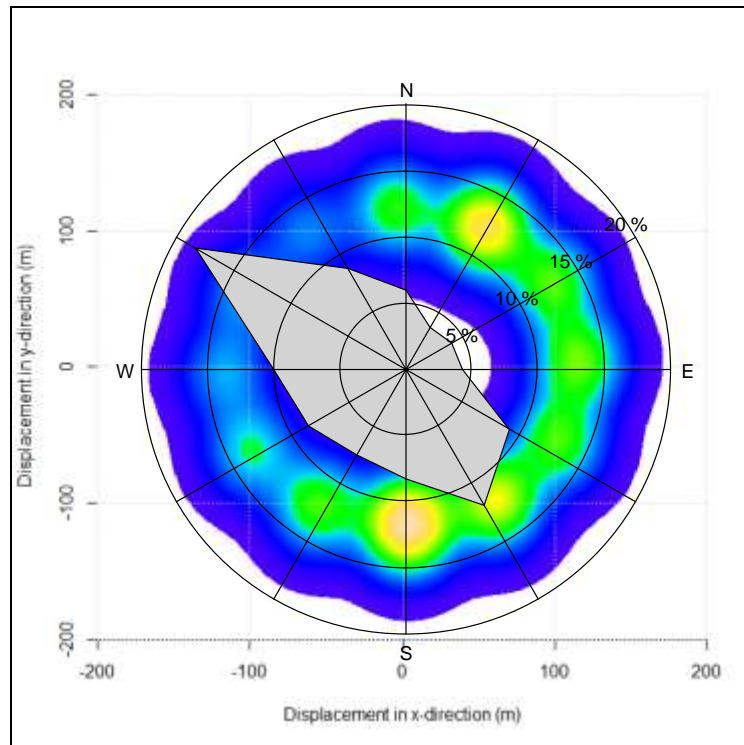


Figure 7J.2: Illustration of landing position when wind direction only varies.

7J.2 WIND SPEED

Now assume that the wind direction is fixed from the 270° sector (chosen for ease of illustration only), and that wind speed in this sector is Weibull-distributed with shape parameter 2.2 and mean 7 ms^{-1} at hub height. Assumptions relating to throw angle, rotational speed, and radial position are fixed at 45° , 14.9 rpm and 45 m, respectively.

The sample of wind speeds simulated for this example is distributed as shown in Figure 7J.1 and a histogram of total displacement from the turbine base as a result of these wind speeds is given in Figure 7J.2. Cut-in and cut-out wind speeds of 4 ms^{-1} and 14 ms^{-1} result in the lower throw distances shown in Figure 7J.4 (corresponding to ice throw when the blades are stationary) whilst the throw distances of 100 m upward correspond to ice thrown when the blades are in motion. Maximum displacement is 156 m.

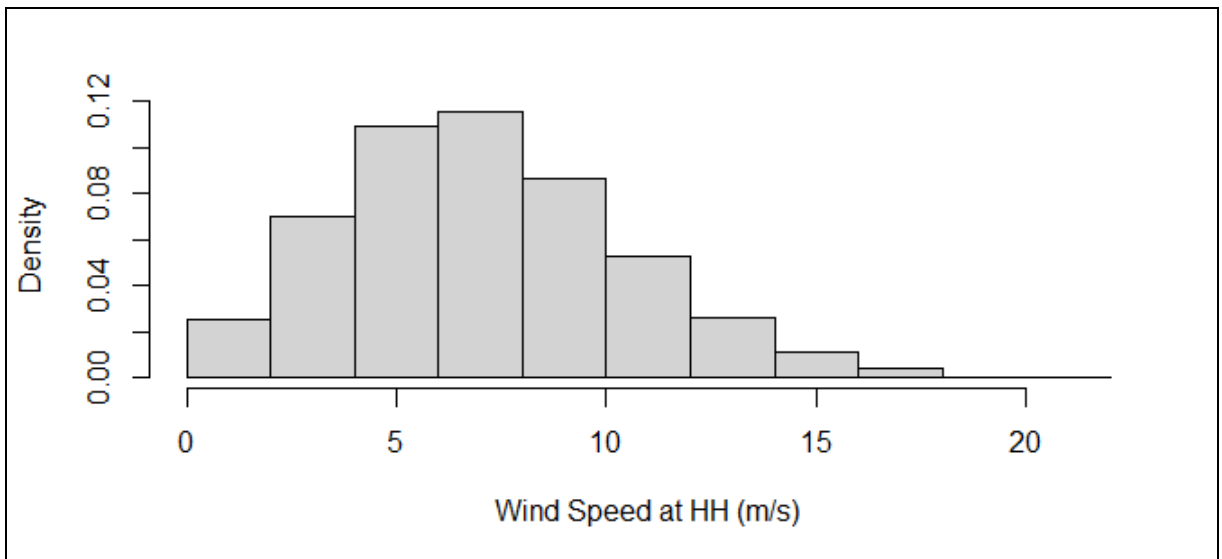


Figure 7J.3: Distribution of wind speeds at hub height.

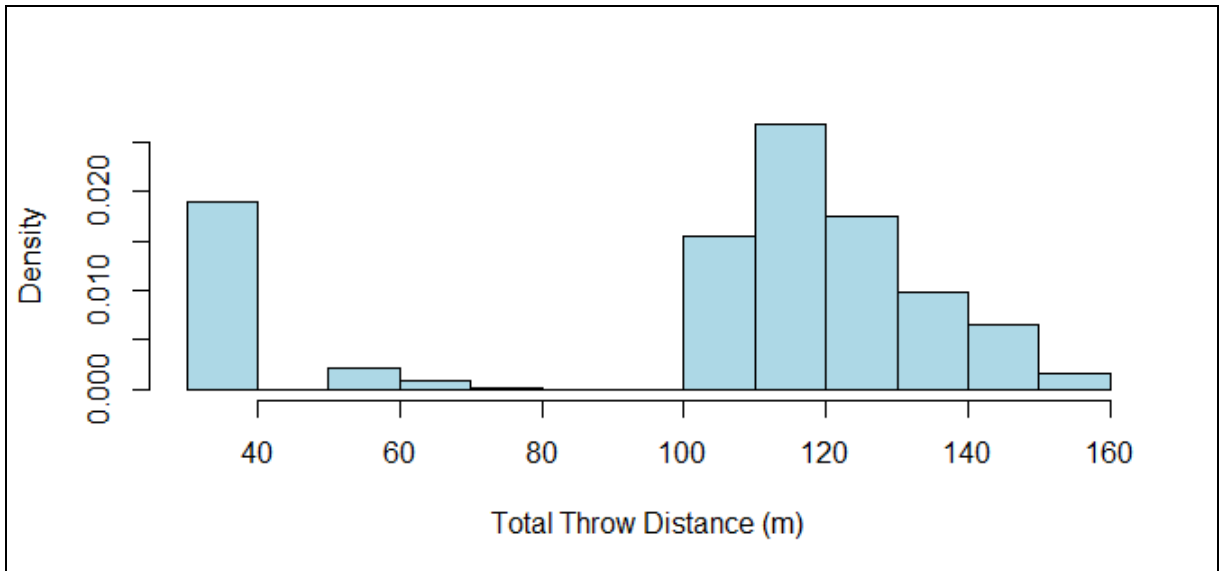


Figure 7J.4: Total displacement.

The relationship between wind speed and throw distance is shown in Figure 7J.3. The steps in the plot at speeds of less than 4 ms^{-1} and greater than 14 ms^{-1} correspond to the cut-in and cut-out speeds of the turbine.

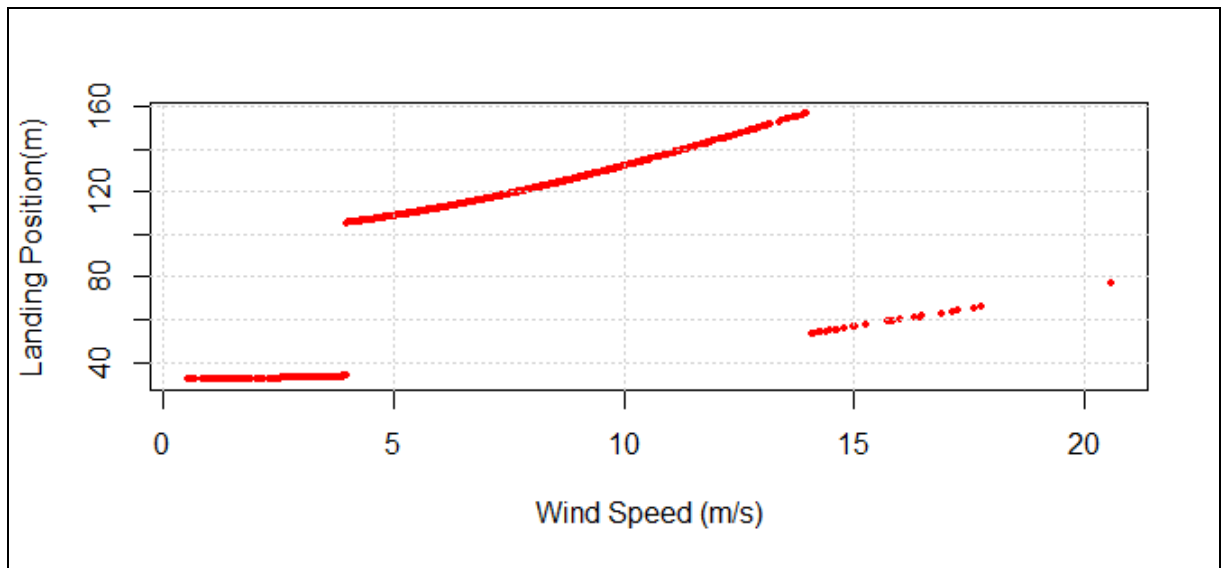


Figure 7J.5: Relationship between wind speed and throw distance.

7J.3 ANGLE OF DETACHMENT

Angles of detachment are assumed to be uniformly distributed around the compass, i.e. detachment from the rotor blade is equally likely at any angle. Angle of detachment is measured relative to the horizontal with the rotor blade rising as per [11].

Given all other parameters take the fixed values used in previous examples, variations in the detachment angle result in the distribution of landing locations shown in Figure 7J.6.

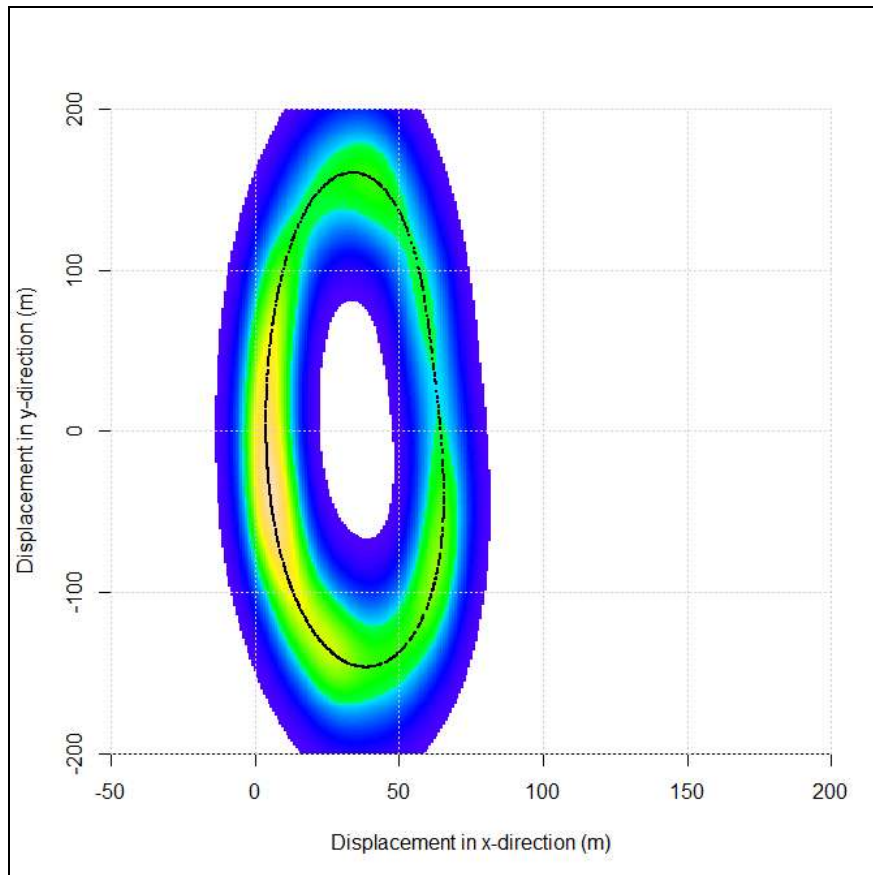


Figure 7J.6: Effect of varying the angle of detachment from the blade.

This shows that there is an area of high density directly under the turbine rotor (which is slightly in front of the tower), and a 'safe area' slightly further out in the x-direction. There is an area of higher density in the negative y-direction than in the positive y-direction due to the rotational direction of the turbine.

7J.4 ROTATIONAL SPEED

The rotational speed of the turbine is assumed to be a function of wind speed as illustrated in Figure 7J.7.

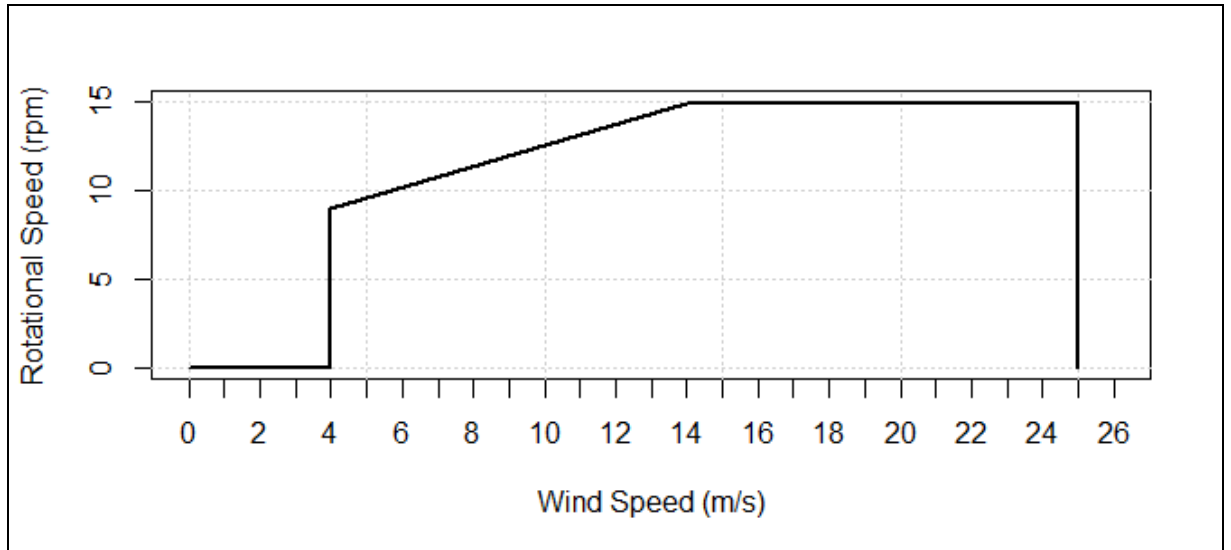


Figure 7J.7: Assumed relationship between rotational speed and wind speed.

This gives a distribution of rotations speeds as per Figure 7J.8. Note the spike at the end, corresponding to a maximum rotor speed of 14.9 rpm, and the observations at a rotor speed of zero, which correspond to turbine cut-in and cut-out.

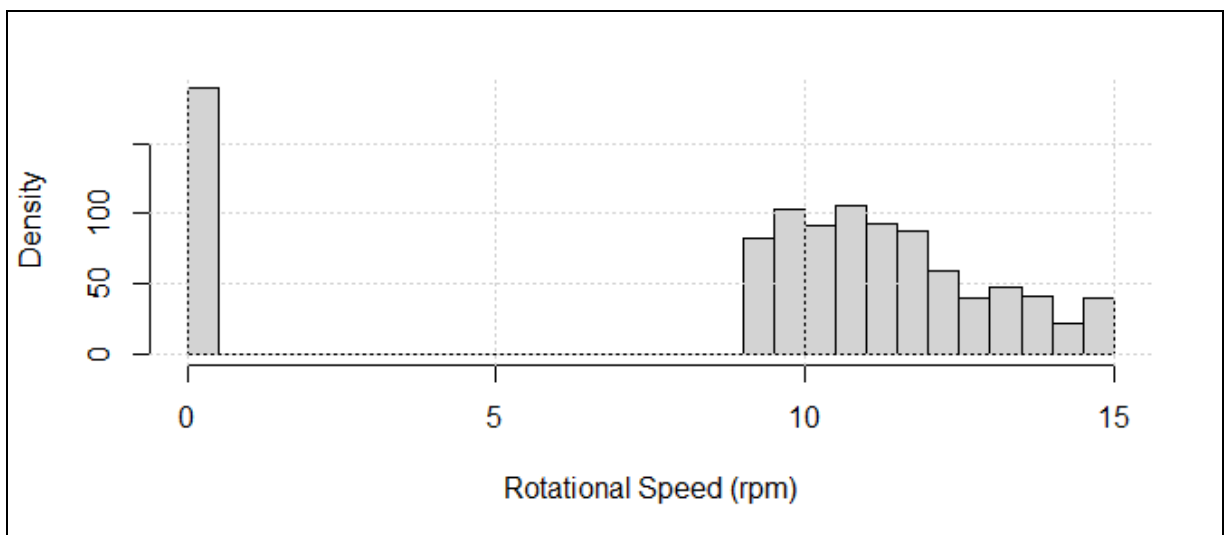


Figure 7J.8: Distribution of variable rotor speed.

This leads to a density of landing positions as shown in Figure 7J.9. This has two areas of high density - one corresponding to ice falling from the blades when not in motion and another which tails off corresponding to the rotor reaching its maximum possible speed before cut-out.

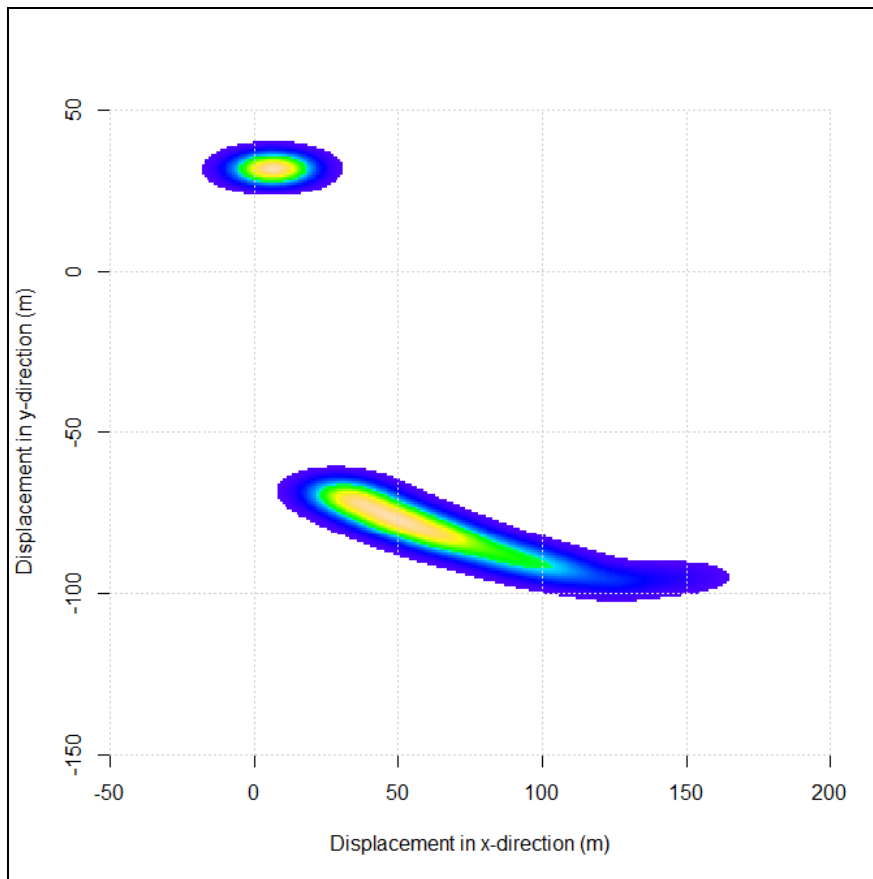


Figure 7J.9: Distribution of impact positions, variable rotor speed.

7J.5 POSITION ALONG BLADE

If the detachment position of the ice along the blade relative to the rotor hub is assumed to be three times more likely at the tip than at the hub as per Figure 7J.10 then this leads to the density of impact locations shown in Figure J7.11.

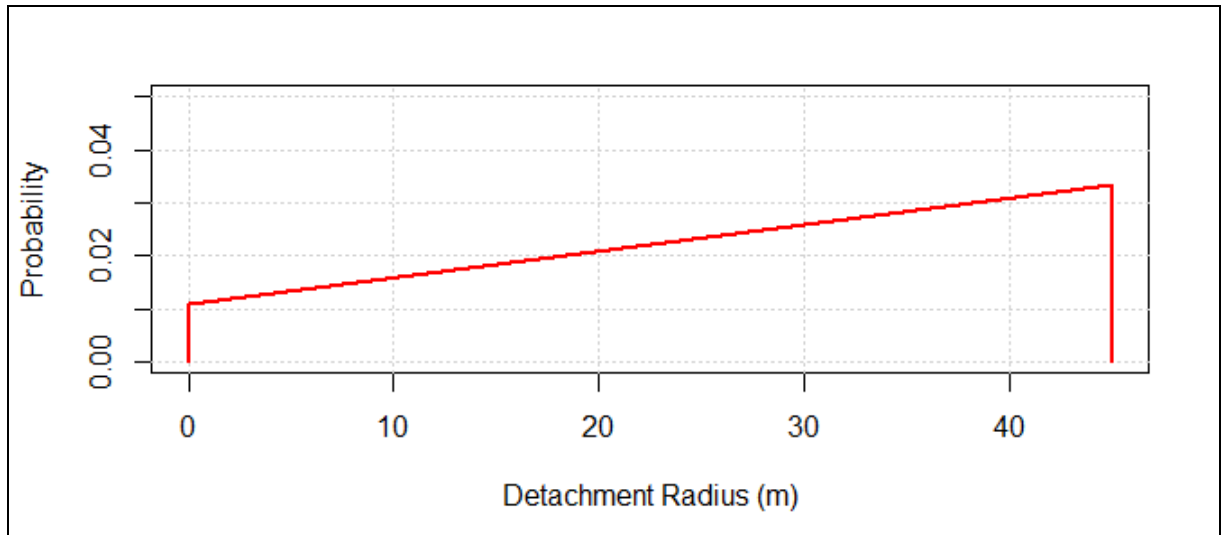


Figure J7.10: Position of detachment along the length of the blade (Radius 45m).

This shows that further displacements are more likely as they correspond to detachment near the top of the blade, which is more probable.

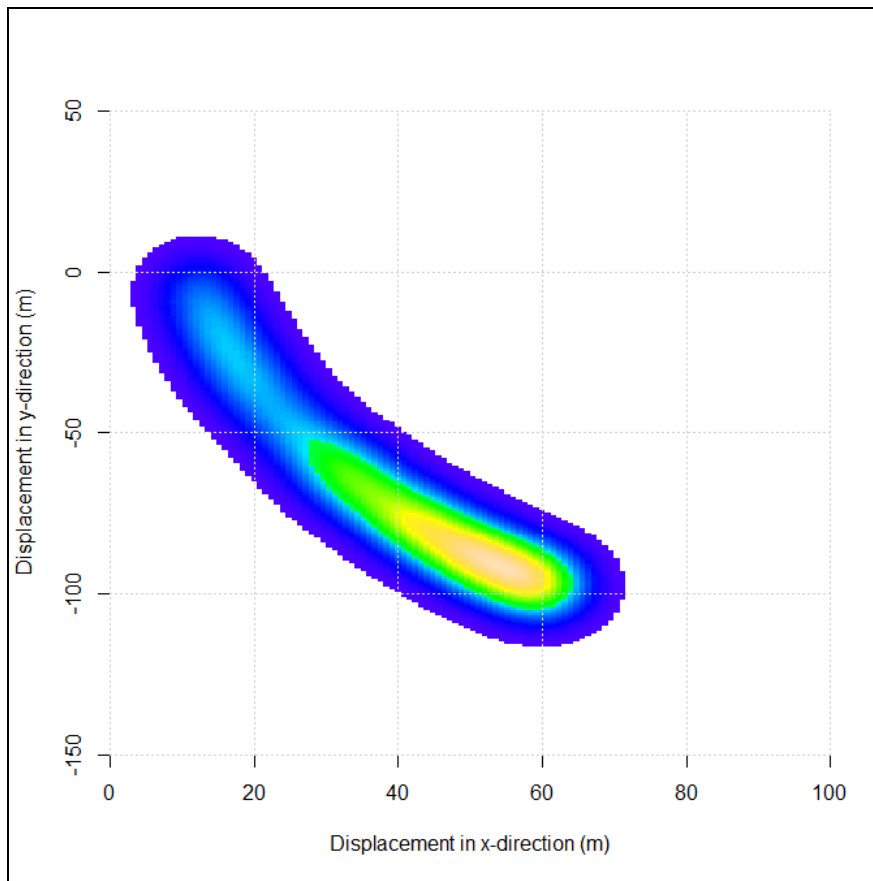


Figure J7.11: Distribution of points of impact with variation in the point of detachment along the blade.

7J.7 SUMMARY

It has been illustrated that the ice throw model works as expected (in terms of the effect of variations in wind direction, wind speed, angle of detachment, rotational speed and release position of ice from the blade). This validates the theoretical aspects of the simulation model being used.

APPENDIX 7K - IEC61400-12-1_DRAFT EQUIVALENT WIND SPEED METHODOLOGY

7K.1 - IEC 61400-12-1,SECTION 8.0 DERIVED RESULTS; SHEAR CORRECTION

19 8.1.2 Shear correction

20 When the wind speed over the turbine rotor is constant with height, the wind speed at hub
21 height is representative of the wind speed over the whole turbine rotor and the use of the hub
22 height wind speed is justified. The assumption of a point wind speed representing the wind
23 speed over the rotor plane can no longer be considered valid for the multi-MW turbines having
24 rotor diameters of the order of 100m or more. It is therefore necessary to define and introduce
25 new parameters which can successfully represent the power curve of a large wind turbine.
26 Such parameters should be able to introduce corrections which account for the wind speed at
27 hub height and the variations of the wind shear over the turbine rotor. In the following, three
28 quantities are defined:

- 29 - The rotor equivalent wind speed
- 30 - The shear correction factor
- 31 - The shear corrected wind speed

32 A power curve based on a wind speed derived from these parameters will have reduced
33 scatter compared to the power curve expressed as a function of the hub height wind speed
34 alone. However data scattering will continue to exist since the ability of the turbine to convert
35 all of the available wind profile kinetic energy may not be the same for all encountered wind
36 profile shapes.

37 8.1.2.1 Wind Shear Exponent

38 The wind shear at a site may be characterized by the wind shear exponent α as calculated by
39 the power law. This parameter is used as a measure of the magnitude of shear for site
40 calibration in Annex C and may be otherwise useful. The power law equation is

$$41 \quad v_z = v_h \left(\frac{z}{H} \right)^\alpha$$

1 Where

2 v_h is the hub height wind speed

3 H is the hub height (m)

4 v_z is the wind speed at height z .

5 α is the wind shear exponent

6 8.1.2.2 Rotor equivalent wind speed

7 The rotor-equivalent wind speed is the wind speed corresponding to the kinetic energy flux
8 through the swept rotor area, when accounting for the vertical shear. For the case that at
9 least three measurement heights are available (see 6.2.2) the rotor equivalent wind speed is
10 defined as

$$11 \quad v_{re} = \left(\sum_{i=1}^n v_i^2 \frac{A_i}{A} \right)^{1/2} \quad (4)$$

12 where

13 n is the number of available measurement heights ($n \geq 3$);

14 v_i is the wind speed measured at height i ;

15 A is the complete area swept by the rotor (i.e. πR^2 with Radius R);

16 A_i is the area of the i th segment, i.e. the segment the wind speed v_i is representative
17 for (refer to 8.1.2.4 for evaluation method).

18 8.1.2.3 Determination of representative rotor segment areas

19 The segments (with areas A_i) shall be chosen in the way that the horizontal separation line
20 between two segments lies exactly in the middle of two measurement points.

21 The segment areas are then derived according to

$$22 \quad A_i = \int_{z_i}^{z_{i+1}} c(z) dz \quad (8)$$

23 where

24 z_i is the height of the i th segment separation line, numbered in the same order as v_i
(either top down or bottom up);

25 $c(z) = 2\sqrt{R^2 - (z - H)^2}$ with R the rotor radius and H the hub height.

26

7K.2 - IEC 61400-12-1, ANNEX Q - DEFINITION OF THE ROTOR EQUIVALENT WIND SPEED UNDER CONSIDERATION OF WIND VEER

1 Q.2 Definition of rotor equivalent wind speed under consideration of wind veer

2 The rotor-equivalent wind speed is the wind speed corresponding to the kinetic energy flux
3 through the swept rotor area, when accounting for the vertical shear and veer. For the case
4 that at least three measurement heights are available (see 6.2.2) the rotor equivalent wind
5 speed is defined as

$$6 \quad v_{re} = \left(\sum_{i=1}^n (v_i \cos(\phi_i))^2 \frac{A_i}{A} \right)^{1/2} \quad (Q.1)$$

7 where

8 n is the number of available measurement heights ($n \geq 3$);

9 v_i is the wind speed measured at height i ;

10 ϕ_i is the angle difference between the wind direction at hub height and segment i

11 A is the complete area swept by the rotor (i.e. πR^2 with Radius R);

12 A_i is the area of the i^{th} segment, i.e. the segment the wind speed v_i is representative for
13 (refer to 8.1.2.2 for evaluation method).

14 Q.3 Measurement of wind veer

15 The rotor equivalent wind speed as defined in formula Q.1 is influenced by the difference of
16 wind direction measurements at various heights relative to hub height. In order to provide
17 accurate measurements of the difference of wind directions, it is important to measure the
18 wind directions at the different height levels with the same type of sensor, i.e. either with one
19 remote sensing device at all heights, or with sensors on the mast at all heights.

APPENDIX 7L - TIME-SERIES COMPARISONS FOR 27 NOVEMBER 2011



Figure 7L.1: Wind speed time-series for 27th November 2012 at M6261, 87m AGL. Comparison between measured data and CFD.

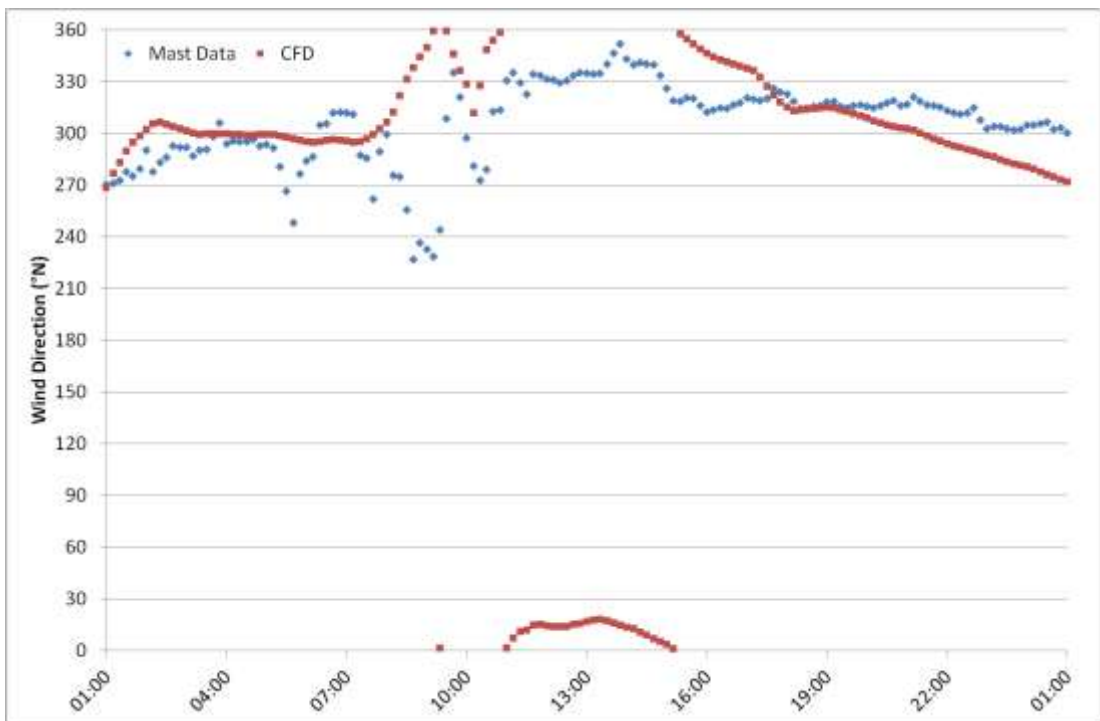


Figure 7L.2: Wind direction time-series for 27th November 2012 at M6261, 85m AGL. Comparison between measured data and CFD.



Figure 7L.3: Potential temperature gradient time-series for 27th November 2011 at M6261, taken between 90m and 10m AGL. Comparison between measured data and CFD.

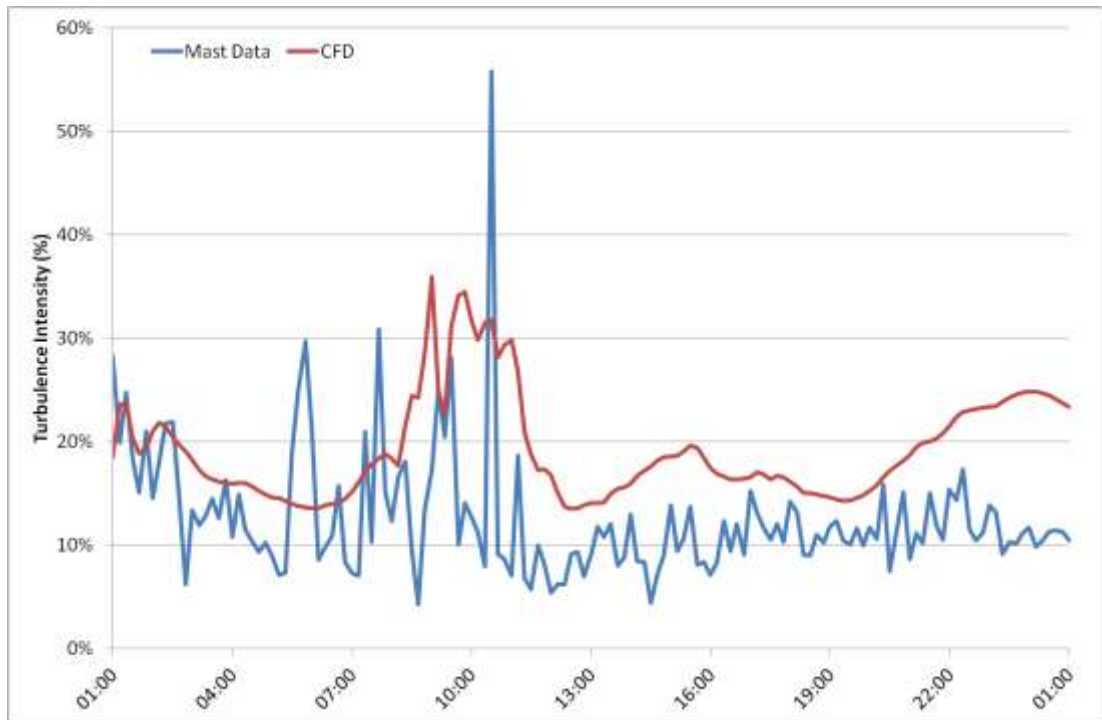


Figure 7L.4: Turbulence intensity time-series for 27th November 2012 at M6261, 87m AGL. Comparison between measured data and CFD.

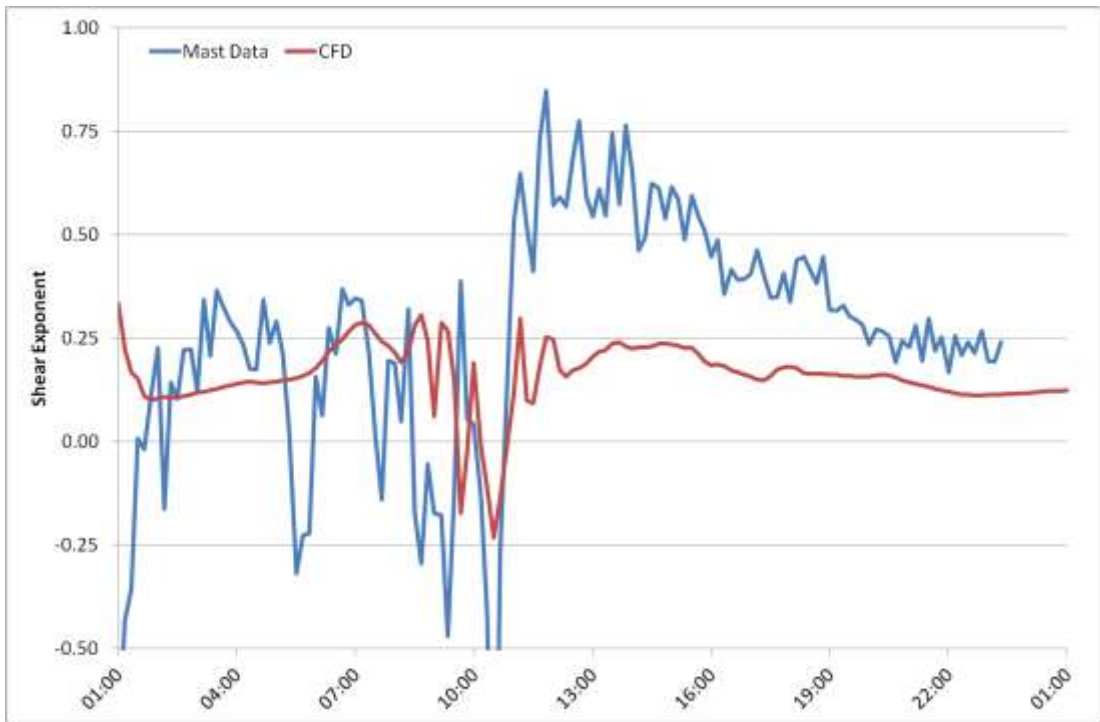


Figure 7L.5: Shear exponent time-series for 27th November 2011 at M6261, taken between 73m and 50m AGL. Comparison between measured data and CFD.

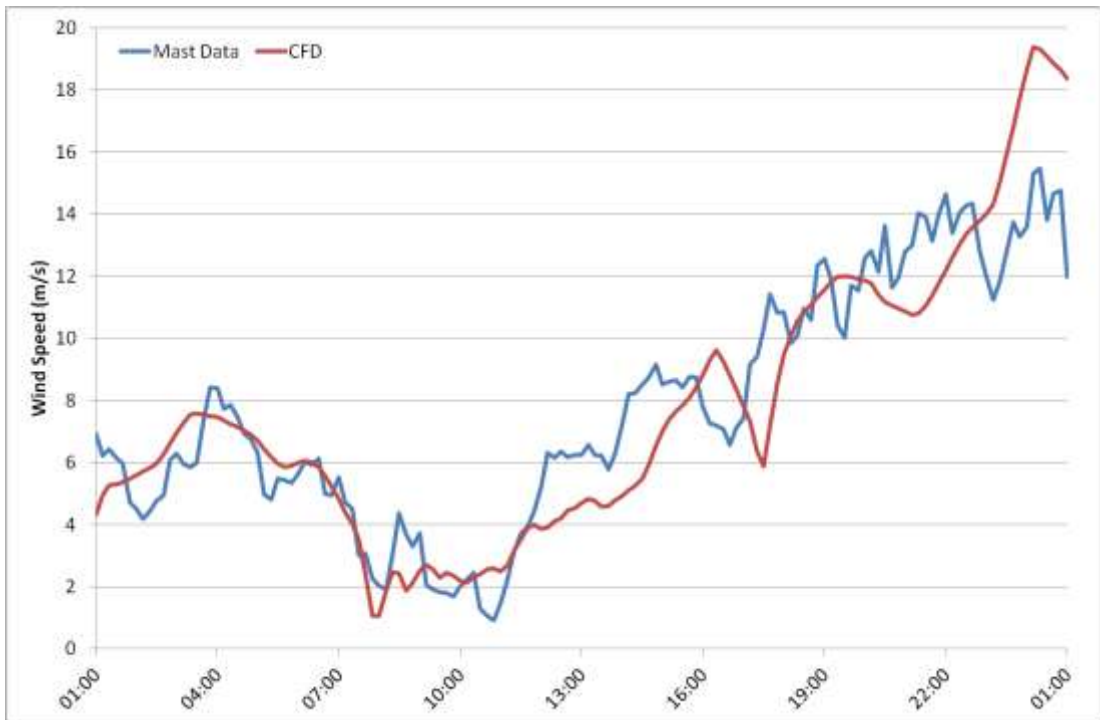


Figure 7L.6: Wind speed time-series for 27th November 2012 at M6282, 87m AGL. Comparison between measured data and CFD.



Figure 7L.7: Wind direction time-series for 27th November 2012 at M6282, 85m AGL. Comparison between measured data and CFD.



Figure 7L.8: Potential temperature gradient time-series for 27th November 2011 at M6282, taken between 90m and 10m AGL. Comparison between measured data and CFD.

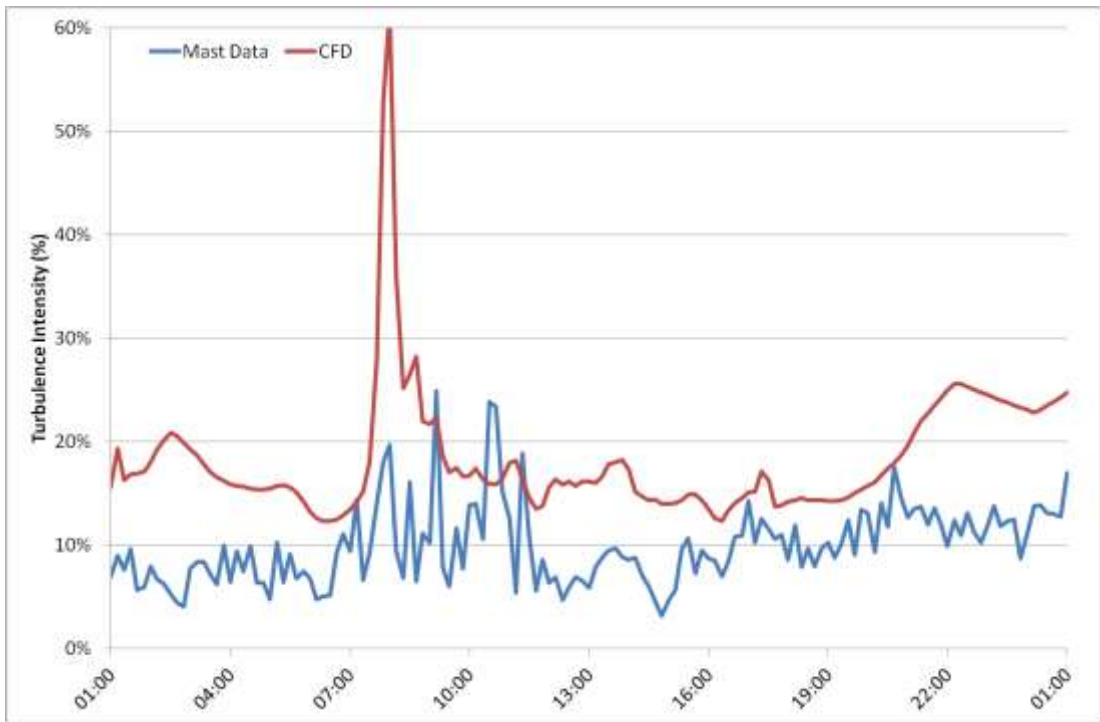


Figure 7L.9: Turbulence intensity time-series for 27th November 2012 at M6282, 87m AGL. Comparison between measured data and CFD.



Figure 7L.10: Shear exponent time-series for 27th November 2011 at M6282, taken between 73m and 50m AGL. Comparison between measured data and CFD.

APPENDIX 7M - TIME-SERIES COMPARISONS FOR 31 DECEMBER 2011



Figure 7M.1: Wind speed time-series for 31st December 2012 at M6261, 87m AGL. Comparison between measured data and CFD.

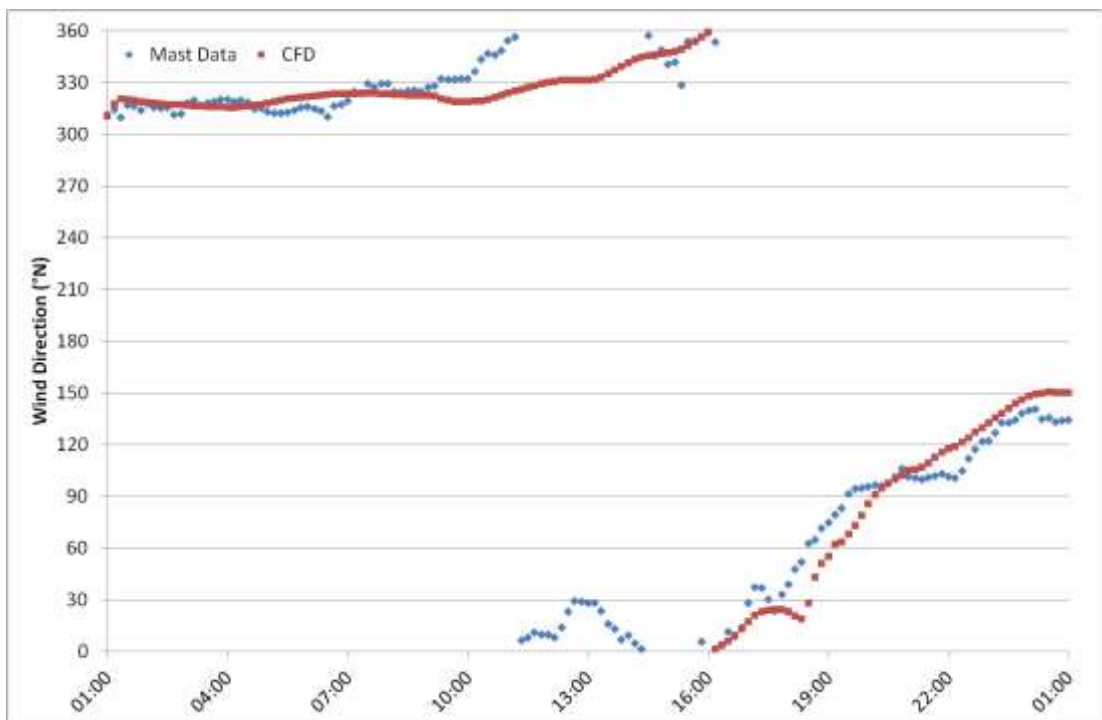


Figure 7M.2: Wind direction time-series for 31st December 2012 at M6261, 85m AGL. Comparison between measured data and CFD.



Figure 7M.3: Potential temperature gradient time-series for 31st December 2011 at M6261, taken between 90m and 10m AGL. Comparison between measured data and CFD.



Figure 7M.4: Turbulence intensity time-series for 31st December 2012 at M6261, 87m AGL. Comparison between measured data and CFD.

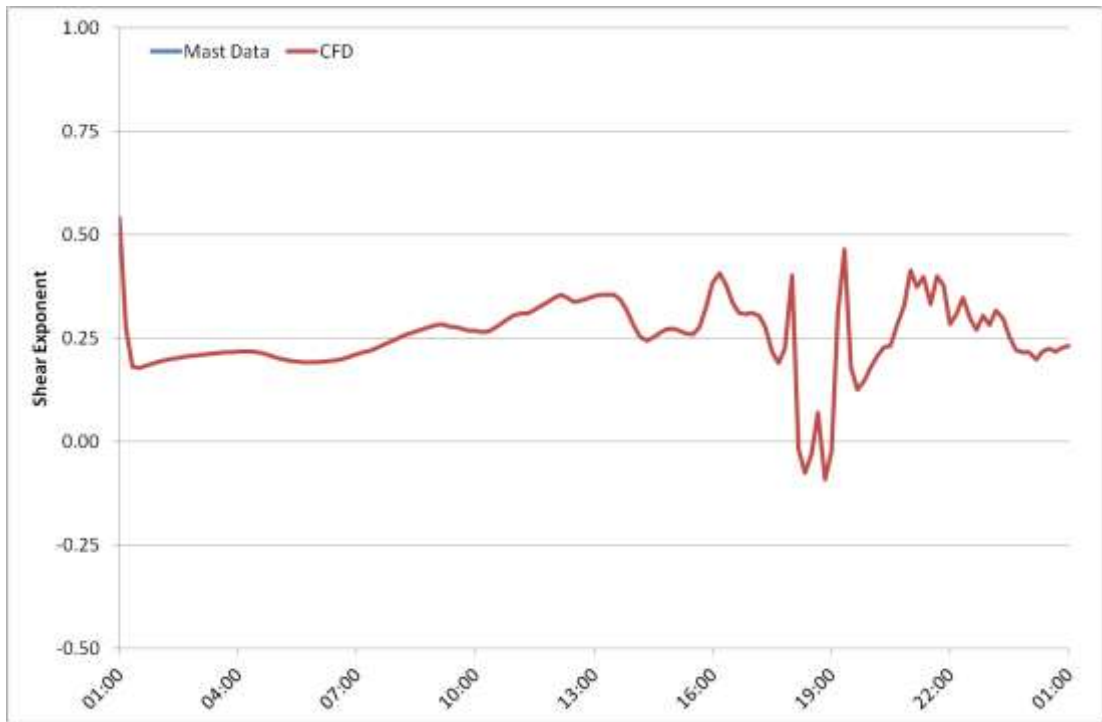


Figure 7M.5: Shear exponent time-series for 31st December 2011 at M6261, taken between 73m and 50m AGL. CFD only, no measured data available for comparison.



Figure 7M.6: Wind speed time-series for 31st December 2012 at M6282, 87m AGL. Comparison between measured data and CFD.

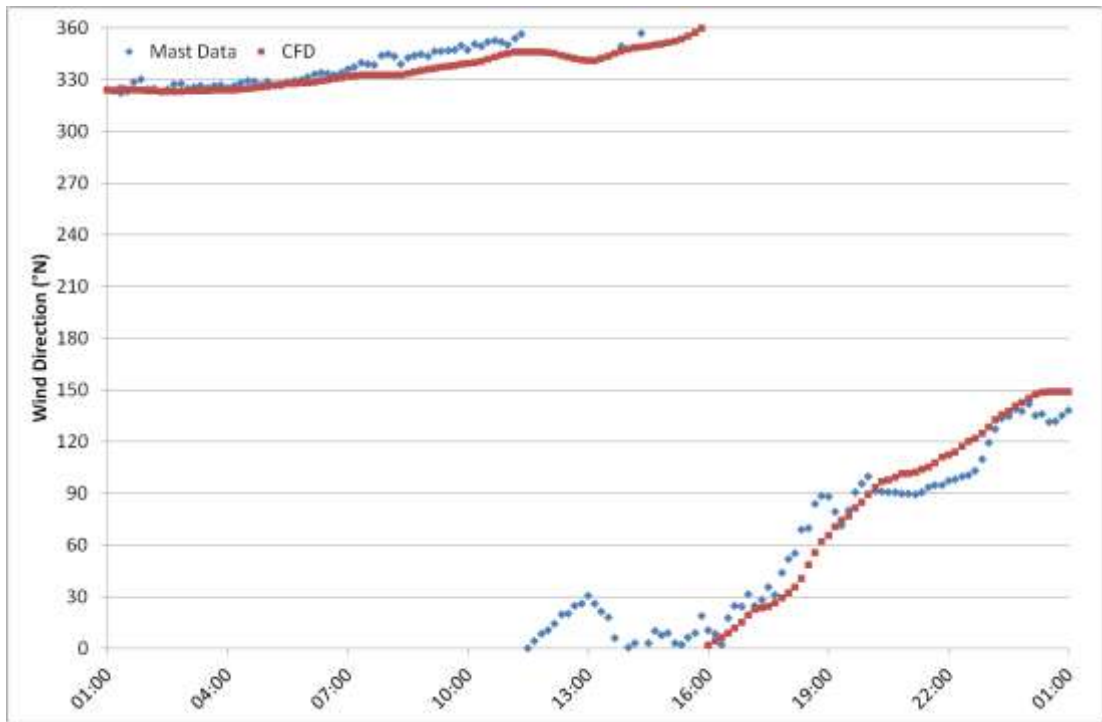


Figure 7M.7: Wind direction time-series for 31st December 2012 at M6282, 85m AGL. Comparison between measured data and CFD.

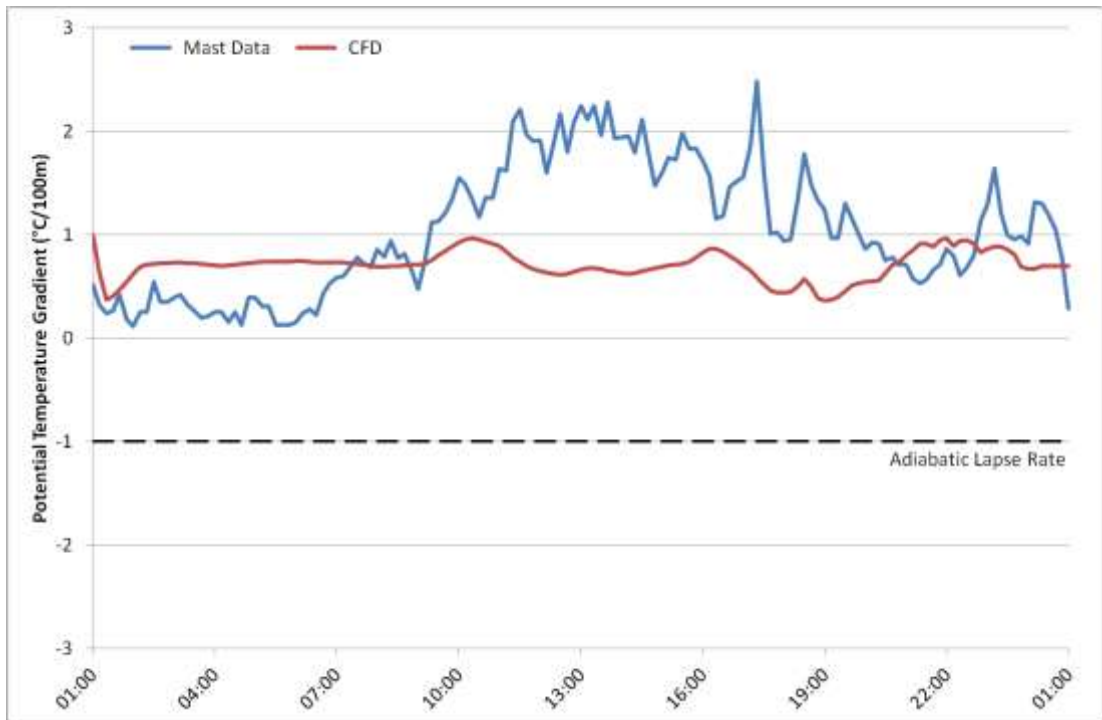


Figure 7M.8: Potential temperature gradient time-series for 31st December 2011 at M6282, taken between 90m and 10m AGL. Comparison between measured data and CFD.

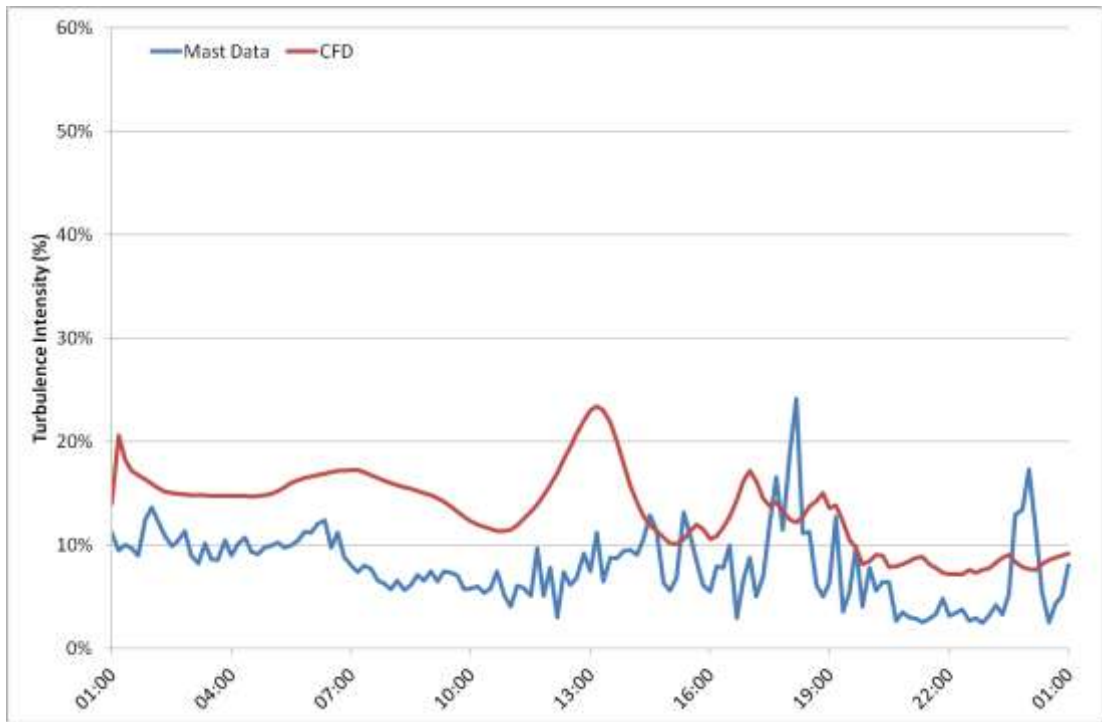


Figure 7M.9: Turbulence intensity time-series for 31st December 2012 at M6282, 87m AGL. Comparison between measured data and CFD.



Figure 7M.10: Shear exponent time-series for 31st December 2011 at M6282, taken between 73m and 50m AGL. Comparison between measured data and CFD.

APPENDIX 7N - TIME-SERIES COMPARISONS FOR 16 JANUARY 2012



Figure 7N.1: Wind speed time-series for 16th January 2012 at M6261, 87m AGL. Comparison between measured data and CFD.



Figure 7N.2: Wind direction time-series for 16th January 2012 at M6261, 85m AGL. Comparison between measured data and CFD.



Figure 7N.3: Potential temperature gradient time-series for 16th January 2011 at M6261, taken between 90m and 10m AGL. Comparison between measured data and CFD.

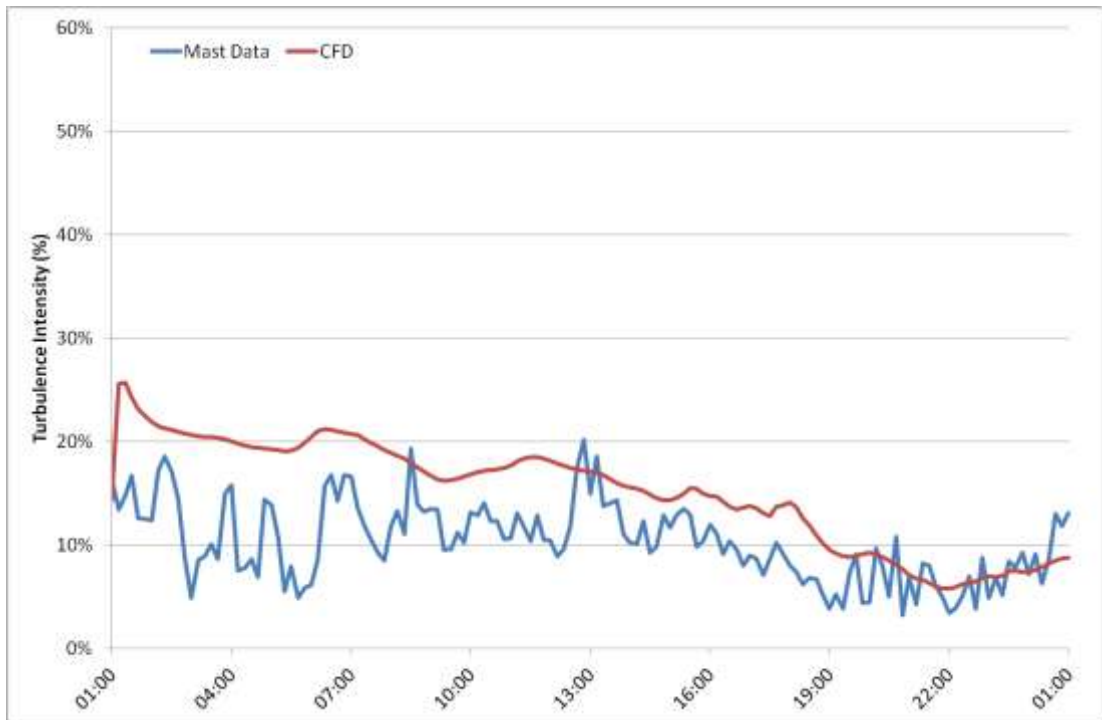


Figure 7N.4: Turbulence intensity time-series for 16th January 2012 at M6261, 87m AGL. Comparison between measured data and CFD.

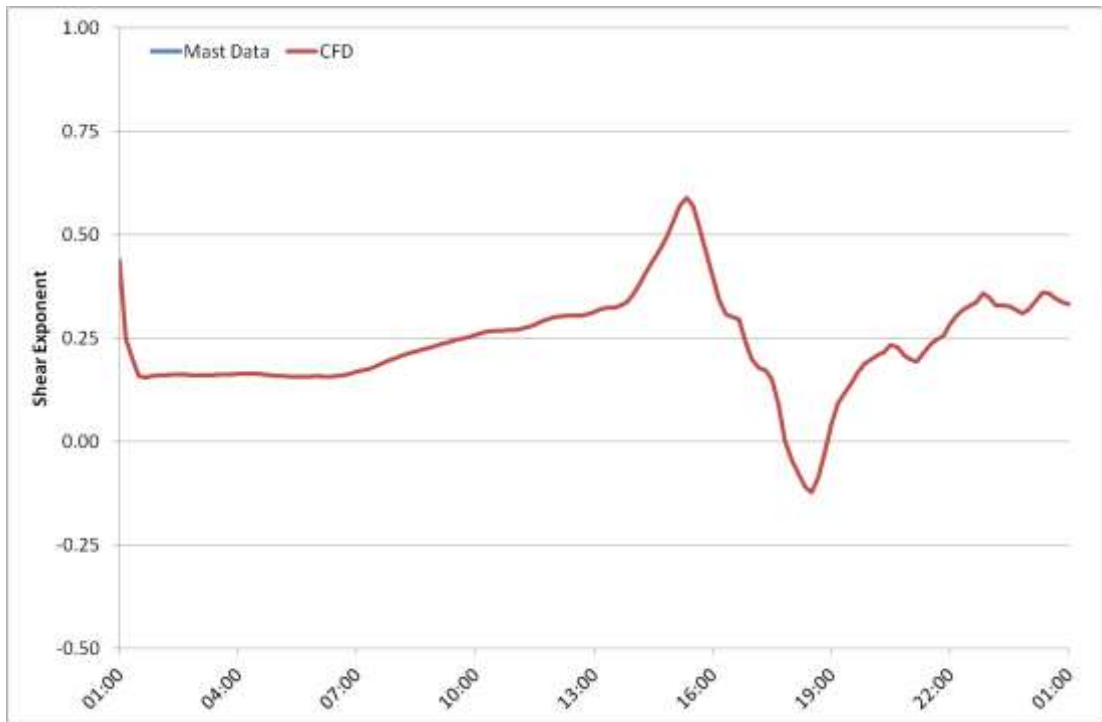


Figure 7N.5: Shear exponent time-series for 16th January 2011 at M6261, taken between 73m and 50m AGL. CFD only, no measured data available for comparison.

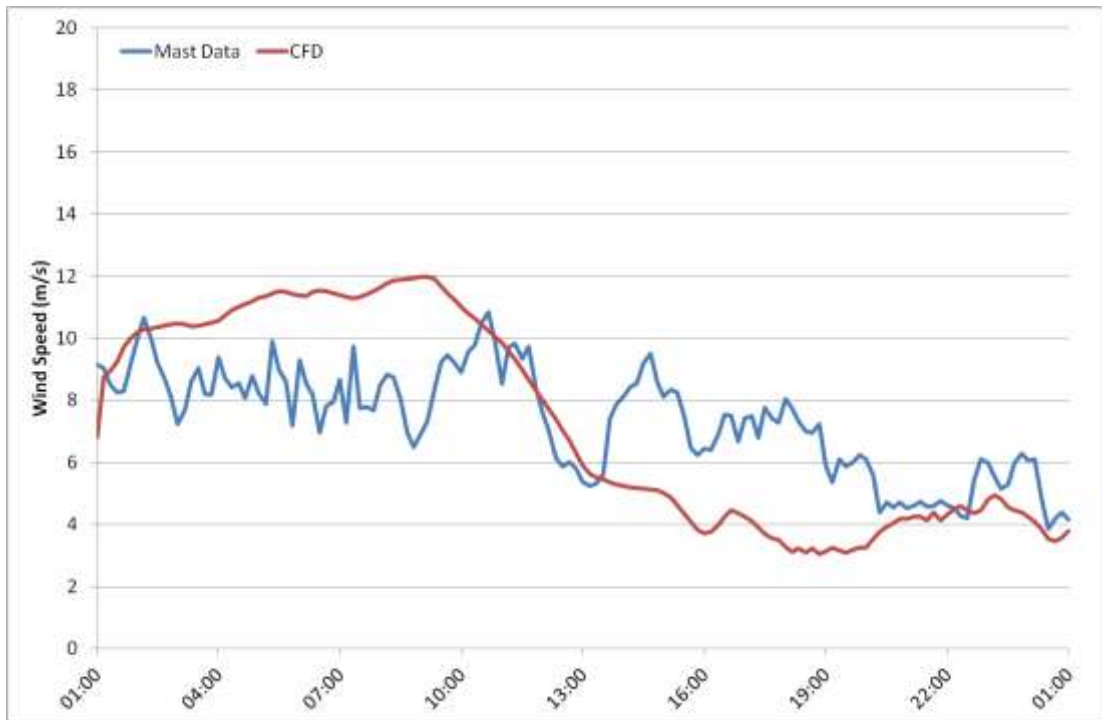


Figure 7N.6: Wind speed time-series for 16th January 2012 at M6282, 87m AGL. Comparison between measured data and CFD.



Figure 7N.7: Wind direction time-series for 16th January 2012 at M6282, 85m AGL. Comparison between measured data and CFD.



Figure 7N.8: Potential temperature gradient time-series for 16th January 2011 at M6282, taken between 90m and 10m AGL. Comparison between measured data and CFD.

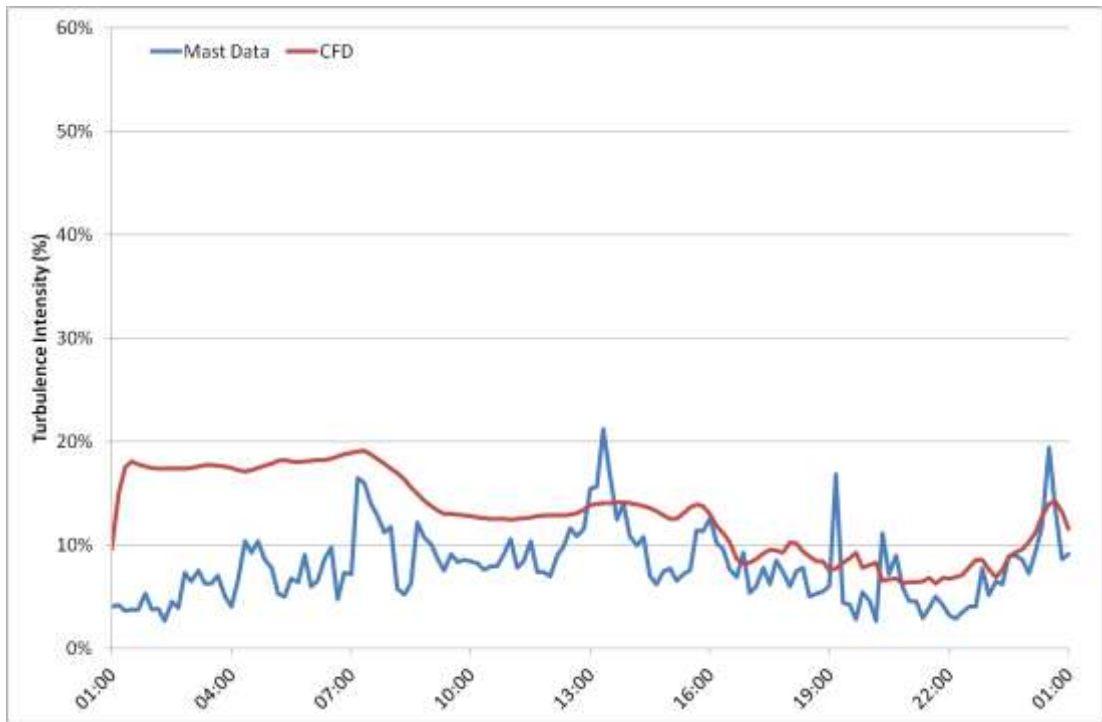


Figure 7N.9: Turbulence intensity time-series for 16th January 2012 at M6282, 87m AGL. Comparison between measured data and CFD.

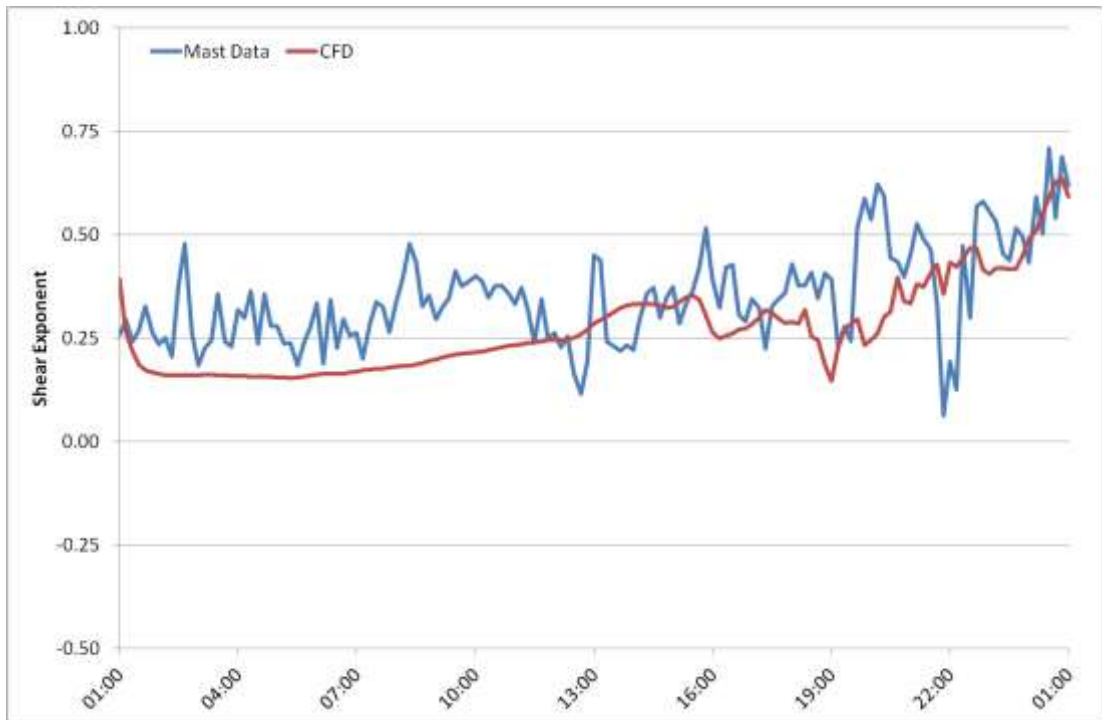


Figure 7N.10: Shear exponent time-series for 16th January 2011 at M6282, taken between 73m and 50m AGL. Comparison between measured data and CFD.

APPENDIX 70 - TIME-SERIES COMPARISONS FOR 17 FEBRUARY 2012

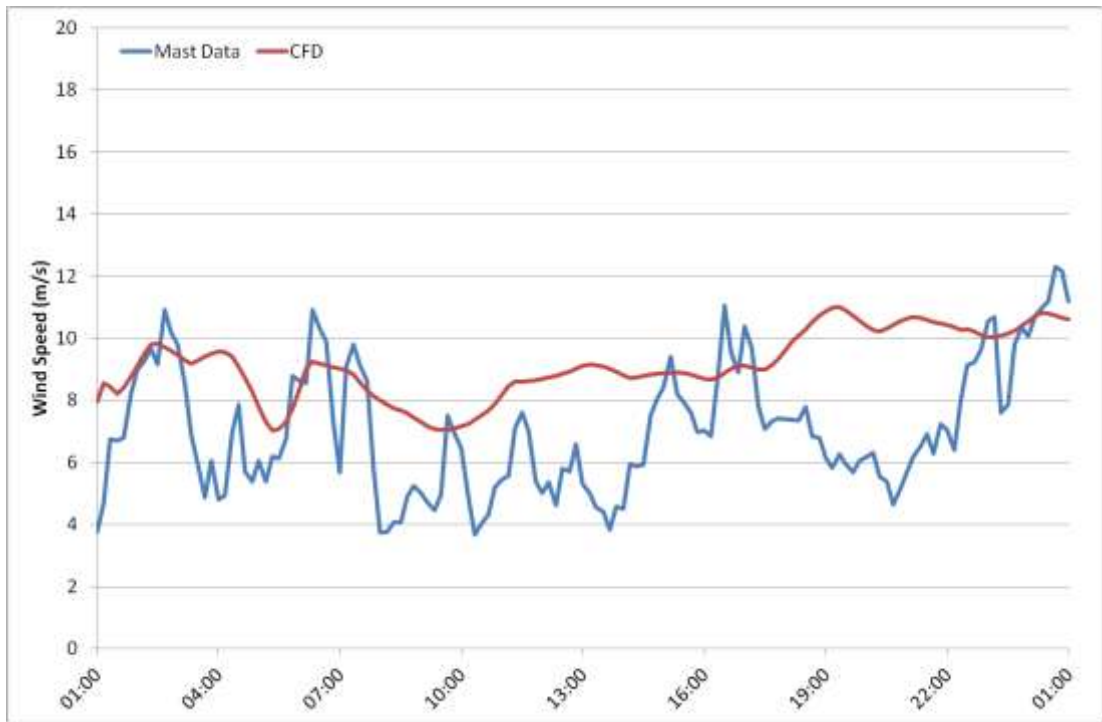


Figure 70.1: Wind speed time-series for 17th February 2012 at M6261, 87m AGL. Comparison between measured data and CFD.



Figure 70.2: Wind direction time-series for 17th February 2012 at M6261, 85m AGL. Comparison between measured data and CFD.



Figure 70.3: Potential temperature gradient time-series for 17th February 2011 at M6261, taken between 90m and 10m AGL. Comparison between measured data and CFD.

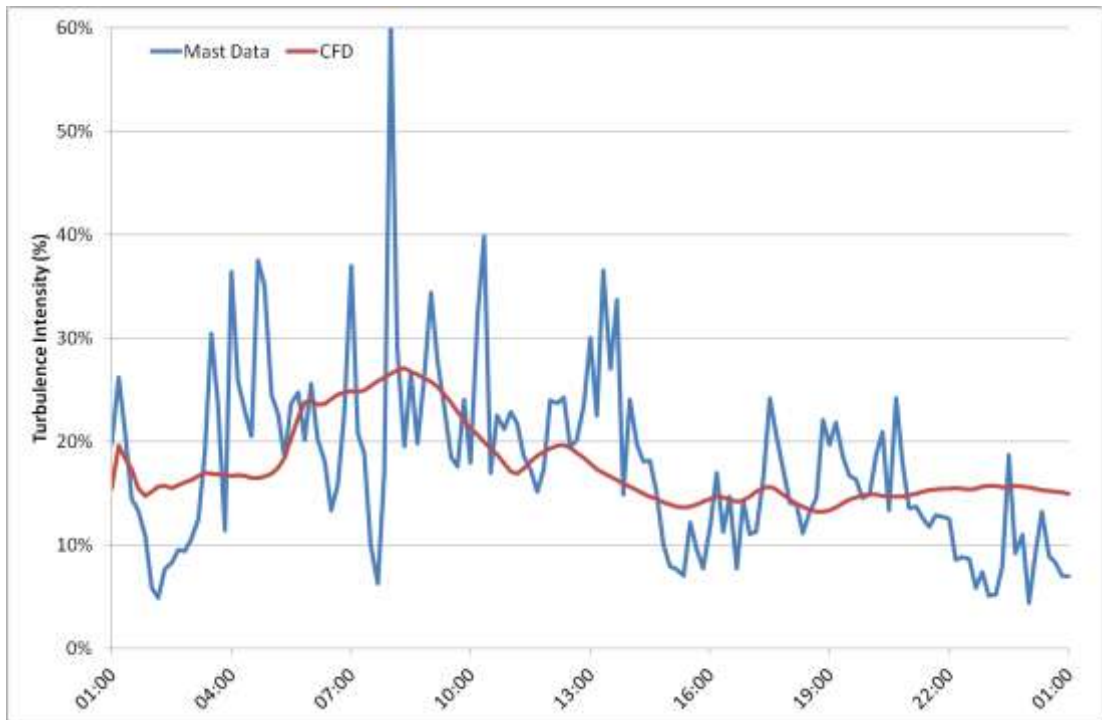


Figure 70.4: Turbulence intensity time-series for 17th February 2012 at M6261, 87m AGL. Comparison between measured data and CFD.



Figure 70.5: Shear exponent time-series for 17th February 2011 at M6261, taken between 73m and 50m AGL. CFD only, no measured data available for comparison.

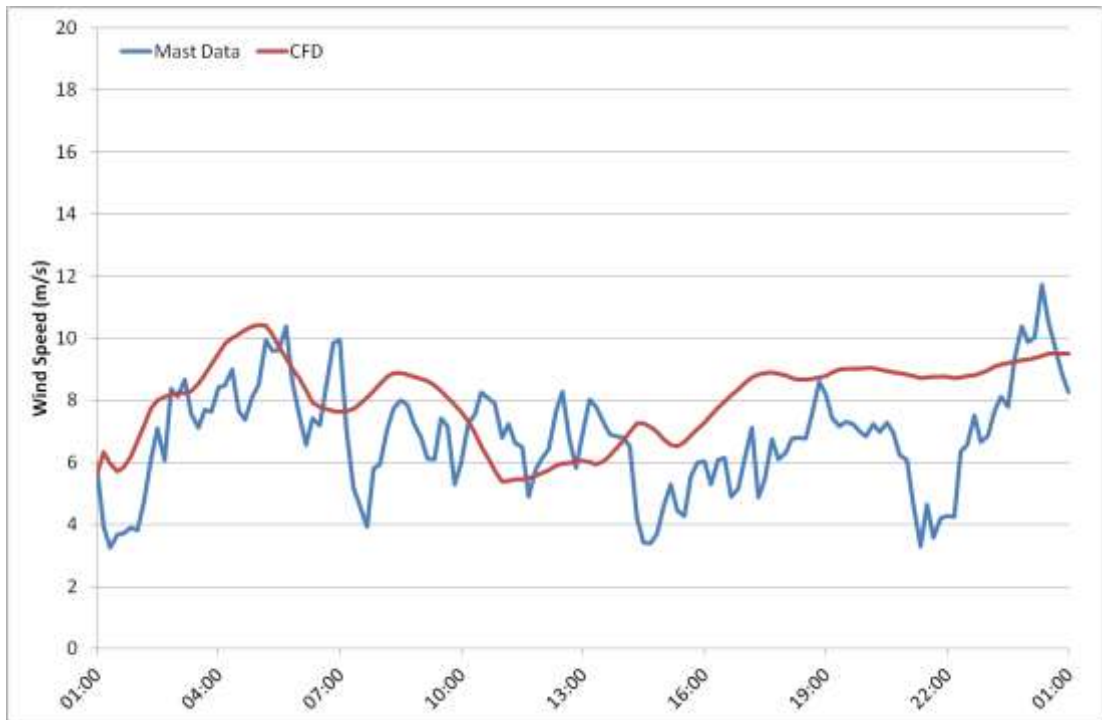


Figure 70.6: Wind speed time-series for 17th February 2012 at M6282, 87m AGL. Comparison between measured data and CFD.



Figure 70.7: Wind direction time-series for 17th February 2012 at M6282, 85m AGL. Comparison between measured data and CFD.

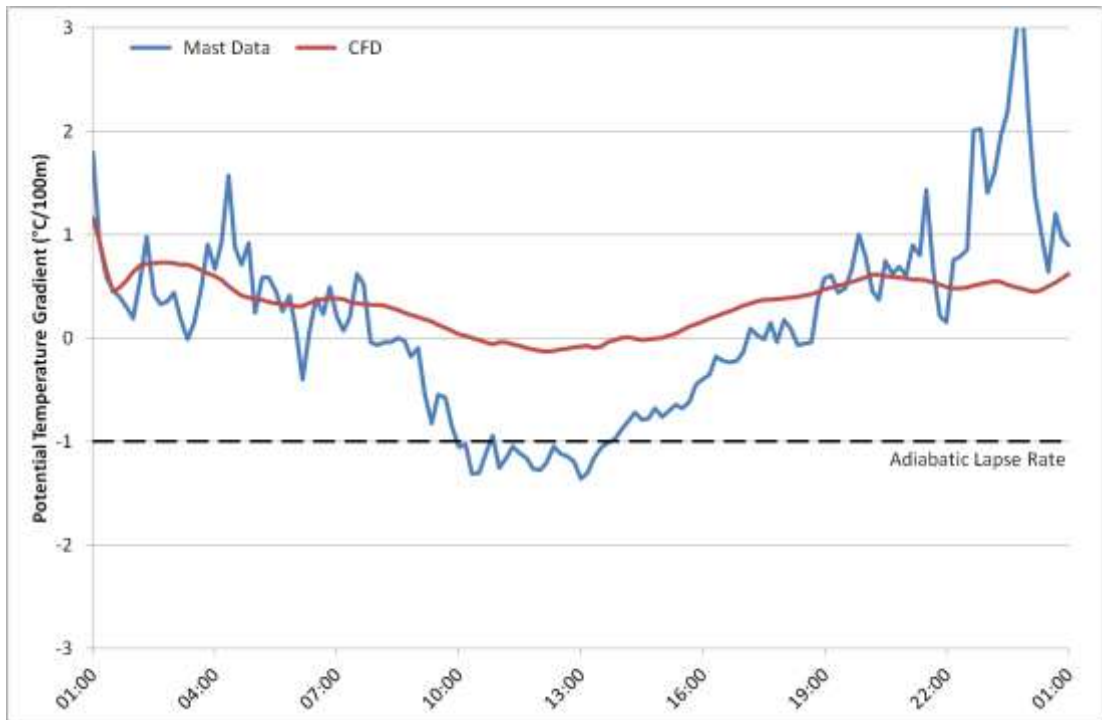


Figure 70.8: Potential temperature gradient time-series for 17th February 2011 at M6282, taken between 90m and 10m AGL. Comparison between measured data and CFD.

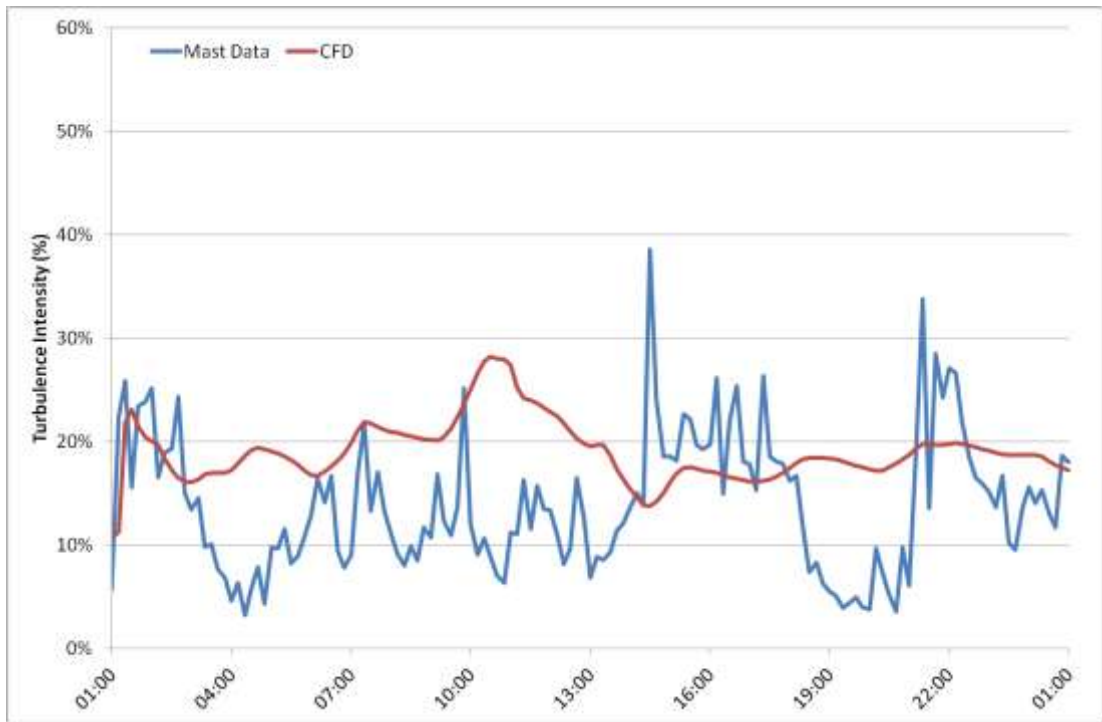


Figure 70.9: Turbulence intensity time-series for 17th February 2012 at M6282, 87m AGL. Comparison between measured data and CFD.

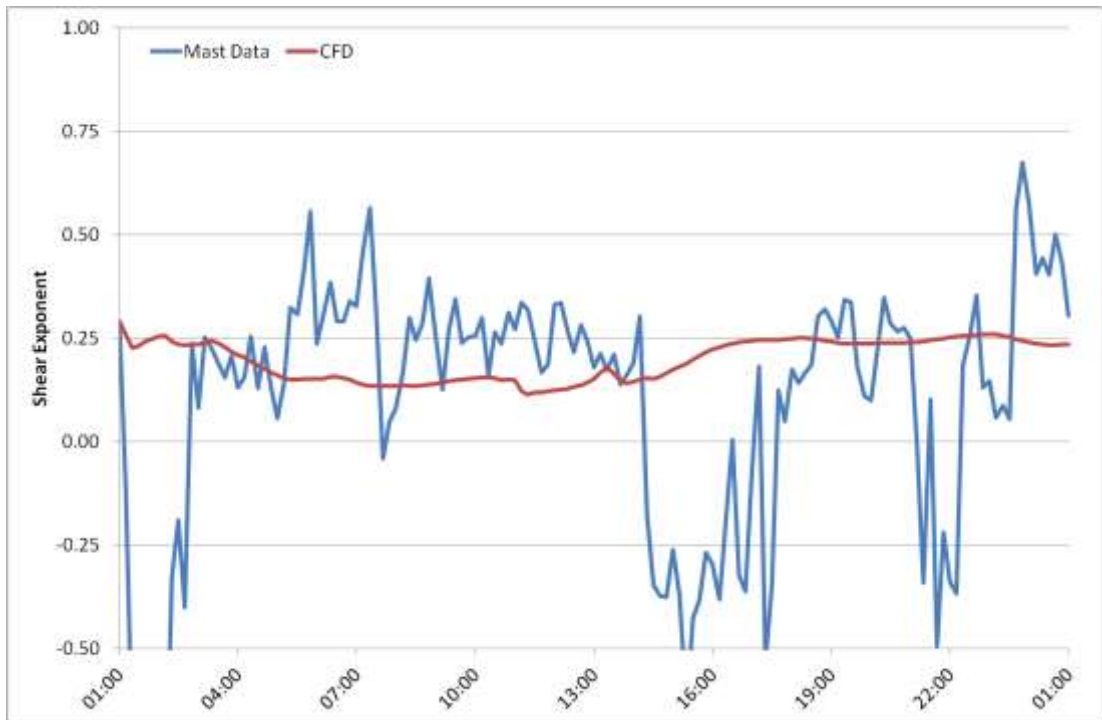


Figure 70.10: Shear exponent time-series for 17th February 2011 at M6282, taken between 73m and 50m AGL. Comparison between measured data and CFD.

APPENDIX 7P - TIME-SERIES COMPARISONS FOR 20 FEBRUARY 2012



Figure 7P.1: Wind speed time-series for 20th February 2012 at M6261, 87m AGL. Comparison between measured data and CFD.

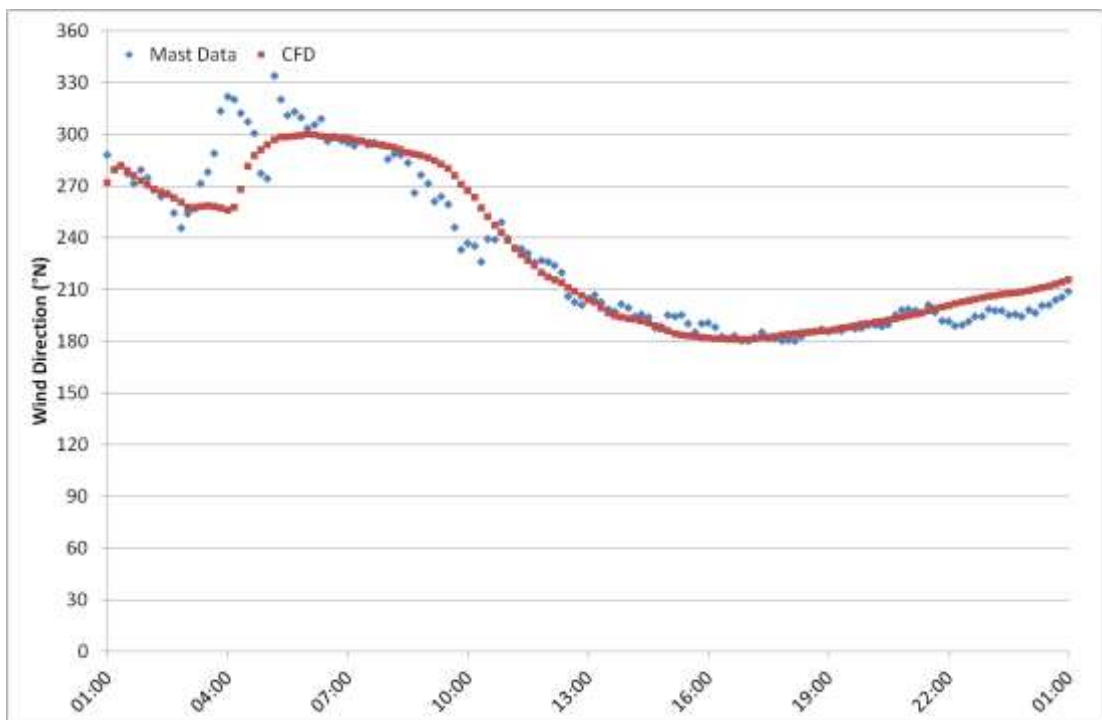


Figure 7P.2: Wind direction time-series for 20th February 2012 at M6261, 85m AGL. Comparison between measured data and CFD.

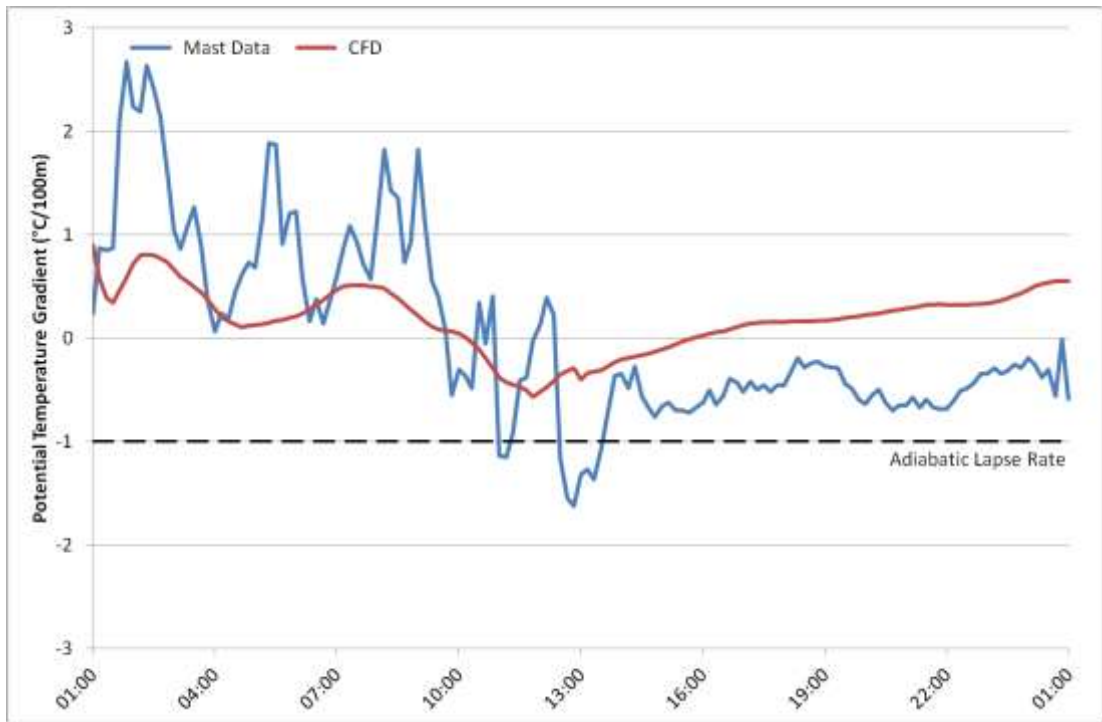


Figure 7P.3: Potential temperature gradient time-series for 20th February 2011 at M6261, taken between 90m and 10m AGL. Comparison between measured data and CFD.

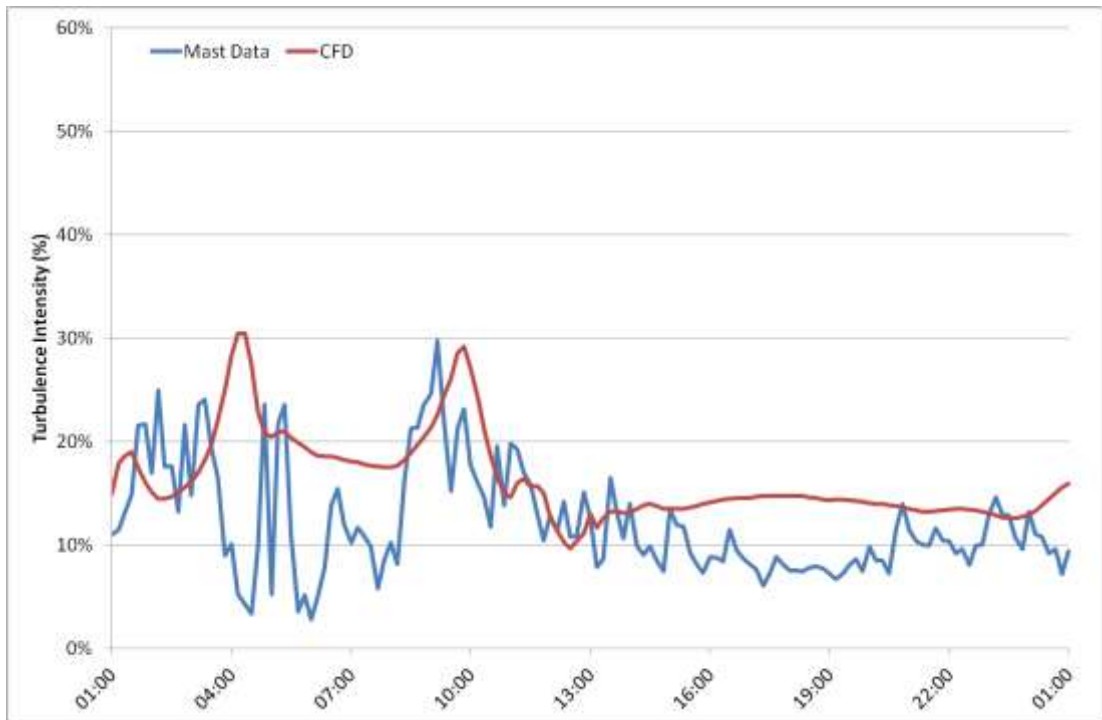


Figure 7P.4: Turbulence intensity time-series for 20th February 2012 at M6261, 87m AGL. Comparison between measured data and CFD.

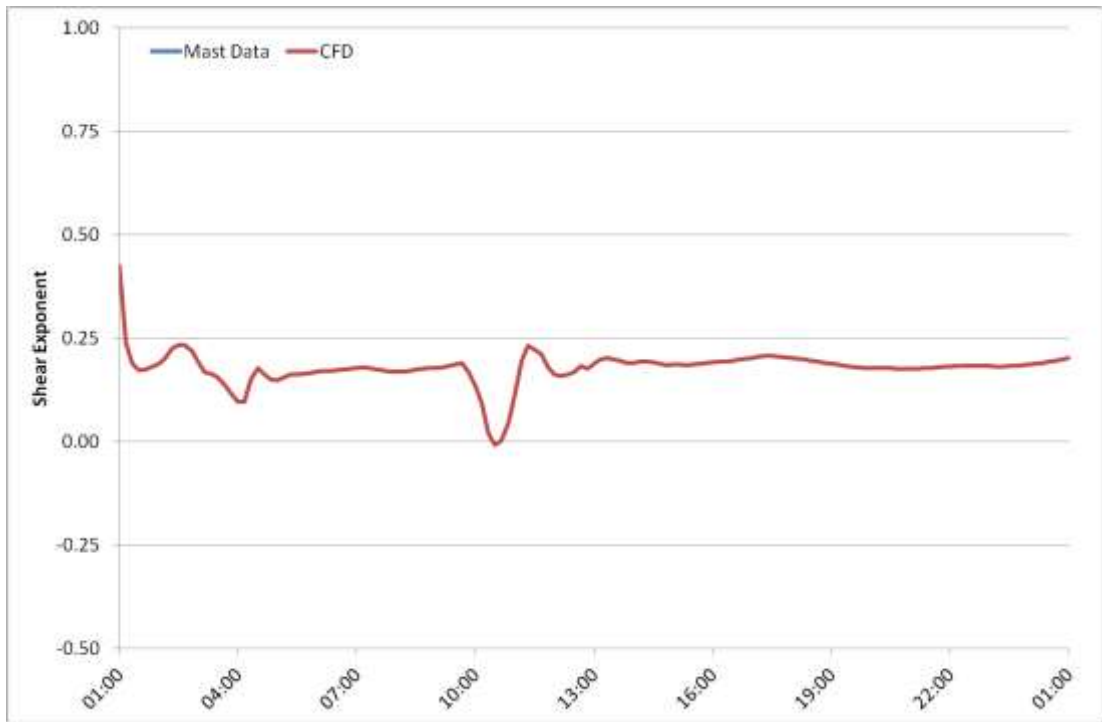


Figure 7P.5: Shear exponent time-series for 20th February 2011 at M6261, taken between 73m and 50m AGL. CFD only, no measured data available for comparison.



Figure 7P.6: Wind speed time-series for 20th February 2012 at M6282, 87m AGL. Comparison between measured data and CFD.

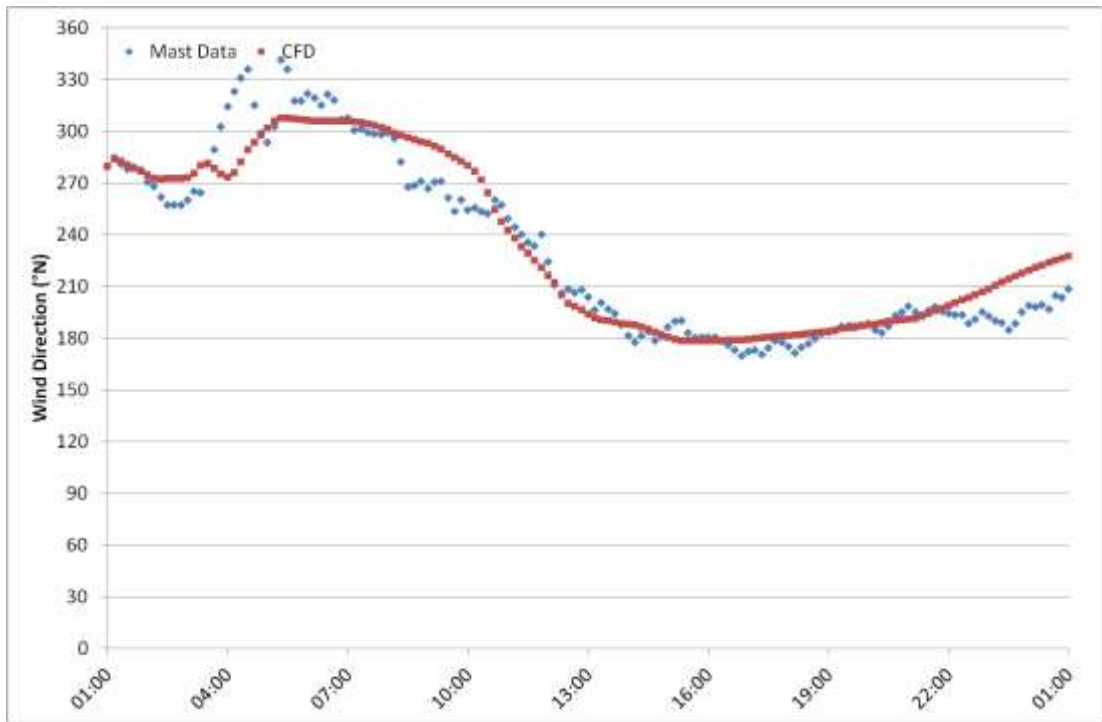


Figure 7P.7: Wind direction time-series for 20th February 2012 at M6282, 85m AGL. Comparison between measured data and CFD.

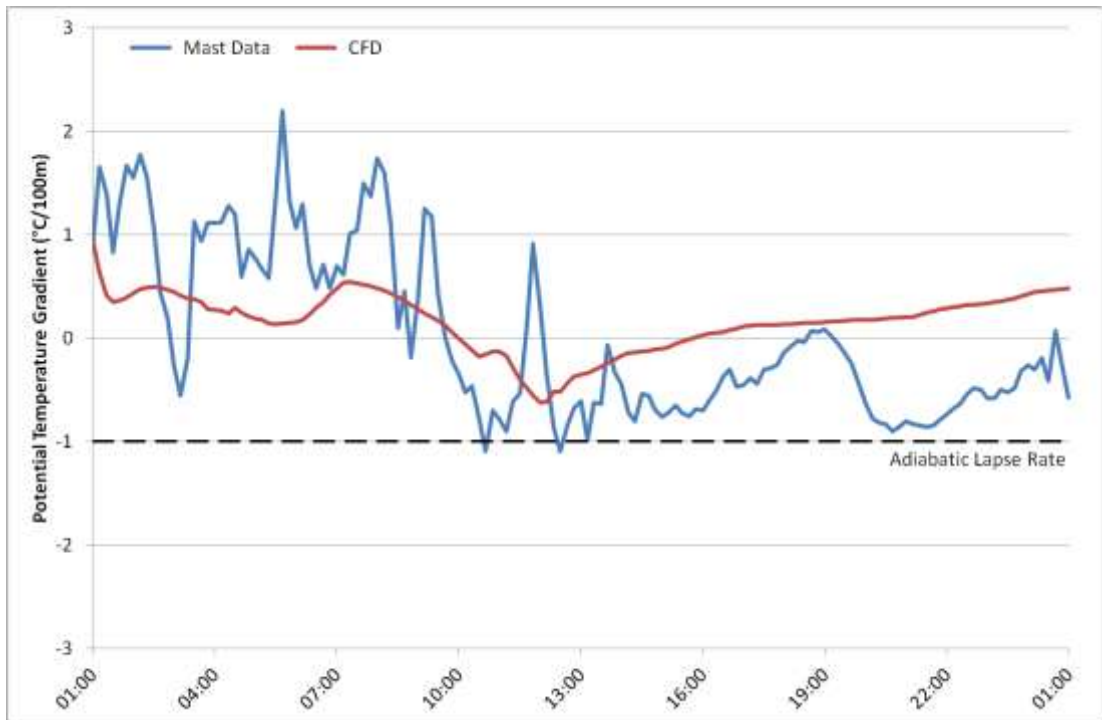


Figure 7P.8: Potential temperature gradient time-series for 20th February 2011 at M6282, taken between 90m and 10m AGL. Comparison between measured data and CFD.

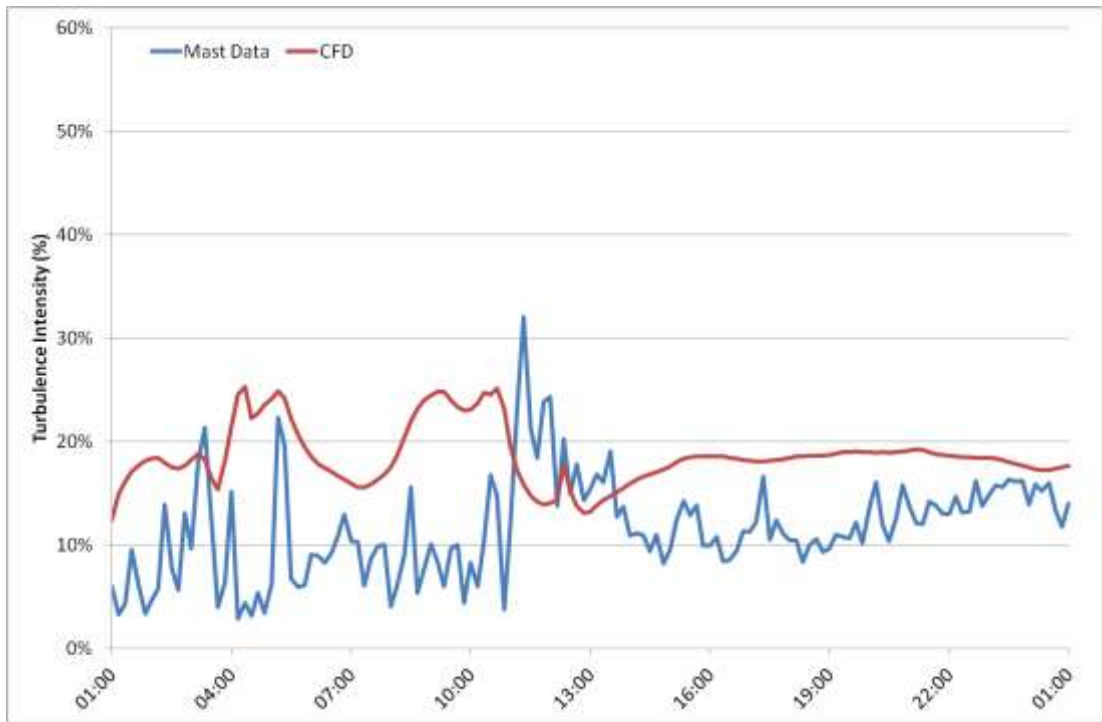


Figure 7P.9: Turbulence intensity time-series for 20th February 2012 at M6282, 87m AGL. Comparison between measured data and CFD.

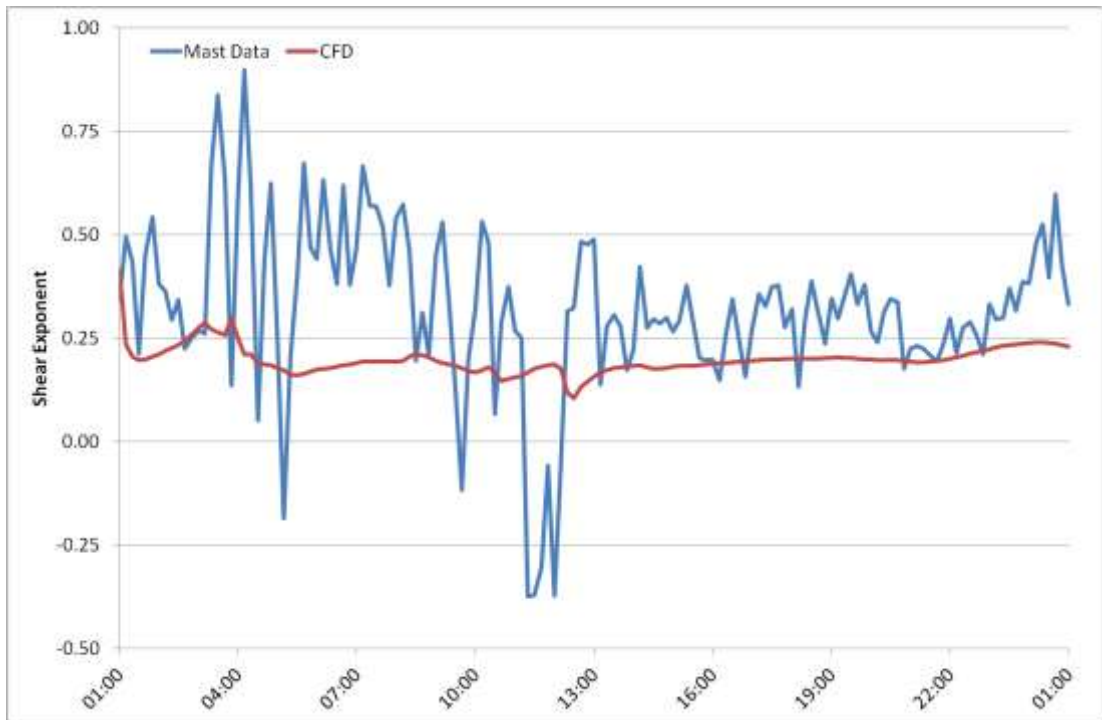


Figure 7P.10: Shear exponent time-series for 20th February 2011 at M6282, taken between 73m and 50m AGL. Comparison between measured data and CFD.

APPENDIX 7Q - TIME-SERIES COMPARISONS FOR 6 APRIL 2012



Figure 7Q.1: Wind speed time-series for 6th April 2012 at M6261, 87m AGL. Comparison between measured data and CFD.

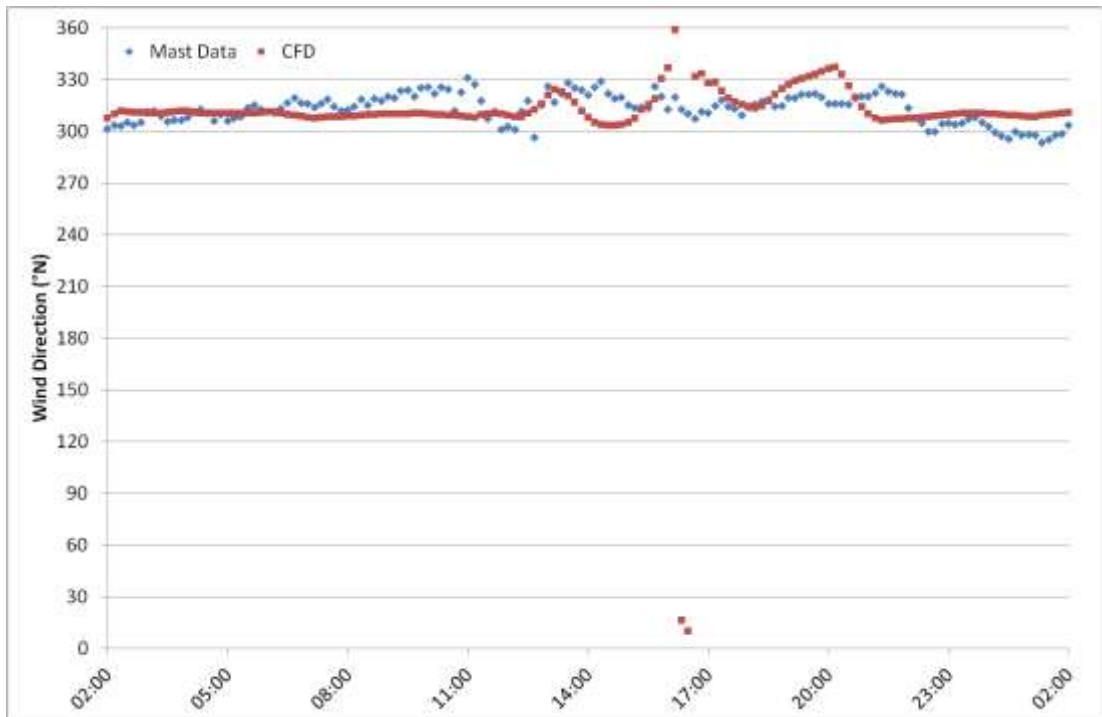


Figure 7Q.2: Wind direction time-series for 6th April 2012 at M6261, 85m AGL. Comparison between measured data and CFD.

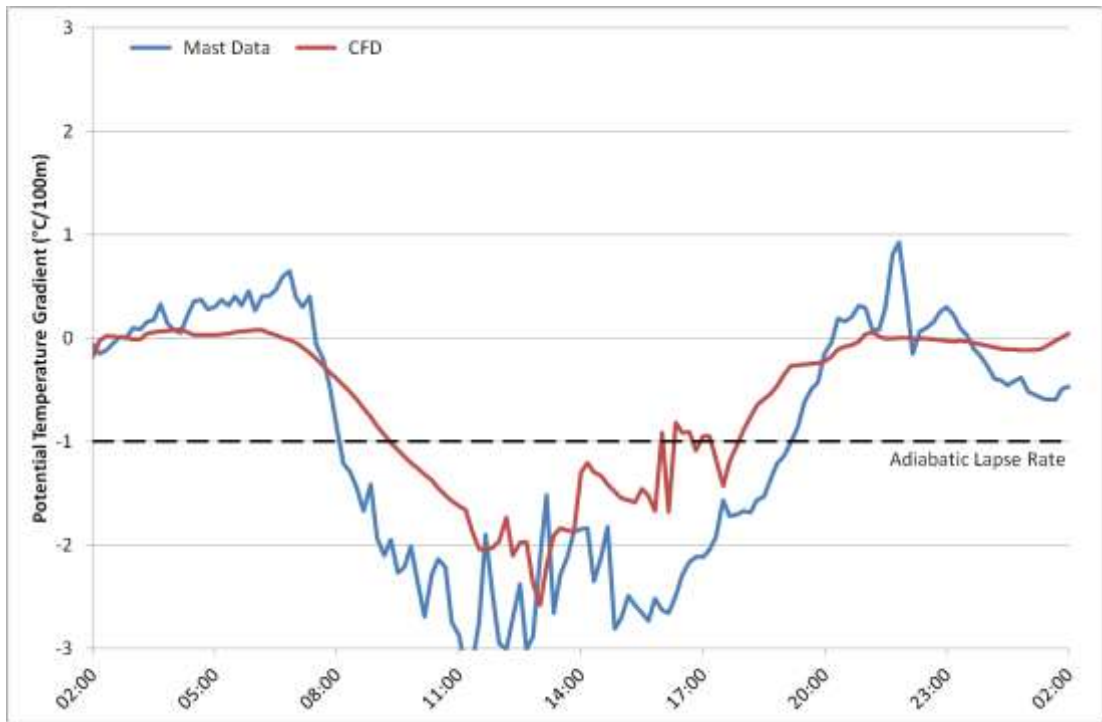


Figure 7Q.3: Potential temperature gradient time-series for 6th April 2011 at M6261, taken between 90m and 10m AGL. Comparison between measured data and CFD.

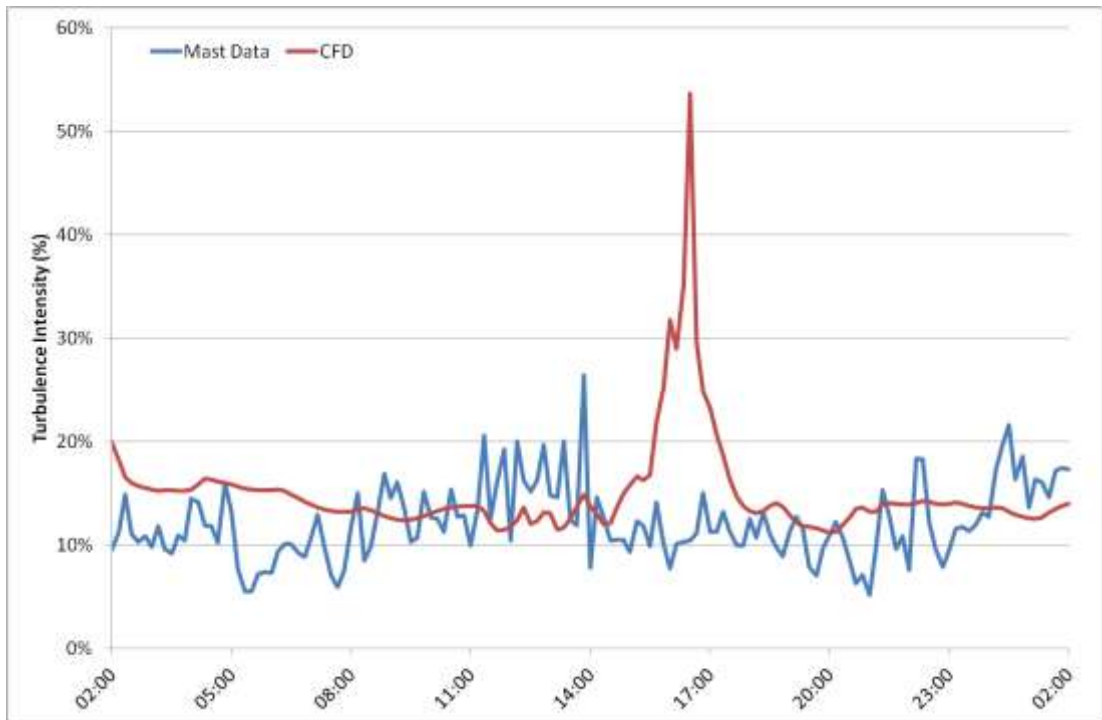


Figure 7Q.4: Turbulence intensity time-series for 6th April 2012 at M6261, 87m AGL. Comparison between measured data and CFD.

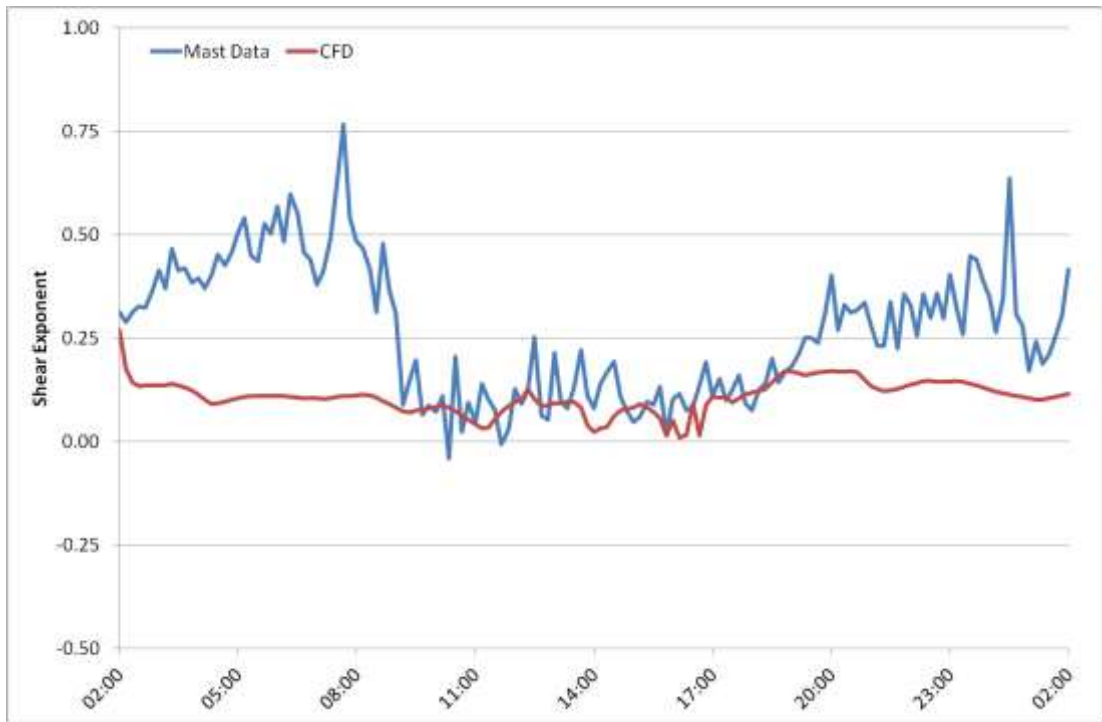


Figure 7Q.5: Shear exponent time-series for 6th April 2011 at M6261, taken between 73m and 50m AGL. Comparison between measured data and CFD.



Figure 7Q.6: Wind speed time-series for 6th April 2012 at M6282, 87m AGL. Comparison between measured data and CFD.

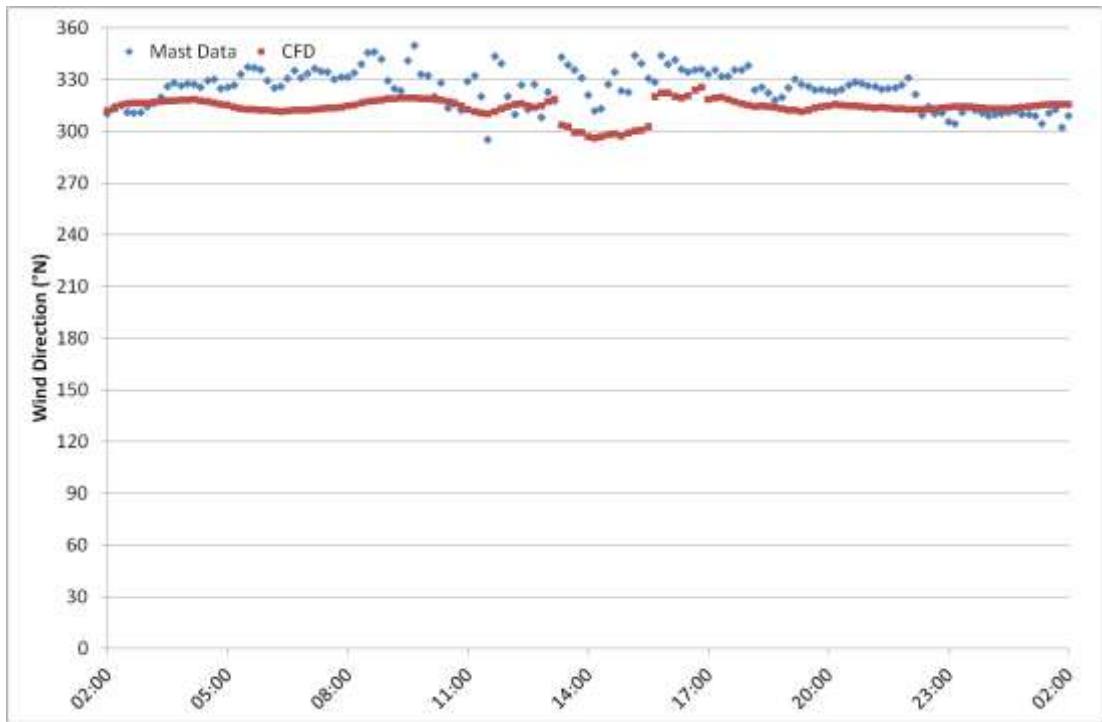


Figure 7Q.7: Wind direction time-series for 6th April 2012 at M6282, 85m AGL. Comparison between measured data and CFD.

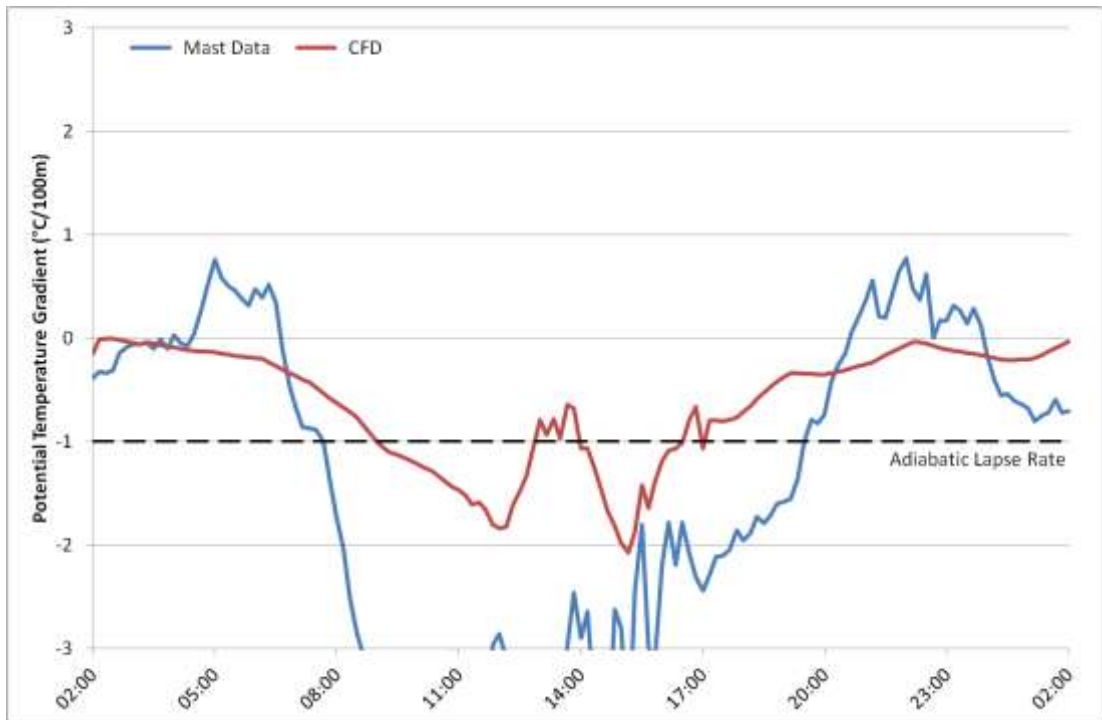


Figure 7Q.8: Potential temperature gradient time-series for 6th April 2011 at M6282, taken between 90m and 10m AGL. Comparison between measured data and CFD.

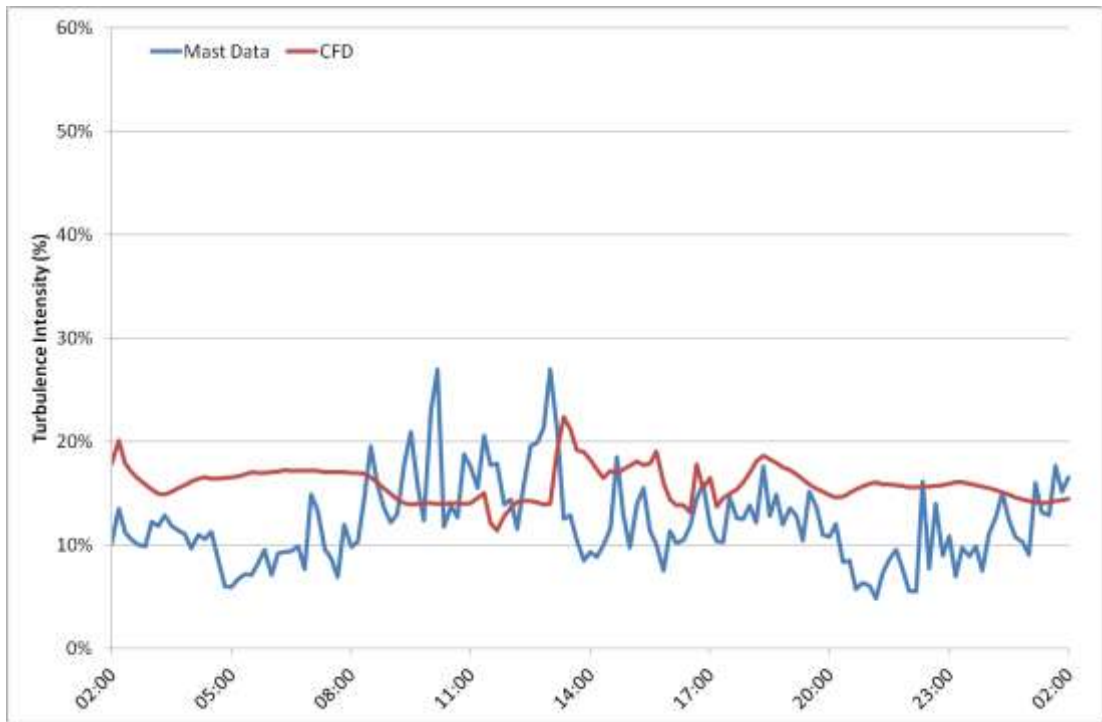


Figure 7Q.9: Turbulence intensity time-series for 6th April 2012 at M6282, 87m AGL. Comparison between measured data and CFD.

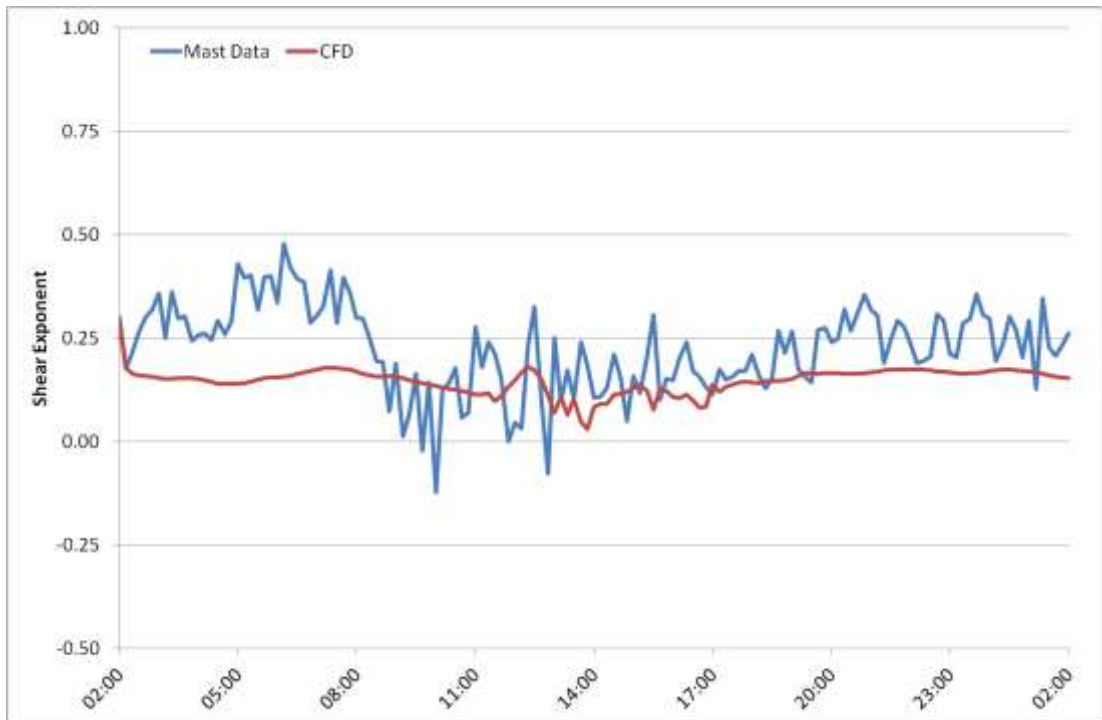


Figure 7Q.10: Shear exponent time-series for 6th April 2011 at M6282, taken between 73m and 50m AGL. Comparison between measured data and CFD.

APPENDIX 7R - TIME-SERIES COMPARISONS FOR 19 APRIL 2012



Figure 7R.1: Wind speed time-series for 19th April 2012 at M6261, 87m AGL. Comparison between measured data and CFD.

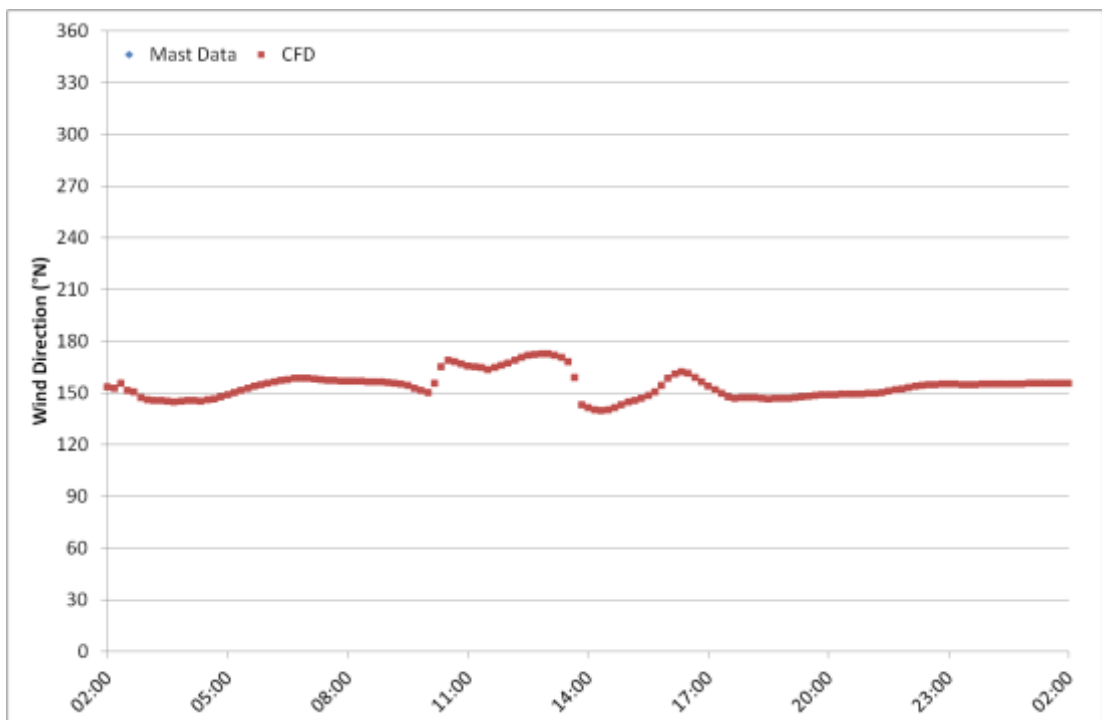


Figure 7R.2: Wind direction time-series for 19th April 2012 at M6261, 85m AGL. CFD only, no measured data available for comparison.

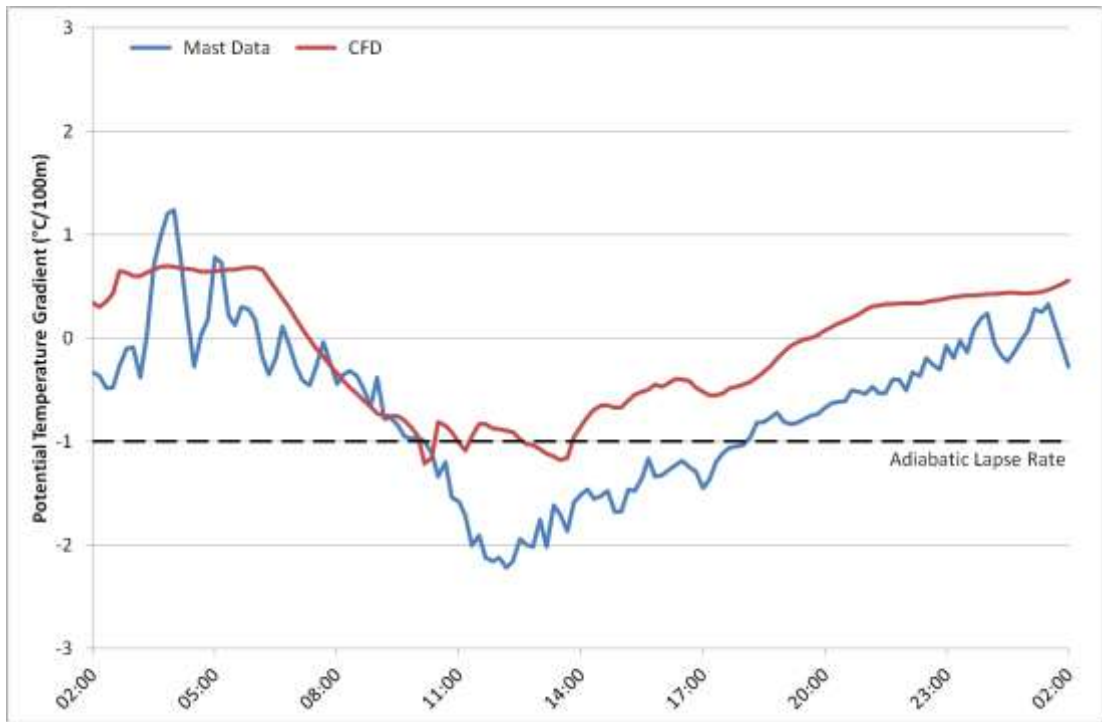


Figure 7R.3: Potential temperature gradient time-series for 19th April 2011 at M6261, taken between 90m and 10m AGL. Comparison between measured data and CFD.

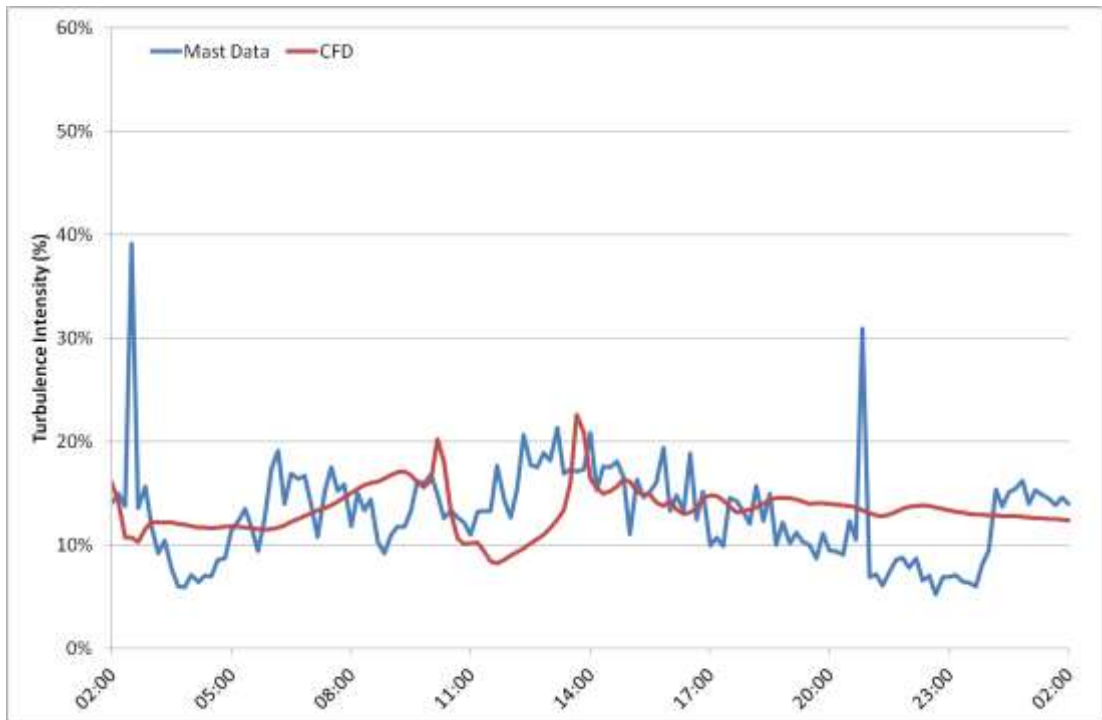


Figure 7R.4: Turbulence intensity time-series for 19th April 2012 at M6261, 87m AGL. Comparison between measured data and CFD.

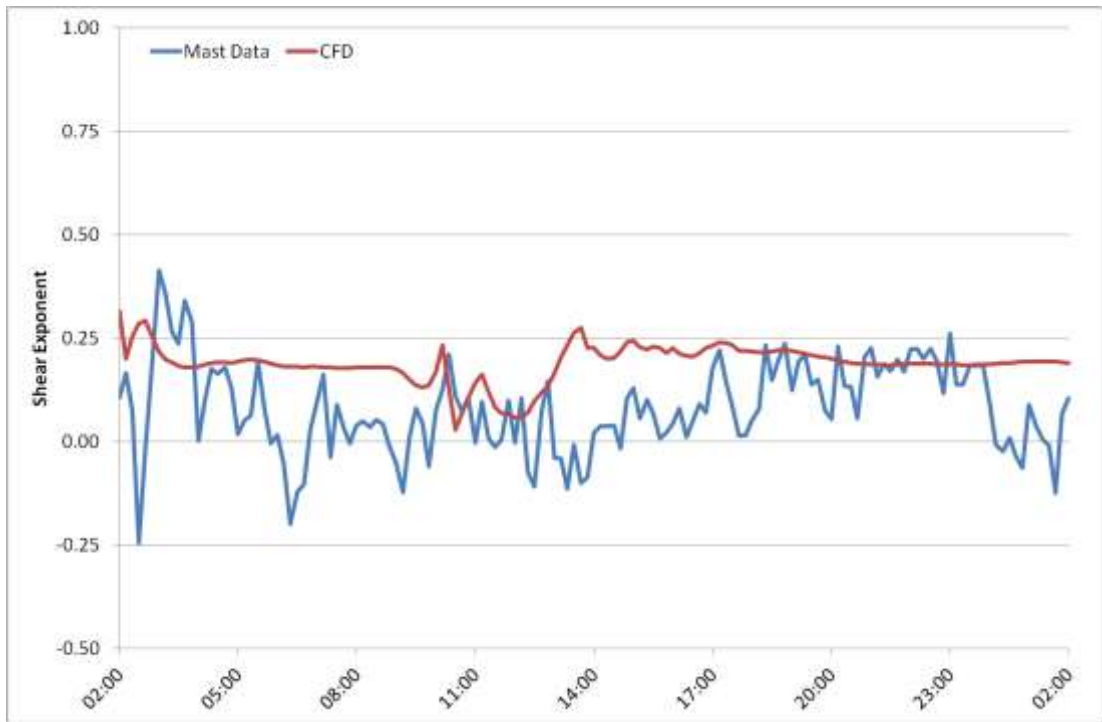


Figure 7R.5: Shear exponent time-series for 19th April 2011 at M6261, taken between 73m and 50m AGL. Comparison between measured data and CFD.

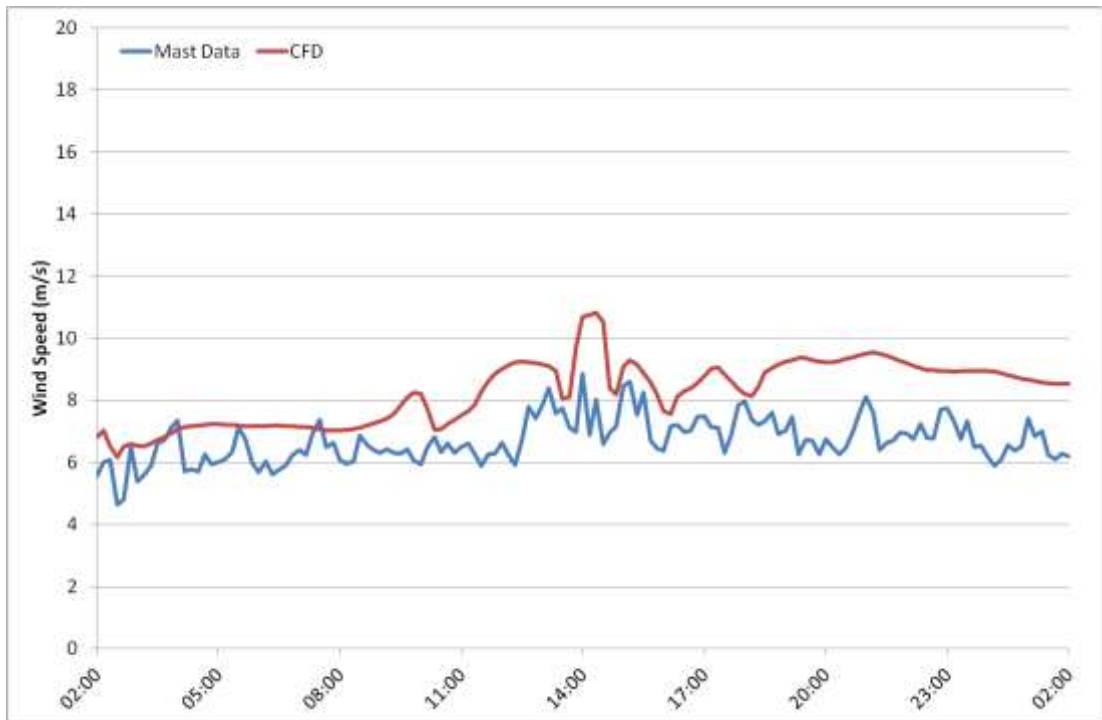


Figure 7R.6: Wind speed time-series for 19th April 2012 at M6282, 87m AGL. Comparison between measured data and CFD.

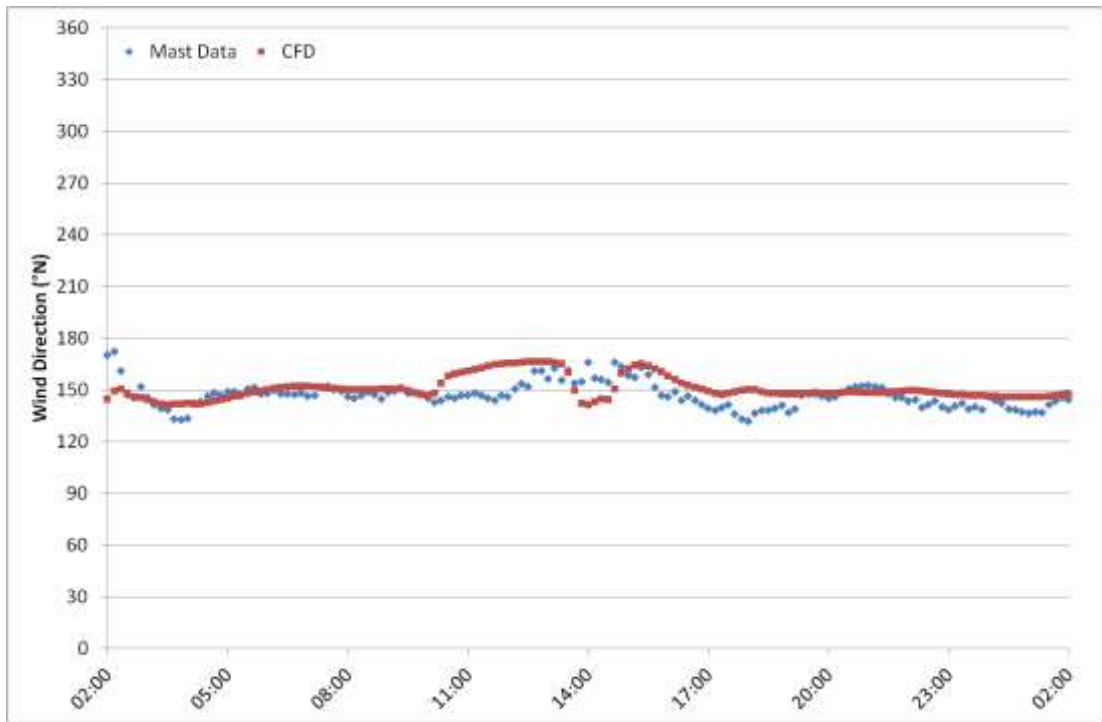


Figure 7R.7: Wind direction time-series for 19th April 2012 at M6282, 85m AGL. Comparison between measured data and CFD.

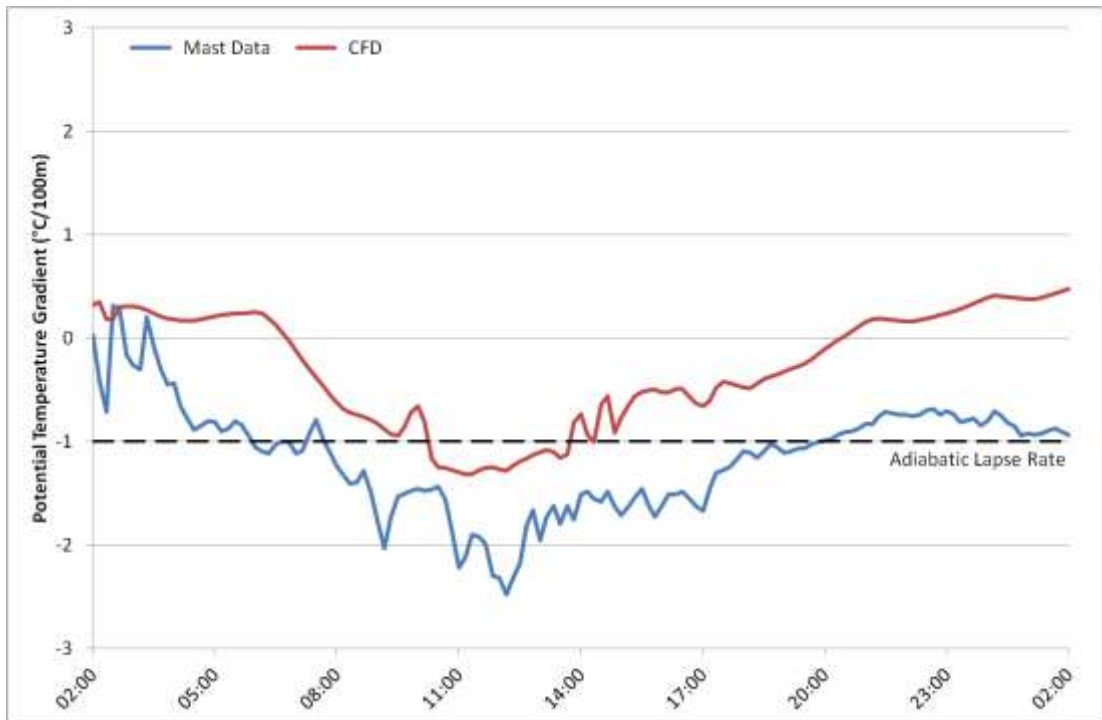


Figure 7R.8: Potential temperature gradient time-series for 19th April 2011 at M6282, taken between 90m and 10m AGL. Comparison between measured data and CFD.

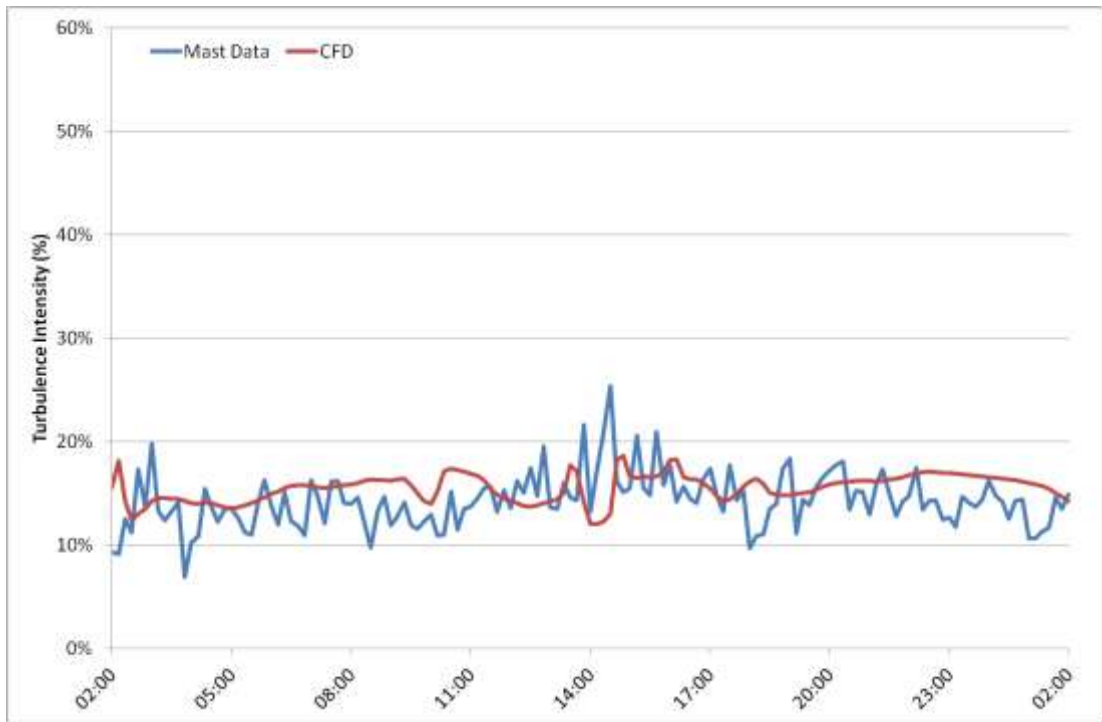


Figure 7R.9: Turbulence intensity time-series for 19th April 2012 at M6282, 87m AGL. Comparison between measured data and CFD.

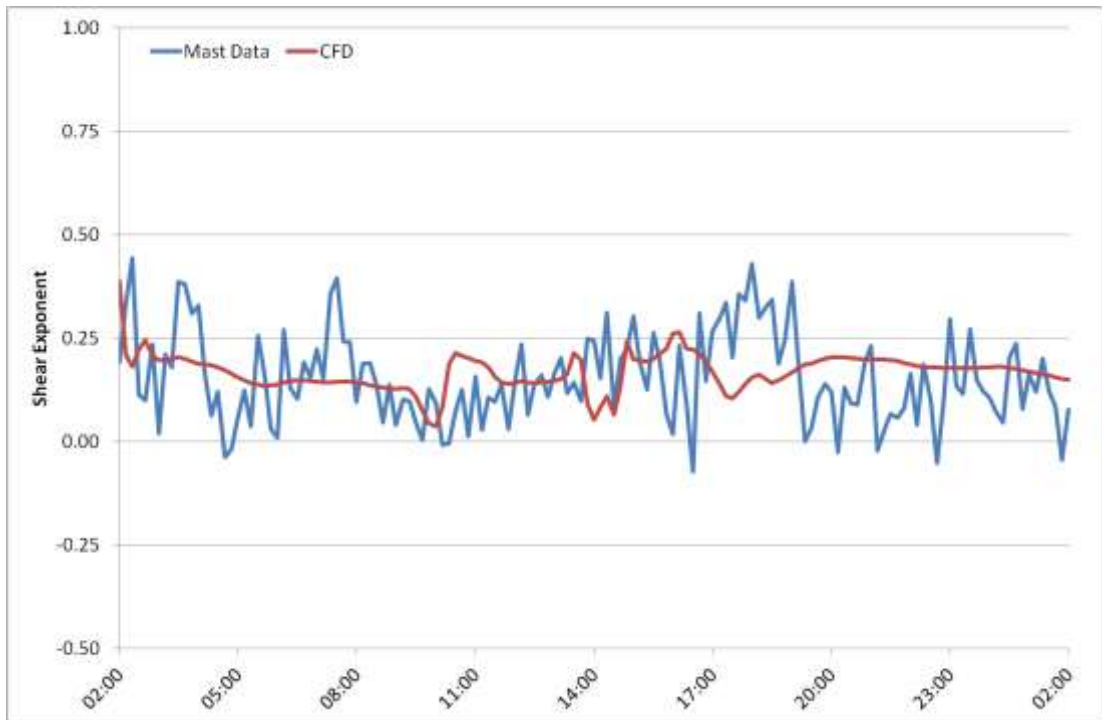


Figure 7R.10: Shear exponent time-series for 19th April 2011 at M6282, taken between 73m and 50m AGL. Comparison between measured data and CFD.

APPENDIX 7S - TIME-SERIES COMPARISONS FOR 16 MAY 2012



Figure 7S.1: Wind speed time-series for 16th May 2012 at M6261, 87m AGL. Comparison between measured data and CFD.



Figure 7S.2: Wind direction time-series for 16th May 2012 at M6261, 85m AGL. Comparison between measured data and CFD.

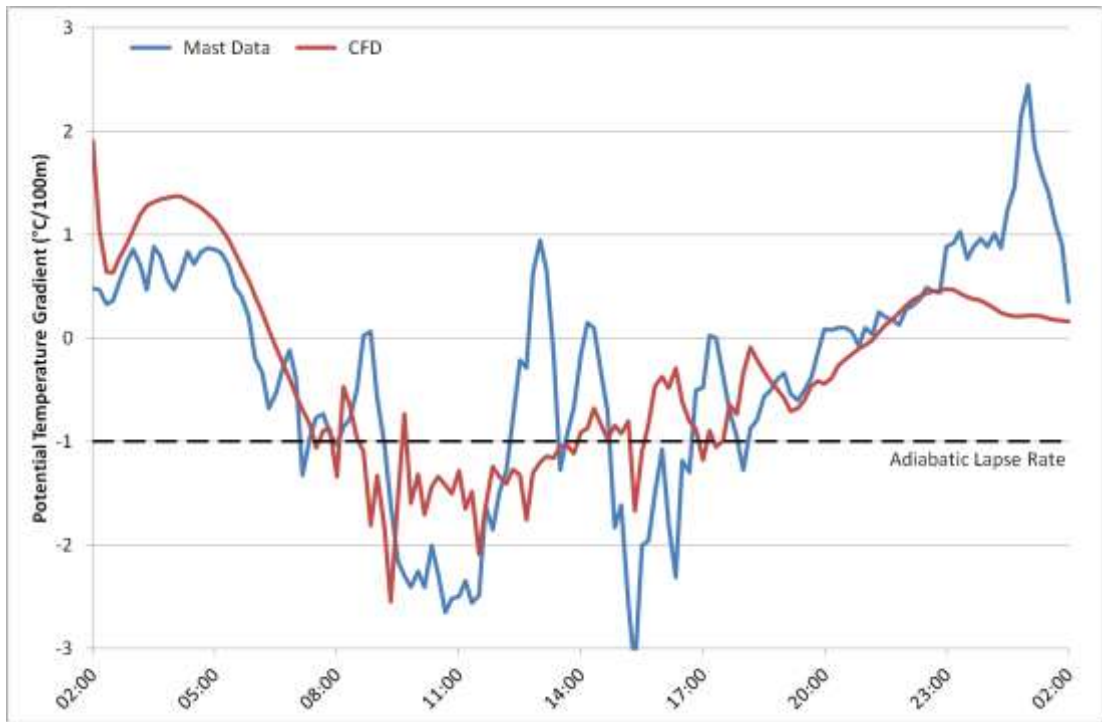


Figure 7S.3: Potential temperature gradient time-series for 16th May 2011 at M6261, taken between 90m and 10m AGL. Comparison between measured data and CFD.

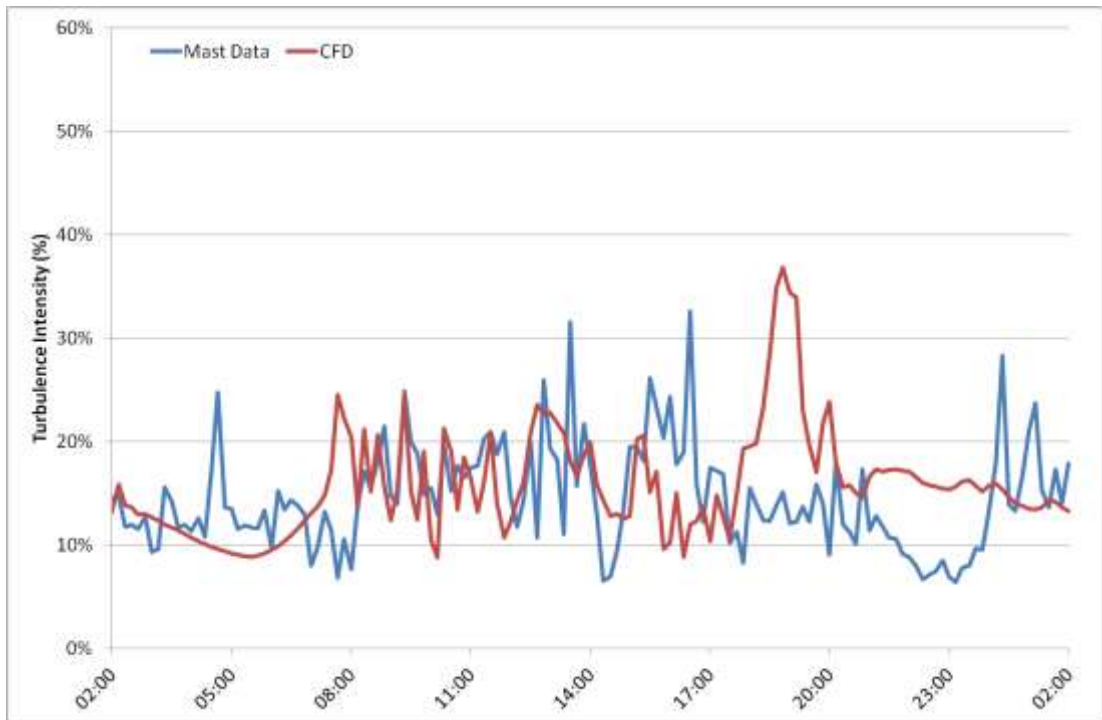


Figure 7S.4: Turbulence intensity time-series for 16th May 2012 at M6261, 87m AGL. Comparison between measured data and CFD.

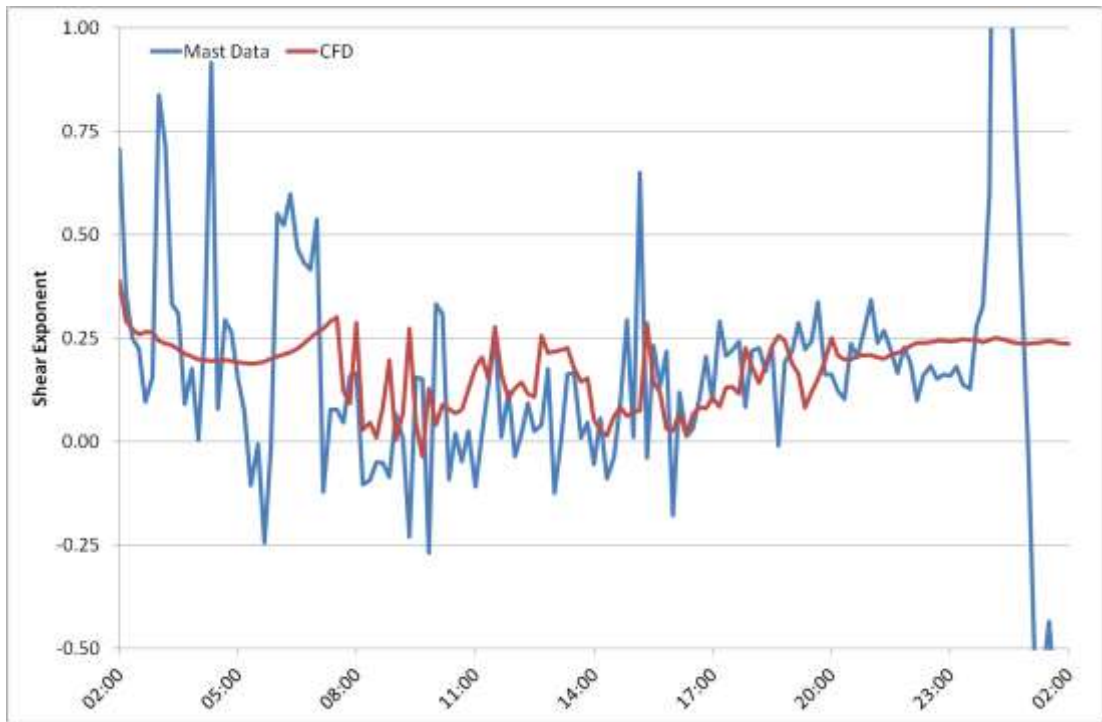


Figure 7S.5: Shear exponent time-series for 16th May 2011 at M6261, taken between 73m and 50m AGL. Comparison between measured data and CFD.

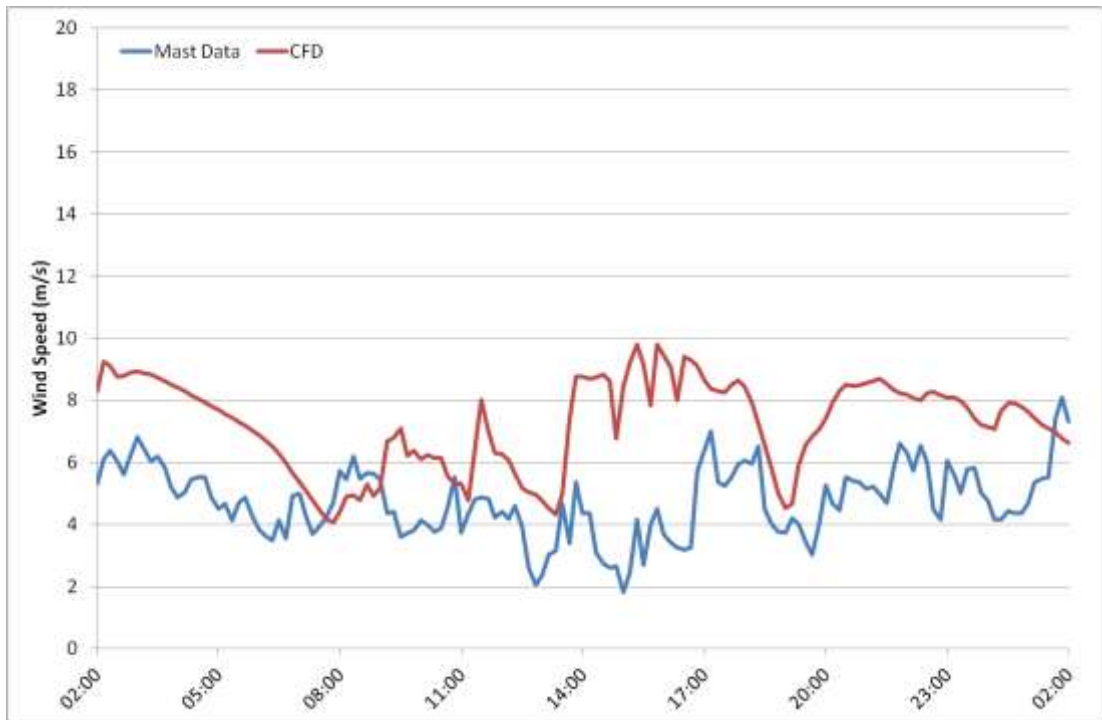


Figure 7S.6: Wind speed time-series for 16th May 2012 at M6282, 87m AGL. Comparison between measured data and CFD.

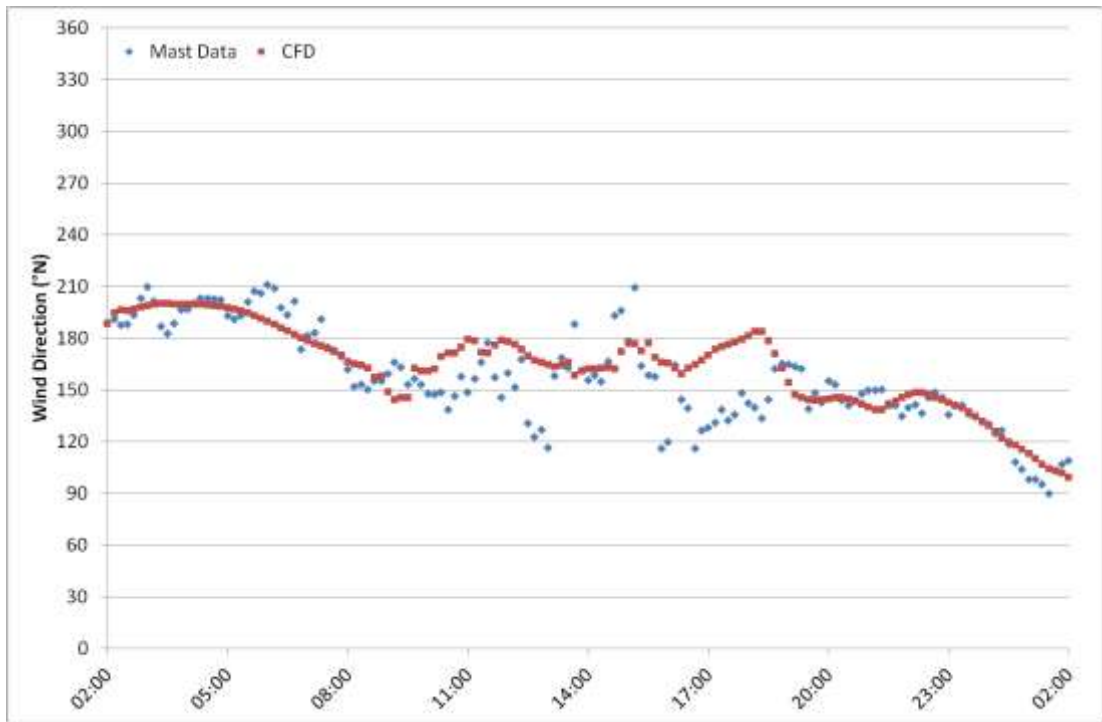


Figure 7S.7: Wind direction time-series for 16th May 2012 at M6282, 85m AGL. Comparison between measured data and CFD.

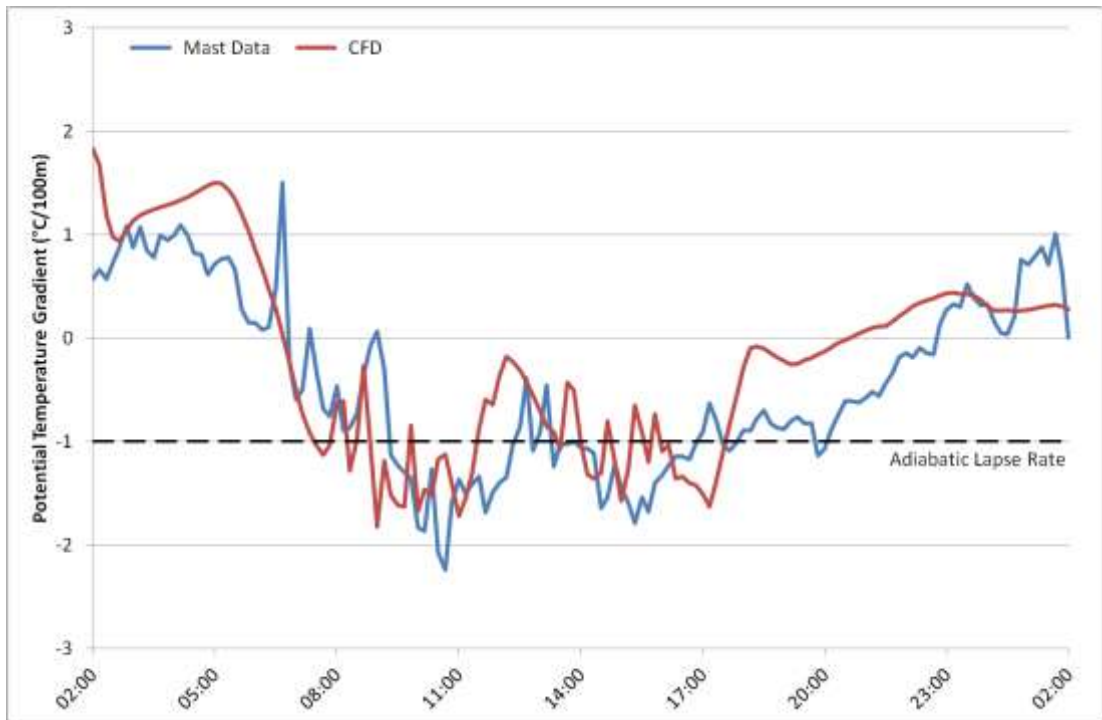


Figure 7S.8: Potential temperature gradient time-series for 16th May 2011 at M6282, taken between 90m and 10m AGL. Comparison between measured data and CFD.

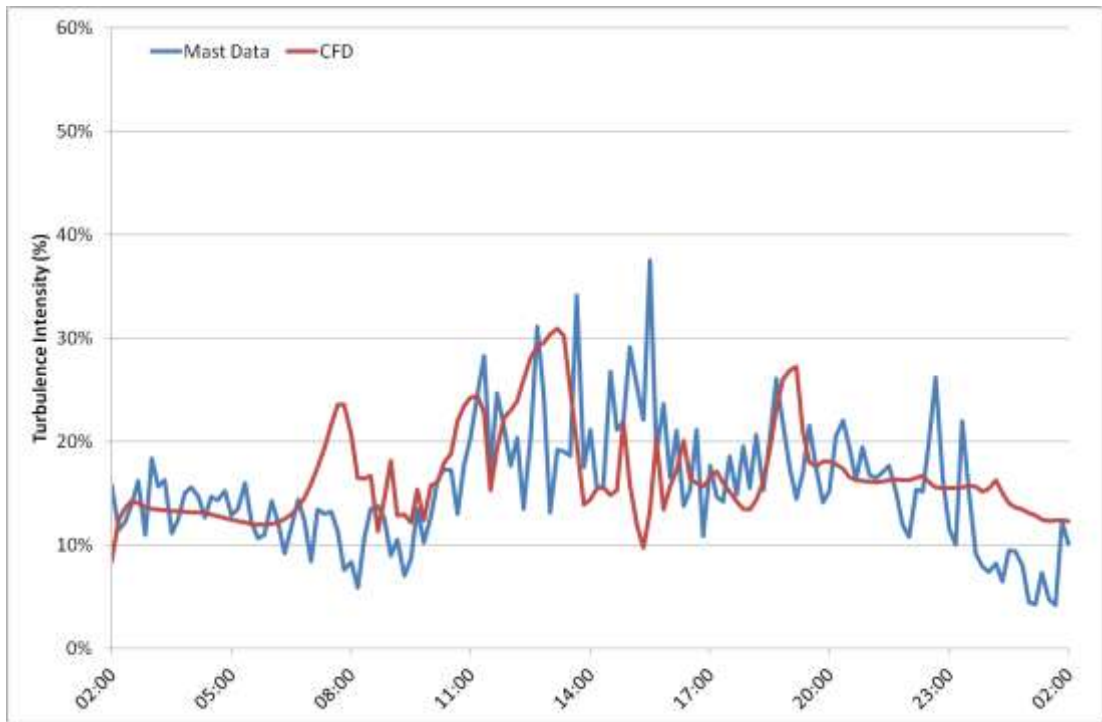


Figure 7S.9: Turbulence intensity time-series for 16th May 2012 at M6282, 87m AGL. Comparison between measured data and CFD.

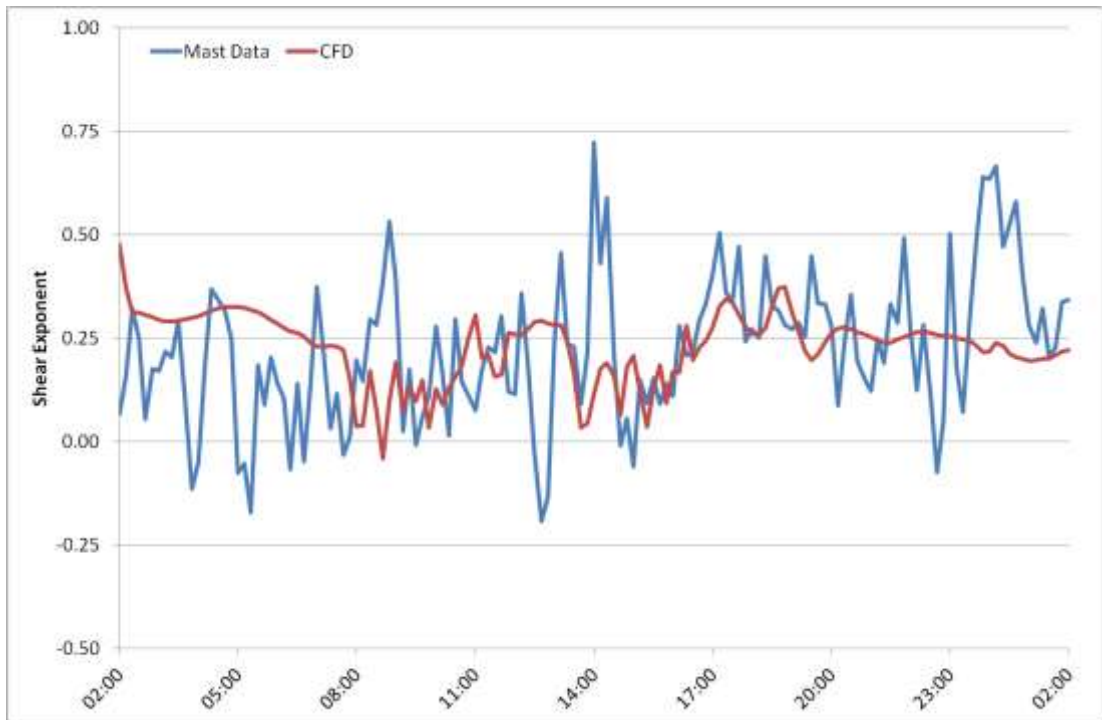


Figure 7S.10: Shear exponent time-series for 16th May 2011 at M6282, taken between 73m and 50m AGL. Comparison between measured data and CFD.

APPENDIX 7T - TIME-SERIES COMPARISONS FOR 27 MAY 2012

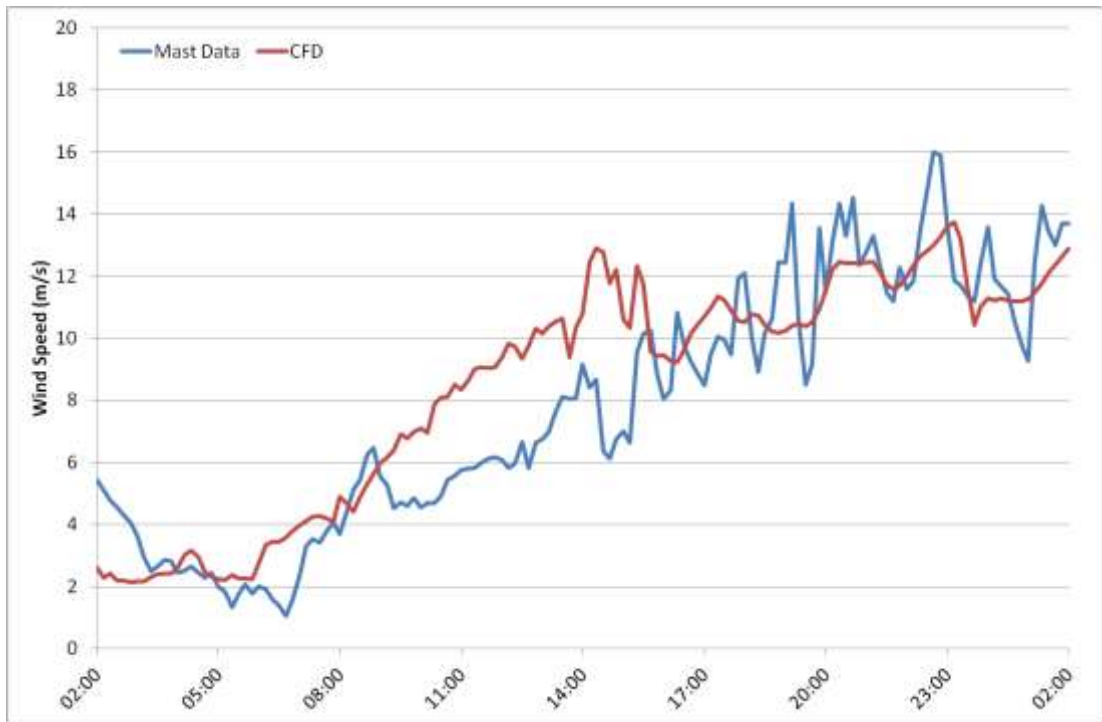


Figure 7T.1: Wind speed time-series for 27th May 2012 at M6261, 87m AGL. Comparison between measured data and CFD.

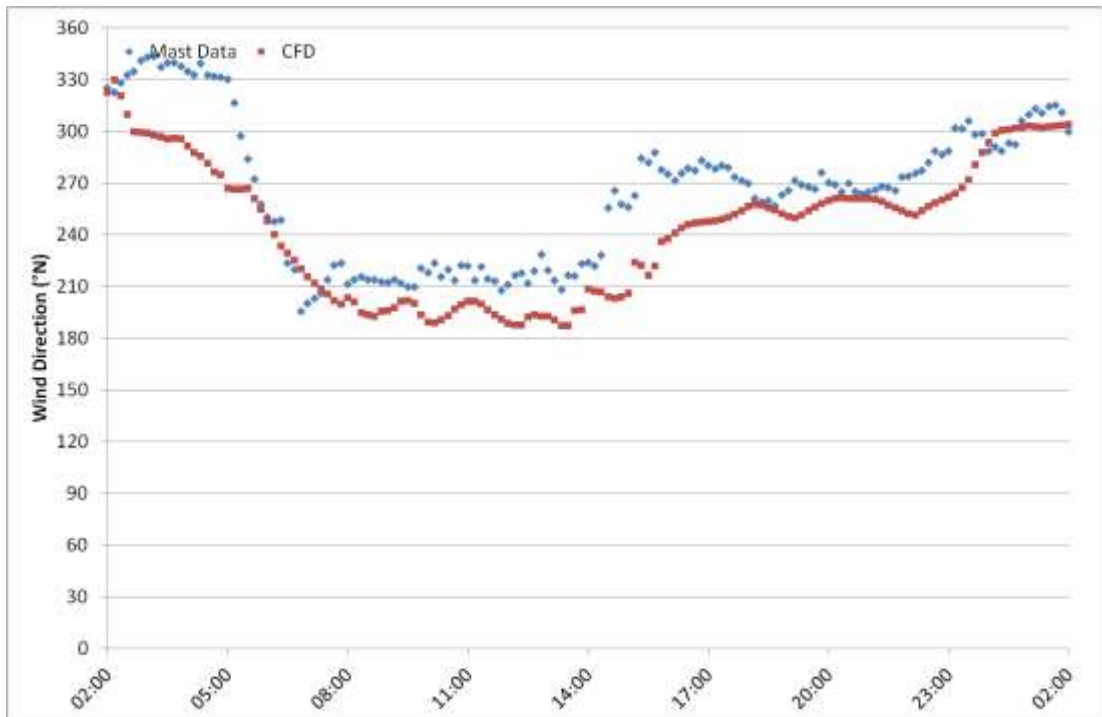


Figure 7T.2: Wind direction time-series for 27th May 2012 at M6261, 85m AGL. Comparison between measured data and CFD.

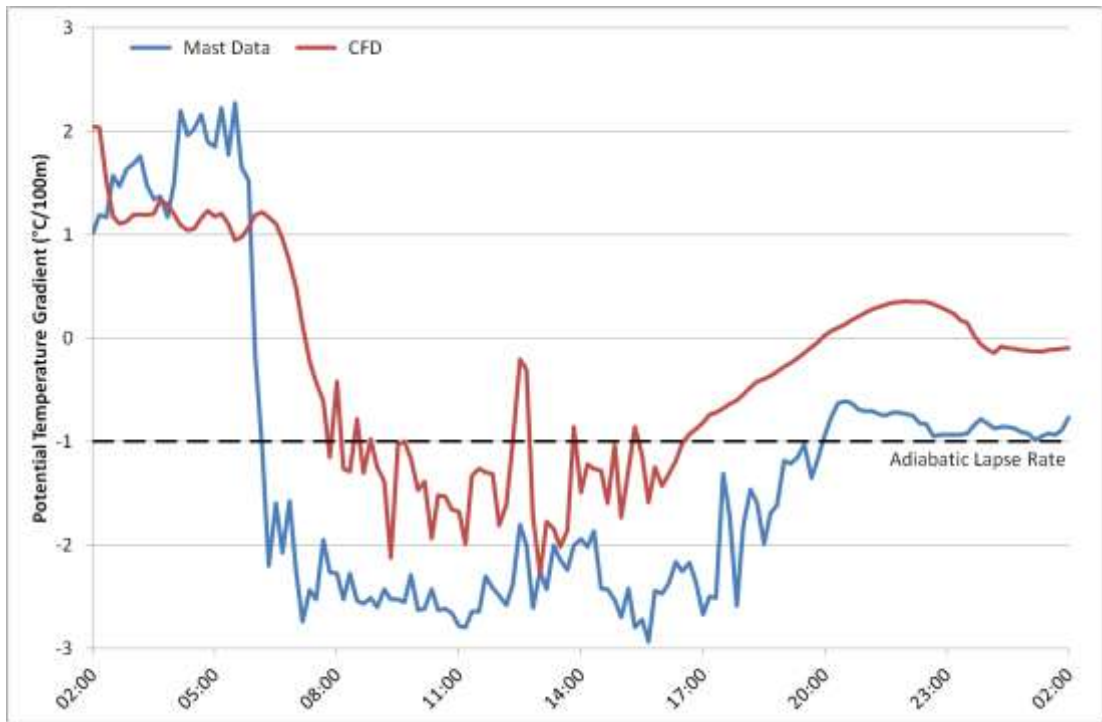


Figure 7T.3: Potential temperature gradient time-series for 27th May 2011 at M6261, taken between 90m and 10m AGL. Comparison between measured data and CFD.

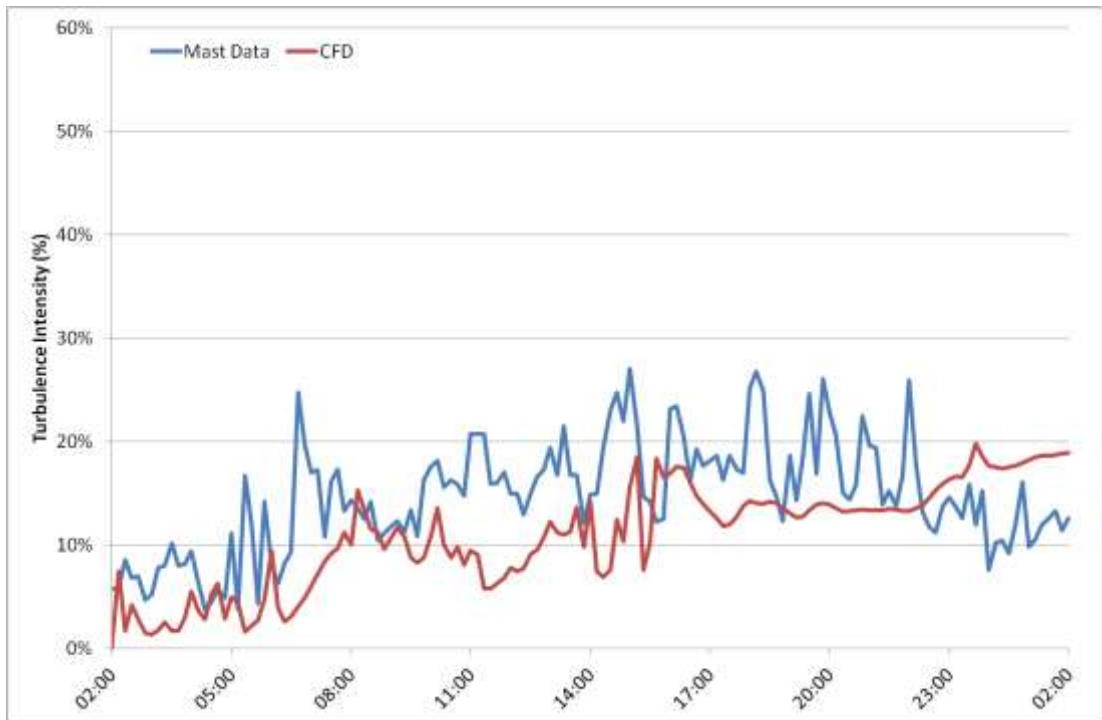


Figure 7T.4: Turbulence intensity time-series for 27th May 2012 at M6261, 87m AGL. Comparison between measured data and CFD.



Figure 7T.5: Shear exponent time-series for 27th May 2011 at M6261, taken between 73m and 50m AGL. Comparison between measured data and CFD.



Figure 7T.6: Wind speed time-series for 27th May 2012 at M6282, 87m AGL. Comparison between measured data and CFD.



Figure 7T.7: Wind direction time-series for 27th May 2012 at M6282, 85m AGL. Comparison between measured data and CFD.

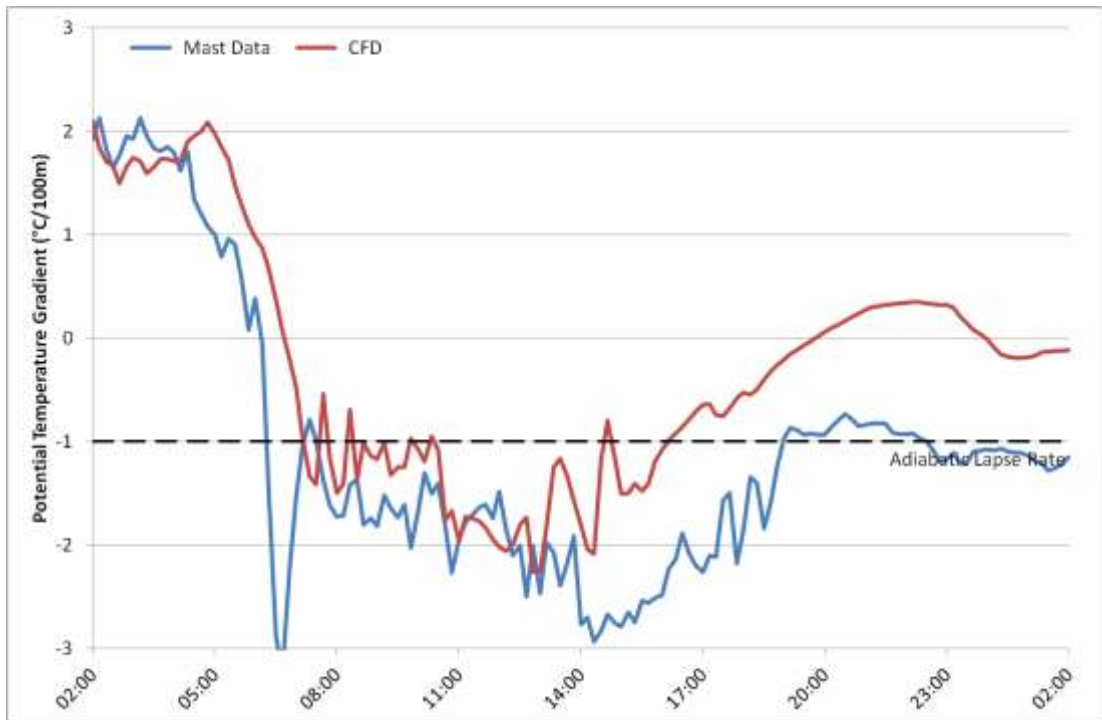


Figure 7T.8: Potential temperature gradient time-series for 27th May 2011 at M6282, taken between 90m and 10m AGL. Comparison between measured data and CFD.

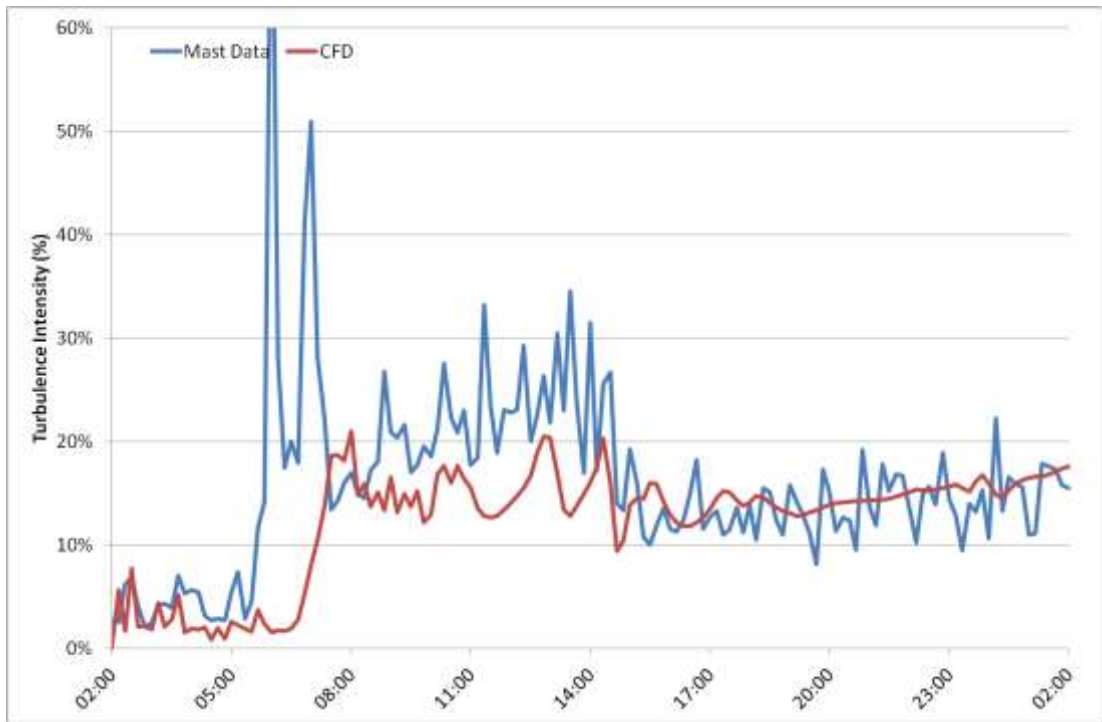


Figure 7T.9: Turbulence intensity time-series for 27th May 2012 at M6282, 87m AGL. Comparison between measured data and CFD.



Figure 7T.10: Shear exponent time-series for 27th May 2011 at M6282, taken between 73m and 50m AGL. Comparison between measured data and CFD.



Thanks to the Swedish Energy Agency, Energimyndigheten, for the funding of this project and to the NV Nordisk Vindkraft AB and Havnäs Vindkraft AB boards for entrusting the work to their technical colleagues in RES Group.

Project Team/Authors:

Alan Derrick, Nicola Atkinson, Iain Campbell, Alex Clerc, Jennifer Cronin, Alan Derrick, Alice Ely, Simon Feeney, Gail Hutton, Marine Lannic, Malcolm MacDonald, Alastair Oram.

Acknowledgments:

Magnus Andersson, Jeremy Bass, Paul Berrie, Richie Cotton, Cody Cox, Victor Donnet, Alan Duckworth, Jonny Flowers, Euan George, Magnus Hopstadius, Loïs Legendre, Lenton McLendon, David Noble, Christer Norlén, Lars Persson, Stephen Peters, Peter Stuart, Min Zhu.

Pilot sponsor: Energimyndigheten